Theoretical and experimental study of the reaction mechanism of several lipoxygenases and hydrolases: governing their product pattern by mutagenesis

Miquel Canyelles Niño

UAB
Universitat Autònoma
de Barcelona

Theoretical and experimental study of the reaction mechanism of several lipoxygenases and hydrolases: governing their product pattern by mutagenesis

Miquel Canyelles Niño

PhD programme in Chemistry

Directors:
Àngels Conzález Lafont
José Maria Lluch López

Department of Chemistry, Faculty of Science

2023

Volume I

Contents

Part I

Introduction

Chapter 1

Introduction

The present PhD Thesis lives in the boundary between chemistry and biology, more accurately, between computational chemistry and molecular biology. Thus, this Thesis will explore biochemical problems from different points of view, giving a complete study of the problem.

During this Thesis a wide variety of Lipoxygenases (LOXs), a family of enzymes, will be studied. The goal is to study the versatility of these enzymes. LOXs are biologically relevant enzymes because they participate in inflammation processes. This role makes them key for the proper function of the immune system. Moreover, LOXs are also used in the industry. Several properties of different LOXs and other enzymes involved in pro-inflammatory and inflammatory resolution will be studied. Moreover, an industrial application of LOXs for the synthesis of Maresin-1 (MaR1) will be explored, both from the computational and experimental points of

view.

With all these studies, the goal of this Thesis is to explore the great versatility of different isoforms of the LOX family. Several isoforms will be studied, focusing on different perspectives such as the chemical mechanism, the regioselectivity, the catalytic properties, the allosteric mechanisms or the interaction with other proteins and biostructures.

1.1 Biological overview of enzymes and substrates

Living organisms have one or more cells. Cells contain a wide variety of chemical entities, among which macromolecules such as proteins or lipid bilayers and organic compounds such as sugars or hormones are two of the most interesting.

In multicellular organisms, there are different kinds of cells with specific roles and functions. Hence, each kind of cell is able to produce different types of enzymes and works with particular organic compounds depending on their genotype and phenotype. These enzymes, defined as biological macromolecules, are able to catalyse chemical reactions[1] that are fundamental for life such as the cleavage of polypeptidic chains or chemical transformations of small molecules with a high level of specificity.

Because multicellular organisms are composed of a large number of cells that constitute a single organism, cells in multicellular systems have to communicate between them. In order to do so, there is biosignalling. It consists on the emission and reception –so the biosynthesis and interaction with– of chemical or physical signals that induce changes in the cellular function, composition and other features[2]. These chemical signals can be endogenous, made up by the organism, or exogenous, introduced into the body from an external source. Inflammation, including its resolution, is

one of the processes driven by biosignals.

1.1.1 Enzymes

Enzymes are biomacromolecules built of aminoacids with a very complex structure and composition which have catalytic properties. Each type of enzyme, thanks to its aminoacidic sequence and three-dimensional structure –which is actually governed by the aminoacidic sequence–, is able to catalyse a given chemical reaction. More than 5000 different enzymes are known today[3]. Consequently, enzymes are present in almost all the biological pathways of any living organism, so they are the key to life.

Even though enzymes are made up only by combining 20 different aminoacids, their function, composition, and structure can be very distinct. Because of these varieties, enzymes have been classified into seven different categories by their chemical reactivity, that is by their catalytic activity[4]. A subfamily of oxidoreductases, the lipoxygenases, and a subfamily of hydrolases, the epoxide hydrolases, will be studied in this Thesis.

1.1.2 Substrates

A substrate is a small chemical compound –at least compared to the size of an enzyme– that can be fitted inside an enzyme in such a way that a reaction can be catalysed over it. In living organisms, substrates have some level of biological relevance, like sugars or lipids.

1.2 Inflammation and its resolution

Inflammation is a biological process that begins with the presence of some kind of stimuli such as infection or injury in a certain tissue that disturbs the cellular homeostasis. The typical physical symptomatology is the ap-

pearance of redness, swelling, heat, and/or pain in the affected region. These symptoms appear in the initial stage –the on-set– of inflammation.[5]

Biologically, inflammation is a very complex process that involves the action of the immune system and the production of a wide variety of pro-inflammatory and pro-resolving mediators from different families of biological and chemical agents, such as cytokines[5]. In this section, Polyunsaturated Fatty Acid (PUFA)-related inflammatory processes will be specifically reviewed.

1.2.1 The immune system and its relationship to inflammation

Living organisms have the immune system, whose function is to protect the organism from diseases and infections[6]. This immune system is very intricate –the higher the organism, the more complex the system is– and involves several kinds of cells, each one with a specific function. In animals, this immune system is mainly built by white blood cells, a family of different cells with immune functions.

As said, one of the most important roles of the immune system is to fight against infections[6]. To do so, there are two immune subsystems: the innate and the adaptive[6]. The first one is not specific to the infecting agent, while the latter acts in a specific way against an agent that has infected previously, so the immune system has learnt how to fight it[5].

The innate immune system is composed of different types of cells, being neutrophils and macrophages two of the most important. Both of them share their principal function: the phagocytosis –that is the ability to ingest and eliminate pathogens and cell debries–[6].

Once there is an infection of a tissue, fluid is accumulated in the affected tissue causing swelling at the region. After that, Polymorphonuclear Neutrophils (PMNs) are the first immune cells to accumulate in the in-

fected tissue. They constitute the major part of the white blood cells. They are the first agents to fight against the exogenous agent by phagocyting it. During the process, they release chemoattractant substances that are able to attract other cells, mainly Macrophages[7].

Macrophages (Mϕs), 'large eaters', are the second type of immune cells that act against infectious agents. As said, they appear after the PMNs thanks to their release of chemoattractants. They are a very interesting type of cells because they have several different phenotypes –that is the behaviour of the cell– which are activated and deactivated by the presence of determined biosignals. These biosignals are composed by different families of biochemical compounds such as cytokines and, more interestingly for the present discussion, lipid mediators of inflammation, which are derivatives of PUFAs[8].

Macrophages (Mϕs) are responsible for inflammation and its resolution too. Their behaviour, as introduced in the previous lines, depends on the active phenotype. Biochemical mediators released by PMNs, as well as by some of the exogenous infecting agents, are mainly Prostaglandins (PGs) and Leukotrienes (LTs), which activate the phenotype 1 of Mϕs[9]. Mϕ 1s fight the infection and cause, as a secondary effect, the inflammation of the tissue. They also have the ability to clean the region of dead PMNs. During its action, Mϕ 1s release small amounts of Specialised Pro-resolving Mediators (SPMs) and other pro-resolving signals that start to accumulate. Once there are enough amounts of these compounds, the phenotype of Mϕs changes from 1 to 2. This change provokes Mϕs to become agents of resolution of the inflammation instead of inflammatory agents[9].

In general terms, Mϕs 1 are associated to pro-inflammatory processes because of their ability to produce pro-inflammatory cytokines, to promote insulin resistance, so no nutrients are stored in the infected tissue thus leading to the death of the infectious agent due to lack of nutrition, and

to produce NO and other reactive oxygen intermediates that are able to phagocyte microbes, bacteria and viruses. At this stage, Mϕs are working on resolving the infection, causing inflammation as a consequence [10].

Figure 1.1 shows, as a summary, the evolution of infection or injury. When a tissue is infected, an edema is formed. Then, PMNs start to accumulate in the infected region and start to release chemoattractants. These chemoattractants then attract other immune cells, Mϕs in this case. The same chemical compounds activate the phenotype 1 of Mϕs, and more biosignalling compounds are released, as well as more infectious agents are removed. After a certain time, Mϕ's phenotype migrates to 2. This makes the process of the resolution of inflammation to start. The whole process ends in the diffusion of Mϕs and the recovery of homeostasis [11;12].

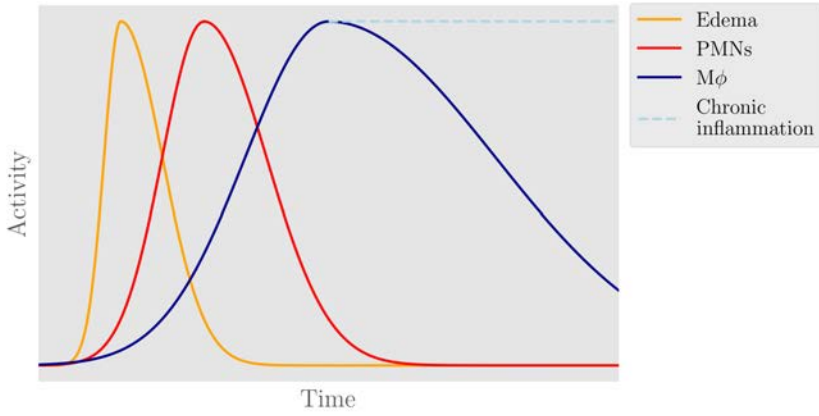

Figure 1.1: Normal evolution of immune system's response after an infection. The evolution of the edema is drawn in yellow, the evolution of the PMNs is plotted in red, the evolution of macrophages is plotted in blue, and the chronic inflammation is indicated as a dashed, light blue line. Adaptation from Serhan et al. [12].

1.2.2 Inflammation from the PUFA's point of view

As reviewed, inflammation is the consequence of the action carried out by PMNs and Mϕs. It is a very sensitive process that typically consists of two stages: inflammation and its resolution. These processes are controlled by the exchange of biosignalling compounds[8].

1.2.2.1 First step: pro-inflammation stage

Once the inflammation process starts and Mϕs get accumulated by the action of PMNs, a big cascade of PUFA derivatives starts. There are two main families of pro-inflammatory signalling molecules derived from Arachidonic Acid (AA): Prostaglandins (PGs) and Leukotrienes (LTs). PGs are synthesised by Cyclooxygenase (COX)-1 and COX-2, while LTs start from the oxidation of AA at the 5^{th} carbon, thus obtaining to 5S-hydroperoxyeicosatetraenoic (5SHpETE) acid, which finally leads to 5S,6S-epoxy-AA, better known as Leukotriene A_4 (LTA_4), the initial compound from which the other LTs are synthesised. Both reactions are carried out by human ALOX5 (*hum*ALOX5), activated by Five-Lipoxigenase-Activating Protein (FLAP) and other cofactors, such as Ca^{2+} and adenosine triphosphate (ATP)[8;13].

Mϕs 1 are specific to the pro-inflammatory stage because of their enzymatic expression profile. They express Lipoxygenase (ALOX)5, FLAP, COX2 and Leukotriene A_4 Hydrolase (LTA_4H) in high amounts, while ALOX15 is expressed in low amounts. All the enzymes that are expressed in high quantities are responsible for the synthesis of pro-inflammatory molecules from the LT and PG families[14].

At this point of the process, if an anti-inflammatory drug –such as Aspirin– is administrated, anti-inflammatory mediators –Lipoxins (LXs), Resolvin (Rv) Es, and Rv Ds, which are biosynthesised by Aspirin-triggered-

COX-2– can act by pushing back the inflammation initiated by LTs and PGs[14].

1.2.2.2 Second step: inflammation resolution

The small amounts of ALOX15 present in Mϕ 1s are able to synthesise small quantities of SPMs or their intermediates that get accumulated during few days after the initiation of the inflammation[9]. These SPMs –or their intermediates– have the ability to change the Mϕ's phenotype by converting to phenotype 2. Among other differences, this second phenotype has a different enzymatic expression profile: the expression of ALOX5 remains high, while the expression of ALOX15 and ALOX15B increases, as well as the expression of ALOX12 in some tissues like the skin, and the expression of FLAP, COX2 and LTA_4H gets decreased[14]. The presence of ALOX15s allows the synthesis of SPMs. Moreover, the disappearance of FLAP produces a change in the regioselectivity of ALOX5, so reducing its ability to synthesise LTA_4. The suppression of the expression of LTA_4H and COXs contributes to limit the presence of pro-inflammatory signalling molecules, too.

There are several different subtypes of Mϕ 2 cells that coexist in a heterogeneous population. They all have differentiated functions: some of them are able to control the pro-inflammatory signals, so the inflammation caused by Mϕ 1s, others work healing wounds, and others accumulate collagen and other agents needed for repairing tissue damage, for example[15].

1.2.2.3 When inflammation resolution does not succeed

In some cases, the inflammation resolution stage fails. When this happens, the inflammation becomes chronic. This chronic inflammation is the underlying cause of lots of diseases, which are the most important cause of

death in the world nowadays[16].

This chronic inflammation takes place when the organism is unable to synthesise SPMs, whose action is to resolve the inflammation (Figure 1.1). The lack of presence of SPMs can be related to several causes, but it opens a door: if the body is not able to generate SPMs, why not to administrate them exogenously? Several studies and patents that explore the treatment of chronic inflammatory diseases with SPMs have been published[17;17–45]. They report good perspectives on this kind of therapeutic approaches.

1.3 Polyunsaturated Fatty Acids and their derivatives

Polyunsaturated Fatty Acids (PUFAs) are a kind of fatty acids, which are long molecules containing an aliphatic tail –which is hydrophobic– and a carboxylic –which is hydrophilic– head[46]. PUFAs are a special kind of fatty acids because they contain two or more unsaturations in their aliphatic moieties.

The structure of fatty acids provides them very interesting chemical features, which makes them key compounds for living organisms. The presence of a hydrophobic tail allows these compounds to interact with non-polar molecules, such as bioactive mediators or hormones. The polar head lets them be soluble in water, even though they usually have low solubility. The presence of these two chemical entities allows fatty acids to build suprachemical structures like micelles or cellular membranes[47]. The addition of polyunsaturations to a fatty acid structure makes them suitable for chemical transformations like peroxidations, as the reactions LOXs are able to perform[48].

The two or more unsaturations that PUFAs contain have a *Z* conformation and are commonly separated by a methylene unit following what

is called a divinylmethane pattern[49].

These PUFAs are not biosynthesised at the same levels in all types of organisms: mammals are not able to synthesise most of them, but fish, algae and plants can biosynthesise significant amounts[50].

1.3.1 PUFA classifications

There are two classifications of PUFAs: one that classifies them by their length and one that classifies them by their number of unsaturations.

If the classification by length is followed, there are two groups: short-chain PUFAs, which have 18 carbons or less, and long-chain PUFAs, which contain 20 or more carbons[51].

There are four main classes of PUFAs if the classification is made by the unsaturations: omega−3 ($\omega-3$), omega−6 ($\omega-6$), omega−9 ($\omega-9$) and conjugated PUFAs[47]. $\omega-3$, $\omega-6$ and $\omega-9$ compounds have non-conjugated unsaturations –one methylene group is placed between two unsaturations– and the unsaturations start in the n^{th} –being n the 3^{rd}, 6^{th}, or 9^{th} carbon starting from the tail, respectively–, while conjugated compounds have their double bonds conjugated.

1.3.1.1 Omega-3 PUFAs

$\omega-3$ PUFAs are all those polyunsaturated fatty acids that have the first unsaturation at the third carbon starting for the methyl group in the tail.

The most relevant $\omega-3$ compounds are Eicosapentaenoic Acid (EPA) and Docosahexaenoic Acid (DHA). The oxidised derivatives of these compounds have anti-inflammatory and inflammation-resolving properties. They are called Resolvin (Rv) E, Resolvin (Rv) D, maresins, and protectins. The first step for the synthesis of these derivatives is carried out by ALOX12, ALOX15, acetylated (by Aspirin) COX2, or P450.

Maresin-1 Maresin-1 (MaR1) is a derivative of DHA. It has two chiral hydroxyl groups separated by a conjugated triene. MaR1 is a very potent inflammation-resolving compound that was detected for the first time in 2012[52]. Its biosynthesis starts by the oxidation of DHA by ALOX12 or ALOX15[53], the epoxidation of the obtained hydroperoxide and a final hydrolysis by an unidentified hydrolase.

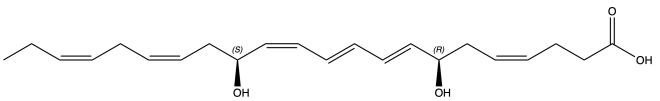

Figure 1.2: Diagram of MaR1's chemical structure

Among other functions, MaR1 has been tested to be effective against many inflammatory diseases such as multiple sclerosis[54], amyotrophic lateral sclerosis[18] or spinal cord injuries[34] among others.

Nonetheless, clinical trials have not been published yet as well as no synthesis upgradable to an industrial scale has been reported. Despite some total organic synthesis have been proposed[55–58], all of them show very low reaction yields, which make them non useful for industrial applications.

1.3.1.2 Omega-6 PUFAs

$\omega-6$ PUFAs are all those polyunsaturated fatty acids that have the first unsaturation at the sixth carbon starting from the methyl group in the tail.

The most relevant $\omega-6$ is Arachidonic Acid (AA). Leukotrienes (LTs) and Prostaglandins (PGs) are two of the most important derivatives of AA and they have pro-inflammatory properties[59]. The first step for the synthesis of these derivatives is carried out by FLAP-activated ALOX5. Lipoxins (LXs), which are the first type of SPMs ever discovered[60], are

derived from AA, too.

1.4 Lipoxygenase family

There are several types of LOXs, classified depending on their regioselectivity[61]. Even though there are different types of LOXs, all of them catalyse oxidations on PUFAs. LOXs are a class of oxidoreductases able to oxygenase the substrate by adding an oxygen molecule. They are metalloenzymes that contain a non-heme Fe atom in their catalytic center, which is the responsible for the redox power of the enzyme. LOXs are present in lots of different types of organisms, such as plants and mammals[48].

1.4.1 General structural features

LOXs have a single polypeptidic chain of around 500 to 700 aminoacids, but they have two differentiated domains. The smallest one is the PLAT domain, located at the N-terminal end of the chain, while the largest one is the catalytic or C-terminal domain.[48]

In LOXs, the two domains do not share the shape, suprachemical features or function: they have very different properties. Besides being linked by the same peptide chain, the two domains interact via non-covalent interactions through an inter-domain plane, which has been reported to be an allosteric site for product synthesis control too.

1.4.1.1 PLAT domain

The Polycystin-1 Lipoxygenase Alpha-Toxin (PLAT) domain, located at the N-terminal in LOXs, is a β-sheet barrel containing from 100 to 150 residues and it is found in other families of enzymes different to LOX[62].

The PLAT domain's function is mainly related to membrane binding. Its hydrophobic character confers the necessary features to interact with the hydrophobic tail of the phospholipids located in the lipid membrane of cells and cellular nucleus[48;63].

Several studies conclude that the presence of the PLAT domain is not essential for the activity of LOXs, but it is related to enhanced catalytic features like higher structural stability –truncated LOXs have higher tendency to liberate the metal atom, and higher substrate selectivity. Moreover, its truncation provokes higher suicidal rates, but, in contrast, enhances the catalytic efficiency –the $^{k_{cat}}/_{K_M}$ ratio–[63].

1.4.1.2 Catalytic domain

The catalytic domain is made of α-helices and contains around 500 residues, depending on the LOX's isoform. This catalytic domain contains the metal atom, typically linked to three or four His, one or none Asn, the carboxylic group of the C-terminal and an OH^- group with an octahedral geometry. Moreover, this sphere of coordinated ligands interact with each other and with the second coordination sphere through a hydrogen-bond network.

The cavity of the enzyme is also located in this domain. It typically has a U shape. The metal is placed at the vertex of the U, so only the region exposed directly to the metal will be the reactive one. Thus, the regioselectivity is governed by two major factors: the depth of the cavity, that lets the substrate go deeper or not, and the presence of hydrophilic residues at the depth of the cavity, which will let establish an interaction with the polar head of the PUFA. Moreover, the cavity has a highly hydrophobic character, which allows the substrate to bind in it by establishing π-π, π-electron and, in some specific cases, electrostatic interactions.

In the catalytic domain there are also oxygen diffusion channels that let the oxygen diffuse from the surface of the enzyme into the substrate's

cavity.

1.4.2 Biological significance of Lipoxygenases

LOXs are key enzymes in several processes that take place both in cells and in organisms. They have three main biological roles: modification of the lipid-protein interactions in membranes through chemical modifications, regulation of the intracellular redox state and synthesis of bioactive lipid mediators[61]. This last role will be explored during this Thesis.

The synthesis of bioactive lipid mediators is a crucial process in mammals and other organisms. Among the plenty of different bioactive mediators derived from different types of chemicals, LOXs are capable of synthesising mediators from fatty acids[13]. These mediators are key for organisms because they are responsible for inflammatory processes, both the pro-inflammatory and the inflammation resolution processes, as reviewed in Section 1.2.2. This double role is possible thanks to the variety of available PUFAs in the organisms, what makes it possible to synthesise a wide variety of mediators, each one with a determined role and target.

1.4.3 Catalytic properties of Lipoxygenases

Non-conjugated PUFAs are the natural substrates of LOXs. Chemically, their most relevant feature in terms of reactivity is that they contain at least a group of two *Z* double bonds with a methylene group in between. This feature is key because of the delocalisation that takes place once one of the hydrogens of the methylene group is abstracted by the enzyme. Thus, the power of LOXs comes from their ability to activate the very unreactive C-H bond[48].

1.4.3.1 Canonic reactivity of LOXs

It is known that the most characteristic reactivity of LOXs is the hydroperoxidation of PUFAs[48]. As Figure 1.3 shows, the mechanism consists of three different steps: the abstraction of a H atom from a methylene position enclosed between two *Z* double bonds, followed by the addition of an oxygen molecule at the $n \pm 2$ position (being n the position of the methylene of the previously abstracted H). Finally, and after the rotation of the peroxide towards the metal atom, the H atom abstracted in the first step is abstracted back from the cofactor to the outer O of the substrate's peroxide.

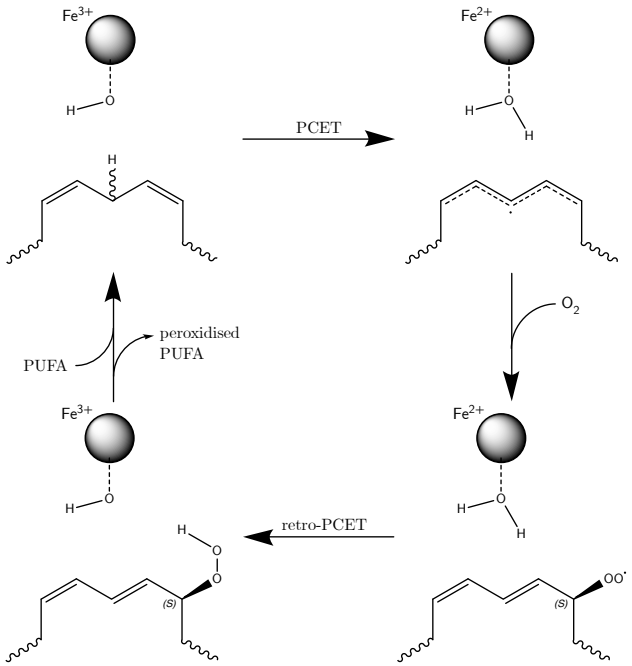

Figure 1.3: Catalytic cycle of LOX's peroxidation on a generic PUFA.

Step 1: Proton-coupled electron transfer The transfer of the proton and the electron may follow a concerted mechanism or not. If the mechanism is concerted, it will follow a Proton-Coupled Electron Transfer (PCET)-like mechanism. Several experimental and computational studies on different kinds of LOXs reported in the bibliography agree that the mechanism is a PCET.

Moreover, kinetic studies have reported that the H-abstraction is generally the Rate Determining Step (RDS) of the global mechanism, meaning that the overall rate of the reaction depends on the relative position of the substrate inside the cavity of the enzyme.

In the PCET mechanism in LOXs, the electron is transferred from the substrate to the metal atom (an Fe in this case) while the H^+ is transferred to OH^- group. However, this does not necessarily mean that the transfers have to take place synchronically, that is the electron and the H^+ transfer as a H atom. On the contrary, Lehnert and Solomon[64] demonstrated that the H^+ starts firstly to transfer, generating a transition state where the Fe and the OH^- keep covalently bonded. Then, a covalent bond is formed between OH^- and H^+ while the C-H bond is not completely broken. This network of bonds is supposed to create a bridge, called *superexchange pathway* by the authors, through which the electron can tunnel from the substrate to the metal. This dependence on the bridge-like bonding network makes the reaction thermochemistry and kinetics dependant on the initial distance between the to-be-abstracted H and the coordinated-to-Fe OH^- group. Nevertheless, this relationship is not necessary proportional[65].

This reaction, the transfer of a H atom (both proton and electron) from the substrate to Fe(III) leads to a Fe(II) atom –it gets reduced by the electron– and to the formation of a radical on the substrate, located on the former divinyil group, which becomes a pentadienyl group.

Step 2: Oxygen addition to pentadienyl group Once the radical pentadienyl group is formed, a molecule of oxygen is added to the $n+2$ or $n-2$ position (being n the methylene position of the abstracted H) of the substrate. The addition takes place following an antarafacial approach –that is, the O_2 molecule is added to the opposed-to-Fe-atom substrate's face–. This dioxygen addition displaces the radical from the pentadienyl to the newly formed peroxide group.

Addition of O_2 takes place in the $n\pm2$ position because of spin electron densities. When there is a delocalisation along the pentadienyl, the outer carbons have higher spin electron densities, so they have a more radical charge. This will allow the O_2 to get added at one of these positions. Moreover, the addition to the $+2$ or -2 positions has been observed to be related to the conformation of the substrate in the cavity. Thus, oxygen diffusion tunnels are needed and they have to point to a certain region of the cavity where the $n\pm2$ carbon (depending on the orientation) is placed.

The antarafacial addition locates the peroxide group far from the cofactor of the enzyme. Thus, a rotation of both the peroxide group and the carbon backbone of the substrate is required to make the outer O point to the cofactor, so the next and final step of the mechanism can take place.

Step 3: Hydrogen abstraction to peroxide group Once the peroxide group is rotated and pointing to the cofactor, there is an abstraction of the initially abstracted H atom –so a back H-transfer– from the H_2O (which gives the proton) and the Fe(II) atom (which gives the electron) to the peroxide group. The final hydroperoxide, which goes back to a non-radical configuration, is obtained as the product of this step.

The mechanism of this retroabstraction is not so well studied compared to the initial H abstraction, so it is not clear which type of mechanism is followed. However, several studies report that the reaction is exergonic

and it is likely to assume that the mechanism is also a PCET.

1.4.3.2 Non-canonic reactivity of LOXs

Even though LOXs are known to be very good at catalysing the stereoselective hydroperoxidation of PUFAs, they are also capable of performing epoxidation on hydroperoxo PUFA derivatives. For instance, LTA_4 is synthesised by ALOX5[66] and 13*S*,14*S*-epoxy-MaR1 (13*S*,14*S*-eMaR1) is synthesised by ALOX12[67] and by ALOX15[53]. Despite this reactivity is known since many decades ago, the mechanism for the formation of the epoxides is still unknown.

1.4.4 Selectivity in Lipoxygenases

LOXs are a family of enzymes with a high regio- and stereo-selectivity. The regioselectivity of each LOX depends on cavity's features, which allow the substrate to expose one or another bisallylic methylene –if available– to the catalytic centre. As previously summarised in Section 1.4.1.2 and discussed in the previous lines, two types of control of the regioselectivity appear in LOXs: the deepness of the substrate inside the cavity and its relative orientation.[68]

On the one hand, a PUFA can get inside the cavity in two orientations: the head can be located in the innermost part of the cavity –in what its called a head-first conformation– or the hydrophobic tail can be the one in the bottom of the cavity in such a way that a tail-first conformation is obtained. This configuration control is mainly achieved by the presence or not of a hydrogen-bond-donor and/or positively-charged residue in the depth of the cavity. If a residue of this kind is present, the carboxylic head of the substrate will be able to create a stable interaction, so it will be possible to achieve the head-first conformation. If there is no positively

charged residue, and taking into account the hydrophobic character of the cavity, the head-first conformation will not be favoured in any way.

The substrate's conformation will also govern the stereospecificity of the product since each conformation faces a different plane of the substrate to the addition, which follows an antarafacial geometry in respect with the Fe atom.[68]

On the other hand, the shape of the cavity controls the deepness of the substrate's binding. The deeper the cavity, the more exposed to the cofactor the outermost methylenes –the ones closer to the entrance of the cavity– will be. For instance, for a tail-first configuration, the cavity of a 12LOX would be deeper than the cavity of a 15LOX. This is possible because LOXs have usually a U-shaped cavity with the Fe complex placed in the vertex of the U in such a way that the methylene moiety from the substrate gets placed in the vertex is the one that will react.

Additionally, the oxygen diffusion tunnels are also governors of the regio- and stereoselectivity. For some LOXs, it has been demonstrated that the presence of an Ala or a Gly residue in the oxygen channel modifies its shape, hence modifying the preferred oxygen addition carbon, and consequentially the chirality of the addition, for the same alignment of the substrate. Mutation studies have delved in this Ala-versus-Gly concept and have demonstrated that the mutation change the regio- and stereoselectivity[69;70]. Thus, the S or R configuration will depend on the conformation of the substrate, on the relative position to the Fe complex, and in some cases on the shape of the oxygen tunnel.

1.5 Enzymes that will be studied

During the present thesis, as commented before, several different enzymes will be studied. The majority of them belong to the LOXs' family, all of

them coming from mammals, although a hydrolase will be studied too.

ALOX5 Formerly known as 5-LOX, it is a LOX isoform that specifically oxidises the C_5 of AA producing 5*S*-HpETE. ALOX5 has also been reported to be able to epoxidate 5*S*-HpETE generating LTA_4[66].

Only the human isoform of 5-LOX will be studied[71]. It contains 674 aminoacids. Contrary to other LOXs, ALOX5 does not have an U-shaped cavity but a straighter one. Moreover, its reactivity and activity is controlled by FLAP.[72;73]

ALOX12 Formerly known as 12-LOX, it is a LOX that specifically oxidises the C_{12} of AA producing 12*S*-HpETE[74;75]. The human variant has been reported to be able to peroxidise other PUFAs like DHA, thus generating 14*S*-hydroperoxy-DHA (14*S*-HpDHA)[76]. It is also capable of epoxidating this kind of substrates generating 13*S*,14*S*-epoxy-DHA as the product of the reaction[53;67].

Only the human's isoform of the ALOX12[77], which contains 663 aminoacids. Additionally, the pig's ALOX15[78] will also be studied since it is reported to behave like a 12LOX[79]. It has 654 aminoacids in its sequence.

ALOX15B Also known as 15-LOX-2 or 8-LOX depending on the organism, it specifically oxidises the C_{15} of AA producing 15*S*-HpETE[80] and/or the C_8, hence producing the 8*S*-HpETE[81]. The mouse isoform has been reported to be able to biosynthesise double oxidation products such as 8*S*,15*S*-diHpETE[82], but no epoxidation capabilities have been reported.

Two isoforms of this enzyme will be studied and compared:

the human and the mouse ones. The human ALOX15B contains 676 aminoacids, while mouse's one contains 677 residues. The mouse's isoform is not 15-lipoxygenating but 8-lipoxygenating, so it mainly produces 8-hydro(per)oxyeicosatetraenoic (H(p)ETE) from AA.

LTA_4H LTA_4H is a hydrolase from the soluble Epoxide Hydrolase (sEH) family, so it is able to perform hydrolysis of soluble epoxides. Typically, they contain a Zn atom and they are able to have very different sizes and tertiary structures. In some cases, hydrolases can have other activities like aminopeptidase's.[83]

In the case of LTA_4H, the product obtained from the hydrolysis of LTA_4 is Leukotriene B_4 (LTB_4), a chiral diol with a very determined conformation of the three double bonds located between the alcohol groups.[84] The transformation is proposed to take place starting from the cleavage of the C_6-O bond of the epoxide of LTA_4 and the addition of a OH^- group to a carbon 7 methylene units away, but the detailed mechanism is still not unravelled. LTA_4H contains around 600 residues and a Zn atom coordinated to two His, a Glu and two water molecules and has a coordination vacancy.[85]

FLAP FLAP is an integral transmembrane protein associated with the enhancement of *hum*ALOX5's LTA_4-synthase activity[86]. Moreover, FLAP is also associated with the binding of free AA molecules spread in the membrane.

Chapter 2

Objectives

The present Chapter aims to define the goals that will be pursued during this Thesis. Two main objectives are defined:

- Study the regio- and stereoselectivity, and the function of different Lipoxygenases and related proteins that intervene in inflammatory processes as a way to understand how they work, which is their role and how punctual mutations can affect the enzymatic behaviour.
- Explore a biocatalytic synthesis pathway for the production of a Specialised Pro-resolving Mediator, Maresin-1, in order to evaluate an alternative biocatalytic synthesis to the total organic synthesis.

For the study of the function and selectivities of inflammation-related proteins, molecular Docking, Molecular Dynamics simulations and Quan-

tum Mechanics/Molecular Mechanics calculations, as well as experimental work, will be employed. In this sense, punctual mutations will be applied to three Lipoxygenases –human and mouse ALOX15Bs and human ALOX5–, in order to understand how the modification of a region of the active site affects the regio- and stereoselectivities of the enzymes. Moreover, the function of two more enzymes, Five-Lipoxigenase-Activating Protein and Leukotriene A_4, will be studied at the atomic level using computational methods in order to precisely define their biological role and catalytic mechanism, respectively.

On the other hand, a pathway for the biocatalytic synthesis of Maresin-1 will be proposed and studied from the computational and experimental points of view. The mechanism of action of human ALOX12 on Docosahexaenoic Acid for the production of the 13*S*,14*S*-epoxy-MaR1 intermediate will be studied, as well as an enzyme will be designed in order to achieve the conversion of this latter intermediate into Maresin-1. Moreover, the designed enzymes will be expressed.

Part II

Background

Chapter 3

Computational Chemistry background

3.1 Introduction

Computational chemistry methods have revolutionised the study of protein roles and enzymatic mechanisms, offering unprecedented insights into the enzyme structure, dynamics, and function. This chapter explores three powerful computational techniques that are commonly applied to the study of enzymes: molecular docking simulations, Molecular Dynamics (MD), and Quantum Mechanics/Molecular Mechanics (QM/MM) methods.

Docking simulations enable the prediction and analysis of binding interactions between small molecules and proteins. By exploring the conformational space, docking simulations identify potential binding sites

and predict binding poses and affinities. MD simulations, on the other hand, simulate the behaviour of atoms and molecules over time, allowing the study of protein dynamics, and conformational changes, for instance. Thus, MD simulations provide insights into the dynamics of protein-ligand complexes. Lastly, QM/MM methods combine Quantum Mechanics (QM) and classical Molecular Mechanics (MM) and are useful for studying enzymatic mechanisms at the atomic level. These methods accurately describe the electronic properties of the active site while capturing the influence of the surrounding molecular environment. The subsequent sections of this chapter will delve deeper into the principles of these computational methods.

3.2 Docking calculations

Molecular docking simulations are the least accurate among the computational chemistry methods used in this Thesis. By approximating the ligand-protein interaction, molecular docking is able to explore the conformational space of the ligand inside the protein's binding site.

For carrying out molecular docking simulations, GOLD[87] will be used as the main software. GOLD is based on the Genetic Algorithm (GA) to generate the positions of the ligands in the protein's cavity. Moreover, a scoring function is used to evaluate the affinity of the generated positions.

3.2.1 Genetic Algorithm in GOLD

As mentioned before, GOLD's docking implementation is based on the GA. In this algorithm, an initial population is generated and evaluated. Then, the best individuals are combined, evaluated and combined again in a new round until convergence is achieved.

For initialising the algorithm, the binding site is defined by a position and a radius.

GOLD's implementation is based on the following scheme:

1. **Representation**: Ligand poses are represented as individuals in a population, with each individual defined by a set of parameters specifying the ligand's conformation and orientation.

2. **Fitness Evaluation**: GOLD evaluates the fitness of each individual using a scoring function that measures how well the ligand fits in the receptor's binding site. The scoring function typically considers factors like shape complementarity, electrostatics, and hydrophobic interactions.

3. **Selection**: Individuals with higher fitness scores are preferentially selected for reproduction, emulating the process of natural selection.

4. **Crossover**: GOLD performs crossover by combining genetic information from selected individuals. This generates offspring with a combination of characteristics from the parent individuals, leading to new ligand poses.

5. **Mutation**: Random changes are introduced to the offspring's parameters through mutation, adding diversity to the population and exploring different regions of the conformational space.

6. **Generation Update**: The offspring replaces less fit individuals in the previous generation, forming the next generation of ligand poses.

7. **Iteration**: Steps 2-6 are repeated for multiple generations, allowing the population to evolve and converge towards ligand poses with improved fitness.

8. **Convergence**: Over iterations, GOLD's genetic algorithm optimizes the ligand poses, aiming to identify the ligand conformations with the best fitness and binding characteristics within the receptor's binding site.

3.2.2 Scoring function

Each pose generated by the GA is evaluated by a scoring function. In this Thesis, the ChemScore[88] function is used. This function is an empirical scoring function, and it also includes the estimated free energy of binding ($\Delta G_{binding}$) in the scoring.

The function expression is the following:

$$\begin{aligned} ChemScore = &\Delta G_{binding} + P_{clash} + C_{internal} \cdot P_{internal} + \\ &(C_{covalent} \cdot P_{covalent} + P_{constrains}) \end{aligned} \tag{3.1}$$

All parameters that appear between parenthesis in Equation 3.1 are optional parameters that only appear if covalent docking is being simulated or if constrains are applied. The other terms are parameters calculated in any type of docking simulations.

$\Delta G_{binding}$ is a product of the addition of several different free energy contributions, as expressed in Equation 3.2.

$$\Delta G_{binding} = \Delta G_0 + \Delta G_{H\ bond} + \Delta G_{metal} + \Delta G_{lipo} + \Delta G_{rot} \tag{3.2}$$

where ΔG_{Hbond} is the hydrogen bonds contribution, the ΔG_{metal} is the contribution by the metal-ligand interactions, the ΔG_{lipo} is the lipophilic contribution, and ΔG_{rot} is the rotation penalisation.

3.3 Classical Molecular Mechanics

Molecular mechanics simulates the behaviour of atoms and molecules by applying classical mechanics principles. This method represents molecules as collections of atoms connected by bonds, with each atom and group of bound atoms defined by specific parameters such as mass, bond lengths, bond angles, or Lennard-Jones parameters, among others.

Classical MM simulations calculate the forces acting on each atom based on their interactions with neighbouring atoms. These interactions are described using mathematical functions called force fields, which model the potential energy of the system as a function of atomic positions. Then, the classical equations of motions for atoms are solved.

In MM, binding interactions are described using a spring model, so each interaction is defined by the mathematical expression of a spring. As a consequence, MM has its own limitations. For example, no electronic structures are explicitly described, so chemical reactivity can not be simulated using this technique. Nonetheless, MM simulations are valuable for studying various molecular properties and phenomena, such as conformational changes or molecular dynamics. They are particularly useful for investigating large biomolecules such as proteins and macromolecular systems like membranes, as well as their interactions with ligands or drugs.

3.3.1 Force Field expression

A force field is the collection of parameters that describe a given system. Any system that needs to be treated using classical MM has to be parametrised, so all the interactions that take place between the atoms in the system are described. In order to generate the parameters that describe the system, several force field libraries that contain standard parameters for common chemical groups such as amino acids are available.

Among them, `AMBER` force fields like `ff14SB`[89] or `ff19SB`[90] are two of the most used ones, and they will be the main force fields employed during this Thesis.

Each force field has its own mathematical expression, so its own set of parameters. A general mathematical expression for the force field can be found in Equation 3.3.

$$E_{MM} = \sum_{bonds} E_{stretching} + \sum_{angles} E_{bending} + \sum_{torsions} E_{torsional} + \sum_{non-bonding} E_{non-bonding} \tag{3.3}$$

with E_{MM} corresponding to the energy of the system with each atom at a certain position. As it can be seen, the total energy is composed by the sum of four different terms, each of them constructed with different mathematical expressions as they represent different kinds of interatomic interactions.

Equation 3.4 describes the energy terms related with bond stretching, so the movement between two connected atoms. The mathematical expression corresponds to a simple harmonic motion, where k_b corresponds to the force constant, l_i to the bond distance at the given structure, and l_0 corresponds to the reference value of the distance. k_b and l_0 are described in the force field, while l_i depends on the atomic positions.

$$\sum_{bonds} E_{stretching} = \sum_{bonds} k_b(l_i - l_0)^2 \tag{3.4}$$

Equation 3.5 describes the energy terms related with angle bending, so the movement between three consequently connected atoms. The mathematical expression corresponds to a simple harmonic motion, where k_θ corresponds to the force constant, θ_i to the angle at the given structure,

and θ_0 corresponds to the reference value of the angle. k_θ and θ_0 are described in the force fields, while l_i depends on the atomic positions.

$$\sum_{angles} E_{bending} = \sum_{angles} k_\theta (\theta_i - \theta_0)^2 \tag{3.5}$$

Equation 3.6 describes the energy terms related to the torsion of a bond, this is the rotation of a bond. The torsion is described for four consecutive connected atoms and describes the relative movement of the two external atoms. k_ϕ is the force constant of the torsion, n is the multiplicity –the number of minimum energy points along the 360° rotation–, ϕ is the dihedral angle at the given structure, and δ is the phase factor –which determines the values of ϕ that corresponds to energy minima–. k_ϕ, n and δ parameters come from the force field, while ϕ_i is the dihedral angle in the punctual structure.

$$\sum_{torsions} E_{torsional} = \sum_{torsions} k_\phi \left[1 + \cos\left(n \cdot \phi - \delta\right)\right] \tag{3.6}$$

Equation 3.7 represents the non-bonding interaction between two atoms, which do not need to be connected. As it can be observed, two terms are present.

$$\begin{aligned} \sum_{non-bonding} E_{non-bonding} = & \sum_{non-bonding} \overbrace{\frac{q_i q_j}{4\pi\epsilon_0 r_{ij}}}^{\text{electrostatic}} + \\ & \sum_{non-bonding} \underbrace{4\epsilon_{ij}\left[\left(\frac{\sigma_{ij}}{r_{ij}}\right)^{12} - \left(\frac{\sigma_{ij}}{r_{ij}}\right)^{6}\right]}_{Van\ der\ Waals} \end{aligned} \tag{3.7}$$

where q_i and q_j represent the net atomic charges of atoms i and j, ϵ_0 is the dielectric constant, and r_{ij} is the distance between i and j in the given

structure. ϵ_{ij} is the depth of the potential well of the energy profile of the interaction and σ_{ij} is the collision distance, so the distance between i and j at which the potential of the described interaction is 0. On the one hand, the electrostatic interactions are described using the Coulomb's law. On the other hand, the van der Waals interactions are described using the Lennard-Jones 12-6 potential[91–93]. This potential properly describes the attractive and repulsive interactions by the r_{ij}^{-6} and r_{ij}^{-12} terms, respectively.

The given mathematical description corresponds to the `AMBER`'s construction of a force field[94]. Nonetheless, other libraries like `CHARMM`[95] or `GROMOS`[96] might include other parameters that describe other interactions like hydrogen bonding.

3.4 Molecular Dynamics

Molecular Dynamics (MD)[97] –here employed for classical dynamics in contraposition to quantum dynamics– is a technique that is used to simulate the behaviour of a molecular system along time. In this Thesis, classical MM (Section 3.3) is used for describing the Potential Energy Surface (PES) on the dynamics, although QM could also be used.

MD is started with an initial configuration of the system –described by the force field and the atomic positions–. The atomic positions are then updated applying a progression algorithm. After each update, the energy is calculated for the new geometry. Then, the geometry is updated considering the energetic calculation.

These set of generated geometries constitute the MD trajectory, which can be further analysed to extract information.

3.4.1 Progression Algorithm

The progression algorithm is the algorithm responsible of the update of the atomic positions in a MD simulation. This progression algorithm is a numerical method for the resolution of the Newton's equations of motion, which are described in Equation 3.8.

$$\vec{F_i}(\vec{r_i}, ..., \vec{r_n}) = -\frac{dV}{d\vec{r_i}} = m_i \frac{d^2\vec{r_i}}{dt^2} \quad \forall_i \tag{3.8}$$

where $\vec{r_i}$ is the position of the atom i and m_i is its mass. $\vec{F_i}$ is the force applied to atom i by the rest of the particles at a potential energy V. One approach to the solution of this equation is to calculate the potential energy surface of the force field using classical MM. However, the equation can not be analytically solved. Thus, numerical methods for the resolution of the Newton's equations are necessary for solving the equations of motion with finite time intervals.

Velocity Verlet integrator[98] is one of these numerical methods for the resolution of Newton's equation of motion. This method is an enhancement of the Verlet integrator which solves its main drawback: the velocity does not appear explicitly in the propagation equation, what prevents the simulation of systems at constant temperature.

The equations of propagation defined by the velocity Verlet integrator for the position and velocity are shown in Equations 3.9.

$$\begin{aligned} \mathbf{x}(t + \Delta t) &= \mathbf{x}(t) + \mathbf{v}(t)\Delta t + \frac{1}{2}\mathbf{a}(t)\Delta t^2 \\ \mathbf{v}(t + \Delta t) &= \mathbf{v}(t) + \frac{\mathbf{a}(t) + \mathbf{a}(t + \Delta t)}{2}\Delta t \end{aligned} \tag{3.9}$$

where $\mathbf{x}$ is the position of the atom, $\mathbf{a}$ is its acceleration, and $\mathbf{v}$ is its velocity. t is the time of the propagation and Δt is the time step.

3.5 Quantum Mechanics

Quantum Mechanics (QM) is a physical theory able to describe the matter at the microscopic scale. QM allows the description of atoms and molecules by explicitly representing the electrons and atomic nuclei. Thus, chemical properties such as reactivity can be properly simulated using this theory.

The Schrödinger equation[99] (Equation 3.10) is the fundamental equation of QM. This equation describes the evolution in time of Ψ of the system. $\hat{H}$ represents the hamiltonian operator, which is an expression involving the system's kinetic and potential energies, while the wavefunction (Ψ) describes the system, so is particular for each one.

$$i\hbar\frac{\partial\Psi}{\partial t} = \hat{H}\Psi \tag{3.10}$$

with $\hbar$ being the Planck's constant divided by 2π, t the time, Ψ the wavefunction, and $\hat{H}$ the hamiltonian operator.

3.5.1 Time-Independent Schrödinger equation

A simplified version of the Schrödinger equation can be generated if the E of the system is considered independent of the time. The Time-Independent Schrödinger equation (Equation 3.11) is then obtained, and it can only be applied on stationary states of quantum systems.

$$\hat{H}\Psi = E\Psi \tag{3.11}$$

The $\hat{H}$ operator can be written as in Equation 3.12.

$$\begin{aligned}\hat{H} = &-\sum_i \frac{\hbar^2}{2m_e}\nabla_i^2 - \sum_k \frac{\hbar^2}{2m_k}\nabla_k^2 \\ &-\sum_i \sum_k \frac{e^2 Z_k}{r_{ik}} + \sum_{i<j} \frac{e^2}{r_{ij}} + \sum_{k<l} \frac{e^2 Z_k Z_l}{r_{kl}}\end{aligned} \tag{3.12}$$

where i and j are electrons, k and l are nuclei, $\hbar$ is the Planck constant divided by 2π, m_e and m_k are the mass of the electron and the nucleus k, respectively, ∇^2 is the Laplacian operator, e is the charge of the electron, Z_k and Z_l represent the atomic number of nuclei k and l, respectively, and r_{ij}, r_{ik} and r_{kl} represent the interparticle distances.

Nonetheless, Equation 3.12 cannot be solved analytically for multi-electronic and multiatomic systems. In order to simplify the equation, the Born-Oppenheimer approximation[100] can be applied. This approximation is based on the idea that since electrons and nuclei have very different masses, their movement can be treated independently in such a way the electrons around a nucleus move much faster. Thus, if nuclei are kept frozen and excluding the internuclei repulsion (V_{NN}), the electronic Schrödinger equation can be obtained (Equation 3.13).

$$\hat{H}_e \Psi_e = E_e \Psi_e \tag{3.13}$$

with $\hat{H}_e$ as expressed in Equation 3.14.

$$\hat{H}_e = -\sum_i \frac{\hbar^2}{2m_e}\nabla_i^2 - \sum_i \sum_k \frac{e^2 Z_k}{r_{ik}} + \sum_{i<j} \frac{e^2}{r_{ij}} \tag{3.14}$$

Then, if the internuclei repulsion term is added, the potential energy equation that corresponds to the potential energy surface is obtained. The equation is expressed in Equation 3.15.

$$V = E_e + V_{NN} \tag{3.15}$$

Although the resolution of this set of equations (Equations 3.13, 3.14 and 3.15) is simplified in comparison with the resolution of the Schrödinger equation (Equations 3.11 and 3.12), it is still very complex for a multielectronic system due to the complexity of the wavefunction of the system.

In order to solve these equations, some approximations can be applied. One of the first approximations for the electronic Schrödinger equation resolution is the Hartree-Fock (HF)[101;102] method. In this approach, each electron is described by a spin-orbital. Electrons are quantum particles with spin of $\pm 1/2$, so the wavefunction is expressed as an anti-symmetric product of their spin-orbitals in the shape of a Slater determinant[103]. Thus, the wavefunction can be expressed as shown in Equation 3.16 if the Hartree-Fock (HF) method is applied.

$$\Psi(1,2,\ldots,N) = \frac{1}{\sqrt{N!}} \sum_{q=1}^{N!} (-1)^{p_q} \hat{P}_q \left\{ \chi_i(1)\chi_j(2)\ldots\chi_k(N) \right\} \tag{3.16}$$

where N is the number of the electrons, χ_i corresponds to the spin-orbitals, $\hat{P}_q$ is the permutation operator, and p_q is the number of transpositions for the permutation q.

By its construction, HF approximation has a main limitation that applies for multielectronic systems. Since the approach considers that each electron perceives the other ones as an average of the electric field, an electron correlation error (E_{corr}) arises between the electrons of different spin. In order to handle this limitation, lots of methods –called post-HF methods– have been developed. Among them, Coupled Cluster methods[104] and the Møller-Plesset Perturbation theory[105] are two of the most common ones. Despite these kind of methods –called *ab initio*– solve the E_{corr} problems, they are computationally very expensive when the number of electrons and atoms is high. As an alternative, Density Functional The-

ory (DFT) methods[106] have also been developed focusing on the inclusion of the E_{corr}, as well as on the application to large systems.

3.5.2 Density Functional Theory

Density Functional Theory (DFT)[106] emerged as alternative to *ab initio* methods[107], with the main advantage that it is computationally less expensive while taking into account the electron correlation missing in the HF method.

DFT is based on the idea that electronic energy can be related to the electron density (ρ) and not only to the explicit electrons. Consequently, E_e can be expressed as a functional of the electron density, so $E_e[\rho]$, so each electron density has an associated electronic energy.

The DFT theory is an evolution of the Thomas-Fermi model[108;109] presented in late 1920s. This model was the first model that related the electronic density with the energy. This model was refined in 1964 by Hohenberg and Kohn[110], who developed the two foundamental theorems of the DFT.

Theorem 1 *Any observable of a non-degenerate ground electronic stationary state can be calculated, exactly in theory, from the electron density of the ground state. Expressed differently, energy is a functional of the electron density of the ground state.*[111]

Accepting Theorem 1, electrons are under the effect of an external potential, which in a molecule is created by the nuclear attraction. As a consequence, this theorem establishes that for a particular external potential ($V_{Ne}(\vec{r})$), $\rho(\vec{r})$ defines the properties of the ground state of a multielectronic system. Therefore, the electronic energy of the ground state can be expressed as shown in Equation 3.17.

$$E_0[\rho] = \int \rho(\vec{r}) V_{Ne}(\vec{r}) dr + F_{HK}[\rho(\vec{r})] \tag{3.17}$$

where $V_{Ne}(\vec{r})$ is the external potential that corresponds to the attractive electron-nucleus interaction, and $F_{HK}[\rho(\vec{r})]$ is the Hohenberg-Kohn functional, which expresses the terms non-dependent of the external potential (Equation 3.18).

$$F_{HK}[\rho(\vec{r})] = T[\rho(\vec{r})] + V_{ee}[\rho(\vec{r})] \tag{3.18}$$

where $T[\rho(\vec{r})]$ encompasses the kinetic energy contributions, while $V_{ee}[\rho(\vec{r})]$ is the combination of the classical and non-classical contributions of the electron-electron interactions. The $T[\rho(\vec{r})]$ term is unknown, whilst $V_{ee}[\rho(\vec{r})]$ is expressed in Equation 3.19.

$$V_{ee}[\rho(\vec{r})] = J[\rho(\vec{r})] + K[\rho(\vec{r})] + J'[\rho(\vec{r})] \tag{3.19}$$

where $J[\rho(\vec{r})]$ is the classical Coulomb interaction, $K[\rho(\vec{r})]$ is the exchange energy, and $J'[\rho(\vec{r})]$ is the potential correlation energy. $J[\rho(\vec{r})]$ expression is known, but $K[\rho(\vec{r})]$ and $J'[\rho(\vec{r})]$ are not.

Theorem 2 *The electron density of a non-degenerate electronic ground state can be calculated determining the density that minimises the energy of the ground state.*[111]

In other words, the second theorem (Theorem 2) says that the energy of the exact ground state energy is always smaller than the energy of any definite, positive trial density (ρ_t), as expressed in Equation 3.20.

$$E_0[\rho_0] \leq E_v[\rho_t] \tag{3.20}$$

3.5.2.1 Kohn-Sham Method

As discussed in the previous section, Equations 3.18 and 3.19 can not be solved. In 1965, Kohn and Sham[112] proposed the first approach to the solution of the $T[\rho(\vec{r})]$, $K[\rho(\vec{r})]$ and $J'[\rho(\vec{r})]$ terms (Equation 3.19). They proposed, assuming that the density of an interacting electron system is the same than the density of the ground state of the system, the description of a fictitious system containing N electrons that do not interact between them. These electrons are described by a set of monoelectronic wave functions (ϕ_i). Thus, the kinetic functional ($T_s[\rho]$) can be calculated using Equations 3.21 and 3.22.

$$T_s[\rho] = -\frac{1}{2}\sum_{i=1}^{N}\langle\phi_i|\nabla_i^2|\phi_i\rangle \tag{3.21}$$

$$\rho(\vec{r}) = \sum_{i=1}^{N}|\phi_i(\vec{r})|^2 \tag{3.22}$$

with T_s referring to a non-real kinetic energy but to the kinetic energy of the non-interacting electron system.

With this approach, Equation 3.17 can be rearranged including the terms introduced by the Kohn-Sham method (Equations 3.21 and 3.22), as expressed in Equation 3.23.

$$E_{DFT}[\rho(\vec{r})] = T_{\mathrm{s}}[\rho(\vec{r})] + \int \rho(\vec{r})V_{ne}(\vec{r})dr + J[\rho(\vec{r})] + E_{\mathrm{xc}}[\rho(\vec{r})] \tag{3.23}$$

where $E_{\mathrm{xc}}[\rho]$ corresponds to the exchange-correlation functional, as expressed in Equation 3.24.

$$E_{\text{xc}}[\rho(\vec{r})] = (T[\rho(\vec{r})] - T_s[\rho(\vec{r})]) + (V_{ee}[\rho(\vec{r})] - J[\rho(\vec{r})]) \tag{3.24}$$

The addition of this E_{xc} term is key for obtaining a reliable energy since it compensates the error introduced by considering that electrons do not interact between them. Thus, it is key to find the best expression since the exact one remains unknown.

Several approaches to this E_{xc} have been proposed. Along this Thesis, the hybrid exchange functional will be used, but there are other methods such as the Local Density Approximation or the Generalized Gradient Approximation.

Hybrid Exchange Functional

Hybrid Exchange functional combines Hartree-Fock corrections with the exchange-correlation functional ($E_{\text{xc}}[\rho]$). The exact exchange derived from a HF calculation is obtained with the Adiabatic Connect Formula, which connects the non-interacting state with the fully interacting state. Its expression can be found in Equation 3.25.

$$E_{\text{xc}}[\rho] = \int_0^1 W_{\text{xc}}[\lambda] d\lambda \tag{3.25}$$

with $W_{\text{xc}}[\lambda]$ representing the exchange-correlation energy of the electronic part of an interacting multielectronic system, and λ as the coupling constant. At $\lambda = 0$, the electrons are not interacting, so it corresponds to the exact exchange at the HF. On the contrary, at $\lambda = 1$, the electrons of the system are interacting, so contributing to the exchange-correlation energy. Based on that idea, the `BHandH` method was proposed by Becke in 1993[113], where $E_{\text{xc}}[\rho]$ is calculated in such a way that $W_{\text{xc}}[\lambda]$ presents

a linear dependency with λ. In this method, λ takes the values 0 and 1, so energy is actually a linear combination of the exact exchange energy calculated by the HF and the DFT methods, respectively, as shown in Equation 3.26.

$$E_{\mathrm{xc}}[\rho] = \frac{1}{2}E_{\mathrm{xc}}^{HF} + \frac{1}{2}E_{\mathrm{xc}}^{DFT} \tag{3.26}$$

Nonetheless, this method lacks of the presence of the dynamic electron correlation. Because of that, Lee, Yang and Parr introduced a correction[114] to an evolved version of the Becke method, which adds three parameters to the original function. The resulting method is called `B3LYP` and is expressed in Equation 3.27.

$$\begin{aligned} E_{\mathrm{xc}}^{\mathrm{B3LYP}} &= (1-a_0)\,E_{\mathrm{x}}^{\mathrm{LSDA}} + a_0 E_{\mathrm{x}}^{\mathrm{HF}} \\ &\quad + a_x \Delta E_{\mathrm{x}}^{\mathrm{B88}} + a_c E_{\mathrm{c}}^{\mathrm{LYP}} + (1-a_c)\,E_{\mathrm{c}}^{\mathrm{VWN}} \end{aligned} \tag{3.27}$$

where $E_{\mathrm{x}}^{\mathrm{LSDA}}$ is the standard local exchange functional, $E_{\mathrm{x}}^{\mathrm{HF}}$ is the exact HF exchange functional, and $\Delta E_{\mathrm{x}}^{\mathrm{B88}}$ is the Becke's gradient correction to the exchange functional including the Lee-Yang-Parr correction to the correlation functional. Nonetheless, the Lee-Yang-Parr correction does not include an easily separable local component, reason why the Vosko-Wilk-Nusair local correlation functional is included to provide different coefficients of the local- and gradient-corrected correlation functionals. As suggested by Becke, $a_0 = 0.2$, $a_x = 0.72$ and $a_c = 0.81$.

3.6 Quantum Mechanics/Molecular Mechanics

QM/MM methods[115] are computational techniques that combine the accuracy of QM with the efficiency of classical MM. These methods provide a framework to study complex systems where both QM and classical re-

gions coexist, such as chemical reactions in solution, enzyme catalysis, or biomolecular interactions.

In the QM/MM methods, the system of interest is divided into two regions: the QM region, which focuses on the part requiring accurate quantum mechanical treatment, and the MM region, which represents the remaining environment. The QM region is described using QM principles (Section 3.5), while the MM region is treated using classical force field models (Section 3.3).

These types of methods where firstly introduced by Warshel and Levitt in 1976[116], when they published the very first study on an enzymatic mechanism using QM/MM methods, but they were not fully accepted until 1990, when the QM-MM coupling details where described by Field, Bash and Karplus. From that point, QM/MM methods started to become more popular and started to be applied to systems beyond enzymes like organometallic compounds or solid-state systems. These methods have become so widespread that in 2013 the Nobel Prize was awarded to Karplus, Levitt and Warshel for the development of these methods[117].

3.6.1 Energy expression and QM-MM interaction schemes

QM/MM methods split the complete system (**S**) into an inner region (**I**), which is treated at the QM level of theory, and an outer region (**O**), which is treated at the MM level of theory. Moreover, a boundary region (**L**) appears where the QM and MM regions interact. A diagram of the system partition is shown in Figure 3.1.

Two different schemes appear for treating how the inner and outer regions interact. On the one hand, there is the subtractive scheme where the total system is treated at the MM level, the contribution of the QM atoms to the MM energy is subtracted, and the QM atoms are treated at the QM level of theory. On the other hand, there is the additive scheme,

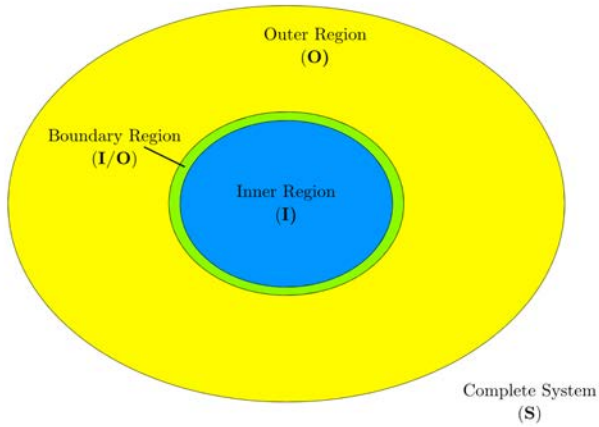

Figure 3.1: Diagram of the complete system, QM (Inner, I), MM (Outer, O) and boundary regions of a QM/MM system Source: Senn and Thiel [115].

where each region is treated separately and an explicit boundary term appears. This scheme is the one used along this Thesis.

3.6.1.1 Additive QM/MM scheme

The additive scheme considers independently the inner and outer regions and adds a boundary region. The energy expression of a system treated with QM/MM methods is expressed in Equation 3.28.

$$E^{add}_{QM/MM}(\mathbf{S}) = E_{MM}(\mathbf{O}) + E_{QM}(\mathbf{I}+\mathbf{L}) + E_{QM-MM}(\mathbf{I},\mathbf{O}) \qquad (3.28)$$

with **I** being the inner region, **O** being the outer region, and **L** being the link atoms. In this case, contrary to the subtractive scheme, only

the atoms in region **O** are treated at the MM level. Link atoms (**L**) are fictitious atoms, usually hydrogens, that are added to the QM region in order to complete the valences of the atoms. The $E_{QM-MM}(\mathbf{I},\mathbf{O})$ term corresponds to the energy term of the interaction between the QM and MM regions. It includes different energetic terms, as expressed in Equation 3.29.

$$E_{QM-MM}(\mathbf{I},\mathbf{O}) = E^{bond}_{QM-MM} + E^{VdW}_{QM-MM} + E^{electrostatic}_{QM-MM} \tag{3.29}$$

where E^{bond}_{QM-MM} represents the energy of the bonding interactions –bond stretching, angle bending and torsional interactions–, E^{VdW}_{QM-MM} is the energy of the Van der Waals interactions between atoms in the inner and in the outer regions, which are usually described by the Lennard-Jones parameters obtained from the force field, and the $E^{electrostatic}_{QM-MM}$ are the electrostatic interactions between atoms in the two regions.

Electrostatic and Van der Waals properties of the atoms in the inner region can change due to the QM treatment, leading to wrong description of these interactions because parameters are obtained from the force field. Van der Waals interactions are short-range interactions, so placing the boundary far enough from the most changing atoms along a reaction process can solve these kind of problems. On the contrary, electrostatic contributions need to be accurately described in order to properly describe the system in terms of energy.

3.6.1.2 Electrostatic embeddings

As said, electrostatic interactions have to be properly treated. Three different embeddings can be used for treating these interactions: the mechanical, the electrostatic, and the polarised embeddings [118].

Mechanical Embedding

It is the simplest embedding. In this embedding, the interactions are considered as MM-MM interactions by a point charge model, so charges are treated as rigid atomic point charges.

This embedding is computationally efficient, but it has some disadvantages. On the one hand, the QM electron density is not modified by the MM atoms. Moreover, PES exploration can lead to discontinuities because of changes in the outer regions. Finally, electrostatic parameters are defined in the force field and they not change even though electron densities change because of the QM treatment of the inner region.

Electrostatic Embedding

In this case, the electrostatic QM-MM interactions are treated at the QM level. A Hamiltonian including these interactions is expressed in Equation 3.30.

$$\hat{H}_{\mathrm{QM-MM}}^{\mathrm{electrostatic}} = -\sum_{i}^{N}\sum_{J\in\mathbf{O}}^{L}\frac{q_J}{|\boldsymbol{x}_i - \boldsymbol{X}_J|} + \sum_{\alpha\in\mathbf{I}+\mathbf{L}}^{M}\sum_{J\in\mathbf{O}}^{L}\frac{q_J Q_\alpha}{|\boldsymbol{X}_\alpha - \boldsymbol{X}_J|} \tag{3.30}$$

where q_J are the MM point charges at $\mathbf{X}_J$, Q_α are the nuclear charges of the QM atoms at $\mathbf{X}_\alpha$, $\mathbf{X}_\alpha$ and $\mathbf{x}_i$ designate nucleus and electron position, respectively. i, J and α are linked to the N electrons, L point charges, and M QM nuclei, respectively.

As expected, this embedding is more accurate since it solves several problems that appear in the mechanical embedding. On the one hand, the QM density is polarised by the environment, in other words, its electronic structure adapts to the changes in the charge distribution of the environ-

ment. On the other hand, charges are not obtained from the force field, so there is no need to derive correct charges for the QM atoms.

Nonetheless, this method has a main drawback in comparison with the mechanical embedding: it is computationally more expensive.

Polarised Embedding

This embedding is an enhancement of the electrostatic embedding. It has the same features but also includes a polarisation on the outer atoms, giving a more accurate description of the inner-outer electrostatic interaction. This polarised embedding works by applying a self-consistent formulation of the interactions at both sides of the boundary.

Chapter 4

Biology background

All the information exposed in this Chapter has been obtained from Nelson et al.[119]*, For Section 4.3, the information has been gathered from Langlais and Korn*[120]*, while for Section 4.4, the information has been obtained from Alberts et al.*[121]*.*

4.1 Introduction

Along the present Chapter the basic knowledge and concepts required for understanding the biological processes behind the experimental work in this Thesis will be presented. Moreover, some biological elements required to comprehend the computational studies will also be reviewed.

4.2 Expression of enzymes in living organisms

As mentioned in the Introduction (Chapter 1), enzymes will be studied not only computationally but experimentally too. These biochemical experiments require the expression of enzymes in a manageable format, so

they can be used as catalysts free from all the cellular machineries and chemicals.

To use enzymes as catalysts, they have to be produced as an aqueous solution. Even though small peptic chains with no more than 100 amino acids –they may have catalytic properties– can be chemically synthesised, the enzymes to be used in this Thesis contain at least 550 residues. Because the proteins of interest in this case have such long chains, biological systems are needed for their production.

In this section, the biochemistry behind the production of enzymes from Desoxyribonucleic Acid (DNA) in living organisms will be reviewed. As it is well known, the genetic code –this is all the information that describes the function and aspect of an organism– is present in all living organisms from any of the existing domains (bacteria, archaea, and eukaryote). The genetic code is stored in a single molecule, the DNA, which consists of a double helical strand made by four different small building blocks called nucleotides: adenosine (A), cytosine (C), guanine (G), and thymine (T). A is complementary to T, while C is complementary to G. This nucleotide complementarity makes the two strands complementary, thus creating one strand that goes in one way –from 3' to 5'– [‖] and another one that goes in the opposite direction –from 5' to 3'–.

In eukaryota, this DNA is located in a specific enclosure called nucleus, while in procaryota (which includes bacteria and archaea) it is spread in the cytosol. Moreover, DNA can also adopt two different shapes: a circular shape (so there is no end in the chain) or a linear shape.

[‖] 3' and 5' are positions of the ribose or deoxyribose rings that are part of Ribonucleic Acid (RNA) and DNA. 3' corresponds to the O placed over the 3rd carbon of the ring starting from the C attached to the base, while 5' corresponds to the the phosphate group attached to the C in the 5th position of the ring.

4.2.1 From DNA to protein

As said, DNA contains all the information that describes the function and aspect of the organism. Within all the information, there are two types of genetic code: the non-coding and the coding codes. The coding code is the one that codifies for proteins, so it contains the descriptors for the synthesis of polypeptidic chains. The non-coding code is the part of the code that contains other information such as the promoter –the initiator– of the transcription.

The production of proteins is driven by the coding genetic code in living organisms. It is a process that requires two differentiated steps: the transcription from DNA to RNA and the translation from RNA to the polypeptidic chain.

Ribonucleic Acid (RNA) is the second type of nucleic acid that is present in living organisms. Unlike DNA, RNA is composed only by one strand. However, it is made also of four building blocks: adenosine (A), cytosine (C), guanine (G) and uracyl (U), which is not present in DNA. There are different types of RNA with different specific functions. The most important ones in protein production are the messenger, the ribosomal and the transfer RNAs.

4.2.1.1 Stage 1: Transcription. From DNA to RNA

As said in the previous lines, RNA is a nucleic acid that is synthesised from DNA. The conversion is carried out by an enzyme called RNA polymerase, which takes the DNA chain at a certain point, called promotor, breaks the interaction between the two strands and starts creating a RNA strand from the 3'-to-5' strand of DNA. This new strand, called immature RNA, is a 5'-to-3' coding strand.

The promotor, the section of the code that precedes the code of interest

and initiates its transcription to RNA, is the responsible for the type of RNA that will be synthesised.

Messenger RNA Messenger Ribonucleic Acid (mRNA) is a type of coding RNA which encodes the sequence of the protein that is going to be produced. Immature RNA strand is further modified in such a way that introns (non-coding regions of the immature RNA) are removed and only exons (coding regions of the immature RNA) are kept in the sequence. Thus, mature mRNA is obtained.

The mRNA is only around the 5 % of the RNA of the cell and it is synthesised by polymerase II.

The code in mRNA consists of a series of triplets of ribonucleic bases called codons. There are 64 possible different combinations of triplets of ribonucleic bases and each of them translates to one of the 20 amino acids or to a *Stop* codon (Table 4.1).

Some amino acids are defined by more than one codon, while others have only one associated codon. There are also four special codons: the AUG, that corresponds to Met and it is the initiation codon for protein synthesis, and the UAA, UAG and UGA, which are called *Stop* codons and do not codify to any amino acid but they terminate the synthesis of the polypeptic chain.

Transfer RNA Transfer Ribonucleic Acid (tRNA) is another type of non-coding RNA. Its main function is to work as a carrier of an amino acid from the cytosol to the ribosome. To do this, tRNAs are able to specifically attach the amino acid to their 3' site. Each tRNA is specific for an amino acid because each of them contains a triad of nucleic bases –called anticodon– that is complementary to the codon that codifies for the amino acid.

Table 4.1: Table of translation from codons to encoded residues

First codon's base	Second codon's base: U		C		A		G	
U	UUU	Phe	UCU	Ser	UAU	Tyr	UGU	Cys
	UUC	Phe	UCC	Ser	UAC	Tyr	UGC	Cys
	UUA	Leu	UCA	Ser	UAA	*Stop*	UGA	*Stop*
	UUG	Leu	UCG	Ser	UAG	*Stop*	UGG	Trp
C	CUU	Leu	CCU	Pro	CAU	His	CGU	Arg
	CUC	Leu	CCC	Pro	CAC	His	CGC	Arg
	CUA	Leu	CCA	Pro	CAA	Gln	CGA	Arg
	CUG	Leu	CCG	Pro	CAG	Gln	CGG	Arg
A	AUU	Ile	ACU	Thr	AAU	Asn	AGU	Ser
	AUC	Ile	ACC	Thr	AAC	Asn	AGC	Ser
	AUA	Ile	ACA	Thr	AAA	Lys	AGA	Arg
	AUG	Met	ACG	Thr	AAG	Lys	AGG	Arg
G	GUU	Val	GCU	Ala	GAU	Asp	GGU	Gly
	GUC	Val	GCC	Ala	GAC	Asp	GGC	Gly
	GUA	Val	GCA	Ala	GAA	Glu	GGA	Gly
	GUG	Val	GCG	Ala	GAG	Glu	GGG	Glu

tRNA corresponds to around the 15 % content of cellular RNA and it is synthesised by polymerase III.

One of the most singular features of tRNA is its shape. As it is represented in Figure 4.1, tRNA have only one strand that folds over itself creating a cloverleaf-like shape that places the charged amino acid and the anticodon in opposite regions of the structure.

Ribosomal RNA Ribosomal Ribonucleic Acid (rRNA) is a type of non-coding RNA. It acts as a catalyst in combination with a ribosome by binding the mRNA and the tRNA.

rRNA corresponds to the 80 % of the total content of RNA in the cell and it is made by polymerase I and III.

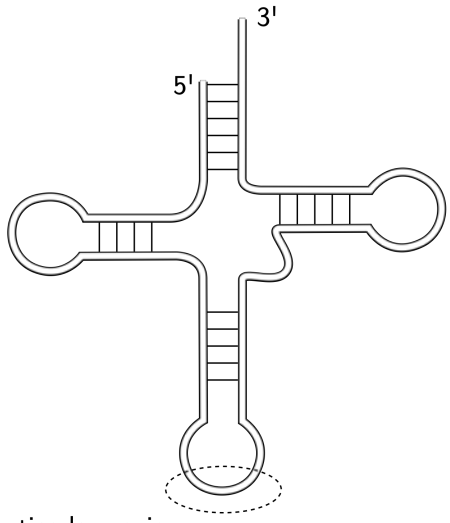

(a) Diagram of a generic tRNA unit

(b) $tRNA^{Glu}$ from Thermus thermophilus *charged with Glu (highlighted in orange). The anticodon is coloured in purple, while the other ribonucleic bases are drawn in yellow.*

Figure 4.1: Diagram (a) **and example** (b) **of a tRNA**

4.2.1.2 Stage 2: Translation: From RNAs to protein

Ribosomes are the protein factories in the cells. Their role in the cell machinery is to create the polypeptic chain by adding up one amino acid after the other following what mRNA dictates.

Ribosomes have two subunits, the major and the minor. They are bigger in eukaryotic cells than in prokaryotic, but their function and way of working is the same. The major subunit has two differentiated regions: the peptic region and the amino acidic region.

All three kinds of RNA that have been reviewed are necessary to carry out the polypeptide synthesis. rRNA binds to other ribosomal proteins and creates the two subunits of the ribosome.

Then, mRNA binds to the inter-subunit space in such a way that it is read from 5' to 3'. Finally, tRNAs are combined with their corresponding amino acid by a process called *charge*.

The charging of the tRNA molecules is carried out by an enzyme called aminoacyl tRNA synthase in two steps. The amino acid is firstly combined with a molecule of ATP, so an aminoacyl-adenosine monophosphate (AMP) complex is obtained as well as a phosphate. Then this complex reacts with the molecule of tRNA, the amino acid-tRNA complex is generated –that is the charged tRNA–, and an AMP is liberated as a subproduct. This reaction takes place with all the different amino acids but it firstly occurs with Met and the tRNA that has the UAC anticodon.

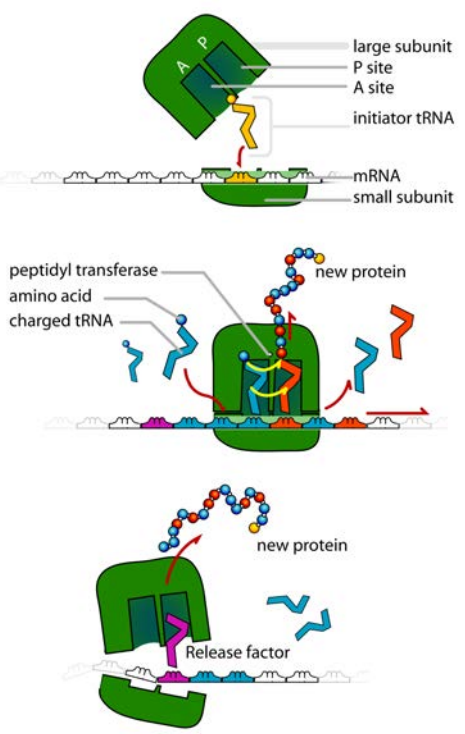

Figure 4.2: Diagram of the expression protein process in ribosome. Initiation step (upper), elongation step (middle) and termination step (lower). Source: LadyofHats [122]

Once everything is set up, the protein production can start. It follows as schematised in Figure 4.2:

Initiation The tRNA charged with the Met amino acid binds to the protein in the peptic site. Then, the second tRNA charged with the amino acid that the mRNA sequence dictates binds to the amino-acyl site of the ribosome. Once both tRNAs are

bound, the ribosome enroles a peptidyl transferase activity: it unbinds the Met from the tRNA by the COO^- site and binds it to the N terminal of the second amino acid. Once the transference has ended, the tRNA of the Met unbinds the ribosome and the other tRNA moves from the aminoacyl site to the peptic site.

As a result, the ribosome is bound to a tRNA linked to the second amino acid of the protein's sequence, which is bonded by its N terminal to the initial Met. The aminoacyl site is free, while the peptic side is occupied by the peptide chain containing the first two amino acids of the sequence. The Met gets outside the ribosome, while the second amino acid keeps linked to its tRNA through the C terminal. Finally, the ribosome moves forward (in the 5' to 3' direction) over the mRNA. This allows more than one ribosome to work on different points of the same mRNA strand.

Elongation The ribosome moves to a new mRNA's codon. The charged tRNA with the anticodon that complements the mRNA's codon binds to the ribosome in the amino-acyl site. The ribosome catalyses the peptic transfer, so the amino acid with the whole peptic chain gets freed by its C terminal and then it is bonded to the N terminal of the new amino acid. Finally the peptic site is freed by the release of the uncharged tRNA and then occupied again by the tRNA charged with the polypeptic chain. As a result, the peptic site remains occupied while the aminoacyl site is freed.

This process is repeated over and over until a stop codon is found in the sequence. Then, the termination step starts.

Termination Once a termination codon is detected, liberation factors are requested and get bound to the ribosome. They free the COO^- group of the terminal amino acid from the tRNA, freeing the polypeptic chain from the tRNA. Once the termination step is done and the complete peptic sequence is liberated, the final structure of the protein can be obtained.

4.2.2 Protein folding

Protein folding is a physical process that occurs to a polypeptide chain and that consists on the adoption of a three-dimensional shape. This process is not driven by any enzyme or organelle –although some enzymes may assist– but it is self-driven.

The functional group of each of the amino acid gives it different chemical properties and inter-residue interaction patterns, which will result in that each unique chain will be folded in a unique three-dimensional structure. The obtained structure is stable, thus becoming a biollogical functionally protein. This three-dimensional structure is possible thanks to the network of non-covalent interactions that are established between the residues.

This three-dimensional structure is the responsible for the functionality of the protein. As said, the three-dimensional structure of the protein locates each side chain of each residue in the required place in order to give it its specific role.

4.2.2.1 Structure of proteins

There are four levels of structure classification:

Primary It is the lowest structural level. It refers to sequence of amino acids in the polypeptic chain with no inter-residue interaction considered.

Secondary It is the second level of structure. It refers to the three-dimensional structures in which pieces of the protein are packed. Two common secondary structures are α-helices and β-sheets. In this two cases, the residues do not interact through their side chains but through the atoms that bond through the peptic bond.

Tertiary It is the highest level of structure classification and it refers to the complete three-dimensional structure, where secondary structures interact. For this tertiary structure, metals or chemical groups, like a heme iron, can be required.

Quaternary It refers to the interaction of different protein units –which can be equal or not–. This union can be needed for the activation of the protein.

4.2.2.2 When protein folding fails

Cells are very complex systems. They contain different organelles, enzymes and macromolecules that generate differentiated regions with different chemical features. Thus, in a single cell there will be regions more or less hydrophilic, regions with higher reducing or oxidising environments, etc.

The combination of these diverse regions with different chemical properties can affect the folding of a protein, making it unsuccessful in some cases.

In order to protect the cell from non-folded or partially-folded proteins, which would have any or non-expected activity, inclusion bodies are formed. Inclusion bodies are aggregates of these wrongly-folded proteins and they have no function in the cell.

Inclusion bodies are often observed when a protein is expressed in a cellular system which is not its natural host, for example when an eukaryote protein is expressed in a procaryote cell. They are also associated to different kinds of diseases.

4.3 Enzyme production for synthetic applications

In the previous section, the production of naturally-present –this is following the dictation of the genetic code contained in the cell– enzymes has been discussed. However, the obtention of enzymes using the specific cell that naturally expresses is not usually suitable for biotechnological applications –like chemical synthesis–.

Enzymes required for biotechnological applications often need some specifications like high solubility, concentration and purity levels. In order to do so, expression systems are used.

An expression system is the combination of a host system and an expression vector that contains the genetic code that will then be translated into the protein. This technique is called recombinant production of enzymes.

Several different host systems are available in the market. They are commonly unicellular systems and they can be both eukaryotic or prokaryotic cells. As an example, bacteria like *Escherichia coli*, yeasts like *Pichia pastoris* or insect cells like *Spodoptera frugiperda* are commonly used as host systems. Each system has characteristic usages and advantages, hence a system or another is used depending on the needs of the protein that is going to be produced.

4.3.1 *Escherichia coli*

E. coli is one of the most widespread expression hosts. Among other advantages, *E. coli* is very useful as an expression system because it is able to produce different types of proteins that can be easily recovered as a soluble solution, it can be easily transformed –that is to incorporate inside the cell the plasmid that codifies for the protein of interest– and it grows fast and in cheap media.

Several different strains of *E. coli* have been developed. These different strains have in common that pathological capabilities have been removed in order to make them suitable for large-scale industrial applications. Besides that, each strain has been developed focusing on solving one or more possible problems in protein production. For example, some of them are able to codify codons not naturally codified in *E. coli*. Others have certain proteases –proteins that work by breaking the peptic bond between two specific amino acids– inhibited. In others the ability to build disulphuric bonds has been enhanced. Nonetheless, the use of *E. coli* is not always optimal: as a prokaryote cell, the expression of eukaryote proteins can be unsuccessful in many cases.

4.3.1.1 Expression vectors for *E. coli*

Since *E. coli* is a bacterium, its DNA is double-stranded, circular and it is spread in the cytosol. In these systems, chromosome, plasmid, and vector are synonyms that refer to the circular piece of DNA that contains genetic code.

Thanks to this configuration, the transformation –that is the process of adding the DNA that codifies for the desired protein– is easily achievable: it is only necessary to generate a channel in the cellular membrane through which the circular DNA in solution can get inside the cell.

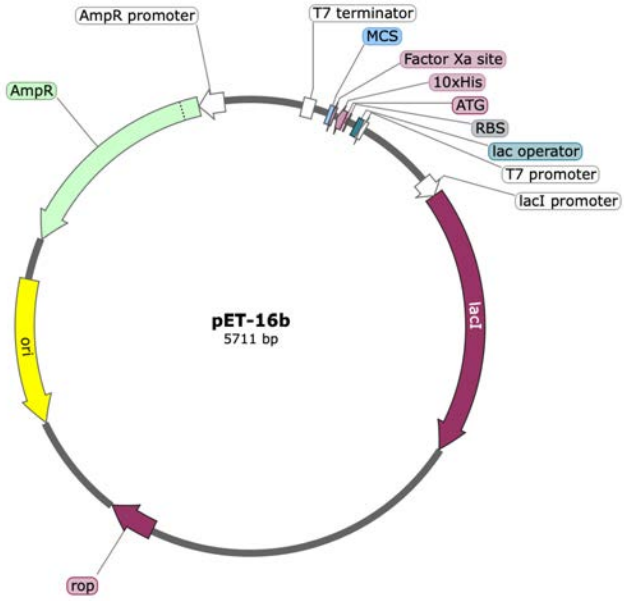

Figure 4.3: Diagram of the different sections of pET16b, one of the most typical expression vectors for *E. coli*

A vector has different sections as Figure 4.3 shows. On the one hand, there is the MCS. Multiple cloning site (MCS) is the point of the DNA where the sequence that codifies for the protein has to be inserted at the vector designing stage. At this point, there are combinations of codons that can be recognised by restriction enzymes –enzymes able to cut specific regions of DNA–, so it is a position where the sequence of the protein can be easily added to the general vector.

This MCS is surrounded by the His tag to the right in some vectors. The His-tag section is a region of codons that codify for a chain of His residues of different length depending on the vector. This His tag is used for the purification of the protein, so it is part of the peptic chain of the expressed protein. It can also be found at the left of the protein's sequence

(the N terminal) or it may be either another kind of tag or it may not be present. It depends on the vector. If the tag is present, an *ATG* codon has to be present previous to the tag, so the expressed protein can include it.

Next to the His-tag, there is the *ATG* codon from the protein's sequence. This codon, as discussed in Section 4.2.1.1, is the starting codon and it codifies to a Met amino acid. This is where the expression of the protein starts.

Also to the right of the MCS, the T7 promoter can be found. This promoter can be different in other families of vectors. Its function is to be recognised by the transcription machinery, so it promotes the protein expression. Before the promoter there is the *lac* operator. It is a piece of genetic code that is inhibited, so the production of the protein can not be carried out although the promoter is recognised. The inhibitor can be easily removed by the addition of induction agents of protein production such as lactose or isopropyl-β-D-thiogalactopyranoside (IPTG). Once the inhibitor is released, the production of the protein can start.

The combination of all these sections will give the cell the ability to recognise the T7 promoter, start the transcription from DNA to RNA from the ATG codon, transcript the His-tag if present, transcript the protein and stop at the T7 termination point.

Moreover, at the left of the MCS in the given example (Figure 4.3), it can be found a section called *AmpR*. This section, called *ampicillin resistance*, is a gene that gives the cell the ability to resist ampicillin, an antibiotic. The vector can contain a resistance gene to a different antibiotic. Thanks to this antibiotic resistance it is possible to distinguish the transformed cells by adding the corresponding antibiotic to the culture media: the cells that will survive will be the transformed ones.

Another relevant section is the one called *ori*. It is the origin of repli-

cation and it is identified by the DNA replication machinery of the cell.

4.4 Biological membranes: composition and function

Biological membranes are cellular components key for life. They play very distinct roles such as the separation of the inside and outside of an organism or an organelle, the control of trespassing molecules or ions, or the storing of transmembrane proteins responsible of signalling or other functions.

Structurally, they are typically 30 Å thick and contain two leaflets. Each leaflet is made of different types of lipids and sterols located with the hydrophilic heads in the outer regions of the membrane, and the hydrophobic tails in the inner region. Thus, they are able to create a bidimensional fluid with a hydrophobic environment in the middle region. Moreover, membranes are not necessarily symmetric, so the composition of the two leaflets can be or not the same. This confers different chemical and physical properties to the membrane.

4.4.1 Membrane composition

The composition of the membranes can be very different depending on the type of membrane –so their cellular location–. They are composed by three different components: phospholipids –the main component–, glycolipids and sterols. Phospholipids (Figure 4.4, left) are glycerol derivatives that contain a phosphatised group in the polar head –there are five possible phosphatised groups– and two fatty acid groups on the hy-

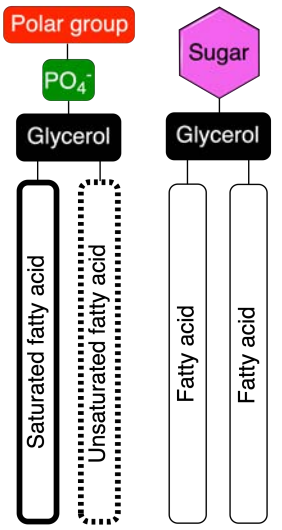

Figure 4.4: Phospholipid (left) **and glycolipid** (right) **schemes.**

drophilic tail, commonly with one of them fully saturated and the other one containing one or more unsaturations. Thus, a great variety of phospholipids can be obtained. Glycolipids are also glycerol derivatives that have a sugar in the hydrophilic head and two lipids on the hydrophobic tail. In opposition with phospholipids, glycolipids are a special kind of lipids that are only found on outer plasmatic membrane.

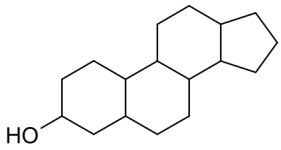

Figure 4.5: Structure of the skeleton of a sterol

Sterols (Figure 4.5) are cyclic compounds made of four fused cycles, three of them of six carbons and the last one of five carbons. Furthermore, they contain a hydroxy group in the first ring. The most common sterol is cholesterol and it can be found in concentrations up to one molecule per ten phospholipid molecules.

4.4.2 Membrane function

As said before, the main function of membranes is separate biological environments like the cell from the outside or the nucleus from the cytosol in eukaryote. However, they also carry out other functions.

The composition of the membrane is important for the development of its function. For example, glycolipids work as recognition sites for other cells and they assist in the formation of tissues[123] and that is why they are found on the outer leaflet of the plasma membrane.

Another very important role of the membranes is the allocation of proteins. Around one third of the human's proteins is a membrane protein, either integral –all the protein crosses the membrane– or peripheral –the protein is submerged in the membrane but it does not cross it–. Four very crucial roles are attributed to this membrane proteins: reception, transport, cell adhesion and catalysis. Protein receptors related with biosignalling are found in the membranes, for example. They are able to

detect a signal on one side of the membrane and transmit it to the other side. Transport proteins are able to take ions or chemicals from one side of the membrane and transport them to the other site. Proteins related to cell adhesion are proteins located in the plasmatic membrane that are able to recognise other proteins from other cells and make the cells interact. Finally, some membrane proteins are also capable of performing enzymatic reactions.

Chapter 5

Experimental methods and techniques

5.1 Introduction

In this section the most important and general methods related to the experimental work carried out during this Thesis will be introduced. Firstly, the general protocol for the protein expression, as well as the most relevant procedures within the protocol, will be presented. Then, analytic chemistry methods used in order to follow the performed reactions and to determine the obtained products will also be reviewed.

5.2 Protein expression

The production of proteins for further application in biotechnological experimentation is a widely used procedure both in investigation and in the industry. Because of this, the production of proteins is a very standardised procedure. The most important methods regarding the expression of proteins and their analysis will be developed below.

5.2.1 General protocol

Let's consider a protein that has to be expressed in a soluble media. Let's consider also that *E. coli* and a suitable vector have been chosen as the expression system. To meet this goal, there is a general order of steps that has to be followed:

1. A *E. coli* strain has to be chosen.

2. A vector is designed from the selected general vector. There are several types of vectors that can be chosen, but some considerations need to be taken: the vector has to be suitable for the length of the protein sequence –there are more appropriate vectors depending on the length of the sequence–. Moreover, the antibiotic resistance has to be considered too –for example, if the *E. coli* strain has a gene that gives it resistance to an antibiotic, it is not optimal to choose a vector that gives resistance to the same antibiotic because then it will not be possible to exclusively select the transformed colonies–.

3. *E. coli* cells have to be treated in order to make them super competent. That is, the cellular membrane is treated in such a way that channels can be opened by applying heat, for example. Therefore, the cells can accept the exogenous plasmid. Competent cells are

also purchasable, so they can be used right away with no previous treatment.

Once the cells are super competent, they can be transformed by mixing them with the vector and applying the appropriate conditions. If channels can be opened by applying heat, for example, the transformation is carried out by heating the cells mixed with the vector in a solution at a specific temperature for a short period of time. Then, it is needed to low the temperature using an ice bath so the holes get closed and the membrane gets back to its natural state. At this point, cells should contain the plasmid in the cytosol.

4. The transformed cells are cultivated in a solid culture media containing the appropriate antibiotic(s). This culture is grown and one or several of the obtained colonies are extracted and transferred to a liquid culture media –containing the antibiotic too–. This liquid culture is grown.

5. Once the concentration of cells is high enough, the expression inductor (for instance, lactose or IPTG) is added. At this point, the cell's machinery focuses on the production of protein and not on cellular reproduction. The cells are incubated for a certain period of time.

6. After the last incubation, cells should contain a high concentration of the desired protein in their cytosol. In order to liberate the protein to the cytosol, the culture is harvested by sonication, a physical process that breaks the cellular membrane, or by the addition of chemical agents such as detergents. Hence, the membrane breaks and the cytosolic content is liberated to the media.

7. At this point, the culture media contains the protein in a soluble form but also the membrane, the organelles and other proteins and

chemicals from the cell. This mixture can be used in some cases as the enzymatic solution. In some other cases, a purification step is needed so a solution containing only the protein of interest is obtained. In order to do so there are several different methods, but one with a high performance uses to be the purification by chelation of the His tag with a Ni-agarose resin. This type of purification is based on affinity chromatography and it can be carried out both manually or automatically.

5.2.2 *Escherichia coli* transformation

The first step for the production of a protein is to obtain a strain of the expression host with the expression vector introduced. This process is called transformation.

Protocol for transformation

The protocol for the transformation of the vast majority of *E. coli* strains goes as follows.

1. Unfreeze the supercompetent cells (around 50 µL of commercial cells) on ice. Thaw them gently to get a homogeneous suspension of cells.
2. Add 1 µL of plasmid DNA [1-10 $\frac{\text{ng}}{\mu\text{L}}$]. Stir gently by inversion to mix.
3. Place the tube on ice for 5 min.
4. Incubate the tube at 42 °C for exactly 30 s.
5. Place the tube back on ice for 2 min.
6. Add 250 µL of super optimal broth with catabolite repression (SOC) medium to the tube. Mix gently to ensure the resuspension of the

cells in the media. Add the corresponding antibiotic(s) depending on the *E. coli* strain and the antibiotic resistance introduced by the expression vector.

7. Incubate the culture at 37 °C at 250 rpm for 60 min.

8. Plate the cells on a solid plate containing culture media and the corresponding antibiotic(s). Place the plate at 37 °C overnight (O/N) until grown-enough colonies are observed.

5.2.3 *Escherichia coli* culture and protein expression induction

Once the cells are transformed, *E. coli* cells are suitable for protein expression. Several methods can be used for the expression of enzymes.

5.2.3.1 Protocol for induction with IPTG

This protocol can be applied to the vast majority of *E. coli* strains.

1. Prepare 2 mL of Luria-Bertani (LB) medium with the appropriate antibiotic(s).

2. Take a colony from the plate using a micropipette tip or an inoculation loop. Insert it in the LB medium.

3. Let the culture grow O/N at 37 °C, 220 rpm.

4. Measure the optical density (OD) at 600 nm with a spectrophotometer. Calculate how much volume of the pre-inoculate is required for an initial OD^{600nm} of 0.02 depending on the culture volume.

5. Prepare the required volume of LB medium and add the appropriate antibiotic(s). Inoculate the culture with pre-inoculate.

6. Let the culture grow until an OD^{600nm} of 0.6-0.8 at 37 °C, 250 rpm.

7. Add IPTG for the final concentration (1 mM or 0.25 mM, for instance).

8. Let the culture grow O/N, at 37 °C, 220 rpm or for 24 h, at 16 °C, 220 rpm. The conditions of incubation for induction will depend on the case.

9. Centrifuge the culture for 20 min, at 10 000 g, 4 °C.

10. Remove the supernatant.

11. Add the required buffer (4 mL/g of pellet) and resuspend the pellet.

12. Sonicate the resuspension.

13. Centrifuge the culture for 20 min, at 10000 *g*, 4 °C. Recover the supernatant and freeze it.

5.2.3.2 Protocol for auto induction

The auto induction protocol goes as follows. This protocol can be applied to the most of *E. coli* strains. The presented protocol below is an adaptation from Fox and Blommel [124].

Solutions

- Growing medium (350 mL):
  - 350 mL of distilled H_2O.
  - 4.8 g of triptone.

  - 9.6 g of yeast extract.

- Salts mix:
  - 221.3 mM of KH_2PO_4.
  - 221.3 mM of Na_2HPO_4.
  - 442.6 mM of NH_4Cl.
  - 44.3 mM of Na_2SO_4.
  - 354.3 mM of $CaCl_2$.
- 1 M of $MgSO_4$.
- 50% (v/v) of glycerol.
- 25% (w/v) of glucose.
- 20% (w/v) of lactose.

All solutions have to be autoclaved, except glucose and lactose solutions that have to be filtered.

Protocol

1. Prepare 10 mL of LB medium with the appropriate antibiotic(s).
2. Take a colony from the plate using a micropipette tip, an inoculation loop, or take a crioball or 2 µL of glycerinate. Insert in the LB medium.
3. Let the culture grow O/N at 37 °C, 220 rpm.
4. Measure the OD at 600 nm. Calculate how much volume of the preinoculate is required for an initial $OD^{600\,nm}$ of 0.02 for 200 mL of culture.

5. Mix 175 mL of growing medium, 22.6 mL of salts' mix, 2 mL of glycerol solution, 2 mL of lactose solution, 400 µL of $MgSO_4$ solution, 400 µL of glucose solution, the appropriate antibiotic and 2 mL of saturated culture.

6. Let the culture grow until an $OD^{600\,nm}$ of 0.6-0.8 at 37 °C, 250 rpm.

7. Low the temperature to 20 °C and let the culture incubate for 48 h.

8. Centrifuge the culture for 20 min, at 10000 g, 4 °C.

9. Remove the supernatant. At this point, the pellet can be frozen for conservation.

10. Add the required buffer (4 mL/g of pellet) and resuspend the pellet.

11. Sonicate the resuspension.

12. Centrifuge the culture for 20 min, at 10000 g, 4 °C. Separate the supernatant and freeze it.

5.2.4 Protein purification

Once the protein is expressed it might be necessary to purify it in order to remove the matrix of proteins and chemical compounds.

Several techniques are available for protein purification. The most common ones are size-exclusion filtering, ion-exchange chromatography, and affinity chromatography. During the present Thesis, two variations of affinity chromatography with Ni are used. As introduced in Section 4.3.1.1, to perform affinity chromatography a His tag has to be introduced in the protein sequence. All proteins expressed during the Thesis will have a His tag in their sequences.

5.2.4.1 Affinity chromatography with FPLC

Fast protein liquid chromatography (FPLC) is an automated liquid chromatographic technique. It is based in the same principles than high-performance liquid chromatography (HPLC). fast protein liquid chromatography (FPLC) is also based on affinity chromatography's principles. Typically, a Ni-agarose is used so a His tag has to be incorporated in the protein's sequence.

The main advantages of FPLC in comparison to the traditional techniques is that FPLC is more reliable, the protein detection in each step can be monitored during the whole process, and it can be automated.

The general protocol starts with the charging of the column. Then, a buffer with a low content of imidazole is injected for a few column volumes. Then, some binding buffer is mixed with elution buffer, which has a higher concentration of imidazole. Then, a gradient that ends up in a 100 % content of elution buffer. Finally, some volume columns of elution buffer are run.

Buffers for purification

- Binding buffer:
  - 0.02 M of Na_2HPO_4.
  - 0.5 M of NaCl.
  - 30 mM of imidazole.
- Elution buffer:
  - 0.02 M of Na_2HPO_4.
  - 0.5 M of NaCl.
  - 1 M of imidazole.

Protocol

1. If required, charge the column with a Ni^{2+} solution. Once charged, install the column in the FPLC.
2. Prepare 10 mL of lysate. Add a cocktail of inhibitors of proteases if needed before.
3. Inject the lysate in the FPLC.
4. Start running the gradient:
   - 4.1. 22 column volumes: 100 % binding buffer, 0 % elution buffer.
   - 4.2. 5 column volumes: 95 % binding buffer, 5 % elution buffer.
   - 4.3. 10 column volumes: Binding buffer from 95 % to 5 % and elution buffer from 5 % to 100 %, respectively.
   - 4.4. 8 column volumes: 0 % of binding buffer, 100 % of elution buffer.

5.2.5 Protein analysis

Several techniques for protein determination have been developed. Nonetheless, each technique gives different information.

One of the most used techniques is electrophoresis, specifically Sodium Dodecyl Sulfate (SDS)-Polyacrylamide Gel Electrophoresis (PAGE). Using this technique, proteins from a protein mixture are separated by their molecular mass, which can be then stained with different techniques. Two of the most common staining techniques will be also reviewed.

5.2.5.1 SDS-PAGE

As said before, SDS-PAGE is a technique that allows the separation of a mixture of proteins by their mass in a gel.

Sodium Dodecyl Sulfate (SDS) is a surfactant that attaches to the protein structure (in a ratio SDS molecule:amino acid 2:1), causing its denaturalisation and giving the protein a negative charge even when the protein is naturally charged. This allows the analysis to be only mass-dependant, avoiding the effects of the tertiary structure and the natural charge of the protein.

Solutions

- Running buffer (25 mM tris(hydroxymethyl)aminomethane (TRIS), 192 mM glycine, 1% SDS):
  - 3 g of TRIS.
  - 14.4 g of glycine.
  - 1 g of SDS.
- Destain solution:
  - 10 % methanol.
  - 30 % of acetic acid 100 %.
- Comassie solution (1 %):
  - 1 g of Comassie R250 solution.
  - 650 mL of distilled water.
  - 300 mL of methanol.
  - 50 mL of acetic acid 100 %.

Protocol for gel preparation

1. Assemble the glass plates in the bracket and put the ensemble in the holder.

2. Prepare the separation gel by mixing in order the following ingredients. Water and acrylamide volumes will depend on the desired gel density. As an example, the following quantities are needed for preparing a 10% polyacrylamide gel:

   - 4.1 mL of H_2O.
   - 3.3 mL of Acrylamide/bis (30 % 37.5:1).
   - 2.5 mL of TRIS-HCl 1.5 M, pH 8.8.
   - 100 µL of SDS, 10 %.
   - 10 µL of N,N,N′,N′-tetramethylethylene-diamine (TEMED).
   - 32 µL of ammonium persulfate (APS), 10 %.

3. After the addition of APS, the polymerisation will immediately start. Transfer quickly the mixture to the glass plates leaving around 2 cm free on top for the stacking gel.

4. Add a thin layer of isopropanol on top of the gel in order to avoid bubbling in the surface of the gel.

5. Let the gel polymerise for around 20 min to 30 min

6. Once polymerisation is complete, the stacking gel can be prepared. Remove carefully the isopropanol with filter paper until total dryness.

7. Mix the following ingredients in order:

   - 6.1 mL of H_2O.
   - 3.3 mL of Acrylamide/bis (30 % 37.5:1).
   - 2.5 mL of TRIS-HCl 0.5 M, pH 6.8.
   - 100 µL of SDS, 10 %.

- 10 µL of TEMED.
- 100 µL of APS, 10 %.

8. Pour the mixture quickly on top of the polymerised separation gel until the top of the glass plates.

9. Place the comb in the gel in order to create the wells for further sample charging. Be careful not to generate air bubbles between the gel and the comb.

10. Let the gel polymerase for around 20 min to 30 min.

Protocol for sample preparation

1. Mix 3 µL to 10 µL of sample with 10 µL of a reductor buffer and water until 21 µL of total sample volume.

2. Place the sample in the thermocycler at 95 °C for 5 min.

Protocol for sample charging and electrophoresis

1. Place the glass plate with the polymerised gel in the clamp gel with a plastic plate. Place the ensemble in the electrophoresis chamber.

2. Fill the space between plates and the camber with running buffer.

3. Remove carefully the comb from the glass plate.

4. Charge in each well the samples and at least one protein ladder.

5. Place the cover, plug into the power supply and configure it at 100 V to 150 V. Run the electrophoresis until the protein ladder reaches the bottom of the gel.

6. Remove the glass plate from the buffer, open it carefully and keep the gel for further staining.

5.2.5.2 Coomassie staining

Once the electrophoresis has run, proteins have to be stained in order to make them visible. Coomassie staining is a method that reveals all the proteins in a non-specific way.

Protocol for staining

1. Place the gel in a container being careful that it does not break.
2. Add Coomassie solution until full coverage of the gel.
3. Cover the container and place it in a shaker for at least 30 min.
4. Remove the staining solution and add destain solution. Clean it by manually shaking and remove the dirty solution.
5. Add clean destain solution again, place the container in the shaker and let it distinct O/N or until gel's destain. Change the solution if too dirty.
6. Remove the last amount of destain solution, dry the gel and scan or photograph it.

5.2.5.3 Western-Blot staining

In opposition to Coomassie staining, Western Blot (WB) is a technique that allows the staining of a specific protein by the use of specific antibodies. WB is a more complex technique that requires a previous transference of the gel to a membrane. Then, it is stained.

Different antibodies can be used for the staining of different proteins. In this case, a generic His-tag antibody will be used since the protein of interest is the only one containing a His-tag. Other protein- or tag-specific antibodies could be used if needed.

Solutions

- Transference solution, 1X (1 L):
  - 18 g of glycine.
  - 3.78 g of TRIS base.
  - 125 mL of methanol.
  - 875 mL of H_2O.
- Tris buffer solution (TBS), 10X (1 L):
  - 24.2 g of TRIS.
  - 80 g of NaCl.
  - 202 g of KCl.
  - 1000 mL of H_2O.
  - pH 7.6.
- TBS, 1X:
  - 100 mL of TBS 10X.
  - 900 mL of H_2O.
- Tween-tris buffer solution (TTBS) 1 L:
  - 100 mL of TBS 10X.
  - 900 mL of H_2O.
  - 1 mL of Tween 20.

Protocol for protein transfer to membrane

1. Prepare of transference sandwich:

    1.1. Prepare two paper filters with a shape similar to the sponges. Prepare a membrane slightly smaller than the paper filter avoiding touching the membrane.

    1.2. Place the membrane in a container and add methanol for 10 min in order to activate it. Clean the membrane with bidistilled water.

    1.3. Keep the gel in transference solution. Humidify all the components of the sandwich with the solution.

    1.4. Mount the sandwich in the cassette by placing a black sponge, a white sponge, the filter paper, the membrane, the gel, the other filter paper, a white sponge and a black sponge.

2. Remove the bubbles between the gel and the membrane in order to ensure a correct transference of the proteins.

3. Place the transference solution in a WB chamber. Place also a freezer ice.

4. Place the cassette into the chamber, add a magnetic stirrer, and start the power supply at 100 V for 1 h under agitation.

5. Remove the sandwich from the chamber, recover the membrane, and cut it with the shape of the gel. Place the membrane in a container and wash it with distilled H_2O for 15 min.

6. Add reversible, all-protein Ponceau staining for some seconds in order to check that the transference has been successful. Once bands are seen, remove the staining solution and wash the membrane with distilled H_2O and destain with transference solution.

Protocol for specific staining

1. Prepare a solution of 5% dehydrated milk and TTBS by mixing 5 g of milk in 100 mL of TTBS.

2. Add 15 mL of the TTBS-milk solution and place the container in a shaker for 1 h.

3. Wash the membrane three times with TTBS for 10 min.

4. Add 3 µL of primary anti-His antibody to 15 mL of TTBS-milk solution.

5. Add the antibody solution to the membrane and place the container in a shaker at 4 °C O/N.

6. Wash the membrane three times with TTBS for 10 min. Remove the last volume of TTBS.

7. Prepare a solution of TTBS-milk with 3 µL of goat anti-mouse secondary antibody.

8. Add the solution to the membrane and incubate it by shaking at room temperature for 1.5 h.

9. Reveal the membrane adding the chemiluminescence solutions to the membrane as the instructions say.

10. Place the treated membrane between two transparent sheets and reveal in a Bio-Rad ChemiDoc system using the chemiluminescence mode.

5.3 Chemical analysis

As mentioned in the Introduction (Chapter 1), the reactants and products treated in this Thesis are small molecules. Moreover, reactions are carried out by enzymes and several of them might be involved in the global process. Thus, the reactants, intermediates and products have to be analysed in order to identify which compounds are obtained and the reactions' yields.

In order to analyse these compounds, HPLC and HPLC-mass spectrometry (MS) techniques will be used in order to identify which compounds are being obtained and how much of them is obtained.

In this Section, the techniques will be introduced but methods will not be developed since they are specific for each system and reaction. Thus, the methods for each analysis will be detailed in the corresponding Chapters.

5.3.1 HPLC

HPLC is an automated chromatographic technique. Its high performance abilities allow this technique to achieve a very high separation of the different chemical compounds using small amounts of mobile phase in a fast, reproducible way.

HPLC instruments are made of four different parts: the injector, the mobile phase, the stationary phase, and the detector.

5.3.1.1 HPLC fundamentals

As said before, HPLC method is a chromatographic technique. Fundamentally, a solution containing one or several chemicals is forced through a stationary phase by the application of pressured mobile phase. The different interaction rates between the compounds and the stationary phase

will be the responsible for the separation of the compounds. The mobile phase pushes the compounds through the column until they get the detector, which registers a signal which is then used for building the chromatogram.

HPLC can be adapted to each analysis by the use of different mobile and stationary phases and detector. Moreover, mobile phases can be adjusted by the use of mixtures of solvents in different amounts and proportions during a single analysis. Thus, each analysis can be optimised, so optimal separation and detection of all of the compounds in a mixture can be achieved.

5.3.1.2 HPLC components

HPLC instruments are composed of at least three parts: the injector, the column and the detector.

Injector The injection of the sample is a crucial step of any HPLC analysis. The whole sample has to be injected at once in order to make the analysis reproducible. Manual injection and automatised injection are possible, but nowadays automised injection is more common.

Column Combined with the mobile phase, the stationary phase is one of the most important parts in an HPLC method. The two most important types of columns are the straight phase (SP), which is made of plain silica, so it is polar; and the reverse phase (RP), which is made of functionalised silica containing typically C_{18} chains, but different types of functionalisation are possible, even chiral groups can be added for separation of chiral compounds. Nowadays, RP columns are much more common.

Detector The detector is the element of the HPLC that will convert the concentration of each sample into a signal, so that the chromatogram can be built. Different detectors are available, both destructive and non-destructive, and the most common ones are UV, Vis, Refractive Index Detector, Charged Aerosol Detector among others.

5.3.2 HPLC-MS

HPLC-MS is a HPLC-derived technique that adds the advantages of mass spectrometry (MS) to HPLC. Thus, each of the HPLC-detected components is further analysed using MS techniques.

5.3.2.1 MS fundamentals

MS is an analytical technique that measures the mass-to-charge ratio of a compound, which has to be either ionic or ionised. Commonly, compounds are ionised by the application of a beam of electrons that will produce a beam of charged moieties which are unique for each molecule. This uniqueness makes the spectrum of a certain molecule unique, so spectra can be used as molecular fingerprints for identification.

5.3.2.2 MS components

MS instruments have three main parts: the ionisation chamber, the mass analyser and the detector.

Ionisation chamber The ionisation chamber is the part of the MS where the compound is ionised by the action of a chemical reaction, an electron beam or a laser. Once ionised, ions are accelerated. The ionisation method is responsible for the fragmentation rates of the analysed compounds.

Mass analyser The mass analyser is the part that separates the ions by their mass-to-charge ratio thanks to the application of a magnetic or electric field. Different analysers such as time-of-flight (TOF) or quadrupole analyser are available.

Detector The detector is the part of the system that quantifies the separated ions. The collected information is used for building the spectrum.

Part III

Lipoxygenases' versatility

Chapter 6

Characterising Human and Mouse ALOX15B and Crossing Their Reaction Specificities

The work presented in this Chapter corresponds to Kakularam et al.[125]*. The publication and the Supporting Information can be found in Chapter SI6. The experiments have been performed by myself at Hartmut Kühn's laboratory at Institut für Biochemie, Charité, Berlin during my stay. The computational studies have been carried out at the UAB.*

6.1 Introduction

Human and mouse ALOX15B isoforms are two enzymes from the ALOX family. Although they share a high identity of 78 % and their foldings are structurally very similar –RMSD of the C_αs of 0.888 Å–, their regioselectivities are different.

*hum*ALOX15B is one of the six ALOXs encoded in the human genome. Its encoding gene is located in the short arm of the chromosome 17[126]. On the other hand, *mou*Alox15b is one of the seven encoded ALOXs by mouse. Its gene is located in a similar region than in the human's genome, but in chromosome 11[126;127].

*hum*ALOX15B was firstly described in 1997[80]. It was reported to be highly expressed in skin, prostate, lungs and cornea. On the other hand,

*mou*Alox15b was firstly described in 1991[81]. Initially, it was reported as an 8-LOX, but it was later related to *hum*ALOX15B and therefore renamed as *mou*Alox15b.

Even though these two enzymes are very similar, their regioselectivities are very different. On the one hand, AA incubation with *hum*ALOX15B produces 15-HETE as the main product[80;128]. On the contrary, the main product of the incubation with *mou*Alox15b is 8-HETE[81].

AA, so no complete study of the enzymatic reactivities including other PUFAs has been ever carried out. In this chapter, a complete view of the regioselectivity exchanging between *hum*ALOX15B and *mou*Alox15b is presented using experimental and computational methods.

6.2 Methods

Experimental and computational techniques have been used for the study presented in this Chapter. On the one hand, incubations with different PUFAs have been carried out with recombinant enzymes. The obtained products have been analysed using HPLC techniques. On the other hand, computational models of the four variants of the enzymes have been prepared and combined with different PUFAs. Docking and MD simulations have been performed.

6.2.1 Experimental Methods

Along this section, a general view of the different techniques and methodologies used for performing the experiments will be given.

Different experiments have been carried out in order to study the enzymatic conversion of the enzymes' variants. AA, EPA, DHA, and LA have been used as substrates. WT *hum*ALOX15B, Asp602Tyr and Val603His *hum*ALOX15B's mutant, WT *mou*Alox15b, and Tyr603Asp

and His604Val *mou*Alox15b's mutant have been expressed and incubated with the substrates.

Sources of the used chemicals for the experiments can be found in Kakularam et al.[125].

6.2.1.1 Cloning, Expression and Mutagenesis

Sequences of the WT *hum*ALOX15B and *mou*Alox15b have been obtained from the NCBI cDNA database[129]. They have been optimised for expression and chemically synthesised by a provider and subcloned into the pET28b(+) vector, so expression sequences containing N-terminal hexa-His-Tag fusion proteins are obtained.

E. coli Rosetta2 (DE3) *pLysS* strain has been used. It has been transformed as described in Reisch et al.[130]. After transformation, one single, isolated clone has been selected. Proteins have been expressed using the expression induction agent IPTG, incubated for 18 h and harvested and homogenised by sonication. Purification has been tested but big activity loss has been detected for the mutant versions, so cell-free supernatant has been used as enzyme source.

Mutant versions of the two enzymes have been prepared using a mutagenesis protocol. WT enzyme-codifying DNA sequences have been incubated with specific primers containing the changes in sequences that correspond to the mutations to be applied. A PCR protocol has been performed and resulting chains have been digested with a restriction enzyme and *E. coli* XL-1 Blue competent cells have been transformed and sequenced to check the success of the mutagenesis. The same expression protocol used for the WT enzymes has been used for the expression of the mutant variants.

The expression levels have been quantified using SDS-PAGE combined with a chemiluminescence method for protein quantification, for which

known amounts of *M. fulvus*'s ALOX have been used for calibration.

6.2.1.2 In Vitro Assays and HPLC analysis

In vitro assays have been performed incubating 100 µM of AA, EPA and DHA with different amounts of enzymatic solution depending on their expression levels.

The obtained products have been analysed by RP-HPLC. A C_{18} column has been used as stationary phase and an ACN:H_2O:CH_3COOH 70:30:0.1 (by volume) mobile phase has been used for all analyses except for EPA incubations, where the employed mixture is 50:50:0.1. The flow rate has been set at $1\,mL\,min^{-1}$. Products have been detected using a UV detector and retention times have been attributed to products by comparison with authentic standards.

SP-HPLC and CP-HPLC have been employed for further, more detailed analysis of LA incubations and 12-HETE's enantiomers separation, respectively. Mobile phases of n-hexane:2-propanol:CH_3COOH 100:2:0.1 and of n-hexane:methanol:ethanol:CH_3COOH 96:3:1:0.1, have been used in conjunction with SP and CP columns, respectively.

6.2.2 Computational Methods

The computational study for this present work has been focused on molecular docking and MD simulations. All four enzymes (WT *hum*ALOX15B, WT *mou*Alox15b, Asp602Tyr and Val603His *hum*ALOX15B's mutant, and Tyr603Asp and His604Val *mou*Alox15b's mutant) have been modelled. For Docking simulations, AA, EPA, DHA and LA have been used as substrates, whilst AA, 8*S*-HETE and 15*S*-HETE have been selected as substrates for the MD simulations.

6.2.2.1 Structure Setup

WT structure of *hum*ALOX15B has been obtained from the X-ray crystallographic structure –PDB ID 4NRE–[131], while WT *mou*Alox15b has been obtained as a predicted structure from the AlphaFold Database[132;133] – UniProt[134] ID O35936–. Since it is a predicted structure, no cofactors are present so they have been extracted from the *hum*ALOX15B structure. The Fe-coordinating residues have been rotated towards the Fe atom to properly describe their interaction.

Mutated enzymes have been manually built using the `Rotamers` module from `UCSF Chimera`[135].

All four built structures have been protonated at the physiological pH of 7.4 using the `ProteinPrepare` tool[136] from `playmolecule.org`.

6.2.2.2 Docking Calculations

Docking simulations have been performed using `GOLD` in its 5.8 version[87]. `ChemScore`[137] has been used as the fitness function for scoring the obtained solutions. AA, EPA, DHA and LA have been used as substrates.

6.2.2.3 MD Simulations

The best scored AA-containing solutions in head- and tail-first orientations with each of the enzymes have been chosen for carrying out the MD simulations. Additionally, the best-scored 8*S*-HETE and 15*S*-HETE tail- and head-first solutions, respectively, have been also chosen for performing MD simulations. Hence, 16 MD simulations have been calculated.

`ff19SB AMBER`'s force field[90] has been chosen for describing the standard residues of the enzymes. Fe and Fe-coordinating residues and cofactor have been parametrised following the Seminario Method[138] using the `MCPB.py`[139] from `AmberTools`[140]. The 6-31G(d)[141]/B3LYP[142] level

of theory has been used using `Gaussian16`[143] for performing the QM calculations, including the force constants and `RESP` charges[144] calculations. Moreover, `RESP` charges for the substrates have also been obtained using the same methods. Substrate's parameters have been obtained from `GAFF AMBER`'s force field[145]. All systems have been solvated with a pre-equilibrated orthorhombic box of OPC water molecules[146], the recommended water model to use in conjunction with the `ff19SB` force field[90]. The limits of the solvation box have been defined at 10 Å from the outermost atom in each direction.

`AMBER20`'s[94] `CUDA`[147;148] version of the `pmemd` program has been used as the MD engine. The initial structures have been minimised. From the minimised structures, temperature has been increased from 0 to 300 K in six steps of 50 K each, followed by 20 ps of equilibration per step. Once heated, 1 ns of NPT simulation at 300 K and 1 atm have been run to stabilise the solvation box. Finally, 10 ns of NVT simulation at 300 K have been carried out followed by 100 ns of production in the same conditions.

6.3 Results and Discussion

Along this section, the experimental and computational results obtained during this study will be explained and discussed in order to give a complete perspective of the study.

6.3.1 Experimental Results

Several experiments have been performed in order to understand how the specificity and selectivity of the different ALOXs change. These experiments mainly involve incubations with different substrates to gain a wide perspective of the behaviour of the WT enzymes and the effects of mutations.

6.3.1.1 Recombinant Expression of Wild-Type ALOX15Bs and mutants

The four enzymes have been expressed as recombinant enzymes in *E. coli* systems. The expression levels of each of the enzymes have been tested and quantified, as explained in Section 6.2.1.1. Results can be found in Table 6.1 and Figure 6.1.

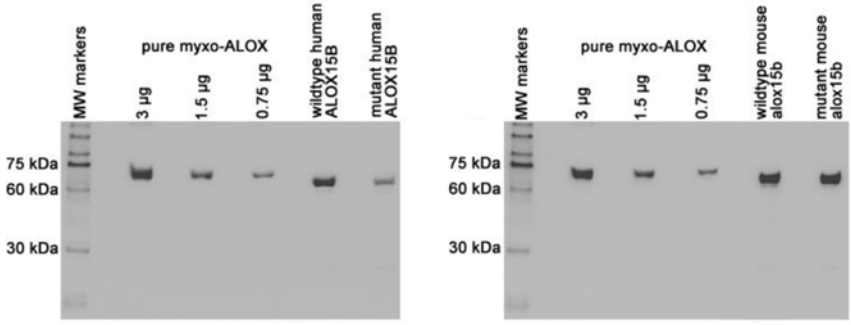

(a) humALOX15B *(b) mouAlox15b*

Figure 6.1: Quantification of the expression levels of the four prepared enzymes.

Table 6.1: Concentration of expressed protein from cell-free supernatants for the expression of the four enzymes.

Enzyme Variant	Expression Level (mg ALOX Protein per L Bacterial Liquid Culture)
WT *hum*ALOX15B	200
WT *mou*Alox15b	700
Asp602Tyr and Val603His mutant of *hum*ALOX15B	170
Tyr603Asp and His604Val mutant of *mou*Alox15b	292

The measured concentrations of the four expressed enzymes are quite different between them (Table 6.1). The purification of the solutions has been tested but a loss of around 90 % on the activity has been observed for the mutants, so cell-free supernatants will be used for the assays.

6.3.1.2 Substrate specificity

Volumes with equivalent activity of each enzymatic solution have been incubated for 5 min with AA, EPA, DHA and LA. The obtained products have been analysed in terms of relative activity towards each substrate and the results have been plotted in Figure 6.2.

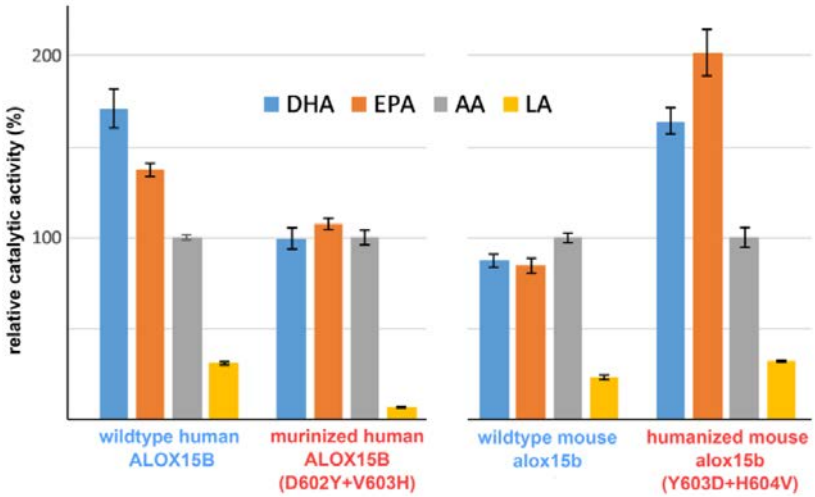

Figure 6.2: Relative activities of WT and mutant versions of humALOX15 and mouAlox15b. AA activity has been set as 100%. All products have been detected by RP-HPLC with a UV detector after 5 min of incubation.

On the one hand, WT *hum*ALOX15B prefers DHA as a substrate, although EPA and AA are also very good substrates. However, LA has been observed not to be a good substrate for this enzyme. These results

are consistent with previous reported data[80]. In comparison, murinised *hum*ALOX15B has a very similar specificity towards DHA, EPA and AA, but LA is not a good substrate.

WT *mou*Alox15b has the same behaviour, although the AA is slightly a better substrate than DHA and EPA. The humanised *mou*Alox15b has a higher specificity for EPA, followed by DHA and AA, respectively. As it happened with the human enzymes, LA is not a good substrate for any of the *mou*Alox15b variants.

6.3.1.3 Murinisation of humALOX15B

The Asp602Tyr and Val603His mutantions applied to *hum*ALOX15B are able to change the products' profile. Whilst WT *hum*ALOX15B converts AA into 15*S*-H(p)ETE, the double mutant's major product is 8*S*-H(p)ETE, the same major product than the WT-*mou*Alox15b's[128]. The analysis of the products' profile has been done for the WT and murinised *hum*ALOX15B variants with AA, DHA, and EPA. Results can be found in Figure 6.3.

The selectivity change for AA and EPA by the murinisation is similar. In both cases, the 8-HETE or 8-HEPE is the major product, while the 15-HETE/HEPE and 5-HETE/HEPE are the minor ones. The case for the DHA is different. The 7-HDHA –equivalent to the 5-HETE– product is the major one, whilst the 17-HDHA –equivalent to the 15-HETE– and the 10-HDHA –equivalent to the 8-HETE– ones are the minor ones. It is interesting to highlight that the behaviour observed for the DHA is new since its products' profile is different from the WT *mou*Alox15b (Figure 6.5). Thus, the double mutant of the *hum*ALOX15B does not mimic completely the WT *mou*Alox15b.

As mentioned in Section 6.3.1.2, LA is not a good substrate of any of the studied enzymes. However, the addition of surfactants –not naturally

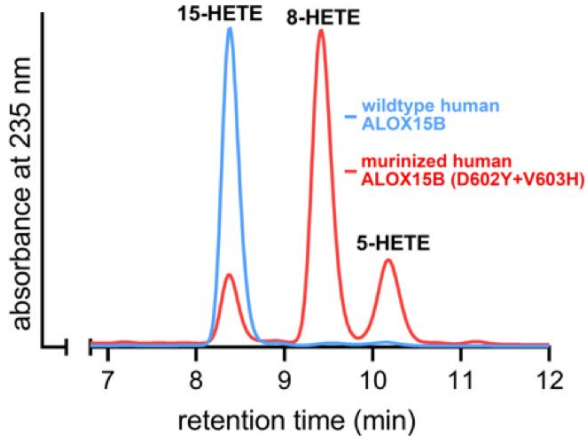

(a) AA as substrate

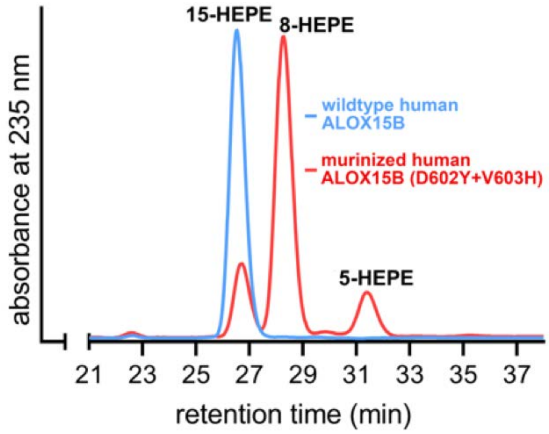

(b) EPA as substrate

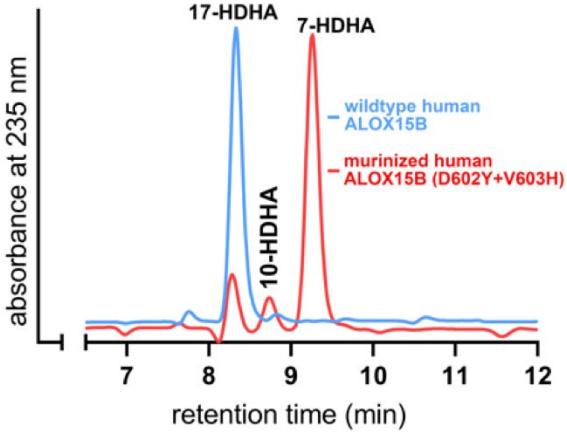

(c) DHA as substrate

Figure 6.3: RP-HPLC-detected products of WT and murinised humALOX15B incubations.

present in mammalian cells– allows the reactivity with ALOX15Bs. The obtained products analysed by SP/CP-HPLC can be found in Figure 6.4.

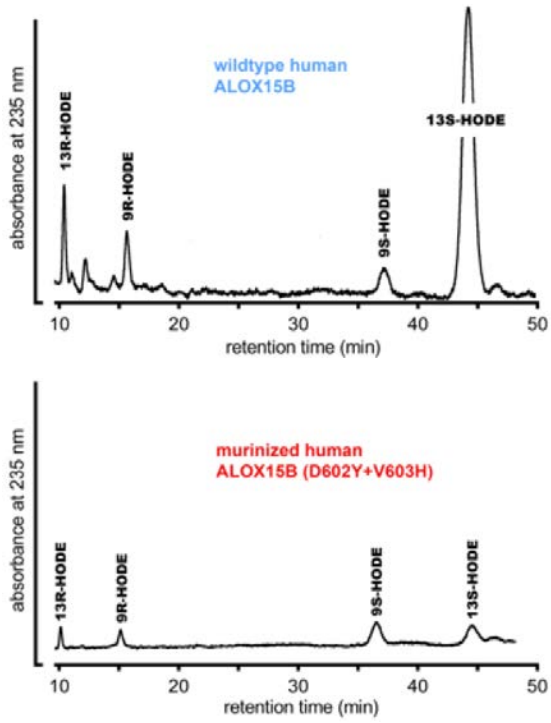

(a) WT humALOX15B

(b) Murinised humALOX15B

Figure 6.4: NP/CP-HPLC-detected products of LA incubations with WT and murinised humALOX15B incubations.

The major product of the incubation with the WT *hum*ALOX15B is 13*S*-HODE. On the other hand, the murinised *hum*ALOX15B is not able to substantially transform LA and a non-racemic mixture of the four possible products –9*S*-, 9*R*-, 13*S*- and 13*R*-HODE– is obtained.

6.3.1.4 Humanisation of mouAlox15b

The same assays have been performed for the WT *mou*Alox15b and its humanised variant. In reported data, 8-HETE has been found to be the major product for the AA incubation with WT *mou*Alox15b, whilst 15-HETE has been found to be the major product for the incubation with the humanised *mou*Alox15b[128]. The obtained results are shown in Figure 6.5.

The humanisation of *mou*Alox15b has converted the products' profile from the 8-HETE/HEPE or 10-HDHA products to the 15-HETE/HEPE or 17-HDHA ones for all three substrates. Thus, the products' profile has become equivalent to the one obtained by incubation with the WT *hum*ALOX15B (Figure 6.3). Thus, the humanisation of *mou*Alox15b mimics the behaviour of the WT *hum*ALOX15B, in opposition to the case of the murinised *hum*ALOX15B.

LA has also been incubated with *mou*Alox15bs' variants in the presence of surfactants. The obtained products can be found in Figure 6.6.

The major product of the incubation with WT *mou*Alox15b is the 9*S*-HODE, whilst for the humanised *mou*Alox15b the major product is the 13*S*-HODE. In this case, in opposition to the *hum*ALOX15B double mutant, the mutation has humanised the products' profile of the *mou*Alox15b.

6.3.1.5 Incubation of HETE isomers

*mou*Alox15b is known to be able to generate double oxygenation products from AA[82]. To understand how the mutations affect the second oxygenation, 8- and 15-HETE have been incubated with the four ALOX15Bs variants. The metabolisation grade of these two substrates by the enzymes can be found in Figure 6.7.

WT *hum*ALOX15B is only able to metabolise 8-HETE, whilst murinised *hum*ALOX15B is mainly able to metabolise 15-HETE, although the ac-

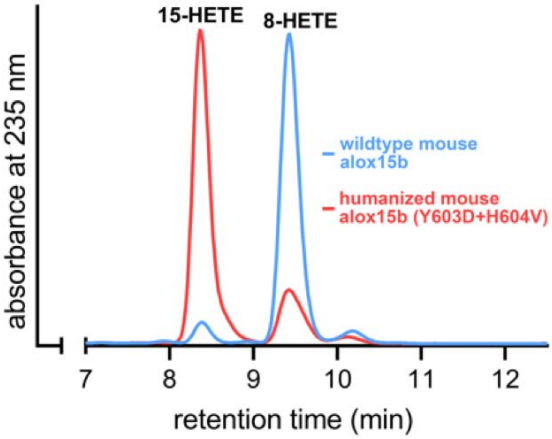

(a) AA as substrate

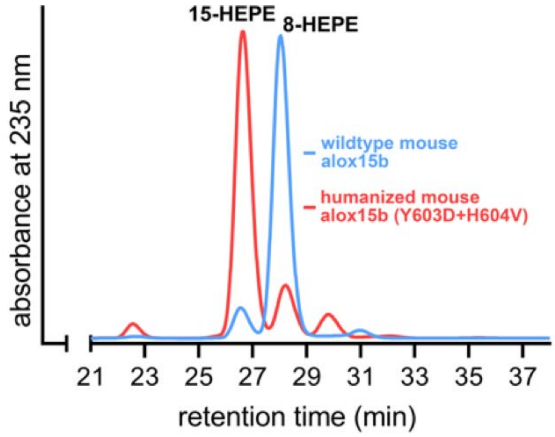

(b) EPA as substrate

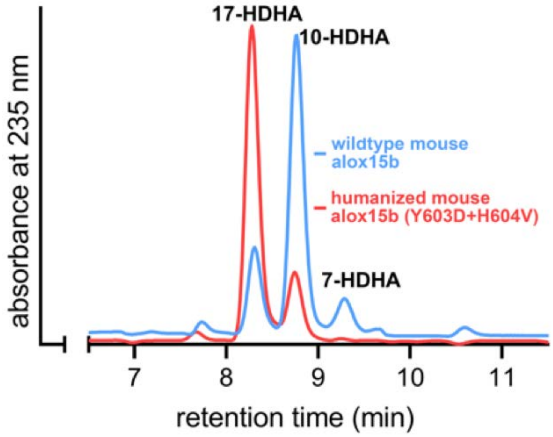

(c) DHA as substrate

Figure 6.5: RP-HPLC-detected products of WT and murinised mouAlox15b incubations.

(a) WT mouAlox15b

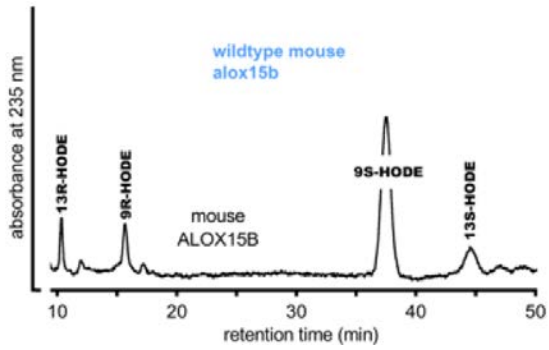

(b) Humanised mouAlox15b

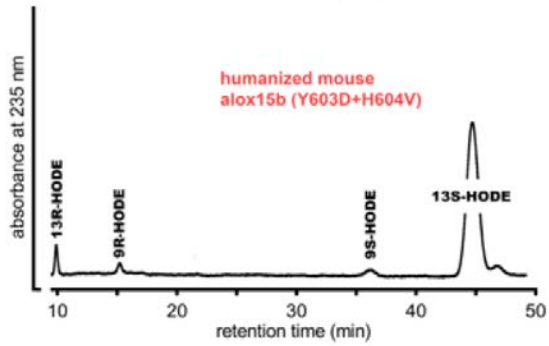

Figure 6.6: NP/CP-HPLC-detected products of LA incubations with WT and murinised mouAlox15b incubations.

tivity is much lower. On the contrary, WT *mou*Alox15b metabolises mainly 15-HETE with a higher activity in comparison with murinised *hum*ALOX15B. Humanised *mou*Alox15b is mainly able to metabolise 8-HETE, like the WT *hum*ALOX15B case. Thus, both mutations are able to mimic the behaviour of the target enzyme.

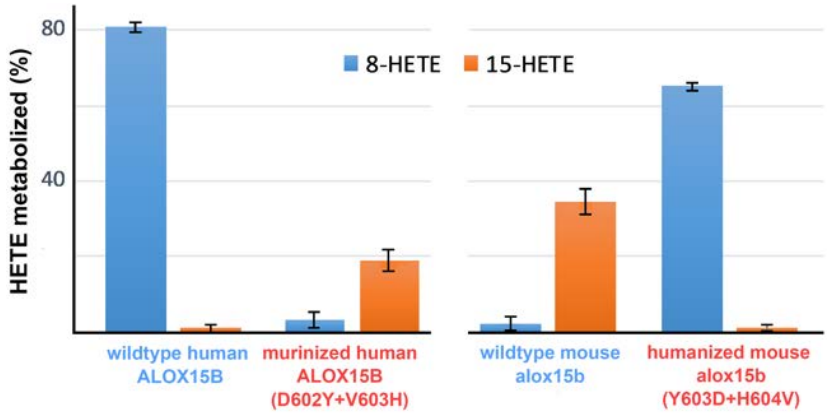

Figure 6.7: Metabolisation grade of 8- and 15-HETE with WT humALOX15B and mouAlox15b and their double mutants.

6.3.1.6 Long-term and high enzymatic concentration incubations of AA

Second oxygenation of AA is possible by a long-term –10 min– incubation with WT *mou*Alox15b. The products' profile of this incubation compared to the incubation during 1 min are available in Figure 6.8.

As it can be observed, a new product, the 8,15-diHETE, is obtained in small amounts when the incubation time is high enough, of 10 min in this case. This product has not been observed in any other incubation performed in this study.

Alternatively, 8,15-diHETE can also been obtained when high amounts of enzyme are used. A comparison of the two assays can be found in Figure 6.9.

As said, the production of the double oxygenated 8,15-diHETE is only detected in long incubation times, but in 10 min or less the concentration of the product is much lower than 8-HETE's concentration. On the other hand, when high concentrations of enzyme are used, the double oxygena-

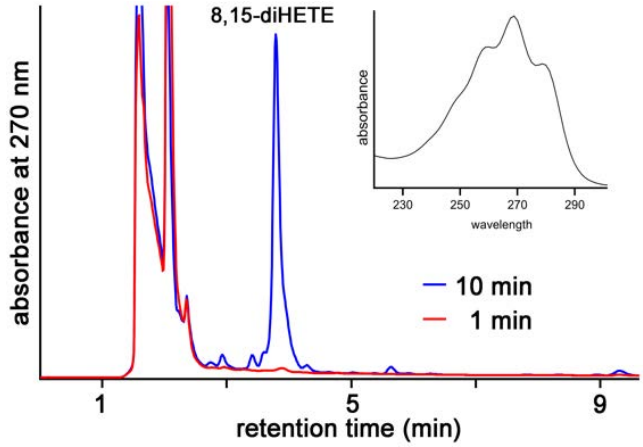

Figure 6.8: Incubation of AA with WT mouAlox15b at different incubation times. At the upper right corner, the UV profile of the double oxygenation profile is shown.

tion product can be detected with addition volumes of enzymatic solution higher than 10 µL. Moreover, when more than 15 µL of enzymatic solution are used, the double oxygenation product becomes the major product and the concentration of 8-HETE gets reduced.

The production of the double oxygenated product can be achieved by two distinct pathways. On the one hand, 8-HETE can be initially produced and then oxygenated again into the double oxygenation product. On the other hand, these steps can take place the other way around, being 15-HETE the first product to be obtained and further transformed into the 8,15-diHETE double-oxygenation derivative. Nonetheless, with the obtained experimental data it can not be established which one of the two pathways is preferred, but this data suggests that the global process is much slower in comparison with the formation of 8-HETE. Consequently, the oxygenation at the C_{15} position has to be a rather slow process.

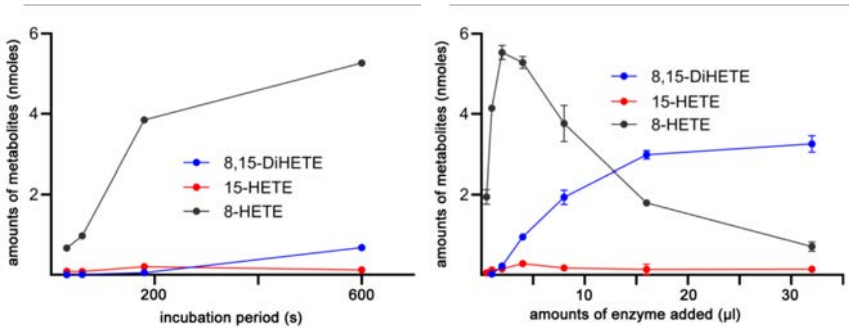

(a) Time-dependent incubation *(b) Concentration-dependent incubation*

Figure 6.9: Incubations of AA with WT mouAlox15b in different conditions.

6.3.2 Computational results

Docking and MD simulations have been performed to obtain a more detailed perspective on the study. On the one hand, docking simulations have been carried out to understand the binding modes of AA, EPA, DHA and LA. On the other hand, enzymatic complexes with AA, 8*S*-HETE and 15*S*-HETE have been prepared for MD simulations.

6.3.2.1 Binding modes of PUFAs in ALOX15Bs

Two binding modes of PUFAs are generally possible in LOXs: the head-first –in which the COO^- is located in the depth of the cavity– and the tail-first –in which the CH_3 is located in the depth of the cavity– alignments. Although *hum*ALOX15B and *mou*Alox15b share a high level of similarity, their regioselectivities are very different, as discussed in Section 6.3.1. *hum*ALOX15B oxygenates AA into 15*S*-HETE, while *mou*Alox15b mainly converts it into 8*S*-HETE. This divergence on the observed major product is thought to be the consequence of different binding modes of the

substrate. In this sense, the tail-first binding mode has to be preferred if the oxygenation takes place with a +2 rearrangement, so for the production of the 8*S*-HETE. On the contrary, the head-first binding mode has to be preferred for the 8*S*-HETE production, leading to oxygenation with a −2 rearrangement. Hence, and according to the experimental results (Section 6.3.1), the tail-first binding mode has to be the preferred in WT *hum*ALOX15B and the head-first mode has to be the preferred in WT *mou*Alox15b.

To investigate this hypothesis, docking simulations have been carried out with AA, EPA, DHA and LA as substrates and the obtained binding modes have been analysed. The respective results are presented in Table 6.2.

In WT *hum*ALOX15B the four substrates are preferentially bound with a tail-first orientation, whilst in WT *mou*Alox15b they prefer to bind with a head-first orientation although high-scored solutions with a tail-first orientation also appear. For the mutant variants, the results tend to be the opposite. The murinised *hum*ALOX15B behaves like the WT *mou*Alox15b, whilst the humanised *mou*Alox15b behaves like the WT *hum*ALOX15B. These results confirm the hypothesis that the binding is different in the two WT enzymes, as well as for the mutants.

The geometry of the two binding modes is similar. In both cases the substrate adopts a U-like shape. An exemplification of the head- and tail-first binding modes can be found in Figure 6.10.

6.3.2.2 Regioselective control in ALOX15Bs with AA as model substrate

Docking simulations have revealed the preferred binding mode for each substrate in each of the four considered ALOX15B variants. For the sake of exemplification, several MD simulations have been run, focusing on

Table 6.2: Free binding energy (in $kJ\,mol^{-1}$) **and orientation of the best five solutions for AA, EPA, DHA and LA's docking simulations with WT humALOX15B, murinised humALOX15B, WT mouAlox15b and humanised mouAlox15b.** Tail-first (TF) orientations are highlighted in blue while head-first (HF) orientations are highlighted in orange.

Substrate	***AA***		***EPA***		***DHA***		***LA***	
Enzyme	ΔG^{bind}	**Orient.**	ΔG^{bind}	**Orient.**	ΔG^{bind}	**Orient.**	ΔG^{bind}	**Orient.**
Human ALOX15B WT	−57.26	TF	−64.38	TF	−69.23	TF	−58.15	TF
	−57.25	TF	−62.69	TF	−67.46	TF	−55.08	TF
	−57.21	TF	−59.66	TF	−62.39	TF	−54.38	TF
	−51.22	HF	−58.93	TF	−56.63	TF	−53.22	TF
	−51.00	TF	−56.36	TF	−55.85	HF	−52.51	TF
Human ALOX15B mut	−39.43	HF	−39.75	TF	−43.77	HF	−35.09	HF
	−39.13	HF	−39.34	HF	−43.71	TF	−34.82	TF
	−39.01	HF	−38.98	HF	−43.56	TF	−34.78	TF
	−38.97	HF	−38.93	TF	−43.51	HF	−34.70	TF
	−38.87	TF	−38.89	TF	−43.44	TF	−34.68	TF
Mouse Alox15b WT	−41.44	HF	−41.47	HF	−45.98	HF	−36.15	HF
	−40.12	TF	−41.19	HF	−45.23	HF	−35.76	TF
	−39.69	TF	−41.04	HF	−44.87	HF	−35.57	TF
	−39.08	TF	−41.02	HF	−44.56	TF	−35.36	TF
	−39.07	TF	−40.88	HF	−44.16	TF	−35.34	TF
Mouse Alox15b mut	−42.56	TF	−43.64	TF	−49.03	TF	−49.03	TF
	−42.56	HF	−43.28	HF	−47.95	TF	−47.95	TF
	−42.52	TF	−42.63	TF	−46.30	TF	−46.30	TF
	−42.12	TF	−42.51	TF	−46.08	TF	−46.08	TF
	−41.65	TF	−42.29	TF	−46.00	TF	−46.00	TF

AA as the reference substrate with its different binding modes. Thus, eight simulations have been carried out with the head- and tail-first binding modes of AA and the four different enzymes –WT *hum*ALOX15B,

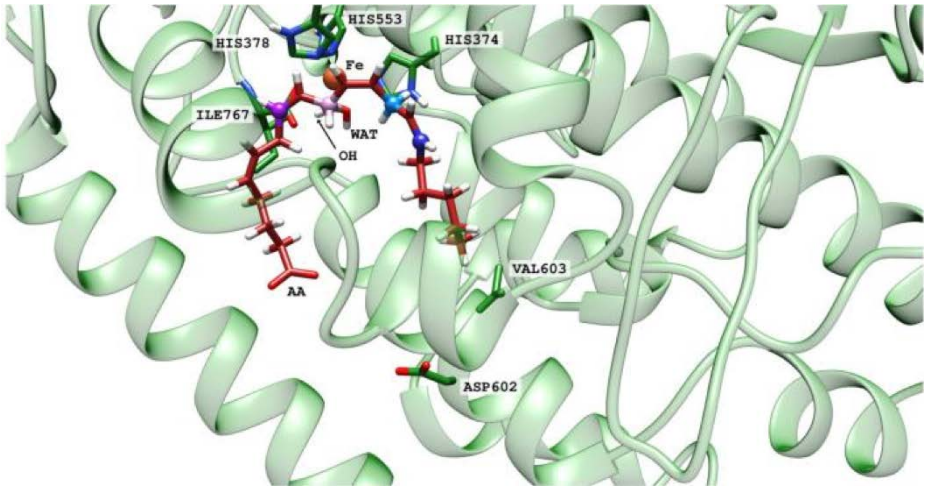

(a) Tail-first

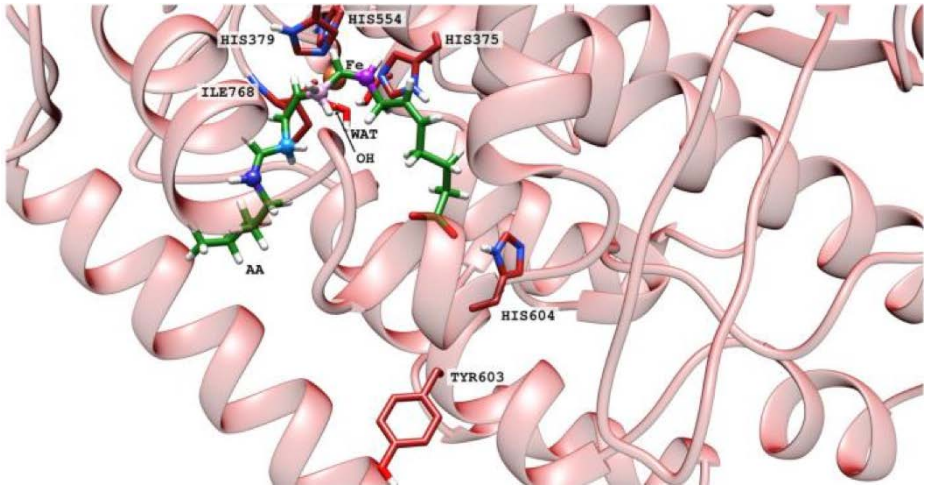

(b) Head-first

Figure 6.10: Binding modes of AA. The tail-first alignment in humALOX15b (a) is drawn in green, and the head-first in mouAlox15b (b) is indicated in red.

Asp602Tyr and Val603His mutant of *hum*ALOX15B, WT *mou*Alox15b, and Tyr603Asp and His604Val mutant of *mou*Alox15b–. 100 ns have been calculated per simulation. The distances between the OH^- group of the cofactor and the three reactive Hs (H_7, H_{10}, and H_{13}) have been measured for each of the simulations. The plots of the distances can be found in Figures 6.11 and SI6.1 for the WTs and mutant variants, respectively. Moreover, average distances for each simulation can be found in Table 6.3.

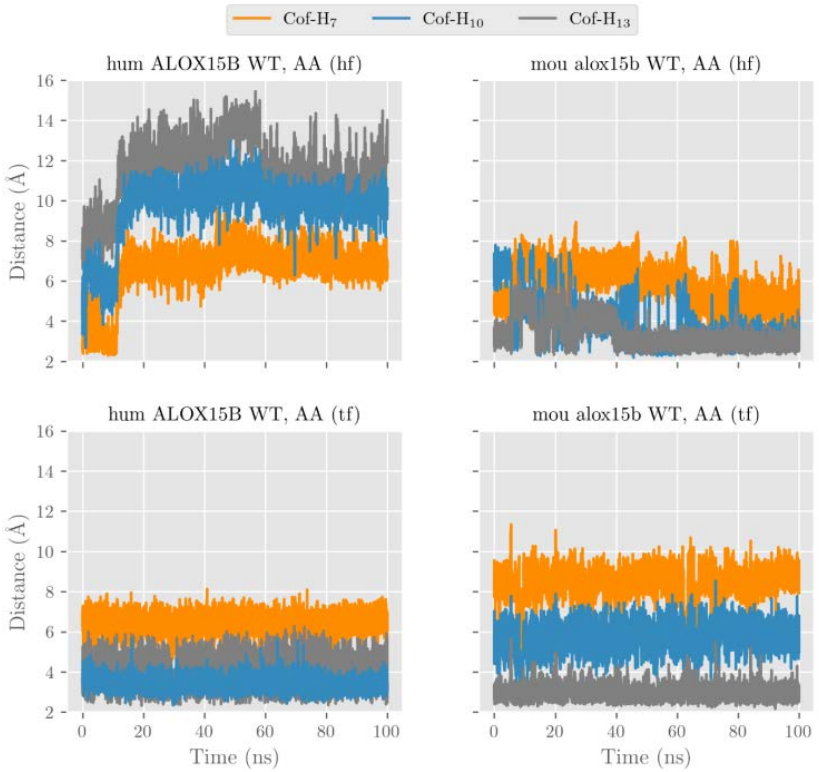

Figure 6.11: Distances from H_7, H_{10}, and H_{13} to OH^- group along the MD simulations for AA and WT *hum*ALOX15B and *mou*Alox15b.

In the case of the head-first orientation in WT *hum*ALOX15B, the

Table 6.3: Average distances from H_7, H_{10}, and H_{13} to OH^- group along the MD simulations for AA and WT *hum*ALOX15B, *mou*Alox15b, and their double mutants. Distances are expressed in Å. HF stands for head-first and TF stands for tail-first alignments.

Substrate's Orientation	Human						Mouse					
	WT			Mutant			WT			Mutant		
	H_7	H_{10}	H_{13}	H_7	H_{10}	H_{13}	H_7	H_{10}	H_{13}	H_7	H_{10}	H_{13}
HF	6.6	9.7	11.4	7.2	5.7	3.4	5.8	3.9	3.4	8.5	6.9	5.5
TF	6.4	3.4	4.2	6.5	4.6	4.8	8.4	5.8	3.0	7.4	4.8	3.2

pair Asp602 and Val603 destabilise the alignment, causing the substrate to move towards the entrance of the cavity, hence loosing the reactivity of the three Hs. On the other hand, the tail-first alignment for the same enzyme is very stable thanks to a hydrogen-bonding interaction of the COO^- moiety with Arg428. The case of the WT *mou*Alox15b is different. The head-first binding mode in this enzyme is stable thanks to the interaction of the COO^- moiety with Tyr603 and His604, as well as the tail-first, which interacts with Arg429 through a hydrogen bond.

The situation for the mutant enzymes is the opposite. The Asp603, Val604 pair of the *mou*Alox15b's mutant destabilises the head-first alignment, while does not have any effect on the tail-first binding mode. On the contrary, the Tyr602, His603 pair of the *hum*ALOX15B's mutant is able to stabilise the head-first binding mode as well as the tail-first one. Again, the tail-first alignments are stabilised thanks to a hydrogen-bonding interaction of the COO^- group with Arg429 or Arg428, respectively.

When analysing the hydrogen-cofactor distances, some trends can be observed. On the one hand, none of the orientations or complexes show a reactive distance with H_7, so no production of 5- or 9-HETE is expected (as Experimental Results have revealed, Section 6.3.1). On the other

hand, both H_{10} and H_{13} show reactive distances in one or both alignments, although no general tendency can be extracted.

In general terms, the synthesis of 15-HETE requires the abstraction of H_{13}, the delocalisation of the radical density over the nascent pentadienyl group from C_{11} to C_{15} and the addition of an O_2 molecule at the $n+2$ carbon (C_{15}), which requires a tail-first orientation[149]. On the other hand, the synthesis of 8-HETE requires the abstraction of H_{10}, the delocalisation over the C_8-C_{12} pentadienyl and the addition of the O_2 molecule at the $n-2$ C_8 carbon, which requires a head-first alignment. Consequently, 15-HETE is produced when the AA binds with a tail-first alignment, while 8-HETE is produced when the alignment is head-first.

As said before, MD simulations have not demonstrated a relationship between the closest-to-OH^- hydrogen and the orientation of the substrate. In a previous publication[65], it was demonstrated that the H-OH^- distance is not the only geometrical feature that affects the potential energy barrier of the hydrogen abstraction reaction. During the hydrogen abstraction, a planar pentadienyl group is formed including the two vicinal double bonds from a bisallylic moiety. Consequently, the abstraction will require a geometrical movement to the planarity of these carbon atoms. The further from the planarity, the higher the potential energy barrier will be. Furthermore, this geometrical movement can be hindered by the presence of close residues, causing an even larger potential energy barrier.

In order to explore if this geometrical feature explains better the hypothesis, MD simulations have been analysed measuring the distance from the C_8C_9 and $C_{11}C_{12}$ double bonds to Leu609 (Leu611 for *mou*Alox15bs) and Ile675 (Ile677 for *mou*Alox15bs) –the two closest residues to these double bonds– and the dihedral angles around C_{10} and C_{13}. A short double-bond–residue distance in combination with dihedral angles far from the planarity –0° or 180°– will translate into a higher barrier, as reported in[65].

Tail-first AA:WT *hum*ALOX15B, tail-first AA:*mou*Alox15b's double mutant, head-first AA:WT *mou*Alox15b, and head-first AA:*hum*ALOX15B's double mutant MD simulations have been analysed. The results are shown in Figures 6.12, SI6.2, SI6.3, and SI6.4, respectively.

Figure 6.12 shows the case for the tail-first binding mode in WT *hum*ALOX15B. As it can be observed, the behaviour of the two carbons' environments is different. On the one hand, the C_8C_9 is very close to Leu609. Moreover, $C_8C_9C_{10}C_{11}$ and $C_9C_{10}C_{11}C_{12}$ dihedral angles are far from the planarity, specially the latter. On the contrary, the $C_{11}C_{12}$ double bond is a little bit further from Leu609 and Ile675 and the $C_{11}C_{12}C_{13}C_{14}$ and $C_{12}C_{13}C_{14}C_{15}$ dihedral angles are close to planarity. According to this data, H_{13} abstraction is more feasible than H_{10} abstraction. The situation is similar for the *mou*Alox15b double mutant (Figure SI6.2).

On the contrary, the case of the head-first AA alignment in the WT *mou*Alox15b and the double mutant of *hum*ALOX15B is the opposite (Figures SI6.3 and SI6.4). The geometrical observations mentioned before behave the other way around in these systems, being the H_{10} the most feasible hydrogen to be abstracted.

6.3.2.3 Specificity and regioselectivity of HETE isomers

As developed in Section 6.3.1.5, 15*S*-HETE and 8*S*-HETE are substrate of ALOX15Bs. Based on the results shown on Figure 6.7, four systems have been prepared choosing the most metabolised HETE isomer for each enzyme. Moreover, docking studies have been carried out to obtain the best alignment for each pair of isomer and enzyme. As a result, for WT *hum*ALOX15B and humanised *mou*Alox15b the best fitting isomer is the 15*S*-HETE with the tail-first alignment, while 8*S*-HETE in the head-first binding mode is the best substrate and alignment for the murinised *hum*ALOX15B and the WT *mou*Alox15b.

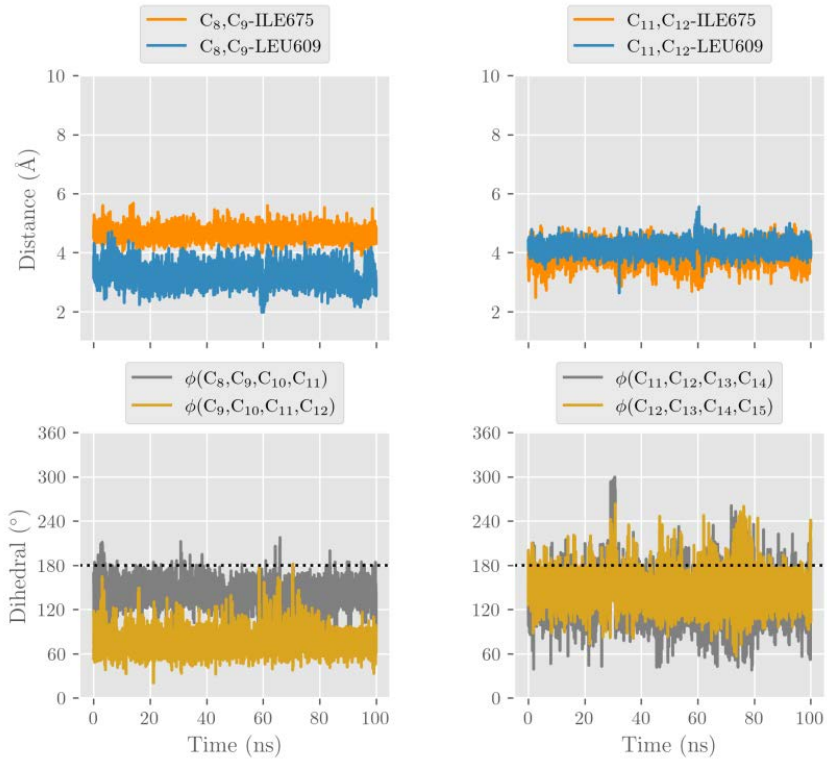

Figure 6.12: Minimum distances from C_8C_9 and $C_{11}C_{12}$ to Leu609 and Ile 675, and dihedral angles around C_{10} and C_{13} along the MD simulation of WT humALOX15B complexed with the tail-first oriented AA.

A 100 ns MD simulation has been calculated for each system. Moreover, distances from the OH^- group of the cofactor to H_7 and H_{10} of 15*S*-HETE, or H_{13} of 8*S*-HETE, have been measured. Results are pictured in Figure 6.13 and average distances are shown in Table 6.4.

Table 6.4: Average distances from OH^- to closest H_7, H_{10}, and/or H_{13} for tail-first 8*S*-HETE:WT humALOX15B, WT mouAlox15b, and humanised mouAlox15b and for head-first 15*S*-HETE:murinised humALOX15B and WT mouAlox15b complexes. Distances are expressed in Å. *n.p.* stands for not possible due to the non bisallylic character of the C, and *n.c.* stands for not calculated since corresponding MD simulation has not been carried out.

Substrate and Orientation	Human						Mouse					
	WT			mut			WT			mut		
	H7	H10	H13	H7	H10	H13	H7	H10	H13	H7	H10	H13
15S-HETE (HF)	n.c.	n.c.	n.c.	6.7	4.0	n.p.	5.6	4.5	n.p.	n.c.	n.c.	n.c.
8S-HETE (TF)	5.8	n.p.	2.8	n.c.	n.c.	n.c.	6.9	n.p.	4.5	6.3	n.p.	5.2

From these results it can be seen that for the 8*S*-HETE-containing systems, the H_{13} is always the closest-to-OH^- hydrogen. As explored in Section 6.3.2.2, this hydrogen abstraction leads to the oxygenation on position C_{15}, so to the production of 8*S*,15*S*-diHETE. Nonetheless, neither the WT *hum*ALOX15B or the humanised *mou*Alox15b are capable of producing 8*S*-HETE, so the 8*S*,15*S*-diHETE cannot be produced from AA using these enzymes.

On the other hand, in the 15*S*-HETE-containing systems, the closest hydrogen is the H_{10}, which leads to the oxygenation at the C_8 position. Hence, the 8*S*,15*S*-diHETE can be obtained with WT *mou*Alox15b and murinised *hum*ALOX15B starting from 8*S*-HETE.

For the formation of the double oxygenated 8*S*,15*S*-diHETE starting from AA by WT *mou*Alox15b another aspect needs to be taken into account. It has been shown that the first oxygenation to 8*S*-HETE is a

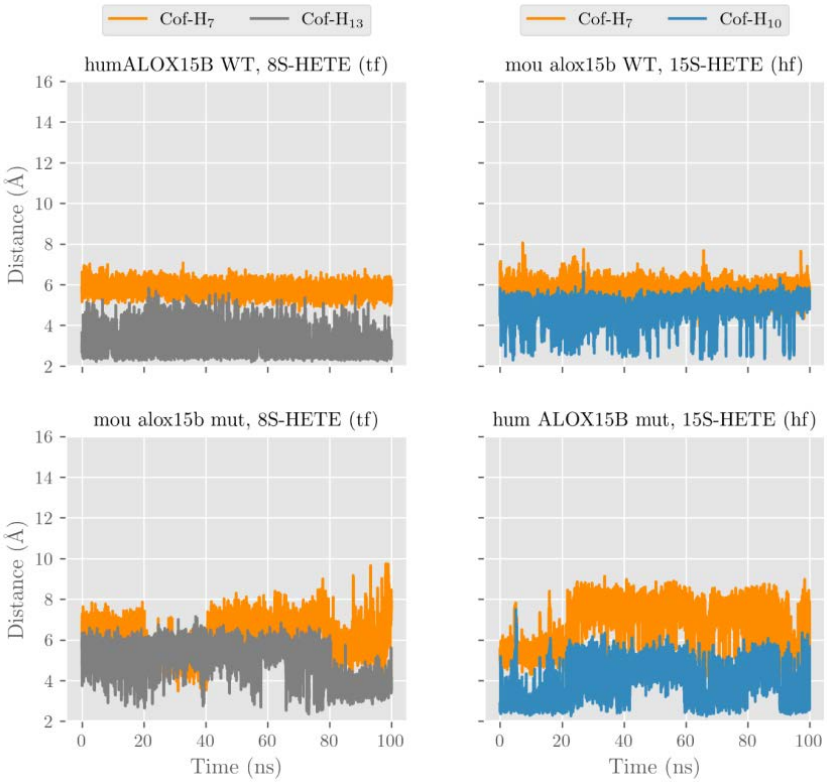

Figure 6.13: Plot of OH^- to closest H_7, H_{10}, and/or H_{13} distances for 8*S*-HETE:WT humALOX15B and humanised mouAlox15b and for 15*S*-HETE:murinised humALOX15B and WT mouAlox15b complexes.

favourable, fast process. On the contrary, the second oxygenation of 8*S*-HETE into 8*S*,15*S*-diHETE is an unfavourable, slow process but actually feasible. In agreement with Table 6.2, the tail-first alignment of AA in WT *mou*Alox15b is not the most preferred, but it is in fact plausible. As a consequence, the tail-first alignment of 8*S*-HETE is also possible. The corresponding MD simulation shows that in this case (Table 6.4, Figure SI6.5), H_{13} is ready to be abstracted, thus yielding to the secondary 15-lipoxygenation. Additionally, Figure 6.7 shows that 8*S*-HETE is somewhat metabolised.

However, an alternative pathway is also possible. It would involve an initial slow, unfavoured oxygenation at C_{15}, which requires an unfavourable tail-first orientation of AA (Table 6.2). After this initial oxygenation, the fast secondary 8-lipoxygenation of the 15-HETE can take place. Thus, 8*S*,15*S*-diHETE would be generated in a slow first step and a fast second step. Both pathways seem to be possible, although both are globally slow since they involve the 15-lipoxygenation, which is always an unfavourable process for WT *mou*Alox15b.

6.4 Conclusions

Incubation assays with different PUFAs, docking simulations and MD simulations have been carried out in order to give a full perspective on the differences between *hum*ALOX15B and *mou*Alox15b and the two double mutants that exchange their regioselectivities, the Asp602Tyr and Val603His mutant of *hum*ALOX15B and the Tyr603Asp and His604Val *mou*Alox15b's mutant. From these experiments and simulations, the products, the preferred binding modes of the substrates and the oxygenation pathways that lead to each of the products have been determined.

It has been demonstrated that the proposed double mutations are ca-

pable of exchanging the products' profiles of the WT enzymes. Furthermore, it has been evidenced that the oxygenation on C_8 –or C_{10} of DHA– requires the head-first alignment of the substrate, while the oxygenation on the C_{15} position –or C_{17} of DHA– requires the tail-first binding mode. Additionally, it has also been observed that WT *mou*Alox15b and murinised *hum*ALOX15B prefer the head-first binding mode although the tail-first alignment is also possible but less favoured, whilst WT *hum*ALOX15B and humanised *mou*Alox15b prefer the tail-first binding mode whereas the head-first orientation is not stable.

Because of these alignment preferences, WT *hum*ALOX15B and humanised *mou*Alox15b produce mainly 15*S*-HETE as the product of AA, whilst WT *mou*Alox15b and murinised *hum*ALOX15B produce mainly 8*S*-HETE as major product, despite they are also capable of producing small amounts of 15*S*-HETE. Moreover, the double oxygenation 8*S*,15*S*-diHETE product can also be synthesised by these two latter enzymes at slow rate.

Chapter 7

Exchanging ALOX5 regioselectivity to emulate ALOX15

The work presented in this Chapter corresponds to Ivanov et al.[150]*. The publication and the Supporting Information can be found in Chapter SI7. Experiments have been performed by scientists at Hartmut Kühn's laboratory at Institut für Biochemie, Charité, Berlin, Germany, while computational studies have been carried out at UAB.*

7.1 Introduction

Human ALOX5 (*hum*ALOX5) is an enzyme member of the LOX family. It is able to synthesise 5*S*-hydro(per)oxy-ETE (5*S*-H(p)ETE) and Leukotriene A_4 (LTA_4)[86]. Nonetheless, the regioselectivity can be changed by applying several mutations following the triad determinant concept[48]. This triad concept was firstly introduced by Borngräber et al.[151] for rabbit 12/15-LOX. It refers to the ability of changing the regioselectivity of a LOX through the mutation of three amino acids located in the bottom of the cavity.

In this Chapter, the application of the triad concept to *hum*ALOX5 is presented. The *hum*ALOX5's mutant that will be investigated was initially reported in 2001 by Schwarz et al. [152]. After identifying and mutating four positions (Phe359, Ala424, Asn425, and Ala603), they were able to obtain a 8*S*- and 15*S*-lipoxygenating mutant although ALOX5 and ALOX15 only share a 64 % of identity. The authors suggested that the regioselectivity change was due to alternative binding modes of the substrate in the reactive cavity.

To confirm this hypothesis, experimental and computational studies of the Phe359Trp, Ala424Ile, Asn425Met, and Ala603Ile quadruple mutant of *hum*ALOX5 are presented.

7.2 Methods

In this section, experimental and computational methods used for the present study will be reviewed.

7.2.1 Experimental Methods

The experimental studies have been performed by scientists in Hartmut Kühn's laboratory in Charité, Berlin, Germany. Thus, the methodology used for carrying out the experiments will be explained in a brief manner for the sake of contextualising the results that will be further explained along Section 7.3.1. More details can be found in Ivanov et al. [150].

7.2.1.1 Chemicals

Different PUFAs and derivatives (as HPLC standards) have been used as substrates: polyenoic fatty acids, 15*S*-HETE, 12*S*-HETE, 5*S*-HETE, 11*S*-deutero-LA and 11*R*-deutero-LA.

7.2.1.2 Cloning, expression and mutagenesis of wild-type and the quadruple mutant of *hum*ALOX5

Sf9 baculovirus-insect cells have been used for final expression, although *E. coli* was initially tested with no success. After removing the His tag coding section from the expression plasmid, *Sf9* cells were transformed following the standard instructions for the Bac-to-Bac Baculovirus Expression System[153]. After expression, cells have been harvested by sonication and the supernatant has been used as the source of enzyme since purification reduces severely the enzymatic activity.

The quadruple mutant has been prepared in three consecutive rounds of mutagenesis. The Phe359Trp mutation is firstly introduced. Then, the Ala424Ile and Asn425Met are introduced at the same time. Finally, the Ala603Ile mutation is introduced. After each step, 5 clones are selected for screening and one of them is also sequenced in order to confirm the presence of the introduced mutation(s).

Enzymatic activities have been assayed and standardised by reaction with fatty acids.

7.2.1.3 Fatty Acid Oxygenase activity

Enzymatic activity of *hum*ALOX5 has been tested by the incubation of the corresponding fatty acid (with a concentration of 40 µM to 100 µM) in 10 µL to 40 µL of lysate mixed in 500 µL of PBS containing 0.4 mM of $CaCl_2$, 0.1 mM of EDTA, 0.1 µg mL^{-1} of dipalmitoylphosphatidyl-choline, and 0.1 mM of ATP.

All incubations have been carried out at room temperature for 5 min. Reactions have been stopped by the addition of $NaBH_4$, followed by acidification with acetic acid to pH 3 and the addition of 0.5 mL of ice-cold ACN. After 15 min of incubation in ice, samples have been centrifuged

and the supernatant has been collected to further analysis.

7.2.1.4 High Performance Liquid Chromatography analysis

HPLC standards of fatty acids derivatives and reactions' products are analysed by RP-HPLC with a C_{18} column and an ACN:H_2O:AcOH 70:30:0.1 mobile phase for single oxygenation products and of 45:55:0.1 for the double oxygenated ones. In the case of LA derivatives, SP-HPLC has been used for better separation. Enantiomers have been separated using a combination of SP- and CP- columns. The products of single oxygenation are detected by UV spectroscopy at 235 nm, while double oxygenated ones are detected at 270 nm.

7.2.2 Computational Methods

Several computational techniques for carrying out the study have been used in order to describe the enzymatic problem at different levels of detail: Molecular Docking simulations, MD simulations and QM/MM calculations.

Computational studies are focused only in AA and LA fatty acids.

7.2.2.1 Protein setup

Protein's structure has been been obtained from the crystallographic coordinates of the subunit A of the model with the PDB ID accession code 3O8Y[72]. Crystallographic agents have been manually removed from the structure. The Phe359Trp, Ala424Ile, Gln425Met, and Ala603Ile mutant has been generated *in silico* from the crystallographic model using the `UCSF Chimera`[135]'s `Rotamers` module.

As a crystallographic model, no hydrogens are present. The protonation has been carried out using `PROpKa3.0`[154] at a pH of 7. The protona-

tion states around Fe have been checked and fixed if needed.

7.2.2.2 Molecular docking simulations

Molecular docking has been used in order to identify the binding modes of AA and LA in the active site of *hum*ALOX5. `GOLD`[87] in its 5.2 version has been used to perform the docking simulations.

For the simulations, protein's coordinates have been kept frozen. Genetic algorithm has been used for generating the ligand's conformations. The cavity has been defined as a sphere of 19 Å around the Fe atom. `ChemScore`[137] has been used as the fitness function.

Four Michaelis complexes have been generated including AA and LA in the head- and tail-first binding modes.

7.2.2.3 Molecular Mechanics parameterisation and solvation

The four systems have been parametrised for further simulations. `ff14SB AMBER`'s force field[89] has been used for parametrising the standard residues. `TIP3P` water molecules[155] have been introduced as the water model. Parameters for AA have been obtained from the literature[156], while LA has been parametrised using the `GAFF AMBER`'s force field[145] as the source of parameters using the `parmchk2` module from `AmberTools`[140]. In both cases, RESP charges[144] have been calculated for both substrates at the HF[101;102]/6-31G(d)[142] level of theory and fitted using the `antechamber` module from `AmberTools` package[140]. Fe environment's parameters have been obtained following the Seminario method[138] through the `MCPB.py` package[139] from the `AmberTools`[140] suite. `Gaussian09`[157] has been used for performing the QM calculations.

The complexes have been solvated in a pre-equilibrated orthorhombic water box. The dimensions of the box have been defined by extending

10 Å in each direction from the outermost atom of the enzyme. Protein's charges have been neutralised by the addition of 20 Na^+ ions.

As a result, a model containing around 75 000 atoms has been created, with around 11000 of them coming from the protein.

The models have been cropped for QM/MM simulations. A drop-solvation model has been created for each model by removing all solvent atoms further than 17 Å from the substrate. The drop-solvation model includes around 12 000 atoms.

7.2.2.4 Molecular Dynamics simulations

The solvated models have been used for performing the MD simulations. To carry out the MD simulations, `pmemd` code in its `CUDA` (GPU) version[147;148] from `AMBER16`[94] has been used.

Prior to the production, an equilibration protocol has been carried out to obtain thermodynamically equilibrated systems. An initial energy minimisation of the solvated models has been carried out. 6000 cycles of energy minimisation using the steepest descent algorithm have been done applying harmonic restraints with a force constant of 5.0 kcal $mol^{-1}Å^{-2}$ to all atoms positions but solvent and counterions. 16000 more minimisation cycles have been performed without applying restraints.

After the minimisation, all four systems have been annealed from 0 to 300 K with gradual increments of 30 K during 20 ps per increment. The weak-coupling Berendsen temperature bath[158] has been used. Next to the heating stage, 1 ns of MD simulation using the NPT ensemble with a temperature of 300 K and a pressure of 1 atm have been calculated to adjust the volume of the solvation box. To control these magnitudes, the weak-coupling Berendsen barostat[158] has been used with isotropic position scaling. Moreover, a harmonic restraint with a force constant of 5.0 kcal $mol^{-1}Å^{-2}$ has been applied to the backbone atoms. Once a den-

sity of around $1\,g\,cm^{-1}$ has been achieved, 10 ns of MD using the NVT ensemble have been performed. No restraint has been applied and the Langevin thermostat adjusted at 300 K has been used. After the equilibration, 200 ns of production have been performed using the same configuration.

During the whole MD simulation, a time step of 2 fs has been used. The SHAKE algorithm[159] has been used to constrain all bonds involving hydrogen atoms. The non-bonding interactions have been treated using the PME method[160] with a cut-off of 10 Å. Van der Waals interactions have been also limited to this cut-off distance.

The analysis of the MD simulations has been carried out with a very preliminary version of the `RCBS.py` code[161], and `UCSF Chimera`[135].

7.2.2.5 Quantum Mechanics/Molecular Mechanics calculations

QM/MM calculations have been performed using the modular `ChemShell` software[162;163] and its `HDLCopt` module[164]. `TURBOMOLE` 7.0[165] has been used as the QM engine, while `DL_POLY` 5[166] has been used for the MM partitions.

The drop-solvated model described in Section 7.2.2.3 has been used as the source of MM force field. The electrostatic embedding has been used to treat the interactions between the QM and the MM partitions and no cut off for the electrostatic interactions has been applied. Hydrogen atoms have been added as link atoms to the boundary bonds in order to complete the atomic valences.

L-BFGS algorithm[167] has been used for the geometric optimisations. The microiterative scheme[168] has been used and all residues with at least one atom in the QM region have been included in the micro region. Only the atoms within a radius of 15 Å centred at C_{11} of LA or AA –around 2000 atoms in both cases– have been set free to move. All the remaining

ones have been kept frozen.

The QM region has been treated at the B3LYP[141]/6-31G(d)[142] level of theory for the H, C, N and O atoms, while Fe has been described with the LANL2DZ basis set[169]. The QM regions include the Fe(III)-OH^- cofactor, the lateral chains of His367, His372, His550 and Asn554 and the COO^- terminal group of Ile673. Moreover, for AA-containing systems the C and H atoms between C_7 and C_{16} have been included, while for the ones containing LA the atoms between C_7 and C_{14} have been included. As a result, two QM region of 73 atoms and of 66 atoms have been obtained, respectively. 8 link atoms have been added in both cases. The QM-MM partitions can be found in Figure 7.1.

7.3 Results and Discussion

The results of the studies about the application of the triad concept to *hum*ALOX5 are presented in this section. A combination of experimental and computational approaches is used in order to give a broad vision of the study.

7.3.1 Experimental results

Experimental results are presented in the first place. Enzyme expression and enzymatic activity on different substrates with both the wild-type and the quadruple mutant of *hum*ALOX5 are going to be outlined.

7.3.1.1 Enzyme expression

As mentioned in the Methods section (Section 7.2.1.2), the expression of wild-type and quadruple mutant of *hum*ALOX5 has been performed using the baculovirus-insect cells *Sf9* system. Supernatants obtained after the lysis of the infected, expressed cells are analysed in order to determine

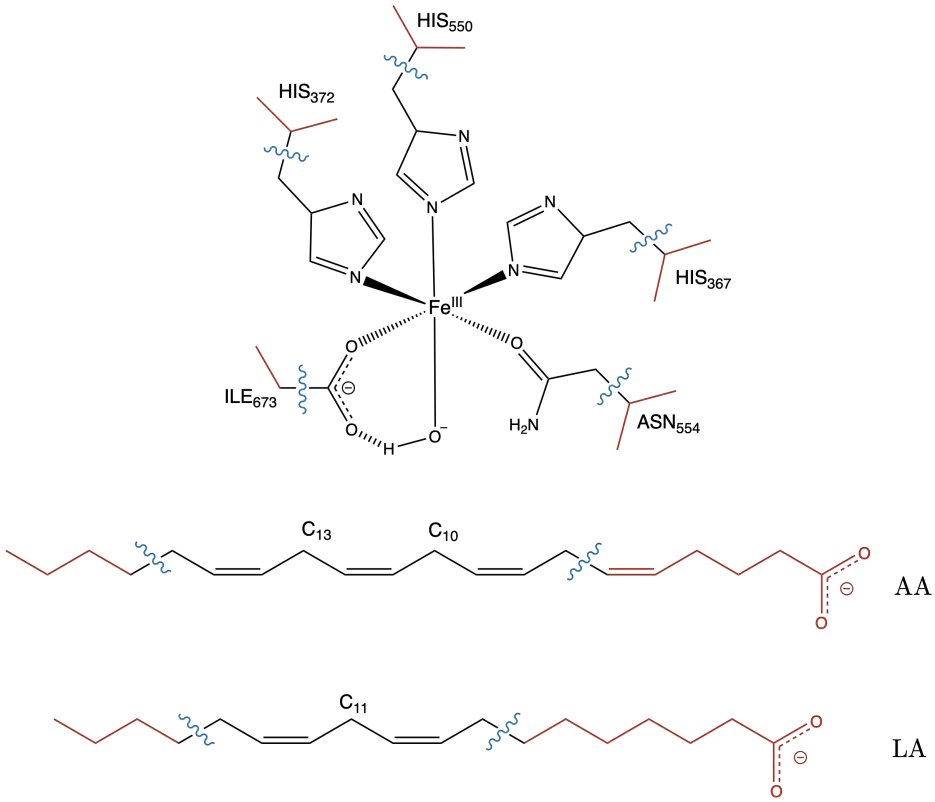

Figure 7.1: QM-MM partitions for the humALOX5 system complexed with AA and LA.

the correct expression of the *hum*ALOX5s. Immunoblotting of the obtained supernatants and pellets has been carried out using an anti-His-tag antibody.

Figure 7.2 shows the results of the immunoblotting assay. As it can be seen, expression in the four samples is observed. In conclusion, wild-type and mutant of *hum*ALOX5 have been obtained as soluble proteins. The expression levels of the two *hum*ALOX5s are similar. The concentration has been measured to be around 12.6 mg/L of culture for the wild-type

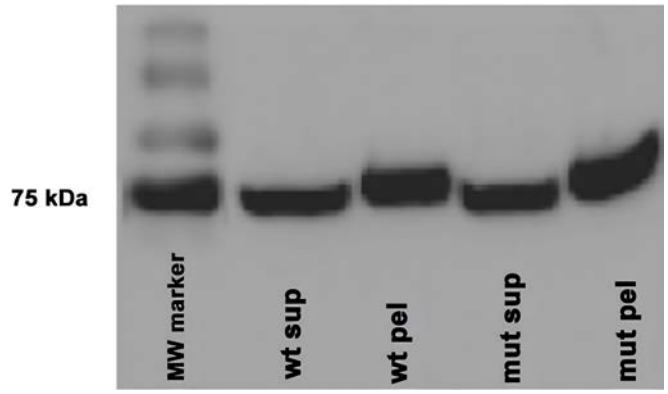

Figure 7.2: Immunoblotting of SDS-PAGE of supernatant and pellet of wild-type and quadruple mutant of *hum*ALOX5 expression samples. 'wt' stands for wild-type and 'mut' corresponds to the *hum*ALOX5 quadruple mutant. 'sup' corresponds to supernatant and 'pel' corresponds to pellet. The first lane is the molecular weight marker.

*hum*ALOX5.

7.3.1.2 Conversion of Arachidonic Acid

After confirming the presence of soluble protein, activity assays have been carried out with 20 µL of supernatant for each version of *hum*ALOX5. Collected samples have been analysed using RP-HPLC and results can be observed in Figure 7.3.

HPLC analysis at 235 nm (Figure 7.3a) reveals a completely different behaviour when the two enzymes are compared. On the one hand, wild-type *hum*ALOX5 produces almost exclusively 5-HETE. On the other hand, the production of 5-HETE in the quadruple mutant is almost completely prevented in favour of the production of 15-HETE and 8/12-HETE –the two isomers coelute–. 8/12-HETE peak has been further analysed by SP-HPLC in order to detect and quantify each of the compounds. The relative production of each product has been calculated. 8-HETE and

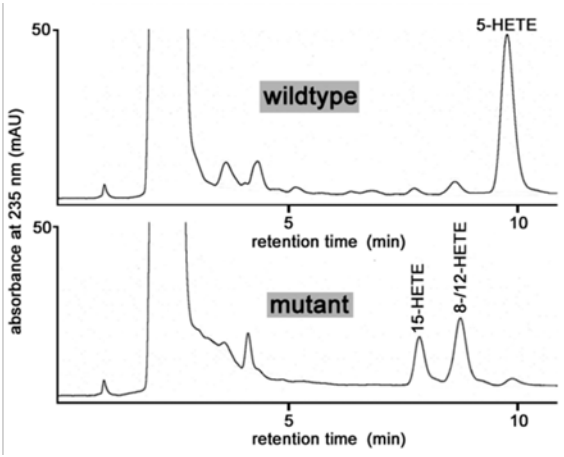

(a) UV detector at 235 nm

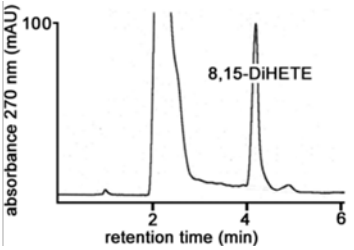

(b) UV detector at 270 nm*, mutant's sample*

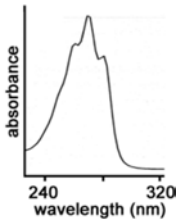

(c) UV spectrum of the product identified in (b)

Figure 7.3: HPLC chromatograms (a, b) **and UV spectrum** (c) **of the products of wild type and *hum*ALOX5's mutant incubation with AA.** All peaks have been assigned by comparing the retention times with the standards' ones.

15-HETE are the major products with similar shares of 46.9±3.5 % and 44.9±4.3 %, respectively, while 12-HETE is the minor product with a share of 8.9±0.1 %.

HPLC analysis at 270 nm reveal the production of a conjugated-triene-containing product. The wild-type *hum*ALOX5 is known by its LTA_4-

synthase activity, but the analysis of the quadruple mutant's products reveals the presence of the dioxygenated 8,15-diHETE –confirmed by comparison with the standard's retention time and UV spectrum–. Thus, the mutation has not only changed the regioselectivity of the enzyme but has also abolished its LTA_4-synthase activity. This results also imply that the mutation reduces significantly the pro-inflammatory capabilities of *hum*ALOX5.

The enantiomeric character of the obtained products has also been assessed using SP/CP-HPLC. The obtained HPLC chromatograms for the wild-type and the quadruple mutant are shown in Figure 7.4.

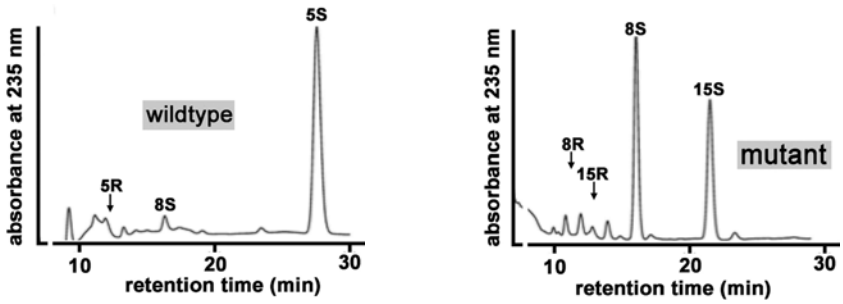

(a) Wild-type *(b) Quadruple mutant*

Figure 7.4: SP/CP-HPLC chromatograms of the wild-type *hum*ALOX5 and the quadruple mutant's products.

As expected, the product of wild-type *hum*ALOX5 is almost enantiomerically pure and it is the 5*S*-H(p)ETE enantiomer. In the case of the quadruple mutant the situation is very similar. 8*S*-HETE and 15*S*-HETE are the major products. For the 12-HETE isomer, a racemic mixture has been detected (data not shown). Thus, the formation of the 8- and 15-HETE isomers is tightly enantiomerically controlled by the enzyme.

If all these experimental results are combined, several ideas can be

obtained. On the one hand, the mutation has introduced a different behaviour of the binding modes. While the preferred binding mode for the wild-type enzyme is the head-first, the introduction of four bulky residues at the bottom of the cavity has allowed also the tail-first binding mode. Moreover, the presence of the mutation's residues changes the cavity's shape, provoking the binding of the head-first mode to be slightly different. AA binds deeper in *hum*ALOX5's mutant cavity than in WT's cavity.

These differences on the geometries of the binding modes are the reason why the *hum*ALOX5 becomes an 8-,15-lipoxygenating LOX, similar to the mouse Alox15b (Chapter 6). A diagram of these geometrical explanation can be found in Figure 7.5.

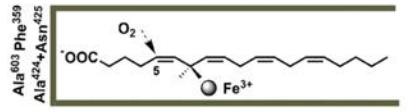

(a) Wild-type humALOX5

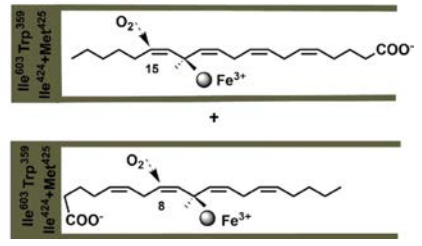

(b) humALOX5 quadruple mutant

Figure 7.5: Diagram of the geometrical differences between the binding on wild-type humALOX5 and its quadruple mutant.

7.3.1.3 Conversion of Linoleic Acid

Incubation of LA with the two versions of *hum*ALOX5 has been carried out to characterise the binding alterations introduced by the quadruple mutant observed for AA.

On the one hand, wild-type *hum*ALOX5 does not accept LA as a substrate. This behaviour is in agreement with the observed for the guinea pig's isoform of ALOX5[170]. The corresponding HPLC chromatogram can be found in Figure 7.6.

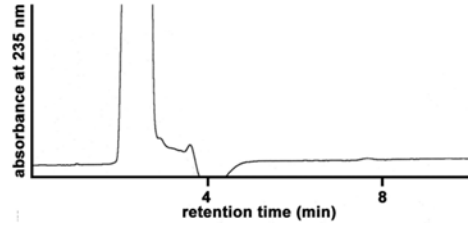

Figure 7.6: HPLC chromatogram of incubation of LA with wild-type humALOX5.

On the other hand, *hum*ALOX5 quadruple mutant does accept LA as a substrate forming 13- and 9-HODE as major and minor products, respectively. Chromatograms of the RP-, SP- and CP-HPLC analysis can be found in Figure 7.7.

Relative quantification of the reaction products for the LA:*hum*ALOX5's mutant incubation has been calculated with the obtained HPLC data. 13-HODE has been found to be the major product with around 80 % of relative share, while 9-HODE is the minor product with around 20 %. Moreover, CP-HPLC has revealed that in both cases the preferred enantiomers are the *S* ones.

From these results it can be observed that the mutation of the residues belonging to the triad determinants changes the binding of LA, allowing a reactive binding that leads to the production of two different derivatives. If the ideas obtained from the study with AA as a substrate are applied to LA, it can be assumed that the mutations allow the two binding modes with reactive geometries. On the one hand, the head-first mode produces the 9-HODE derivative in the same way than the mutant produces 8-

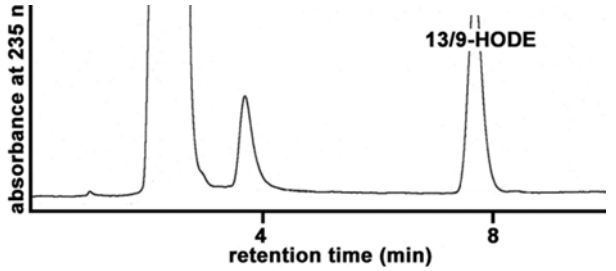

(a) RP-HPLC

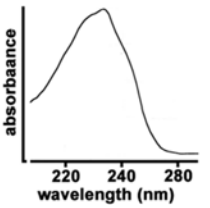

(b) UV profile of products from (a)

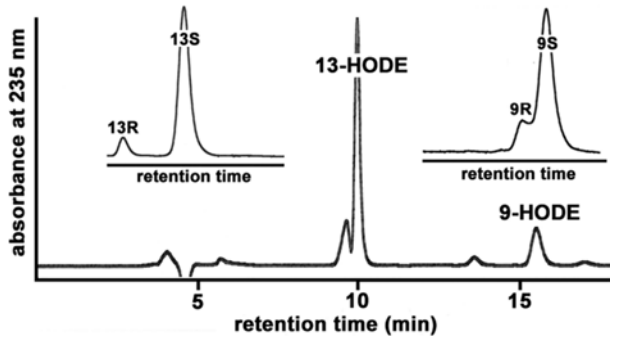

(c) NP- (large) and CP-HPLC (small)

Figure 7.7: RP-, SP- and CP-HPLC chromatograms of LA incubation with *hum*ALOX5 quadruple mutant.

HETE from AA. On the other hand, 13-HODE is synthesised following the 15-lipoxygenating activity of the quadruple mutant, which requires the tail-first binding mode of the substrate.

Geometry of the hydrogen abstraction

It is known that LOXs' mechanism follows an antarafacial geometry between the abstracted H and the addition of the O_2. Thus, the *S* enantiomer is formed by the initial abstraction of the pro-*S* hydrogen of the

reactive methylene. In the case of the formation of the 13*S*-HODE isomer, this translates to the initial abstraction of the pro-*S* H_{11}.

To confirm that this geometrical feature is conserved in *hum*ALOX5's quadruple mutant, incubations with the 11*R*- and 11*S*-deuterated-LA have been performed. The 11*S* isotopomer is found to be oxygenated at a low rate, while for the 11*R* isotopomer the rates are comparable with the ones for the non-deuterated substrate. Primary isotopic effect has been calculated and it is greater than 30.

The products of the reaction with both isotopomers (with a 10-fold higher concentration of the enzyme for the 11*S* isotopomer) have been analysed using HPLC techniques. Chromatograms can be found in Figure 7.8.

The obtained products have been quantified. For the 11*R* isotopomer, 13-HODE is the major product with a relative share of 80.1±0.6 %. 9-HODE is the minor product with a share of 19.9±0.6 %. These results are identical to the ones observed for the incubation with the non-deuterated LA, which indicates that the pro-*R* hydrogen of the C_{11} methylene is not involved in the mechanism.

On the contrary, the results for the 11*S* isotopomer are very different. The major product is the 9-HODE with a relative share of 79.1±2.5 % while it is of 20.9±2.5 % for 13-HODE. These results reveal that the abstracted hydrogen of the non-deuterated LA is the pro-*S*. Thus, the antarafacial geometry is conserved in the *hum*ALOX5 quadruple mutant.

These results confirm the parallelism between the mutant's 8- and 15-lipoxygenating activities on AA, which depends on the binding mode (Chapter 6) and for LA applies for the production of 9- and 13-HODE, respectively.

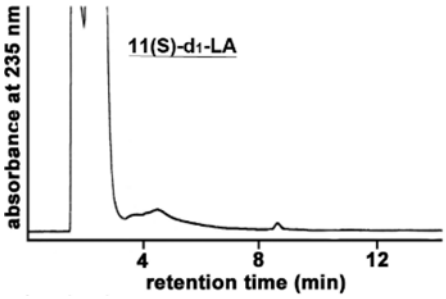

*(a) RP-HPLC of 11*S

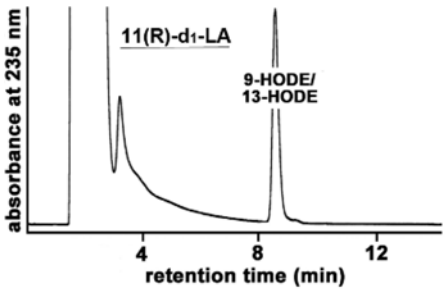

*(b) RP-HPLC of 11*R

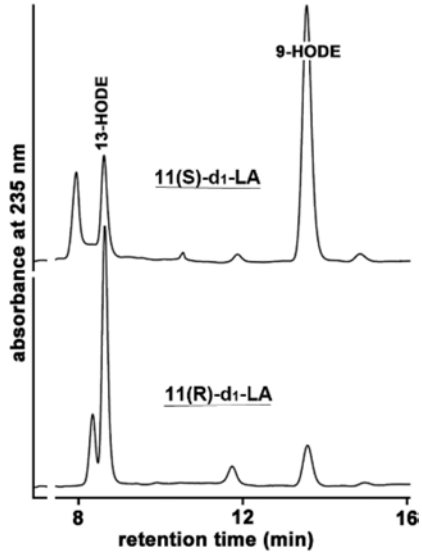

*(c) NP-HPLC of 11*S *(upper) and 11*R *(lower) isotopomer incubation*

Figure 7.8: RP- and NP-HPLC chromatograms of the analysis of 11*S*- and 11*R*-deutero-LA incubated with the *hum*ALOX5 quadruple mutant.

7.3.1.4 Conversion of Linolenic Acids

Oxygenation of α-LA has been studied. Incubations of the substrate with the wild-type *hum*ALOX5 and its quadruple mutant have been carried out and the products have been analysed using HPLC. On the one hand, α-LA is not a substrate of wild-type *hum*ALOX5. On the contrary, the quadruple mutant is able to convert α-LA into 13-HOTrE(n-3). Chromatograms for each incubation can be found in Figure SI7.1.

The case for γ-LA is similar. γ-LA has been found not to be a good substrate for wild-type *hum*ALOX5 but it is for the quadruple mutant. HPLC chromatograms can be found in Figure SI7.2. *hum*ALOX5's quadruple mutant's major product is 13-HOTrE(n-6) while the minor product is 10-HOTrE(n-6).

7.3.1.5 Conversion of Eicosapentaenoic Acid

EPA has been found to be substrate of the two versions of *hum*ALOX5. The wild-type enzyme converts EPA selectively to 5-HEPE with a 3-fold higher rate in comparison to AA. On the other hand, it is not such a good substrate for the quadruple mutant. Its major oxygenation products are 12-HEPE and 15-HEPE. The corresponding HPLC chromatograms can be found in Figure SI7.3.

7.3.1.6 Conversion of Docosahexaenoic Acid

DHA is substrate of the wild-type and the mutant versions of *hum*ALOX5. The wild-type enzyme is able to convert DHA into 7-HDHA, although 14- and 17-HDHA have been also detected but are associated with auto-oxygenation processes as they are present in the substrate solution. This conversion has a 35 % lower rate in comparison to AA.

The activity rate of the quadruple mutant is similar, although different products are obtained. In this case the major obtained derivatives are 10- and 17-HDHA.

The corresponding HPLC chromatograms can be found in Figure SI7.4.

7.3.2 Computational results

Computational results are presented in this section. These studies have been focused on the quadruple mutant structure and AA and LA have been

used as substrates. For the study, docking simulations, MD simulations and QM/MM calculations have been carried out.

7.3.2.1 Docking studies

Docking simulations have been done in order to generate initial structures for the MD simulations. For each system –AA:*hum*ALOX5's mutant, and LA:*hum*ALOX5 mutant–, the highest-scored solution has been chosen for the head- and the tail-first binding modes. Thus, four models have been generated as a result.

7.3.2.2 Molecular Dynamics simulations

Four MD simulations of 200 ns have been carried out, one for each of the models. The C_7, C_{10}, C_{13}-OH^- distances have been measured for the quadrupole mutant of *hum*ALOX5 complexed with AA, while C_{11}-OH^- distances have been measured for the complexes with LA.

Arachidonic Acid

The evolution of the analysed distances for the head- and tail-first binding modes of AA is shown in Figure 7.9.

During the first 100 ns of the head-first conformation (Figure 7.9a), C_{13} methylene is the closest to the OH^- group, although some structures with a close distance with C_{10} have also been found. These observed distances explain the formation of 15-HETE, which might start with the abstraction of a H from the C_{13} methylene and continues with the addition of the O_2 molecule at C_{15}. Moreover, the presence of structures with a close distance between C_{10} and the OH^- group explains the formation of 8- and 12-HETE, which might be obtained by the initial abstraction

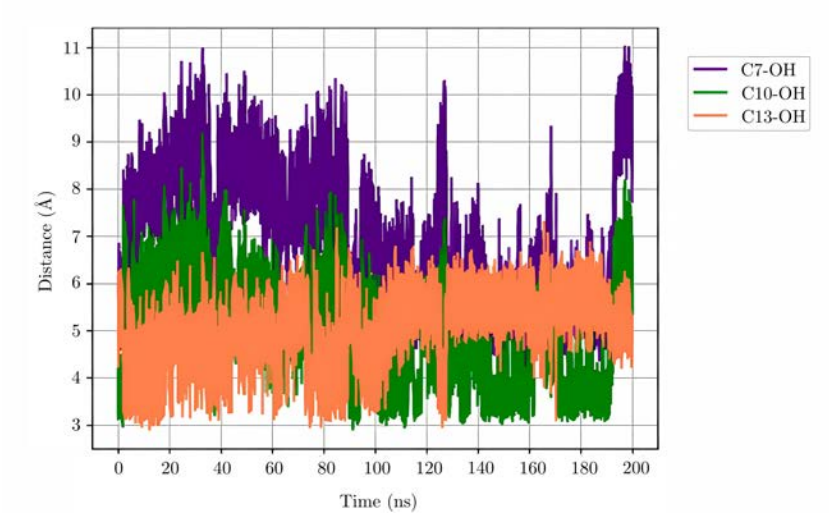

(a) Head-first orientation

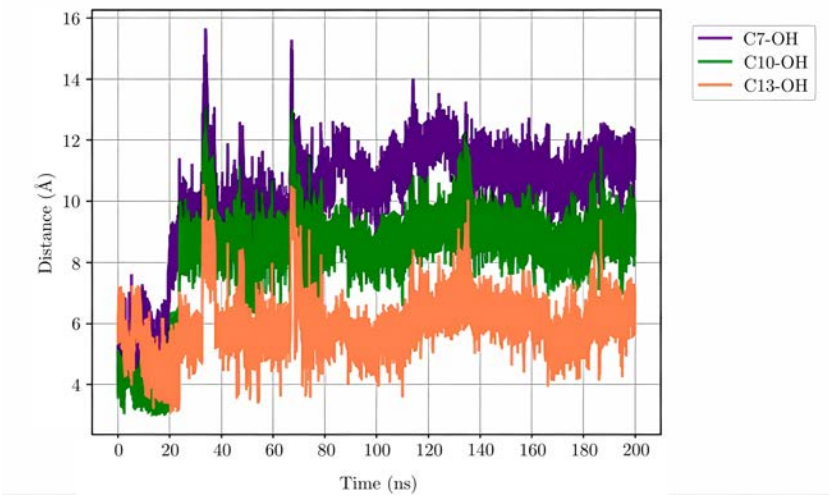

(b) Tail-first orientation

Figure 7.9: C_7, C_{10}, C_{13}-OH^- group distances for the AA:*hum*ALOX5's quadruple mutant complex during 200 ns of MD simulation.

Table 7.1: Average, minimum and maximum distances between C_7, C_{10}, and C_{13} and OH^- group from the cofactor for the AA:*hum*ALOX5's quadruple mutant system along the MD simulations for the head- and tail-first binding modes.

Orientation	Type	Distance (Å)		
		C_7-OH^-	**C_{10}-OH^-**	**C_{13}-OH^-**
Head-first	**Average**	**7.02**	**4.95**	**5.00**
	Minimum	3.99	2.91	2.90
	Maximum	11.02	9.18	7.30
Tail-first	**Average**	**10.23**	**8.29**	**5.94**
	Minimum	4.05	2.99	3.07
	Maximum	15.63	13.01	10.54

of a H in the C_{10} and the addition of the O_2 molecule at C_8 and C_{12}, respectively.

Moreover, during the second half of the MD simulation, C_{10} gets closer to the OH^- group than C_{13}, meaning that 8- and 12-HETE will be preferentially obtained with this binding mode. During the complete simulation, no structures with a close distance between C_7 and the OH^- group are observed. Thus, the formation of 5-HETE is not plausible with this quadruple mutant. This is in agreement with the experimental results (Section 7.3.1.2). Distances during the MD simulations are summarised in Table 7.1.

Figure 7.9b and Table 7.1 reveal that for the tail-first binding mode of the AA:*hum*ALOX5's quadruple mutant complex all distances are greater than the observed for the head-first system. C_7 is too far away from the OH^- group to be reactive. C_{10} is also far away but some reactive positions have been detected, whilst C_{13} is close enough for the hydrogen abstraction to take place. Thus, 15-HETE will obtained as the major product from

AA in the tail-first binding mode, while 8- and 10-HETE will be the minor products.

Although analysis of the methylene-OH^- distance leads to the observations above mentioned, experimentally it has been demonstrated that the oxygen addition can take place at the $n-2$ position only if the binding mode is the head-first, while it can be at the $n+2$ if the binding mode is the tail-first[149]. Thus, the only products that can be obtained from AA with the head-first binding mode are 8-HETE and 11-HETE, which has not been experimentally detected. On the contrary, the tail-first mode will lead to the production of 15-HETE and, in lower quantities, of 12-HETE. These results are in agreement with the experimental data, which indicate that 8- and 15-HETE are obtained in similar quantities (Section 7.3.1.2).

Linoleic Acid

LA contains only one reactive methylene. Two MD simulations of 200 ns have been simulated with the head- and the tail-first binding modes. In both cases, C_{11} has been found close to the OH^- group, with average distances of 4.48 and 5.17 Å for the head- and tail-first modes, respectively. These data suggests that reactivity can take place in any of the binding modes on C_{11} for LA. The C-OH^- distances plots can be seen in Figure SI7.5.

Substrates' binding modes comparison

For the sake of comparison, each binding mode of the two substrates has been overlayed and aligned. The comparison can be found in Figure 7.10.

In the head-first binding mode (Figure 7.10) it can be seen that both

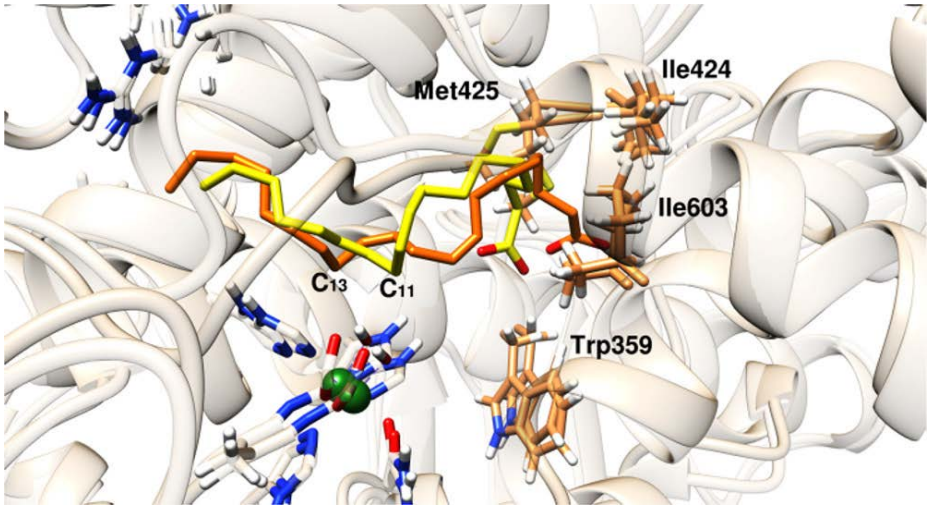

(a) Head-first

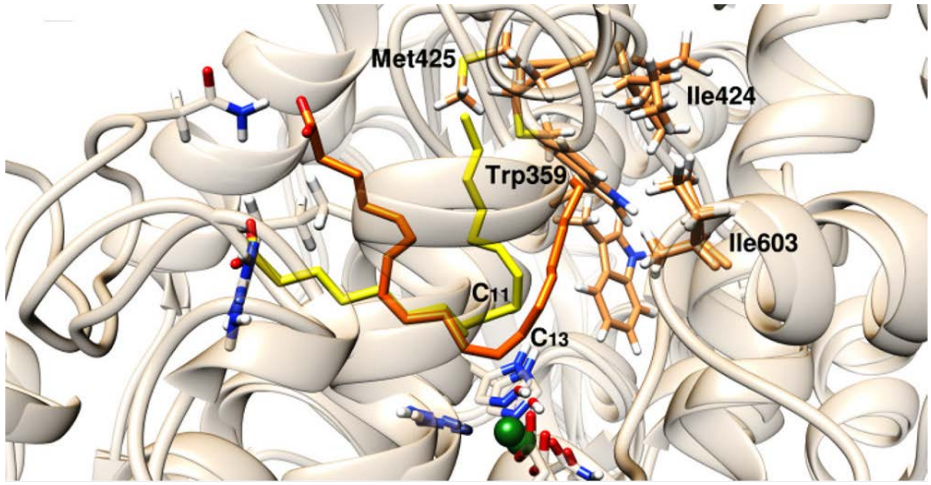

(b) Tail-first

Figure 7.10: Comparison of AA and LA binding modes at the catalytic centre of *hum*ALOX5 quadruple mutant. AA is drawn in orange and LA is drawn in yellow.

substrates fit in the same region of the cavity. C_{13} from AA and LA's C_{11} are close to the cofactor, although the C_{11} from LA is placed closer to the bottom of the cavity.

The case of the tail-first binding mode is different. The heads and tails of the substrates are located in slightly different regions, whilst the reactive methylenes (C_{13} for AA, and C_{11} for LA) are located in the same region.

7.3.2.3 Quantum Mechanics/Molecular Mechanics Simulations

Several structures from the MD simulations have been selected. Only precatalytic structures with a close distance between a reactive methylene and the OH^- group from the cofactor have been chosen. From the selected structures, H-abstraction scan calculations have been performed in order to obtain the potential energy barrier of the reaction.

Arachidonic Acid

For the AA-containing complex three frames with a H-OH^- distance lower than 3 Å for the C_{13} and three more for the C_{10} have been selected. Only structures corresponding to the head-first binding mode have been chosen in order to compare the regioselectivity since MD simulations have not been conclusive in this regarding. The obtained results can be found in Table 7.2.

For the tail-first binding mode, MD simulations have concluded that hydrogen abstraction can only take place on the C_{13} methylene.

The ranges of the potential energy barriers are similar for both processes (from 19.7 to 22.6 kcal/mol for the H_{13} abstraction and from 19.3 to 21.5 kcal/mol for the H_{10} abstraction), meaning that neither of the processes is preferred in terms of potential energy.

Table 7.2: Potential energy barriers (in kcal/mol) **of the hydrogen abstraction of H_{13} and H_{10} for the head-first AA:*hum*ALOX5's quadruple mutant system.**

Abstracted hydrogen	$\Delta E^{\ddagger}$
H_{13}	19.7
	22.6
	20.9
H_{10}	21.0
	19.3
	21.5

In conjunction with the experimental results, these results explain the formation of 8-HETE, which starts from the abstraction of one of the H_{10} and follows with the addition of the O_2 molecule on C_8, the $n-2$ methylene.

Linoleic Acid

For the LA-containing complex, the study has been focused on the reaction capabilities depending on the binding mode since there is only one reactive methylene. Three pre-catalytic frames have been selected for the head-first conformation, while only one has been selected for the tail-first conformation. Potential energy barriers can be found in Table 7.3.

Table 7.3 shows that the average potential energy barrier for the H_{11} abstraction in the head-first mode is 19.7 kcal/mol, while the barrier for the abstraction in the tail-first mode is 19.3 kcal/mol. These results indicate that there is not a preferred binding mode for the hydrogen abstraction in the LA:*hum*ALOX5's quadruple mutant system.

In combination with the experimental results, these data translate into

Table 7.3: Potential energy barriers (in kcal/mol) **of the H_{11} abstraction for the head- and tail-first conformations of the LA:*hum*ALOX5's quadruple mutant system.**

Binding mode	$\Delta E^{\ddagger}$
Head-first	23.2
	14.2
	21.7
Tail-first	19.3

the idea that 9-HODE formation requires the head-first binding mode since O_2 is added to the $n-2$ carbon. On the other hand, 13-HODE is generated from the tail-first mode with the addition of the O_2 molecule to the $n+2$ carbon.

7.4 Conclusions

The triad determinants is a group of residues located in the bottom of the cavity of LOXs that determines the regioselectivity of the ALOX. Thus, the mutation of these residues can exchange the regioselectivity of a certain ALOX to mimic another one.

In the present case, the triad concept has been applied to *hum*ALOX5. Through the mutation of four positions –Phe359Trp, Ala424Ile, Asn425Met, and Ala603Ile–, *hum*ALOX5 has been converted into a 8-,15-lipoxygenating ALOX5. The enzymatic capabilities of the new mutant have been experimentally tested with different PUFAs. Moreover, computational studies have been carried out in order to clarify the experimental observations.

In conclusion, the applied mutations have been able to modify the binding of the substrate in two different ways. On the one hand, the binding mode already observed for the wild-type ALOX5 –the head-first–

gets modified. The addition of bulkier residues in the bottom of the cavity causes a displacement in the position of the head of the substrate, producing a shift on the exposed-to-reactivity methylene and exchanging the regioselectivity from a 5- to a 8-lipoxygenating ALOX. On the other hand, the mutations have allowed the introduction of a tail-first binding mode that allows the reactivity on C_{10} and C_{13} –preferentially–, generating 12- and 15-HETE, respectively. Thus, *hum*ALOX5 has become an 8-,15-lipoxygenating ALOX5 with the application of the Phe359Trp, Ala424Ile, Asn425Met, and Ala603Ile mutations.

Chapter 8

Exploring FLAP in an AA-containing membrane

The Supporting Information can be found in Chapter SI8.

8.1 Introduction

Five-Lipoxigenase-Activating Protein (FLAP) is a 161 residues long, homotrimeric, transmembrane protein associated with *hum*ALOX5. It was discovered in 1990 while testing the MK-886 inhibitor, which was initially designed to be a *hum*ALOX5 inhibitor. Unexpectedly, it was found to be bound to a novel protein. This protein was identified, cloned and expressed and it was found to be a 18 kDa protein [171]. Its sequence was then compared to the LOX family and no similarities were found. Surprisingly, it shares a 31 % of identity with LTC_4S, another transmembrane protein responsible of the LTC_4 synthesis from LTA_4. From this finding, and including other proteins from the same family later discovered, the MAPEG family of proteins was defined.

In 2007, the first crystallographic structures of FLAP were reported (PDB IDs 2Q7R and 2Q7M[172]). In 2020, new crystallographic structures (PDB IDs 6VGI and 6VGC[173]) were published. However, none of these structures is complete.

Structurally, FLAP contains three monomers. Each monomer has four helices α, one of them significantly longer than the other three (Figure 8.1a). Moreover, FLAP monomers have three distinct regions. The top (residues 140 to 161) and bottom (residues 24 to 62 and 94 to 113) regions are hydrophilic, while the central region (residues 1 to 23, 63 to 93, and 114 to 139) is mainly hydrophobic. As expected, this hydrophobic region allows the transmembrane location (Figure 8.1b).

Two biological roles have been associated with FLAP. On the one hand, FLAP has been reported to be responsible for the regulation of *hum*ALOX5's activity through their interaction, which is assisted by ATP and Ca^{2+}. On the other hand, FLAP has also been associated with the binding of free AA located in the nuclear envelope and ER's membrane. AA is obtained from AA-containing phospholipids by cPLA$_2$α. This AA-binding role of FLAP will be studied in this Chapter.

8.2 Methods

For the study of the FLAP's AA-binding function, MD simulations of the membrane-embedded protein will be carried out in order to understand the dynamic role of the protein.

8.2.1 Model setup

As mentioned before, no complete crystallographic structure is available. Nonetheless, an AlphaFold[132;133] predicted model of the complete sequence of a FLAP's monomer is available (UniProt[134] ID P20292[175]).

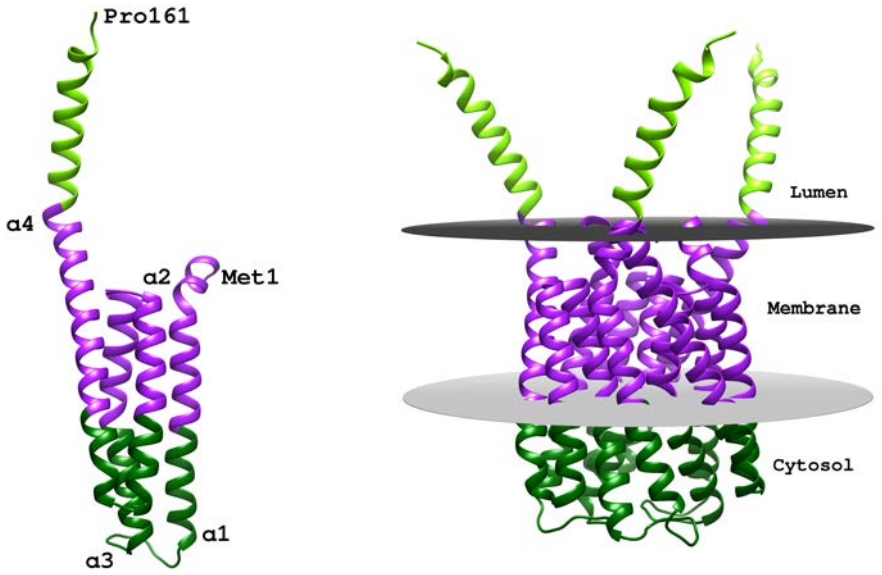

(a) Structure of a FLAP's monomer.

(b) FLAP structure in the predicted position in ER's membrane.

Figure 8.1: Structure of FLAP's monomer and trimer with the predicted embedding in ER membrane. Purple indicates the hydrophobic region, dark and light green indicate the hydrophilic region, and grey planes indicate the membrane's limits, which have been predicted using the PPM server[174]. The dark grey disc is the lumenal limit, while the light grey disc indicates the cytosolic limit[172]. First and last residues of the monomer and helices' names are indicated in the structure (a).

To build the trimeric model, the predicted monomeric structure has been triplicated and each monomer has been aligned to each monomer of the crystallographic structure with PDB ID 2Q7R. This trimer has been protonated at physiological pH (7.4) using the `ProteinPrepare` module[136] from `playmolecule.org` website.

`CHARMM-GUI`[176]'s `Membrane Builder`[177–180] module has been used for

building the membrane model. The protonated model of FLAP has been used as input and automatically aligned using the PPM2.0 server[181] from `CHARMM-GUI`. Since FLAP is located in the ER's membrane, a realistic model of an ER membrane has been built[182]. The composition of the membrane can be found in Table 8.1. 41 molecules of free AA have been added to the membrane for the study of the AA-binding function of FLAP. An initial width and depth (X and Y axis, respectively) of 100 Å has been set. The system has been solvated with a water box of 15 Å of thickness at each side of the membrane. 0.15 M of KCl and of 0.015 M of $CaCl_2$ salts have been used for neutralising the protein's charge and add physiological salts. After the system's preparation, the final dimensions of the systems are 120.9 Å × 120.9 Å × 123.4 Å. The initial solvated model can be found in Figure 8.2.

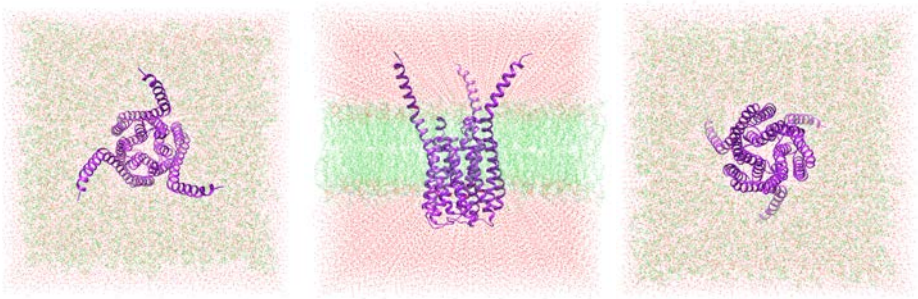

(a) Top view *(b) Frontal view* *(c) Bottom view*

Figure 8.2: Top, frontal and bottom views of the solvated FLAP-membrane system. The protein is drawn in purple, the membrane is drawn in green, and the solvent is drawn in red.

`CHARMM36m`[183] force field has been used as the source of parameters for the protein. The TIP3P water model[146] has been chosen for the solvation. The membrane components have been parametrised using the `CHARMM36` force field for lipids[184]. After preparing the system, the parameters have

Table 8.1: Composition of ER membrane with AA for FLAP-membrane simulation. 'Lipid Head/Tail' column indicates, in order, the composition of the lipid with the phospho- group, the length and unsaturation of the lipid bonded at the position 1 of the glycerol molecule, and the length and unsaturation of the lipid bonded at the position 2 of the glycerol. The structure of each component is drawn in Figure SI8.1.

Component Name	**Lipid Head/Tail**	**Composition in membrane (%)**
POPC	PC(16:0/18:1(9Z))	16
PLPC	PC(16:0/18:2(9Z,12Z))	18
SAPC	PC(18:0/20:4(5Z,8Z,11Z,14Z))	27
POPE	PE(16:0/18:1(9Z))	5
PSPE	PE(16:0/18:0)	8
SAPE	PE(18:0/20:4(5Z,8Z,11Z,14Z))	7
SAPI	PI(18:0/20:4(5Z,8Z,11Z,14Z))	3
SLPI	PI(18:0/18:2(9Z,12Z))	3
OLPS	PS(18:1(9Z)/18:2(9Z,12Z))	3
PSM	SM(d18:1/16:0)	4
POPA	PA(16:0/18:1(9Z))	1
Cholesterol		5

been obtained in the `AMBER` format[185].

8.2.2 Molecular Dynamics simulations

MD simulations have been carried out using the GPU (`CUDA`) version of the `pmemd` software[147;148] from `AMBER22`[140], which has been used as the MD engine.

An initial short minimisation of 500 cycles using the steepest descent algorithm and 500 cycles using the conjugated gradient algorithm have been calculated using the CPU `pmemd` version, followed by a longer minimisation of 10000 cycles employing the same algorithms for half of the cycles

each, respectively. Two heating stages have been carried out restraining all the atoms except the solvent and ions. In the first one, a heating from 0 K to 100 K has been done for 5 ps. For the second one, the temperature has been increased until 310.15 K for 100 ps. This temperature has been set for the rest of MD stages. Once the requested temperature has been achieved, two semiisotropic NPT steps of 1 ns each have been done for equilibration. The pressure has been applied on the XY plane –the plane parallel to the membrane–. A restrain on the backbone has been applied to the protein's backbone for the first step. For the second one, restrains have only been applied to C_α.

A timestep of 2 fs has been used for all the MD stages. The long-range interactions have been treated using the PME scheme with a cut off of 10 Å.

After the equilibration protocol, 100 ns of production have been carried out using the same NPT configuration but without restraints. After this production, additional 500 ns of production have been calculated using the hydrogen mass repartitioning method as implemented in `AMBER`[186] and a timestep of 4 fs.

Only the last stage has been analysed. The `RCBS.py`[161] package, an implementation of the `MDAnalysis`[187;188] `Python` module has been used for the MD analysis. The `membrane-curvature`[189] package has been used for the analysis of the membrane's curvature. Structure drawings have been prepared using `UCSF Chimera`[135].

8.3 Results

Two distinct behaviours of FLAP will be studied from the last 500 ns of MD production. On the one hand, how FLAP effects and gets affected by the membrane will be studied in terms of curvature of the membrane,

FLAP's RMSD, and RMSF. On the other hand, FLAP's role in capturing AA will also be explored.

8.3.1 FLAP's stability

In order to explore the stability of FLAP, the RMSD of the protein has been measured. The corresponding plot can be found in Figure 8.3.

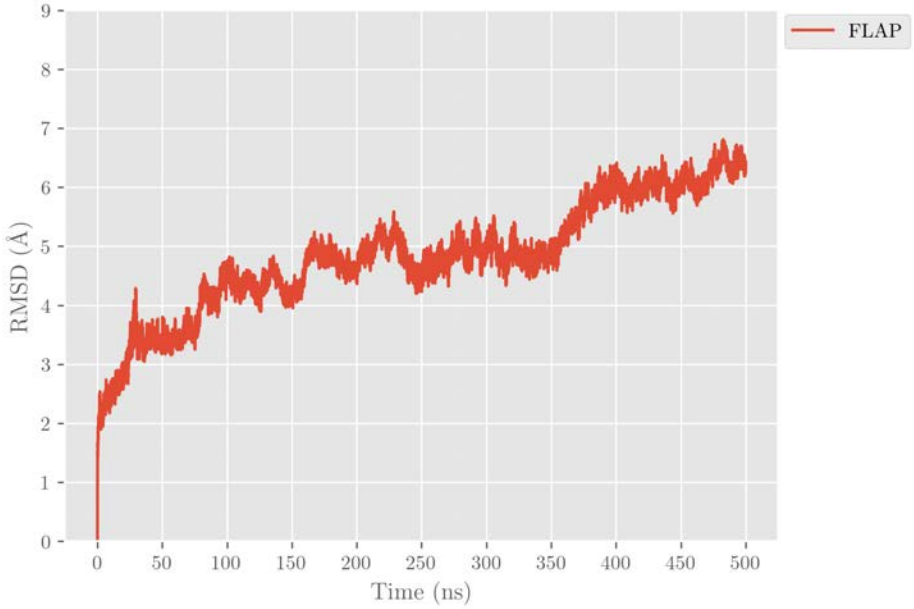

Figure 8.3: All-atom RMSD of the FLAP trimer.

The RMSD plot (Figure 8.3) reveals a great movement of FLAP structure during the trajectory. Nonetheless, the three monomers do not contribute equally to the global movement of FLAP trimer (Figure SI8.2). To identify which are the most mobile residues and the differences between the monomers, the residue-wise RMSF has been measured for all three monomers. The measured values are plotted in Figure 8.4.

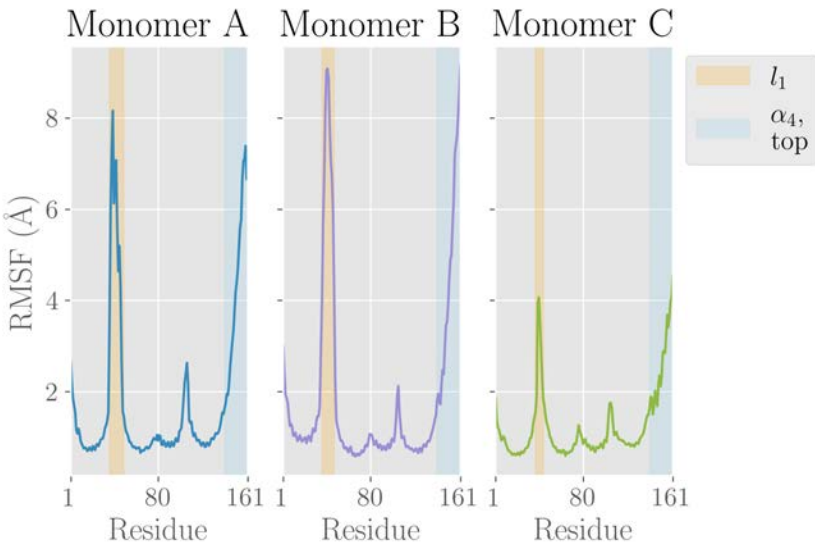

Figure 8.4: Residue-wise RMSF for each monomer of FLAP. Regions with high mobility, l_1 –the loop that links helices α_1 and α_2– and the topmost region of helix α_4 for each monomer are indicated in orange and blue, respectively.

The RMSF measure (Figure 8.4) reveals that there are two highly mobile regions –which structurally correspond to opposite regions of the protein– in all monomers and that they are not equally mobile in each monomer. Thus, two movements of different FLAP's regions have been found. For better visualisation of the movements, a comparison of FLAP's structure in the initial and final frames of the analysed trajectory is available in Figure 8.5.

On the one hand, the helices located at the protein's top bend from the solvent to the top of the membrane, with residues Phe138, Phe139 and Gly140 acting as a hinge. As a consequence, a role for this helices emerges: they act as an anchor for FLAP, so it cannot cross the membrane towards the cytosol. A visual analysis of the trajectory reveals that the bending of

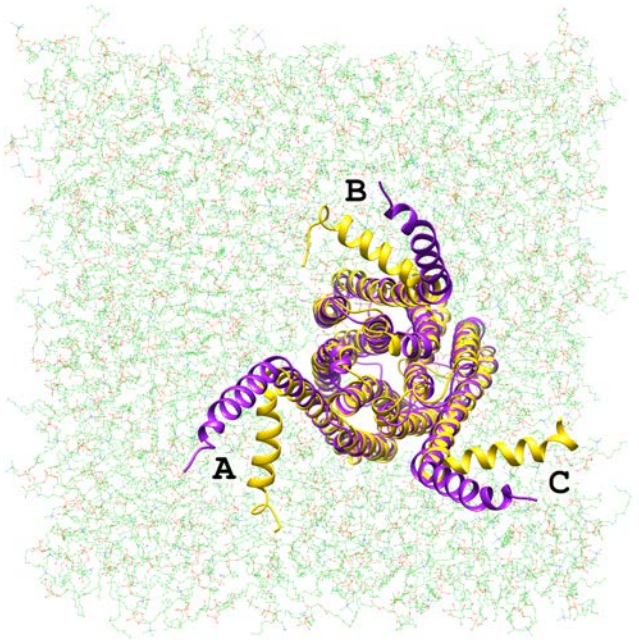

(a) Top view

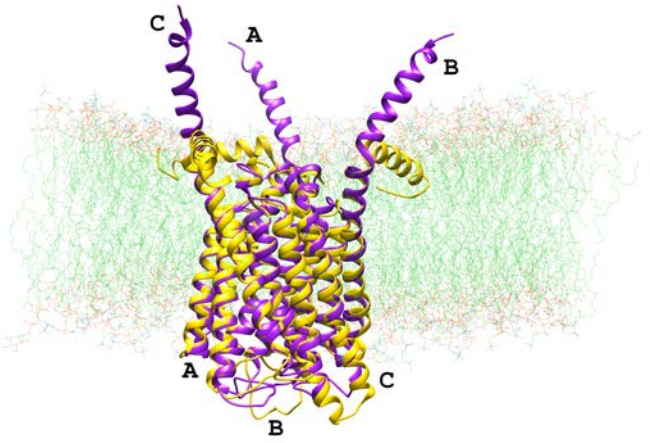

(b) Frontal view

Figure 8.5: Top and frontal views of the initial and final frames of the MD production. The protein's structure in the first frame of the production is drawn in purple, while the protein's structure in the last frame of the production is drawn in yellow. The membrane corresponds to the final frame and is drawn in green. Monomers are indicated with the corresponding labels.

helix α_4 of monomer C happens the first, followed by monomer A and B. This is one of the reasons why the RMSD increases along the trajectory for monomers A and B but not for C and hence why the RMSF is lower for monomer C than for the other ones.

On the other hand, the loops that link the helices α_1 and α_2 (l_1) found on the bottom of the each monomer move also significantly except for monomer C, as the RMSF plot reveals (Figure 8.4). The initial structure of FLAP of the MD production stage shows that l_1 has 8 residues (from Gln37 to Arg44), while l_1 of monomer A has 14 residues (from Thr36 to Ala49) and l_1 of monomer B has 12 residues (from Thr36 to Thr47). This difference on the l_1 length makes the loop much more flexible for monomers A and B than for monomer C, and it can be observed along the trajectory. Structurally, l_1s of monomers A and B keep bending from the centre of the trimer to the outermost part and the closest α_1 and α_2 residues pack and unpack into the helices accompanying the loop's bending.

8.3.2 FLAP effect on the membrane

It is known that some transmembrane proteins are able to modify the membrane's shape inducing a curvature. This curvature can be associated with several biological processes such as the association of proteins –transmembrane or not–, transport between the two sites of the membrane, or even with the shape of the organelle.[190]

To understand how FLAP affects the membrane's shape, the membrane's curvature has been analysed. The mean curvature can be found in Figure 8.6.

As it can be observed, the membrane is curved along the trajectory as the non-planar mean curvature indicates. The region around FLAP is the most curved region, with a mean curvature of 0.2. Nonetheless, three small regions around FLAP are significantly less curved than the

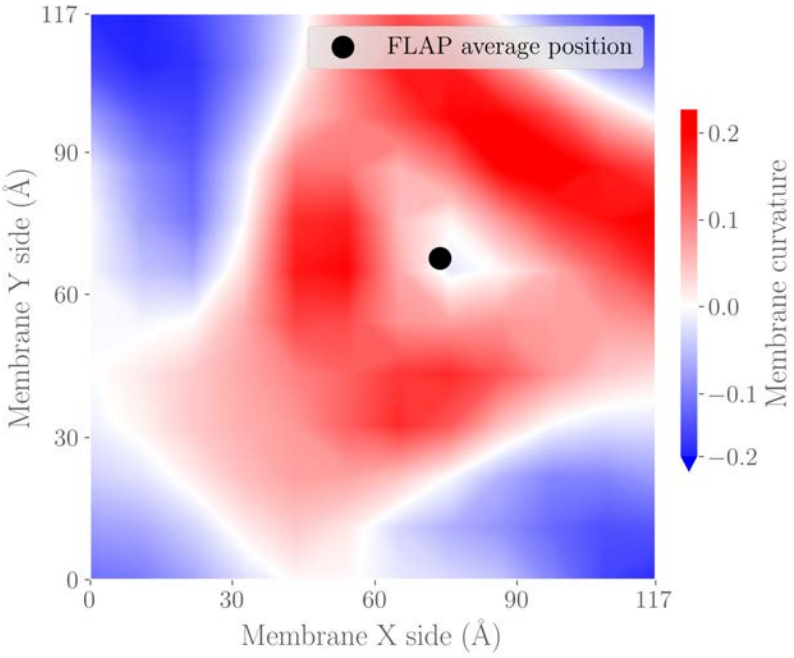

Figure 8.6: Mean membrane's curvature. Red indicates a convex curvature, while blue indicates a concave curvature. A curvature 0 means plane and ± 1 curvature is a sphere. The mean position of the FLAP is indicated as a black dot.

rest of the membrane that circumscribes the protein. These three regions correspond to the topmost regions where helix α_4 that bend towards the membrane are located. Nonetheless, this curvature-inducing effect is local. The regions of the membrane close to the model's edges curve concavely –in the opposite way than FLAP's surrounding–, so it can be expected that in a bigger model the membrane's edges would get flat, as it happens in some small regions of this model like the region from 30 Å to 60 Å along Y axis and from 0 Å to 10 Å along X axis (Figure 8.6), for instance.

8.3.3 Arachidonic Acid binding

One of the roles attributed to FLAP is its ability to bind free AA molecules spread in the membrane. To study this function, the AAs that are close to FLAP have been analysed. Thus, the number of contacting AAs in each frame has been measured. The corresponding plot can be found in Figure 8.7.

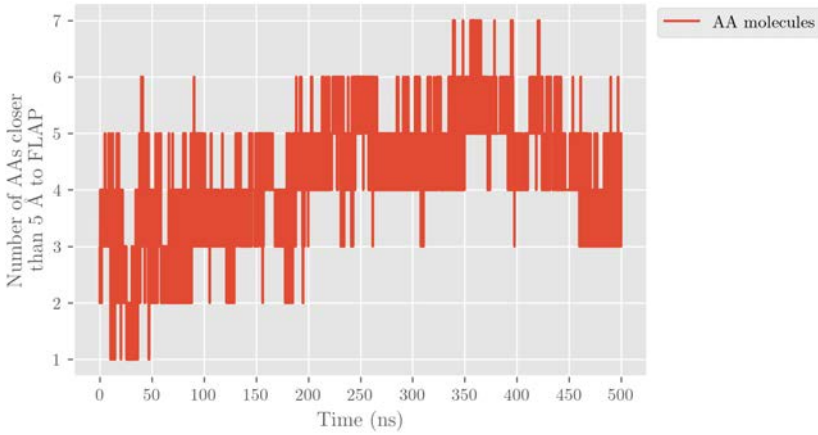

Figure 8.7: Number of close AA molecules to FLAP along the trajectory.

As Figure 8.7 shows, the number of AAs close to FLAP increases along the trajectory concentrating up to 7 molecules out of the 41 total spread ones in the membrane. The FLAP's AA-contacting residues have been analysed to identify if there are residues that play a key function in the AA-binding role of FLAP. Lots of residues in the hydrophobic region have been identified, suggesting that the AA-binding role is a global behaviour of the protein.

It is relevant to mention that the reported crystallographic structures of FLAP containing inhibitors, such as MK-886, indicate that they bind in

the inter-monomer regions. In order to identify if this region is the same where the contacting AAs bind, hence if the inhibitor acts by blocking the AA-binding region of FLAP, the residues that enclose the inhibitor have been analysed. Among hydrophobic residues, two hydrophilic residues have been detected: the Arg35 and the Arg117, each of them belonging to a different monomer (A and C in this case). These two residues are capable of interacting with the COO^- group of the AA through a saline bridge, which is strong enough to establish a stable interaction. AA binding to these residues have been studied.

Among other AA molecules, the one numbered as residue 511 (AA511) has been detected to interact with these residues. The minimum distances to Arg35 and Arg117 are plotted along the MD trajectory in Figure 8.8.

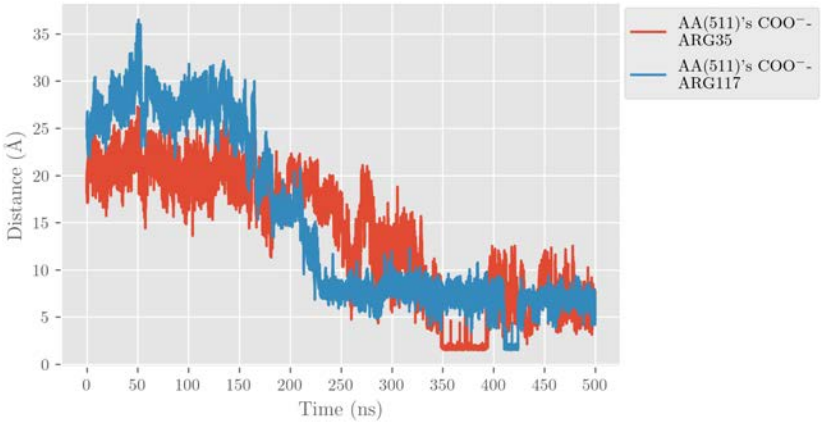

Figure 8.8: AA511's COO^- distance to Arg35 and Arg117 along the trajectory.

The trajectory of this AA molecule has been analysed visually and in terms of distance to FLAP. The migration process can be found in Figure 8.9, while the minimum FLAP-AA511 distance along the MD production can be found in Figure SI8.4. This plot reveals that this molecule

is interacting with FLAP along all the MD production, but the interaction does not initially take place in the inter-monomer expected region.

Along the trajectory, the molecule explores the surface of FLAP towards the monomer A's Arg35. Around time 225 ns of trajectory the AA511 starts to interact with Arg35 of monomer A and Arg117 of monomer C. The interaction with Arg35 is weak during most of the migration process except for around 50 ns (from 350 ns to 395 ns), but the interaction with Arg117 is constant for the last half of the trajectory. During this migration process, the position of monomer C does not change significantly, whilst monomer A moves and pushes monomer B.

Thus, AA511 migration ends up with the AA molecule located in the inter-monomer region, which is in accordance to the inhibitor's position in the reported crystallographic models. Moreover, the AA molecule gets stabilised in this region for about half of the trajectory, suggesting that this region is the final target of the free AA molecules spread in membrane.

8.4 Conclusions

The study of FLAP embedded in a free-AA-containing membrane has given good perspectives on the two FLAP roles that were subject of exploration.

On the one hand, it has been seen that the FLAP is stable in the membrane and that it changes its conformation through a movement of the upper –lumenal– helices, which assists its anchoring and enhances its exposition to the membrane.

On the other hand, it has been confirmed that the FLAP is able to bind the AA molecules spread in the membrane. Moreover, this behaviour, combined with the migration process to the inter-monomer region, confirms its ability to capture the free AA molecules and transport them to

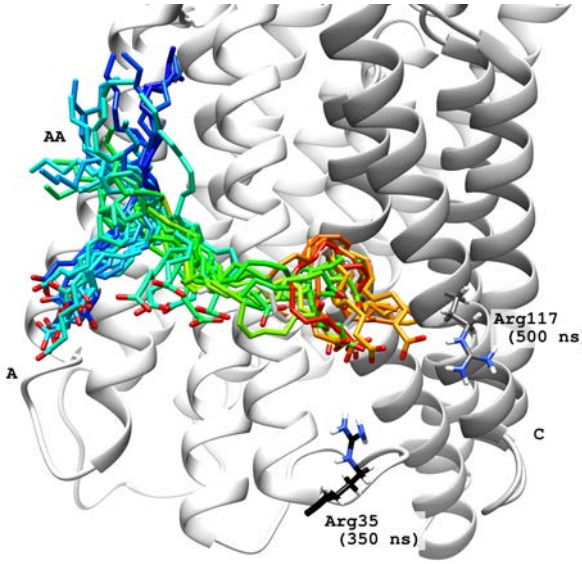

(a) Frontal view

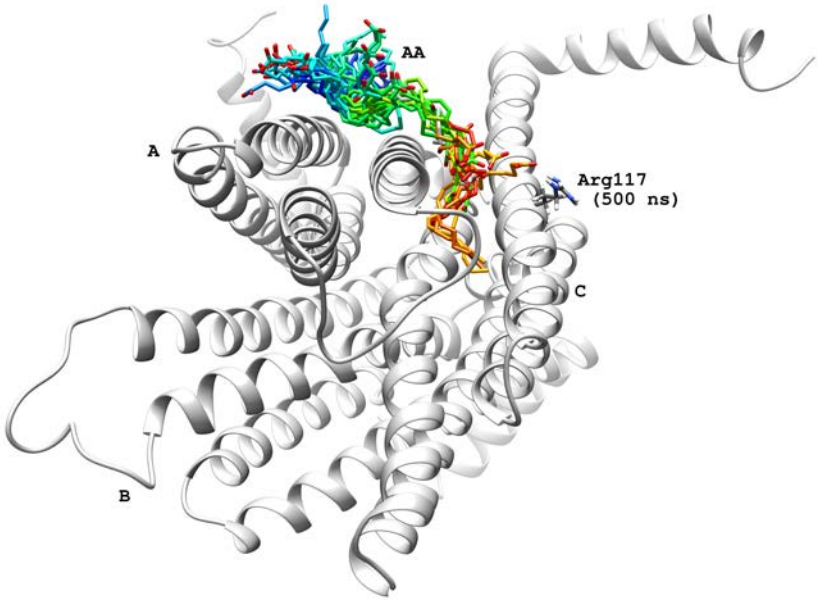

(b) Bottom view

Figure 8.9: Migration process of AA511 on FLAP's surface along the trajectory. FLAP's structure at 500 ns is drawn in white. Arg35 position at 350 ns is drawn in black (in a), while Arg117 at 500 ns is drawn in gray. Rainbow coloring of AA indicates the time along the trajectory, from blue (time 0 ns) to red (time 500 ns). A, B and C labels indicate each of the monomers.

the target binding region. From this location, these bound AA molecules might be transferred to *hum*ALOX5, since it is known that some kind of interaction takes place between these two proteins –FLAP and *hum*ALOX5– and that FLAP has a role in enhancing *hum*ALOX5 activity and in feeding it with AA molecules for their conversion into LTA_4 [191].

8.5 Future work

During this Chapter, molecular details of FLAP's role in binding AA have been described. Nonetheless, in the Introduction Section (Section 8.1) another FLAP's function was mentioned: the regulation of *hum*ALOX5 activity, mainly related with its LTA_4-synthase role. Nonetheless, how FLAP and *hum*ALOX5 interact and how FLAP regulates *hum*ALOX5 remains unknown. [86]

The interaction between these two proteins has been object of study for several decades, but no details have never been reported. Nonetheless, it is known that FLAP is responsible for providing AA to *hum*ALOX5. In 2021, Gilbert et al. [192] reported that *hum*ALOX5's structure shows a closed conformation of the helix α_2. They built a model that combines the FLAP and *hum*ALOX5 structures aligned to the membrane as predicted by PPM2.0 [181]. Nonetheless, they discussed that the closed conformation of helix α_2 blocks a substrate channel to the active centre. To explore this, they generated a *hum*ALOX5 conformer with an elongated, or open, conformation of the helix α_2. With this conformation, a new channel to the active site located in the membrane-interacting site of *hum*ALOX5 opens.

However, these models do not properly describe the interaction. Moreover, the models are based on manual alignments using incomplete crystallographic structures, which in the case of FLAP have been demonstrated

to be different in comparison to the structures from the presented MD simulation. To delve in this FLAP-*hum*ALOX5 interaction, it was needed to explore the FLAP behaviour in the first place since no molecular detail has never been reported.

As the starting point of the FLAP-*hum*ALOX5 interaction study, a protein-in-membrane–protein docking has been performed using the LightDock software[193–196]. A drawing of the model is available in Figure 8.10.

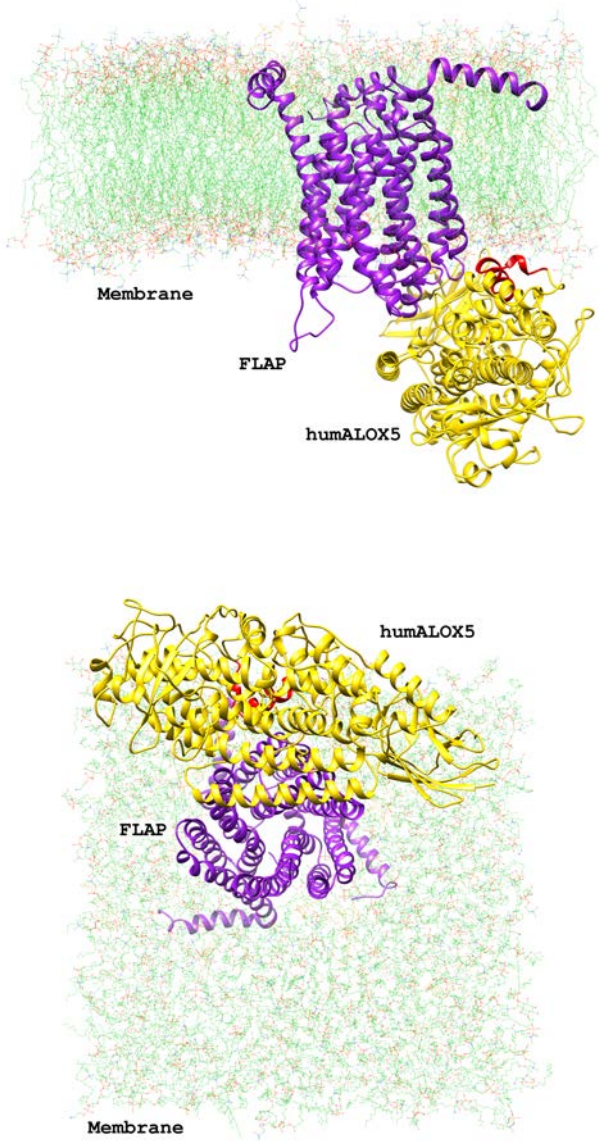

Figure 8.10: Initial model of humALOX5 and FLAP, embedded in the membrane, for the study of FLAP-humALOX5 interaction. hALOX5 is coloured in yellow, hALOX5's helix α_2 is coloured in red, FLAP is drawn in purple and membrane is drawn in green. Labels specify each part of the system.

Chapter 9

Computational study on the conversion from LTA_4 to LTB_4 driven by LTA_4H

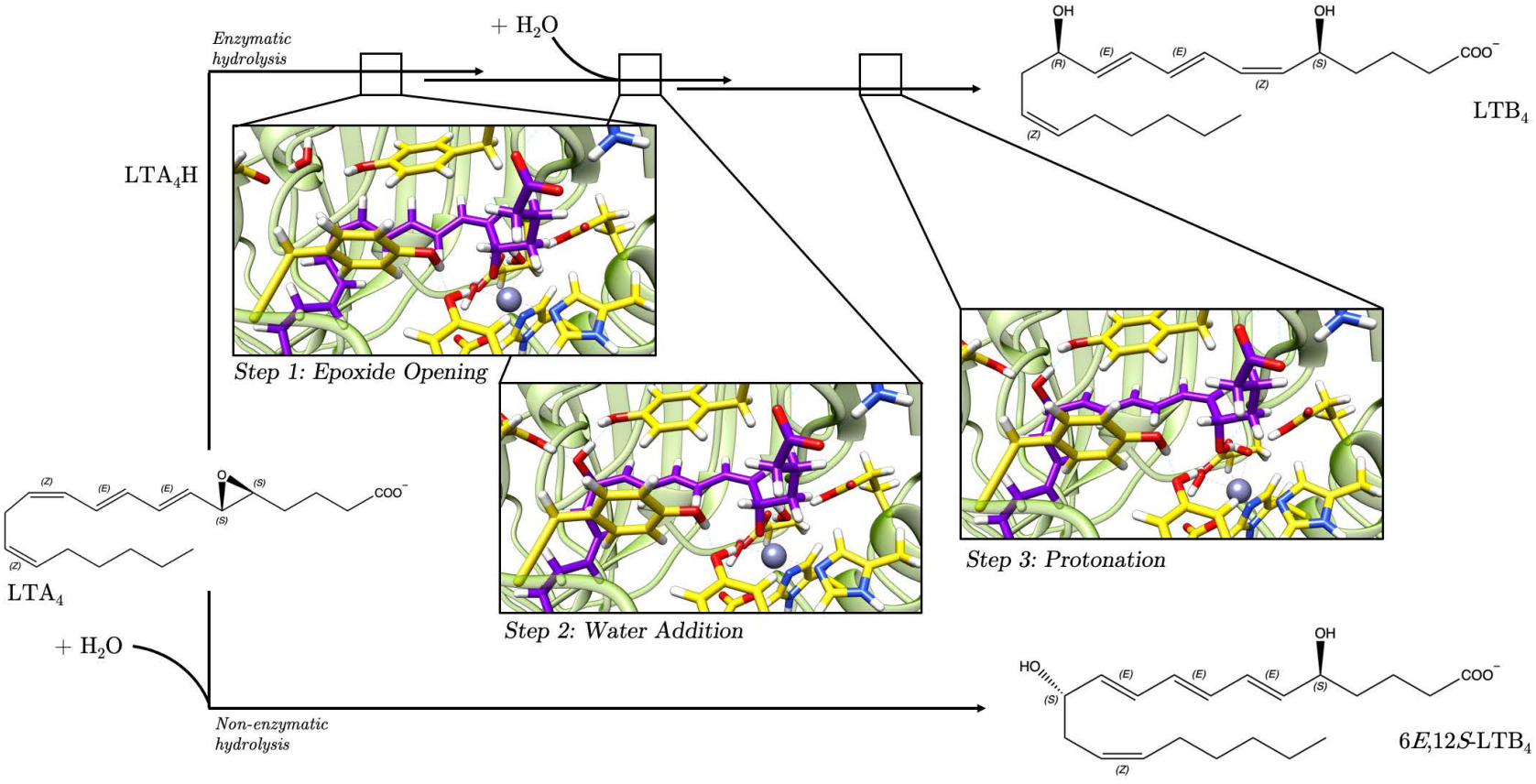
Enzymatic hydrolysis
+ H_2O
LTA_4H
LTB_4
Step 1: Epoxide Opening
Step 2: Water Addition
Step 3: Protonation
LTA_4
+ H_2O
Non-enzymatic hydrolysis
$6E,12S$-LTB_4

The work presented in this Chapter corresponds to Canyelles-Niño et al.[197]*. The publication and the Supporting Information can be found in Chapter SI9.*

9.1 Introduction

The enzymatic conversion of Leukotriene A_4 (LTA_4) to LTB_4 is quite an interesting reaction. A scheme of the reaction can be found in Figure 9.1. As it can be observed, the conversion is a hydrolysis reaction that is unique due to two features: the addition of the OH^- group takes place seven methylene units away from the leaving group (the O from the epoxide that deattaches from the C_6 bond, the bond with C_5 remains intact) in a 1,7-S_N reaction. Moreover, the addition takes place in a very stereochemical-controlled way and the reaction defines the conformation of a double bond next to the leaving group. The overall process is driven by LTA_4H.

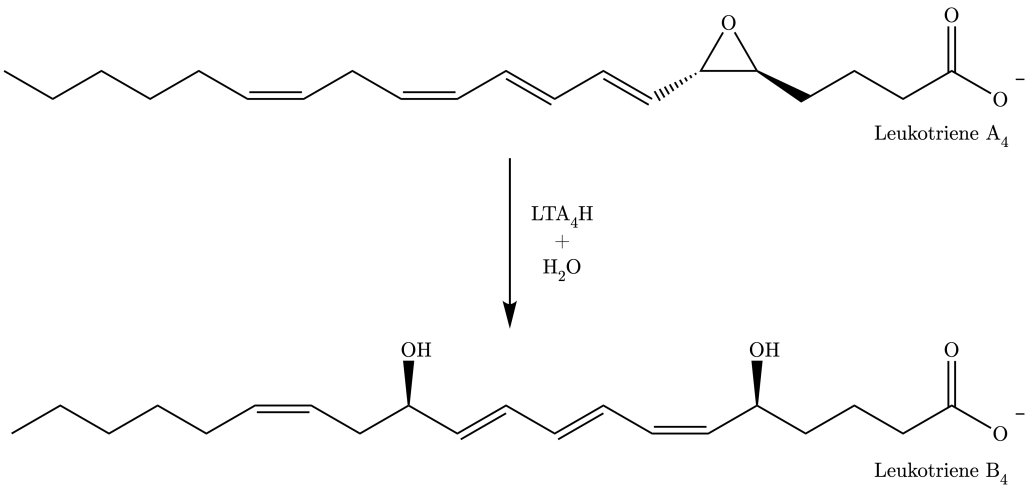

Figure 9.1: LTA_4 to LTB_4 reaction driven by LTA_4H.

Leukotriene A_4 Hydrolase (LTA_4H) (EC 3.3.2.6[198], Figure 9.2) is a zinc-containing, monomeric metalloenzyme.

Even though it is labelled as a hydrolase, LTA_4H has a dual activity: it can act as a hydrolase[199] or as an amino-peptidase[200]. In the latter case, LTA_4H is able to cleave the Pro-Gly-Pro polypeptide through a hydrolysis of the peptic bond between the N-terminal residue and the central amino acid. On the other hand, LTA_4H acts as a hydrolase by the addition of a water molecule on LTA_4 in a highly stereo-, regioselective way to produce LTB_4[201]. The hydrolysis reaction can be found in Figure 9.1.

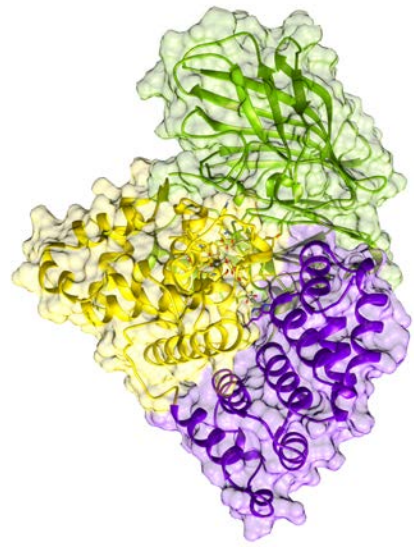

Figure 9.2: LTA_4:LTA_4H Michaelis complex. The N-term domain is drawn in green, the catalytic domain in yellow and the C-term domain in purple.

As reviewed in Section 1.2.2.1, Leukotriene A_4 (LTA_4) is a LT, a derivative of AA biosynthesised by *hum*ALOX5. As a LT, LTA_4 and its derivatives are lipid mediators involved in the pro-inflammation stage of an inflammatory process. As it can be observed in Figure 9.1, LTA_4 has an epoxide with a triene system next to it. This chemical structure makes LTA_4 very reactive, with a half-life time of around 3 s [202].

Thus, LTA_4 is converted into two different, initial derivatives: LTB_4 and LTC_4. LTB_4 [203] is the hydrolised derivative of LTA_4 and is the last one of its route, while LTC_4 is a glutathionated derivative, converted by LTC_4S [204]. From LTC_4, other LTs such as LTD_4 and LTE_4 are obtained through consequent transformations [201].

In the present Chapter, the conversion from LTA_4 to LTB_4 by the action of LTA_4H will be studied from a theoretical point of view, with a focus on the regio- and stereoselectivities of the enzyme.

9.1.1 Reactivity approach to LTB_4 biosynthesis

The conversion from LTA_4 to LTB_4 is a very stereoselective process. The step-by-step conversion is schematised in Figure 9.3. The first step starts from LTA_4. Through a S_N reaction, the unprotonated LTB_4 is obtained. During the reaction, the C_6-C_7 double bond is defined with a *Z* conformation, and the OH^- is added with an *R* stereochemistry at C_{12}. A final protonation of this intermediate leads to LTB_4.

A S_N1 mechanism has been proposed by Stsiapanava et al. [85]. In this proposal, the Zn atom acts as a Lewis acid and is responsible for the opening of the epoxide. Then, a water molecule is added to C_{12}, and the opened epoxide gets finally protonated.

Furthermore, a mechanistic study using computational methods has been published by Mu and Xu [205]. In this investigation, the authors discussed the Epoxide Ring Opening (ERO) reaction and the protonation of

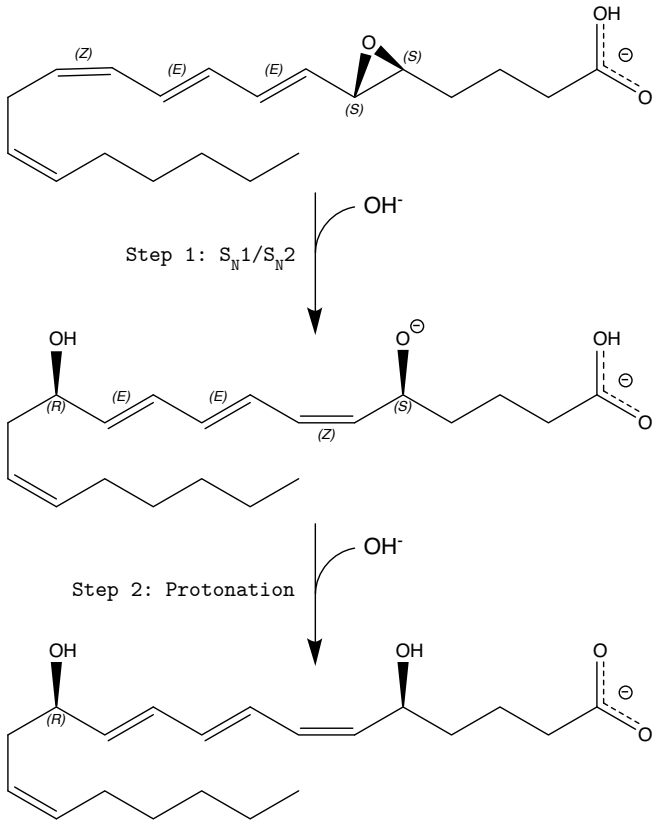

Figure 9.3: Step-by-step conversion from LTA_4 to LTB_4.

the opened epoxide by building a bidimensional PES of the two reactions. The result is that the two reactions are independent, being the ERO the first one. Nonetheless, this paper is incomplete because of two different reasons: the chosen model was not the latest available in that moment and it did not contain Zn-coordinating water molecules that seem to be key for the reactivity[85]. Moreover, the study was focused only on the reactivity around the epoxide ring, so neither the addition of the water molecule nor the stereoselectivity of the reaction were considered.

Thus, available literature has not unravelled the S_N character of the reaction (uni- or bimolecular), as well as the role of the enzyme regarding the stereochemical properties.

9.2 Computational methods

In this Section the computational methodology including protein setup and computational features will be reviewed.

9.2.1 Protein setup

In 2001, the first X-ray structure of LTA_4H was published[206]. Since then, almost 70 structures have been reported under the P09960 `UniProt's ID`[134]. Several of them correspond to the WT version of the enzyme, although other ones include different mutations. For this study, a structure of the LTA_4H complexed with LTA_4 and containing the Asp375Asn mutation (PDB ID 5NI6[85]) has been selected. This structure consists of a mutant version of LTA_4H complexed with LTA_4 in its catalytic centre.

The crystal contains two different poses for LTA_4. From these, the pose with LTA_4 interacting with Arg563 and Lys565 has been selected, since these interactions have been found to be key for substrate anchoring and hence for the hydrolase activity[84]. Moreover, the mutation has been reverted through an Asn375Asp mutation using the `rotamers` module from `UCSF Chimera`[135] in order to obtain the WT variant of the enzyme.

9.2.1.1 Protonation status

The WT LTA_4:LTA_4H complexed structure was protonated at pH 7.0 using the `ProteinPrepare`[136] module from `playmolecule.org`.

All obtained protonations were kept except for Glu271 and Glu296. In contrast with the literature[85], `PROpKa`'s protonation results suggests

that Glu271 is unprotonated while Glu296 is protonated. Both residues interact with the same Zn-coordinated water molecule (Wat1) through a hydrogen bond, which can lead to unclear protonation states.

Moreover, previous bibliography indicates that only Glu271 is crucial for hydrolase activity[207], while the mutation of Glu296 does not have any effect on the enzymatic activity[208]. Furthermore, the only available computational study proposed that Glu271 is the one actually protonated.

Due to these reasons, the idea that the initially-obtained protonation might not be the proper one was reinforced. In order to unravel the protonation state of the Zn environment, the two initial configurations (protonated Glu271 and unprotonated Glu296, and unprotonated Glu271 and protonated Glu296) have been built. Both have been optimised at the QM/MM level (Section 9.2.4 for further details), leading both of them to the same result: Glu271 is deprotonated while Glu296 is protonated. This is going to be the initial structure.

9.2.2 Solvated model and Molecular Mechanics parameterisation

The crystallographic, QM/MM-optimised structure has been chosen for building the solvated model.

Zn and its environment have been parametrised following the Seminario Method[138] using `MCPB.py`[139] from `AmberTools`[94]. Residues within a radius of 3.0 Å from the Zn atom have been selected, including His295, His299, Glu318, Wat1 and Wat2. Gaussian16[143] has been used as the QM software. No further optimisation has been performed since the structure has been previously optimised at the QM/MM level. RESP charges[144] and frequencies have been obtained at the B3LYP[141]/6-31G(d)[142] level. From the calculated frequencies, MM parameters have been finally obtained.

LTA_4 has been optimised at the B3LYP[141]/6-31G(d)[142] level and from

there RESP charges[144] have been obtained. Parameters have been obtained using the `parmchk2` module from `AmberTools`[94] and using the `GAFF2` force field[145].

The `tleap` module from `AmberTools`[94] package has been used for combining the obtained custom parameters with the `ff14SB AMBER`'s force field[89] for standard residues. As the authors recommend[89], TIP3P model[155] has been chosen as the solvent model. Using `tleap`[94], a pre-equilibrated orthorhombic box of waters has been built. 9 Na^+ atoms have been added to the water box to neutralise the protein's charge. The limits of the box have been defined at 10 Å from the outermost protein's atom in each direction. As a result, a box with dimensions of 78.7 Å × 116.5 Å × 94.7 Å containing roughly 72000 atoms, almost 10000 of them from the protein, has been obtained.

Once parameters and topology files have been obtained, parameters have been manually modified using the `parmed` module from `AmberTools`[94]. From the QM/MM-optimised structure, two hydrogen-bond interactions between Wat1 and the epoxide's oxygen atom of LTA_4, and the hydrogen of Tyr378 and the epoxide have been detected. To describe these interactions, a bond with a force constant of 25 $kcal \cdot mol^{-1} \cdot Å^{-2}$ has been manually added between these atoms.

9.2.3 Molecular Dynamics simulation

MD simulations have been performed in GPUs using the `CUDA`[147;148] version of the AMBER's[94] `pmemd` module from `AMBER`[94] in its 18 version.

An initial MM minimisation stage has been performed. Three sets of 5000 steps have been carried out using the steepest descent method followed by 5000 steps using the conjugate gradient method. For the first set, protein's movement has been restrained applying a 150 $kcal \cdot mol^{-1} \cdot Å^{-2}$ force. For the second set, the same restrain has been applied to the atoms

of the backbone of the protein. For the third set, no restraints have been applied. During minimisation and the following stages, PME method[160] has been used with a cut-off of 9 Å for all the Lennard-Jones interactions.

Following the minimisation stage, the system has been heated to 300 K. In order to do so, 10 steps 200 ps have been applied increasing the temperature 30 K per step. For this stage and the following ones the SHAKE algorithm[159] has been activated for all atoms except for LTA_4's epoxide-interacting hydrogens.

A 5 ns NPT equilibration stage has been done until density equilibration at $1.025\,\mathrm{g\,mL^{-1}}$. A restraint of $5\,\mathrm{kcal{\cdot}mol^{-1}{\cdot}\AA^{-2}}$ has been applied to the backbone of the protein. Pressure and temperature have been set at 1 atm and 300 K, respectively, and are controlled using the Berendsen thermostat and barostat[158].

Finally, a 10 ns NVT equilibration stage has been carried out before the production of 150 ns. The volume of the water box has been kept from the last frame of the NPT stage, while temperature has been set at 300 K. From the 150 ns of production, only the last 100 ns have been used for analysis.

For MD simulation's analysis, `RCBS.py` package[161] and `MDAnalysis` Python package[187;188] have been used.

9.2.4 Quantum Mechanics/Molecular Mechanics simulations

For the QM/MM calculations, the solvated model of the crystallographic structure has been used. The water box has been cropped: only waters within a radius of 17 Å from the substrate have been kept. All atoms from the protein have been kept. Thus, around 11000 atoms have been considered for the QM/MM calculations. The same `AMBER` parameters built in Section 9.2.2 have been used for describing the MM atoms.

The active region has been defined by selecting all atoms within a

sphere with a radius of 15 Å centred at the oxygen of the epoxide of the substrate. Thus, around 3000 atoms have been set as free-to-move. All the other atoms have been kept frozen.

The QM zone has been manually defined (Figure 9.4). All atoms interacting directly with Zn have been selected, as well as the lateral chains of the corresponding residues. Moreover, residues Glu271 and Glu296 have been also selected due to its hydrogen-bond interaction with Zn-coordinated water molecules and their possible involvement in the reaction. Asp375 and its closest hydrogen-bonding-interacting water molecule have also been chosen due to their involvement in the reaction mechanism. Finally, the epoxide and the triene of the substrate have been considered as QM atoms, as well as C_4 and C_{13} methylenes, which have been added in order to locate the QM/MM boundaries in more neutral regions.

QM/MM calculations have been performed using the modular interface `ChemShell`[162;163] in its 3.7 version. `DL_POLY 5.0`[166] has been selected as the MM engine, while `TURBOMOLE 7.0`[165] has been used as the QM engine.

QM atoms are described at the DFT level by the B3LYP hybrid functional[141]. 6-31G(d) Pople's basis set[142] has been used for describing H, C, N and O atoms, while for Zn Stuttgart RLC ECP basis set[209] has been chosen.

QM/MM minima optimisations and scan calculations have been performed using the `DL-FIND` module[210] from `ChemShell`. HDLC[164] coordinates have been used in combination with the microiterative scheme[168], for which all residues with at least one QM atom have been considered. Energy optimisations have been done using the L-BFGS algorithm[167], setting the tolerance at 0.0045 Bohr for optimisations to minima and at 0.01 Bohr for scan calculations. For scan calculations, harmonic potentials with a force constant of 3.0 Hartree·Bohr^{-2} or 3.0 Hartree·rad^{-2} have been applied to at least one bond, bond distances difference, or angle.

For TS search, `HDLCopt` module[164] from `ChemShell` has been used. The atoms directly involved in the reactivity have been considered as the core, for which P-RFO algorithm[164] has been used. L-BFGS[167] has been used for all the other atoms. HDLC coordinates have been used for describing the positions of the atoms. Microiterative scheme[168] has not been used due to software limitations. For the calculations, tolerance has also been set at 0.0045 Bohr. Frequencies have been calculated using the `force` module from `ChemShell` and considering all atoms in the QM region. Frequencies have been analysed for confirming the nature of the stationary structures.

A self-implementation of the Dijsktra algorithm[211] has been used for obtaining MEPs from bidimensional PESs.

9.3 Results and discussion

Along this Section a description of the enzyme and its reactivity regarding the conversion from LTA_4 to LTB_4 will be presented.

9.3.1 Structural analysis

The crystallographic structure has been studied. LTA_4 has been found to occupy the main cavity of the enzyme in a head-first conformation. The L-shaped, hydrophobic cavity contains Arg563 and Lys565 in its bottom, a pentacoordinated Zn in the middle and Asp375 with a hydrogen-bonding-interacting water in the vertex of the L shape.

As said in Section 9.2.1, Arg563 and Lys565 are the responsible of the anchoring of the carboxylic head of LTA_4. Moreover, the fitting of the substrate places the epoxide near the Zn atom. Zn is pentacoordinated to His295, His299, Glu318 and two water molecules with an octahedral geometry (RMSD against ideal octahedron of 0.490 Å, Figure SI9.1), so a

vacancy is available. A representation of the Zn's environment is drawn in Figure 9.5. In fact, the epoxide of the substrate is geometrically occupying the vacancy but in the second sphere of coordination. This epoxide positioning is also helped by two hydrogen-bonding interactions with Tyr383 and one of the Zn-coordinated water molecules.

Furthermore, two Tyrs, Tyr267 and Tyr378, enclose the triene of the LTA_4 in the cavity. Non-bonding interactions between the protein and the substrate are summarised in Figure 9.6. As it will be discussed in the following Sections, Tyr267 and Tyr378 have a key role in the selectivity of LTA_4H.

Finally, LTA_4's binding mode has been also studied. As explained before, the carboxylate head interacts with Arg563 and Lys565 through a water that acts as a bridge. C_{12} is close to a water molecule that interacts through a hydrogen bond with Asp375. H_6-C_6-C_7-H_7 has a dihedral angle of around 65°, which is neither *Z* nor *E*, but pro-*Z*. This will be important in the following Sections in order to unravel the stereochemical and conformational control of the enzyme on the reaction.

9.3.2 Molecular Dynamics simulations

Structural analysis of the QM/MM-optimised structure has lead to some conclusions. Nonetheless, these conclusions might only be applicable to the optimised structure. In order to confirm the observations, MD simulations have been analysed. From the produced 150 ns, the last 100 ns have been analysed.

After confirming the stability of both the substrate and the backbone of the protein by RMSD measurements (Figure SI9.2), three features have been analysed: the stability of the epoxide-Zn interaction, the presence of a water bridging between Asp375 and C_{12} and the C_6-C_7 conformation.

9.3.2.1 Epoxide stability in the active site

In Section 9.3.1, two interactions were detected and the epoxide was found to be placed in the second sphere of interaction of Zn. In the present Section, these interactions are analysed along the MD simulation. In Figure SI9.3 the evolution of distances from epoxide to Zn, Tyr383 and Wat1 can be found.

All three distances are very stable along the MD. These results lead to the conclusion that the epoxide ring is in a very stable position and that all three interactions are actually occurring.

9.3.2.2 Water stability around Asp375 and C_{12}

Another key parameter to study is the presence and behaviour of water molecules around C_{12} and Asp375, which has been demonstrated to be necessary for the reaction[85]. In order to study this, a bridging water between Asp375 and C_{12} has been searched along the MD trajectory.

The search of the bridging water has been done in the following way: for each frame, water molecules closer than 3 Å (there has to be a hydrogen-bonding interaction) to Asp375 and closer than 5 Å to C_{12} have been searched. Then, the two lists of water molecules are compared and the matching ones are selected. Finally, if more than one water molecule is bridging, the closest-to-C_{12} one is selected. If there is only one water molecule, it is the selected one.

Using this algorithm, the closest bridging waters have been detected. The distances from water molecules to Asp375 and C_{12} along the MD trajectory have been plotted in Figure 9.7. 96% of the frames present a water molecule satisfying these criteria. Nonetheless, it has been found that even though the water molecules are very stable in that position, different water molecules exchange along the trajectory.

9.3.2.3 C_6-C_7 conformation

The conformation of the C_6-C_7 bond, the single bond located between the epoxide and the triene in the reactant, is a conformationally-defined double bond in the final product while in the reactant it is a rotatable single bond. Thus, some kind of conformational regulation controlled by the enzyme has to take place. To analyse the behaviour of the C_6-C_7 bond, the H_6-C_6-C_7-H_7 dihedral angle has been measured along the trajectory. The obtained results are plotted in Figure 9.8, in such a way that any value under $-90°$ is considered pro-*Z* and any value over $-90°$ is considered pro-*E*.

As it can be observed in Figure 9.8, in most of the frames (91%), the conformation of C_6-C_7 bond is pro-*Z*, while the pro-*E* conformation is observed only in the 9% of frames. These results reveal that the enzyme is able to control the conformation of the double bond before the reaction starts.

9.3.3 Quantum Mechanics/Molecular Mechanics simulations

QM/MM calculations have been done in order to unravel several different features that cannot be studied using MD simulations such as the reactivity.

Solvated, cropped crystallographic structure model (Section 9.2.4) has been selected for carrying out the QM/MM calculations.

9.3.3.1 S_N character of the conversion

In order to clarify the S_N character of the reaction corresponding to the first part of the reaction (Figure 9.3), a bidimensional PES has been prepared. For building the bidimensional PES, an ERO-defining reaction coordinate has been used as the first coordinate ($r_c^1 = d(C_6^{\mathrm{LTA_4}} - O^{\mathrm{LTA_4}})$),

and water addition (defined as the breaking of the O-H bond of the water molecule Wat3 and the formation of the C_{12}-O bond, $r_c^2 = (d(O^{WAT3} - H^{WAT3}) - d(C_{12}^{LTA_4} - O^{WAT3}))$ has been selected as the second reaction coordinate. The remaining geometrical parameters have been fully optimised following the methodology detailed in Section 9.2.4.

The bidimensional PES and the identified MEP are plotted in Figure 9.9. As it can be seen, two independent, orthogonal reactions can be identified. The first step shows the evolution starting on R along the ERO coordinate (r_c^1) while the Water Addition coordinate (r_c^2) is kept invariant. Thus, the INT1 structure is obtained, which further evolves to INT2 only through the Water Addition coordinate (r_c^2) in the second step of the mechanism.

This two-step mechanism confirms that the first reaction of the conversion follows a S_N1 mechanism. This kind of mechanism requires the presence of a positive charge in the electrophilic group (the triene in the present case). Therefore, a NBO analysis has been performed. From the analysis, a charge of +0.71 au delocalised over the triene moiety (C_6–C_{12}) has been obtained confirming the S_N1 character of the mechanism.

INT2 has been structurally studied. Surprisingly, the obtained product is not the expected LTB_4 but the 6*E*,12*S*-LTB_4 isomer. The initial structure (crystallographic, QM/MM-optimised structure) has been analysed and LTA_4 shows an initial $\varphi(H_6 - C_6 - C_7 - H_7)$ of $-65.6°$, which is clearly a pro-*Z* configuration. A detailed structural analysis of the structures along the MEP has revealed that during the first step of the mechanism –the ERO reaction– the C_6–C_7 bond suddenly defines with an *E* conformation whilst the bond is acquiring the double bond character. Moreover, it is interesting to mention that not only the conformation of the double bond is surprising, but the stereochemistry of the water addition is also the opposite to the expected, suggesting some kind of relation

between these two geometrical features.

9.3.3.2 Stereochemical control of the reaction

In order to unravel the reasons behind the conformational control, another bidimensional PES has been built. The two explored coordinates are the following: the ERO ($r_c^1 = d(C_6^{\mathrm{LTA}_4} - O^{\mathrm{LTA}_4})$) and the rotation of the C_6–C_7 bond ($r_c^3 = \varphi(H_6 - C_6 - C_7 - H_7)$).

The initial structure of the reactant has been reobtained starting from the INT2 structure found in Section 9.3.3.1. As the PES shows (Figure 9.9), hysteresis has been detected. INT2 has a much lower potential energy compared to the rest of the stationary points, suggesting that a less energetic global conformation has been found. Thus, the Water Addition reaction has been firstly studied in the backwards direction, leading to INT1. Then, the ERO reaction has been explored in the backwards direction too. The reactant has been obtained. Structurally, only minor movements have been detected except for Wat3, which is much closer to C_{12} in the new reactant structure. A comparison of both structures can be found in Figure SI9.4. The RMSD of the residues with at least one QM atom is 0.81 Å, confirming that the overall movement is quite small.

From this new reactant, the bidimensional PES with the coordinates mentioned before has been built. It is plotted in Figure 9.10. Three minima have been detected: one corresponding to the reactant and the two other ones corresponding to the *E* and *Z* INT1s. From the reactant to each of the INT1s the corresponding MEP has been obtained, as shown in the Figure 9.10. The potential energy barrier of the path to the *E* isomer is 7.9 kcal/mol, whilst for the path to the *Z* isomer is 11.6 kcal/mol.

Moreover, the reason behind the stereochemical control of the water addition has also been cleared up. A detailed structural analysis of the two INT1s has led to the answer. In Figure 9.11 a representation of the ge-

ometries corresponding to the reactant and to the Z and E INT1s can be found. As the Figure illustrates, the geometry of substrate's triene is the opposite for the E and Z INT1 isomers in relation with the enzyme's cavity. Thus, the conformational control of the C_6-C_7 bond determines also the relative position of the whole triene in the cavity. As a consequence, the exposed-to-Wat3 face of the triene is the opposed in each case, leading to the $12S$ and $12R$ additions, respectively.

At this point, it has been unravelled that the first step of the mechanism is the opening of the epoxide ring, followed by the Water Addition to C_{12}. Moreover, for the first time the Z isomer has been identified but the ERO leading to the E isomer has been found to be more favourable in terms of potential energy. Thus, the complete mechanism for each of the paths needs to be studied in order to unravel the reasons behind the specificity of LTA_4H.

9.3.3.3 Complete *E* and *Z* paths

As said, the complete mechanisms starting from the reactant to the product have been studied. The first steps' energy barriers are obtained from the stationary structures located in the last bidimensional PES mentioned above and plotted in Figure 9.10, and fully optimising them to TSs or minima. From the optimised INT1 structures, water additions have been studied for each path. For these reactions, the addition has been performed adding the OH^- group to C_{12}'s exposed face, thus leading to alcohols with the opposed chirality, as discussed before. Finally, the protonation of the oxygen from the epoxide has been studied. As a result, a diagram of the potential energies of the stationary structures localised along each path has been built in Figure 9.12.

As discussed in Section 9.3.3.2 and plotted in Figure 9.12, the potential energy barrier is lower for the E path compared to the Z one by

3.7 kcal/mol (7.9 and 11.6 kcal/mol, respectively) for the first step of the mechanism, the ERO. Nonetheless, in the second step a crossing appears. The Water Addition reaction has a much lower relative potential energy barrier of 8.6 kcal/mol (15.9 kcal/mol taking the reactant as the reference) in the Z path compared to the 12.9 kcal/mol (18.7 kcal/mol taking the reactant as the reference) corresponding to the E path. Finally, the protonation step has also a lower potential energy barrier for the Z path of 3.8 kcal/mol (14.4 kcal/mol when taking the reactant as the reference). For the E path this barrier is 5.2 kcal/mol (17.8 kcal/mol if the reactant is taken as the reference). Thus, the second step of the mechanism is the RDS of the global path. The path that leads to the 6Z,12R-LTB_4, also known simply as LTB_4, is the one with the lowest potential energy barrier (globally 15.9 kcal/mol, 2.8 kcal/mol lower than for the E path).

In Figures 9.13, 9.15 and 9.17 a drawing of the different stationary structures along the E path can be found. In Figures 9.14, 9.16 and 9.18, the same drawing but for the Z path can be found. E and Z drawings of the same stationary structure are placed one next to the other for easier comparison. In Figures SI9.5–SI9.10 a closer view of each stationary structure focusing on the atoms directly involved in the reaction can be found.

As said before, the Z path (Figures 9.14, 9.16 and 9.18) is the one with the lowest potential energy barrier. Let's focus first on it. In Table 9.1 the most relevant distances that will be discussed in the following lines for the Z path are shown. For better visualisation, all these values have been plotted in Figure SI9.11.

As repeatedly said before, the first step of the reaction is the ERO (Figure 9.14). Along this reaction coordinate, the C_6 and $O_{epoxide}$ bond gets broken starting at a distance of 1.47 Å in R to 2.40 Å in INT1 going through a distance of 1.92 Å in the TS1. On the contrary, the C_5–$O_{epoxide}$

Table 9.1: Relevant distances and the dihedral angle of the stationary structures along the *Z* path. Distances (defined by two atoms) are in Å and dihedral angles (defined by four atoms) are in °.

Pro-*Z* Reaction Path	**R**	**TS1**	**INT1**	**TS2**	**INT2**	**TS3**	**P**
Zn-O_{epox}	3.39	2.94	1.99	1.97	1.95	2.45	2.96
O_{epox}-C_5	1.45	1.41	1.39	1.39	1.39	1.41	1.43
O_{epox}-C_6	1.47	1.92	2.40	2.41	2.42	2.37	2.39
H(Wat1)-O_{epox}	1.75	1.65	2.42	2.46	2.49	1.39	1.02
O(Wat1)-H(Wat1)	0.99	1.00	0.97	0.97	0.98	1.09	1.59
O(Wat3)-C_{12}	3.84	3.69	3.69	1.82	1.53	1.53	1.53
H(Wat3)-O(Asp375)	1.71	1.69	1.67	1.36	1.03	1.03	1.03
O(Wat3)-H(Wat3)	0.99	0.99	0.99	1.11	1.53	1.53	1.53
H_6-C_6-C_7-H_7	−65.6	−15.9	−7.1	1.5	1.5	−0.5	−0.7

bond, so its distance, does not significantly change. At the same time, the distance from the O_{epox} to Zn gets shortened, from 3.39 Å to 1.99 Å, revealing the Lewis acid role of the metal. The free vacancy in the coordination sphere of Zn is now occupied by the $O_{epoxide}$. Simultaneously, the distance of the initially hydrogen-bonding hydrogen of Wat1 has increased from 1.75 Å to 2.42 Å, so the interaction weakens. All the other distances have not changed substantially, even though the distance between O(Wat3) and C_{12} has slightly shortened due to electrostatic attraction between the negatively-charged O of Wat3 and the positively-charged triene (Section 9.3.3.1). During this step, the dihedral angle between H_6-C_6-C_7-H_7, which describes the Z/E character of the C_6-C_7 bond, has suffered an important change: it has rotated from −65.6°, which is pro-*Z*, to −15.9° in the TS1 to −7.1° in INT1, which translates into a well-defined *Z* configuration of the new double bond.

The evolution of this first reaction in terms of geometry determines the next one, the water addition. As discussed in Section 9.3.3.2, the *Z* configuration exposes the *R* face of the C_{12} to the water addition. Thus, the final alcohol group will be added in the 12*R* position. This reaction evolves in terms of distances as follows: the distance between O(Wat3) and C_{12} gets shortened from 3.69 Å in INT1 to 1.82 Å in TS2 and to 1.53 Å in INT2, showing that a new bond between these atoms has been formed. On the other hand, the distance between O(Wat3) and H(Wat3) has grown from 0.99 Å in INT1 to 1.11 Å in TS1 and to the final distance of 1.53 Å in INT2. This evolution shows that the bond gets broken. This H(Wat3) protonates the Asp375 as the evolution of the H(Wat3)-O(Asp375) distance shows: it starts at 1.36 Å in INT1, evolves to 1.36 Å in TS1 and to a final distance of 1.03 Å.

At this point, the conversion from LTA_4 to (6*Z*, 12*R*-)LTB_4 is almost done and only the protonation of the initially opened epoxide ring is remaining. In this step of the mechanism, the H(Wat1) travels from Wat1 to $O_{epoxide}$, starting at a distance of 2.49 Å in INT2 to a distance of 1.39 Å in TS2 to a final distance of 1.02 Å in the P *Z*. At the same time, the bond between H(Wat1) and O(Wat1) breaks. The distance between these atoms starts at 0.98 Å to 1.09 Å to 1.59 Å, respectively. As a consequence, the $O_{epoxide}$ leaves the first coordination sphere of Zn. The distance between $O_{epoxide}$ and Zn starts at 1.95 Å in INT2, it is 2.45 Å in TS2 and ends at 2.96 Å in the P *Z*.

The case of the *E* path (Figures 9.13, 9.15 and 9.17) is quite similar except for some details that will be explained in the following lines. The most relevant geometrical values along the path are shown in Table 9.2.

During the first step of the mechanism of the *E* path, the ERO reaction, the bond between C_6–$O_{epoxide}$ gets broken. Its distance starts at 1.47 Å in R, then elongates to 2.04 Å in TS1 and in INT1 is 2.20 Å. The dis-

Table 9.2: Relevant distances and the dihedral angle of the stationary structures along the *E* path. Distances (defined by two atoms) are in Å and dihedral angle (defined by four atoms) are in °.

Pro-*E* Reaction Path	**R**	**TS1**	**INT1**	**TS2**	**INT2**	**TS3**	**P**
Zn-O_{epox}	3.39	2.64	1.98	1.93	1.92	3.26	2.96
O_{epox}-C_5	1.45	1.40	1.39	1.39	1.39	1.44	1.43
O_{epox}-C_6	1.47	2.04	2.20	2.30	2.32	2.39	2.34
H(Wat1)-O_{epox}	1.75	1.66	3.00	3.12	3.12	0.97	1.02
O(Wat1)-H(Wat1)	0.99	1.00	0.98	0.98	0.98	2.39	1.59
O(Wat3)-C_{12}	3.84	3.68	3.66	1.79	1.51	1.50	1.50
H(Wat3)-O(Asp375)	1.71	1.66	1.66	1.32	1.01	1.01	1.01
O(Wat3)-H(Wat3)	0.99	1.00	1.00	1.12	1.60	1.64	1.62
H_6-C_6-C_7-H_7	294.4	196.9	183.7	178.1	177.5	180.7	181.5

tance between C_5–$O_{epoxide}$ does not significantly change. Simultaneously, a bond between Zn and $O_{epoxide}$ appears, revealing again the Lewis-acid role of the metal. All other distances either do not change significantly or evolve as in the *Z* path. As expected, the H_6-C_6-C_7-H_7 dihedral evolves in the opposed way as it does in the *Z* path. It starts in a pro-*Z* conformation, with a dihedral of $-65.6°$, or 294.4° as shown in Table 9.2. In TS1, this dihedral evolves to 196.9°, showing a clear pro-*E* conformation. In INT1, this bond has finally rotated until a full *E* conformation with a dihedral of 183.7°. From now on this bond will have a *E* conformation, with a dihedral of around 180±3° in all the stationary structures along the path.

The addition of the water molecule to C_{12} evolves in a similar way than for the *Z* path. Nonetheless, the C_{12}'s exposed face is not the *R* but the *S* due to the opposed conformation of the C_6–C_7 double bond,

as discussed in Section 9.3.3.2. Thus, the distances that change the most along the path are the ones involving Wat3 and C_{12}. The O(Wat3)–C_{12} bond is formed and its distances are 3.66 Å, 1.79 Å and 1.51 Å for INT1, TS1 and INT2, respectively. At the same time, the O(Wat3)–H(Wat3) bond gets broken. Its distances are 1.00 Å, 1.12 Å and 1.60 Å, respectively. Finally, as observed in the *Z* path, the H(Wat3) protonates Asp375. The distances along the three stationary structures are 1.66 Å, 1.32 Å and 1.01 Å, respectively.

At this point of the mechanism, the 6*E*,12*R*-LTB_4 isomer is almost obtained, only the protonation of the epoxide's oxygen is remaining. $O_{epoxide}$ gets protonated by the donation of a proton from Wat1, so the distances involving Wat1 and $O_{epoxide}$ will be the ones with the greatest changes. As said, the $O_{epoxide}$–H(Wat1) bond is formed. Its distance starts at 3.12 Å for INT2, evolves to 0.97 Å in TS3 and ends at 1.02 Å in P-*E*. The evolution of the H(Wat1)–O(Wat1) distance is the opposite. Its distances are 0.98 Å, 2.39 Å and 1.59 Å, respectively. As observed in the *Z* path, epoxide's oxygen–Zn coordination has also been lost. Along this step the distances for this bond are 1.92 Å, 3.26 Å and 2.96 Å, respectively. All the other distances have not changed significantly.

9.3.3.4 Non-covalent interactions as governors of the stereochemistry

In Section 9.3.3.3, the complete *Z* and *E* paths have been explained at the atomic level. Overall, both paths are very similar. The mechanism is the same except for the conformation of the C_6-C_7 conformation, which controls the face of the addition. Thus, no explanation of the stereochemical control has emerged from the analysis of the atoms directly involved in the reaction.

In the gas phase (at the B3LYP/6-31G(d) level of theory), the 6*E*,12*S*-

LTB_4 isomer is 0.3 kcal/mol more stable than LTB_4 in terms of potential energy, thus indicating that the first one is the most favourable one in non-enzymatic conditions. When LTA_4H is involved, the mechanism to LTB_4 is favoured, implying that either the formation of the Z isomer is favoured or the formation of the E isomer is hindered.

The answer can be found in the non-covalent interactions in the cavity of LTA_4. A structural analysis of the substrate and the lateral chains of the residues that shape the cavity has been done along both paths. As explained in Section 9.3.1, the cavity is enclosed by the lateral chains of Tyr267 and Tyr378, two aromatic, polar residues. Tyr267 is interacting by its OH group with Asp375-bridging water molecules, while Tyr378 is interacting also by its OH group with Tyr383, one of the residues interacting with the epoxide in R. Thanks to these interactions, the position of both Tyrs is stable. As said, these two residues have an aromatic ring which can interact non-covalently with other delocalised systems such as the triene of the substrate. This type of interaction is called π-π interaction and can appear with different geometries, being the most common ones the face-to-face and the edge-to-face. Between these two, the face-to-face interaction is the strongest one.

The angle between the closest plane to the aromatic ring of Tyr267 and Tyr378 and the closest plane to the triene moiety of the substrate has been measured for all the stationary structures along the path. The results are plotted in Figure 9.19.

Figure 9.19 shows that the interaction with Tyr267 is quite similar in both cases. Moreover, the geometry is neither an edge-to-face nor a face-to-face. The combination of these two facts indicates that the interaction is too weak to have any significant effect on the reaction. On the other hand, the behaviour of the interaction between the triene system and Tyr378 is the contrary in the two paths. In the case of the Z path, the interaction

has an edge-to-face geometry. As said some lines above, this interaction is weak, consequently easy to break. Moreover, it is conserved along the first two steps of the mechanism. On the other hand, the geometry of the same interaction in the *E* path is face-to-face. This stronger interaction will allow a lower barrier of the first step of the mechanism, but breaking the interaction is required at the second step. This interaction's loss is the reason behind the greater height of the energy barrier of the second step of the *E* mechanism.

Experimental works with an isoform of the LTA_4H from *Xanopus laevis*, which among other mutations has a Phe instead of a Tyr in the 378 position (which can not interact with Tyr383), and with Tyr378Phe-mutated versions of human LTA_4H[212] support the role of Tyr378 in the control of the stereochemistry of the substrate's double bonds. The authors determined that these versions of LTA_4H are not only able to synthesise the LTB_4 but other isomers such as the 6*E*,8*Z*-LTB_4, demonstrating the key role of Tyr378. Now its mechanism of control has been unravelled. Nevertheless, the 6*E*,12*S* isomer detected as the product of the *E* path has never been reported as a product of any LTA_4H isoform.

As a summary, in the *Z* path an edge-to-face interaction is created when the epoxide ring is opened and the C_6-C_7 bond acquires a *Z* conformation. This interaction will not need to be broken in the following steps. On the other hand, this same interaction has a face-to-face geometry for the *E* path, which stabilises the INT1 structure lowering the potential energy barrier of the epoxide ring opening. However, this stacking interaction has to be broken in the second step of the mechanism, contributing to a higher potential energy barrier in the water addition reaction.

9.4 Conclusions

LTB_4 is a very potent pro-inflammatory mediator with a very determined stereochemistry, which is required for its biological activity. The double bonds of the central triene system have the 6*Z*,8*E*,10*E* conformations, while the OH group at the C_5 position has the *S* chirality and the OH group at C_{12} has the *R* chirality. The conformation of the Δ^8 and Δ^{10} double bonds and the chirality of the C_5's OH group are determined from the reactant, while the conformation of the Δ^6 double bond and the chirality of the OH group at C_{12} are determined by LTA_4H.

The mechanism and stereochemical control of the enzyme have been unravelled in this Chapter. As a summary, the reaction takes place in three steps through an 1,7-S_N1 mechanism: the epoxide ring gets opened and stabilised over the Zn cation –which acts as a Lewis acid stabilising the negatively charged O from the epoxide–, a water molecule is added as an OH^- group at the C_{12} carbon and the oxygen from the epoxide is protonated. All these steps take place with a high stereochemical control. In this sense, the C_6-C_7 becomes a double bond with a *Z* conformation when the epoxide ring is opened, exposing the *R* face of C_{12} to the addition of the water molecule. Thus, the chirality of the water addition is controlled by the conformation of the C_6-C_7 bond, which is 6 methylene units away. Furthermore, the control of the conformation of the new double bond is given by the generation of a π-π stacking interaction with Tyr378, which is weaker for the *Z* path compared to the *E* one. For the generation of the 6*E*,12*S*-LTB_4 isomer, the π-πstacking interaction has a face-to-face geometry which would need to be broken in the water addition step, contributing then to a higher barrier. In the case of the *Z* path, the cleavage of the interaction is not needed and, if it was, it would not contribute that much to the barrier because of its weakness, which is determined by its geometry.

Moreover, MD simulations suggest that in more than the 90% of the frames the initial conformation of the C_6–C_7 bond is pro-*Z*, implying then that this is the preferred starting conformation. In addition, even when the starting conformation is closer to a pro-*E* conformation, the preferred path is the *Z* too.

The study of the mechanism of the Leukotriene A_4 Hydrolase is a clear example of the highly interesting properties of enzymes, not only fastening the reactions by lowering the energy barrier but also by controlling the chirality and stereochemistry of the synthesised products.

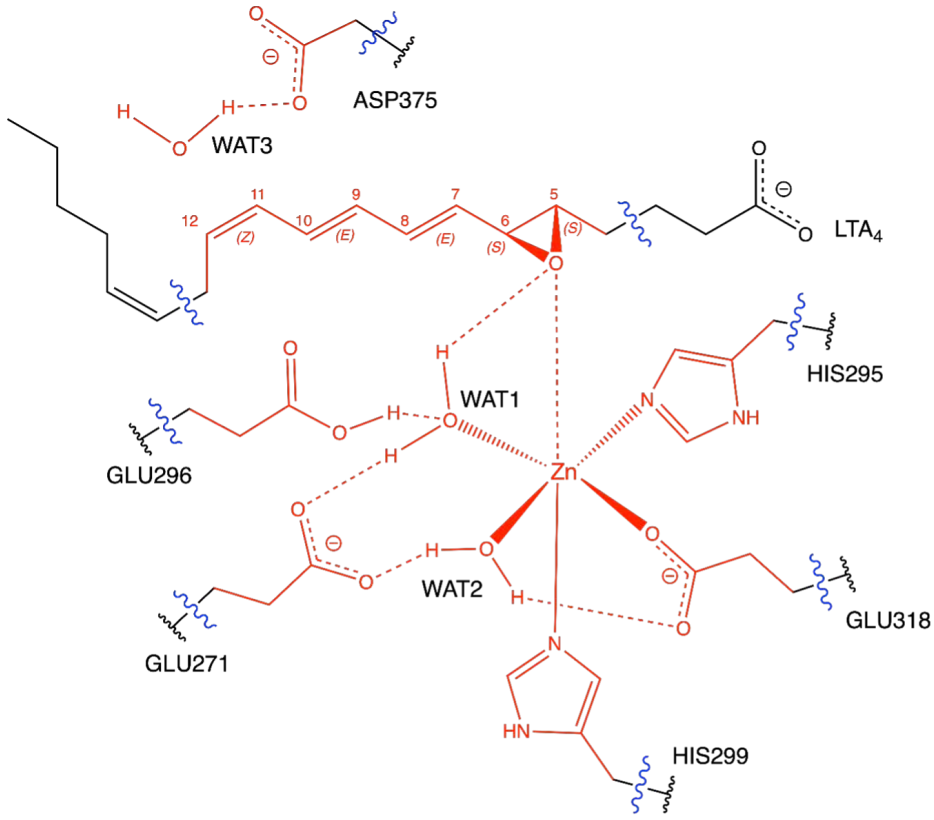

Figure 9.4: QM/MM partition scheme. QM atoms are drawn in red, QM/MM frontiers are depicted in blue, and MM atoms are drawn in black.

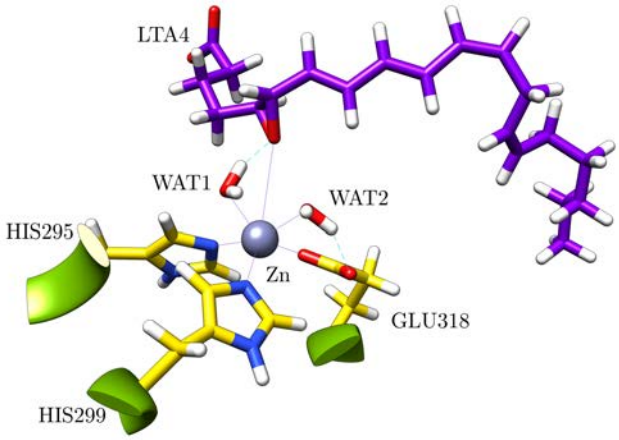

Figure 9.5: Geometry and coordination of Zn in LTA_4H.

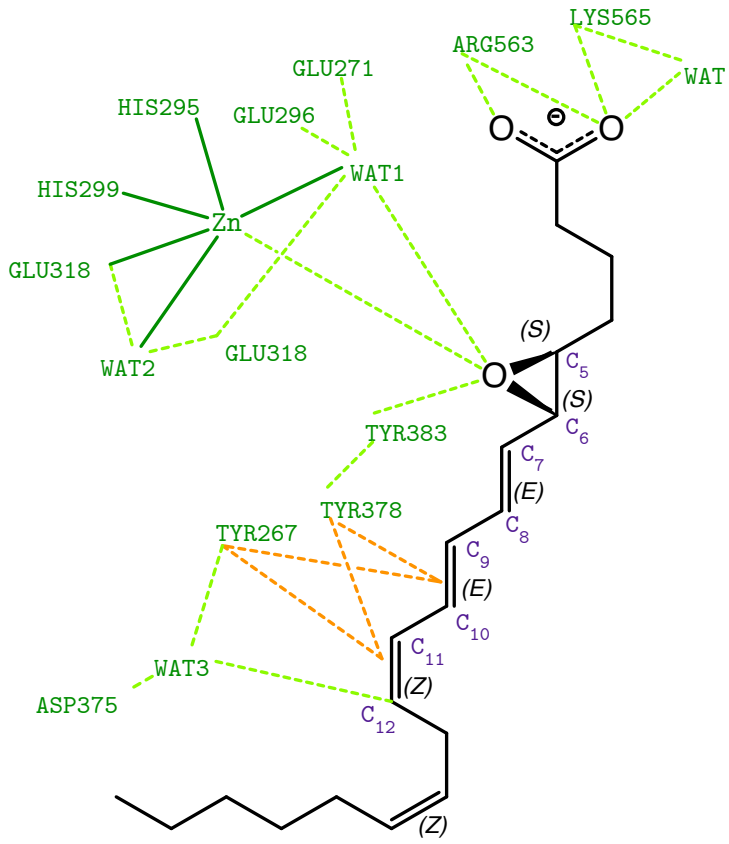

Figure 9.6: Enzyme-substrate non-covalent interactions. Covalent interactions are drawn in full lines, hydrogen-bond interactions are drawn in green, dashed lines and π-stacking interactions are drawn in orange, dash lines.

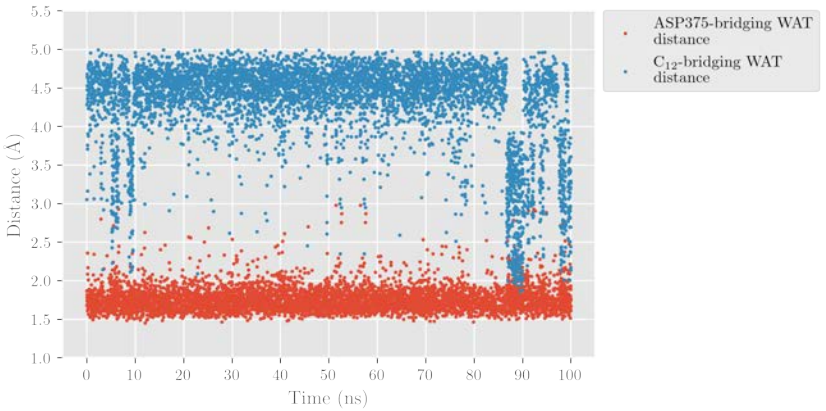

Figure 9.7: Distances of closest water molecule bridging Asp375 and C_{12} vs. time along the trajectory. Asp375-Wat distances are plotted in red while C_{12}-Wat distances are plotted in blue.

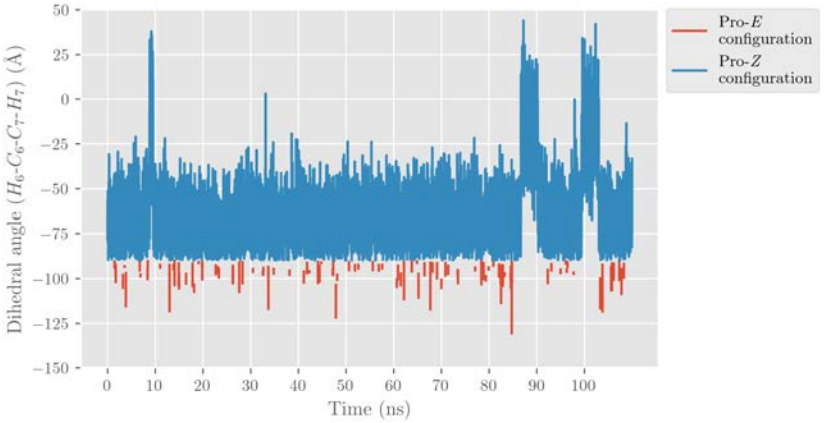

Figure 9.8: H_6-C_6-C_7-H_7 dihedral angle evolution along the MD simulation. Pro-*E* values ($\varphi < -90°$) are plotted in red while pro-*Z* values ($\varphi > -90°$) are plotted in blue.

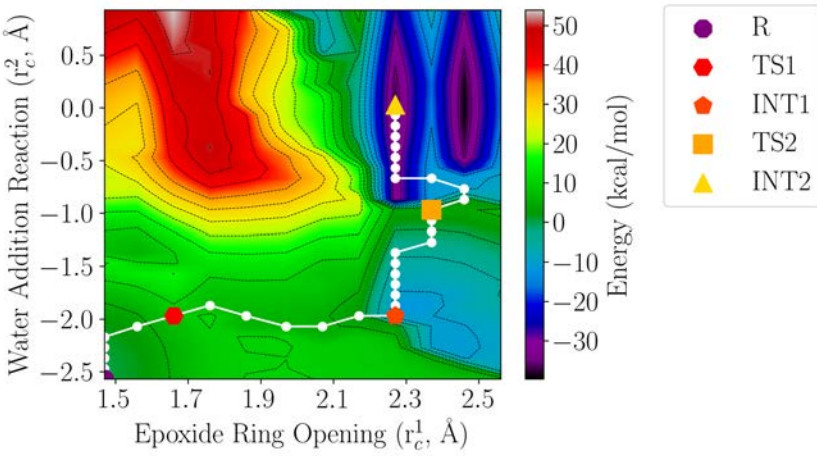

Figure 9.9: Two-dimensional PES of the ERO and water addition reactions coordinates. White lines and dots represent the MEP, polygons correspond to stationary structures identified along the MEP and dashed lines represent the isoenergetic lines with intervals of 5 kcal/mol.

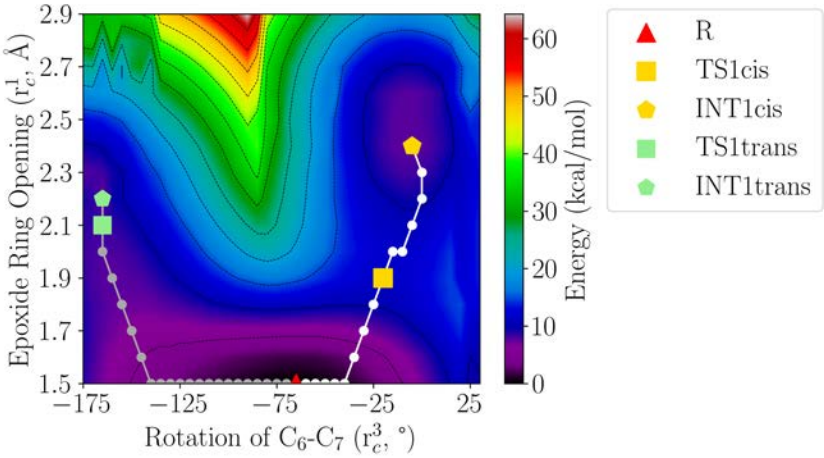

Figure 9.10: Two-dimensional PES of the Epoxide Ring Opening and C_6-C_7 rotation coordinates. White and grey lines and dots represent the MEPs, polygons correspond to stationary structures identified along the MEPs and dashed lines represent the isoenergetic lines with intervals of 5 kcal/mol.

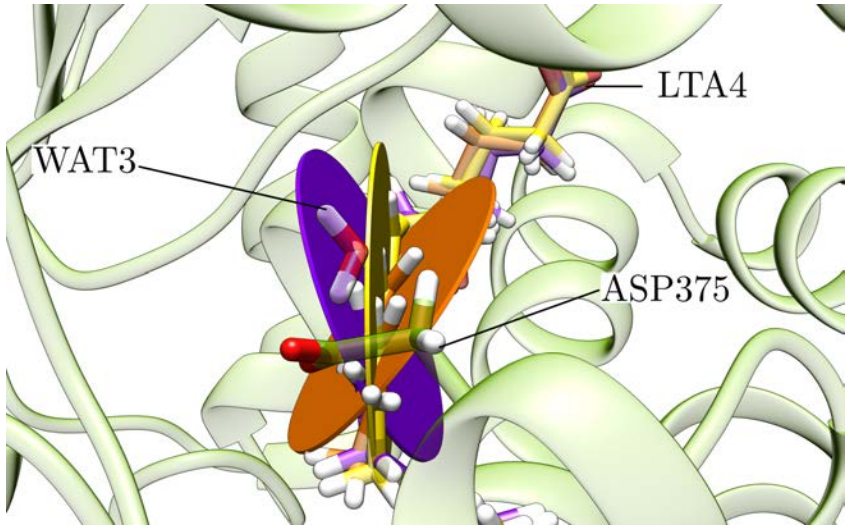

Figure 9.11: Representation of the planes of the trienes for the R, INT1-*E* and INT1-*Z* with respect to the Asp375-interacting water molecule WAT3. The plane corresponding to the R is drawn in yellow, in orange the one corresponding to INT1-*E* and in violet the corresponding to INT1-*Z*.

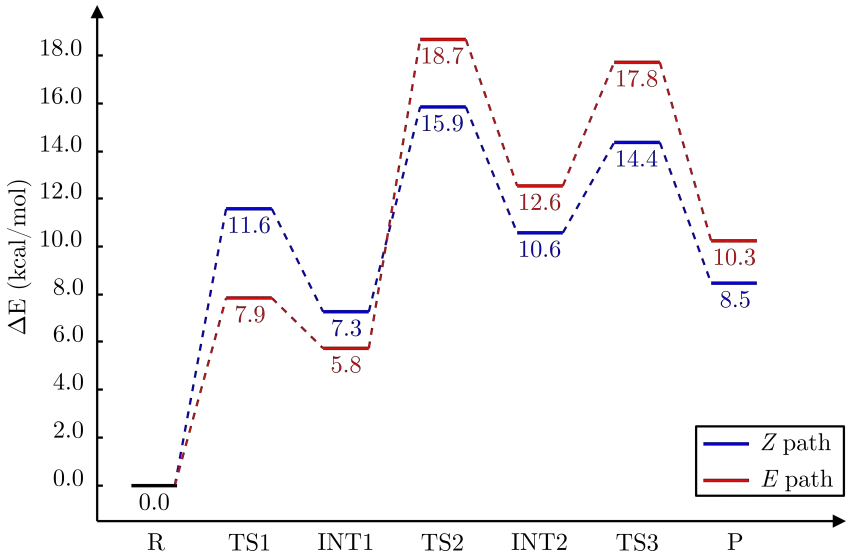

Figure 9.12: Potential energy diagram of the stationary structures along the *E* and *Z* paths from LTA_4 to LTB_4. *E* path is plotted in red while *Z* path is in blue.

(a) R

(b) TS1-E

(c) INT1-E

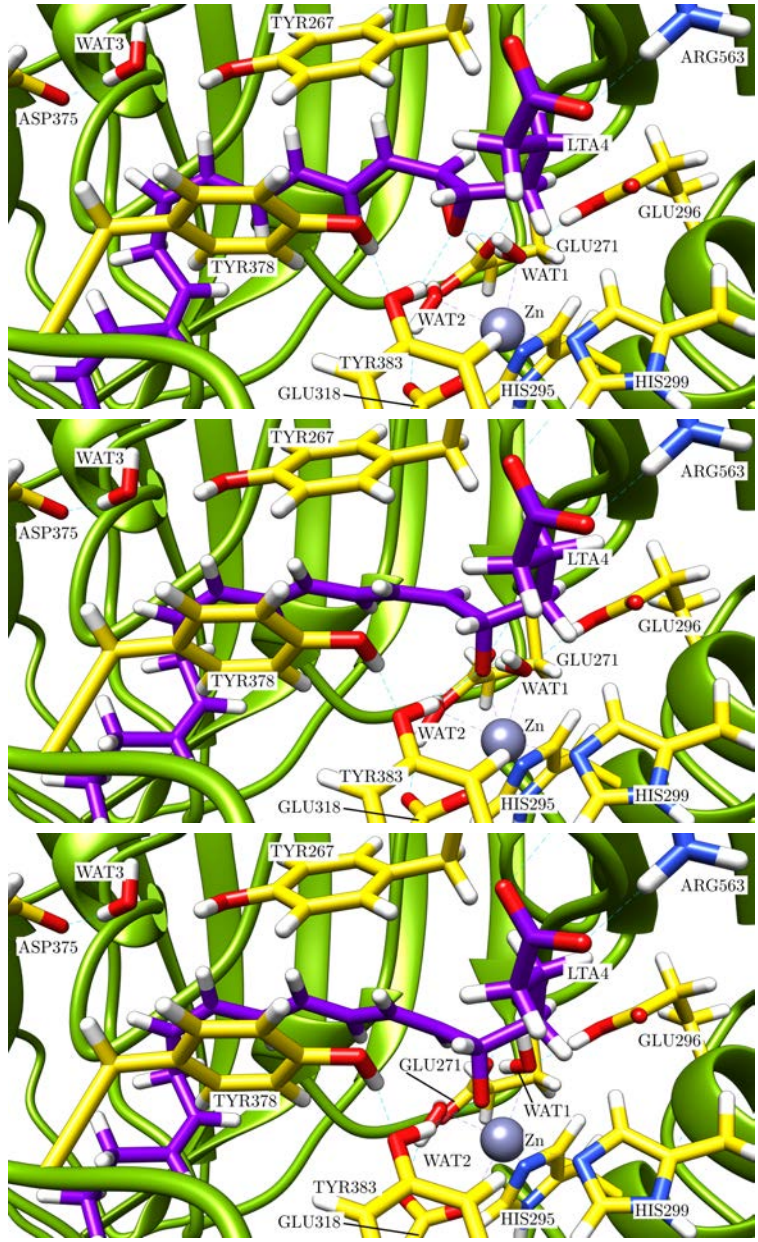

Figure 9.13: Stationary structures along Epoxide Ring Opening reaction for *E* path.

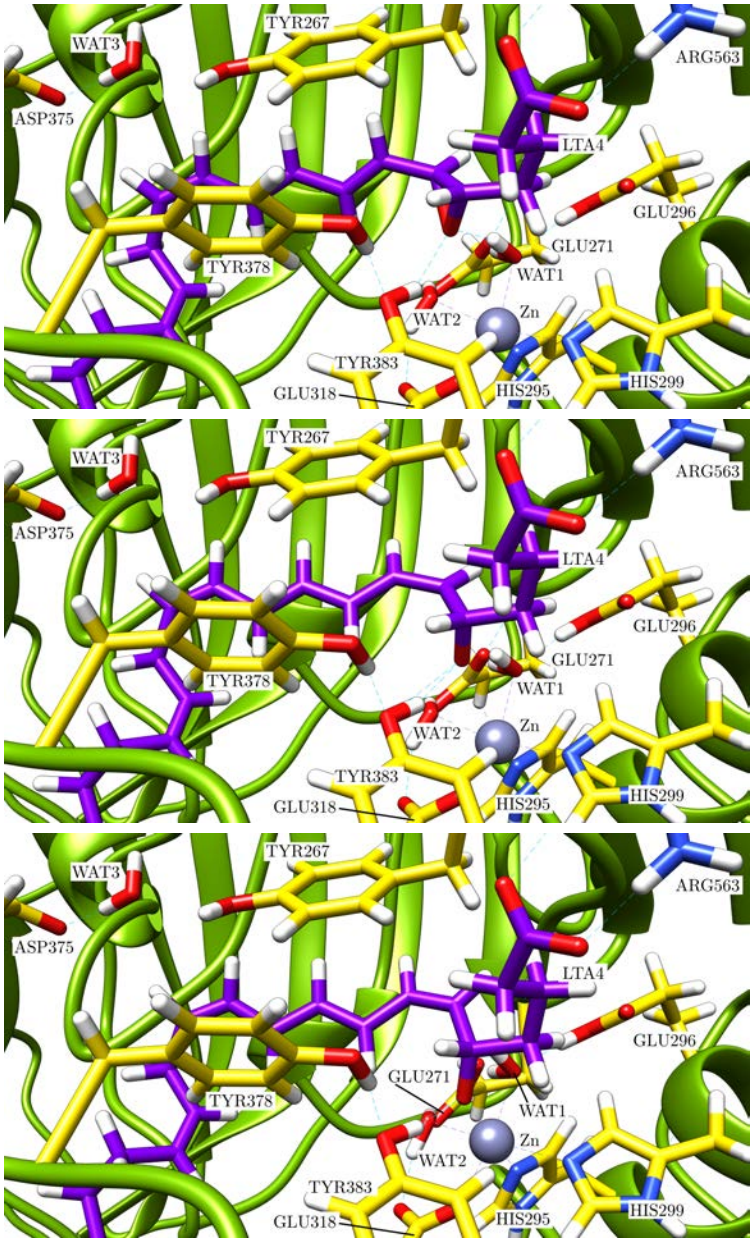

(a) R

(b) TS1-Z

(c) INT1-Z

Figure 9.14: Stationary structures along Epoxide Ring Opening reaction for *Z* path.

(a) *INT1*-E

(b) *TS2*-E

(c) *INT2*-E

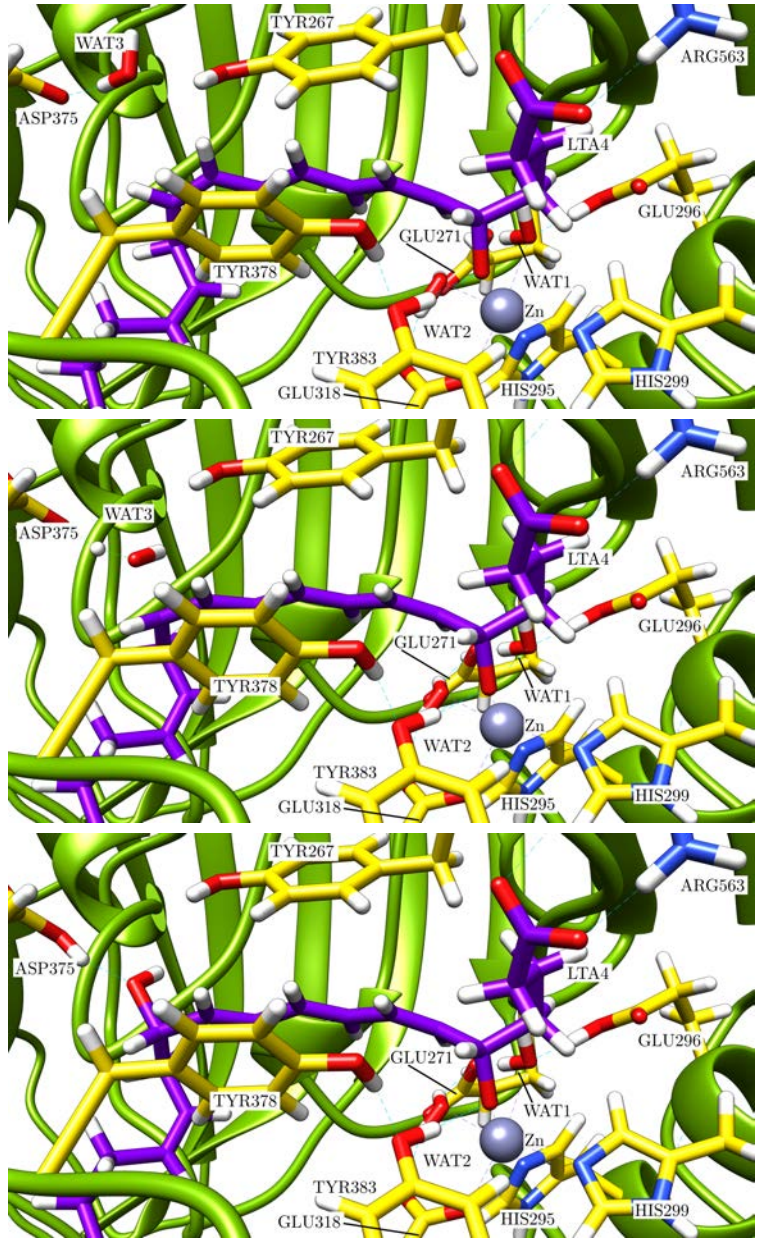

Figure 9.15: Stationary structures along Water Addition reaction for *E* path.

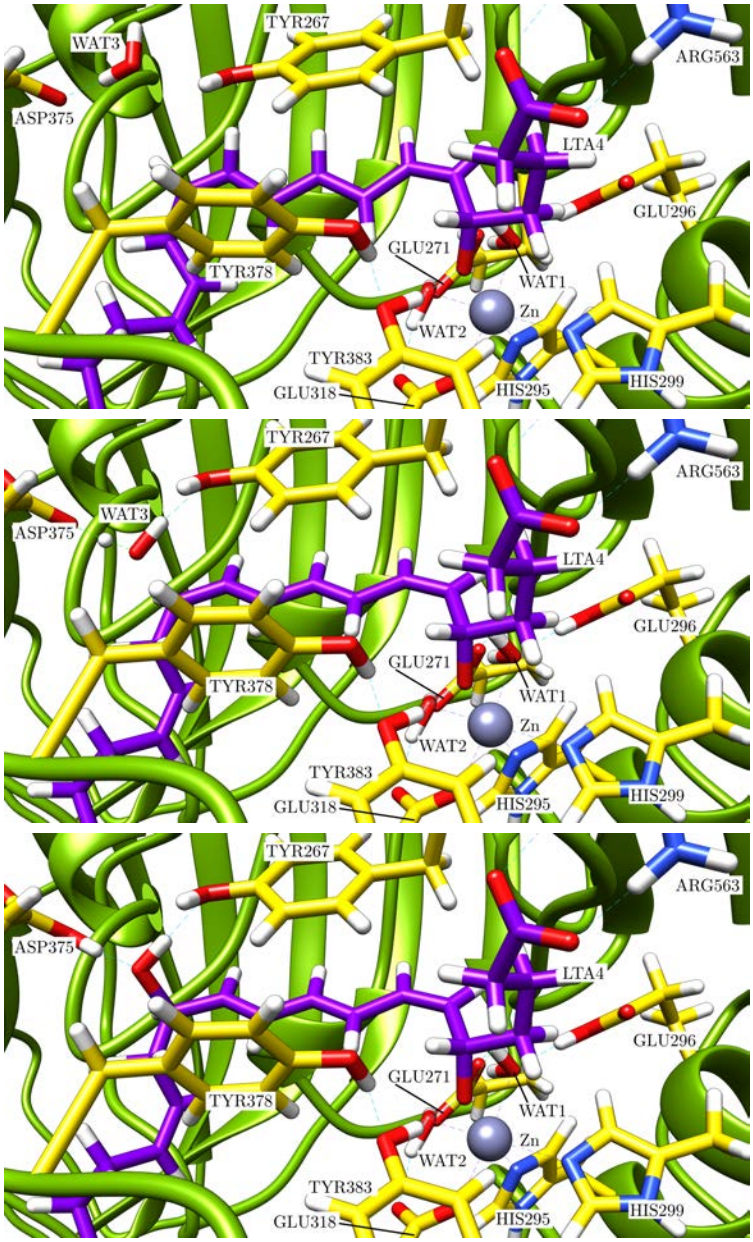

(a) INT1-Z

(b) TS2-Z

(c) INT2-Z

Figure 9.16: Stationary structures along Water Addition reaction for Z path.

(a) *INT2*-E

(b) *TS3*-E

(c) *P*-E

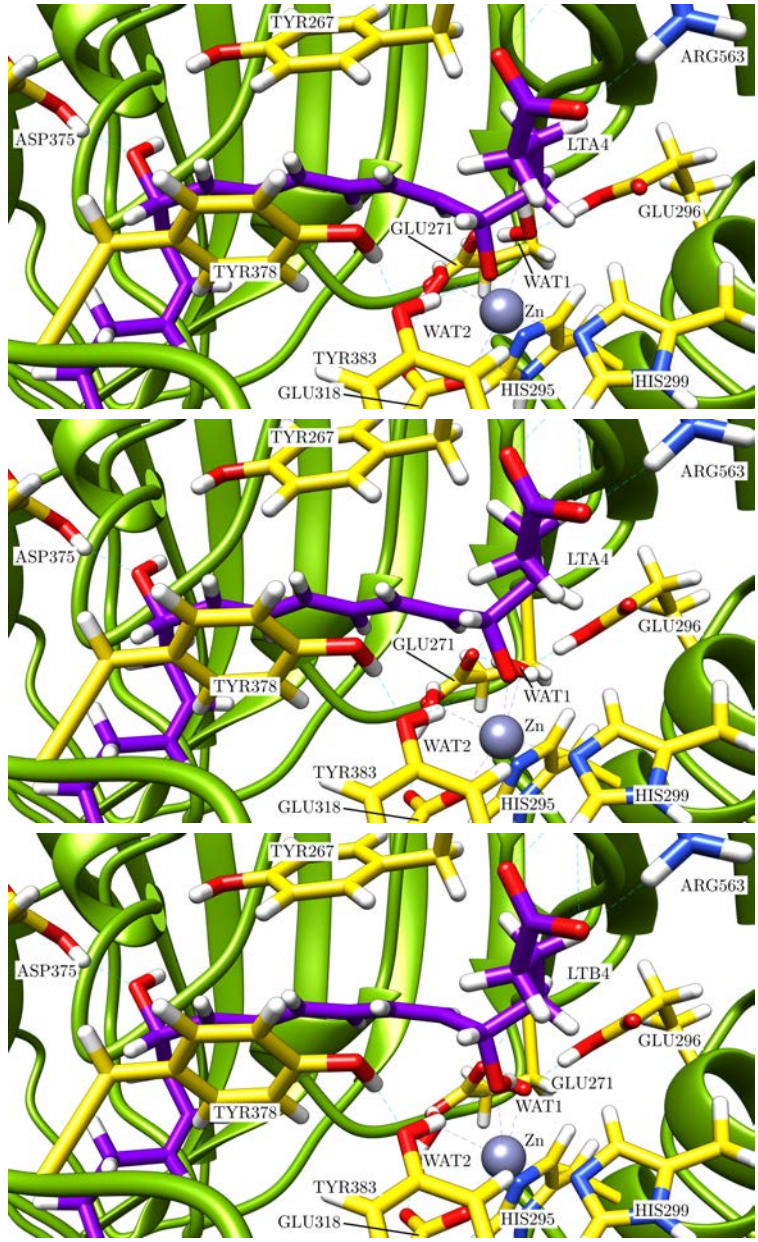

Figure 9.17: Stationary structures along Protonation reaction for *E* path.

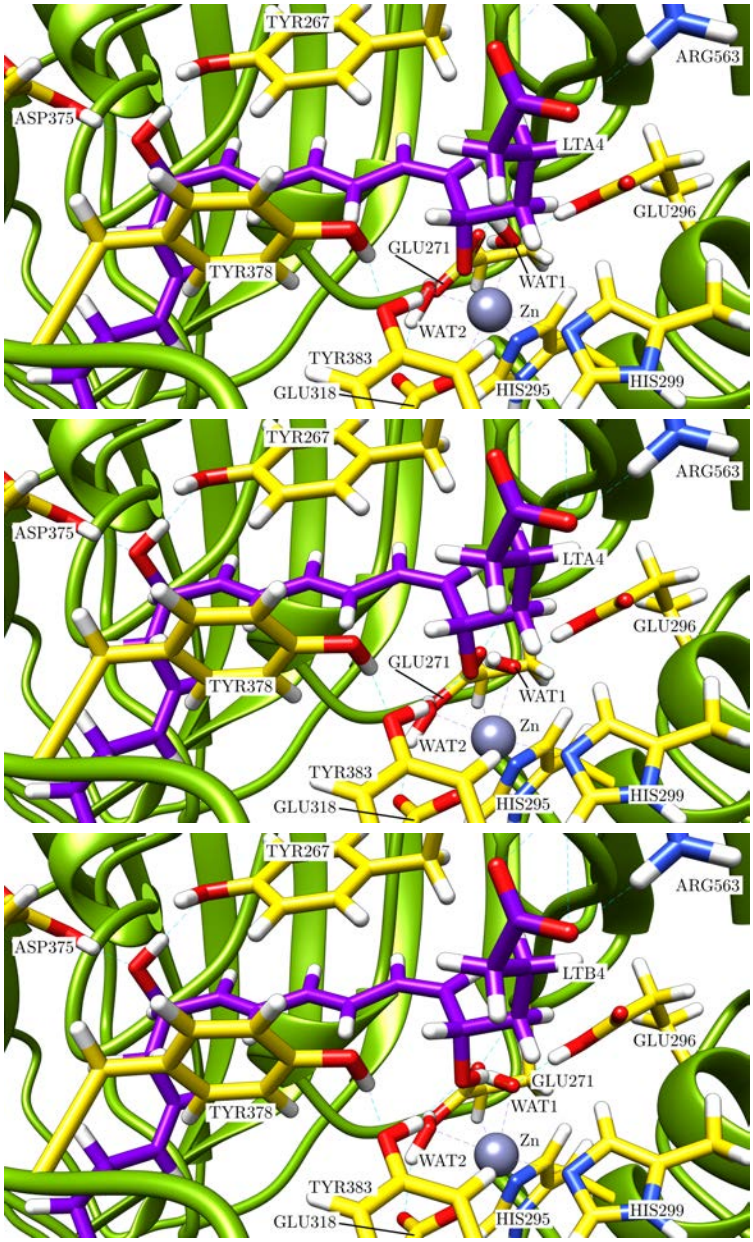

(a) INT2-Z

(b) TS3-Z

(c) P-Z

Figure 9.18: Stationary structures along Protonation reaction for Z path.

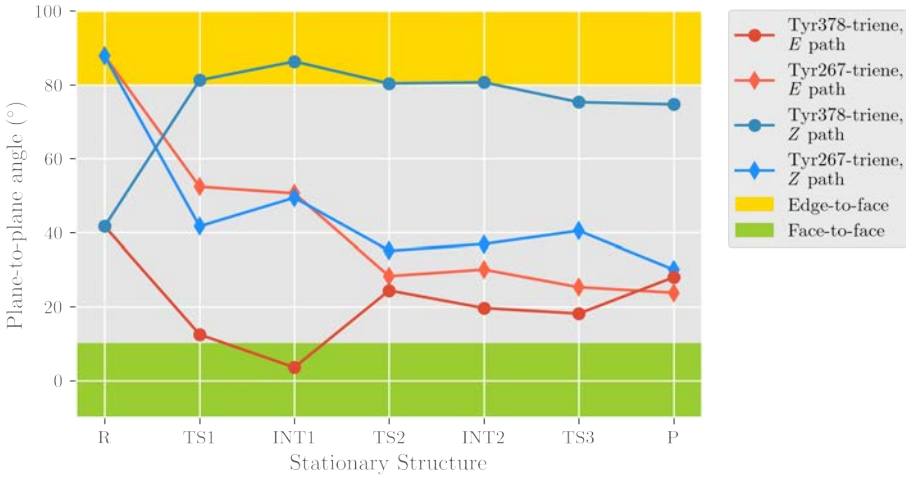

Figure 9.19: Angle between the closest plane to Tyr267 and Tyr378's aromatic atoms and closest plane to the triene atoms of the substrate. In blue, the angles for the Z path have been plotted, while the angles for the E path have been plotted in red. Additionally, a region in yellow and a region in green have been coloured highlighting the regions where π-πinteractions are edge-to-face or face-to-face, respectively.

Part IV

Biocatalytic synthesis of Maresin-1

Chapter 10

Introduction: Biocatalytic synthetic routes to Maresin-1 from Docosahexaenoic Acid

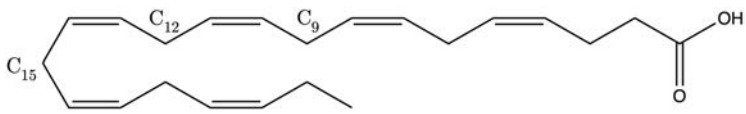

DHA

Hydroperoxidation

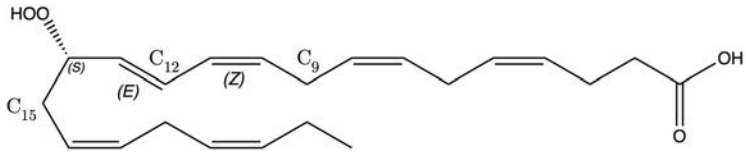

14*S*-HydroperoxyDHA

Epoxidation

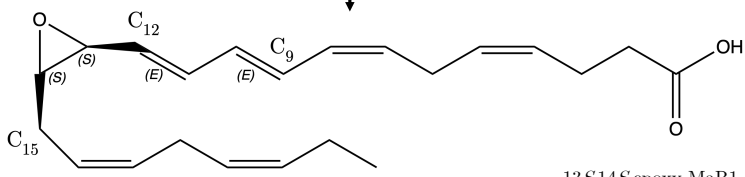

13*S*,14*S*-epoxy-MaR1

Hydrolysis

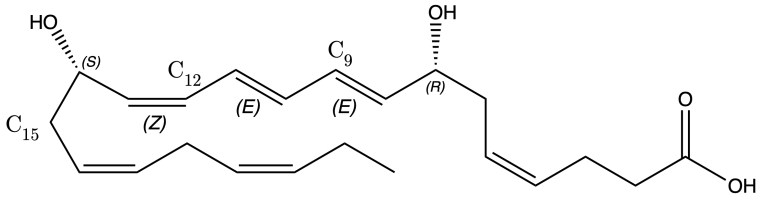

Maresin 1

10.1 Introduction

Maresin-1 (MaR1) (Figure 10.1b), from **ma**crophage mediators in **re**solving **in**flammation, is a very potent SPM. It is the first compound of the Maresin family ever reported[213]. It is a double-oxidised derivative of DHA (Figure 10.1a), with a controlled stereochemistry of the conformation of the double bonds and the chirality of the alcohol groups. Among other functions, MaR1 is able to regulate the phenotype of Mϕs toward a homeostatic, tissue-protective one[67], as described in Sections 1.2.1 and 1.2.2. Moreover, it is also a very potent phagocyte director –even more than other EPA- and DHA-derived SPMs like RvE_1, PD_1, PGE_1 and 7*S*,14*S*-diHDHA[214]–, as well as it is an inhibitor of neutrophil recruitment and

a stimulator of Mϕs efferocytosis[67] –that is the clearance of apoptotic cells[215]–.

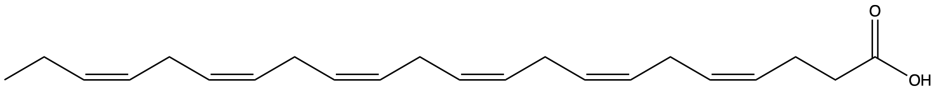

(a) Docosahexaenoic Acid (DHA)

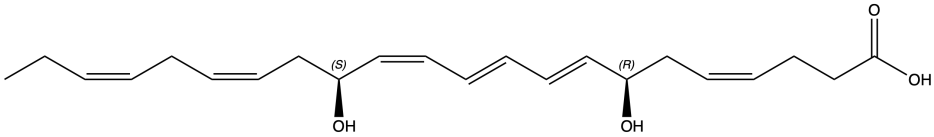

(b) Maresin-1 (MaR1)

Figure 10.1: Structures of DHA and MaR1.

Docosahexaenoic Acid (DHA) (Figure 10.1a), the initial compound of the MaR1 biosynthetic route, is an $\omega-3$ PUFA that has 22 carbon atoms in its skeleton and 6 double bonds starting from the 3$^{\text{rd}}$ carbon atom, counting from the terminal methylene (Section 1.3.1.1). As a PUFA, DHA has a methylene-interrupted structure of the double bonds that makes it suitable for reactions like the reviewed in Sections 1.3 and 1.4.3 and studied in Chapter 6 and 7.

The biocatalytic synthesis of Maresin-1 (MaR1) is a very stereochemically controlled process that takes place in Mϕs. As said, it is a derivative of DHA. The synthesis and stereochemical control is driven by different enzymes that cover the different steps of the biotransformation. This synthesis involves three consecutive steps: hydroperoxidation, epoxidation and hydrolysis. Initially, it was thought that the first two steps were carried out specifically by ALOX12[216]. Nonetheless, it has been recently reported that ALOX15 is also capable of performing these two reactions and even that ALOX15 is better at the epoxidation step[53]. Unfortunately, the enzyme responsible for the final hydrolysis has not been identified yet,

although it is thought to be a sEH.

10.2 Hydroperoxidation: from Docosahexaenoic Acid to 14*S*-hydroperoxy-DHA

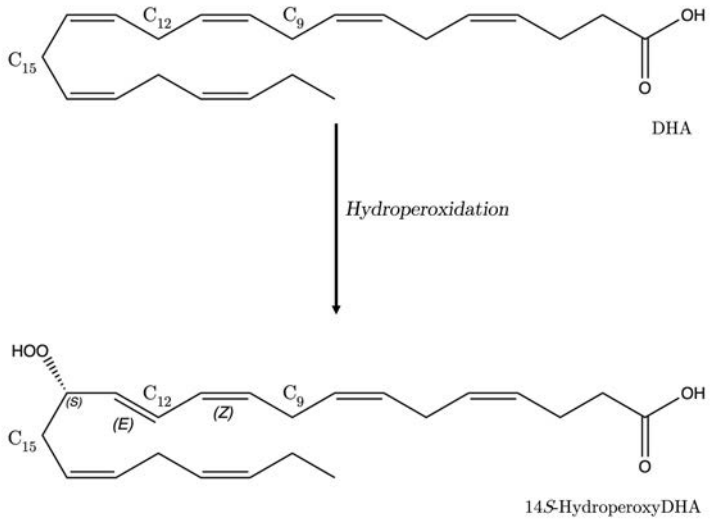

Figure 10.2: Scheme of the first step of the biocatalytic synthesis of MaR1, the hydroperoxidation.

As said before, the first step of the reaction is the hydroperoxidation of DHA (Figure 10.2). In order to evolve to MaR1, the oxidation has to take place at the C_{14} position, so an initial abstraction of H_{12} is needed (Section 1.4.3.1).

Experimentally, it has been demonstrated that ALOX12 and ALOX15 are suitable for performing this reaction[53;216]. Nonetheless, ALOX12 is the best enzyme known for this transformation.

Although no molecular details about this reaction are available neither for ALOX12 nor for ALOX15, several publications have reported the

reactivity on AA for the conversion to 12*S*-HpETE and 15*S*-HpETE, respectively[217–220].

10.3 Epoxidation: from 14*S*-hydroperoxy-DHA to 13*S*,14*S*-epoxy-MaR1

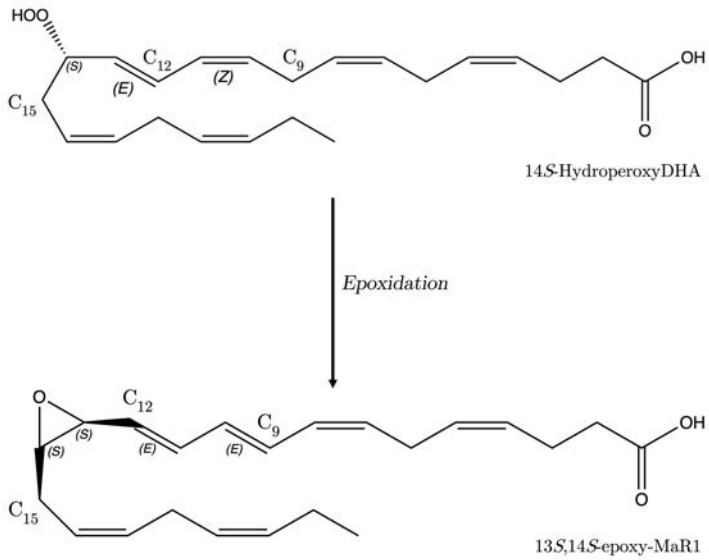

Figure 10.3: Scheme of the second step of the biocatalytic synthesis of MaR1, the epoxidation.

The second step of the biosynthetic route to MaR1 is the epoxidation of 14*S*-HpDHA to 13*S*,14*S*-eMaR1 (Figure 10.3). This reaction is not a canonic reaction of LOX –which is the addition of a molecule of oxygen to the substrate–. The formation of 13*S*,14*S*-eMaR1 can be achieved by ALOX12[53;67] and ALOX15[53], but no mechanistic details have never been reported for ALOX12, ALOX15 nor for any other LOX.

The formation of 13*S*,14*S*-eMaR1 by ALOX12 was firstly described

in Dalli et al.[67] by comnparison to the total organic synthesis' product, followed by the incubation of human macrophages with the compound, which lead to the formation of MaR1 at low temperatures and other non-enzymatic products at higher temperatures. Moreover, it has also been described[53] that ALOX15 is a better enzyme for the production of the 13*S*,14*S*-eMaR1 intermediate. Nonetheless, the step-by-step reaction mechanism has not been described for any of these systems.

A competitive reaction to the formation of the epoxide has also been described for both *hum*ALOX12 and *hum*ALOX15. The product of this reaction is the 7*S*,14*S*-*EZE*-diHDHA. This compound has small stereochemical differences with MaR1 but a similar bioactivity, although lower[214]. The reactions' competition has been observed to depend on the concentration of the reactant, so some kind of allosteric control on the enzyme is thought to take place[53].

10.4 Hydrolysis: from 13*S*,14*S*-epoxy-MaR1 to MaR1

The final step to MaR1 is the enzymatic hydrolysis of 13*S*,14*S*-eMaR1 (Figure 10.4). No enzyme has been reported to be responsible of this hydrolysis. Nonetheless, two major products of the non-enzymatic hydrolysis have been reported[53] and none of them corresponds to MaR1 but are 7*S*/7*R*,14*S*-*EEE*-diHDHA and 13*S*/13*R*,14*S*-*EEZ*-diHDHA[221]. Consequently, stereoselective hydrolysis of 13*S*,14*S*-eMaR1 to MaR1 has to take place by the action of a hydrolase.

Due to the chemical features of 13*S*,14*S*-eMaR1, which are very similar to the ones observed for LTA_4, an equivalent path is proposed. LTA_4H was initially suggested to be the responsible of the hydrolysis, but contrary to the expected, a inhibition of LTB_4 formation was detected, so LTA_4H-

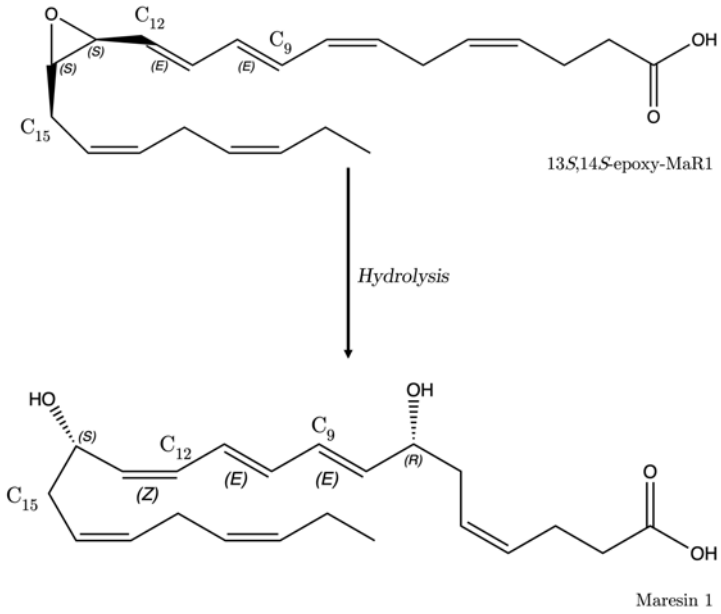

Figure 10.4: Scheme of the third step of the biocatalytic synthesis of MaR1, the hydrolysis.

inhibition properties were attributed to 13*S*,14*S*-eMaR1. To solve this, and based on the knowledge acquired from the study of the LTA_4:LTA_4H complex and its reactivity, a mutated version of the LTA_4H will be designed for the hydrolysis of 13*S*,14*S*-eMaR1, the last step of the biocatalytic synthesis of MaR1.

Chapter 11

Conversion of Docosahexaenoic Acid by pig ALOX15/*pig*12LOX

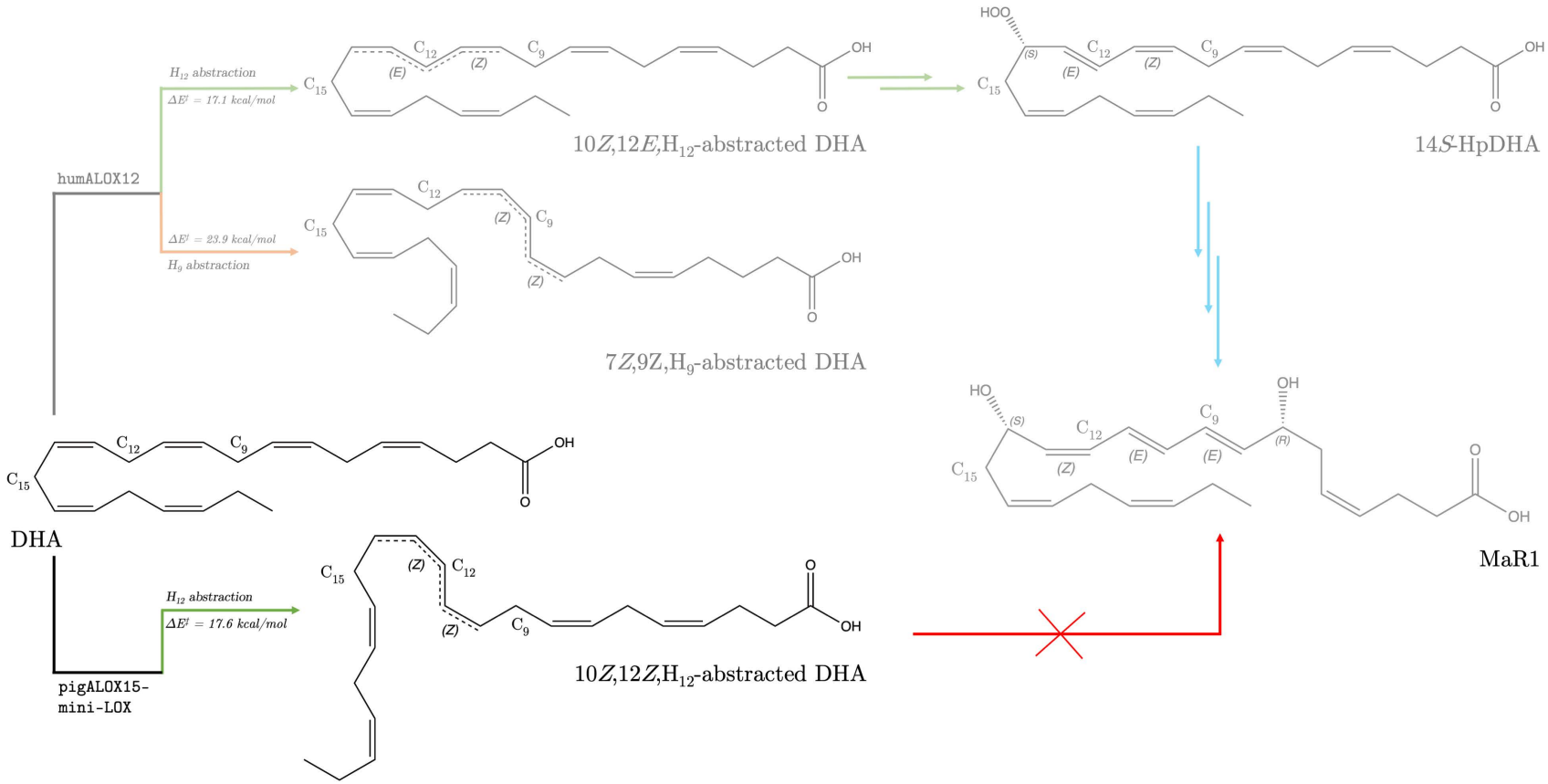
humALOX12
H_{12} abstraction
$\Delta E^{\ddagger}$ = 17.1 kcal/mol
$\Delta E^{\ddagger}$ = 23.9 kcal/mol
H_9 abstraction
10Z,12E,H_{12}-abstracted DHA
7Z,9Z,H_9-abstracted DHA
14S-HpDHA
MaR1
DHA
pigALOX15-mini-LOX
H_{12} abstraction
$\Delta E^{\ddagger}$ = 17.6 kcal/mol
10Z,12Z,H_{12}-abstracted DHA

The work presented in this Chapter is corresponds tos Canyelles-Niño et al.[222]*. The Supporting Information can be found in Chapter SI11, while the publication can be found in Chapter SI12.*

11.1 Introduction

The computational study of the conversion from DHA to MaR1 starts with the hydroperoxidation of DHA by ALOX12. When the present computational study of this conversion started, only one complete structure of a 12LOX was available: the pig's (*Sus Scrofa*) 12LOX. This enzyme is in fact a *pig*ALOX15 that has naturally evolved to a 12LOX able to convert AA into 12*S*-HETE. Experimental studies confirms its ability to oxidise DHA into 14*S*-HpDHA[223].

Along this Chapter, the mechanism of hydroperoxidation of DHA at the C_{14} position will be studied computationally starting from the abstraction of H_{12}, as the general mechanism of LOXs suggests (Section 1.4.3.1).

A focus on the stereochemistry of the product is required for a proper study of the biosynthetic route to MaR1.

11.2 Computational Method

In this section, the computational methods used for the study of the peroxidation of DHA by *pig*ALOX15 will be explained

11.2.1 Protein setup

The initial structure of the protein is a X-Ray structure obtained from the Protein Data Bank. It is not a complete model of the enzyme but contains only the catalytic domain of the *pig*ALOX15 enzyme. This model is known as *pig*ALOX15-*mini*-LOX. Its accession PDB ID is `3RDE`.

The inhibitor bounded in the active site for the crystallisation has been removed for building the initial model. As a X-Ray model, the protein does not contain hydrogens, which have been added at a pH 7 by `PROpKa 3`[154] through the `ProteinPrepare` module from `PlayMolecule`[136]. For the protonation, Fe and OH^- groups have been kept for better description of the Fe environment's pK_as.

11.2.2 Molecular docking simulations

Since the initial structure does not contain DHA, molecular docking has been employed to generate an initial structure for MD and QM/MM simulations.

`GOLD` software[87], in its 5.8 version, was employed for the docking calculations. The protonated structure has been used as the receptor, while DHA has been used as the ligand. Fe is kept with the default geometry. Exploration of the conformational space has been set with a radius of 20 Å around the Fe atom and `ChemScore`[137] is chosen as the fitness function.

100 solutions have been obtained and clustered by RMSD with a threshold of 1.5 Å. Solutions have been ranked by their score, although estimated binding energies given by `ChemScore` have also been analysed.

11.2.2.1 Building and parameterisation of solvated Michaelis complex

For MD simulations, the DHA:*pig*ALOX15 Michaelis complex has been built, solvated and parametrised. From molecular docking simulations, the best ranked solution for DHA has been selected. Its parameters have been obtained from the `AMBER`'s `GAFF2` force field[145]. Charges have been obtained from the QM-optimised structure at the B3LYP[141]/6-31G(d)[142] level. From this structure, RESP charges[144] have been calculated at the same level.

Parameters and charges for the Fe atom and its environment have been calculated following the Seminario Method[138] using `MCPB.py`[139] from the `AmberTools` package[140]. All Fe-coordinating residues (His361, His366, His551, His555, Ile663 and OH^-) have been included in the model. The system has been optimised at the B3LYP[141]/6-31G(d)[142] level of theory. RESP charges[144] have been obtained at the same level of theory for the complete system –including backbone atoms–, while frequencies have been obtained for the simplified system –which does not contain the backbone atoms–. From these frequences, MM parameters have been obtained. All QM calculations for Fe environment and for the substrate have been carried out using `Gaussian16`[143].

Solvation and parameterisation of the complex have been performed using the `tleap` software from the `AmberTools` suite[140]. `ff14SB`[89] has been used as the force field for describing the protein's residues, aside of the Fe-coordinated ones. The TIP3P model[155] has been chosen for describing the water molecules, following the `ff14SB`'s authors[89] recommendation.

All parameters have been combined and an orthorhombic box of 10 Å from the outermost atom in each direction has been built. Na^+ ions have been added for protein's charge neutralisation.

A final model of about 64000 atoms, almost 9000 from the protein, has been obtained. The complete system has been used for MD simulations. For QM/MM simulations, the solvated model has been cropped to a drop-solvation model. Only protein atoms and water molecules with at least one atom within a radius of 17 Å around the substrate have been kept. All other solvent molecules have been removed. A model of around 12000 atoms has been obtained.

11.2.3 Molecular Dynamics simulations

MD simulations have been carried out using the GPU (`CUDA`) version of the `pmemd` software[147;148] from `AMBER16`[94]. The SHAKE algorithm[159] has been used in all stages. PME method[160] has been employed for the treatment of the non-bonding interactions. The cut-off has been set at 9 Å. Temperature and pressure have been controlled using the Berendsen bath[158].

A five-stage preproduction has been performed until a equilibrated system has been obtained. Three steps of minimisation have been initially run including 10000 steps of energy minimisation employing the steepest descent and conjugate gradient algorithms for half of the steps each. In the first step, a harmonic restraint with a force constant of 5.0 kcal $mol^{-1}Å^{-2}$ has been applied to all atoms from the protein, cofactor and substrate. For the second step, the same restraint has been applied only to the backbone atoms, whilst for the third step no restraints have been applied.

The energy-minimised system has been heated from 0 K to 300 K in ten steps. For each step the temperature has been increased 30 K during 20 ps under constant volume conditions. A restraint with a force constant of 5.0 kcal $mol^{-1}Å^{-2}$ has been applied to all non-solvent atoms.

Once the system has been heated to 300 K, 1 ns of NPT simulation has been performed at 1 atm until density stabilisation at around $1\,\mathrm{g\,mL^{-1}}$. For this stage, a restraint with a force constant of $5.0\,\mathrm{kcal\ mol^{-1}\,\AA^{-2}}$ has been also applied to all non-solvent atoms.

Finally, 10 ns of NVT simulation at 300 K have been carried out. No restraints have been applied and the volume from the last frame of the NPT stage has been used.

Two replicas of 100 ns each have been calculated starting from the last frame of the preproduction.

11.2.4 Quantum Mechanics/Molecular Mechanics calculations

The drop-solvation model has been used for the QM/MM calculations. All atoms around 15 Å from the DHA's C_{12} have been set as active (around 2200 atoms), while the rest have been kept frozen for all the calculations.

The QM region (Figure 11.1) includes the Fe atom, the lateral chains of the Fe-coordinated residues –only the terminal carboxylate for Ile663–, the OH^- cofactor and the atoms from the C_6 methylene to the C_{18} methylene of the DHA. A total of 77 atoms, plus seven link atoms, constitute the QM region. This part is described using the B3LYP[141] DFT. H, C, N and O atoms are described using the 6-31G(d) Pople's basis set[142], while Fe atom is described using the LANL2DZ ECP basis set[169]. Fe atom is in the high spin configuration, so the multiplicity of the partition is 6. The total charge is +1. MM atoms have been treated using the parametrised model (Section 11.2.2.1).

QM/MM interactions have been treated using the electrostatic embedding scheme, using also the charge shift algorithm to avoid overpolarisation effects. A cut off for the electrostatic interactions has been set at 10 Å.

Optimisations and scan of reaction coordinates have been performed

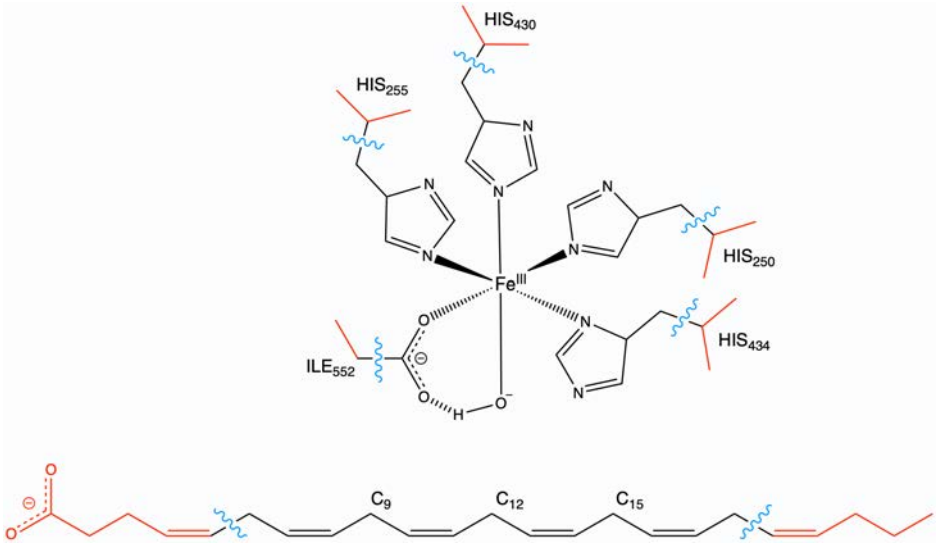

Figure 11.1: QM/MM partitions in the DHA/*pig*ALOX15 system. QM atoms are drawn in black, while MM atoms are depicted in red and QM-MM boundaries are drawn as blue, wavy lines.

employing the L-BFGS algorithm[167], combined with the use of a microiterative scheme[168] including all residues with at least one atom in the QM region to the *micro* partition. For TS search, the dimer method[224;225] has been used without the microiterative scheme due to limitations on the software implementation.

`ChemShell`[162;163] in its 3.7 version has been used as the QM/MM software. `Turbomole`[165], version 7.0, has been used for the QM calculations, while `DL_POLY` 5.0[166] has been used for treating the MM region. For geometry optimisations, `DL-FIND`[210] has been used, which includes all algorithms and schemes described before. HDLC[164] coordinates have been used for describing the atomic positions.

11.2.5 Simulations analysis, plots and pictures

MD simulations have been analysed using `RCBS.py`[161], an implementation of the `MDAnalysis`[187;188] `Python` package. Structure drawings have been prepared using `UCSF Chimera`[135].

11.3 Computational results

In this section the results of the computational study will be discussed. The results obtained from MD simulations and QM/MM calculations will be presented.

11.3.1 Molecular docking simulations

As explained in Section 11.2, docking simulations have been carried out in order to obtain an initial pose of DHA in *pig*ALOX15's cavity. From the 100 obtained solutions, no head-first posing has been observed to occupy the U-shaped cavity. On the contrary, the best solutions show a tail-first conformation with a proper U shape and with the C_9 and C_{12} located close to the OH^- group.

11.3.2 Molecular Dynamics simulations

The two produced replicas of MD simulation have been analysed. Stability of the system has been studied through RMSD analysis of the backbone of the protein and the substrate (Figure SI11.1). After confirming the stability of the system along the trajectories, several features of the substrate-enzyme interactions have been analysed.

11.3.2.1 Non-covalent interactions between DHA and *pig*ALOX15

Molecular docking simulations confirmed the unique tail-first posing of the DHA in the active site of *pig*ALOX15. Using MD simulations, the most important interactions that make this configuration stable have been studied.

Interactions with DHA's carboxylate

DHA has a carboxylate group in its head, which is able to stablish hydrogen-bonding interactions with the lateral chains of different amino acids of the protein. A search of the most common interactions of this kind has identified one possible interaction with Arg403, a residue found in the entrance of the cavity. Nonetheless, this interaction is not very strong, as Figure 11.2 reveals. Thus, the carboxylate of the substrate weakly interacts with Arg403 but interacts with several water molecules during the whole trajectory. Some of this water molecules are able to bridge between the COO^- group and the Arg403, thus stabilising their interaction.

An interaction between the carboxylate and His596 has been described for the AA/*hum*ALOX12 system[226]. The *hum*ALOX12 and *pig*ALOX15 sequences have been aligned and it has been found that for *pig*ALOX15, the residue in the same position is a Gln. The COO^--Gln595 interaction has been checked visually and in terms of distances and it has been found that due to the position of the Gln in the inner part of the entrance and the greater length of the DHA in comparison with AA –it has two more carbons in its skeleton–, this interaction is not possible, as Figure SI11.2 reveals.

$\pi - \pi$ interactions with double bonds

π-π interactions also appear in this system due to the presence of double bonds (Δ^4, Δ^7, Δ^{10}, Δ^{13}, Δ^{16}, and Δ^{19}). The U shape of the cavity allows

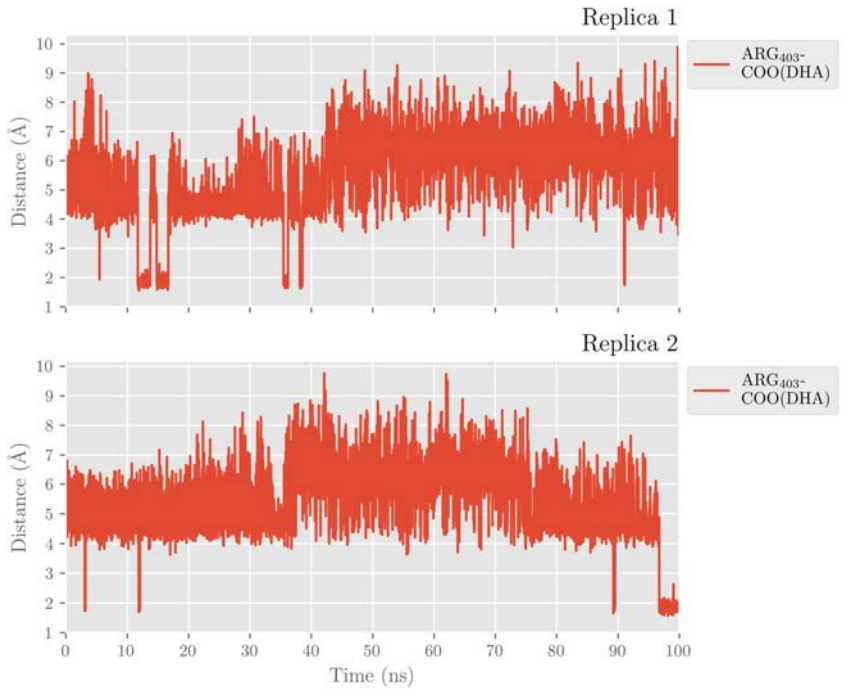

Figure 11.2: Evolution of the distance between DHA's COO^- and Arg403 for the two replicas of MD simulation.

each double bond to interact with different aromatic residues of the cavity, thus allowing a better stabilisation of the substrate. The most relevant interactions will be explained.

All interactions are plotted in Figure 11.3. As the plots show, the interaction behave in a similar way in the two replicas. Both Δ^4 and Δ^7 interact with Phe175. As it can be seen, both interactions take place simultaneously and both have similar strength. The interaction between Δ^{10} and His366 is weak along most of the trajectories, while the Δ^{16}-Phe415 is stronger although after 50 ns the distance increases around 1 Å. The interaction between Δ^{13} and Phe415 is the weakest. It starts at a long distance that increases around 3 Å after 40 ns. Furthermore, the

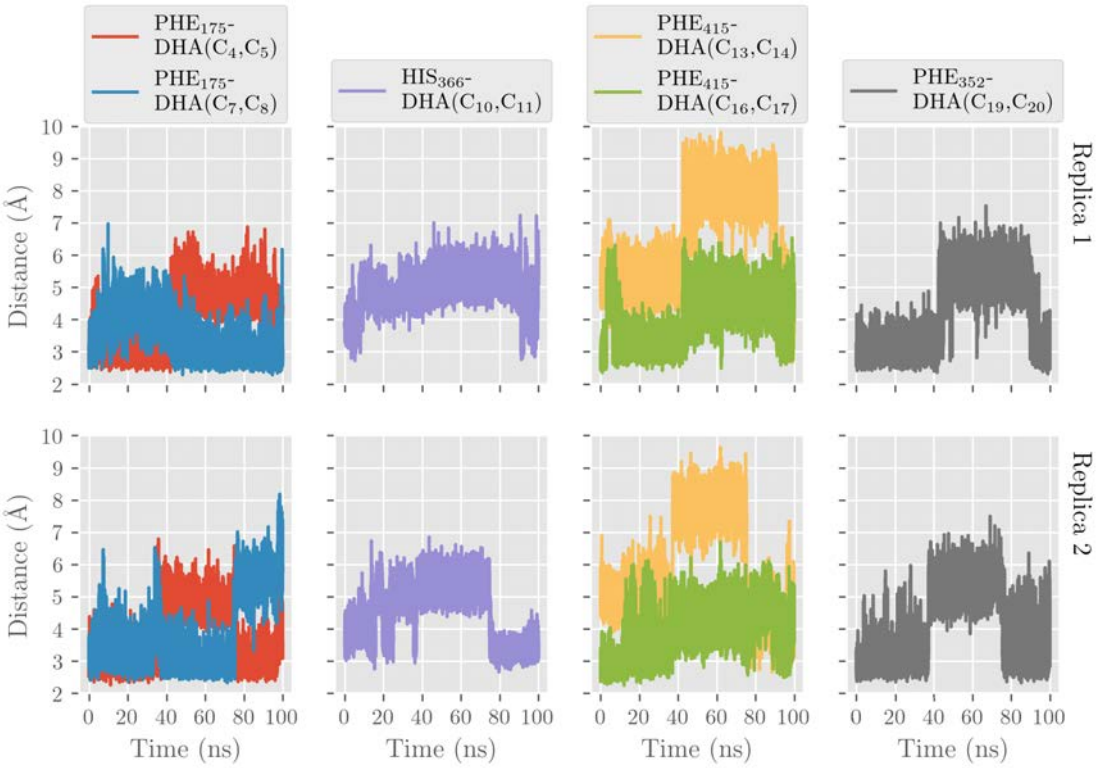

Figure 11.3: Distances for the interactions of Δ^4, Δ^{107}, Δ^{10}, Δ^{13}, Δ^{16}, and Δ^{19} with the closest aromatic residues in each case.

interaction between the Δ^{19} and Phe352 is strong during most of the trajectories, although in certain moments it gets weakened. Thus, all described π-π interactions occur at some point of the two replicas and contribute to the binding of DHA.

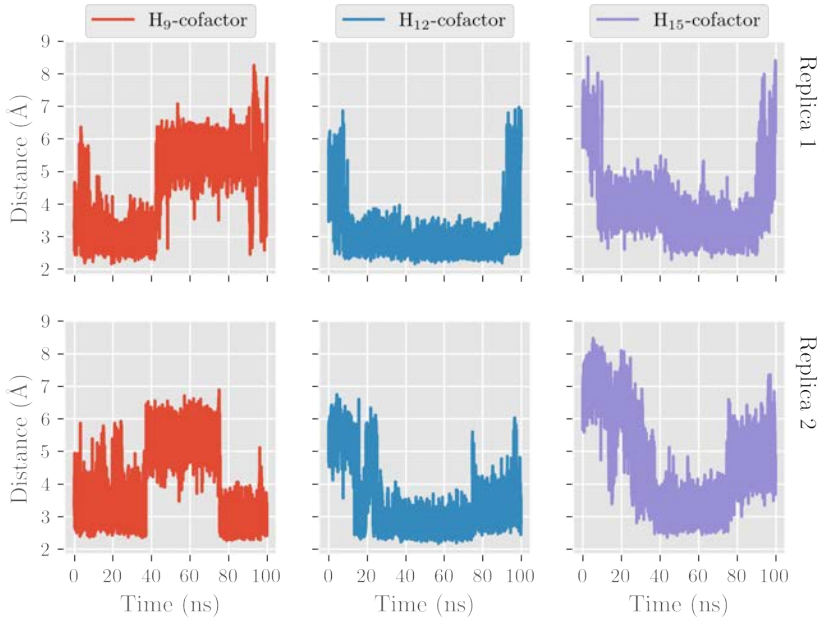

Figure 11.4: Distances from H_9 (in red)**, H_{12}** (in blue)**, and H_{15}** (in purple) **to OH^- group versus time for replicas 1 and 2 of MD simulation.**

11.3.2.2 Regio- and stereoselectivity analysis

In order to study the regioselectivity of the hydrogen abstraction by *pig*ALOX15, the distances from the C_9, C_{12} and C_{15} methylenes to the O atom of the Fe-coordinated OH^- group have been studied. The results are plotted in Figure 11.4.

As Figure 11.4 shows, H_{12} remains the closest to OH^- during most of the time in the two trajectories. Moreover, structures with short H-OH^- distances for H_9 and H_{15} can also be found, although it can be observed that when H_9 is closer, H_{15} is further to OH^-, and vice versa. Thus, 83 % of the frames show reactive H-OH^- distance (< 4 Å) for H_{12}, while 50 %

show reactivity for H_9 and 54 % show reactivity for H_{15}.

The results of these simulations indicate that *pig*ALOX15 transforms mainly DHA into 14-H(p)DHA, but it is able also to transform it into 11- and 17-H(p)DHA[227] with lower probability. These results are in agreement with experimental evidences[76], which report a relative share of 76 % for 14-H(p)DHA and of 24 % for 17-H(p)DHA.

Even though distance is a very relevant parameter for establishing the regioselectivity of PUFA oxidation by LOXs, it is not the only one. As discussed in Section 6.3.2.2 for the AA:ALOX15B systems, the hydrogen-abstraction reaction requires a planar pentadienyl group in the product, the two double bonds around the methylene from which the hydrogen is abstracted has to rotate to a planar conformation[65]. This rotation contributes to the energy barrier of the abstraction, so the further to the planarity, the higher the energy barrier. Furthermore, the rotation is more energetically expensive if there appears steric hindrance with close residues. Thus, the planarity of the vicinal double bonds is also studied as a parameter that influences the stereoselectivity. In addition, the initial geometry of the double bonds helps to prognosticate the conformation of the nascent double bond after the abstraction. In this sense, if the angle between the bonds is greater than 90°, the conformation of the double bond will be *Z*, while if it is lower than 90°, it will be *E*. The angle between the nascent double bonds is analysed as the planar angle between the planes built by C_{n+2}, C_{n+1} and C_n, and C_n, C_{n-1} and C_{n-2}, being n the number of the methylene.

Figure 11.5: Planar angle around C_9 (in red) **and C_{12}** (in blue) **versus time for replica 1 of MD simulations.**

Only C_9 and C_{12} have been studied because these are the methylenes involved in the biocatalytic synthetic route to MaR1 (Chapter 10). Results

of the analysis of replica 1 are plotted in Figure 11.5. The plots show a similar behaviour for both C_9 and C_{12} vicinal double bonds' geometry. For the whole trajectory both planar angles are around 90°. In both cases the value is greater than 90°, meaning that the expected conformation of the new obtained double bond is *Z* in both cases. With these results, for the H_{12} abstraction the conformation of the nascent Δ^{12} is expected to be *Z* instead of the described *E* stereochemistry for 14*S*-HpDHA, as mentioned in Section 10.2. QM/MM calculations will confirm or refute this preliminary observations.

11.3.3 Quantum Mechanics/Molecular Mechanics calculations

From the first MD replica, H_{12} abstraction will be studied using QM/MM methods as described in Section 11.2.4. Ten frames will be selected from the replica, from which a scan of the hydrogen abstraction will be calculated using a two-distance-difference reaction coordinate: $r_c = d(O_{cof} - H_n) - d(C_n - H_n)$. All stationary structures have been optimised to minima for Rs and Ps and to TS for TSs.

11.3.3.1 Selection of frames

Ten frames have been selected as precatalytic structures from the replica 1 of MD simulations. In order to select the frames for QM/MM calculations, two parameters have been defined as selection criteria: the distances between H_9 and the OH^- group and from the latter to H_{12} have to be under 4 Å.

An initial filtering of all the frames of the replica has been carried out. 39 % of the frame satisfy the imposed criteria. From this filtering, ten frames have been randomly selected, choosing one frame per around 10 ns of trajectory. Frames 940, 1548, 1709, 2132, 2515, 3020, 3556, 4502, 5758,

and 9207 have been selected. In all cases, H_{12proS} has found to be the nearest H_{12} to OH^-, so it will be the abstracted hydrogen.

11.3.3.2 H_{12} abstraction

Due to preliminary results obtained from the analysis of the planar angles from MD simulations (Section 11.3.2.2), H_{12} abstraction has been studied. Obtained barriers, reaction energies and stereochemistry of the product are presented in Table 11.1.

Table 11.1: H_{12proS}-OH^- initial distances, potential energy barriers and reaction energies of the QM/MM-optimised structures for the H_{12} abstraction process. Distances (defined by two atoms) are in Å and energies are in kcal/mol. Pentadienyl stereochemistry defines $\mathbf{\Delta^{10}}$ and $\mathbf{\Delta^{12}}$. $\boldsymbol{\Delta E^{\ddagger}_{AV}}$ is the exponential average potential energy barrier[228].

Frame	$d^{react}_{H_{12proS}-OH^-}$	$\Delta E^{\ddagger}$	ΔE	Pentadienyl Stereochemistry
0940	3.2	20.9	−12.5	ZZ
1548	3.0	19.8	−11.8	ZZ
1709	2.9	24.5	−12.4	ZZ
2132	2.8	22.1	−9.7	ZZ
2515	3.2	27.2	−8.9	ZZ
3020	2.8	19.8	−10.8	ZZ
3556	3.2	24.5	−9.9	ZZ
4502	2.7	15.9	−16.1	ZZ
5758	2.6	20.4	−12.1	ZZ
9207	2.6	22.6	−13.1	ZZ
$\boldsymbol{\Delta E^{\ddagger}_{AV}}$		17.6		

The exponential average potential energy barrier for the ten analysed frames is 17.6 kcal/mol. This barrier reveals that the H_{12proS} abstraction by *pig*ALOX15 is a feasible process that would lead eventually to 14*S*-HpDHA. Nonetheless, according to the MD simulations' predictions, the stereochemistry of all the hydrogen-abstraction products is *ZZ* for the Δ^{10} and Δ^{12} bonds. As explained in Section 11.3.2.2, this configuration of the pentadienyl would not lead to 14-hydroxy-4*Z*,7*Z*,10*Z*,12***E***,16*Z*,19*Z*-DHA but to the 14-hydroxy-4*Z*,7*Z*,10*Z*,12***Z***,16*Z*,19*Z*-DHA isomer, which is not adequate for the further biosynthesis of MaR1.

11.4 Conclusions

The calculations presented in this Chapter have shown the correct regioselectivity for the production of 14-H(p)DHA of the conversion from DHA by *pig*ALOX15 starting at the preferred abstraction of H_{12}.

However, the calculations also reveal that the stereoselectivity of the conversion is not the expected because it leads to the 10*Z*,12*Z*-14*S*-HpDHA isomer, which will not lead to MaR1 but to an isomer.

Chapter 12

Peroxidation: Formation of 14*S*-hydroperoxy-DHA from Docosahexaenoic Acid by human ALOX12

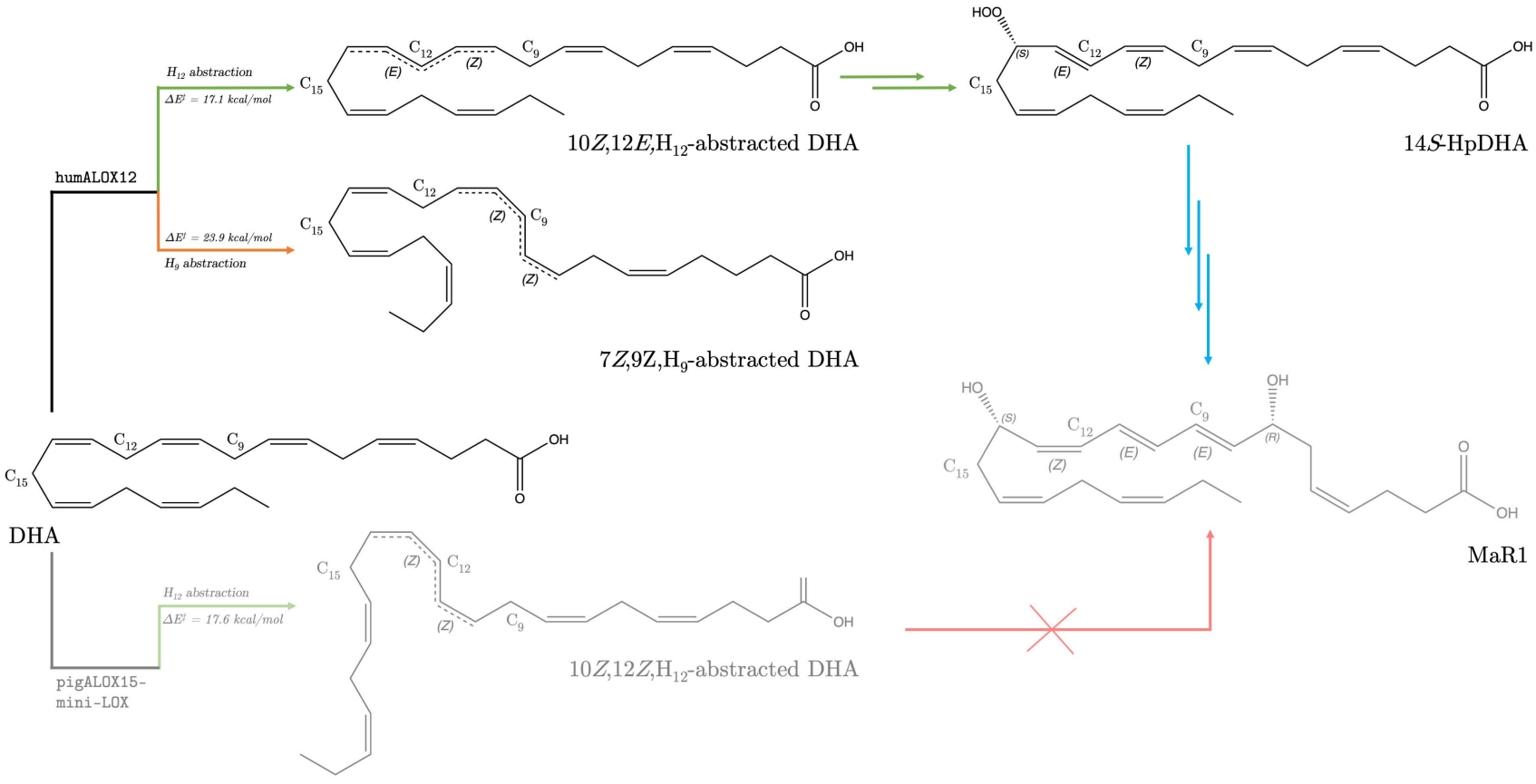
humALOX12
H_{12} abstraction
$\Delta E^{\ddagger}$ = 17.1 kcal/mol
$\Delta E^{\ddagger}$ = 23.9 kcal/mol
H_9 abstraction
10Z,12E,H12-abstracted DHA
14S-HpDHA
7Z,9Z,H9-abstracted DHA
DHA
MaR1
pigALOX15-mini-LOX
H_{12} abstraction
$\Delta E^{\ddagger}$ = 17.6 kcal/mol
10Z,12Z,H12-abstracted DHA

The work presented in this Chapter corresponds to Canyelles-Niño et al.[222]*. The publication and the Supporting Information can be found in Chapter SI12.*

12.1 Introduction

The study of the oxygenation of DHA by *pig*ALOX15 led to the production of 14-hydroxy-4*Z*,7*Z*,10*Z*,12***Z***,16*Z*,19*Z*-DHA instead of the expected 14-hydroxy-4*Z*,7*Z*,10*Z*,12***E***,16*Z*,19*Z*-DHA for MaR1 biosynthesis. This led to the conclusion that *pig*ALOX15 is not able to generate the fully described 14*S*-HpDHA but an isomer. Thus, the need to study the *hum*ALOX12 isoform rised again, but no usable X-ray structure was available.

In July 2021, AlphaFold[132;133], an artificial intelligence-based system for predicting the folding of a protein from its amino acidic sequence, was publicly launched. A computationally-predicted 3D structure of *hum*ALOX12 isoform was then available.

This structure will be used for the study of the conversion from DHA to 14*S*-HpDHA by *hum*ALOX12. This chapter will cover the first step of the MaR1 biosynthesis.

12.2 Computational methods

In this section the structure and computational methods used for the study will be reviewed.

12.2.1 Protein setup

A X-ray structure of the *hum*ALOX12 isoform is available from the Protein Data Bank by the accession code 3D3L. Nonetheless, this structure is not useful for enzymatic mechanisms' studies because it does not correspond to the complete enzyme. Some α-helices are not properly described and some loops are missing, as well as the PLAT domain.

The first available version of *hum*ALOX12 on the AlphaFold database[132;133] [accessed on October, 2022] has been used as the protein's structure (accession UniProt ID[134] P18054).

AlphaFold's *hum*ALOX12 structure does not contain metals, cofactors, or hydrogens. Fe atom and OH^- group have been added aligning the *hum*ALOX12 structure with the *pig*ALOX15's one. For the protonation, the Fe-, OH^--containing structure has been used. `PROpKa` 3[154] has been used for the protonation at a pH 7.0 through the `ProteinPrepare` module[136] from `playmolecule.org` website. Protonation has been carried out including the added cofactor.

12.2.2 Molecular docking simulations

The computational method used for the docking simulations is the same than the described for the DHA:*pig*ALOX15 system in Section 11.2.2.

The protein model described in Section 12.2.1 has been used. `GOLD`'s 5.8 version has been used for carrying out the docking simulations.

12.2.3 Building and parameterisation of solvated Michaelis complex

The solvation and parameterisation of the DHA:*hum*ALOX12 system has been done as explained in Section 11.2.2.1. In the present case, the parametrisation of the Fe environment has been done including His360, His365, His540, Asn544, the carboxylate from Ile663, and the OH^- group. The `ff19SB` forcefield[90] has been employed as the source of parameters for the standard protein residues. The final system contains almost 80000 atoms, while the drop-solvation model contains roughly 12000 atoms.

12.2.4 Molecular Dynamics simulations

MD simulations have been done as detailed in Section 11.2.3. `AMBER20`[140] has been used as the MD engine. 2 replicas of 200 ns of production each have been carried out.

12.2.5 Quantum Mechanics/Molecular Mechanics calculations

The QM/MM calculations have been performed following the same method as described in Section 11.2.4. Nonetheless, the QM zone is different because the Fe environment is different. The QM/MM partition for the DHA:*hum*ALOX12 system can be found in Figure 12.1.

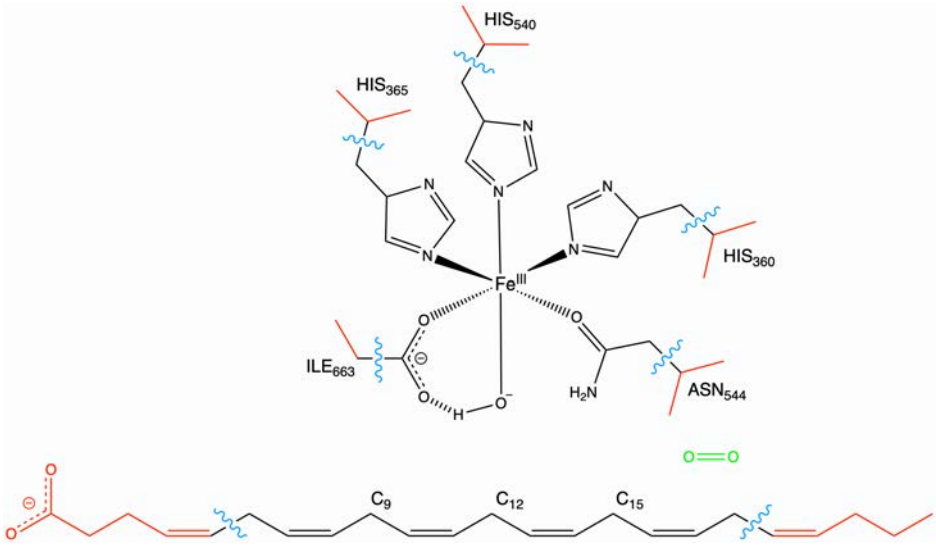

Figure 12.1: QM/MM partitions for the DHA:*hum*ALOX12 system. QM atoms are drawn in black, while MM atoms are depicted in red and QM-MM boundaries are drawn as blue, wavy lines. O_2 is drawn in green and it is only added for the study of the O_2 addition reaction and the following ones.

12.3 Computational results

The computational results obtained from the study of the DHA conversion to 14*S*-HpDHA carried out by *hum*ALOX12 will be exposed in this section.

12.3.1 Molecular docking simulations

Molecular docking simulations have been used for generating an initial DHA:*hum*ALOX12 Michaelis complex as explained in Section 12.2.2. 100 poses have been generated and clustered by RMSD with a threshold of 1.5 Å. No head-first solution with a U-shaped binding mode has been obtained, whilst the top-ranked poses correspond to U-shaped, tail-first orientations. The best-ranked solution has been selected as the starting

position for the MD simulations.

12.3.2 Molecular Dynamics simulations

Two replicas starting from the last frame of the preproduction have been calculated. The RMSD versus time plots for the two replicas are depicted in Figure 12.2.

Figure 12.2: RMSD versus time for replica 1 and 2 of DHA:*hum*ALOX12 Michaelis complex.

RMSD along time for the majority of replica 1 and for the whole replica 2 shows stability of the complex. Nonetheless, in replica 1 an important movement of DHA inside *hum*ALOX12 is observed at 140 ns, followed by a conformational change of *hum*ALOX12 that starts 20 ns after.

12.3.2.1 Conformations of *hum*ALOX12

The *hum*ALOX12's conformational change previously described has been visually analysed. Two different conformations have been observed. They correspond to a closed conformation (the initial one) and to an open conformation. A comparison of both conformations can be seen in Figure 12.3. This conformational change is known to happen in LOXs and it is described as a pendulum-like movement of the PLAT domain in respect to the catalytic domain. It has been previously reported in the literature by SAXS experiments[63;229].

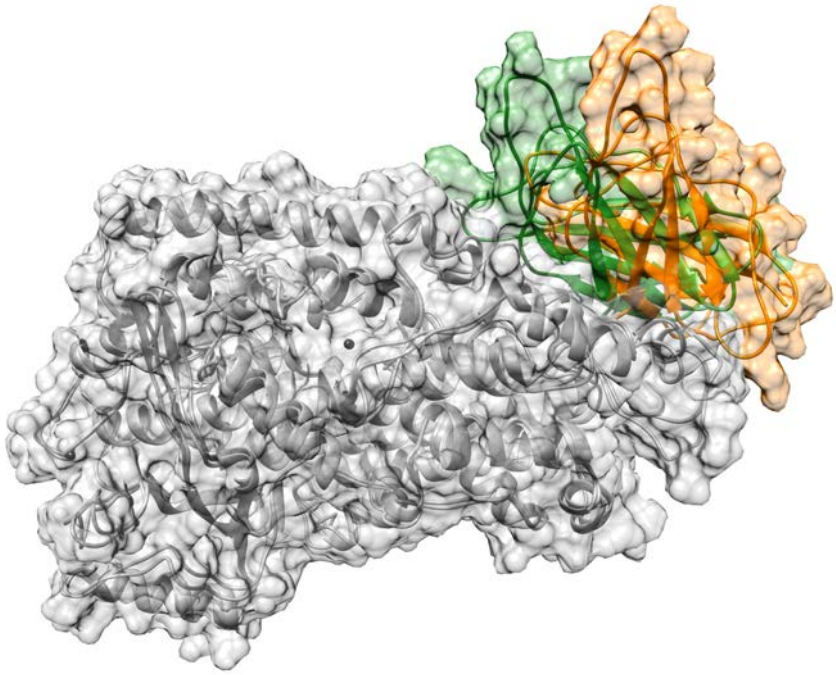

Figure 12.3: Closed (in green) **and open** (in orange) **conformations of *hum*ALOX12 observed in replica 1.** The catalytic domain is drawn in grey. The Fe atom is drawn in black as a reference for the active site.

The two frames drawn in the comparison in Figure 12.3 show a domain COGs distance of 42.3 Å in the closed conformation and of 47.3 Å in the open conformation. Moreover, the angle between the longest axes of the ellipsoid of each domain is 38.2° and 58.8°, respectively.

In order to study how the conformational change takes place during replica 1, the COGs distance during the replica has been analysed. The results are plotted in Figure 12.4. As the plot shows, the distance starts to increase at 160 ns and at 180 ns the open conformation is achieved.

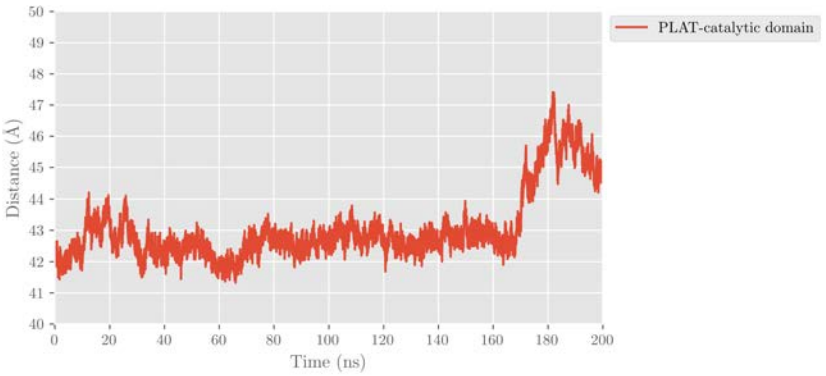

Figure 12.4: Distance of catalytic and PLAT domains' COMs during replica 1 of MD simulation.

Inter-residue interactions in closed and open conformations

The opening of the PLAT domain also affects the inter-residue interactions. In the open conformation, there is a loss in the secondary structure of the helix αthat goes from the residue 408 to 418. This helix distortion causes a movement of Phe414, which rotates blocking the depth of the cavity. The consequences will be seen in the next lines. Ile408 also moves approaching to the DHA's tail.

DHA's binding mode in closed and open conformations

As described in Figure 12.2, the conformation of DHA in the *hum*ALOX12's cavity changes before the enzyme's conformation does. DHA's binding in the cavity has been visually analysed and it is drawn in Figure 12.5.

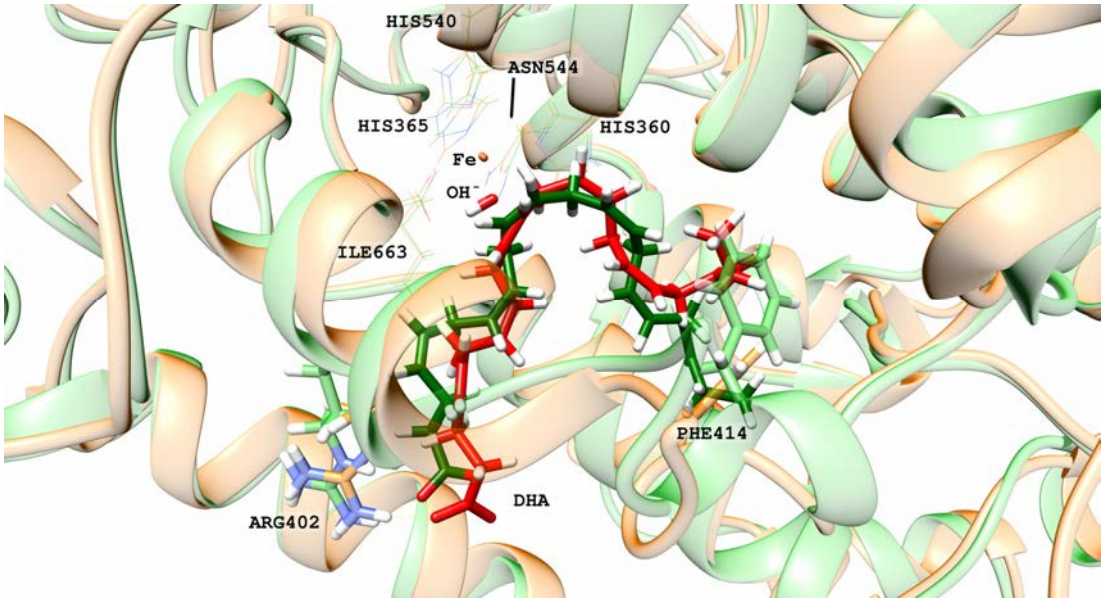

Figure 12.5: Overlay of DHA's binding in closed (in green) **and open** (in orange) **conformations of *hum*ALOX12.**

In Section 12.3.1, molecular docking calculations predicted a U-shaped binding mode for DHA in *hum*ALOX12's cavity. This binding mode has been confirmed while *hum*ALOX12 stays in the closed conformation. Nonetheless, in the open conformation the shape of the bottom of the cavity changes, with Phe414 as the most moved lateral chain. Phe414 rotates and the deepest region of the cavity gets blocked, forcing the tail of the substrate to move. Thus, the U shape is lost.

Depth of *hum*ALOX12's cavity

In the closed conformation, the depth of the cavity is enclosed by Phe352, Ala417, Cys559 and Gln590. The movement of Phe414 blocks the access to these residues but opens the access to Ile357, His425 and Ile408. Ile408 is moved due to the loss of its helix's secondary structure, as explained before. In Figure 12.6, a drawing of the binding focusing on the depth of the cavity can be found.

12.3.2.2 Non-covalent interactions between DHA and *hum*ALOX12

Two different binding modes of DHA have been found, each one of them corresponding to each of the *hum*ALOX12's detected conformations. Only the relative position of Phe414 has been detected to be different in the two conformations, but maybe other interactions change.

The different interactions that take place between *hum*ALOX12 and DHA have been studied.

Interactions with DHA's carboxylate

In the case of the DHA:*pig*ALOX15 complex, an interaction between DHA's carboxylate and *pig*ALOX15's Arg403 was found (Section 11.3.2.1). An Arg in the same position has been found in *hum*ALOX12. It is the Arg402. The distance between the substrate's carboxylate and Arg402's hydrogens has been analysed for the two replicas. Moreover, the region around Arg402 has been analysed in order to find other residues able to interact with the carboxylate. Gln406 has been found. The two distances have been plotted in Figure 12.7.

Figure 12.7 shows that there is an interaction between the DHA's COO^- group and Arg402, which is not present in the *pig*ALOX15 case (Section 11.3.2.1). Moreover, an interaction with Gln406 is present although it is weak.

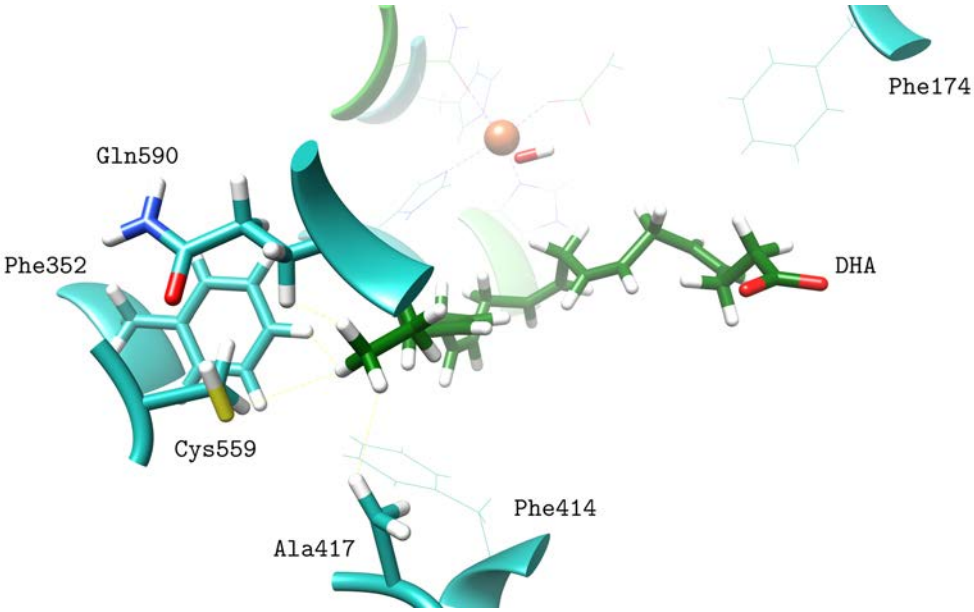

(a) Closed conformation

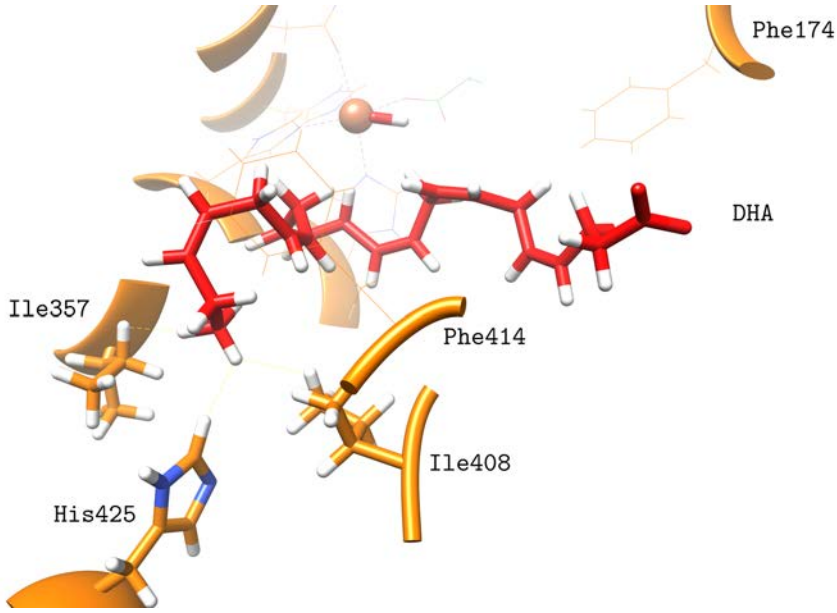

(b) Open conformation

Figure 12.6: Residues in the depth of the cavity for the closed (upper, in green) **and open** (lower, in orange) **conformations of *hum*ALOX12.**

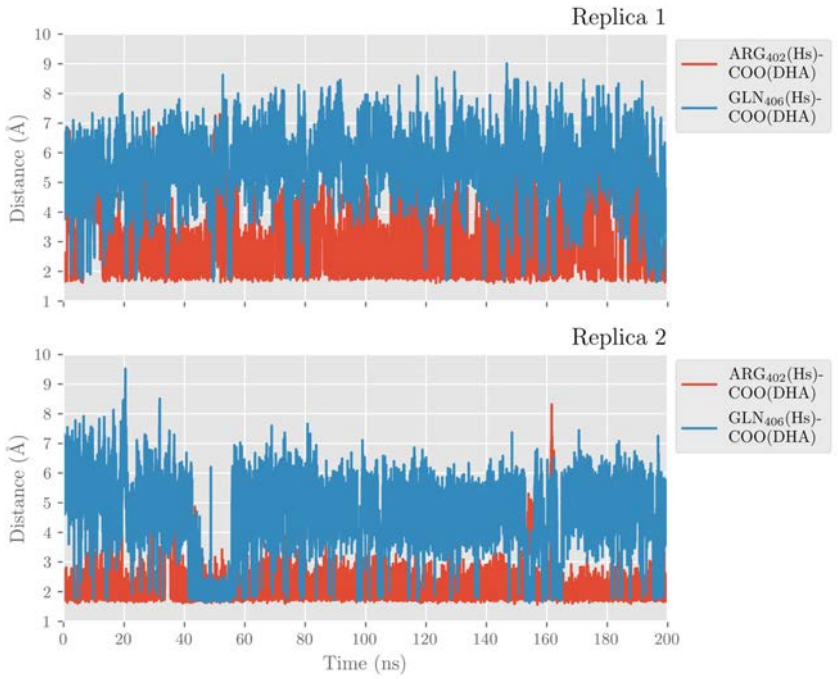

Figure 12.7: Distance from DHA's carboxylate to Arg402's (in red) **and Gln406's** (in blue) **hydrogens versus time for replica 1 and 2.**

This interaction with Arg402, that appears in a few specific moments in *pig*ALOX15 (with Arg403 in that case) (Section 11.3.2.1), has to be related –in the human case– with some interaction between Arg402 and a close residue. Its environment has been restudied and an interaction with Gln406 has been detected. The interaction between Arg402's hydrogens and Gln406's oxygen –the hydrogen-donor–hydrogen-acceptor pair that can interact between these two residues– has been analysed. The results for replica 1 are plotted in Figure 12.8.

Gln406's position along the trajectories has been analysed and it has been observed that the lateral chain flips repeatedly away from the en-

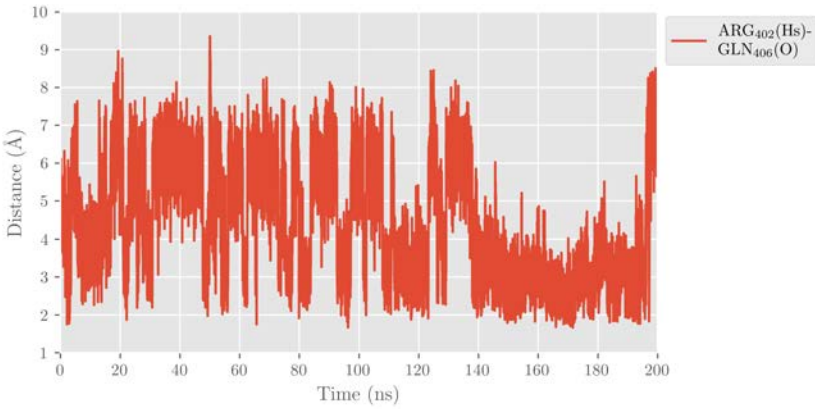

Figure 12.8: Shortest distance between the Arg402's hydrogens and Gln406's oxygen versus time for replica 1.

trance of the cavity and back. This movement causes the detected intermitency of the Gln406 interaction with DHA and Arg402. On the contrary, Arg402 remains pointing to the cavity for the whole trajectories thanks to a salt bridge with helix α_2's Glu175.

As it can be seen in Figure 12.8, an interaction between Arg402 and Gln406 is present. This interaction is thought to assist the proper position of Arg402 for its interaction with the substrate's carboxylate.

Nevertheless, experimental works[226] have reported that the mutation of Arg402 to a hydrophobic Leu residue does not change significantly the reactivity of *hum*ALOX12 with DHA. From the learnt from the studies of the DHA binding with *pig*ALOX15 and with *hum*ALOX12, two theories are possible: the mutation removes the interaction with Arg402 and the COO^- group interacts with Gln406 or the mutation removes both interactions with COO^- and the DHA's binding becomes similar to that seen in the *pig*ALOX15's case (Section 11.3.2.1).

With respect to the closed and open conformations of *hum*ALOX12,

there is no difference in the interaction with Arg402 or Gln406. Nonetheless, the interaction between the two residues gets stronger in the open conformation, as it can be seen in Figure 12.8.

Analogously to the case of *pig*ALOX15, no interaction has been observed to take place between DHA and His596. In *hum*ALOX12 it is also placed in the inner region of the entrance preventing the interaction with the long-chain DHA, although it happens with shorter-chain PUFAs such as AA[226].

$\pi - \pi$ interactions with double bonds

As it happens with *pig*ALOX15, between DHA and *hum*ALOX12 π-π interactions take place between DHA's double bonds and aromatic groups of enzyme's residues. As in the case of *pig*ALOX15, Δ^4 and Δ^7 interact with Phe174. A plot of the distances between the double bonds and Phe174 can be found in Figure 12.9. In replica 1 Phe174 stabilises initially the Δ^4 bond, whilst it remains further to Δ^7. After 150 ns, Phe174 gets closer to Δ^7 and further to Δ^4. This happens when DHA moves towards the entrance of the cavity right before *hum*ALOX12's conformational change. On the contrary, in replica 2 the interaction with both double bonds is very similar along the whole trajectory.

Other π-π interactions also take place. Δ^{10} interacts with His365, Δ^{13} and Δ^{16} interact with Phe414 and Δ^{19} interacts with Phe352. The measured distances can be found in Figure SI12.1. The behaviour in the two replicas is different, specially for the Δ^{10}-His365 interaction, which is present in replica 1 despite it weakens after 150 ns, but it is not observed in replica 2. Δ^{10} and Δ^{16} interactions with Phe414 are strong at the start but weaken for replica 1 in the very first nanoseconds. They remain stable for replica 2. The interaction between Δ^{19} and Phe352 is strong in the two replicas except when the open conformation of *hum*ALOX12 is achieved

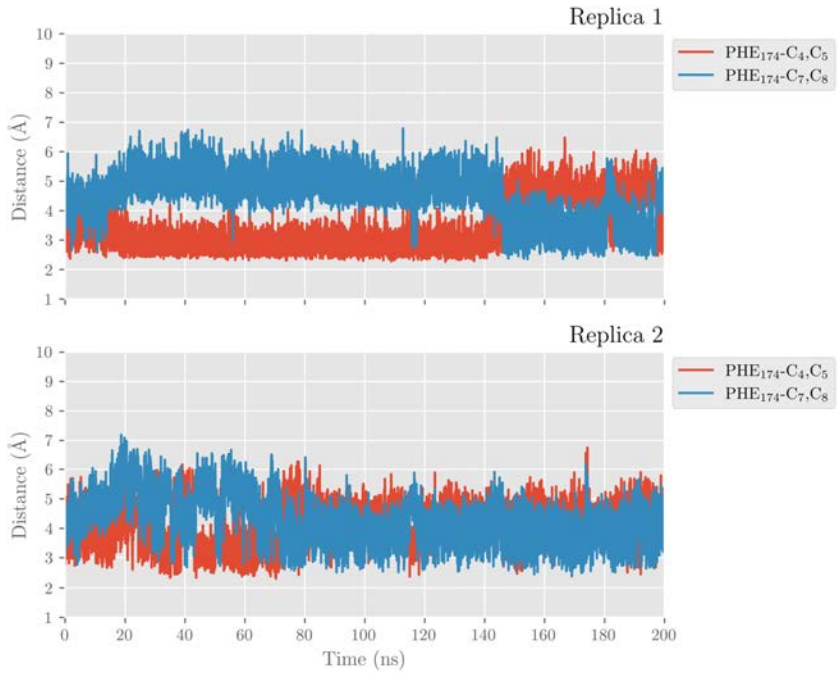

Figure 12.9: Shortest distances between Δ^4 and Δ^7 to Phe174 versus time for replica 1 and 2 of MD simulation.

in replica 1. However, no significant changes like the observed for Phe174 take place.

In Figure 12.10 a representation of DHA and the residues that participate in the π-π interactions is drawn.

12.3.2.3 Regio- and stereoselectivity analysis

The regioselectivity of the hydrogen-abstraction reaction carried out by *hum*ALOX12 over DHA has been studied by analysing the H_9, H_{12} and H_{15}-OH^- distances during the two replicas. The results are plotted in Figure 12.11. As a summary, experimental studies[76;226] reveal that the major product (with a relative share of 76 %) is 14*S*-HpDHA, which is obtained

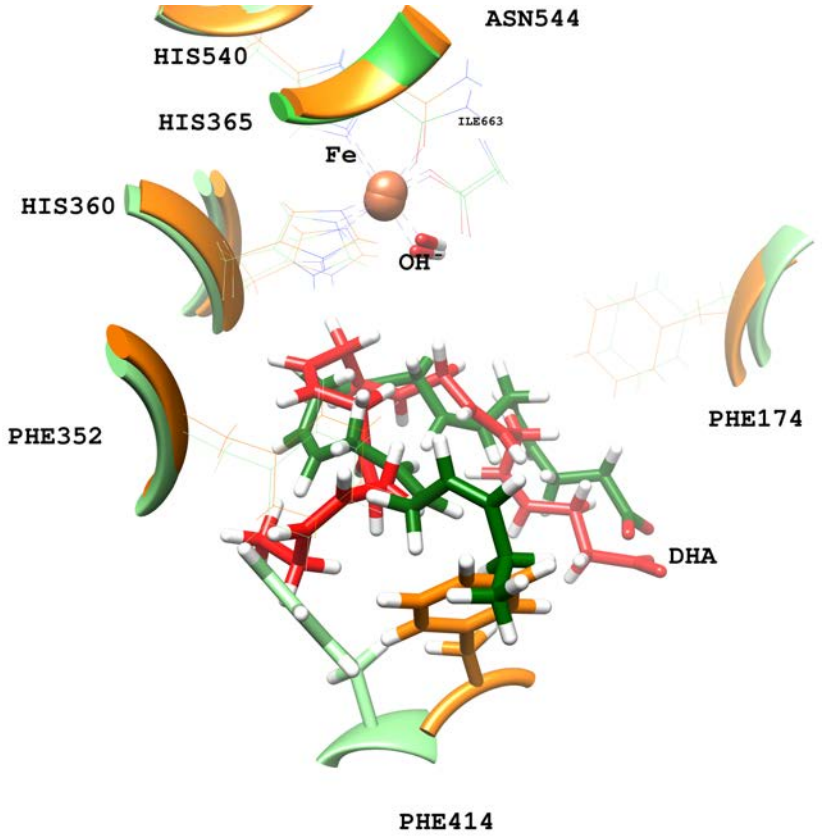

Figure 12.10: Main π-π-interacting *hum*ALOX12's residues with DHA. The closed conformation is drawn in green while the open conformation is drawn in orange.

starting from the abstraction of H_{12}. 17-HpDHA is also obtained experimentally as a minor product and it is obtained by the initial abstraction of H_{15}.

The plots reveal a general tendency for the two replicas. H_9 is generally as close to the OH^- group as H_{12}, whilst H_{15} is the furthest. H_{12} is at a reactive distance from the cofactor during the two trajectories.

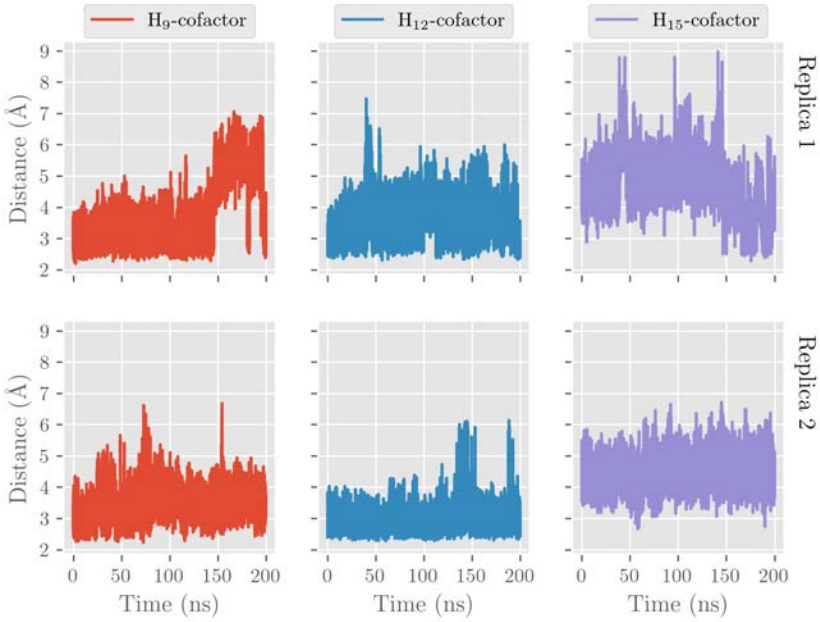

Figure 12.11: Distances between H_9, H_{12} and H_{15} to OH^- group versus time for replica 1 and 2. Distances for H_9 are plotted in red, for H_{12} in blue, and for H_{15} in purple**.**

In replica 2, H_9 remains closer (average distance of 2.99 Å) than H_{15} (4.49 Å) for the whole trajectory. The average distance for H_{12} is 3.44 Å, meaning that it is the most reactive hydrogen together with H_9.

In replica 1 the scenario changes after 150 ns. In the first part of the trajectory –when *hum*ALOX12 is in the closed conformation–, the H_9-OH^- group distance is 3.14 Å in average. At the same time, the H_{12}-OH^- distance is greater (average distance of 3.60 Å). Concluding only from these distances' analysis, 11-HpDHA should be the major product –15-HDHA can not be produced since the DHA binding is tail-first [149]–. H_{15} is the farthest hydrogen from the cofactor. After 150 ns, the PLAT domain opens and DHA moves towards the entrance. H_9 gets farther from

the cofactor while H_{15} gets closer.

Statistical analysis has been done for the H-OH^- distances. The imposed criteria is that the distance has to be shorter than 4 Å. With this criteria, the results are the following for replica 1: 73 % of the frames satisfy the criteria for H_9, 74 % for H_{12} and 10 % for H_{15}. From these results it can be concluded that H_{15} has the lowest probability of being abstracted, while the probabilities for the H_9 and H_{12} abstractions are very similar if only distance is considered.

As introduced in Chapter 10, the biosynthesis of MaR1 is a very stereoselective process. For this process, the synthesis of 14*S*-HpDHA has to lead to the 14-hydroxy-4*Z*,7*Z*,10*Z*,12*E*,16*Z*,19*Z*-DHA isomer, with the 10*Z* and 12*E* bonds conformationally defined. The double bonds close to C_9 and C_{12} –the two most reactive methylenes– are analysed in terms of planar angles to study the conformation of the nascent double bond.

A plot containing the angles between the planes defined by C_7, C_8 and C_9, and by C_9, C_{10} and C_{11} ($\Pi(C_7C_8C_9) - \Pi(C_9C_{10}C_{11})$, and between the planes defined by C_{10}, C_{11} and C_{12}, and by C_{12}, C_{13} and C_{14} ($\Pi(C_{10}C_{11}C_{12}) - \Pi(C_{12}C_{13}C_{14})$ can be found in Figure 12.12. As a reference, a planar angle (as defined in the present case) above 90° is pro-*ZZ*, while if it is under 90°, the bond is pro-*ZE*.

The planar bond around C_9 is around 110° for the whole trajectory. Consequently, the expected double bond conformation for the Δ^7 and Δ^9 is *ZZ*. For C_{12} two different behaviours are detected, corresponding to the two conformations of *hum*ALOX12. During the first 150 ns of the trajectory, the planar angle is mostly under 90°. As a consequence, the expected conformation for the Δ^{10},Δ^{12} is *ZE*. When the PLAT domain opens, the planar angle starts to fluctuate between the two possible conformations of the nascent Δ^{12}.

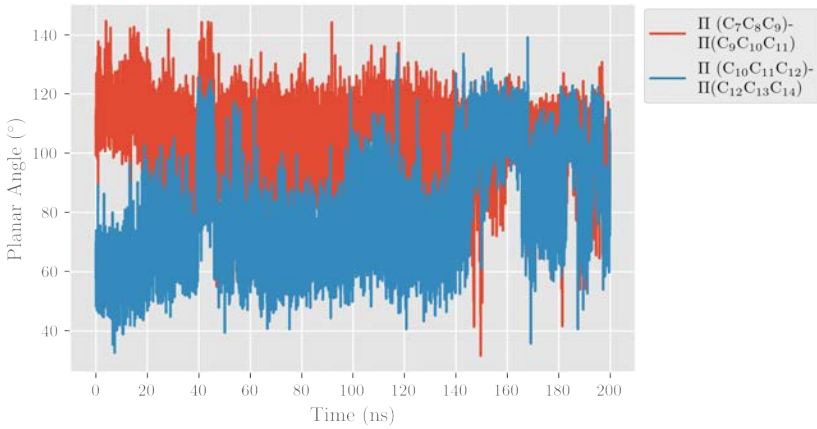

Figure 12.12: Planar angles around C_9 and C_{12} versus time for replica 1 of MD simulations. Planar angle around C_9 is plotted in red, while C_{12} is plotted in blue.

12.3.3 Quantum Mechanics/Molecular Mechanics calculations

The complete oxygenation mechanism from DHA to 14*S*-HpDHA will be studied at the QM/MM level according to the methodology described in Section 12.2.5. Initially, ten frames from the MD replica 1 will be studied in order to analyse the regioselectivity of *hum*ALOX12.

12.3.3.1 Overall mechanism

The formation of 14*S*-HpDHA takes place following a four-steps mechanism that involves both the OH^- group –which acts as a H^+ acceptor and donor– and the Fe atom, which is involved in redox reactions. A scheme of the mechanism can be seen in Figure 12.13.

Each step will be studied in consecutive reactions, taking the product of the previous step as the reactant of the following one. As a result, the

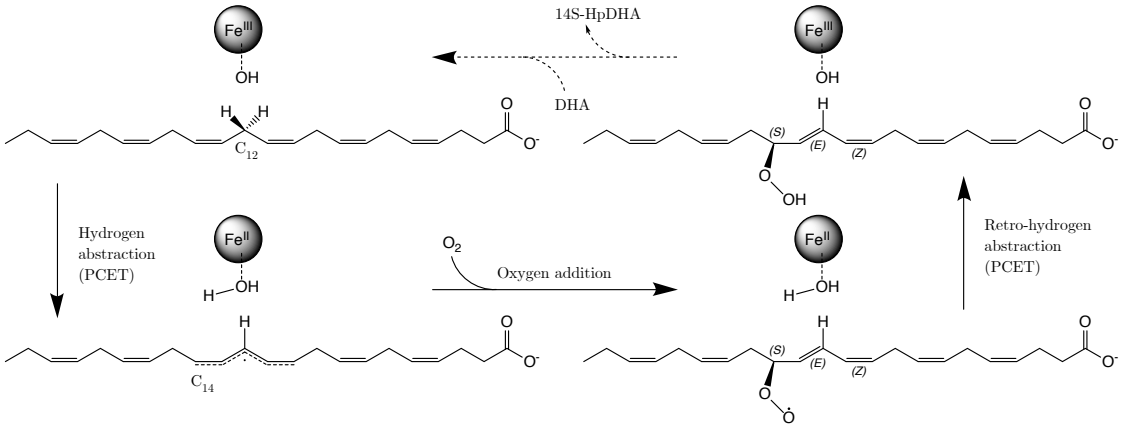

Figure 12.13: Scheme of the mechanism of conversion from DHA to 14S-HpDHA driven by humALOX12. Adapted from Figure 1.3.

step-by-step mechanism of the whole process will be studied.

12.3.3.2 Selection of frames

Ten frames from replica 1 of the DHA:*hum*ALOX12 Michaelis complex's MD simulation are selected. The selection has been done randomly and choosing one frame per each 20 ns in order to obtain representative structure for the whole simulation.

The statistical analysis carried out in Section 12.3.2.3 has been used for selecting the frames. H_9 and H_{12} to OH^- distances have been used, so all selected frames satisfy both criteria. Thus, 29 % of frames have a H_9- and H_{12}-OH^- distance under 4 Å.

As a result, frames 322, 2253, 4986, 6993, 8721, 10106, 12860, 14423, 18168 and 19729 have been selected. 8 of these frames correspond to the close conformation of *hum*ALOX12, while the two others correspond to the open conformation.

12.3.3.3 H abstractions

Hydrogen abstractions have been studied as the first step of the mechanism. A scan of the hydrogen abstraction from DHA to the OH^- group has been performed for each frame and each hydrogen using a two-distances-difference reaction coordinate: $r_c = d(O_{\mathrm{cof}} - H_{\mathrm{n}}) - d(C_{\mathrm{n}} - H_{\mathrm{n}})$. All frames from the MD simulation have been optimised to a minimum, as well as the product obtained from each scan. The maximum-energy structure in each path has been optimised to TS. The obtained results are given in Tables 12.1 and SI12.1. In Table 12.1 only the abstractions with the lowest potential energy barriers are shown.

From Table 12.1 it can be concluded that the abstraction of H_{15} (both the pro-*S* and the pro-*R* hydrogens) is the least feasible process. On the contrary, the abstraction of $H_{12\mathrm{pro}S}$ is the one with the lowest exponential average energy barrier ($\Delta E^{\ddagger}_{AV} = 17.1\,\mathrm{kcal/mol}$), while the abstraction of $H_{9\mathrm{pro}R}$ is the second one ($\Delta E^{\ddagger}_{AV} = 23.9\,\mathrm{kcal/mol}$). From these results, it can be concluded that the regioselectivity of *hum*ALOX12 favours the abstraction of hydrogens in the following order: H_{12}, H_9 and H_{15}. Moreover, as observed for other LOXs[230], all processes are exoergic.

From Table SI12.1, more conclusions can be obtained. If initial distances are compared to energy barriers, it can be concluded that there is no direct correlation, so that a shorter distance does not necessarily translate into a lower barrier. This observation has been reported before[65]. In Section 12.3.2.3, the planarity of the double bonds around C_9 and C_{12} was analysed and it was observed that C_{12}'s environment was closer to planarity than C_9's environment. Moreover, the profiles in discussion have been visually analysed and it has been seen that H_9 abstraction requires a rotation of the Δ^7 to achieve planarity. Furthermore, this rotation suffers steric hindrance because of the presence of the lateral chain of the terminal Ile663. Thus, it can be concluded that the further from the planarity

Table 12.1: Initial H-OH$^-$ distance of the QM/MM-optimised structure, potential energy barrier, reaction energy and stereochemistry of the pentadienyl for the abstraction of H_{12proS} and H_{9proR} for the ten selected frames. Distances are in Å and energies are in kcal/mol. Exponential average energy barriers[228] are included in the last row.

	H_{12proS}				H_{9proR}			
Frame	$d^{react}_{H-OH^-}$ [a]	$\Delta E^{\ddagger}$	ΔE	**Pentadienyl Stereochemistry**	$d^{react}_{H-OH^-}$ [a]	$\Delta E^{\ddagger}$	ΔE	**Pentadienyl Stereochemistry**
322	3.5	15.9	−18.3	*ZE*	3.5	36.4	−13.9	*ZZ*
2253	5.4	20.5	−19.0	*ZE*	3.5	23.4	−19.1	*ZZ*
4986	5.4	19.3	−17.0	*ZE*	5.0	35.0	−14.1	*ZZ*
6993	3.9	18.0	−18.5	*ZE*	3.1	29.7	−14.5	*ZZ*
8721	5.0	21.9	−17.3	*ZE*	3.3	22.7	−13.6	*ZZ*
10,106	5.5	24.3	−16.8	*ZE*	3.4	25.6	−17.4	*ZZ*
12,860	5.2	22.9	−18.5	*ZE*	3.9	29.2	−15.3	*ZZ*
14,423	4.1	21.8	−19.1	*ZE*	3.4	27.5	−13.6	*ZZ*
18,168	3.7	17.1	−17.0	*ZE*	3.3	31.8	−13.8	*ZZ*
19,729	3.4	17.1	−17.0	*ZE*	3.9	43.7	−18.4	*ZZ*
$\Delta E^{\ddagger}_{AV}$		17.1				23.9		

[a] H stands for H_{12proS}; [b] H stands for H_{9proR}.

the C_{n-2}-C_{n+2} pentadiene is, the higher tends to be the barrier. More specifically, the harder the steric hindrance of this rotation, the higher tends to be the barrier. This geometrical behaviour is not observed in the H_{12} abstraction. In this case, only a small, not hindred rotation is required. This is why the H-abstraction barrier for $H_{12pro\mathit{S}}$ is 6.8 kcal/mol lower than for $H_{9pro\mathit{R}}$.

In Table 12.1 the stereochemistry of the pentadienyl is also described. In all cases, the conformation of the double bonds –Δ^7 and Δ^9 for H_9 and Δ^{10} and Δ^{12} for H_{12}– is *ZZ* for the abstraction of $H_{9pro\mathit{R}}$ and *ZE* for the $H_{12pro\mathit{S}}$. Thus, the expected major product to be obtained in the following steps is the 14-hydroxy-4*Z*,7*Z*,10*Z*,12*E*,16*Z*,19*Z*-DHA, which is the appropriate intermediate for MaR1 biosynthesis. Moreover, these results confirm the initial ideas emerged from the analysis of the planar angles during the MD simulation (Section 12.3.2.3).

The effect of *hum*ALOX12's conformation has to be also pointed out. If the barriers from frame 322 to 12860 –which correspond to the closed conformation– are compared to the one from 14423 –which corresponds to an intermediate conformation between the open and closed conformations– and with the ones from frames 18168 and 19729 –which correspond to the open conformation–, the same behaviour can be observed. For all frames, the barrier for the $H_{12pro\mathit{S}}$'s abstraction is always lower than the barrier for the $H_{9pro\mathit{R}}$'s abstraction, even when the OH^- group to $H_{12pro\mathit{S}}$ initial distance is larger than to $H_{9pro\mathit{R}}$. Nonetheless, it is also remarkable that the barriers for the abstraction of $H_{9pro\mathit{R}}$ for the frames corresponding to the open conformation –18168 and 19729– are higher than for the closed one, with the exception of the frame 4986. This is in agreement with the displacement of the DHA towards the entry of the cavity observed in the open conformation (Section 12.3.2.3), which is responsible for a more hindered abstraction, although the $H_{9pro\mathit{R}}$ to the OH^- group distances are

short enough to be reactive.

As an example, the stationary structures along the $H_{12pro}S$'s abstraction for frame 8721 can be found in Figure 12.14.

12.3.3.4 O_2 Addition

The second step of the mechanism has been studied (Figure 12.13) from the H_{12}-abstracted radicals. The addition has been studied on C_{14}, so the 14*S*-HpDHA intermediate will be obtained.

The study of the addition has been done as follows. Around the C_{14} of the H_{12}-abstracted DHA radical –optimised as a minimum–, a sphere of O_2 molecules has been built. The molecules have been located along the x, y and z Cartesian axes and along the bisector axes contained in the xy, xz and yz. Thus, 26 positions have been generated for each of the frames. O_2 molecules have been positioned in such a way that the inner O atom is placed at 3 Å and the molecular axis is over the built axis. For each frame, a first filter has been applied and all positions with a clash with a protein's atom has been removed. A single-point evaluation of each structure has been carried out and the positions with an energy greater than 100 kcal/mol compared to the energetically lowest structure have been removed. For the least energetic structures, the addition has been studied. It has been defined with the reaction coordinate $r_c^{O_2\ addition} = d(O - C_{14})$, which has been explored with a negative step –so the bond formation is studied–. The obtained products have been optimised to minima. The reaction coordinates have been explored backwards in order to refine the addition paths for each frame. The new reactants have been optimised and the bond formation have been explored again. The refined potential energy barriers have been obtained and the results are shown in Table 12.2 for the three frames that have converged –8721, 10106 and 18167–. For the sake of example, the stationary structures obtained for

(a) *R*

(b) *TS*

(c) *P*

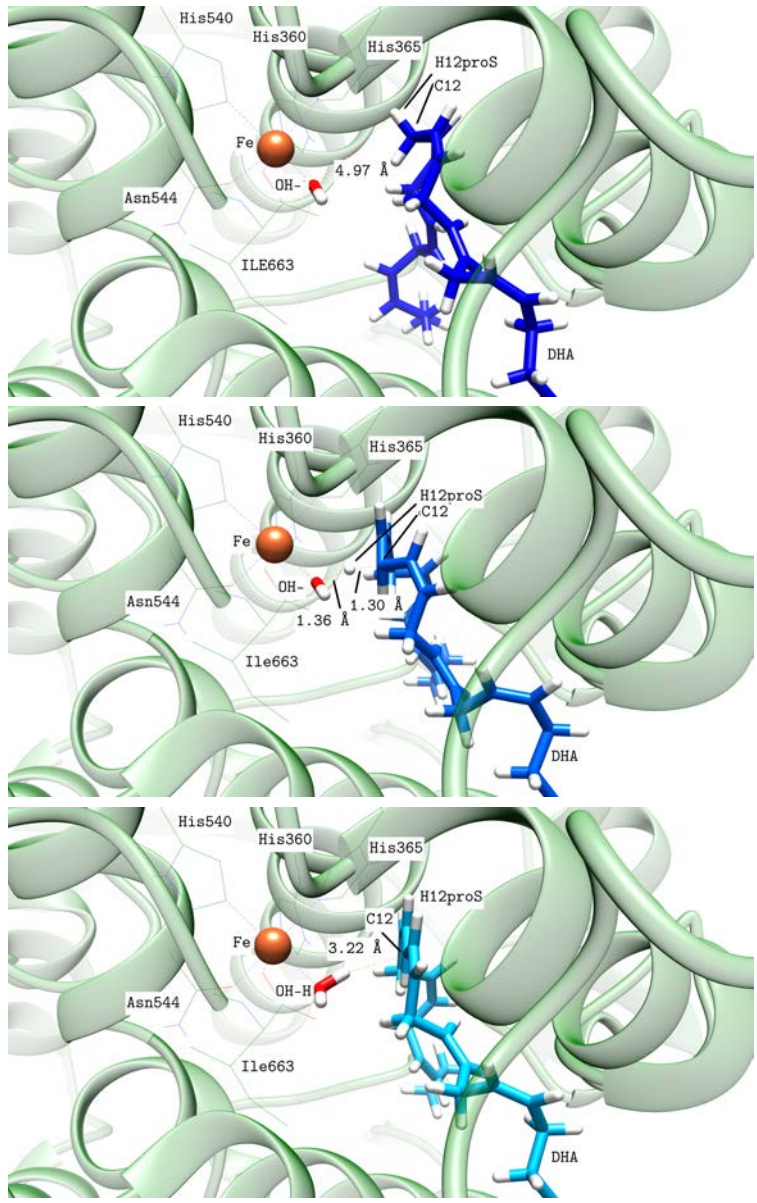

Figure 12.14: Structures along the H_{12proS}-abstraction pathway for frame 8721. Key distances in each case are included in the Figures.

Table 12.2: Initial O_2-C_{14} distance of the refined, QM/MM-optimised reactant, the potential energy barrier, the chirality of the obtained product and the geometry of the addition for the frames 8721, 10106 and 18167. Distances are in Å and energies are in kcal/mol.

Frame	$d^{react}_{O_2-C_{14}}$	$\Delta E^{\ddagger}$	Chirality of Product	Geometry of Addition
8721	3.2	3.0	*S*	Antarafacial
10106	3.2	4.3	*S*	Antarafacial
18167	3.1	3.1	*S*	Antarafacial

the O_2 addition path of the frame 8721 are depicted in Figure 12.15.

As it can be seen in Table 12.2, all additions have an antarafacial geometry, meaning that the O_2 molecule is added in the opposite face with respect to the Fe atom. Moreover, the final chirality of the product is *S*. Again, the conformation of the *hum*ALOX12 does not affect the O_2 addition, as it can be seen when the barriers corresponding to the frame 18167 –open conformation– are compared with the barriers from frames 8721 and 10106.

For the three paths, the obtained product after the last step of the mechanism is the 14*S*-hydroperoxy-4*Z*,7*Z*,10*Z*,12*E*,16*Z*,19*Z*-DHA.

12.3.3.5 Retro-hydrogen Abstraction Reaction

The final step of the oxygenation of DHA by *hum*ALOX12 is the retro-hydrogen abstraction of the initially abstracted H_{12} to the peroxide group and leads to the final 14*S*-HpDHA. Along this step, the Fe(II)-H_2O group recovers its initial Fe(III)-OH^- state.

As discussed in the previous Section, the geometry of the addition is antarafacial. This means that the peroxide group is located in the opposite

(a) *R*

(b) *TS*

(c) *P*

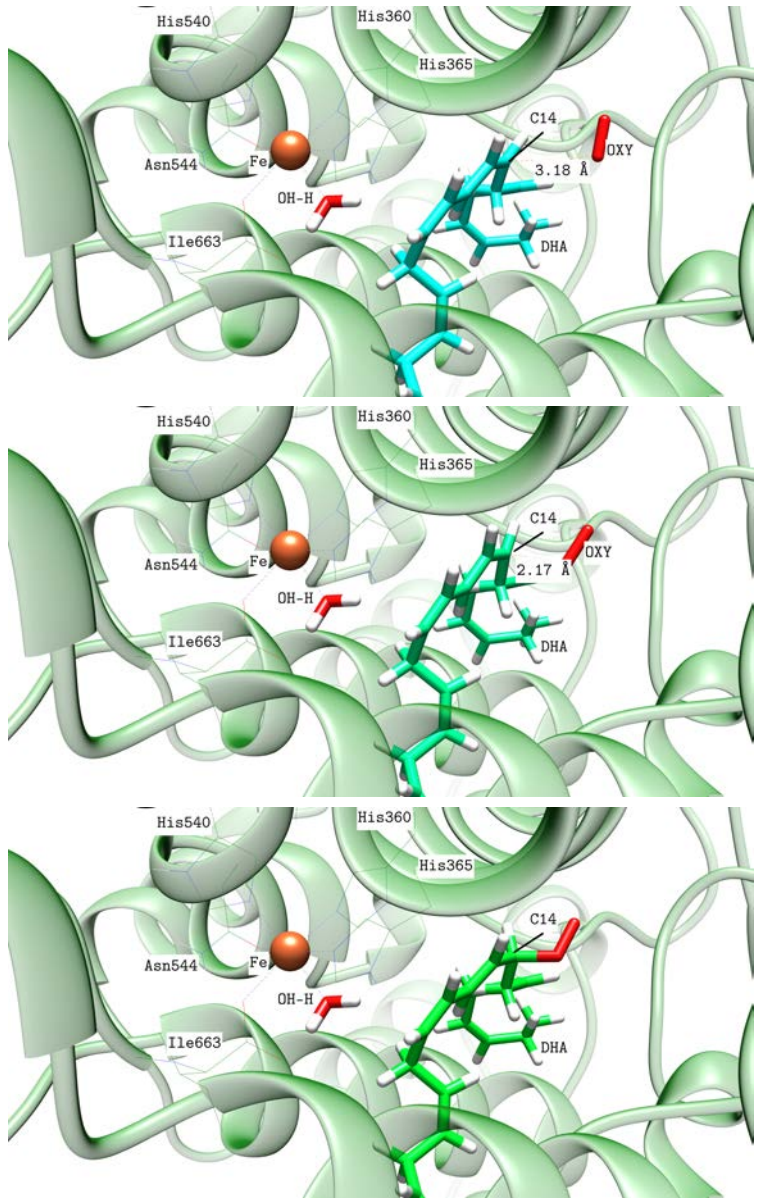

Figure 12.15: Structures along the O_2 addition pathway for frame 8721. Key distances in each case are included in the Figures.

face with respect to the Fe atom, so an initial rotation of the C skeleton is required in order to achieve a geometry suitable for the retro-hydrogen abstraction.

Two different rotations have been tested: the rotation of the dihedral defined by $C_{12}C_{13}C_{14}C_{15}$ and of the $C_{13}C_{14}C_{15}C_{16}$ torsion. For the three studied paths, the lowest barrier has been obtained with the rotation of the $C_{13}C_{14}C_{15}C_{16}$ torsion (between 5.8 kcal/mol and 6.6 kcal/mol) and all three have located the peroxide in the same face as the Fe atom. The results are shown in Table 12.3. A representation of the stationary structures along this step can be found in Figure 12.16.

After this initial reorganisation, the retro-hydrogen abstraction reaction can be performed. The reaction coordinate has been defined as $r_c = d(O_{\text{cof}} - H_{12}) - d(O^{outer}_{\text{peroxide}} - H_{12})$ –H is labelled as H_{12} since it is the one linked to C_{12} in R–. For frames 8721 and 18168 the pathway has been obtained but for the frame 10106 it has not due to convergence problems. In the two obtained paths, two steps have been found: an initial reorganisation that approaches the peroxide to the cofactor and the hydrogen abstraction itself. The obtained results for the two steps are also shown in Table 12.3. A representation of the stationary structures along the retro-hydrogen abstraction (including the reorganisation) for frame 8721 can be found in Figure 12.17.

12.3.3.6 Complete mechanism for frame 8721

During the last Sections, the complete step-by-step mechanism for the conversion of DHA into 14*S*-HpDHA has been reported. This mechanism consists of three reactions and two reorganisations previous to the last reaction. Along this section, the complete mechanism will be summarised. The frame 8721 will be used as example.

In order to generate a consistent energy profile of the complete process,

(a) *R*

(b) *TS*

(c) *P*

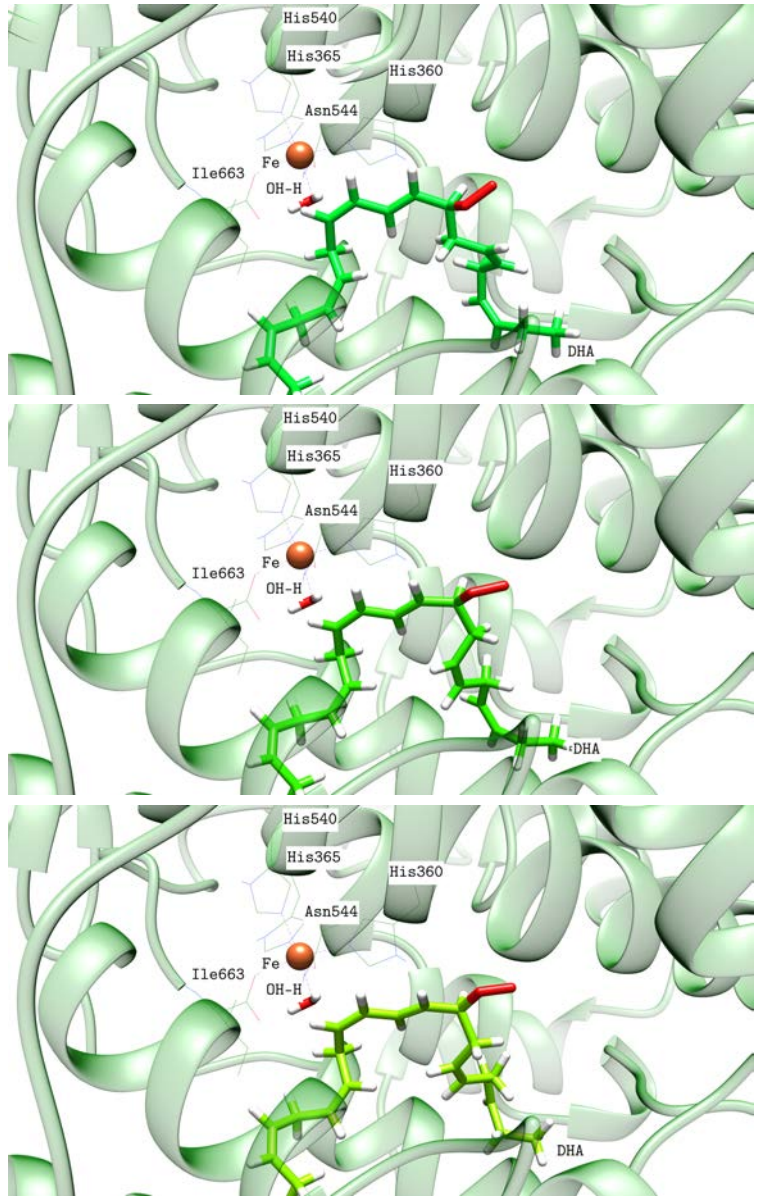

Figure 12.16: Structures along the carbon skeleton rotation for frame 8721.

(a) TS1

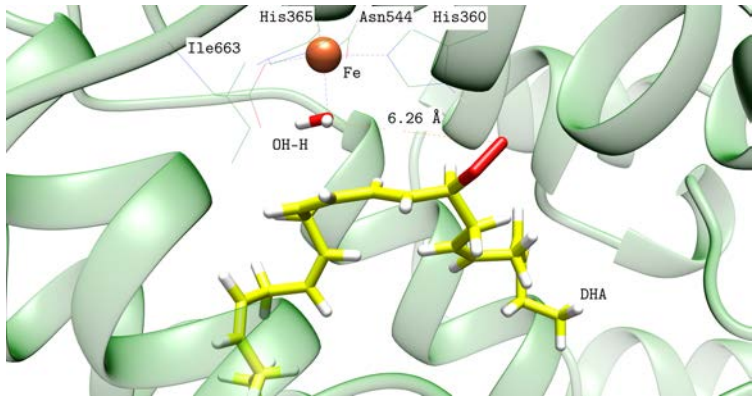

(b) INT1

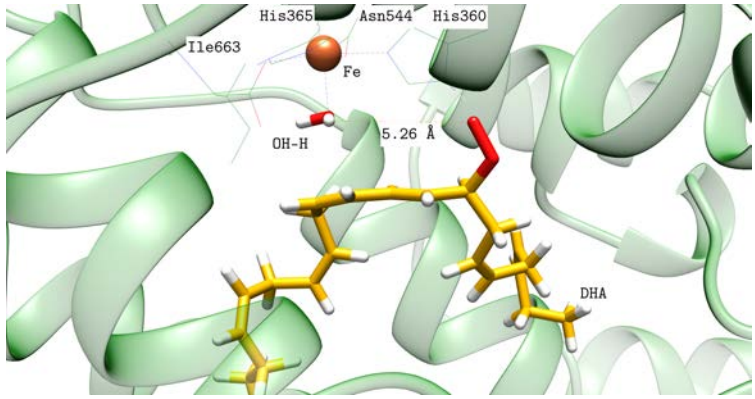

(c) TS2

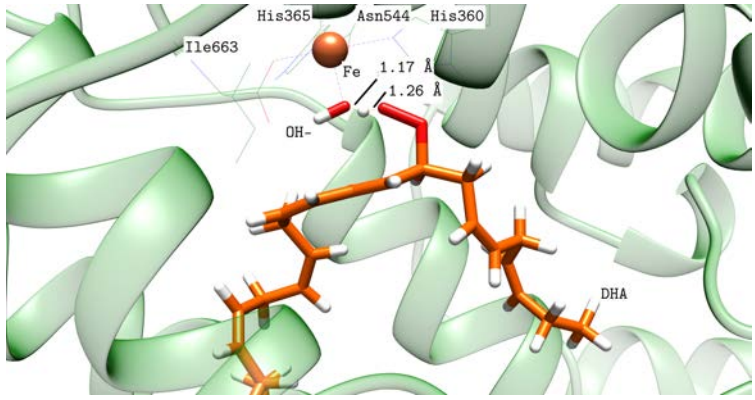

(d) P

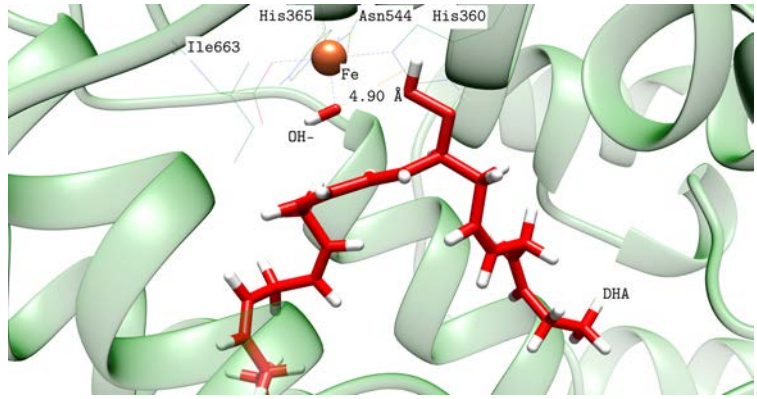

Figure 12.17: Structures along the retro-hydrogen abstraction for frame 8721. Key distances in each case are included in the figures. The structure of the reactant can be found in Figure 12.16c.

an O_2 has been added to the stationary structures along the hydrogen abstraction. The dioxygen molecule has been added at the surface of the cavity and its position has been optimised at the QM/MM level. The O_2 has been finally placed at 12.1 Å in the same axis than the addition.

The energetic diagram of the complete mechanism from DHA to 14*S*-HpDHA can be found in Figure 12.18. As it can be observed, two regions

Table 12.3: Barriers for the several steps along retro-hydrogen abstraction reaction: carbon skeleton rotation, substrate reorganisation and retro-hydrogen abstraction for frames 8721, 10106 and 18168. Energies are in kcal/mol.

Frame	$\Delta E^{\ddagger}_{C\ rotation}$	$\Delta E^{\ddagger}_{reorg}$	$\Delta E^{\ddagger}_{retro-Habs}$
8721	6.6	10.2	33.3
10106	5.8	-	-
18168	5.9	13.1	20.6

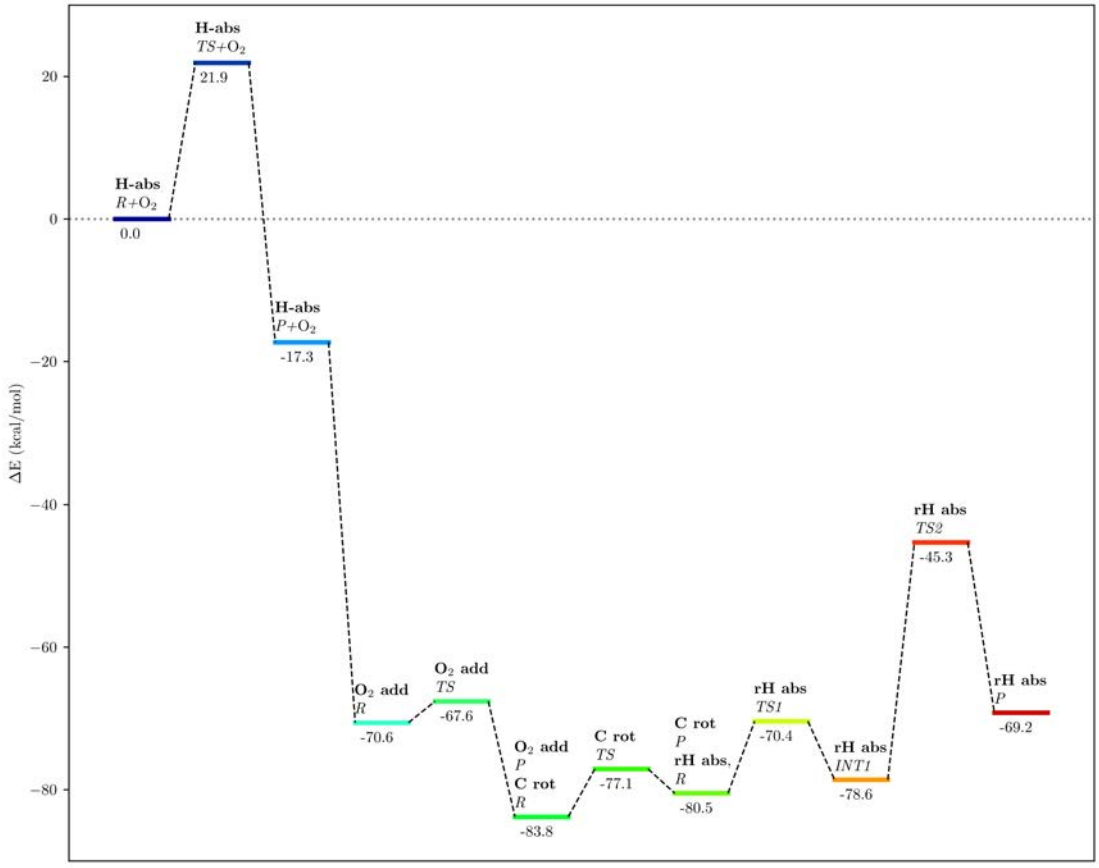

Figure 12.18: Energy profile of the complete peroxidation mechanism of DHA by *hum*ALOX12. The profile corresponds to the mechanism studied for frame 8721. The zero of energy corresponds to the DHA:*hum*ALOX12 Michaelis complex with an O_2 molecule place at 12.1 Å from C_{14}.

can be detected. The first one corresponds to the hydrogen abstraction step of the mechanism, which is the RDS of the reaction. Once the DHA radical has been obtained, the entrance of the O_2 molecule in the cavity generates a falloff of the energy of 53.3 kcal/mol. Then, the O_2 addition, the rotation of the skeleton of carbons and the final retro-hydrogen abstraction take place energetically below the first step of the mechanism.

12.4 Conclusions

During the present Chapter the formation of the regio-, stereoselective 14*S*-HpDHA product from DHA carried out by *hum*ALOX12 has been depicted in a step-by-step manner. Using MD simulations, the stereoselective control has been depicted and it has been confirmed by QM/MM calculations. Moreover, the regioselectivity of *hum*ALOX12 has been also studied. As a conclusion, it has been found that both the distance and the initial relative position of the double bonds around the reactive methylene contribute to the potential energy barrier. The stereochemistry of the O_2 addition has also been studied at QM/MM level and it has been demonstrated to happen with an *S* configuration and following an antarafacial geometry. The global mechanism goes as follows: firstly a hydrogen (H_{12} preferrentially) is abstracted, then a molecular O_2 is added to the antarafacial face respect the Fe atom. After the formation of the peroxide group, the skeleton of carbons rotates so the peroxide adopts a suprafacial geometry respect the Fe atom, and, finally, the initially abstracted hydrogen gets retroabstracted to the peroxide group. As a product, the fully reported 14*S*-hydroperoxy-4*Z*,7*Z*,10*Z*,12*E*,16*Z*,19*Z*-DHA is obtained.

A conformational change of the protein has been detected during one of the MD replicas. The PLAT and the catalytic domain separate from each other, thus generating a bigger interdomain space and inducing a

geometrical change of the cavity's bottom. This new cavity changes the DHA's binding mode from the known U shape to a more distorted one. This binding mode change induces also a global movement of the DHA towards the entrance of the cavity. After this moment, the H_9 is located further from the OH^- cofactor, while the H_{15} is closer. The distance from H_{12} to the OH^- group does not change significantly. Furthermore, this new, open conformation of *hum*ALOX12 does not change the regio- and stereoselective features of the enzyme over DHA.

Chapter 13

Epoxidation: Formation of 13*S*,14*S*-epoxy-MaR1 from 14*S*-hydroperoxy-DHA by human ALOX12

13.1 Introduction

In the previous Chapter (Chapter 12), the enzymatic mechanism of the conversion from DHA into 14*S*-HpDHA was described using MD simulations and QM/MM calculations. The biosynthetic pathway that leads to the production of MaR1 is known to involve a second reaction carried out by *hum*ALOX12[53;67], although *hum*ALOX15 is reported to be more efficient for this step[53]. This reaction consists on a dehydration where the 14*S*-HpDHA intermediate epoxides, leading to the 13*S*,14*S*-eMaR1 intermediate of the MaR1 biosynthesis.

Nonetheless, the epoxidation reaction is allosterically regulated[53], so the higher the concentration of 14*S*-HpDHA, the lower the production of 13*S*,14*S*-eMaR1 and the greater the production of 7*S*,14*S*-diHDHA.

The mechanism of the epoxidation is still unknown and no molecular details have been reported yet, but experimental evidences confirm this kind of reactivity in LOXs[53;67;231;232].

It is known that the reactant must be a hydroperoxide group with an available methylene group 5 carbon units away from the OOH moiety, enclosed between a vinyl and a diene group. It is suggested that the reaction starts with the abstraction of a hydrogen from this methylene –the C_9 in the present case– promoted by the Fe(III)-OH^- cofactor. As a product of the hydrogen abstraction, a radical is formed on the substrate, which is delocalised in a heptatrienyl system –which includes the vinyl and diene groups–. Simultaneously, the cofactor changes to the Fe(II)$-H_2O$ state. At some point of the reaction, there is a homolytic cleavage of the O–O bond of the hydroperoxide and the O bonded to the carbon of the substrate cycles over the nearest carbon of the delocalised triene system, forming an epoxide. The global reaction is schematised in Figure 13.1

As said before, the step-wise mechanism is unknown. Two different activation pathways are possible after the hydrogen abstraction. On the one hand, the mechanism can be activated by the transference of a hydrogen –the proton and the electron– to the peroxide, thus causing the homolytic cleavage[231;232]. Alternatively, the mechanism can be activated by the transference of an electron to the peroxide group, thus provoking the homolytic cleavage.

To study the step-by-step mechanism of the epoxidation of 14*S*-HpDHA, the obtained products in Chapter 12 for frames 8721 and 18168 will be used as the starting structures.

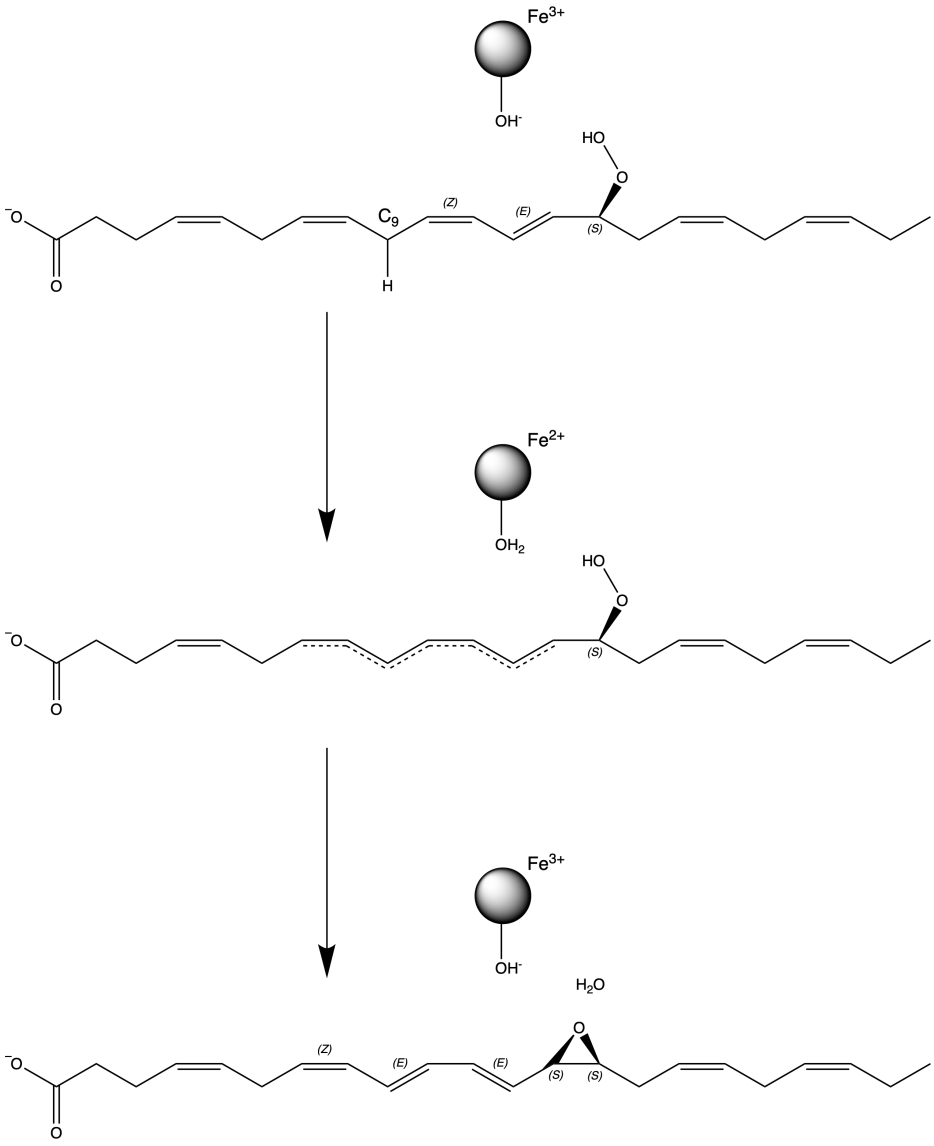

Figure 13.1: Scheme of the epoxidation reaction of 14*S*-HpDHA by humALOX12.

13.2 Methods

For the study of the epoxidation of 14*S*-HpDHA into 13*S*,14*S*-eMaR1 by *hum*ALOX12, QM/MM calculations have been carried out.

13.2.1 System setup

The drop-solvation models (Section 12.2.3) of the frames 8721 and 18168 of the replica 1 of the MD simulatiosn of the DHA:*hum*ALOX12 complex (Sections 12.2.4 and 12.3.2), after the QM/MM simulations that led to the 14*S*-HpDHA intermediate, have been used. No modifications have been applied to the structures' coordinates nor to the solvation model.

13.2.2 Quantum Mechanics/Molecular Mechanics calculations

The same methodology used for the study of the conversion from DHA to 14*S*-HpDHA has been used for the present study (Section 12.2.5).

The same QM/MM setup has been used, as well as the same QM-MM partition (Figure 12.1). `ChemShell` 3.7[162;163] has been used for the QM/MM calculations. Turbomole 7.0[165] is used as the QM engine, while `DL_POLY` 5.0[166] is used as the MM engine.

13.3 Computational results

In this section the computational results of the 14*S*-HpDHA epoxidation by *hum*ALOX12 will be described.

13.3.1 Hydrogen abstraction

As explained in the Introduction Section (Section 13.1), the initial step of the mechanism is the abstraction of the H_9. For the study of this step, a

r_2 coordinate has been defined with the equation $r_2 = d(C_9 - H_{9\text{proS}}) - d(H_{9\text{proS}} - O_{\text{cofactor}})$. The obtained results can be found in Table 13.1. Only the abstraction of $H_{9\text{proS}}$ has been calculated since it is the closest H_9 to the OH^- group. Additionally, $H_{9\text{proS}}$ is found between the Fe atom and the $H_{9\text{proR}}$, so the abstraction of the latter is prevented.

Table 13.1: Initial distance, $\Delta E^{\ddagger}$ and ΔE of the $H_{9\text{proS}}$ abstraction from 14S-HpDHA for frames 8721 and 18168. Distances are in Å and energies are expressed in kcal/mol.

Frame	***hum*ALOX12's conformation**	$d^{react}_{H-OH^-}$	$\Delta E^{\ddagger}$	ΔE
8721	Closed	2.86	31.6	-14.7
18168	Open	3.65	41.0	-1.6

As Table 13.1 reveals, the abstraction of $H_{9\text{proS}}$ has a much lower potential energy barrier for frame 8721 than for frame 18168. The reaction's potential energy is also lower for the frame 8721 than for 18168. Additionally, the potential energy barrier for the frame 18168 is too high for a feasible hydrogen abstraction (see Tables 7.2, 7.3, 11.1, 12.1, and 12.3 for reference barriers of different hydrogen abstraction processes).

Thus, the data shown in Table 13.1 demonstrates that the open conformation of *hum*ALOX12 makes the potential energy barrier of the $H_{9\text{proS}}$ abstraction higher, while destabilising the radical intermediate. On the contrary, the closed conformation lowers the energy barrier and stabilises the product.

After this initial hydrogen abstraction, a radical delocalised in a heptatriene system enclosed between a methylene group and the hydroperoxide group of 14*S*-HpDHA has been obtained. Moreover, during the course of the reaction, the Fe(III)-OH^- cofactor is reduced and protonated by the transference of the H atom, so the Fe(II)-H_2O state of the cofactor is

obtained. From this intermediate, epoxidation can take place.

13.3.2 Epoxidation

The epoxidation can only take place from the radical product of the H_{9proS} abstraction, and the obtained epoxide is localised on C_{13} –because it is the closest-to-peroxide C of the radical heptatriene– and C_{14} –because it is the C bonded to the peroxide–. As mentioned before, two distinct mechanisms for the epoxidation are possible, but no mechanistic details have never been reported. Unpublished studies from our Group have reported high potential energy barriers for the hydrogen transference mechanism in similar systems. Hence, the epoxidation will be studied following the electron transfer mechanism.

For the electron transfer to take place, the Fe centre has to release an electron and transfer it to the peroxide group. This transfer has to take place through an ISET, which requires the cleavage of a bond during the reaction.

An ISET mechanism has been suggested by Smyrniotis et al.[232], although no step-by-step mechanism is detailed. A step-wise mechanism that obeys the ISET mechanism is proposed here. According to it, the H_2O molecule formed from the H_9 abstraction and which is coordinated to the Fe atom decoordinates –it is known to be labile[233]– and the peroxide occupies the free vacancy in the Fe's coordination sphere, so coordinating to the Fe atom. Once the peroxide is coordinated, the electron can be transferred and the peroxide bond can break and the epoxide can be formed over C_{13}.

13.3.2.1 Reorganisation of the substrate

The two proposed mechanisms require the OOH moiety to be close to the Fe-H_2O cofactor. Nonetheless, the starting distance between Fe and the

outer oxygen of the peroxide group in the H_{9proS}-abstracted intermediate is 6.4 Å. Since it is a very long distance, an initial reorganisation of the substrate will be explored in order to approach the peroxide group to the iron. For this reorganisation, a r_1 reaction coordinate is defined with the equation $r_1 = -d(Fe_{cofactor} - O_{outer}^{peroxide})$. Table 13.2 shows the results of this reorganisation.

Table 13.2: Distances of reactant and product, $\Delta E^{\ddagger}$ and ΔE of the substrate's reorganisation prior to the epoxidation. Distances are expressed in Å and energies are in kcal/mol.

Frame	$d^{react}_{Fe^{cof.}-O^{perox.}_{outer}}$	$\Delta E^{\ddagger}$	ΔE	$d^{prod}_{Fe^{cof.}-O^{perox.}_{outer}}$
8721	6.4	11.5	3.5	4.6

13.3.2.2 Testing reaction coordinates for peroxide's coordination to Fe

Several reaction coordinates obey the mechanism where the OOH moiety coordinates to the Fe atom. Four of them have been designed and tested. r_1 –the same coordinate than the one used for the substrate's reorganisation (Section 13.3.2.1)–, r_2 and r_4 reaction coordinates have been tested to find the best descriptor. Their equations are

$$r_1 = -d(Fe_{cof.} - O_{outer}^{perox}), \tag{13.1}$$

$$r_2 = d(Fe_{cof.} - O_{cof.}) - d(Fe_{cof.} - O_{outer}^{perox}), \tag{13.2}$$

$$\begin{aligned} r_4^A = {} & 2{\cdot}d(O_{outer}^{perox} - O_{inner}^{perox}) \\ & -d(Fe_{cof.} - O_{outer}^{perox}) - d(O_{inner}^{perox} - C_{13}^{subs}), \end{aligned} \tag{13.3}$$

and

$$\begin{aligned} r_4^B =& d(Fe_{cof.} - O_{cof.}) + d(O_{outer}^{perox} - O_{inner}^{perox}) \\ & - d(Fe_{cof.} - O_{outer}^{perox}) - d(O_{inner}^{perox} - C_{13}^{subs}) \end{aligned} \tag{13.4}$$

All these reaction coordinates have been used to partially explore the PES. Scan calculations have been run for each of the reaction coordinates but stopped if unfeasible structures have been obtained. The results of the partial explorations can be found in Table 13.3.

Table 13.3: Explored reaction coordinates and energies of the highest energy point along the coordinate. ΔE^{max} corresponds to the maximum potential energy along the coordinate. Italics in energy values indicate that the structure is a TS, so the energy corresponds to $\Delta E^{\ddagger}$. All energies are expressed in kcal/mol. "Eq." stands for Equation.

r_c	r_c equation	ΔE^{max}
r_1	Eq. 13.1	43.4
r_2	Eq. 13.2	*38.6*
r_4^A	Eq. 13.3	54.7
r_4^B	Eq. 13.4	*49.3*

The PES exploration using the r_1 reaction coordinate (Equation 13.1) has led to a high potential energy structure of 43.4 kcal/mol where both the peroxide and the cofactor's H_2O are coordinated ($d(Fe_{cof.} - O_{outer}^{perox}) = 2.23$ Å and $d(Fe_{cof.} - O_{cof.}) = 2.0$ Å, respectively), so the Fe center gets coordinated to seven ligands with a face-capped octahedral geometry.

During the PES exploration using the r_4^A reaction coordinate, a minimum-energy structure has been obtained at $r_4^A = -1.6$ Å. This structure corresponds to a 13,14-diol with a radical located over the C_{14}'s oxygen atom and the cofactor remaining at the same initial Fe(II)-H_2O state. The cleavage of the C_{13}-OH bond requires a barrier of more than 80 kcal/mol –from

around -25 kcal/mol to 55 kcal/mol–, which makes this process unfeasible.

An alternative r_4 coordinate, the r_4^B, has also been tested. Along this coordinate, a TS-like structure has been obtained. Along the coordinate, the water molecule decoordinates the Fe atom, the outer oxygen of the hydroperoxide moiety approaches the Fe centre, and the peroxide bond gets elongated before the hydroperoxide approach to the Fe. Although the reaction coordinate geometrically explores the reaction as expected, the reaction barrier is more than 10 kcal/mol higher than the observed for the r_2. This makes this coordinate no the most appropriate among the tested ones.

The PES exploration using the r_2 is the one that gives the lowest potential energy among the tested r_cs. Thus, this r_2 coordinate is the best candidate for exploring the proposed ISET mechanism in this system. The $\Delta E^{\ddagger}$ of the coordinate is high, at least in comparison to other energy barriers obtained along this Thesis. However, energy barriers for a reactivity like the explored in this Section have never been reported for LOX, hence no reference values can be compared. Moreover, if the whole path is considered starting from the initial DHA reactant –so the peroxidation (Chapter 12) and epoxidation reactions are understood as consecutive reactions–, the TS structure along this r_2 coordinate remains 41.8 kcal/mol under the energy of the initial DHA.

After the TS, the reaction coordinate evolves in such a way that the water molecule moves away from the Fe atom but the OOH moiety does not get closer. An intermediate structure is obtained with a relative potential energy of 17.5 kcal mol, in which the water molecule from the cofactor is decoordinated from the Fe atom but the hydroperoxide group has not coordinate yet. The structure of the obtained intermediate is drawn in Figure 13.2.

The reaction coordinate after the intermediate has been visually anal-

ysed and it has been found that the OOH moiety approaches the Fe atom between the Fe-coordinating His360 and His365, as Figure 13.2 shows. To avoid this geometry and approach to the free coordination vacancy, the heptratriene requires to move towards Leu597, but the H_2O is occupying the region at the last obtained point along the r_2 coordinate. Hence, the H_2O needs to free the region, so the heptatriene-OOH moieties can reorganise and the OOH group can adopt a better angle for its coordination with the Fe atom. Similar studies in our Group with related systems using shorter, more flexible substrates (5*S*-HpETE) reveal that the coordination of the OOH can be achieved after the H_2O release when the OOH group approaches the proper site of the Fe coordination sphere. Thus, it is expected that after the reorganisation of the leaving H_2O molecule and the substrate, the coordination can be achieved.

Once the exploration of this reaction coordinate is completed, a last step consisting in the closure of the epoxide ring on C_{13} is required for completing the epoxidation mechanism.

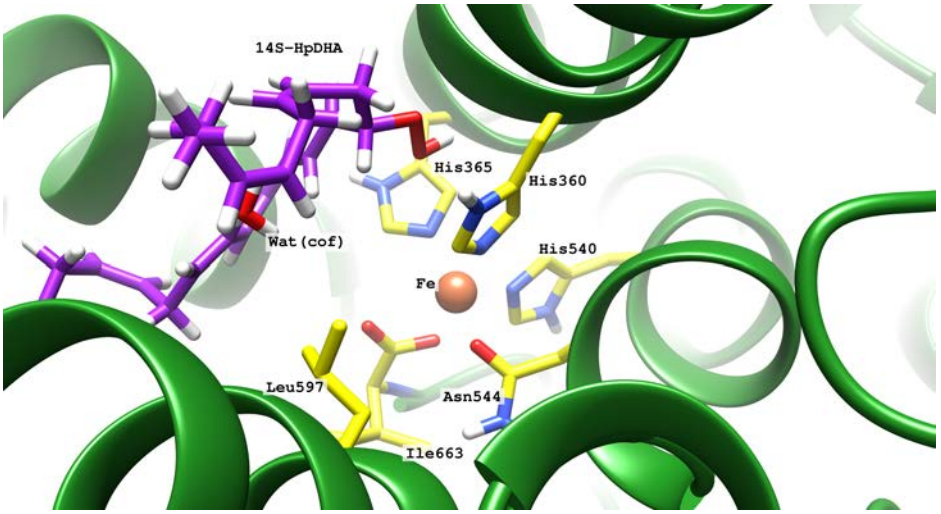

(a) Lateral view

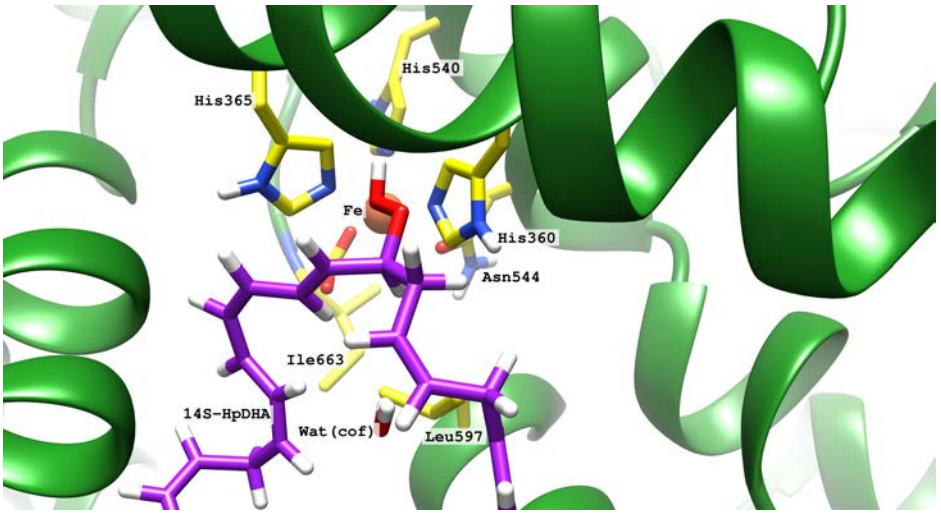

(b) Frontal view

Figure 13.2: Structure after TS of r_2 reaction coordinate for epoxidation reaction. The substrate is drawn in purple, the protein's backbone is coloured in green and the lateral chains of the relevant residues of the protein are drawn in yellow.

Chapter 14

Design of LTA_4H mutants for hydrolysis of eMaR1

Along the present Chapter, the design of several mutants of LTA_4H for the last step of the MaR1's synthesis will be presented. Nevertheless, the designed sequences are protected under Industrial Property Protection. In order to avoid any conflict of interest, the designed mutations will not be revealed, but the results that emerge from their application will be presented. The Supporting Information can be found in Chapter SI14.

14.1 Introduction

As explained in Chapter 10, Section 10.4, the enzyme responsible of biosynthetic the hydrolysis of 13*S*,14*S*-eMaR1 to MaR1 –the last step of the conversion from DHA– is unknown. Nonetheless, the reaction is known to be a stereospecific 1,7-S_N reaction, like the one studied in Chapter 9.

In order to bypass the lack of a known enzyme for this last conversion, the knowledge learnt from the study of the mechanism of LTA_4H on its natural substrate LTA_4 (Chapter 9) has been applied to the design of several mutants of LTA_4H capable of converting 13*S*,14*S*-eMaR1 into MaR1.

14.2 Computational Methods

The same methodology described in Section 9.2 has been used to carry out the simulations required for the design of the mutated LTA_4H's versions Mutated models have been set up as explained in Sections 9.2.1 and 9.2.2, while mutations have been manually added using the `rotamers` module from `UCSF Chimera`[135]. The substrate has been added manually to the different mutants aligning as close as possible the triene system and the epoxide ring to the same moieties from the crystallographic position of LTA_4 in LTA_4H. A comparison of the fitting of the two substrates can be found in Figure 14.1. MD simulations have been performed as described in Section 9.2.3. No QM/MM calculations have been carried out.

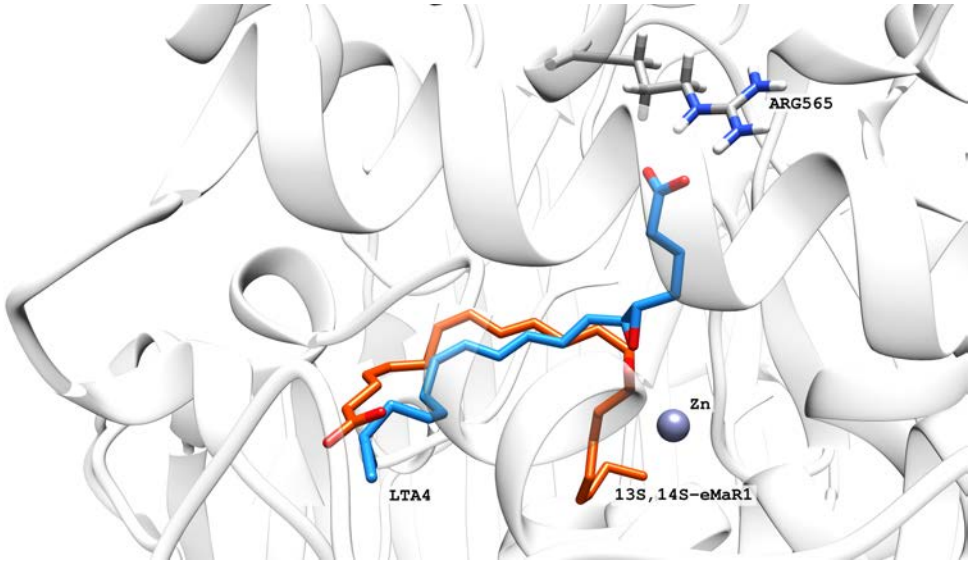

Figure 14.1: Comparison of LTA_4's and 13S,14S-eMaR1's bindings in LTA_4H. Zn and Arg565 have been added for reference.

14.3 Results

Two different sets of mutations have been designed focusing on two different aspects of the substrate-enzyme binding. Firstly, the interaction of the polar head of the substrate has been relocated. Additionally, mutations for improving the fitting of the tail of the 13*S*,14*S*-eMaR1 –which has two more carbons in comparison with LTA_4– have also been designed. Along this Section, the MD simulations with different mutants of LTA_4H will be analysed.

14.3.1 Swapping the binding mode of the substrate

LTA_4 and 13*S*,14*S*-eMaR1 are two oxidised fatty acids that share the same chemical features but with opposed geometries. On the one hand, in LTA_4 there is an epoxide ring that is located on C_5 and C_6, close to the carboxylic acid of the molecule. 13*S*,14*S*-eMaR1 has the same chemical moiety but closer to the tail, on C_{13} and C_{14}. On the other hand, the triene system is closer than the epoxide to the hydrophobic tail in the LTA_4's case, while for the 13*S*,14*S*-eMaR1 it is closer to the carboxylic head.

Along Chapter 9, it has been discussed that the epoxide has to be placed close to the Zn cation of the catalytic centre, while the C_7 methylene of 13*S*,14*S*-eMaR1 has to be placed close to Asp375. To satisfy this geometrical features, as described in Section 9.3.1, the LTA_4 has to fit in a head-first orientation with the carboxylic acid interacting with Lys563 and Arg565. On the contrary, to satisfy these same geometrical features 13*S*,14*S*-eMaR1 has to bind with the opposed orientation –this is the tail-first orientation– to be able to react. If its orientation is not inverted in respect with LTA_4's binding mode in LTA_4H, the 13*S*,14*S*-eMaR1 does not react and it actually behaves as an inhibitor[67].

In order to achieve the inversion of the substrate's orientation, two regions of the cavity have to be mutated. On the one hand, COO^--interacting residues –Lys563 and Arg565– found at the bottom of the cavity have to be removed to avoid the head-first binding mode. Simultaneously, the hydrophobic entrance of the cavity has to be mutated so a residue able to interact with the COO^- group is added to stabilise the tail-first orientation.

A first model has been generated applying these mutations and MD simulations have been carried out. On the one hand, RMSD of the substrate and the backbone, and distances from the epoxide of 13*S*,14*S*-eMaR1 to Zn, the hydrogen of Tyr381 and the hydrogen of Wat1 that points to the epoxide have been analysed in order to determine the stability of the binding. The corresponding plots can be found in Figures SI14.1 and SI14.2. As it can be observed, RMSDs show that after 12 ns of simulation time there is a slight relocation of the substrate, which is propagated to the backbone after 6 ns. Nonetheless, the 13*S*,14*S*-eMaR1's epoxide binding to the Zn environment keeps stable during the whole simulation, as the stable distances show in Figure SI14.2. This data reveals that the applied mutations allow a stable binding of the substrate with a tail-first conformation with the epoxide located close to the Zn.

The conformation of the C_{12}-C_{13} has also been analysed along the MD simulation. The corresponding plot can be found in Figure 14.2.

As observed in the RMSD's plot (Figure SI14.1), the geometry of the substrate changes after 12 ns of simulation time. This change on the geometry can be attributed to a change on the conformation of the ligand where the C_{12}-C_{13} bond goes from around $-90°$ to get stabilised between 0 and 90°, generating always a pro-*Z* conformation, which is the expected one for the double bond in MaR1.

A visual inspection of the MD simulation suggests that the tail of the

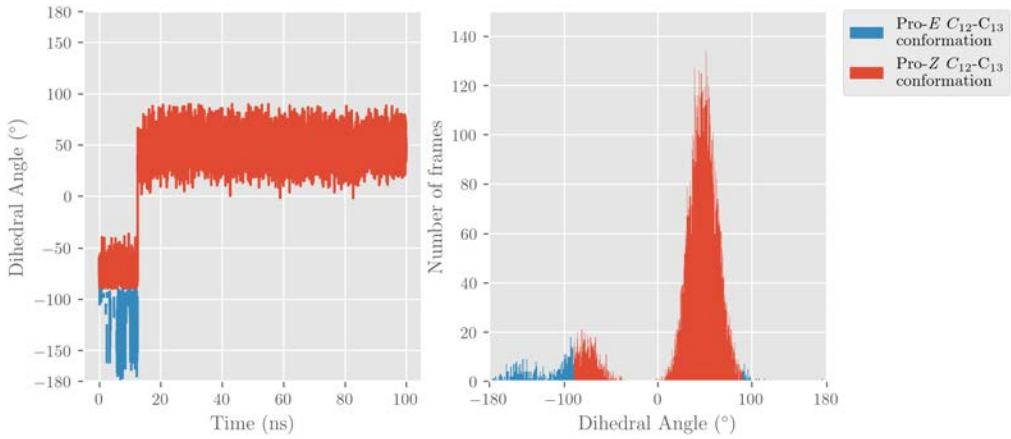

Figure 14.2: Plot and histogram of the dihedral angle of H_{12}-C_{12}-C_{13}-H_{13} along the MD simulation of the eMaR1:LTA_4H's mutant 0. Frames where the C_{12}-C_{13} of LTA_4 shows a pro-Z conformation are coloured in red, while the ones showing a pro-E conformation are coloured in blue.

substrate does not fit well in the depth of the cavity, while the substrate's head and triene system remain in the same position. This is the reason behind the geometry change, which causes the binding geometry to be different from the observed for the LTA_4 natural substrate. A comparison between LTA_4 and 13S,14S-eMaR1 reveals that while in the first case there are only four carbon atoms of the molecule's skeleton in the depth of the cavity, for 13S,14S-eMaR1 there are seven carbon atoms. In Figure 14.1, these atoms correspond to the substrates' extrems on the right of the drawing, close to the Arg565. The atoms at the left are located in the entrance on the cavity.

14.3.2 Giving space to eMaR1's tail

As concluded in the previous Section, the tail of 13*S*,14*S*-eMaR1 does not properly fit in the bottom of LTA_4H's cavity. Since 13*S*,14*S*-eMaR1 has more carbons placed in the cavity's bottom, some space needs to be generated to allow a better substrate's fitting. To do so, two bulky residues located in the depth of the cavity that have been determined not to be essential neither for the substrate's reactivity nor for its binding have been mutated to two smaller residues. Two different sets of mutations (from now on set A and set B) have been generated and combined with the mutations presented in the previous Section.

The stabilities of the protein and the substrate along the MD simulations have been analysed by RMSD and distances from the substrate's epoxide. The corresponding plots can be found in Figures SI14.5 and SI14.6 for the mutant 0 with the set A of mutations at the depth of the cavity and in Figures SI14.3 and SI14.4 for the mutant 0 with the set B. RMSDs show that the enzyme's backbone is structurally stable, as well as the substrate in both cases. No geometry changes have been observed. The distances from the epoxide to the Zn atom are similar in the two cases and similar also to the LTA_4:LTA_4H system (Section 9.3.2.1, Figure SI9.3).

The conformational analysis of the C_{12}-C_{13} bond has also been carried out. The plots of the H_{12}-C_{12}-C_{13}-H_{13} dihedral angle for each system can be found in Figure 14.3.

The analysis of the conformation of the C_{12}-C_{13} reveals that the substrate geometry is the same in the two cases, although a few pro-*E* conformations are obtained for the mutant with the set B of mutations in the depth of the cavity. Because set A of mutations of the cavity's bottom show slightly better results, this set is chosen.

Thus, it can be concluded that the best mutant is the one containing the set A of mutations in the depth of the cavity.

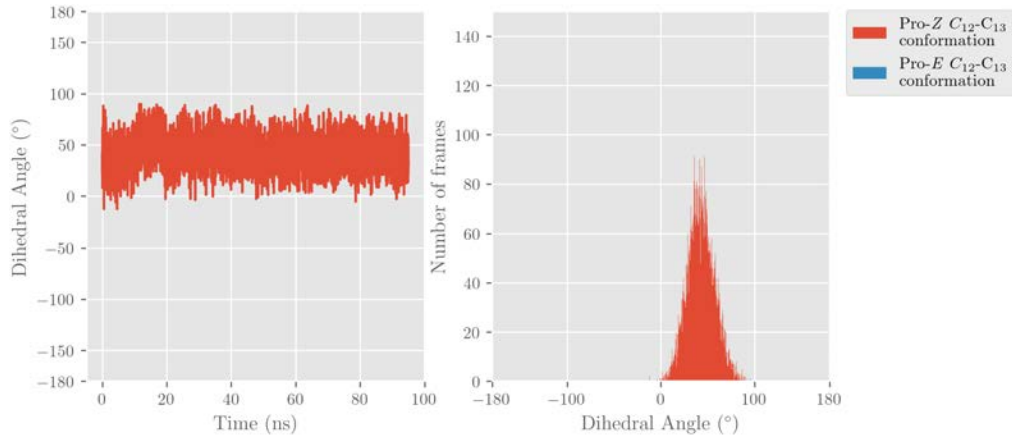

(a) Mutant 0 with set A of mutations in the bottom of the cavity

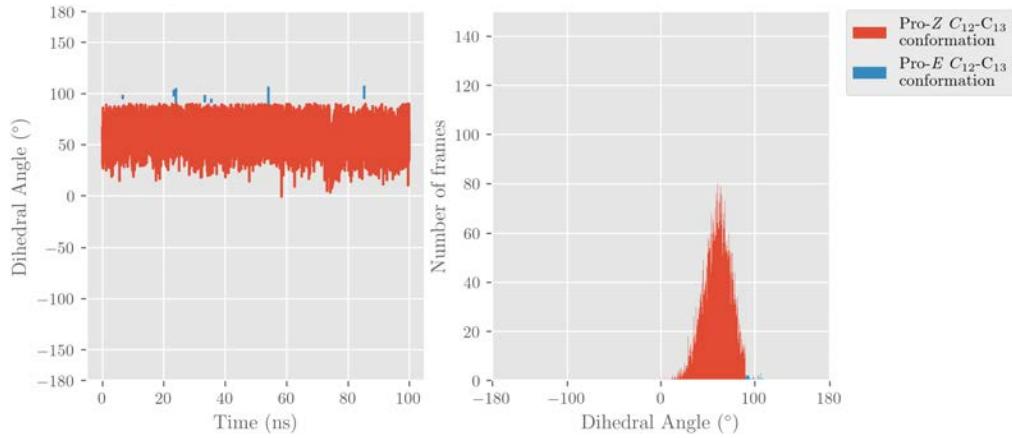

(b) Mutant 0 with set B of mutations in the bottom of the cavity

Figure 14.3: Dihedral angle of H_{12}-C_{12}-C_{13}-H_{13} along the MD simulation of the 13*S*,14*S*-eMaR1:LTA_4H's mutant 0 with mutations in the depth of the cavity. Frames where the C_{12}-C_{13} bond of 13*S*,14*S*-eMaR1 shows a pro-*Z* conformation are coloured in red, while the ones showing a pro-*E* conformation are coloured in blue.

14.3.3 Exploring alternative mutations for COO^-'s interaction

The mutations applied in the previous Sections had allowed the inversion of the binding orientation and the fitting of the substrate's tail. However, only one mutation for the binding with the substrate's head has been tested. The mutation at the entrance requires the introduction of a bulkier residue in comparison with the original residue. This mutation might block the entrance of the substrate, so it might prevent completely the reactivity of the enzyme. Two alternatives to the initially proposed mutation for the COO^-'s binding have been tested. Thus, three mutants have been generated also including the removal of the originally COO^--interacting residues and the mutation that allows a better fitting of the substrate's tail.

The structural and substrate's stability have been firstly analysed by means of RMSDs. The corresponding plots can be found in Figures SI14.6, SI14.8, and SI14.10 for the mutant 1, 2 and 3, respectively. All plots reveal that both the enzyme's backbone and the substrate are stable, although a small movement of the substrate is observed for mutants 2 and 3. Moreover, the relevant distances from the epoxide's O to Zn, Wat1 and Tyr381 have been analysed. The resulting plots can be found in Figures SI14.6, SI14.8 and SI14.10. The three mutants show a stable interaction with the epoxide ring, as the plots reveal.

The C_{12}-C_{13} conformation have also been analysed for each of these three mutants. The corresponding plots can be found in Figures 14.3a and 14.4.

The plots reveal that in the three cases the conformation is pro-*Z*, with values between 0 and 90°, during the most of the three MD simulations. This data confirms that the three mutants allow a substrate's binding with the proper conformation of the C_{12}-C_{13} bond, which will have a *Z*

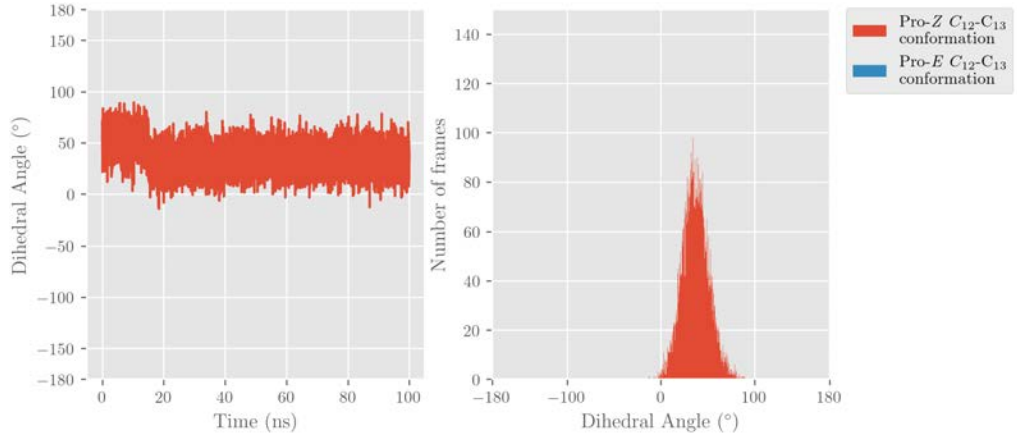

(a) Mutant 2

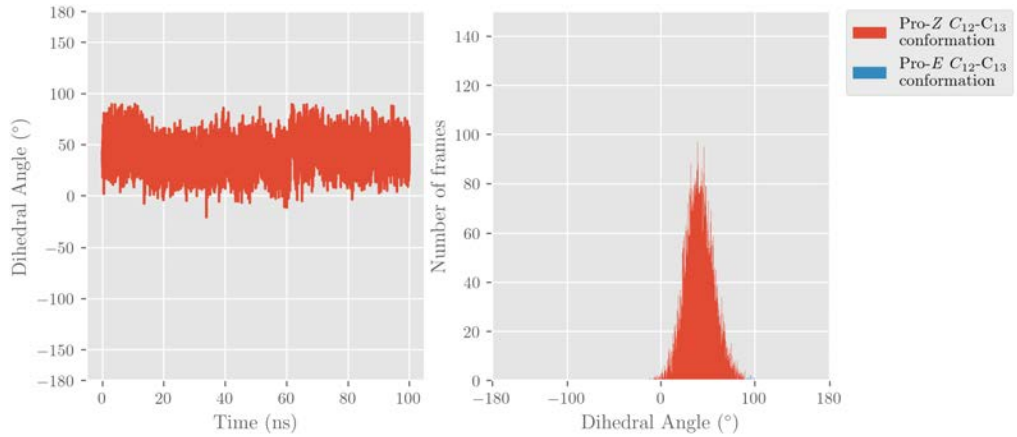

(b) Mutant 3

Figure 14.4: Dihedral angle of H_{12}-C_{12}-C_{13}-H_{13} along the MD simulation of the eMaR1:LTA_4H's mutants 2 and 3. Frames where the C_{12}-C_{13} of eMaR1 shows a pro-Z conformation are coloured in red, while the ones showing a pro-E conformation are coloured in blue.

conformation after the first step of the mechanism (Chapter 9).

There is another parameter that has not been yet analysed for any of the mutants. This is the distance from C_7 and Asp375 to a bridging water molecule –a water molecule close to C_7 and Asp375 at the same time–. The corresponding plots can be found in Figure 14.5.

The three plots are very similar. For all three mutants, more than the 85 % of the frames have a water molecule close enough to both C_7 and Asp375 to be added to C_7 as explained in Chapter 9.

14.4 Conclusions

LTA_4H has been mutated in order to allow the addition of a water molecule to 13*S*,14*S*-eMaR1 regiospecifically on C_7 to obtain MaR1. Three final mutants have been designed with five mutations in each of the mutants.

The stability and orientation of the substrate, the conformation of the C_{12}-C_{13} bond and the presence of bridging water molecules near Asp375 and C_7 have been analysed for the MD simulations calculated for each mutant. All the analysed geometrical features show that the applied mutations might be suitable for the obtention of MaR1.

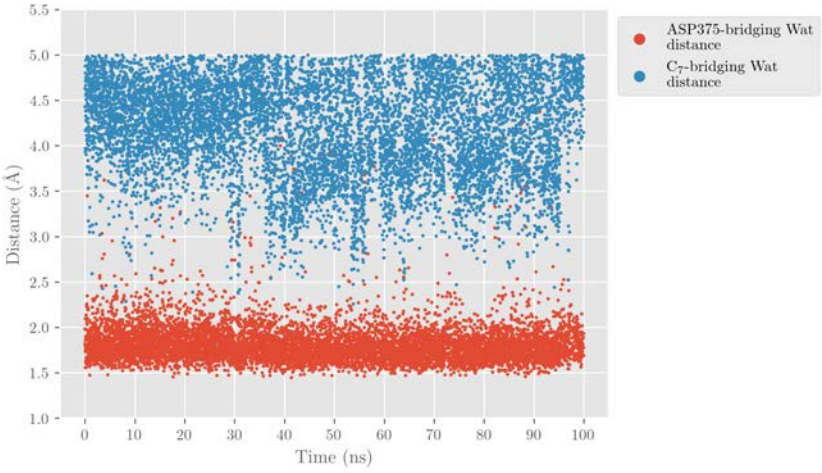

(a) Mutant 1, 86 % of frames have a bridging water molecule

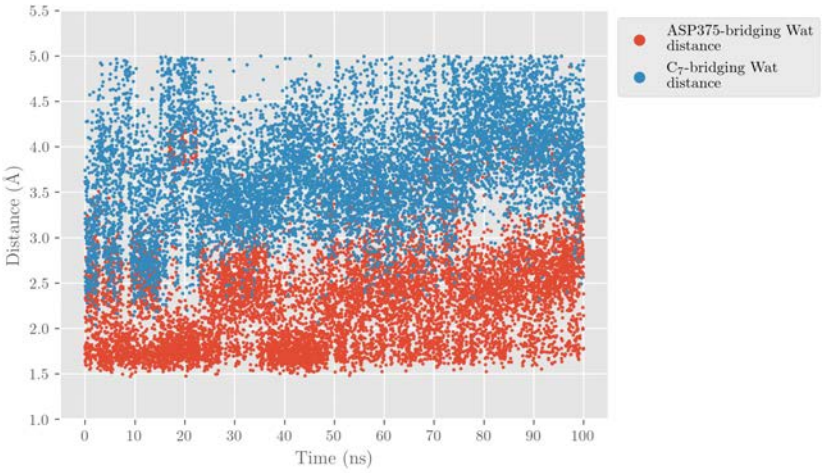

(b) Mutant 2, 99 % of frames have a bridging water molecule

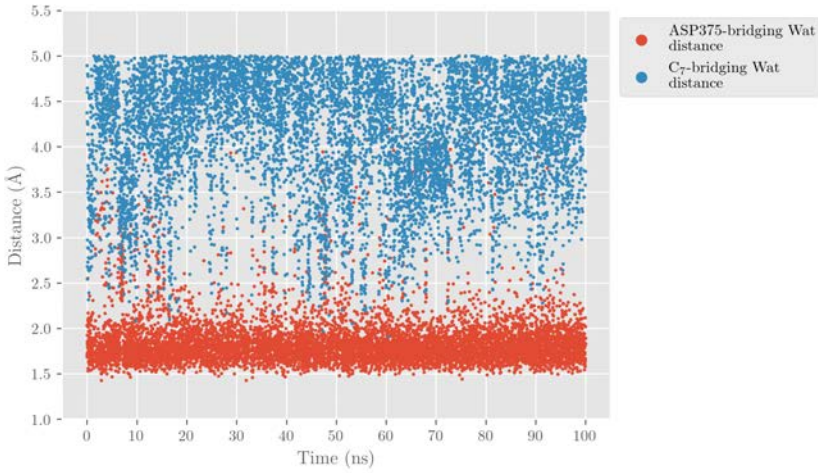

(c) Mutant 3, 88 % of frames have a bridging water molecule

Figure 14.5: Distance of closest water molecule bridging C_7 and Asp375 along the MD simulations of the 13S,14S-eMaR1:LTA_4H's mutants 1, 2 and 3. Only water molecules closer than 5 Å to C_7 and Asp375 have been considered.

Chapter 15

Experimental synthesis of MaR1 from DHA

The Supporting Information can be found in Chapter SI15.

15.1 Introduction

Along this Chapter, all experiments related to the experimental synthesis of MaR1 will be discussed. Expression and purification of the several enzymes reported in Part IV are described.

For these experiments, the protocols and techniques exposed in Chapter 5 have been used. Nonetheless, the conditions of each experiment will be detailed in each case.

15.2 Expression and purification of LTA_4H and its mutants

In Chapter 14.4, mutants of LTA_4H have been designed with the intention of performing the hydrolysis of 13*S*,14*S*-eMaR1 into MaR1. In this Section, the expression and purification of the WT and the designed mutants will be discussed.

15.2.1 Transformation of *E. coli*

DNA sequence that codifies for WT LTA_4H has been obtained from the UniProt database[134] with the accession code P09960-1[234]. The pET-16b vector has been chosen to host the codifying sequence. Mutations have been added into the WT sequence, so four sequences have been generated. The synthesis of these sequences has been requested to a manufacturer.

E. coli BL21 (DE3) strain has been selected as host and has been transformed following the protocol described in Section 5.2.2. After the transformations, cells have been plated. Plates have been incubated O/N and several colonies have been obtained for each of the LTA_4H variants. 4 isolated colonies of each transformant have been selected, grown in aqueous media and stored for further use.

15.2.2 Expression of LTA_4H

Expression conditions have been tested for the WT and mutant 1 of LTA_4H. A colony of each transformant has been chosen. Cultures of each transformant have been prepared following the protocol described in Section 5.2.3. Two different expression conditions have been tested: 1 mM of IPTG, 6 h and O/N incubation, 50 mL of culture, and 37 °C; and 0.25 mM of IPTG, 24 h of incubation, 200 mL of culture, and 20 °C. Several samples have been extracted at different times for the high IPTG concentration

conditions, while for the low ones only control and 24 h samples have been collected. All samples have been analysed with SDS-PAGE. The resulting gels are shown in Figures 15.1 and 15.2. The conditions of each experiment are detailed in each of the images.

If both SDS-PAGE gels (Figures 15.1 and 15.2) are compared, it can be seen that the low IPTG concentration conditions (24 h of incubation time, 0.25 mM of IPTG, 20 °C) are the best conditions for the expression of WT LTA_4H and its mutant 1 since the bands on the SDS-PAGE gel are more intense. Thus, these conditions have been applied to the expression of mutant 2 and 3 of LTA_4H. A Comassie-stained SDS-PAGE comparing the soluble and insoluble samples of the expression of WT LTA_4H and its mutant 1, 2 and 3 at low IPTG conditions can be found in Figure SI15.1.

15.2.3 Purification of LTA_4H variants

Expressed WT and LTA_4H's mutants have been purified using the FPLC purification method (Section 5.2.4.1) using the hexa-His tag expressed together with the protein. SDS-PAGE gels have been stained with Comassie solution containing the samples from the purification fractions. The obtained gels can be found in Figures 15.3, SI15.2, SI15.3 and SI15.4. For some of the gels, sample after dialysis has been added.

Figure 15.3 shows the results of the purification of WT LTA_4H. As it can be observed, the purified sample contains mainly the target enzyme along with small quantities of other enzymes. Figure 15.3a shows the SDS-PAGE gel of the different samples collected along the FPLC purification. Moreover, Figure 15.3b shows the FPLC chromatogram. In this plot, the abscissa axis represents the volume of elutant solution added. The ordinate axis on the left represents the UV absorbance at 280 nm –which is proportional to the concentration of protein by the Lambert-Beer's law–, while the ordinate axes on the right represents the percent-

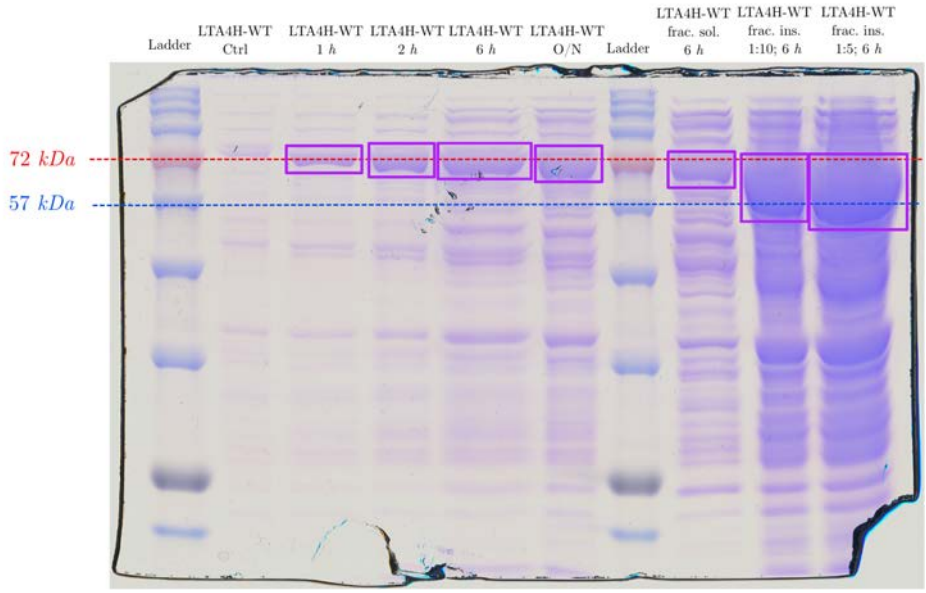

(a) WT LTA_4H

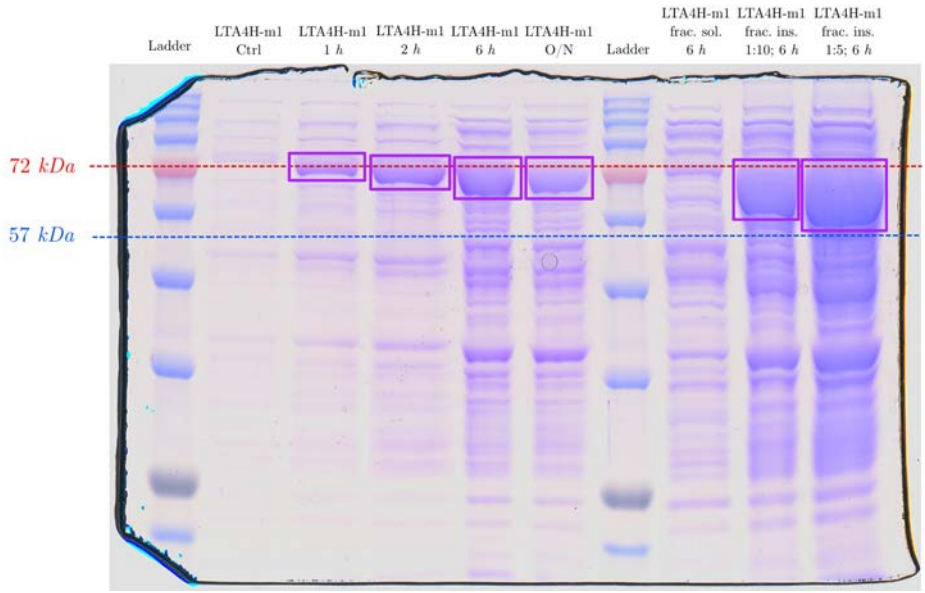

(b) Mutant 1 of LTA_4H

Figure 15.1: Comassie-stained SDS-PAGE gel of expression of WT and mutant 1 of LTA_4H at high IPTG concentration conditions. Overnight incubation, 1 mM of IPTG, 37 °C. 72 kDa and 57 kDa weight marks are indicated with red and blue dashed lines, respectively. Bands corresponding to LTA_4H's are indicated with a purple square. "Ctrl" labels refer to samples taken before the addition of IPTG. "frac. sol." is the soluble fraction, whilst "frac. ins." is the insoluble fraction.

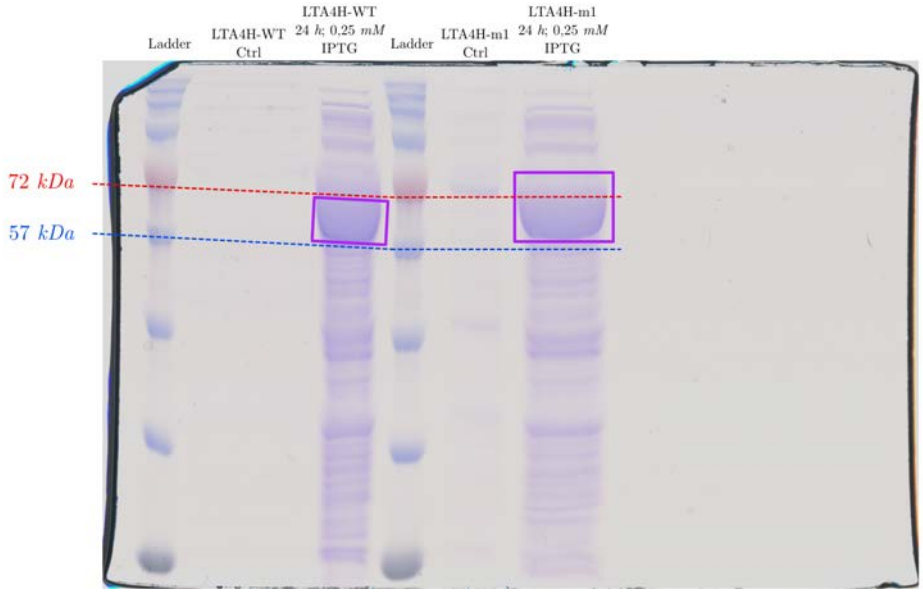

Figure 15.2: Comassie-stained SDS-PAGE gel of supernatant samples of expression of WT and mutant 1 of LTA$_4$H at low IPTG concentration conditions. 24 h of incubation time, 0.25 mM of IPTG, 20 °C. 72 kDa and 57 kDa weight marks are indicated with red and blue dashed lines, respectively. Bands corresponding to LTA$_4$H's are indicated with a purple square.

age of the elutant containing 1 M of imidazole solution in respect with the total composition of elutant volume. In this purification technique, the protein that does not contain a His tag should elute at the beginning of the purification, while His-tag-containing proteins –the target protein– elute when the concentration of imidazole is high due to imidazole's better Ni^{2+}-chelating properties. In the present case, the target protein elutes at a imidazole's concentration of 1 M and it elutes completely in only 3 mL of elutant (from 28 mL to 30 mL). As said before, the elution fractions

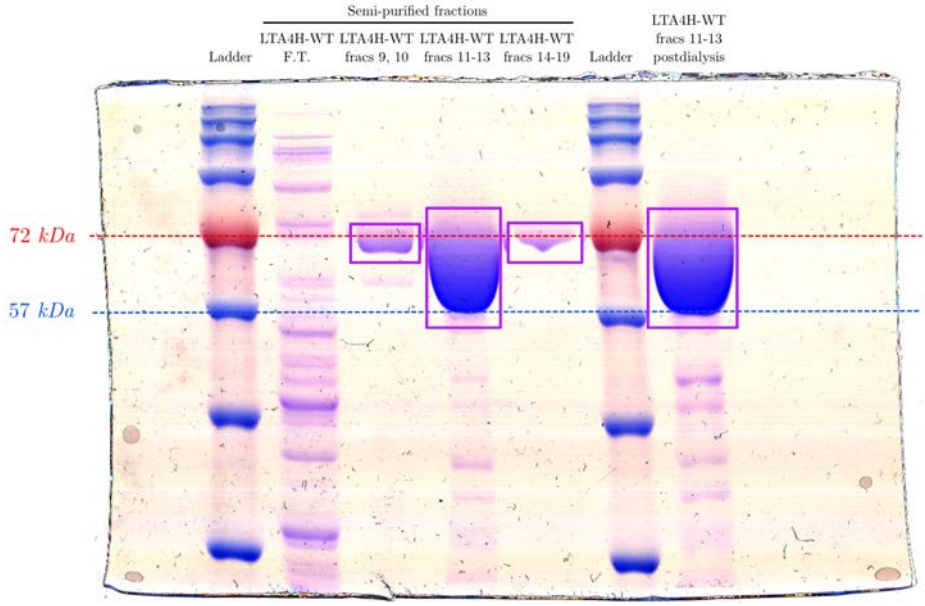

(a) Comassie-stained SDS-PAGE

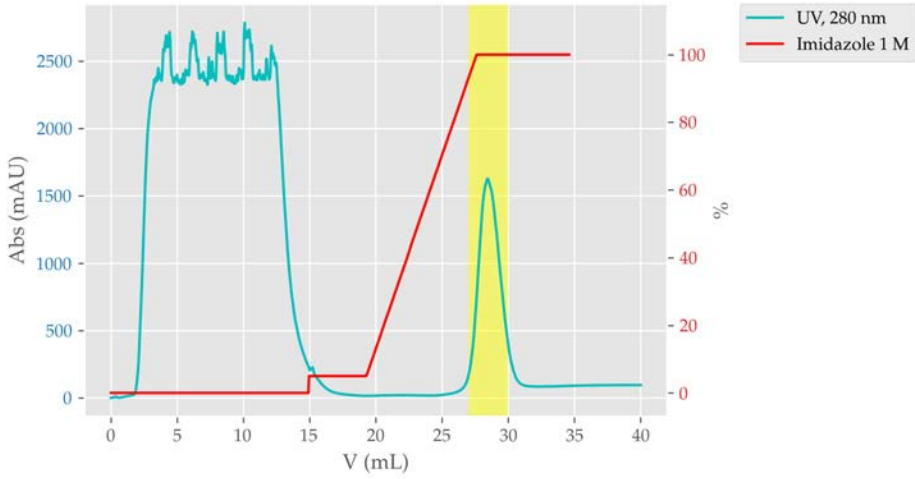

(b) UV measure and imidazole concentration along the FPLC purification

Figure 15.3: FPLC purification of WT LTA_4H. For (a), 72 kDa and 57 kDa weight marks are indicated with red and blue dashed lines, respectively. Bands corresponding to LTA_4H's are indicated with a purple box. For (b), yellow region indicates the elution volume where the purified protein is detected.

that contain the purified protein are dialysed in order to remove the imidazole from the solution. This process has been carried out for the WT and mutants of LTA_4H, although a sample after dialysis is not present in mutants 1 and 2's gels (Figures SI15.2 and SI15.3). The protein concentration of each purified LTA_4H's variant can be found in Table 15.1. As the Table shows, the WT variant is the one expressed with the highest concentration. Among the mutants, the one expressed with the highest concentration is the mutant 1.

Table 15.1: Concentration of purified protein for each LTA_4H variant.

LTA_4H variant	Concentration ($mg\,mL^{-1}$)
WT	3.46
Mutant 1	2.80
Mutant 2	1.46
Mutant 3	0.36

15.3 Expression and purification of humALOX12

As shown in the previous section, the expression and purification of the several LTA_4H mutants have been carried out successfully. However, in order to test their activity for the conversion of 13*S*,14*S*-eMaR1 into MaR1 the 13*S*,14*S*-eMaR1 intermediate has to be prepared. Although it has been synthesised before by Dalli et al.[67], no details are provided in the publication. Hence, its organic synthesis cannot be replicated in a straightforward manner. Also, this synthesis scapes the goal of this Thesis. Alternatively, and following the computational studies performed in this Thesis (Chapter 12 and 13), it is proposed to adapt the biosynthesis of MaR1 to the lab. The biosynthetic pathway requires the use of *hum*ALOX12 for the conversion of DHA into 14*S*-HpDHA and then into 13*S*,14*S*-eMaR1. Then, the

three designed mutants of LTA_4H can be tested for the final hydrolysis into MaR1.

In order to test the proposed pathway, *hum*ALOX12 will be expressed using *E. coli* as host. Nonetheless, no bacterial expression protocol using this system has been reported, although it has been achieved using a baculovirus-insect cell system[63;218]. Thus, a new protocol for *hum*ALOX12's expression has to be designed and tested. Moreover, the expressed cells will need to be purified in order to remove all the cellular machineries and chemicals which can react with the reaction intermediates (14*S*-HpDHA and 13*S*,14*S*-eMaR1).

15.3.1 Transformation of *E. coli* cells

The BL21(DE3) strain of *E. coli* has been used again as the host cell. The plasmid was already available in Biochemize's facilities. It corresponds to the *hum*ALOX12 embedded in the pET-16b vector, which includes a His tag. Nonetheless, no detailed information of the sequence is available. The transformation has been carried out following the protocol described in Section 5.2.2.

After the transformation and O/N culture in antibiotic-containing agar-LB plates, four isolated colonies have been extracted from the plate. All four of them have been let grow O/N and have been kept at $-80\,^{\circ}C$ after the collection of a sample per colony. The samples have been treated to extract the DNA. The plasmid concentration has been measured for each sample and it can be found in Table 15.2. As the Table shows, the plasmid concentration is similar in all the colonies, thus indicating that the transformation is consistent.

As commented in previous lines, no details of the used sequence were available. In order to check that the sequence actually corresponds to the *hum*ALOX12, the obtained DHA sample from colony number four

Table 15.2: Plasmid concentrations of each of the BL21 (DE3)/pET-16b-humALOX12 transformant colonies.

Colony	Concentration $\left(\frac{ng}{\mu L}\right)$
C1	79,8
C2	95,8
C3	84,6
C4	94,8
Average	88,75

has been sequenced starting from the T7 promoter of the pET-16b vector. Current DNA sequencing techniques only allow to analyse the first around 1100 pair bases with a good-enough resolution, so only the T7 promoter region and the first 238 of the protein's sequence will be obtained from the analysis. The obtained nucleic sequence can be found in Figure SI15.4, the translated-to-amino acid sequence can be found in Figure SI15.5, and the comparison between the obtained sequence and the reported sequence in UniProt[134] under the P18054 ID[77] can be found in Figure 15.4.

As Figure 15.4 shows, the first 234 residues are the same in the analysed sample than in the UniProt's P18054 sequence. The residues 235 to 237 are not the same but this is not remarkable since current DNA sequencing techniques lose resolution at the last residues. Thus, it can be concluded that the codifying sequence with which *E. coli* cells have been transformed corresponds to the *hum*ALOX12's sequence.

15.3.2 Expression of humALOX12

Once it has been confirmed that the cells are transformed and that the used plasmid codifies to *hum*ALOX12, protein expression can be carried out. In order to do so, three different protocols will be followed to stablish which one is the best for *hum*ALOX12's expression. Thus, expression with IPTG

```
C4       MGRYRIRVATGAWLFSGSYNRVQLWLVGTRGEAELELQLRPARGE    45
P18054   MGRYRIRVATGAWLFSGSYNRVQLWLVGTRGEAELELQLRPARGE    45

C4       EEEFDHDVAEDLGLLQFVRLRKHHWLVDDAWFCDRITVQGPGACA    90
P18054   EEEFDHDVAEDLGLLQFVRLRKHHWLVDDAWFCDRITVQGPGACA    90

C4       EVAFPCYRWVQGEDILSLPEGTARLPGDNALDMFQKHREKELKDR   135
P18054   EVAFPCYRWVQGEDILSLPEGTARLPGDNALDMFQKHREKELKDR   135

C4       QQIYCWATWKEGLPLTIAADRKDDLPPNMRFHEEKRLDFEWTLKA   180
P18054   QQIYCWATWKEGLPLTIAADRKDDLPPNMRFHEEKRLDFEWTLKA   180

C4       GALEMALKRVYTLLSSWNCLEDFDQIFWGQKSALAEKVRQCWQDD   225
P18054   GALEMALKRVYTLLSSWNCLEDFDQIFWGQKSALAEKVRQCWQDD   225

C4       ELFSYQFLNGANP    238
P18054   ELFSYQFLNRCEP    238
```

Figure 15.4: Comparison of the colony 4 (C4)**'s sequence and the UniProt's P18054 sequence** (P18054)**.**

at high and low concentrations (protocol described in Section 5.2.3.1) and autoinduction (protocol described in Section 5.2.3.2) are tested.

The three protocols are applied simultaneously, so three different sets of samples are obtained. The tested experimental conditions are the following: 1 mM of IPTG, 37 °C, for 6 h and O/N; 0.25 mM of IPTG, 20 °C for 24 h; and autoinduction with lactose instead of IPTG at 20 °C for 48 h. The corresponding Comassie-stained SDS-PAGE gel is shown in Figure 15.5.

Figure 15.5 shows that no overexpression of *hum*ALOX12 at around 75 kDa is found for any of the tested conditions. Nevertheless, all samples

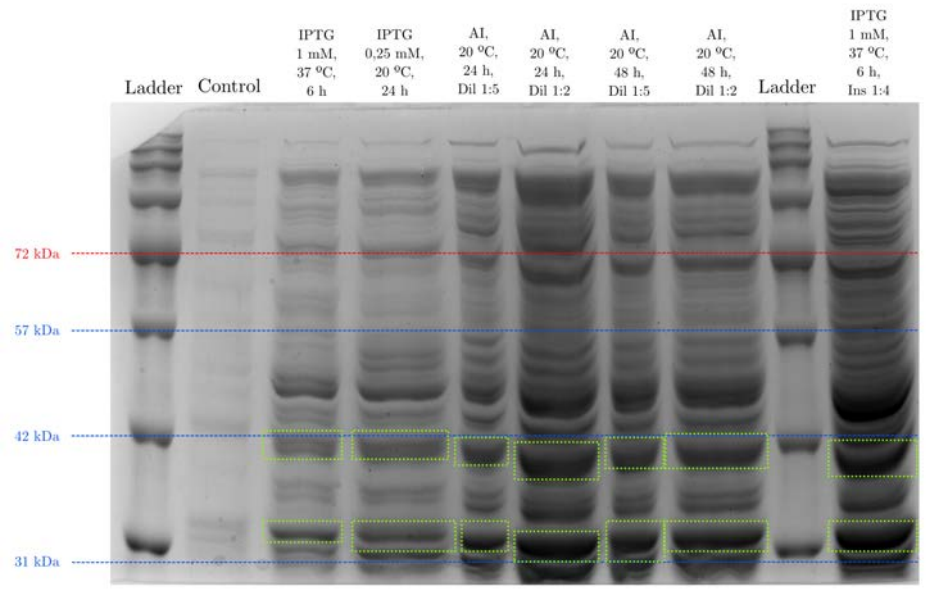

Figure 15.5: Comassie-stained SDS-PAGE gel of humALOX12 expression with different experimental conditions. Extraction time and experimental conditions for each sample are indicated in the header of each lane. Green boxes indicate overexpression bands. Red and blue, dashed lines indicate molecular weight marks. AI stands for "auto induction".

contain high-concentration bands at around 42 kDa and 31 kDa. If the molecular masses of these two bands are summed up, a molecular mass of around 72 kDa, which approximately corresponds to *hum*ALOX12 fragmented in two pieces. In order to confirm this hypothesis, WB staining has been applied to the same SDS-PAGE, so if any of the detected fragments correspond to *hum*ALOX12, it has to be detected. The corresponding SDS-PAGE gel stained with WB with His-tag antibodies can be found in Figure 15.6.

Figure 15.6 confirms that there is no band associated with *hum*ALOX12

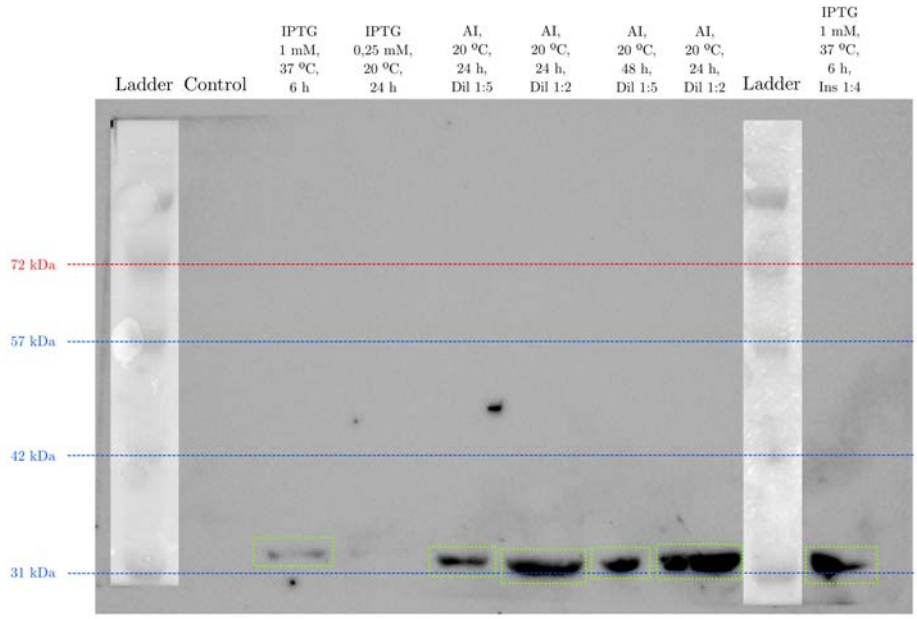

Figure 15.6: WB-stained SDS-PAGE gel of humALOX12 expression with different experimental conditions. Extraction time and experimental conditions for each sample are indicated in the header of each lane. Green boxes indicate overexpression bands. Red and blue, dashed lines indicate molecular weight marks.

at 75 kDa of molecular mass. Furthermore, it also confirms that the band detected at 31 kDa corresponds to a fragment of *hum*ALOX12. Hence, the band at 42 kDa is associated to the remaining fragment of *hum*ALOX12.

Nonetheless, these tests have revealed that the best expression conditions are the autoinduction (Section 5.2.3.2), as the more intense bands indicate (Figure 15.6).

The *hum*ALOX12's fragmentation can be caused by various factors such as the presence of a proteases –a family of enzymes able to recognise and cleave certain amino acid sequences–, or the lack of cellular machinery

that assists the protein folding, for example. In order to discard that proteases are the cause behind the fragmentation, a protease inhibitor cocktail has been added to the cellular suspension before sonication. SDS-PAGE gels have been repeated but the same results have been obtained (data not shown). Thus, the *hum*ALOX12's degradation cannot be attributed to the action of proteases.

15.3.3 Using previously transformed *E. coli* strains

A first transformation of *E. coli* with the same *hum*ALOX12 plasmid used in Section 15.3.1 was performed in Biochemize's laboratory before starting this Thesis. Nonetheless, the applied transformation protocol is not available, reason why the transformation has been redone following a standard protocol (Section 15.3.1). Expression results using this transformed strain report that *hum*ALOX12 is expressed without fragmentation (Figures 15.7 and 15.8).

The autoinduction expression protocol has been applied to this previously transformed strain since it has been demonstrated to be the best protocol (Section 15.3.2). The corresponding Comassie-stained and WB-stained SDS-PAGE gels are available in Figures 15.7 and 15.8, respectively. In this gels, samples from the expression of the previously transformed transformant (Section 15.3.2) have also been included for the sake of comparison. From know on, samples transformed and expressed during this Thesis will be referenced as "UAB", whilst samples from transformation carried out previous to the starting of this Thesis will be referenced as "BCZ".

As Figures 15.7 and 15.8 show, the "BCZ" transformants are capable of expressing the protein with a molecular weight of around 72 kDa, which approximately corresponds to the molecular weight of the complete *hum*ALOX12 (75 kDa). A Comassie-stained gel of the expression of the

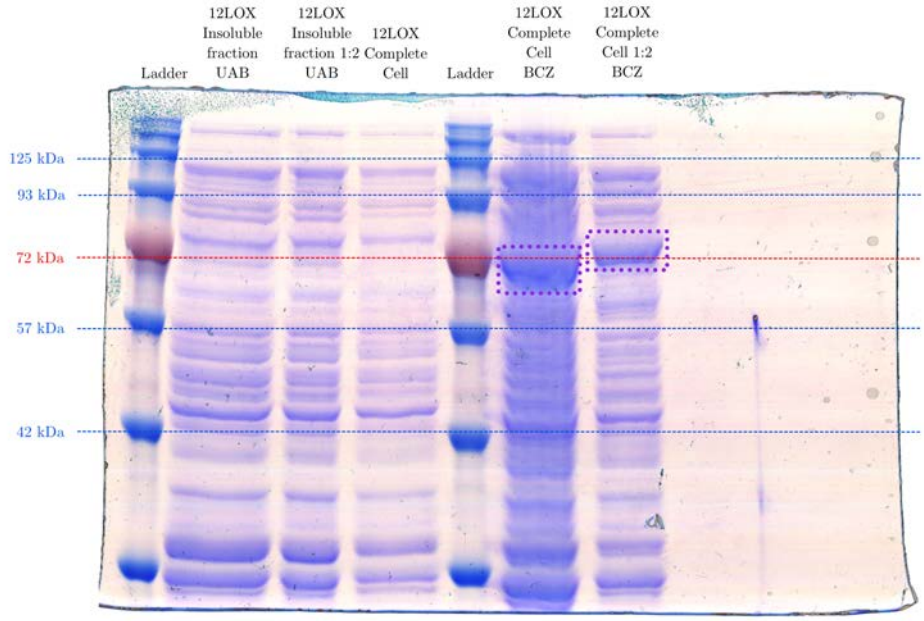

Figure 15.7: Comassie-stained SDS-PAGE gels of autoinduction expression of "UAB" and "BCZ" transformants. Bands that correspond to humALOX12 are boxed in purple. Red and blue, dashed lines indicate molecular weight marks.

"BCZ" transformants can be found in Figure 15.9.

Figure 15.9 reveals that great quantities of expressed protein are detected from the first 24 h of incubation time, although soluble and insoluble samples reveal that most of the expressed protein ends up in the insoluble fraction, so it cannot be used. Nonetheless, small amounts of soluble protein have been obtained, so purification can be performed.

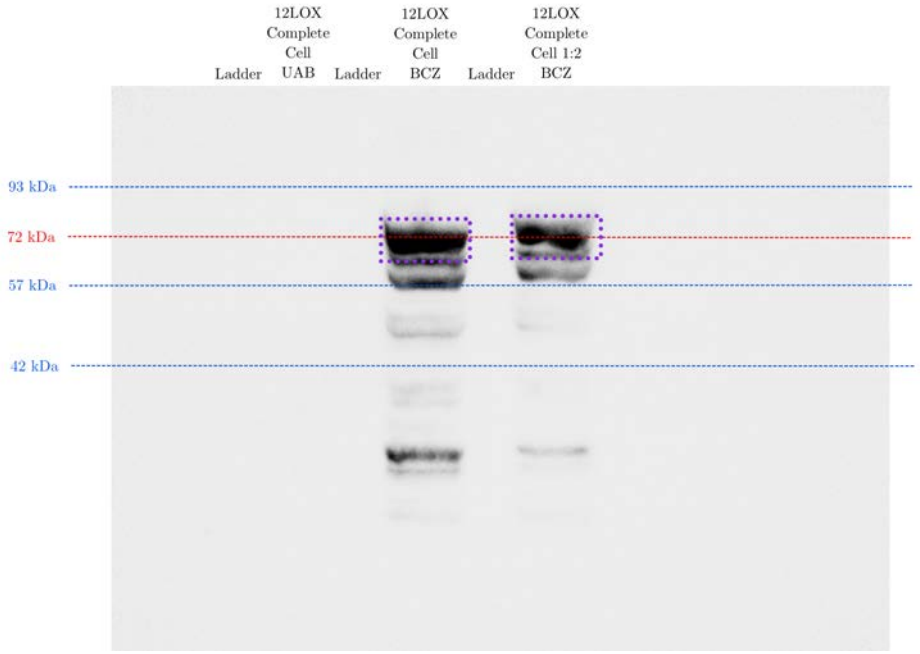

Figure 15.8: His-tag WB-stained SDS-PAGE gels of autoinduction expression of "UAB" and "BCZ" transformants. Bands that correspond to humALOX12 are boxed in purple. Red and blue, dashed lines indicate molecular weight marks.

15.3.4 Purification of humALOX12

As said before, small amounts of soluble, not fragmented *hum*ALOX12 have been obtained using the "BCZ" *E. coli* strain. In order to be useful for incubation with DHA, *hum*ALOX12 has to be purified so reaction intermediates of the DHA to MaR1 conversion are not degraded by cellular chemicals. As for LTA_4H and its mutants (Section 15.2.3), the purification has been carried out with FPLC. The FPLC chromatogram and the related Comassie-stained gel can be found in Figure 15.10 and SI15.6.

FPLC chromatogram (Figure 15.10) reveals that no protein has been

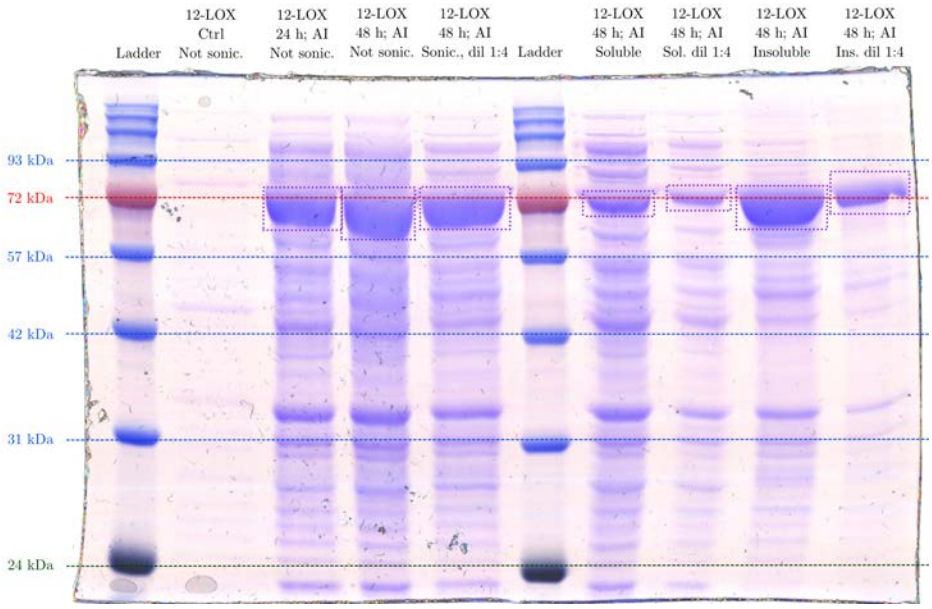

Figure 15.9: Comassie-stained SDS-PAGE gel of "BCZ" expression. Bands that correspond to humALOX12 are boxed in purple. "Sonic" refers to the sonication of the cells, "sol" corresponds to the soluble fraction, and "ins" corresponds to the insoluble sample. Red and blue, dashed lines indicate molecular weight marks.

purified. High values of UV absorbance can only be found in volumes from 4 mL to 12 mL, which correspond to the flow-through –the fraction that contains all proteins that do not interact with the purification column–. Once the imidazole concentration increases (from 17 mL), all protein chelated with the column's Ni atoms should be freed, so carried with the mobile phase. However, no His-tag-containing protein, Ni-interacting is detected. SDS-PAGE gel confirms this observation (Figure SI15.6). As it can be seen, protein at around 75 kDa (the molecular mass of *hum*ALOX12) is only detected in the pre-purification and flow-through

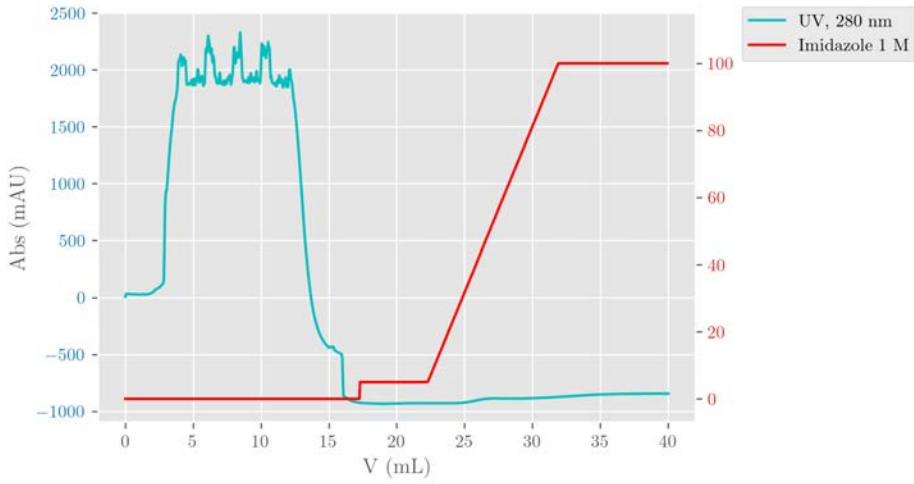

Figure 15.10: FPLC purification chromatogram of humALOX12 expression from "BCZ" transformants. Blue line corresponds to the UV measure along the purification, while red line corresponds to the percentage of 1 M imidazole solution added to the mobile phase.

samples, as well as in the insoluble ones, which have been added as reference.

Hence, it can be concluded that although the molecular mass of the expressed protein corresponds to the *hum*ALOX12's one, there is some kind of unidentified expression problem. The DNA sequencing of the plasmid confirmed the presence of a His tag, so if the protein was complete, purification should have been successful. Consequently, the prepared *hum*ALOX12 cannot be used for the biocatalytic synthesis of MaR1.

15.3.5 Other tested systems

In order to solve all these expression problems, lots of different tests have been carried out besides the addition of inhibitors of proteases, as mentioned in Section 15.3.2.

On the one hand, the *hum*ALOX12's plasmid has been resynthesised and transformation and expression has been tested again with new transformants. Rosetta and Rosetta 2 pLysS *E. coli* strains have been tested. Moreover, a plasmid based on a vector that contains a fusion protein (pET-32) has also been tested. Nonetheless, none of the tested expression systems have led to the expression of complete, purificable *hum*ALOX12 (data not shown).

15.4 Conclusions and future work

Along this Chapter LTA_4H and its three designed mutants have been prepared using bacterial systems and purified successfully. On the contrary, *hum*ALOX12 has been also expressed using bacterial systems but the purification has not been successful, hence it has not been used due to the incompatibility between the cellular chemicals and the highly unstable MaR1 reaction intermediates.

Beyond this Thesis, experimental groups that collaborate with our Theoretical Group are currently trying to develop new methods to express a purified *hum*ALOX12. In the moment this goal is accomplished, the suitability of our theoretical design of the hydrolase to produce MaR1 will be assessed.

Part V

Conclusions

Chapter 16

General conclusions

Along this Thesis, a wide variety of Lipoxygenases and LOX-related enzymes have been studied from the computational and experimental points of view. The computational work has been carried out applying different computational techniques that allow the study of different aspects of the systems. The applied techniques are molecular docking, Molecular Dynamics (MD) and Quantum Mechanics/Molecular Mechanics (QM/MM). On the other hand, the experimental works have been focused on protein expression using bacterial systems, protein purification and substrate incubation with the expressed enzymes. Moreover, HPLC and HPLC-MS/MS analytical techniques have been applied for the detection of the incubation products in order to establish the enzymatic activity and products' profile.

Among the variety of studied LOXs and related enzymes, human ALOX5 (*hum*ALOX5), human ALOX12 (*hum*ALOX12), pig ALOX15 (*pig*ALOX15),

human ALOX15B (*hum*ALOX15B), mouse Alox15b (*mou*Alox15b), Five-Lipoxigenase-Activating Protein (FLAP) and Leukotriene A_4 Hydrolase (LTA_4H) have been studied. Mutations have been applied to *hum*ALOX5, *hum*ALOX15B and *mou*Alox15b to modify the enzymatic regioselectivity and products' profile. For *hum*ALOX12, *pig*ALOX15 and LTA_4H, the enzymatic mechanism at the molecular level has been unravelled for the DHA substrate for LOXs and for the LTA_4 for the hydrolase. For FLAP, the AA binding role has been studied in a membrane system.

At the end of each Chapter, the conclusions of the corresponding investigation are given. Here, the general conclusions of all investigations are summarised below.

- LOXs are highly regio- and stereoselective enzymes that catalyse the hydroperoxidation of PUFAs. In this case, the regioselectivity is controlled by the cavity shape, philicity character of its bottom, and the steric hindrance of cavity enclosing residues. The stereoselective control is mainly driven by the oxygen diffusion tunnels location in combination with the substrate's conformation.

- LOXs are also capable of reacting on hydro(pero)xy-PUFAs substrates through two distinct reactivities: a second hydroperoxidation or an epoxidation.

- LOXs control the regioselectivity in two different ways: the relative conformation of the substrate –tail- or head-first– and the depth of the cavity. As it has been demonstrated, this control can be modulated changing the residues at the depth of the cavity. Thus, the presence or absence of a hydrogen-bond-capable residue in the bottom of the cavity modulates the substrate's conformation. Moreover, the bulkier the residues in the bottom are, the smaller is the cavity.

  More specifically:

  - *hum*ALOX5, *hum*ALOX15B and *mou*Alox15b's regioselectivities can be modulated by the mutation of residues in the bottom of the binding cavity. In particular, *hum*ALOX5 can be converted into a 15-lipoxygenating LOX applying the Phe359Trp, Ala424Ile, Asn425Met, and Ala603Ile mutations.
  - *hum*ALOX15B and *mou*Alox15b are two LOXs that are codified from the same gene but have different regioselectivities. Their regioselectivities can be exchanged by the application of the Asp602Tyr and Val603His mutations on *hum*ALOX15B for its murinisation, and Tyr603Asp and His604Val mutations on *mou*Alox15b for its humanisation.

- LTA_4H is also a highly regio- and stereoselective enzyme that catalyses the hydrolysis of LTA_4. In this case, the regioselective control is driven by the position of the water-binding residue (Asp375), while the stereoselective control is assisted by the enclosing Phe378 residue, which establishes a π-π stacking interaction in such a way that the *Z* path has a global lower potential energy path in comparison with the *E* path. Moreover, this stereoselective control involves the control of the water addition, which takes place seven methylene units away from the nascent double bond.

- FLAP has been demonstrated to be capable of attracting spread AA molecules along the membrane. Moreover, it has been demonstrated that the inter monomer region is the final destination of the FLAP-interacting AA molecules by the study of the migration process of AA511 from FLAP's surface to the inter-monomer domain.

Moreover, specific conclusions regarding the biocatalytic synthesis of MaR1 have also been obtained:

- *pig*ALOX15 has been demonstrated not to be suitable for the biocatalytic synthesis of MaR1 because of the wrong conformation of the Δ^{10} double bond of the 14*S*-HpDHA intermediate. However, it has been demonstrated that *hum*ALOX12 converts successfully DHA into 14*S*-HpDHA with the proper conformation of all the double bonds.

- The knowledge acquired from the mechanistic study of LTA_4H with LTA_4 as substrate has helped to design LTA_4H mutants that can hydrolyse the 13*S*,14*S*-eMaR1 intermediate specifically into MaR1.

- The experimental expression and purification of the WT LTA_4H and the different mutants designed in this Thesis to produce MaR1 from 13*S*,14*S*-eMaR1 has been successfully achieved, although they have not been experimentally tested for the 13*S*,14*S*-eMaR1 conversion into MaR1 because the 13*S*,14*S*-eMaR1 intermediate has not been obtained in spite of the many tried attempts.

- The experimental expression of *hum*ALOX12 has been achieved, although its purification has not, which is key for 14*S*-HpDHA and 13*S*,14*S*-eMaR1 intermediates synthesis. Hence, the intermediate 13*S*,14*S*-eMaR1 has not been prepared and the capacity of LTA_4H mutants designed in this Thesis for 13*S*,14*S*-eMaR1 generation could not been tested.

In summary, LOXs are a small family of very similar enzymes involved in inflammatory processes with a very specific reactivity, both in terms of substrate specificity and in terms of regio- and stereoselectivities. This two features change among the family components. Nonetheless, their selectivities can be modulated, so the regio- and stereospecificities of a specific LOX can be achieved by the modification of the cavity's depth of another

LOX. Because of this, the different isoforms of each LOX might show punctual mutations that change its behaviour depending on the mammalian species.

Moreover, the synthesis of MaR1 from DHA has been achieved computationally. Thus, the steps required for its synthesis are well established but they have not been experimentally tested due to expression and purification problems of *hum*ALOX12. Nonetheless, the lack of knowledge of the enzyme responsible of 13*S*,14*S*-eMaR1 conversion into MaR1 has been bypassed with the design of mutants of LTA_4H, an enzyme with the same reactivity but on LTA_4. The designed mutants have been successfully expressed and purified but have not been tested. Thus, additional experimental work is needed in order to assess the suitability of the proposed biocatalytic synthesis of MaR1.

As a final remark, this Thesis demonstrates that enzymes are not only capable of accelerating reactions, but they are also useful for driving the chemical reaction to obtain regio- and stereoselective products in a highly controlled way. This behaviour is very important in complex biological processes such as inflammations, since the role of different isomer, for instance, can be completely opposite. In this sense, highly selective enzymes like LTA_4H are key.

Bibliography

[1] V. Gold, editor. *The IUPAC Compendium of Chemical Terminology: The Gold Book*. International Union of Pure and Applied Chemistry (IUPAC), Research Triangle Park, NC, 4 edition, 2019. doi: 10.1351/goldbook. URL https://goldbook.iupac.org/.

[2] 28: Biosignaling - Capstone Volume I, December 2018. URL https://bio.libretexts.org/Bookshelves/Biochemistry/Fundamentals_of_Biochemistry_(Jakubowski_and_Flatt)/Unit_IV_-_Special_Topics/28%3A_Biosignaling_-_Capstone_Volume_I.

[3] I. Schomburg, A. Chang, S. Placzek, C. Söhngen, M. Rother, M. Lang, C. Munaretto, S. Ulas, M. Stelzer, A. Grote, M. Scheer, and D. Schomburg. BRENDA in 2013: integrated reactions, kinetic data, enzyme function data, improved disease classification: new options and contents in BRENDA. *Nucleic Acids Research*, 41(D1):D764–D772, November 2012. ISSN 0305-1048, 1362-4962. doi: 10.1093/nar/gks1049. URL http://academic.oup.com/nar/article/41/D1/D764/1052948/BRENDA-in-2013-integrated-reactions-kinetic-data.

[4] N. C. of the International Union of Biochemistry and Molecu-

lar Biology (NC-IUBMB). Enzyme Nomenclature. URL https://iubmb.qmul.ac.uk/enzyme/.

[5] R. Medzhitov. Origin and physiological roles of inflammation. *Nature*, 454(7203):428–435, July 2008. ISSN 0028-0836, 1476-4687. doi: 10.1038/nature07201. URL https://www.nature.com/articles/nature07201.

[6] L. Sompayrac. *How the immune system works*. Wiley Blackwell, Hoboken, NJ, sixth edition edition, 2019. ISBN 978-1-119-54219-3 978-1-119-54220-9.

[7] G. Bannenberg and C. N. Serhan. Specialized pro-resolving lipid mediators in the inflammatory response: An update. *Biochimica et Biophysica Acta (BBA) - Molecular and Cell Biology of Lipids*, 1801(12):1260–1273, December 2010. ISSN 13881981. doi: 10.1016/j.bbalip.2010.08.002. URL https://linkinghub.elsevier.com/retrieve/pii/S1388198110001800.

[8] D. Crean and C. Godson. Specialised lipid mediators and their targets. *Seminars in Immunology*, 27(3):169–176, May 2015. ISSN 10445323. doi: 10.1016/j.smim.2015.05.002. URL https://linkinghub.elsevier.com/retrieve/pii/S1044532315000469.

[9] C. Yunna, H. Mengru, W. Lei, and C. Weidong. Macrophage M1/M2 polarization. *European Journal of Pharmacology*, 877:173090, June 2020. ISSN 00142999. doi: 10.1016/j.ejphar.2020.173090. URL https://linkinghub.elsevier.com/retrieve/pii/S0014299920301825.

[10] S. A. Amici, J. Dong, and M. Guerau-de Arellano. Molecular Mechanisms Modulating the Phenotype of Macrophages and Microglia. *Frontiers in Immunology*, 8:1520, November 2017. ISSN

1664-3224. doi: 10.3389/fimmu.2017.01520. URL http://journal.frontiersin.org/article/10.3389/fimmu.2017.01520/full.

[11] T. A. Wynn, A. Chawla, and J. W. Pollard. Macrophage biology in development, homeostasis and disease. *Nature*, 496(7446):445–455, April 2013. ISSN 0028-0836, 1476-4687. doi: 10.1038/nature12034. URL http://www.nature.com/articles/nature12034.

[12] C. N. Serhan, N. Chiang, J. Dalli, and B. D. Levy. Lipid Mediators in the Resolution of Inflammation. *Cold Spring Harbor Perspectives in Biology*, 7(2):a016311, February 2015. ISSN 1943-0264. doi: 10.1101/cshperspect.a016311. URL http://cshperspectives.cshlp.org/lookup/doi/10.1101/cshperspect.a016311.

[13] D. Steinhilber, editor. *Lipoxygenases in inflammation*. Springer Berlin Heidelberg, New York, NY, 2016. ISBN 978-3-319-27764-6.

[14] O. Werz, J. Gerstmeier, S. Libreros, X. De La Rosa, M. Werner, P. C. Norris, N. Chiang, and C. N. Serhan. Human macrophages differentially produce specific resolvin or leukotriene signals that depend on bacterial pathogenicity. *Nature Communications*, 9(1):59, January 2018. ISSN 2041-1723. doi: 10.1038/s41467-017-02538-5. URL https://www.nature.com/articles/s41467-017-02538-5.

[15] Y. Yao, X.-H. Xu, and L. Jin. Macrophage Polarization in Physiological and Pathological Pregnancy. *Frontiers in Immunology*, 10:792, April 2019. ISSN 1664-3224. doi: 10.3389/fimmu.2019.00792. URL https://www.frontiersin.org/article/10.3389/fimmu.2019.00792/full.

[16] D. Furman, J. Campisi, E. Verdin, P. Carrera-Bastos, S. Targ, C. Franceschi, L. Ferrucci, D. W. Gilroy, A. Fasano, G. W. Miller,

A. H. Miller, A. Mantovani, C. M. Weyand, N. Barzilai, J. J. Goronzy, T. A. Rando, R. B. Effros, A. Lucia, N. Kleinstreuer, and G. M. Slavich. Chronic inflammation in the etiology of disease across the life span. *Nature Medicine*, 25(12):1822–1832, December 2019. ISSN 1078-8956, 1546-170X. doi: 10.1038/s41591-019-0675-0. URL http://www.nature.com/articles/s41591-019-0675-0.

[17] N. Saito-Sasaki, Y. Sawada, and M. Nakamura. Maresin-1 and Inflammatory Disease. *International Journal of Molecular Sciences*, 23(3):1–11, 2022. ISSN 14220067. doi: 10.3390/ijms23031367.

[18] K. Ohuchi, Y. Ono, M. Joho, K. Tsuruma, S. Ogami, S. Yamane, M. Funato, H. Kaneko, S. Nakamura, H. Hara, and M. Shimazawa. A Docosahexaenoic Acid-Derived Pro-resolving Agent, Maresin 1, Protects Motor Neuron Cells Death. *Neurochemical Research*, 43(7): 1413–1423, 2018. ISSN 15736903. doi: 10.1007/s11064-018-2556-1. URL http://dx.doi.org/10.1007/s11064-018-2556-1.

[19] A. Sánchez-Fernández, S. Zandee, M. Mastrogiovanni, M. Charabati, H. Rubbo, A. Prat, and R. López-Vales. Administration of Maresin-1 ameliorates the physiopathology of experimental autoimmune encephalomyelitis. *Journal of Neuroinflammation*, 19(1):1–18, 2022. ISSN 17422094. doi: 10.1186/s12974-022-02386-1. URL https://doi.org/10.1186/s12974-022-02386-1.

[20] L. Balas and T. Durand. Dihydroxylated E,E,Z-docosatrienes. An overview of their synthesis and biological significance. *Progress in Lipid Research*, 61:1–18, 2016. ISSN 18732194. doi: 10.1016/j.plipres.2015.10.002. URL http://dx.doi.org/10.1016/j.plipres.2015.10.002.

[21] I. C. León, S. Quesada-Vázquez, N. Sáinz, E. Guruceaga, X. Es-

coté, and M. J. Moreno-Aliaga. Effects of maresin 1 (MaR1) on colonic inflammation and gut dysbiosis in diet-induced obese mice. *Microorganisms*, 8(8):1–16, 2020. ISSN 20762607. doi: 10.3390/microorganisms8081156.

[22] X. Fang, H. Wang, T. Ye, X. Fu, X. Tan, Y. Zeng, J. Fan, and Y. Xu. Low serum Maresin-1 levels are associated with non-alcoholic fatty liver disease: a cross-sectional study. *Lipids in Health and Disease*, 20(1):1–9, 2021. ISSN 1476511X. doi: 10.1186/s12944-021-01518-5.

[23] N. Chiang, S. Libreros, P. C. Norris, X. De La Rosa, and C. N. Serhan. Maresin 1 activates LGR6 receptor promoting phagocyte immunoresolvent functions. *Journal of Clinical Investigation*, 129 (12):5294–5311, 2019. ISSN 15588238. doi: 10.1172/JCI129448.

[24] D. Li, M. Wang, J. Ye, J. Zhang, Y. Xu, Z. Wang, M. Zhao, D. Ye, and J. Wan. Maresin 1 alleviates the inflammatory response, reduces oxidative stress and protects against cardiac injury in LPS-induced mice. *Life Sciences*, 277(November 2020), 2021. ISSN 18790631. doi: 10.1016/j.lfs.2021.119467.

[25] J. Gu, L. Luo, Q. Wang, S. Yan, J. Lin, D. Li, B. Cao, H. Mei, B. Ying, L. Bin, F. G. Smith, and S. W. Jin. Maresin 1 attenuates mitochondrial dysfunction through the ALX/cAMP/ROS pathway in the cecal ligation and puncture mouse model and sepsis patients. *Laboratory Investigation*, 98(6):715–733, 2018. ISSN 15300307. doi: 10.1038/s41374-018-0031-x. URL `http://dx.doi.org/10.1038/s41374-018-0031-x`.

[26] T. Yang, G. Xu, P. T. Newton, A. S. Chagin, S. Mkrtchian, M. Carlström, X. M. Zhang, R. A. Harris, M. Cooter, M. Berger, K. R. Maddipati, K. Akassoglou, and N. Terrando. Maresin 1 attenuates

neuroinflammation in a mouse model of perioperative neurocognitive disorders. *British Journal of Anaesthesia*, 122(3):350–360, 2019. ISSN 14716771. doi: 10.1016/j.bja.2018.10.062.

[27] Y. Wang, A. Leppert, S. Tan, B. van der Gaag, N. Li, M. Schultzberg, and E. Hjorth. Maresin 1 attenuates pro-inflammatory activation induced by β-amyloid and stimulates its uptake. *Journal of Cellular and Molecular Medicine*, 25(1):434–447, 2021. ISSN 15821838. doi: 10.1111/jcmm.16098.

[28] T. W. Jung, H. S. Park, G. H. Choi, D. Kim, S. H. Ahn, D. S. Kim, T. Lee, and J. H. Jeong. Maresin 1 attenuates pro-inflammatory reactions and ER stress in HUVECs via PPARα-mediated pathway. *Molecular and Cellular Biochemistry*, 448(1-2):335–347, 2018. ISSN 15734919. doi: 10.1007/s11010-018-3392-y. URL `http://dx.doi.org/10.1007/s11010-018-3392-y`.

[29] R. E. E. Abdulnour, J. Dalli, J. K. Colby, N. Krishnamoorthy, J. Y. Timmons, S. H. Tan, R. A. Colas, N. A. Petasis, C. N. Serhan, and B. D. Levy. Maresin 1 biosynthesis during platelet-neutrophil interactions is organ-protective. *Proceedings of the National Academy of Sciences of the United States of America*, 111(46):16526–16531, 2014. ISSN 10916490. doi: 10.1073/pnas.1407123111.

[30] S. Jin, H. Chen, Y. Li, H. Zhong, W. Sun, J. Wang, T. Zhang, J. Ma, S. Yan, J. Zhang, Q. Tian, X. Yang, and J. Wang. Maresin 1 improves the Treg/Th17 imbalance in rheumatoid arthritis through miR-21. *Annals of the Rheumatic Diseases*, 77(11):1644–1652, 2018. ISSN 14682060. doi: 10.1136/annrheumdis-2018-213511.

[31] Q. Sun, Y. Wu, F. Zhao, and J. Wang. Maresin 1 inhibits transforming growth factor-β1-induced proliferation, migration and differenti-

ation in human lung fibroblasts. *Molecular Medicine Reports*, 16(2): 1523–1529, 2017. ISSN 17913004. doi: 10.3892/mmr.2017.6711.

[32] S. Tang, C. Gao, Y. Long, W. Huang, J. Chen, F. Fan, C. Jiang, and Y. Xu. Maresin 1 Mitigates High Glucose-Induced Mouse Glomerular Mesangial Cell Injury by Inhibiting Inflammation and Fibrosis. *Mediators of Inflammation*, 2017:1–11, 2017. ISSN 14661861. doi: 10.1155/2017/2438247.

[33] R. Li, Y. Wang, Z. Ma, M. Ma, D. Wang, G. Xie, Y. Yin, P. Zhang, and K. Tao. Maresin 1 Mitigates Inflammatory Response and Protects Mice from Sepsis. *Mediators of Inflammation*, 2016, 2016. ISSN 14661861. doi: 10.1155/2016/3798465.

[34] I. Francos-Quijorna, E. Santos-Nogueira, K. Gronert, A. B. Sullivan, M. A. Kopp, B. Brommer, S. David, J. M. Schwab, and R. López-Vales. Maresin 1 promotes inflammatory resolution, neuroprotection, and functional neurological recovery after spinal cord injury. *Journal of Neuroscience*, 37(48):11731–11743, 2017. ISSN 15292401. doi: 10.1523/JNEUROSCI.1395-17.2017.

[35] J. Wei, W. Su, Y. Zhao, Z. Wei, Y. Hua, P. Xue, X. Zhu, Y. Chen, and G. Chen. Maresin 1 promotes nerve regeneration and alleviates neuropathic pain after nerve injury. *Journal of Neuroinflammation*, 19(1):1–16, 2022. ISSN 17422094. doi: 10.1186/s12974-022-02405-1. URL `https://doi.org/10.1186/s12974-022-02405-1`.

[36] R. Huang, L. Vi, X. Zong, and G. S. Baht. Maresin 1 resolves aged-associated macrophage inflammation to improve bone regeneration. *FASEB Journal*, 34(10):13521–13532, 2020. ISSN 15306860. doi: 10.1096/fj.202001145R.

[37] R. Li, Y. Wang, E. Zhao, K. Wu, W. Li, L. Shi, D. Wang, G. Xie, Y. Yin, M. Deng, P. Zhang, and K. Tao. Maresin 1, a Proresolving Lipid Mediator, Mitigates Carbon Tetrachloride-Induced Liver Injury in Mice. *Oxidative Medicine and Cellular Longevity*, 2016, 2016. ISSN 19420994. doi: 10.1155/2016/9203716.

[38] M. V. Olsen, A. V. Lyngstadaas, J. A. Bair, R. R. Hodges, T. P. Utheim, C. N. Serhan, and D. A. Dartt. Maresin 1, a specialized proresolving mediator, stimulates intracellular [Ca2+] and secretion in conjunctival goblet cells. *Journal of Cellular Physiology*, 236(1): 340–353, 2021. ISSN 10974652. doi: 10.1002/jcp.29846.

[39] E. Albuquerque-Souza, F. Schulte, T. Chen, M. Hardt, H. Hasturk, T. E. Van Dyke, M. Holzhausen, and A. Kantarci. Maresin-1 and Resolvin E1 Promote Regenerative Properties of Periodontal Ligament Stem Cells Under Inflammatory Conditions. *Frontiers in Immunology*, 11(September):1–15, 2020. ISSN 16643224. doi: 10.3389/fimmu.2020.585530.

[40] R. López-Vales, I. Francos-Quijorna, J. M. Schwab, and D. Samuel. Maresins for use in the treatment of cns injuries, January 2019. URL `https://patents.google.com/patent/WO2019016580A1/en`.

[41] F. Munir, M. B. Jamshed, N. Shahid, S. A. Muhammad, A. Bhandari, and Q. Y. Zhang. Protective effects of Maresin- 1 against inflammation in experimentally induced acute pancreatitis and related lung injury. *American Journal of Physiology - Gastrointestinal and Liver Physiology*, 317(3):G333–G341, 2019. ISSN 15221547. doi: 10.1152/AJPGI.00078.2019.

[42] Z. Gu, G. J. Lamont, R. J. Lamont, S. M. Uriarte, H. Wang, and D. A. Scott. Resolvin D1, resolvin D2 and maresin 1 activate the

GSK3β anti-inflammatory axis in TLR4-engaged human monocytes. *Innate Immunity*, 22(3):186–195, 2016. ISSN 17534267. doi: 10.1177/1753425916628618.

[43] R. López-Vales, A. Sánchex-Fernández, and A. Martínez-Muriana. Specialized pro-resolving lipid mediators for use in the treatment of neurodegenerative diseases and/or autoimmune diseases, July 2018. URL `https://patents.google.com/patent/WO2018134230A1/en?q=(maresin)&inventor=Ruben+LOPEZ+VALES&oq=inventor:(Ruben+LOPEZ+VALES)+maresin`.

[44] W. Xian, Y. Wu, W. Xiong, L. Li, T. Li, S. Pan, L. Song, L. Hu, L. Pei, S. Yao, and Y. Shang. The pro-resolving lipid mediator Maresin 1 protects against cerebral ischemia/reperfusion injury by attenuating the pro-inflammatory response. *Biochemical and Biophysical Research Communications*, 472(1):175–181, 2016. ISSN 10902104. doi: 10.1016/j.bbrc.2016.02.090. URL `http://dx.doi.org/10.1016/j.bbrc.2016.02.090`.

[45] T. L. Cezar, R. M. Martinez, C. d. Rocha, C. P. Melo, D. L. Vale, S. M. Borghi, V. Fattori, J. A. Vignoli, D. Camilios-Neto, M. M. Baracat, S. R. Georgetti, W. A. Verri, and R. Casagrande. Treatment with maresin 1, a docosahexaenoic acid-derived pro-resolution lipid, protects skin from inflammation and oxidative stress caused by UVB irradiation. *Scientific Reports*, 9(1):1–14, 2019. ISSN 20452322. doi: 10.1038/s41598-019-39584-6. URL `http://dx.doi.org/10.1038/s41598-019-39584-6`.

[46] G. P. Moss, P. a. S. Smith, and D. Tavernier. Glossary of class names of organic compounds and reactivity intermediates based on structure (IUPAC Recommendations 1995). *Pure and Applied*

Chemistry, 67(8-9):1307–1375, January 1995. ISSN 1365-3075. doi: 10.1351/pac199567081307. URL https://www.degruyter.com/document/doi/10.1351/pac199567081307/html.

[47] E. Tvrzicka, L.-S. Kremmyda, B. Stankova, and A. Zak. Fatty Acids as Biocompounds: Their Role in Human Metabolism, Health and Disease - a Review. Part 1: Classification, Dietary Sources and Biological Functions. *Biomedical Papers*, 155(2):117–130, June 2011. ISSN 12138118, 18047521. doi: 10.5507/bp.2011.038. URL http://biomed.papers.upol.cz/doi/10.5507/bp.2011.038.html.

[48] I. Ivanov, D. Heydeck, K. Hofheinz, J. Roffeis, V. B. O'Donnell, H. Kuhn, and M. Walther. Molecular enzymology of lipoxygenases. *Archives of Biochemistry and Biophysics*, 503(2):161–174, November 2010. ISSN 00039861. doi: 10.1016/j.abb.2010.08.016. URL https://linkinghub.elsevier.com/retrieve/pii/S0003986110003516.

[49] A. C. Rustan and C. A. Drevon. Fatty Acids: Structures and Properties. In John Wiley & Sons, Ltd, editor, *eLS*. Wiley, 1 edition, September 2005. ISBN 978-0-470-01617-6 978-0-470-01590-2. doi: 10.1038/npg.els.0003894. URL https://onlinelibrary.wiley.com/doi/10.1038/npg.els.0003894.

[50] J. A. Kenar, B. R. Moser, and G. R. List. Naturally Occurring Fatty Acids. In *Fatty Acids*, pages 23–82. Elsevier, 2017. ISBN 978-0-12-809521-8. doi: 10.1016/B978-0-12-809521-8.00002-7. URL https://linkinghub.elsevier.com/retrieve/pii/B9780128095218000027.

[51] M. Cholewski, M. Tomczykowa, and M. Tomczyk. A Comprehensive Review of Chemistry, Sources and Bioavailability of Omega-3 Fatty

Acids. *Nutrients*, 10(11):1662, November 2018. ISSN 2072-6643. doi: 10.3390/nu10111662. URL http://www.mdpi.com/2072-6643/10/11/1662.

[52] C. N. Serhan, J. Dalli, S. Karamnov, A. Choi, C. Park, Z. Xu, R. Ji, M. Zhu, and N. A. Petasis. Macrophage proresolving mediator maresin 1 stimulates tissue regeneration and controls pain. *The FASEB Journal*, 26(4):1755–1765, April 2012. ISSN 0892-6638, 1530-6860. doi: 10.1096/fj.11-201442. URL https://onlinelibrary.wiley.com/doi/abs/10.1096/fj.11-201442.

[53] C. Freedman, A. Tran, B. E. Tourdot, C. Kalyanaraman, S. Perry, M. Holinstat, M. P. Jacobson, and T. R. Holman. Biosynthesis of the Maresin Intermediate, 13S,14S-Epoxy-DHA, by Human 15-Lipoxygenase and 12-Lipoxygenase and Its Regulation through Negative Allosteric Modulators. *Biochemistry*, 59(19): 1832–1844, May 2020. ISSN 0006-2960, 1520-4995. doi: 10.1021/acs.biochem.0c00233. URL https://pubs.acs.org/doi/10.1021/acs.biochem.0c00233.

[54] I. Zahoor, M. Nematullah, S. Mir, M. E. Ahmed, R. Rattan, and G. Shailendra. Pro-resolution lipid mediator Maresin-1 reduces inflammation, promotes neuroprotection, and prevents disease progression in multiple sclerosis model of autoimmunity. *The Journal of Immunology*, 210(1_Supplement): 85.08–85.08, May 2023. ISSN 0022-1767, 1550-6606. doi: 10.4049/jimmunol.210.Supp.85.08. URL https://journals.aai.org/jimmunol/article/210/1_Supplement/85.08/264493/Pro-resolution-lipid-mediator-maresin-1-reduces.

[55] K. Sasaki, D. Urabe, H. Arai, M. Arita, and M. Inoue. To-

tal Synthesis and Bioactivities of Two Proposed Structures of Maresin. *Chemistry - An Asian Journal*, 6(2):534–543, February 2011. ISSN 18614728. doi: 10.1002/asia.201000494. URL https://onlinelibrary.wiley.com/doi/10.1002/asia.201000494.

[56] A. R. Rodriguez and B. W. Spur. Total synthesis of the macrophage derived anti-inflammatory lipid mediator Maresin 1. *Tetrahedron Letters*, 53(32):4169–4172, August 2012. ISSN 00404039. doi: 10.1016/j.tetlet.2012.05.143. URL https://linkinghub.elsevier.com/retrieve/pii/S0040403912009434.

[57] J. E. Tungen, M. Aursnes, J. Dalli, H. Arnardottir, C. N. Serhan, and T. V. Hansen. Total Synthesis of the Anti-inflammatory and Pro-resolving Lipid Mediator MaR1 (n-3 DPA). Utilizing an sp3-sp3 Negishi Cross-Coupling Reaction. *Chemistry - A European Journal*, 20(45):14575–14578, November 2014. ISSN 09476539. doi: 10.1002/chem.201404721. URL https://onlinelibrary.wiley.com/doi/10.1002/chem.201404721.

[58] J. E. Tungen, M. Aursnes, and T. V. Hansen. Stereoselective synthesis of Maresin-1. *Tetrahedron Letters*, 56(14):1843–1846, April 2015. ISSN 00404039. doi: 10.1016/j.tetlet.2015.02.080. URL https://linkinghub.elsevier.com/retrieve/pii/S0040403915003615.

[59] M. M. Papamichael, C. Katsardis, D. Tsoukalas, C. Itsiopoulos, and B. Erbas. Plasma lipid biomarkers in relation to BMI, lung function, and airway inflammation in pediatric asthma. *Metabolomics*, 17(7):63, July 2021. ISSN 1573-3882, 1573-3890. doi: 10.1007/s11306-021-01811-5. URL https://link.springer.com/10.1007/s11306-021-01811-5.

[60] C. N. Serhan, M. Hamberg, and B. Samuelsson. Trihydroxyte-

traenes: A novel series of compounds formed from arachidonic acid in human leukocytes. *Biochemical and Biophysical Research Communications*, 118(3):943–949, February 1984. ISSN 0006291X. doi: 10.1016/0006-291X(84)91486-4. URL https://linkinghub.elsevier.com/retrieve/pii/0006291X84914864.

[61] H. Kuhn, S. Banthiya, and K. van Leyen. Mammalian lipoxygenases and their biological relevance. *Biochimica et Biophysica Acta (BBA) - Molecular and Cell Biology of Lipids*, 1851(4):308–330, April 2015. ISSN 13881981. doi: 10.1016/j.bbalip.2014.10.002. URL https://linkinghub.elsevier.com/retrieve/pii/S138819811400211X.

[62] A. Bateman and R. Sandford. The PLAT domain: a new piece in the PKD1 puzzle. *Current Biology*, 9(16):R588–S2, August 1999. ISSN 09609822. doi: 10.1016/S0960-9822(99)80380-7. URL https://linkinghub.elsevier.com/retrieve/pii/S0960982299803807.

[63] A. M. Aleem, J. Jankun, J. D. Dignam, M. Walther, H. Kühn, D. I. Svergun, and E. Skrzypczak-Jankun. Human Platelet 12-Lipoxygenase, New Findings about Its Activity, Membrane Binding and Low-resolution Structure. *Journal of Molecular Biology*, 376(1): 193–209, February 2008. ISSN 00222836. doi: 10.1016/j.jmb.2007.11.086. URL https://linkinghub.elsevier.com/retrieve/pii/S0022283607015860.

[64] N. Lehnert and E. I. Solomon. Density-functional investigation on the mechanism of H-atom abstraction by lipoxygenase. *JBIC Journal of Biological Inorganic Chemistry*, 8(3):294–305, February 2003. ISSN 0949-8257, 1432-1327. doi: 10.1007/s00775-002-0415-6. URL http://link.springer.com/10.1007/s00775-002-0415-6.

[65] P. Saura, R. Suardíaz, L. Masgrau, J. M. Lluch, and González-

Lafont. Unraveling How Enzymes Can Use Bulky Residues To Drive Site-Selective C–H Activation: The Case of Mammalian Lipoxygenases Catalyzing Arachidonic Acid Oxidation. *ACS Catalysis*, 4 (12):4351–4363, December 2014. ISSN 2155-5435, 2155-5435. doi: 10.1021/cs5006103. URL https://pubs.acs.org/doi/10.1021/cs5006103.

[66] C. A. Rouzer, T. Matsumoto, and B. Samuelsson. Single protein from human leukocytes possesses 5-lipoxygenase and leukotriene A4 synthase activities. *Proceedings of the National Academy of Sciences*, 83(4):857–861, February 1986. ISSN 0027-8424, 1091-6490. doi: 10.1073/pnas.83.4.857. URL https://pnas.org/doi/full/10.1073/pnas.83.4.857.

[67] J. Dalli, M. Zhu, N. A. Vlasenko, B. Deng, J. Z. Haeggström, N. A. Petasis, and C. N. Serhan. The novel 13S,14S-epoxy-maresin is converted by human macrophages to maresin 1 (MaR1), inhibits leukotriene A4 hydrolase (LTA4H), and shifts macrophage phenotype. *The FASEB Journal*, 27(7):2573–2583, July 2013. ISSN 0892-6638, 1530-6860. doi: 10.1096/fj.13-227728. URL https://onlinelibrary.wiley.com/doi/abs/10.1096/fj.13-227728.

[68] M. E. Newcomer and A. R. Brash. The structural basis for specificity in lipoxygenase catalysis: Specificity in Lipoxygenases. *Protein Science*, 24(3):298–309, March 2015. ISSN 09618368. doi: 10.1002/pro.2626. URL https://onlinelibrary.wiley.com/doi/10.1002/pro.2626.

[69] G. Coffa and A. R. Brash. A single active site residue directs oxygenation stereospecificity in lipoxygenases: Stereocontrol is linked to the position of oxygenation. *Proceedings of the National Academy*

of Sciences, 101(44):15579–15584, November 2004. ISSN 0027-8424, 1091-6490. doi: 10.1073/pnas.0406727101. URL https://pnas.org/doi/full/10.1073/pnas.0406727101.

[70] P. Saura, R. Suardíaz, L. Masgrau, González-Lafont, E. Rosta, and J. M. Lluch. Understanding the Molecular Mechanism of the Ala-versus-Gly Concept Controlling the Product Specificity in Reactions Catalyzed by Lipoxygenases: A Combined Molecular Dynamics and QM/MM Study of Coral 8R-Lipoxygenase. *ACS Catalysis*, 7(7):4854–4866, July 2017. ISSN 2155-5435, 2155-5435. doi: 10.1021/acscatal.7b00842. URL https://pubs.acs.org/doi/10.1021/acscatal.7b00842.

[71] ALOX5 - Polyunsaturated fatty acid 5-lipoxygenase - Homo sapiens (Human) | UniProtKB | UniProt, . URL https://www.uniprot.org/uniprotkb/P09917/entry.

[72] N. C. Gilbert, S. G. Bartlett, M. T. Waight, D. B. Neau, W. E. Boeglin, A. R. Brash, and M. E. Newcomer. The Structure of Human 5-Lipoxygenase. *Science*, 331(6014):217–219, January 2011. ISSN 0036-8075, 1095-9203. doi: 10.1126/science.1197203. URL https://www.science.org/doi/10.1126/science.1197203.

[73] O. Rådmark, O. Werz, D. Steinhilber, and B. Samuelsson. 5-Lipoxygenase, a key enzyme for leukotriene biosynthesis in health and disease. *Biochimica et Biophysica Acta (BBA) - Molecular and Cell Biology of Lipids*, 1851(4):331–339, April 2015. ISSN 13881981. doi: 10.1016/j.bbalip.2014.08.012. URL https://linkinghub.elsevier.com/retrieve/pii/S138819811400167X.

[74] M. Hamberg and B. Samuelsson. Prostaglandin Endoperoxides. Novel Transformations of Arachidonic Acid in Human Platelets.

Proceedings of the National Academy of Sciences, 71(9):3400–3404, September 1974. ISSN 0027-8424, 1091-6490. doi: 10.1073/pnas.71.9.3400. URL https://pnas.org/doi/full/10.1073/pnas.71.9.3400.

[75] C. D. Funk, L. B. Funk, G. A. FitzGerald, and B. Samuelsson. Characterization of human 12-lipoxygenase genes. *Proceedings of the National Academy of Sciences*, 89(9):3962–3966, May 1992. ISSN 0027-8424, 1091-6490. doi: 10.1073/pnas.89.9.3962. URL https://pnas.org/doi/full/10.1073/pnas.89.9.3962.

[76] L. Kutzner, K. Goloshchapova, D. Heydeck, S. Stehling, H. Kuhn, and N. H. Schebb. Mammalian ALOX15 orthologs exhibit pronounced dual positional specificity with docosahexaenoic acid. *Biochimica et Biophysica Acta (BBA) - Molecular and Cell Biology of Lipids*, 1862(7):666–675, July 2017. ISSN 13881981. doi: 10.1016/j.bbalip.2017.04.001. URL https://linkinghub.elsevier.com/retrieve/pii/S1388198117300616.

[77] ALOX12 - Polyunsaturated fatty acid lipoxygenase ALOX12 - Homo sapiens (Human) | UniProtKB | UniProt, . URL https://www.uniprot.org/uniprotkb/P18054/entry.

[78] ALOX15 - Polyunsaturated fatty acid lipoxygenase ALOX15 - Sus scrofa (Pig) | UniProtKB | UniProt, . URL https://www.uniprot.org/uniprotkb/P16469/entry.

[79] H. Suzuki, K. Kishimoto, T. Yoshimoto, S. Yamamoto, F. Kanai, Y. Ebina, A. Miyatake, and T. Tanabe. Site-directed mutagenesis studies on the iron-binding domain and the determinant for the substrate oxygenation site of porcine leukocyte arachidonate 12-lipoxygenase. *Biochimica et Biophysica Acta (BBA) - Lipids and*

Lipid Metabolism, 1210(3):308–316, January 1994. ISSN 00052760. doi: 10.1016/0005-2760(94)90234-8. URL https://linkinghub.elsevier.com/retrieve/pii/0005276094902348.

[80] A. R. Brash, W. E. Boeglin, and M. S. Chang. Discovery of a second 15S-lipoxygenase in humans. *Proceedings of the National Academy of Sciences*, 94(12):6148–6152, June 1997. ISSN 0027-8424, 1091-6490. doi: 10.1073/pnas.94.12.6148. URL https://pnas.org/doi/full/10.1073/pnas.94.12.6148.

[81] G. Fürstenberger, H. Hagedorn, T. Jacobi, E. Besemfelder, M. Stephan, W. Lehmann, and F. Marks. Characterization of an 8-lipoxygenase activity induced by the phorbol ester tumor promoter 12-O-tetradecanoylphorbol-13-acetate in mouse skin in vivo. *Journal of Biological Chemistry*, 266(24):15738–15745, August 1991. ISSN 00219258. doi: 10.1016/S0021-9258(18)98471-1. URL https://linkinghub.elsevier.com/retrieve/pii/S0021925818984711.

[82] M. Jisaka, C. Iwanaga, N. Takahashi, T. Goto, T. Kawada, T. Yamamoto, I. Ikeda, K. Nishimura, T. Nagaya, T. Fushiki, and K. Yokota. Double dioxygenation by mouse 8S-lipoxygenase: Specific formation of a potent peroxisome proliferator-activated receptor α agonist. *Biochemical and Biophysical Research Communications*, 338(1):136–143, December 2005. ISSN 0006291X. doi: 10.1016/j.bbrc.2005.08.029. URL https://linkinghub.elsevier.com/retrieve/pii/S0006291X05017250.

[83] J. Gautheron and I. Jéru. The Multifaceted Role of Epoxide Hydrolases in Human Health and Disease. *International Journal of Molecular Sciences*, 22(1):13, December 2020. ISSN 1422-0067. doi:

10.3390/ijms22010013. URL https://www.mdpi.com/1422-0067/22/1/13.

[84] P. C. Rudberg, F. Tholander, M. Andberg, M. M. Thunnissen, and J. Z. Haeggström. Leukotriene A4 Hydrolase. *Journal of Biological Chemistry*, 279(26):27376–27382, June 2004. ISSN 00219258. doi: 10.1074/jbc.M401031200. URL https://linkinghub.elsevier.com/retrieve/pii/S002192582085399X.

[85] A. Stsiapanava, B. Samuelsson, and J. Z. Haeggström. Capturing LTA4 hydrolase in action: Insights to the chemistry and dynamics of chemotactic LTB4 synthesis. *Proceedings of the National Academy of Sciences*, 114(36):9689–9694, September 2017. ISSN 0027-8424, 1091-6490. doi: 10.1073/pnas.1710850114. URL https://pnas.org/doi/full/10.1073/pnas.1710850114.

[86] J. Z. Haeggström and C. D. Funk. Lipoxygenase and Leukotriene Pathways: Biochemistry, Biology, and Roles in Disease. *Chemical Reviews*, 111(10):5866–5898, October 2011. ISSN 0009-2665, 1520-6890. doi: 10.1021/cr200246d. URL https://pubs.acs.org/doi/10.1021/cr200246d.

[87] G. Jones, P. Willett, R. C. Glen, A. R. Leach, and R. Taylor. Development and Validation of a Genetic Algorithm for Flexible Docking. *Journal of Molecular Biology*, 267(3):727–748, April 1997. ISSN 00222836. doi: 10.1006/jmbi.1996.0897. URL https://linkinghub.elsevier.com/retrieve/pii/S0022283696908979.

[88] M. K. Annamala, K. K. Inampudi, and L. Guruprasad. Docking of phosphonate and trehalose analog inhibitors into M. tuberculosis mycolyltransferase Ag85C: Comparison of the two scoring fitness functions GoldScore and ChemScore, in the GOLD software.

Bioinformation, 1(9):339–350, January 2007. ISSN 0973-2063. URL https://www.ncbi.nlm.nih.gov/pmc/articles/PMC1891722/.

[89] J. A. Maier, C. Martinez, K. Kasavajhala, L. Wickstrom, K. E. Hauser, and C. Simmerling. ff14SB: Improving the Accuracy of Protein Side Chain and Backbone Parameters from ff99SB. *Journal of Chemical Theory and Computation*, 11(8):3696–3713, August 2015. ISSN 1549-9618, 1549-9626. doi: 10.1021/acs.jctc.5b00255. URL https://pubs.acs.org/doi/10.1021/acs.jctc.5b00255.

[90] C. Tian, K. Kasavajhala, K. A. A. Belfon, L. Raguette, H. Huang, A. N. Migues, J. Bickel, Y. Wang, J. Pincay, Q. Wu, and C. Simmerling. ff19SB: Amino-Acid-Specific Protein Backbone Parameters Trained against Quantum Mechanics Energy Surfaces in Solution. *Journal of Chemical Theory and Computation*, 16(1):528–552, January 2020. ISSN 1549-9618, 1549-9626. doi: 10.1021/acs.jctc.9b00591. URL https://pubs.acs.org/doi/10.1021/acs.jctc.9b00591.

[91] J. E. Jones. On the determination of molecular fields.—I. From the variation of the viscosity of a gas with temperature. *Proceedings of the Royal Society of London. Series A, Containing Papers of a Mathematical and Physical Character*, 106(738):441–462, October 1924. ISSN 0950-1207, 2053-9150. doi: 10.1098/rspa.1924.0081. URL https://royalsocietypublishing.org/doi/10.1098/rspa.1924.0081.

[92] J. E. Jones. On the determination of molecular fields. —II. From the equation of state of a gas. *Proceedings of the Royal Society of London. Series A, Containing Papers of a Mathematical and Physical Character*, 106(738):463–477, October 1924. ISSN

0950-1207, 2053-9150. doi: 10.1098/rspa.1924.0082. URL https://royalsocietypublishing.org/doi/10.1098/rspa.1924.0082.

[93] J. E. Lennard-Jones. Cohesion. *Proceedings of the Physical Society*, 43(5):461–482, September 1931. ISSN 0959-5309. doi: 10.1088/0959-5309/43/5/301. URL https://iopscience.iop.org/article/10.1088/0959-5309/43/5/301.

[94] D. A. Case, T. E. Cheatham, T. Darden, H. Gohlke, R. Luo, K. M. Merz, A. Onufriev, C. Simmerling, B. Wang, and R. J. Woods. The Amber biomolecular simulation programs. *Journal of Computational Chemistry*, 26(16):1668–1688, December 2005. ISSN 0192-8651, 1096-987X. doi: 10.1002/jcc.20290. URL https://onlinelibrary.wiley.com/doi/10.1002/jcc.20290.

[95] B. R. Brooks, C. L. Brooks, A. D. Mackerell, L. Nilsson, R. J. Petrella, B. Roux, Y. Won, G. Archontis, C. Bartels, S. Boresch, A. Caflisch, L. Caves, Q. Cui, A. R. Dinner, M. Feig, S. Fischer, J. Gao, M. Hodoscek, W. Im, K. Kuczera, T. Lazaridis, J. Ma, V. Ovchinnikov, E. Paci, R. W. Pastor, C. B. Post, J. Z. Pu, M. Schaefer, B. Tidor, R. M. Venable, H. L. Woodcock, X. Wu, W. Yang, D. M. York, and M. Karplus. CHARMM: The biomolecular simulation program. *Journal of Computational Chemistry*, 30(10):1545–1614, July 2009. ISSN 0192-8651, 1096-987X. doi: 10.1002/jcc.21287. URL https://onlinelibrary.wiley.com/doi/10.1002/jcc.21287.

[96] W. F. Van Gunsteren, X. Daura, and A. E. Mark. GROMOS Force Field. In N. L. Allinger, T. Clark, J. Gasteiger, P. A. Kollman, H. F. Schaefer, and P. R. Schreiner, editors, *Encyclopedia of Computational Chemistry*, page cga011. John Wiley &

Sons, Ltd, Chichester, UK, April 2002. ISBN 978-0-470-84501-1. doi: 10.1002/0470845015.cga011. URL https://onlinelibrary.wiley.com/doi/10.1002/0470845015.cga011.

[97] B. J. Alder and T. E. Wainwright. Studies in Molecular Dynamics. I. General Method. *The Journal of Chemical Physics*, 31(2): 459–466, August 1959. ISSN 0021-9606, 1089-7690. doi: 10.1063/1.1730376. URL https://pubs.aip.org/jcp/article/31/2/459/1031509/Studies-in-Molecular-Dynamics-I-General-Method.

[98] L. Verlet. Computer "Experiments" on Classical Fluids. I. Thermodynamical Properties of Lennard-Jones Molecules. *Physical Review*, 159(1):98–103, July 1967. ISSN 0031-899X. doi: 10.1103/PhysRev.159.98. URL https://link.aps.org/doi/10.1103/PhysRev.159.98.

[99] E. Schrödinger. An Undulatory Theory of the Mechanics of Atoms and Molecules. *Physical Review*, 28(6):1049–1070, December 1926. ISSN 0031-899X. doi: 10.1103/PhysRev.28.1049. URL https://link.aps.org/doi/10.1103/PhysRev.28.1049.

[100] M. Born and R. Oppenheimer. Zur Quantentheorie der Molekeln. *Annalen der Physik*, 389(20):457–484, 1927. ISSN 00033804, 15213889. doi: 10.1002/andp.19273892002. URL https://onlinelibrary.wiley.com/doi/10.1002/andp.19273892002.

[101] D. R. Hartree. The Wave Mechanics of an Atom with a Non-Coulomb Central Field. Part II. Some Results and Discussion. *Mathematical Proceedings of the Cambridge Philosophical Society*, 24(1):111–132, January 1928. ISSN 0305-0041, 1469-8064. doi: 10.1017/S0305004100011920. URL

https://www.cambridge.org/core/product/identifier/S0305004100011920/type/journal_article.

[102] V. Fock. Näherungsmethode zur Lösung des quantenmechanischen Mehrkörperproblems. *Zeitschrift für Physik*, 61(1-2):126–148, January 1930. ISSN 1434-6001, 1434-601X. doi: 10.1007/BF01340294. URL http://link.springer.com/10.1007/BF01340294.

[103] J. C. Slater. The Theory of Complex Spectra. *Physical Review*, 34(10):1293–1322, November 1929. ISSN 0031-899X. doi: 10.1103/PhysRev.34.1293. URL https://link.aps.org/doi/10.1103/PhysRev.34.1293.

[104] J. Čížek. On the Correlation Problem in Atomic and Molecular Systems. Calculation of Wavefunction Components in Ursell-Type Expansion Using Quantum-Field Theoretical Methods. *The Journal of Chemical Physics*, 45(11):4256–4266, December 1966. ISSN 0021-9606, 1089-7690. doi: 10.1063/1.1727484. URL https://pubs.aip.org/jcp/article/45/11/4256/211247/On-the-Correlation-Problem-in-Atomic-and-Molecular.

[105] C. Møller and M. S. Plesset. Note on an Approximation Treatment for Many-Electron Systems. *Physical Review*, 46(7):618–622, October 1934. ISSN 0031-899X. doi: 10.1103/PhysRev.46.618. URL https://link.aps.org/doi/10.1103/PhysRev.46.618.

[106] W. Kohn, A. D. Becke, and R. G. Parr. Density Functional Theory of Electronic Structure. *The Journal of Physical Chemistry*, 100 (31):12974–12980, January 1996. ISSN 0022-3654, 1541-5740. doi: 10.1021/jp960669l. URL https://pubs.acs.org/doi/10.1021/jp960669l.

[107] C. J. Cramer. Ab Initio Implementations of Hartree-Fock Molecular Orbital Theory. In *Essentials of computational chemistry: theories and models*, pages 165–202. J. Wiley, West Sussex, England ; New York, 2nd edition, 2002. ISBN 978-0-471-48551-3 978-0-471-48552-0.

[108] E. Fermi. *Collected papers (note E memorie): Italy 1921-1968*. Collected papers (note E memorie). University of Chicago Press, 1962. URL https://books.google.es/books?id=mNPuQKFMlvsC.

[109] L. H. Thomas. The calculation of atomic fields. *Mathematical Proceedings of the Cambridge Philosophical Society*, 23(5):542–548, January 1927. ISSN 0305-0041, 1469-8064. doi: 10.1017/S0305004100011683. URL https://www.cambridge.org/core/product/identifier/S0305004100011683/type/journal_article.

[110] P. Hohenberg and W. Kohn. Inhomogeneous Electron Gas. *Physical Review*, 136(3B):B864–B871, November 1964. ISSN 0031-899X. doi: 10.1103/PhysRev.136.B864. URL https://link.aps.org/doi/10.1103/PhysRev.136.B864.

[111] J. Andrés and J. Beltrán. Capítulo 2: Métodos de la Química Cuántica. In *Química teórica y computacional*. Universitat Jaume I. Servei de Comunicació i Publicacions, 2013. ISBN 978-84-15443-27-8.

[112] W. Kohn and L. J. Sham. Self-Consistent Equations Including Exchange and Correlation Effects. *Physical Review*, 140(4A):A1133–A1138, November 1965. ISSN 0031-899X. doi: 10.1103/PhysRev.140.A1133. URL https://link.aps.org/doi/10.1103/PhysRev.140.A1133.

[113] A. D. Becke. A new mixing of Hartree–Fock and local density-functional theories. *The Journal of Chemical Physics*, 98(2):1372–1377, January 1993. ISSN 0021-9606, 1089-7690. doi: 10.1063/1.464304. URL https://pubs.aip.org/jcp/article/98/2/1372/821432/A-new-mixing-of-Hartree-Fock-and-local-density.

[114] C. Lee, W. Yang, and R. G. Parr. Development of the Colle-Salvetti correlation-energy formula into a functional of the electron density. *Physical Review B*, 37(2):785–789, January 1988. ISSN 0163-1829. doi: 10.1103/PhysRevB.37.785. URL https://link.aps.org/doi/10.1103/PhysRevB.37.785.

[115] H. M. Senn and W. Thiel. QM/MM Methods for Biomolecular Systems. *Angewandte Chemie International Edition*, 48(7):1198–1229, February 2009. ISSN 14337851. doi: 10.1002/anie.200802019. URL https://onlinelibrary.wiley.com/doi/10.1002/anie.200802019.

[116] A. Warshel and M. Levitt. Theoretical studies of enzymic reactions: Dielectric, electrostatic and steric stabilization of the carbonium ion in the reaction of lysozyme. *Journal of Molecular Biology*, 103(2):227–249, May 1976. ISSN 00222836. doi: 10.1016/0022-2836(76)90311-9. URL https://linkinghub.elsevier.com/retrieve/pii/0022283676903119.

[117] The Nobel Prize in Chemistry 2013, October 2013. URL https://www.nobelprize.org/prizes/chemistry/2013/prize-announcement/.

[118] H. Lin and D. G. Truhlar. QM/MM: what have we learned, where are we, and where do we go from here? *Theoretical Chemistry Accounts*, 117(2):185, February 2007. ISSN 1432-881X, 1432-2234.

doi: 10.1007/s00214-006-0143-z. URL https://link.springer.com/10.1007/s00214-006-0143-z.

[119] D. L. Nelson, M. M. Cox, and A. L. Lehninger. *Principles of Biochemistry*. Macmillan learning. W.H. Freeman, New York NY, seventh edition edition, 2017. ISBN 978-1-319-10824-3 978-1-4641-2611-6.

[120] C. Langlais and B. Korn. Recombinant Protein Expression in Bacteria. In *Encyclopedic Reference of Genomics and Proteomics in Molecular Medicine*, pages 1609–1616. Springer, Berlin, Heidelberg, 2006. ISBN 978-3-540-29623-2. doi: 10.1007/3-540-29623-9_4800. URL https://doi.org/10.1007/3-540-29623-9_4800.

[121] B. Alberts, A. Johnson, J. Lewis, M. Raff, K. Roberts, and P. Walter. The Lipid Bilayer. In *Molecular Biology of the Cell. 4th edition*. Garland Science, 2002. URL https://www.ncbi.nlm.nih.gov/books/NBK26871/.

[122] LadyofHats. Diagram showing how proteins are produced with tRNA mRNA and ribosomes, October 2008. URL https://commons.wikimedia.org/wiki/File:TRNA_ribosomes_diagram_en.svg.

[123] R. L. Schnaar. Glycolipid-mediated cell–cell recognition in inflammation and nerve regeneration. *Archives of Biochemistry and Biophysics*, 426(2):163–172, June 2004. ISSN 00039861. doi: 10.1016/j.abb.2004.02.019. URL https://linkinghub.elsevier.com/retrieve/pii/S0003986104000943.

[124] B. G. Fox and P. G. Blommel. Autoinduction of Protein Expression. *Current Protocols in Protein Science*, 56(1), April

2009. ISSN 1934-3655, 1934-3663. doi: 10.1002/0471140864.ps0523s56. URL https://currentprotocols.onlinelibrary.wiley.com/doi/10.1002/0471140864.ps0523s56.

[125] K. R. Kakularam, M. Canyelles-Niño, X. Chen, J. M. Lluch, González-Lafont, and H. Kuhn. Functional Characterization of Mouse and Human Arachidonic Acid Lipoxygenase 15B (ALOX15B) Orthologs and of Their Mutants Exhibiting Humanized and Murinized Reaction Specificities. *International Journal of Molecular Sciences*, 24(12):10046, January 2023. ISSN 1422-0067. doi: 10.3390/ijms241210046. URL https://www.mdpi.com/1422-0067/24/12/10046.

[126] H. Kuhn, L. Humeniuk, N. Kozlov, S. Roigas, S. Adel, and D. Heydeck. The evolutionary hypothesis of reaction specificity of mammalian ALOX15 orthologs. *Progress in Lipid Research*, 72:55–74, October 2018. ISSN 0163-7827. doi: 10.1016/j.plipres.2018.09.002. URL https://www.sciencedirect.com/science/article/pii/S0163782718300018.

[127] C. D. Funk, X.-S. Chen, E. N. Johnson, and L. Zhao. Lipoxygenase genes and their targeted disruption. *Prostaglandins & other Lipid Mediators*, page 10, 2002.

[128] M. Jisaka, R. B. Kim, W. E. Boeglin, and A. R. Brash. Identification of Amino Acid Determinants of the Positional Specificity of Mouse 8S-Lipoxygenase and Human 15S-Lipoxygenase-2. *Journal of Biological Chemistry*, 275(2):1287–1293, January 2000. ISSN 00219258. doi: 10.1074/jbc.275.2.1287. URL https://linkinghub.elsevier.com/retrieve/pii/S002192581831247X.

[129] N. L. of Medicine (US). National Center for Biotechnology Information. URL https://www.ncbi.nlm.nih.gov/nucleotide/.

[130] F. Reisch, K. R. Kakularam, S. Stehling, D. Heydeck, and H. Kuhn. Eicosanoid biosynthesis in marine mammals. *The FEBS Journal*, 288(4):1387–1406, February 2021. ISSN 1742-464X, 1742-4658. doi: 10.1111/febs.15469. URL https://onlinelibrary.wiley.com/doi/10.1111/febs.15469.

[131] M. J. Kobe, D. B. Neau, C. E. Mitchell, S. G. Bartlett, and M. E. Newcomer. The Structure of Human 15-Lipoxygenase-2 with a Substrate Mimic. *Journal of Biological Chemistry*, 289(12): 8562–8569, March 2014. ISSN 00219258. doi: 10.1074/jbc.M113.543777. URL https://linkinghub.elsevier.com/retrieve/pii/S0021925820523521.

[132] J. Jumper, R. Evans, A. Pritzel, T. Green, M. Figurnov, O. Ronneberger, K. Tunyasuvunakool, R. Bates, A. Žídek, A. Potapenko, and others. Highly accurate protein structure prediction with AlphaFold. *Nature*, 596(7873):583–589, 2021.

[133] M. Varadi, S. Anyango, M. Deshpande, S. Nair, C. Natassia, G. Yordanova, D. Yuan, O. Stroe, G. Wood, A. Laydon, A. Žídek, T. Green, K. Tunyasuvunakool, S. Petersen, J. Jumper, E. Clancy, R. Green, A. Vora, M. Lutfi, M. Figurnov, A. Cowie, N. Hobbs, P. Kohli, G. Kleywegt, E. Birney, D. Hassabis, and S. Velankar. AlphaFold Protein Structure Database: massively expanding the structural coverage of protein-sequence space with high-accuracy models. *Nucleic Acids Research*, 50(D1):D439–D444, January 2022. ISSN 0305-1048, 1362-4962. doi: 10.1093/nar/gkab1061. URL https://academic.oup.com/nar/article/50/D1/D439/6430488.

[134] The UniProt Consortium. UniProt: the universal protein knowledgebase. *Nucleic Acids Research*, 45(D1):D158–D169, January 2017. ISSN 0305-1048, 1362-4962. doi: 10.1093/nar/gkw1099. URL https://academic.oup.com/nar/article-lookup/doi/10.1093/nar/gkw1099.

[135] E. F. Pettersen, T. D. Goddard, C. C. Huang, G. S. Couch, D. M. Greenblatt, E. C. Meng, and T. E. Ferrin. UCSF Chimera visualization system for exploratory research and analysis. *Journal of Computational Chemistry*, 25(13):1605–1612, October 2004. ISSN 0192-8651, 1096-987X. doi: 10.1002/jcc.20084. URL https://onlinelibrary.wiley.com/doi/10.1002/jcc.20084.

[136] G. Martínez-Rosell, T. Giorgino, and G. De Fabritiis. PlayMolecule ProteinPrepare: A Web Application for Protein Preparation for Molecular Dynamics Simulations. *Journal of Chemical Information and Modeling*, 57(7):1511–1516, July 2017. ISSN 1549-9596, 1549-960X. doi: 10.1021/acs.jcim.7b00190. URL https://pubs.acs.org/doi/10.1021/acs.jcim.7b00190.

[137] M. L. Verdonk, J. C. Cole, M. J. Hartshorn, C. W. Murray, and R. D. Taylor. Improved protein-ligand docking using GOLD. *Proteins: Structure, Function, and Bioinformatics*, 52(4):609–623, August 2003. ISSN 08873585. doi: 10.1002/prot.10465. URL https://onlinelibrary.wiley.com/doi/10.1002/prot.10465.

[138] J. M. Seminario. Calculation of intramolecular force fields from second-derivative tensors. *International Journal of Quantum Chemistry*, 60(7):1271–1277, 1996. ISSN 0020-7608, 1097-461X. doi: 10.1002/(SICI)1097-461X(1996)60:7⟨1271::AID-QUA8⟩3.0.CO;

2-W. URL https://onlinelibrary.wiley.com/doi/10.1002/(SICI)1097-461X(1996)60:7<1271::AID-QUA8>3.0.CO;2-W.

[139] P. Li and K. M. Merz. MCPB.py: A Python Based Metal Center Parameter Builder. *Journal of Chemical Information and Modeling*, 56(4):599–604, April 2016. ISSN 1549-9596, 1549-960X. doi: 10.1021/acs.jcim.5b00674. URL https://pubs.acs.org/doi/10.1021/acs.jcim.5b00674.

[140] D. A. Case, H. M. Aktulga, K. Belfon, I. Y. Ben-Shalom, J. T. Berryman, S. R. Brozell, D. S. Cerutti, T. E. Cheatham III, G. A. Cisneros, V. W. D. Cruzeiro, T. A. Darden, N. Forouzesh, G. Giambaşu, T. Giese, M. K. Gilson, H. Gohlke, A. W. Goetz, J. Harris, S. Izadi, S. A. Izmailov, K. Kasavajhala, M. C. Kaymak, E. King, A. Kovalenko, T. Kurtzman, T. S. Lee, P. Li, C. Lin, J. Liu, T. Luchko, R. Luo, M. Machado, V. Man, M. Manathunga, K. Merz, Y. Miao, O. Mikhailovskii, G. Monard, H. Nguyen, K. A. O'Hearn, A. Onufriev, F. Pan, S. Pantano, R. Qi, A. Rahnamoun, D. R. Roe, C. Roitberg, A. Sagui, S. Schott-Verdugo, A. Shajan, J. Shen, C. L. Simmerling, N. R. Skrynnikov, J. Smith, J. Swails, R. C. Walker, J. Wang, J. Wang, H. Wei, X. Wu, Y. Wu, Y. Xiong, Y. Xue, D. M. York, S. Zhao, Q. Zhu, and P. A. Kollman. Amber 2023, 2023.

[141] A. D. Becke. Density-functional thermochemistry. III. The role of exact exchange. *The Journal of Chemical Physics*, 98(7):5648–5652, April 1993. ISSN 0021-9606, 1089-7690. doi: 10.1063/1.464913. URL https://pubs.aip.org/jcp/article/98/7/5648/842114/Density-functional-thermochemistry-III-The-role-of.

[142] P. C. Hariharan and J. A. Pople. The influence of polarization functions on molecular orbital hydrogenation energies. *Theoretica*

Chimica Acta, 28(3):213–222, 1973. ISSN 0040-5744, 1432-2234. doi: 10.1007/BF00533485. URL http://link.springer.com/10.1007/BF00533485.

[143] M. J. Frisch, G. W. Trucks, H. B. Schlegel, G. E. Scuseria, M. A. Robb, J. R. Cheeseman, G. Scalmani, V. Barone, G. A. Petersson, H. Nakatsuji, X. Li, M. Caricato, A. V. Marenich, J. Bloino, B. G. Janesko, R. Gomperts, B. Mennucci, H. P. Hratchian, J. V. Ortiz, A. F. Izmaylov, J. L. Sonnenberg, D. Williams-Young, F. Ding, F. Lipparini, F. Egidi, J. Goings, B. Peng, A. Petrone, T. Henderson, D. Ranasinghe, V. G. Zakrzewski, J. Gao, N. Rega, G. Zheng, W. Liang, M. Hada, M. Ehara, K. Toyota, R. Fukuda, J. Hasegawa, M. Ishida, T. Nakajima, Y. Honda, O. Kitao, H. Nakai, T. Vreven, K. Throssell, J. A. Montgomery, Jr., J. E. Peralta, F. Ogliaro, M. J. Bearpark, J. J. Heyd, E. N. Brothers, K. N. Kudin, V. N. Staroverov, T. A. Keith, R. Kobayashi, J. Normand, K. Raghavachari, A. P. Rendell, J. C. Burant, S. S. Iyengar, J. Tomasi, M. Cossi, J. M. Millam, M. Klene, C. Adamo, R. Cammi, J. W. Ochterski, R. L. Martin, K. Morokuma, O. Farkas, J. B. Foresman, and D. J. Fox. Gaussian16 Revision B.01, 2016.

[144] R. Woods and R. Chappelle. Restrained electrostatic potential atomic partial charges for condensed-phase simulations of carbohydrates. *Journal of Molecular Structure: THEOCHEM*, 527(1-3): 149–156, August 2000. ISSN 01661280. doi: 10.1016/S0166-1280(00)00487-5. URL https://linkinghub.elsevier.com/retrieve/pii/S0166128000004875.

[145] J. Wang, R. M. Wolf, J. W. Caldwell, P. A. Kollman, and D. A. Case. Development and Testing of a General AMBER Force Field. *Journal of Computational Chemistry*, 25(9):1157–1174, July 2004.

ISSN 0192-8651, 1096-987X. doi: 10.1002/jcc.20035. URL https://onlinelibrary.wiley.com/doi/10.1002/jcc.20035.

[146] S. Izadi, R. Anandakrishnan, and A. V. Onufriev. Building Water Models: A Different Approach. *The Journal of Physical Chemistry Letters*, 5(21):3863–3871, November 2014. ISSN 1948-7185, 1948-7185. doi: 10.1021/jz501780a. URL https://pubs.acs.org/doi/10.1021/jz501780a.

[147] A. W. Götz, M. J. Williamson, D. Xu, D. Poole, S. Le Grand, and R. C. Walker. Routine Microsecond Molecular Dynamics Simulations with AMBER on GPUs. 1. Generalized Born. *Journal of Chemical Theory and Computation*, 8(5):1542–1555, May 2012. ISSN 1549-9618, 1549-9626. doi: 10.1021/ct200909j. URL https://pubs.acs.org/doi/10.1021/ct200909j.

[148] R. Salomon-Ferrer, A. W. Götz, D. Poole, S. Le Grand, and R. C. Walker. Routine Microsecond Molecular Dynamics Simulations with AMBER on GPUs. 2. Explicit Solvent Particle Mesh Ewald. *Journal of Chemical Theory and Computation*, 9(9):3878–3888, September 2013. ISSN 1549-9618, 1549-9626. doi: 10.1021/ct400314y. URL https://pubs.acs.org/doi/10.1021/ct400314y.

[149] H. Kuhn. Structural basis for the positional specificity of lipoxygenases. *Prostaglandins & Other Lipid Mediators*, 62(3):255–270, August 2000. ISSN 10988823. doi: 10.1016/S0090-6980(00)00084-8. URL https://linkinghub.elsevier.com/retrieve/pii/S0090698000000848.

[150] I. Ivanov, A. B. Golovanov, C. Ferretti, M. Canyelles-Niño, D. Heydeck, S. Stehling, J. M. Lluch, González-Lafont, and H. Kühn. Mutations of Triad Determinants Changes the Substrate Alignment

at the Catalytic Center of Human ALOX5. *ACS Chemical Biology*, 14(12):2768–2782, 2019. ISSN 15548937. doi: 10.1021/acschembio.9b00674.

[151] S. Borngräber, M. Browner, S. Gillmor, C. Gerth, M. Anton, R. Fletterick, and H. Kühn. Shape and Specificity in Mammalian 15-Lipoxygenase Active Site. *Journal of Biological Chemistry*, 274(52):37345–37350, December 1999. ISSN 00219258. doi: 10.1074/jbc.274.52.37345. URL https://linkinghub.elsevier.com/retrieve/pii/S002192581953099X.

[152] K. Schwarz, M. Walther, M. Anton, C. Gerth, I. Feussner, and H. Kuhn. Structural Basis for Lipoxygenase Specificity. *Journal of Biological Chemistry*, 276(1):773–779, January 2001. ISSN 00219258. doi: 10.1074/jbc.M005114200. URL https://linkinghub.elsevier.com/retrieve/pii/S0021925818443013.

[153] V. A. Luckow, S. C. Lee, G. F. Barry, and P. O. Olins. Efficient generation of infectious recombinant baculoviruses by site-specific transposon-mediated insertion of foreign genes into a baculovirus genome propagated in Escherichia coli. *Journal of Virology*, 67(8):4566–4579, August 1993. ISSN 0022-538X, 1098-5514. doi: 10.1128/jvi.67.8.4566-4579.1993. URL https://journals.asm.org/doi/10.1128/jvi.67.8.4566-4579.1993.

[154] M. H. M. Olsson, C. R. Søndergaard, M. Rostkowski, and J. H. Jensen. PROPKA3: Consistent Treatment of Internal and Surface Residues in Empirical pKa Predictions. *Journal of Chemical Theory and Computation*, 7(2):525–537, February 2011. ISSN 1549-9618, 1549-9626. doi: 10.1021/ct100578z. URL https://pubs.acs.org/doi/10.1021/ct100578z.

[155] W. L. Jorgensen, J. Chandrasekhar, J. D. Madura, R. W. Impey, and M. L. Klein. Comparison of simple potential functions for simulating liquid water. *The Journal of Chemical Physics*, 79(2): 926–935, July 1983. ISSN 0021-9606, 1089-7690. doi: 10.1063/1.445869. URL `https://pubs.aip.org/jcp/article/79/2/926/776316/Comparison-of-simple-potential-functions-for`.

[156] P. Tosco. A Mechanistic Hypothesis for the Aspirin-Induced Switch in Lipid Mediator Production by Cyclooxygenase-2. *Journal of the American Chemical Society*, 135(28):10404–10410, July 2013. ISSN 0002-7863, 1520-5126. doi: 10.1021/ja402870k. URL `https://pubs.acs.org/doi/10.1021/ja402870k`.

[157] M. J. Frisch, G. W. Trucks, H. B. Schlegel, G. E. Scuseria, M. A. Robb, J. R. Cheeseman, G. Scalmani, V. Barone, G. A. Petersson, H. Nakatsuji, X. Li, M. Caricato, A. Marenich, J. Bloino, B. G. Janesko, R. Gomperts, B. Mennucci, H. P. Hratchian, J. V. Ortiz, A. F. Izmaylov, J. L. Sonnenberg, D. Williams-Young, F. Ding, F. Lipparini, F. Egidi, J. Goings, B. Peng, A. Petrone, T. Henderson, D. Ranasinghe, V. G. Zakrzewski, J. Gao, N. Rega, G. Zheng, M. Liang, W. Hada, M. Ehara, J. Toyota, K. Fukuda, R. Hasegawa, M. Ishida, T. Nakajima, Y. Honda, O. Kitao, H. Nakai, T. Vreven, K. Throssell, J. A. Montgomery Jr., J. E. Peralta, F. Ogliaro, M. Bearpark, J. J. Heyd, E. Brothers, K. N. Kudin, V. N. Staroverov, T. Keith, R. Kobayashi, J. Normand, K. Raghavachari, A. Rendell, J. C. Burant, S. S. Iyengar, M. Tomasi, J. Cossi, J. M. Millam, M. Klene, C. Adamo, R. Cammi, J. W. Ochterski, K. Martin, R. L. Morokuma, O. Farkas, J. B. Foresman, and D. J. Fox. Gaussian09 revision B.01, 2009.

[158] H. J. C. Berendsen, J. P. M. Postma, W. F. Van Gunsteren,

A. DiNola, and J. R. Haak. Molecular dynamics with coupling to an external bath. *The Journal of Chemical Physics*, 81(8):3684–3690, October 1984. ISSN 0021-9606, 1089-7690. doi: 10.1063/1.448118. URL https://pubs.aip.org/jcp/article/81/8/3684/565473/Molecular-dynamics-with-coupling-to-an-external.

[159] J.-P. Ryckaert, G. Ciccotti, and H. J. Berendsen. Numerical integration of the cartesian equations of motion of a system with constraints: molecular dynamics of n-alkanes. *Journal of Computational Physics*, 23(3):327–341, March 1977. ISSN 00219991. doi: 10.1016/0021-9991(77)90098-5. URL https://linkinghub.elsevier.com/retrieve/pii/0021999177900985.

[160] P. P. Ewald. Die Berechnung optischer und elektrostatischer Gitterpotentiale. *Annalen der Physik*, 369(3):253–287, 1921. ISSN 00033804, 15213889. doi: 10.1002/andp.19213690304. URL https://onlinelibrary.wiley.com/doi/10.1002/andp.19213690304.

[161] M. Canyelles-Niño. dynamicsUAB/RCBS.py: 0.2.0, February 2023. URL https://zenodo.org/record/7626048.

[162] P. Sherwood, A. H. De Vries, M. F. Guest, G. Schreckenbach, C. A. Catlow, S. A. French, A. A. Sokol, S. T. Bromley, W. Thiel, A. J. Turner, S. Billeter, F. Terstegen, S. Thiel, J. Kendrick, S. C. Rogers, J. Casci, M. Watson, F. King, E. Karlsen, M. Sjøvoll, A. Fahmi, A. Schäfer, and C. Lennartz. QUASI: A general purpose implementation of the QM/MM approach and its application to problems in catalysis. *Journal of Molecular Structure: THEOCHEM*, 632(1-3):1–28, August 2003. ISSN 01661280. doi: 10.1016/S0166-1280(03)00285-9. URL https://linkinghub.elsevier.com/retrieve/pii/S0166128003002859.

[163] S. Metz, J. Kästner, A. A. Sokol, T. W. Keal, and P. Sherwood. ChemShell—a modular software package for QM/MM simulations. *WIREs Computational Molecular Science*, 4(2):101–110, March 2014. ISSN 1759-0876, 1759-0884. doi: 10.1002/wcms.1163. URL https://onlinelibrary.wiley.com/doi/10.1002/wcms.1163.

[164] S. R. Billeter, A. J. Turner, and W. Thiel. Linear scaling geometry optimisation and transition state search in hybrid delocalised internal coordinates. *Physical Chemistry Chemical Physics*, 2(10): 2177–2186, 2000. ISSN 14639076, 14639084. doi: 10.1039/a909486e. URL http://xlink.rsc.org/?DOI=a909486e.

[165] TURBOMOLE V7.2 2017, a development of University of Karlsruhe and Forschungszentrum Karlsruhe GmbH, 1989-2007, TURBOMOLE GmbH, since 2007; available from http://www.turbomole.com.

[166] W. Smith and T. Forester. DL_poly_2.0: A general-purpose parallel molecular dynamics simulation package. *Journal of Molecular Graphics*, 14(3):136–141, June 1996. ISSN 02637855. doi: 10.1016/S0263-7855(96)00043-4. URL https://linkinghub.elsevier.com/retrieve/pii/S0263785596000434.

[167] D. C. Liu and J. Nocedal. On the limited memory BFGS method for large scale optimization. *Mathematical Programming*, 45(1-3):503–528, August 1989. ISSN 0025-5610, 1436-4646. doi: 10.1007/BF01589116. URL http://link.springer.com/10.1007/BF01589116.

[168] J. Kästner, S. Thiel, H. M. Senn, P. Sherwood, and W. Thiel. Exploiting QM/MM Capabilities in Geometry Optimization: A

Microiterative Approach Using Electrostatic Embedding. *Journal of Chemical Theory and Computation*, 3(3):1064–1072, May 2007. ISSN 1549-9618, 1549-9626. doi: 10.1021/ct600346p. URL https://pubs.acs.org/doi/10.1021/ct600346p.

[169] P. J. Hay and W. R. Wadt. Ab initio effective core potentials for molecular calculations. Potentials for the transition metal atoms Sc to Hg. *The Journal of Chemical Physics*, 82(1):270–283, January 1985. ISSN 0021-9606, 1089-7690. doi: 10.1063/1.448799. URL https://pubs.aip.org/jcp/article/82/1/270/219079/Ab-initio-effective-core-potentials-for-molecular.

[170] K. Ochi, T. Yoshimoto, S. Yamamoto, K. Taniguchi, and T. Miyamoto. Arachidonate 5-lipoxygenase of guinea pig peritoneal polymorphonuclear leukocytes. Activation by adenosine 5'-triphosphate. *The Journal of Biological Chemistry*, 258(9):5754–5758, May 1983. ISSN 0021-9258.

[171] R. A. F. Dixon, R. E. Diehl, E. Opas, E. Rands, P. J. Vickers, J. F. Evans, J. W. Gillard, and D. K. Miller. Requirement of a 5-lipoxygenase-activating protein for leukotriene synthesis. *Nature*, 343(6255):282–284, January 1990. ISSN 0028-0836, 1476-4687. doi: 10.1038/343282a0. URL https://www.nature.com/articles/343282a0.

[172] A. D. Ferguson, B. M. McKeever, S. Xu, D. Wisniewski, D. K. Miller, T.-T. Yamin, R. H. Spencer, L. Chu, F. Ujjainwalla, B. R. Cunningham, J. F. Evans, and J. W. Becker. Crystal Structure of Inhibitor-Bound Human 5-Lipoxygenase-Activating Protein. *Science*, 317(5837):510–512, July 2007. ISSN 0036-8075, 1095-9203.

doi: 10.1126/science.1144346. URL https://www.science.org/doi/10.1126/science.1144346.

[173] J. D. Ho, M. R. Lee, C. T. Rauch, K. Aznavour, J. S. Park, J. G. Luz, S. Antonysamy, B. Condon, M. Maletic, A. Zhang, M. J. Hickey, N. E. Hughes, S. Chandrasekhar, A. V. Sloan, K. Gooding, A. Harvey, X.-P. Yu, S. D. Kahl, and B. H. Norman. Structure-based, multi-targeted drug discovery approach to eicosanoid inhibition: Dual inhibitors of mPGES-1 and 5-lipoxygenase activating protein (FLAP). *Biochimica et Biophysica Acta (BBA) - General Subjects*, 1865(2):129800, February 2021. ISSN 03044165. doi: 10.1016/j.bbagen.2020.129800. URL https://linkinghub.elsevier.com/retrieve/pii/S0304416520303111.

[174] A. L. Lomize, S. C. Todd, and I. D. Pogozheva. Spatial arrangement of proteins in planar and curved membranes by PPM3.0. *Protein Science*, 31(1):209–220, January 2022. ISSN 0961-8368, 1469-896X. doi: 10.1002/pro.4219. URL https://onlinelibrary.wiley.com/doi/10.1002/pro.4219.

[175] ALOX5AP - Arachidonate 5-lipoxygenase-activating protein - Homo sapiens (Human) | UniProtKB | UniProt, . URL https://www.uniprot.org/uniprotkb/P20292/entry#subcellular_location.

[176] S. Jo, T. Kim, V. G. Iyer, and W. Im. CHARMM-GUI: A web-based graphical user interface for CHARMM. *Journal of Computational Chemistry*, 29(11):1859–1865, August 2008. ISSN 01928651. doi: 10.1002/jcc.20945. URL https://onlinelibrary.wiley.com/doi/10.1002/jcc.20945.

[177] S. Jo, J. B. Lim, J. B. Klauda, and W. Im. CHARMM-GUI Membrane Builder for Mixed Bilayers and Its Application to

Yeast Membranes. *Biophysical Journal*, 97(1):50–58, July 2009. ISSN 00063495. doi: 10.1016/j.bpj.2009.04.013. URL https://linkinghub.elsevier.com/retrieve/pii/S0006349509007917.

[178] E. L. Wu, X. Cheng, S. Jo, H. Rui, K. C. Song, E. M. Dávila-Contreras, Y. Qi, J. Lee, V. Monje-Galvan, R. M. Venable, J. B. Klauda, and W. Im. CHARMM-GUI Membrane Builder toward realistic biological membrane simulations. *Journal of Computational Chemistry*, 35(27):1997–2004, October 2014. ISSN 01928651. doi: 10.1002/jcc.23702. URL https://onlinelibrary.wiley.com/doi/10.1002/jcc.23702.

[179] J. Lee, D. S. Patel, J. Ståhle, S.-J. Park, N. R. Kern, S. Kim, J. Lee, X. Cheng, M. A. Valvano, O. Holst, Y. A. Knirel, Y. Qi, S. Jo, J. B. Klauda, G. Widmalm, and W. Im. CHARMM-GUI Membrane Builder for Complex Biological Membrane Simulations with Glycolipids and Lipoglycans. *Journal of Chemical Theory and Computation*, 15(1):775–786, January 2019. ISSN 1549-9618, 1549-9626. doi: 10.1021/acs.jctc.8b01066. URL https://pubs.acs.org/doi/10.1021/acs.jctc.8b01066.

[180] S. Park, Y. K. Choi, S. Kim, J. Lee, and W. Im. CHARMM-GUI Membrane Builder for Lipid Nanoparticles with Ionizable Cationic Lipids and PEGylated Lipids. *Journal of Chemical Information and Modeling*, 61(10):5192–5202, October 2021. ISSN 1549-9596, 1549-960X. doi: 10.1021/acs.jcim.1c00770. URL https://pubs.acs.org/doi/10.1021/acs.jcim.1c00770.

[181] M. A. Lomize, I. D. Pogozheva, H. Joo, H. I. Mosberg, and A. L. Lomize. OPM database and PPM web server: resources for positioning of proteins in membranes. *Nucleic Acids Research*,

40(D1):D370–D376, January 2012. ISSN 1362-4962, 0305-1048. doi: 10.1093/nar/gkr703. URL https://academic.oup.com/nar/article-lookup/doi/10.1093/nar/gkr703.

[182] I. D. Pogozheva, G. A. Armstrong, L. Kong, T. J. Hartnagel, C. A. Carpino, S. E. Gee, D. M. Picarello, A. S. Rubin, J. Lee, S. Park, A. L. Lomize, and W. Im. Comparative Molecular Dynamics Simulation Studies of Realistic Eukaryotic, Prokaryotic, and Archaeal Membranes. *Journal of Chemical Information and Modeling*, 62 (4):1036–1051, February 2022. ISSN 1549-9596, 1549-960X. doi: 10.1021/acs.jcim.1c01514. URL https://pubs.acs.org/doi/10.1021/acs.jcim.1c01514.

[183] J. Huang, S. Rauscher, G. Nawrocki, T. Ran, M. Feig, B. L. De Groot, H. Grubmüller, and A. D. MacKerell. CHARMM36m: an improved force field for folded and intrinsically disordered proteins. *Nature Methods*, 14(1):71–73, January 2017. ISSN 1548-7091, 1548-7105. doi: 10.1038/nmeth.4067. URL https://www.nature.com/articles/nmeth.4067.

[184] R. Venable, A. Sodt, B. Rogaski, H. Rui, E. Hatcher, A. MacKerell, R. Pastor, and J. Klauda. CHARMM All-Atom Additive Force Field for Sphingomyelin: Elucidation of Hydrogen Bonding and of Positive Curvature. *Biophysical Journal*, 107(1):134–145, July 2014. ISSN 00063495. doi: 10.1016/j.bpj.2014.05.034. URL https://linkinghub.elsevier.com/retrieve/pii/S0006349514005724.

[185] J. Lee, X. Cheng, J. M. Swails, M. S. Yeom, P. K. Eastman, J. A. Lemkul, S. Wei, J. Buckner, J. C. Jeong, Y. Qi, S. Jo, V. S. Pande, D. A. Case, C. L. Brooks, A. D. MacKerell, J. B. Klauda, and W. Im. CHARMM-GUI Input Generator for NAMD,

GROMACS, AMBER, OpenMM, and CHARMM/OpenMM Simulations Using the CHARMM36 Additive Force Field. *Journal of Chemical Theory and Computation*, 12(1):405–413, January 2016. ISSN 1549-9618, 1549-9626. doi: 10.1021/acs.jctc.5b00935. URL https://pubs.acs.org/doi/10.1021/acs.jctc.5b00935.

[186] C. W. Hopkins, S. Le Grand, R. C. Walker, and A. E. Roitberg. Long-Time-Step Molecular Dynamics through Hydrogen Mass Repartitioning. *Journal of Chemical Theory and Computation*, 11(4):1864–1874, April 2015. ISSN 1549-9618, 1549-9626. doi: 10.1021/ct5010406. URL https://pubs.acs.org/doi/10.1021/ct5010406.

[187] R. Gowers, M. Linke, J. Barnoud, T. Reddy, M. Melo, S. Seyler, J. Domański, D. Dotson, S. Buchoux, I. Kenney, and O. Beckstein. MDAnalysis: A Python Package for the Rapid Analysis of Molecular Dynamics Simulations. pages 98–105, Austin, Texas, 2016. doi: 10.25080/Majora-629e541a-00e. URL https://conference.scipy.org/proceedings/scipy2016/oliver_beckstein.html.

[188] N. Michaud-Agrawal, E. J. Denning, T. B. Woolf, and O. Beckstein. MDAnalysis: A toolkit for the analysis of molecular dynamics simulations. *Journal of Computational Chemistry*, 32(10):2319–2327, July 2011. ISSN 01928651. doi: 10.1002/jcc.21787. URL https://onlinelibrary.wiley.com/doi/10.1002/jcc.21787.

[189] E. Barreto-Ojeda. MDAnalysis MembraneCurvature Tool, October 2021. URL https://github.com/MDAnalysis/membrane-curvature/.

[190] C. Kluge, M. Pöhnl, and R. A. Böckmann. Spontaneous local membrane curvature induced by transmembrane proteins. *Biophys-*

ical Journal, 121(5):671–683, March 2022. ISSN 00063495. doi: 10.1016/j.bpj.2022.01.029. URL https://linkinghub.elsevier.com/retrieve/pii/S0006349522000790.

[191] M. Peters-Golden and T. Brock. 5-Lipoxygenase and FLAP. *Prostaglandins, Leukotrienes and Essential Fatty Acids*, 69(2-3):99–109, August 2003. ISSN 09523278. doi: 10.1016/S0952-3278(03)00070-X. URL https://linkinghub.elsevier.com/retrieve/pii/S095232780300070X.

[192] N. C. Gilbert, M. E. Newcomer, and O. Werz. Untangling the web of 5-lipoxygenase-derived products from a molecular and structural perspective: The battle between pro- and anti-inflammatory lipid mediators. *Biochemical Pharmacology*, 193:114759, November 2021. ISSN 00062952. doi: 10.1016/j.bcp.2021.114759. URL https://linkinghub.elsevier.com/retrieve/pii/S0006295221003750.

[193] B. Jiménez-García, J. Roel-Touris, M. Romero-Durana, M. Vidal, D. Jiménez-González, and J. Fernández-Recio. LightDock: a new multi-scale approach to protein–protein docking. *Bioinformatics*, 34(1):49–55, January 2018. ISSN 1367-4803, 1367-4811. doi: 10.1093/bioinformatics/btx555. URL https://academic.oup.com/bioinformatics/article/34/1/49/4103399.

[194] J. Roel-Touris, B. Jiménez-García, and A. M. J. J. Bonvin. Integrative modeling of membrane-associated protein assemblies. *Nature Communications*, 11(1):6210, December 2020. ISSN 2041-1723. doi: 10.1038/s41467-020-20076-5. URL https://www.nature.com/articles/s41467-020-20076-5.

[195] J. Roel-Touris, A. M. J. J. Bonvin, and B. Jiménez-García. LightDock goes information-driven. *Bioinformatics*, 36(3):950–

952, February 2020. ISSN 1367-4803, 1367-4811. doi: 10.1093/bioinformatics/btz642. URL https://academic.oup.com/bioinformatics/article/36/3/950/5550626.

[196] B. Jiménez-García, J. Roel-Touris, and D. Barradas-Bautista. The LightDock Server: Artificial Intelligence-powered modeling of macromolecular interactions. *Nucleic Acids Research*, 51(W1): W298–W304, July 2023. ISSN 0305-1048, 1362-4962. doi: 10.1093/nar/gkad327. URL https://academic.oup.com/nar/article/51/W1/W298/7151343.

[197] M. Canyelles-Niño, González-Lafont, and J. M. Lluch. Theoretical Characterization of the Step-by-Step Mechanism of Conversion of Leukotriene A4 to Leukotriene B4 Catalysed by the Enzyme Leukotriene A4 Hydrolase. *International Journal of Molecular Sciences*, 23(6):3140, March 2022. ISSN 1422-0067. doi: 10.3390/ijms23063140. URL https://www.mdpi.com/1422-0067/23/6/3140.

[198] A. Bairoch. The ENZYME database in 2000. *Nucleic Acids Research*, 28(1):304–305, January 2000. ISSN 13624962. doi: 10.1093/nar/28.1.304. URL https://academic.oup.com/nar/article-lookup/doi/10.1093/nar/28.1.304.

[199] B. Samuelsson and C. D. Funk. Enzymes involved in the biosynthesis of leukotriene B4. *The Journal of Biological Chemistry*, 264(33): 19469–19472, November 1989. ISSN 0021-9258.

[200] A. Stsiapanava, U. Olsson, M. Wan, T. Kleinschmidt, D. Rutishauser, R. A. Zubarev, B. Samuelsson, A. Rinaldo-Matthis, and J. Z. Haeggström. Binding of Pro-Gly-Pro at the

active site of leukotriene A4 hydrolase/aminopeptidase and development of an epoxide hydrolase selective inhibitor. *Proceedings of the National Academy of Sciences*, 111(11):4227–4232, March 2014. ISSN 0027-8424, 1091-6490. doi: 10.1073/pnas.1402136111. URL https://pnas.org/doi/full/10.1073/pnas.1402136111.

[201] B. Samuelsson, S.-E. Dahlén, J. Lindgren, C. A. Rouzer, and C. N. Serhan. Leukotrienes and Lipoxins: Structures, Biosynthesis, and Biological Effects. *Science*, 237(4819):1171–1176, September 1987. ISSN 0036-8075, 1095-9203. doi: 10.1126/science.2820055. URL https://www.science.org/doi/10.1126/science.2820055.

[202] J. S. Dickinson and R. C. Murphy. Mass spectrometric analysis of leukotriene A4 and other chemically reactive metabolites of arachidonic acid. *Journal of the American Society for Mass Spectrometry*, 13(10):1227–1234, October 2002. ISSN 1044-0305. doi: 10.1016/S1044-0305(02)00456-7. URL https://pubs.acs.org/doi/10.1016/S1044-0305%2802%2900456-7.

[203] S. Crooks and R. Stockley. Leukotriene B4. *The International Journal of Biochemistry & Cell Biology*, 30(2):173–178, March 1998. ISSN 13572725. doi: 10.1016/S1357-2725(97)00123-4. URL https://linkinghub.elsevier.com/retrieve/pii/S1357272597001234.

[204] O. Rådmark, C. Malmsten, and B. Samuelsson. Leukotriene A4: Enzymatic conversion to leukotriene C4. *Biochemical and Biophysical Research Communications*, 96(4):1679–1687, October 1980. ISSN 0006291X. doi: 10.1016/0006-291X(80)91367-4. URL https://linkinghub.elsevier.com/retrieve/pii/0006291X80913674.

[205] X. Mu and D. Xu. QM/MM Molecular Dynamics Investigations

of the Substrate Binding of Leucotriene A4 Hydrolase: Implication for the Catalytic Mechanism. *The Journal of Physical Chemistry B*, 122(29):7253–7263, July 2018. ISSN 1520-6106, 1520-5207. doi: 10.1021/acs.jpcb.8b04203. URL https://pubs.acs.org/doi/10.1021/acs.jpcb.8b04203.

[206] M. M. Thunnissen, P. Nordlund, and J. Z. Haeggström. Crystal structure of human leukotriene A(4) hydrolase, a bifunctional enzyme in inflammation. *Nature Structural Biology*, 8(2):131–135, February 2001. ISSN 1072-8368. doi: 10.1038/84117.

[207] P. C. Rudberg, F. Tholander, M. M. G. Thunnissen, and J. Z. Haeggström. Leukotriene A4 Hydrolase/Aminopeptidase. *Journal of Biological Chemistry*, 277(2):1398–1404, January 2002. ISSN 00219258. doi: 10.1074/jbc.M106577200. URL https://linkinghub.elsevier.com/retrieve/pii/S002192582087940X.

[208] A. Wetterholm, J. F. Medina, O. Rådmark, R. Shapiro, J. Z. Haeggström, B. L. Vallee, and B. Samuelsson. Leukotriene A4 hydrolase: abrogation of the peptidase activity by mutation of glutamic acid-296. *Proceedings of the National Academy of Sciences*, 89 (19):9141–9145, October 1992. ISSN 0027-8424, 1091-6490. doi: 10.1073/pnas.89.19.9141. URL https://pnas.org/doi/full/10.1073/pnas.89.19.9141.

[209] F. Schautz, H.-J. Flad, and M. Dolg. Quantum Monte Carlo study of Be 2 and group 12 dimers M 2 (M = Zn, Cd, Hg). *Theoretical Chemistry Accounts: Theory, Computation, and Modeling (Theoretica Chimica Acta)*, 99(4):231–240, July 1998. ISSN 1432-881X, 1432-2234. doi: 10.1007/s002140050331. URL http://link.springer.com/10.1007/s002140050331.

[210] J. Kästner, J. M. Carr, T. W. Keal, W. Thiel, A. Wander, and P. Sherwood. DL-FIND: An Open-Source Geometry Optimizer for Atomistic Simulations. *The Journal of Physical Chemistry A*, 113 (43):11856–11865, October 2009. ISSN 1089-5639, 1520-5215. doi: 10.1021/jp9028968. URL https://pubs.acs.org/doi/10.1021/jp9028968.

[211] E. W. Dijkstra. A Note on Two Problems in Connexion with Graphs. *Numerische Mathematik*, 1(1):269–271, December 1959. ISSN 0029-599X, 0945-3245. doi: 10.1007/BF01386390. URL http://link.springer.com/10.1007/BF01386390.

[212] M. J. Mueller, M. Blomster, U. C. Oppermann, H. Jörnvall, B. Samuelsson, and J. Z. Haeggström. Leukotriene A4 hydrolase: protection from mechanism-based inactivation by mutation of tyrosine-378. *Proceedings of the National Academy of Sciences*, 93(12):5931–5935, June 1996. ISSN 0027-8424, 1091-6490. doi: 10.1073/pnas.93.12.5931. URL https://pnas.org/doi/full/10.1073/pnas.93.12.5931.

[213] M. Shinohara, V. Mirakaj, and C. N. Serhan. Functional Metabolomics Reveals Novel Active Products in the DHA Metabolome. *Frontiers in Immunology*, 3, 2012. ISSN 1664-3224. doi: 10.3389/fimmu.2012.00081. URL http://journal.frontiersin.org/article/10.3389/fimmu.2012.00081/abstract.

[214] C. N. Serhan, R. Yang, K. Martinod, K. Kasuga, P. S. Pillai, T. F. Porter, S. F. Oh, and M. Spite. Maresins: novel macrophage mediators with potent antiinflammatory and proresolving actions. *Journal of Experimental Medicine*, 206(1):15–23,

January 2009. ISSN 1540-9538, 0022-1007. doi: 10.1084/jem.20081880. URL https://rupress.org/jem/article/206/1/15/54203/Maresins-novel-macrophage-mediators-with-potent.

[215] A. M. deCathelineau and P. M. Henson. The final step in programmed cell death: phagocytes carry apoptotic cells to the grave. *Essays in Biochemistry*, 39:105–117, October 2003. ISSN 0071-1365, 1744-1358. doi: 10.1042/bse0390105. URL https://portlandpress.com/essaysbiochem/article/doi/10.1042/bse0390105/78070/The-final-step-in-programmed-cell-death-phagocytes.

[216] C. N. Serhan, J. Dalli, R. A. Colas, J. W. Winkler, and N. Chiang. Protectins and maresins: New pro-resolving families of mediators in acute inflammation and resolution bioactive metabolome. *Biochimica et Biophysica Acta (BBA) - Molecular and Cell Biology of Lipids*, 1851(4):397–413, April 2015. ISSN 13881981. doi: 10.1016/j.bbalip.2014.08.006. URL https://linkinghub.elsevier.com/retrieve/pii/S1388198114001619.

[217] T. Hada, N. Ueda, Y. Takahashi, and S. Yamamoto. Catalytic properties of human platelet 12-lipoxygenase as compared with the enzymes of other origins. *Biochimica et Biophysica Acta (BBA) - Lipids and Lipid Metabolism*, 1083(1):89–93, April 1991. ISSN 00052760. doi: 10.1016/0005-2760(91)90128-5. URL https://linkinghub.elsevier.com/retrieve/pii/0005276091901285.

[218] X.-S. Chen, A. R. Brash, and C. D. Funk. Purification and characterization of recombinant histidine-tagged human platelet 12-lipoxygenase expressed in a baculovirus/insect cell system. *European Journal of Biochemistry*, 214(3):845–852, June 1993. ISSN

0014-2956, 1432-1033. doi: 10.1111/j.1432-1033.1993.tb17988.x. URL https://onlinelibrary.wiley.com/doi/10.1111/j.1432-1033.1993.tb17988.x.

[219] J. J. Prusakiewicz, M. V. Turman, A. Vila, H. L. Ball, A. H. Al-Mestarihi, V. D. Marzo, and L. J. Marnett. Oxidative metabolism of lipoamino acids and vanilloids by lipoxygenases and cyclooxygenases. *Archives of Biochemistry and Biophysics*, 464(2):260–268, August 2007. ISSN 00039861. doi: 10.1016/j.abb.2007.04.007. URL https://linkinghub.elsevier.com/retrieve/pii/S0003986107001890.

[220] A. T. Wecksler, C. Jacquot, W. A. Van Der Donk, and T. R. Holman. Mechanistic Investigations of Human Reticulocyte 15- and Platelet 12-Lipoxygenases with Arachidonic Acid. *Biochemistry*, 48(26):6259–6267, July 2009. ISSN 0006-2960, 1520-4995. doi: 10.1021/bi802332j. URL https://pubs.acs.org/doi/10.1021/bi802332j.

[221] B. Deng, C.-W. Wang, H. H. Arnardottir, Y. Li, C.-Y. C. Cheng, J. Dalli, and C. N. Serhan. Maresin Biosynthesis and Identification of Maresin 2, a New Anti-Inflammatory and Pro-Resolving Mediator from Human Macrophages. *PLoS ONE*, 9(7):e102362, July 2014. ISSN 1932-6203. doi: 10.1371/journal.pone.0102362. URL https://dx.plos.org/10.1371/journal.pone.0102362.

[222] M. Canyelles-Niño, González-Lafont, and J. M. Lluch. Hydroperoxidation of Docosahexaenoic Acid by Human ALOX12 and pigALOX15-mini-LOX. *International Journal of Molecular Sciences*, 24(7):6064, March 2023. ISSN 1422-0067. doi: 10.3390/ijms24076064. URL https://www.mdpi.com/1422-0067/24/7/6064.

[223] I. Ivanov, H. Kuhn, and D. Heydeck. Structural and functional biology of arachidonic acid 15-lipoxygenase-1 (ALOX15). *Gene*, 573 (1):1–32, November 2015. ISSN 03781119. doi: 10.1016/j.gene.2015.07.073. URL https://linkinghub.elsevier.com/retrieve/pii/S0378111915009142.

[224] G. Henkelman and H. Jónsson. A dimer method for finding saddle points on high dimensional potential surfaces using only first derivatives. *The Journal of Chemical Physics*, 111(15):7010–7022, October 1999. ISSN 0021-9606, 1089-7690. doi: 10.1063/1.480097. URL https://pubs.aip.org/jcp/article/111/15/7010/475160/A-dimer-method-for-finding-saddle-points-on-high.

[225] J. Kästner and P. Sherwood. Superlinearly converging dimer method for transition state search. *The Journal of Chemical Physics*, 128(1):014106, January 2008. ISSN 0021-9606, 1089-7690. doi: 10.1063/1.2815812. URL https://pubs.aip.org/jcp/article/128/1/014106/928095/Superlinearly-converging-dimer-method-for.

[226] A. M. Aleem, W.-C. Tsai, J. Tena, G. Alvarez, J. Deschamps, C. Kalyanaraman, M. P. Jacobson, and T. Holman. Probing the Electrostatic and Steric Requirements for Substrate Binding in Human Platelet-Type 12-Lipoxygenase. *Biochemistry*, 58(6):848–857, February 2019. ISSN 0006-2960, 1520-4995. doi: 10.1021/acs.biochem.8b01167. URL https://pubs.acs.org/doi/10.1021/acs.biochem.8b01167.

[227] S. C. Perry, C. Kalyanaraman, B. E. Tourdot, W. S. Conrad, O. Akinkugbe, J. C. Freedman, M. Holinstat, M. P. Jacobson, and T. R. Holman. 15-Lipoxygenase-1 biosynthesis of 7S,14S-diHDHA implicates 15-lipoxygenase-2 in biosynthesis of resolvin D5. *Journal*

of Lipid Research, 61(7):1087–1103, July 2020. ISSN 00222275. doi: 10.1194/jlr.RA120000777. URL https://linkinghub.elsevier.com/retrieve/pii/S0022227520435862.

[228] S. Romero-Téllez, A. Cruz, L. Masgrau, González-Lafont, and J. M. Lluch. Accounting for the instantaneous disorder in the enzyme–substrate Michaelis complex to calculate the Gibbs free energy barrier of an enzyme reaction. *Physical Chemistry Chemical Physics*, 23(23):13042–13054, 2021. ISSN 1463-9076, 1463-9084. doi: 10.1039/D1CP01338F. URL http://xlink.rsc.org/?DOI=D1CP01338F.

[229] W. Shang, I. Ivanov, D. I. Svergun, O. Y. Borbulevych, A. M. Aleem, S. Stehling, J. Jankun, H. Kühn, and E. Skrzypczak-Jankun. Probing Dimerization and Structural Flexibility of Mammalian Lipoxygenases by Small-Angle X-ray Scattering. *Journal of Molecular Biology*, 409(4):654–668, June 2011. ISSN 00222836. doi: 10.1016/j.jmb.2011.04.035. URL https://linkinghub.elsevier.com/retrieve/pii/S0022283611004505.

[230] P. Li, A. V. Soudackov, and S. Hammes-Schiffer. Fundamental Insights into Proton-Coupled Electron Transfer in Soybean Lipoxygenase from Quantum Mechanical/Molecular Mechanical Free Energy Simulations. *Journal of the American Chemical Society*, 140 (8):3068–3076, February 2018. ISSN 0002-7863, 1520-5126. doi: 10.1021/jacs.7b13642. URL https://pubs.acs.org/doi/10.1021/jacs.7b13642.

[231] J. Jin, Y. Zheng, W. E. Boeglin, and A. R. Brash. Biosynthesis, isolation, and NMR analysis of leukotriene A epoxides: substrate chirality as a determinant of the cis or trans epoxide configura-

tion. *Journal of Lipid Research*, 54(3):754–761, March 2013. ISSN 00222275. doi: 10.1194/jlr.M033746. URL https://linkinghub.elsevier.com/retrieve/pii/S002222752041939X.

[232] C. J. Smyrniotis, S. R. Barbour, Z. Xia, M. S. Hixon, and T. R. Holman. ATP Allosterically Activates the Human 5-Lipoxygenase Molecular Mechanism of Arachidonic Acid and 5(S)-Hydroperoxy-6(E),8(Z),11(Z),14(Z)-eicosatetraenoic Acid. *Biochemistry*, 53 (27):4407–4419, July 2014. ISSN 0006-2960, 1520-4995. doi: 10.1021/bi401621d. URL https://pubs.acs.org/doi/10.1021/bi401621d.

[233] L. M. Brines, M. K. Coggins, P. C. Y. Poon, S. Toledo, W. Kaminsky, M. L. Kirk, and J. A. Kovacs. Water-Soluble Fe(II)–H2O Complex with a Weak O–H Bond Transfers a Hydrogen Atom via an Observable Monomeric Fe(III)–OH. *Journal of the American Chemical Society*, 137(6):2253–2264, February 2015. ISSN 0002-7863, 1520-5126. doi: 10.1021/ja5068405. URL https://pubs.acs.org/doi/10.1021/ja5068405.

[234] LTA4H - Leukotriene A-4 hydrolase - Homo sapiens (Human) | UniProtKB | UniProt. URL https://www.uniprot.org/uniprotkb/P09960/entry.

Acronyms

α-LA α-linolenic acid.

γ-LA γ-linolenic acid.

$\omega-3$ omega−3.

$\omega-6$ omega−6.

$\omega-9$ omega−9.

***hum*ALOX12** human ALOX12.

***hum*ALOX15B** human ALOX15B.

***hum*ALOX5** human ALOX5.

***mou*Alox15b** mouse Alox15b.

***pig*ALOX15** pig ALOX15.

13*S*,14*S*-eMaR1 13*S*,14*S*-epoxy-MaR1.

14*S*-HpDHA 14*S*-hydroperoxy-DHA.

5*S*-H(p)ETE 5*S*-hydro(per)oxy-ETE.

A adenosine.

AA Arachidonic Acid.

ALOX Lipoxygenase.

ALOX15B ALOX15B.

AMP adenosine monophosphate.

APS ammonium persulfate.

ATP adenosine triphosphate.

C cytosine.

COG center of geometry.

COM center of mass.

COX Cyclooxygenase.

CP chiral phase.

cPLA$_2\alpha$ cytosolic Phospholipase A$_2\alpha$.

DFT Density Functional Theory.

DHA Docosahexaenoic Acid.

DNA Desoxyribonucleic Acid.

ECP Effective Core Potential.

EDTA etylendiamintetraacetic acid.

EPA Eicosapentaenoic Acid.

ER endoplasmic reticulum.

ERO Epoxide Ring Opening.

FLAP Five-Lipoxigenase-Activating Protein.

FPLC fast protein liquid chromatography.

G guanine.

GA Genetic Algorithm.

H(p)DHA hydro(per)oxy-DHA.

H(p)ETE hydro(per)oxyeicosatetraenoic.

HDHA hydroxy-DHA.

HDLC Hybrid Delocalised Coordinates.

HEPE hydroxyeicosapentaenoic.

HETE hydroxyeicosatetraenoic.

HF Hartree-Fock.

HODE hydroxyoctadecadienoic.

HOTrE hydroxyoctadecatrienoic.

HpDHA hydroperoxy-DHA.

HpETE hydroperoxyeicosatetraenoic.

HPLC high-performance liquid chromatography.

INT intermediate.

IPTG isopropyl-β-D-thiogalactopyranoside.

ISET inner-sphere electron transfer.

L-BFGS low-memory Broyden-Fletcher-Goldfard-Shanno.

LA Linoleic Acid.

LB Luria-Bertani.

LOX Lipoxygenase.

LT Leukotriene.

LTA_4 Leukotriene A_4.

LTA_4H Leukotriene A_4 Hydrolase.

LTB_4 Leukotriene B_4.

LTC_4 Leukotriene C_4.

LTC_4S Leukotriene C_4 Synthase.

LTD_4 Leukotriene D_4.

LTE_4 Leukotriene E_4.

LX Lipoxin.

Mϕ Macrophage.

MAPEG membrane-associated proteins in eixosanoid and glutathione metabolism.

MaR1 Maresin-1.

MCS multiple cloning site.

MD Molecular Dynamics.

MEP Minimum Energy Path.

MM Molecular Mechanics.

mRNA messenger Ribonucleic Acid.

MS mass spectrometry.

NBO Natural Bond Orbital.

O/N overnight.

OD optical density.

P Protectin.

P product.

P-RFO partitioned rational function optimiser.

PAGE Polyacrylamide Gel Electrophoresis.

PBS Phosphate-buffered solution.

PCET Proton-Coupled Electron Transfer.

PCR Polymerase Chain Reaction.

PES Potential Energy Surface.

PG Prostaglandin.

PLAT Polycystin-1 Lipoxygenase Alpha-Toxin.

PME Particle Mesh Ewald.

PMN Polymorphonuclear Neutrophil.

PUFA Polyunsaturated Fatty Acid.

QM Quantum Mechanics.

QM/MM Quantum Mechanics/Molecular Mechanics.

R reactant.

RDS Rate Determining Step.

RESP Restrained Electrostatic Potential.

RMSD root-mean-square deviation.

RMSF root-mean-square fluctuation.

RNA Ribonucleic Acid.

RP reverse phase.

rRNA ribosomal Ribonucleic Acid.

Rv Resolvin.

S_N nucleophillic substitution.

SAXS Small-angle X-ray scattering.

SDS Sodium Dodecyl Sulfate.

sEH soluble Epoxide Hydrolase.

SOC super optimal broth with catabolite repression.

SP straight phase.

SPM Specialised Pro-resolving Mediator.

T thymine.

TBS tris buffer solution.

TEMED N,N,N′,N′-tetramethylethylene-diamine.

TRIS tris(hydroxymethyl)aminomethane.

tRNA transfer Ribonucleic Acid.

TS Transition State.

TTBS tween-tris buffer solution.

U uracyl.

WB Western Blot.

WT wild-type.

List of Figures

List of Tables

UAB
Universitat Autònoma
de Barcelona

Theoretical and experimental study of the reaction mechanism of several lipoxygenases and hydrolases: governing their product pattern by mutagenesis

Miquel Canyelles Niño

PhD programme in Chemistry

Directors:
Àngels Conzález Lafont
José Maria Lluch López

Department of Chemistry, Faculty of Science

2023

Volume II: Supporting Information

Contents

Chapter SI6

Characterising Human and Mouse ALOX15B and Crossing Their Reaction Specificities

SI6.1 Publication

International Journal of
Molecular Sciences

MDPI

Article

Functional Characterization of Mouse and Human Arachidonic Acid Lipoxygenase 15B (ALOX15B) Orthologs and of Their Mutants Exhibiting Humanized and Murinized Reaction Specificities

Kumar R. Kakularam [1,†], Miquel Canyelles-Niño [2,3,†], Xin Chen [1], José M. Lluch [2,4], Àngels González-Lafont [2,4] and Hartmut Kuhn [1,*]

[1] Department of Biochemistry, Charité–Universitätsmedizin Berlin, Corporate Member of Freie Universität Berlin and Humboldt Universität zu Berlin, D-10117 Berlin, Germany; kumar.1416@gmail.com (K.R.K.); xin.chen2@charite.de (X.C.)
[2] Departament de Química, Universitat Autònoma de Barcelona, 08193 Barcelona, Spain; miquel.canyelles@uab.cat (M.C.-N.); josemaria.lluch@uab.cat (J.M.L.); angels.gonzalez@uab.cat (À.G.-L.)
[3] Arquebio S.L., 08005 Barcelona, Spain
[4] Institut de Biotecnologia i de Biomedicina (IBB), Universitat Autònoma de Barcelona, 08193 Barcelona, Spain
* Correspondence: hartmut.kuehn@charite.de; Tel.: +49-30-450528040
† These authors contributed equally to this work.

Abstract: The arachidonic acid lipoxygenase 15B (ALOX15B) orthologs of men and mice form different reaction products when arachidonic acid is used as the substrate. Tyr603Asp+His604Val double mutation in mouse arachidonic acid lipoxygenase 15b humanized the product pattern and an inverse mutagenesis strategy murinized the specificity of the human enzyme. As the mechanistic basis for these functional differences, an inverse substrate binding at the active site of the enzymes has been suggested, but experimental proof for this hypothesis is still pending. Here we expressed wildtype mouse and human arachidonic acid lipoxygenase 15B orthologs as well as their humanized and murinized double mutants as recombinant proteins and analyzed the product patterns of these enzymes with different polyenoic fatty acids. In addition, in silico substrate docking studies and molecular dynamics simulation were performed to explore the mechanistic basis for the distinct reaction specificities of the different enzyme variants. Wildtype human arachidonic acid lipoxygenase 15B converted arachidonic acid and eicosapentaenoic acid to their 15-hydroperoxy derivatives but the Asp602Tyr+Val603His exchange murinized the product pattern. The inverse mutagenesis strategy in mouse arachidonic acid lipoxygenase 15b (Tyr603Asp+His604Val exchange) humanized the product pattern with these substrates, but the situation was different with docosahexaenoic acid. Here, Tyr603Asp+His604Val substitution in mouse arachidonic acid lipoxygenase 15b also humanized the specificity but the inverse mutagenesis (Asp602Tyr+Val603His) did not murinize the human enzyme. With linoleic acid Tyr603Asp+His604Val substitution in mouse arachidonic acid lipoxygenase 15b humanized the product pattern but the inverse mutagenesis in human arachidonic acid lipoxygenase 15B induced racemic product formation. Amino acid exchanges at critical positions of human and mouse arachidonic acid lipoxygenase 15B orthologs humanized/murinized the product pattern with C20 fatty acids, but this was not the case with fatty acid substrates of different chain lengths. Asp602Tyr+Val603His exchange murinized the product pattern of human arachidonic acid lipoxygenase 15B with arachidonic acid, eicosapentaenoic acid, and docosahexaenoic acid. An inverse mutagenesis strategy on mouse arachidonic acid lipoxygenase 15b (Tyr603Asp+His604Val exchange) did humanize the reaction products with arachidonic acid and eicosapentaenoic acid, but not with docosahexaenoic acid.

Keywords: eicosanoids; lipids; metabolism; fatty acids; inflammation; atherosclerosis

Citation: Kakularam, K.R.; Canyelles-Niño, M.; Chen, X.; Lluch, J.M.; González-Lafont, À.; Kuhn, H. Functional Characterization of Mouse and Human Arachidonic Acid Lipoxygenase 15B (ALOX15B) Orthologs and of Their Mutants Exhibiting Humanized and Murinized Reaction Specificities. *Int. J. Mol. Sci.* **2023**, *24*, 10046. https://doi.org/10.3390/ijms241210046

Academic Editor: Claudiu T. Supuran

Received: 16 March 2023
Revised: 6 June 2023
Accepted: 8 June 2023
Published: 12 June 2023

Int. J. Mol. Sci. **2023**, *24*, 10046

1. Introduction

In the human genome, six different arachidonate lipoxygenase (*ALOX*) genes have been detected [1] and these genes encode for six functionally distinct ALOX isoforms). In the reference genome of mice, an orthologous enzyme exists for each human ALOX isoform, but in addition a functional *Aloxe12* gene [1,2] encoding for the Aloxe12 has been identified [3]. In humans, the *ALOXE12* gene is a corrupted pseudogene [1,2]. The human *ALOX15B* gene is located in a common *ALOX* gene cluster present on the short arm of chromosome 17 [2]. The mouse *Alox15b* gene is located in a similar *Alox* gene cluster that is localized in a synthetic region on chromosome 11 [1,2].

ALOX-isoforms are lipid peroxidizing enzymes that convert polyunsaturated fatty acids to the corresponding hydroperoxides [4,5]. In cellular systems these peroxides are rapidly reduced to the corresponding alcohols [6]. Alternatively, the peroxides are further converted to more complex secondary ALOX products such as pro-inflammatory leukotrienes [7] or anti-inflammatory resolvins, maresins, and protectins [8,9], which are collectively named specialized pro-resolving mediators (SPMs). Although the biosynthetic pathways of SPMs are rather diverse and although the SPM-induced intracellular signaling mechanisms are far from clear [9], these compounds exhibit a large number of interesting bioactivities [9]. The majority of ALOX isoforms prefer free polyenoic fatty acids as the substrate and under in vivo conditions the formation of ALOX products is limited by the liberation of the polyenoic fatty acids (PUFAs) from cellular ester lipids [10]. However, some isoforms, in particular human ALOX15 and human ALOX15B accept esterified polyenoic fatty acids as the substrate even if they are presented in complex lipid-protein-assemblies, such as nanodiscs [11,12], biomembranes [13–15], and different classes of lipoproteins [16–18].

In 1997, human ALOX15B was first described as AA 15-lipoxygenating enzyme, which is high level expressed in human skin, in the prostate, in the lungs and in the cornea [19]. The enzyme was cloned from hair routes and has been implicated in hair growth and skin development [19]. Later experiments indicated that the enzyme is also expressed in human monocytes when these cells are differentiated in vitro to macrophages. Stimulation of these cells with the Th2 cytokines interleukins-4 and -13 upregulated the expression of the enzyme [20]. When human peripheral monocytes are long-term stimulated with toll-like receptor-2/4 agonists, ALOX15B expression is also upregulated and this treatment induced a switch in the lipid mediator profile produced by these cells [21]. Despite these findings the biological relevance of ALOX15B orthologs is far from clear. A recent review nicely summarizes the potential biological functions of human ALOX15B, but this paper also indicates that there is no unifying concept for the biological role of ALOX15B [22].

Mouse Alox15b was first described in 1991 in phorbol ester-treated mouse skin [23]. This enzyme, which was later on cloned and expressed as recombinant protein [24] converted exogenous arachidonic acid to 8-HETE and it was therefore originally called mouse 8-LOX [23]. Today we know that this enzyme constitutes the mouse ortholog of human ALOX15B and it should therefore be called Alox15b. Mouse and human ALOX15B share a high (78%) degree of amino acid identity and the two *ALOX15B* genes have similar structures [1]. They both span some 10 Mbp and consist of 14 exons and 13 introns. Thus, from a structural point of view, the two enzymes are very similar. On the other hand, the two enzymes exhibit different catalytic properties, and these data suggest that their biological functions in mice and men might be different. One of the most striking differences between the two ALOX15B orthologs is their different product pattern when arachidonic acid is sued as the substrate. Human ALOX15B [19,25] catalyzes the stereospecific oxygenation of AA to 15S-HpETE (15S-hydroperoxy-5Z,8Z,11Z,13E-eicosatetraenoic acid). In contrast, mouse Alox15b [23] converts the same substrate to 8S-HpETE (8S-hydroperoxy-5Z,9,9E,11Z,14Z-eicosatetraenoid acid). Interestingly, such differences in the product mixture of the two enzymes were not observed when complex substrates such as AA-containing phospholipids and/or AA containing phospholipid loaded nanodiscs were used as the substrate [11]. In fact, with these substrates 15-HETE was identified as the major oxygenation product for mouse and human ALOX15B orthologs [11].

The molecular basis for the differential product patterns of mouse and human ALOX15B has been explored and in vitro mutagenesis studies indicated that the Tyr603Asp+His604Val mutant of mouse Alox15b formed similar reaction products as wildtype human ALOX15B [25]. An inverse mutagenesis strategy (Asp602Tyr+Val603His exchange in human ALOX15B) partially murinized the product pattern of the human enzyme [25]. To test whether the product pattern of mouse Alox15b can also be humanized in vivo, knock-in mice were recently created, which express the humanized AA 15-lipoxygenting Tyr603Asp+His604Val double mutant of mouse Alox15b instead of the AA 8-lipoxygenating mouse wildtype enzyme [26]. These mice are viable and breed normally [26], but the erythrocyte parameters of male knock-in individuals are compromised [26].

As indicated above, the Asp602Tyr+Val603His exchange murinized the product pattern of human ALOX15B with arachidonic acid and an inverse mutagenesis strategy on mouse Alox15b (Tyr603Asp+His604Val exchange) humanized the product mixture of this enzyme. However, whether this humanization of mouse Alox15b and murinization of human ALOX15B can also be observed when other polyenoic fatty acid are used as substrate has not been explored in detail. To fill this gap, we expressed the four enzyme variants as recombinant proteins and tested under strictly comparable experimental conditions their reaction specificities with different substrates (oxygenated and non-oxygenated polyenoic fatty acids). We found that human and mouse ALOX15B orthologs exhibit differential reaction specificities with all free polyenoic fatty acid derivatives tested (AA, EPA, DHA, LA, 15-HETE, and 8-HETE) and that the product pattern of the mouse enzyme can be humanized by Tyr603Asp+His604Val exchange. When an inverse mutagenesis strategy was applied for human ALOX15B, the product mixture was murinized for AA and EPA oxygenation, but the major DHA oxygenation product was identified as 7-HDHA. Thus, with this substrate fatty acid the product pattern was not murinized. To explore the molecular basis for the observed functional differences we carried out substrate docking studies and performed molecular dynamics simulations, and the obtained in silico data are consistent with our experimental observations.

2. Results

2.1. Recombinant Expression of Mouse and Human ALOX15B Orthologs and of Selected Mutants

Human ALOX15B oxidizes arachidonic acid to 15-HETE but its D602Y+V603H mutant forms a 2:1 mixture of 8-HETE and 12-HETE [25]. Thus, with arachidonic acid the D602Y+V603H double mutant of human ALOX15B forms similar products as wildtype mouse Alox15b. On the other hand, mouse Alox15b forms almost exclusively to 8-HETE from AA but its Y603D+H604V mutant dominantly produces 15-HETE [25] and thus, this enzyme mutant forms humanized reaction products [25].

To test whether murinization of human ALOX15B and humanization of mouse Alox15b ortholog can also be seen when other substrate fatty acids are used, we expressed the four enzyme species (wildtype human ALOX15B, D602Y+V603H mutant of human ALOX15B, wildtype mouse Alox15b, and Y603D+H604V mutant of mouse Alox15b) as his-tag fusion proteins in *E. coli* and quantified the expression levels of the four enzyme variants by quantitative immunoblotting using an anti-his-tag antibody (Figure 1). The expression levels of the different recombinant proteins are summarized in (Table 1). It can be seen that all ALOX15B variants are well expressed in *E. coli* and that mouse Alox15b reached an expression level of about 700 mg Alox15b protein per liter bacterial liquid culture. Next, we attempted to purify the recombinant proteins by affinity chromatography on Ni-agarose gel. The two wildtype enzymes could well be purified as catalytically active proteins employing this purification technique.

Int. J. Mol. Sci. **2023**, *24*, 10046

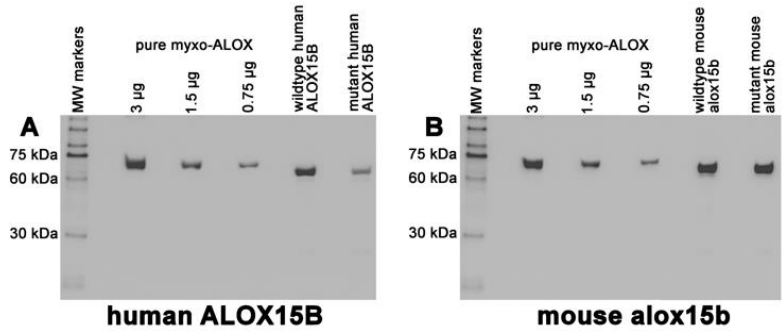

Figure 1. Quantification of the expression levels of human and mouse ALOX15B variants. ALOX15B variants were expressed in *E. coli* and aliquots of the bacterial lysis supernatants were analyzed by quantitative immunoblotting (see Section 4). A total of 1 µL human wildtype supernatant; 1.1 µL human D602Y+V603H mutant supernatant; 0.5 µL wildtype mouse supernatant; 1.2 µL mouse Y603D+H604V supernatant. The band intensity scale was calibrated applying known amounts of the pure recombinant N-terminal his-tag fusion protein of *M. fulvus* ALOX. (**A**) Human ALOX15B, (**B**) Mouse Alox15b.

Table 1. Expression levels of the different recombinant ALOX15B variants. ALOX15B variants were expressed in *E. coli* and bacterial lysis supernatants were prepared as described in Section 4. Aliquots of the lysis supernatants were analyzed by quantitative immunoblotting using an anti-hist-tag antibody for specific staining of the ALOX bands. SDS-PAGE and immunoblotting were carried out as described in Section 4. The band intensity scale was calibrated by applying known amounts (3 µg, 1.5 µg, 0.75 µg) of the pure recombinant N-terminal his-tag fusion protein of *M. fulvus* ALOX as the reference protein [27].

Enzyme Variant	Expression Level (mg ALOX Protein per L Bacterial Liquid Culture)
Wildtype human ALOX15B	200
Wildtype mouse Alox15b	700
D602Y+V603H mutant (human ALOX15B)	170
Y603D+H604V mutant (mouse Alox15b)	292

Unfortunately, the D602Y+V603H mutant of human ALOX15B lost more than 90% of its catalytic activity during the purification procedure. To ensure strict comparability of the functional data we used crude enzyme preparations (bacterial lysate supernatant) for functional characterization.

2.2. Mouse and Human ALOX15B Variants Prefer C20 and C22 Polyenoic Fatty Acids over Linoleic Acid (C18)

To test the substrate specificity of human and mouse ALOX15B variants in vitro activity assays using linoleic acid (LA), 5,8,11,14,17-eicosapentaenoic acid (EPA), arachidonic acid (AA), and 4,7,10,13,16,19-docosahexaenoic acid (DHA) as ALOX substrates were performed. When we set the catalytic activity of the different enzyme variants with AA 100% and calculated the relative catalytic activities with the other polyenoic fatty acids we found (Figure 2A, left columns) that wildtype human ALOX15 prefers DHA as substrate. EPA and AA were also oxygenated with relatively high reaction rates, but linoleic acid was not a good substrate for this enzyme. This data is consistent with previous reports on the substrate specificity of human ALOX15B [19].

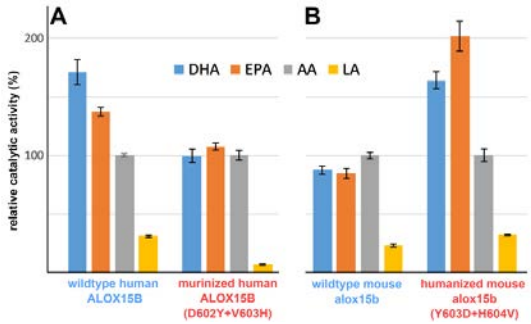

Figure 2. Substrate specificity of human and mouse ALOX15 variants with different polyunsaturated fatty acids. ALOX15B variants were expressed in *E. coli* and aliquots of the bacterial lysis supernatants were incubated in vitro for 5 min with different polyunsaturated fatty acids. After the incubation period the produced hydroperoxy fatty acids were reduced to their more stable hydroxy derivatives and products carrying a conjugated diene chromophore were quantified by RP-HPLC. Two incubation samples were set up for each fatty acid substrate and each sample was analyzed twice. The product formation from AA by each enzyme preparation was set 100% and the relative amounts of conjugated dienes formed from the other substrates were calculated. (**A**) Human ALOX15B, (**B**) mouse Alox15b.

When we tested the substrate specificity of the human ALOX15B D602Y+V603H double mutant DHA, EPA and AA were equally well oxygenated but LA was not a good substrate (Figure 2A, right columns). Similar experiments were subsequently carried out with mouse Alox15b and its Y603D+H604V double mutant. The wildtype enzyme converted DHA, EPA, and AA with similar reaction rates but here again, LA was not a good substrate (Figure 2B, left columns). For the mouse Alox15b Y603D+H604V double mutant EPA was the preferred polyenoic fatty acid substrate followed by DHA and AA. For this enzyme variant, LA was also not a good substrate in the absence of detergents (Figure 2B, right columns). The addition of sodium cholate improved the substrate behavior of LA [28] and this effect might be related to the allosteric properties of this enzyme [29]. However, since cholate is absent in most mammalian cells at these relatively high concentrations, we did not test the impact of this detergent on the reaction rate and on the product pattern in this study.

It should be stressed at this point that the data shown in Figure 2 characterize the product mixtures formed by the four different recombinant enzymes during a 5 min incubation period (end point measurements). Unfortunately, more detailed kinetic studies could not be carried out since our crude enzyme preparation did not allow spectrophotometric measurements following the increase in absorbance at 235 nm (formation of conjugated dienes).

2.3. D602Y+V603H Exchange Partly Murinized the Reaction Products Formed by Human ALOX15B with EPA and AA but Altered the Product Pattern with DHA in a Different Way

Human ALOX15B converts AA to 15-H(p)ETE [19,25] but D602Y+V603H exchange partly murinized the product pattern [25]. In fact, for this double mutant 8S-H(p)ETE was identified as major AA oxidation product. Whether such murinization of the product pattern can also be observed with other substrates has not been explored. To answer this question, we incubated wildtype human ALOX15B and its D602Y+V603H double mutant with different polyenoic fatty acids and analyzed the reaction products by RP-HPLC. As shown in Figure 3A, 15-H(p)ETE was the almost exclusive AA oxygenation product formed by the wildtype enzyme. However, for the D602Y+V603H double mutant a mixture of 8-H(p)ETE, 15-H(p)ETE, and 5-H(P)ETE was analyzed. This data confirmed the previous finding that D602Y+V603H exchange partly murinized the product mixture of human ALOX15B [25] but our results also indicate that the mutant enzyme formed a

Int. J. Mol. Sci. **2023**, *24*, 10046

significant share of 5-HETE as minor (15–20% of the total conjugated dienes formed) side product. Interestingly, combined NP/CP-HPLC indicated that this minor side product was completely chiral (5S-HETE), suggesting that the 5S-HETE formation was completely enzyme-controlled.

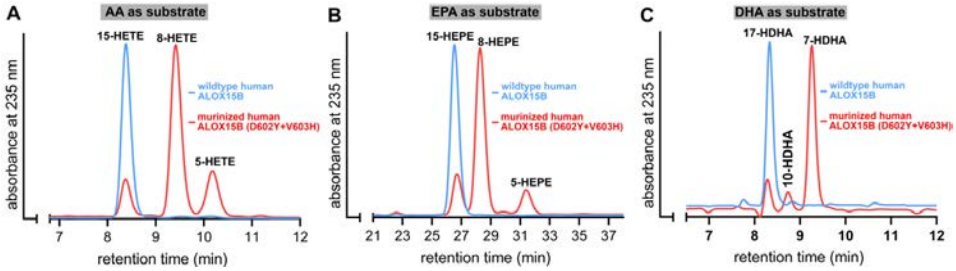

Figure 3. D602Y+V603H exchange partly murinized the product mixture of human ALOX15B with different polyenoic fatty acids. ALOX15B variants were expressed in *E. coli* and aliquots of the bacterial lysis supernatants were used to perform in vitro activity assays were carried out as described in the legend of Figure 2. Representative partial RP-HPLC chromatograms are shown. The chemical identity of the conjugated dienes formed during the 5 min incubation period was concluded by co-chromatography with authentic standards. Oxygenation products of AA and DHA were analyzed isocratically using a solvent system consisting of acetonitrile/water/acetic acid (70/30/0.1, by vol). The EPA oxygenation products were analyzed isocratically with the solvent system acetonitrile/water/acetic acid (50/50/0.1, by vol). (**A**) Arachidonic acid as substrate, (**B**) eicosapentaenoic acid as substrate, (**C**) docosahexaenoic acid as substrate.

Similar incubations were performed with EPA (Figure 3B) and DHA (Figure 3C). As expected from the product profile of AA oxygenation, 15-HEPE was the major EPA oxygenation product formed by wildtype human ALOX15B. In contrast, 8-HEPE was the major EPA oxygenation product formed by the D602Y+V603H double mutant of human ALOX15B. In addition, smaller amounts of 15-H(p)EPE and 5-H(p)EPE were found. Thus, the oxygenation products formed from AA and EPA by wildtype human ALOX15B and its D602Y+V603H double mutant were very similar. In contrast, with DHA the situation was somewhat different. Wildtype human ALOX15B oxygenated this highly unsaturated polyenoic fatty acid almost exclusively to 17-HDHA and this simple product pattern could be predicted on the basis of the analysis of the AA and EPA oxygenation products. Interestingly, the major DHA oxidation product formed by the D602Y+V603H double mutant was not 10-HDHA (the equivalent DHA oxygenation product of 8-HETE) but 7-HDHA instead. This product is the equivalent DHA oxygenation product of 5-HETE. 17-HDHA and 10-HDHA were also detected in minor quantities.

2.4. Y603D+H604V Mutation Humanized the Product Pattern of Mouse Alox15b with AA, EPA and DHA

Mouse Alox15b converts AA to 8-HETE but the Y603D+H604V exchange humanized the product mixture of this enzyme [25]. For this mutant, 15S-HETE was identified as the major AA oxidation product [25]. When we incubated mouse Alox15b and its Y603D+H604V mutant with AA we confirmed these results. 8-HETE was the major wildtype enzyme product whereas the Y603D+H604V double mutant produced 15-HETE (Figure 4A). When EPA was used as the substrate, 8-HEPE was analyzed as the major oxygenation product of the wildtype enzyme, but 15-HEPE was dominantly formed by the Y603D+H604V double mutant (Figure 4B).

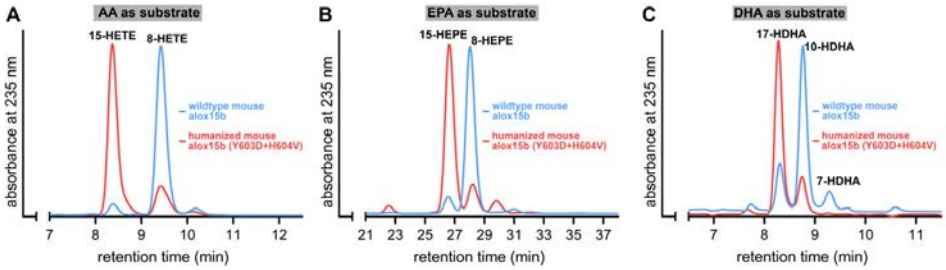

Figure 4. The Y603D+H604V exchange humanized the product pattern of mouse Alox15b with different polyenoic fatty acids. Mouse Alox15b variants were expressed in *E. coli* and aliquots of the bacterial lysis supernatants were used to perform in vitro activity assays as described in the legend of Figure 2. Representative partial RP-HPLC chromatograms are shown. The chemical identity of the conjugated dienes formed during the 5 min incubation period was concluded by co-chromatography with authentic standards. Oxygenation products of AA and DHA were analyzed isocratically using a solvent system consisting of acetonitrile/water/acetic acid (70/30/0.1, by vol). The EPA oxygenation products were analyzed isocratically with the solvent system acetonitrile/water/acetic acid (50/50/0.1, by vol). (**A**) Arachidonic acid as substrate, (**B**) eicosapentaenoic acid as substrate, (**C**) docosahexaenoic acid as substrate.

Finally, we explored the DHA oxygenation products formed by these two enzyme variants and found that, as expected from the product profiles of AA and EPA oxygenation, 10-HDHA was mainly formed by the wildtype enzyme whereas 17-HDHA dominated the product pattern produced by the Y603D+H604V double mutant (Figure 4C). Taken together these data indicated that the Y603D+H604V exchange humanized the product pattern of mouse Alox15b not only with AA but also with EPA and DHA. The outcome of the DHA experiments was of particular interest since the inverse mutagenesis strategy of human ALOX15B (D602Y+V603H exchange) murinized the reaction products of AA and EPA oxygenation by human ALOX15 (Figure 3A,B) but not the product pattern of DHA oxygenation (Figure 3C).

2.5. D602Y+V603H Exchange in Human ALOX15B and Y603D+H604V Mutation of Mouse Alox15b also Altered the Reaction Products of Linoleic Acid Oxygenation

In the absence of detergents, linoleic acid was not a good substrate for either human or mouse ALOX15B (Figure 2). Nevertheless, we analyzed the product mixture formed by the four different enzyme variants from these polyenoic fatty acids, which abundantly occurs in most mammalian cells. For this purpose, in vitro activity assays were carried out (Figure 2), and the conjugated dienes formed were prepared by RP-HPLC and further analyzed by the combined normal phase/chiral phase HPLC (NP/CP-HPLC). With linoleic acid as the substrate only four major ALOX products (13*S*-HODE, 13*R*-HODE, 9*S*-HODE, 9*R*-HODE) can be formed and all of them are well separated by our combined NP/CP-HPLC analytical protocol.

As expected, the major LA oxygenation product of wildtype human ALOX15B was 13*S*-HODE. 13*R*-HODE and the two 9-HODE enantiomers (9*S*- and 9*R*-HODE) were only formed in small amounts (Figure 5A). Interestingly, the major LA oxygenation product formed by the mouse wildtype Alox15b was 9S-HODE and here again, the other HODE isomers were only minor side products (Figure 5C). The human ALOX15B D602Y+V603H double mutant exhibited only a very low catalytic activity with this fatty acid and here we observed a complex mixture of all four LA oxygenation products. However, 9- and 13-HODE were not complete racemic mixtures since for each positional isomer the S-enantiomer prevailed (*S*/*R*-ratio of 7:3) for the two positional isomers. The Y603D+H604V double mutant of mouse Alox15b dominantly formed 13*S*-HODE and thus, the product pattern of the mouse Alox15b with linoleic acid was fully humanized.

Int. J. Mol. Sci. **2023**, *24*, 10046

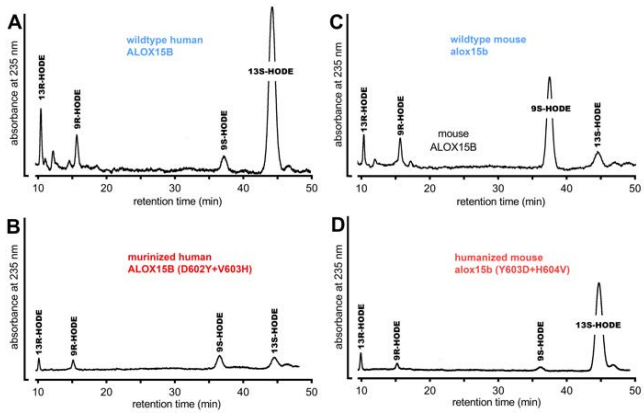

Figure 5. Product patterns of mouse and human wildtype ALOX15 orthologs and of their murinized (D602Y+V603H) and humanized (Y603D+H604V) double mutants using linoleic acid as the substrate. The different ALOX15B variants were expressed as N-terminal his-tag fusion proteins in *E. coli* and aliquots of the bacterial lysis supernatants were used to perform in vitro activity assays (Figure 2). The conjugated dienes formed during the incubation period were prepared by RP-HPLC and were further analyzed by NP/CP-HPLC. Representative partial RP-HPLC chromatograms are shown. The chemical identity of the conjugated dienes formed during the incubation period was concluded by co-chromatography with authentic standards. The chromatographic conditions of NP/CH-HPLC are described in detail in Section 4. (**A**) Wildtype human ALOX15B, (**B**) murinized human ALOX15B (D602Y+V603H), (**C**) wildtype mouse Alox15B, (**D**) humanized mouse Alox15b (Y603D+H604V).

2.6. MD Simulations Suggest an Alternative Fatty Acid Binding at the Active Site of Human and Mouse ALOX15 Orthologs

Human and mouse ALOX15 orthologs share a high degree of amino acid conservation but the catalytic properties of the two enzymes are remarkably different. Human ALOX15B oxygenates AA and EPA to the 15-oxygenation products (Figure 3A,B) whereas mouse Alox15b dominantly forms the 8-oxygenation products from these two PUFAs. A plausible explanation for the different product patterns was an inverse substrate alignment at the active site of the two enzymes. For 15-HETE formation by human ALOX15B a tail-first substrate alignment at the active site can be suggested [30]. Such substrate binding allows hydrogen abstraction from C13 and [+2] radical rearrangement. In contrast, 8-lipoxygenation by mouse Alox15b may involve head-first substrate alignment, hydrogen abstraction from C10, and [−2] radical rearrangement.

To test these hypotheses, we have carried out docking calculations of the substrates AA, EPA, DHA, and LA at the active sites of the four enzyme variants. For each case, we have selected the five more stable structures and classified them according to the preference of tail-first (TF) or head-first (HF) substrate alignment. The results are shown in Table 2. Despite the limited accuracy of such docking calculations, it can be seen that the four substrates preferentially tend to adopt a tail-first alignment in wildtype human ALOX15B and in the Y603D+H604V mutant of mouse Alox15b. In contrast, a head-first orientation was preferred in the D602Y+V603H mutant of human ALOX15B and in wildtype mouse Alox15b. To visualize these results, images of the tail-first alignment of AA (the carboxylate pointing to the protein surface, Figure 6A) in wildtype human ALOX15B, and of the head-first alignment of AA in wildtype mouse Alox15b (the carboxylate facing to the bottom of the enzyme, Figure 6B) are illustrated. In both cases, AA adopts a U-shaped structure in the substrate binding pocket.

Table 2. The five most stable structures of the substrates AA, EPA, DHA, and LA at the active sites of the four enzymes, according to docking calculations. Total free energy change (kJ/mol) that occurs on ligand binding and substrate alignment (Tail-first (TF) or Head-first (HF)). The TF solutions are highlighted in blue, and the HF solutions in pink.

Substrate	***AA***		***EPA***		***DHA***		***LA***	
Enzyme	**ΔG^{bind}**	**Orient.**	**ΔG^{bind}**	**Orient.**	**ΔG^{bind}**	**Orient.**	**ΔG^{bind}**	**Orient.**
Human ALOX15B WT	−57.26	TF	−64.38	TF	−69.23	TF	−58.15	TF
	−57.25	TF	−62.69	TF	−67.46	TF	−55.08	TF
	−57.21	TF	−59.66	TF	−62.39	TF	−54.38	TF
	−51.22	HF	−58.93	TF	−56.63	TF	−53.22	TF
	−51.00	TF	−56.36	TF	−55.85	HF	−52.51	TF
Human ALOX15B mut	−39.43	HF	−39.75	TF	−43.77	HF	−35.09	HF
	−39.13	HF	−39.34	HF	−43.71	TF	−34.82	TF
	−39.01	HF	−38.98	HF	−43.56	TF	−34.78	TF
	−38.97	HF	−38.93	TF	−43.51	HF	−34.70	TF
	−38.87	TF	−38.89	TF	−43.44	TF	−34.68	TF
Mouse Alox15b WT	−41.44	HF	−41.47	HF	−45.98	HF	−36.15	HF
	−40.12	TF	−41.19	HF	−45.23	HF	−35.76	TF
	−39.69	TF	−41.04	HF	−44.87	HF	−35.57	TF
	−39.08	TF	−41.02	HF	−44.56	TF	−35.36	TF
	−39.07	TF	−40.88	HF	−44.16	TF	−35.34	TF
Mouse Alox15b mut	−42.56	TF	−43.64	TF	−49.03	TF	−49.03	TF
	−42.56	HF	−43.28	HF	−47.95	TF	−47.95	TF
	−42.52	TF	−42.63	TF	−46.30	TF	−46.30	TF
	−42.12	TF	−42.51	TF	−46.08	TF	−46.08	TF
	−41.65	TF	−42.29	TF	−46.00	TF	−46.00	TF

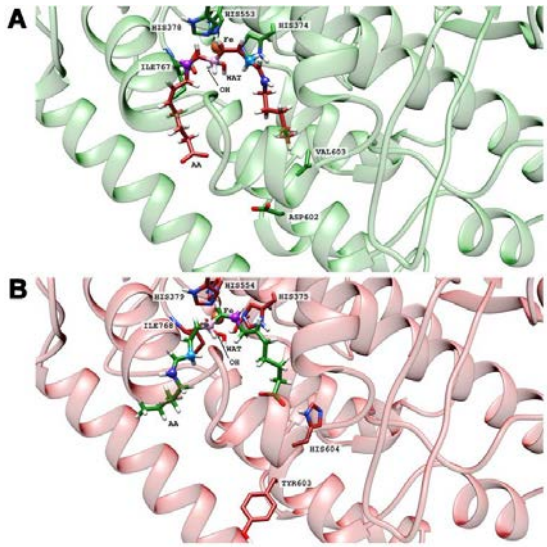

Figure 6. Tail-first alignment of AA (**A**) in wildtype human ALOX15B in green, and head-first alignment of AA (**B**) in wildtype mouse Alox15b in pink.

Int. J. Mol. Sci. **2023**, *24*, 10046

After our docking calculations revealed the preferred substrate alignment for each enzyme-substrate complex, we employed molecular dynamics (MD) simulations to explore which hydrogen atoms are located at a suitable position for productive hydrogen abstraction from a bisallylic methylene. In principle, AA involves three different bisallylic methylene groups and each of these carbon atoms carry two hydrogen atoms, which can be abstracted during initial hydrogen removal. To explore which of these hydrogen atoms are suitable candidates for hydrogen abstraction, we focused on AA and ran eight MD simulations (100 ns each). These simulations mirror both HF and TF substrate orientation at the active site of the four different enzyme species (wildtype human ALOX15B, D602Y+V603H mutant of human ALOX15B, wildtype mouse Alox15b, and Y603D+H604V mutant of mouse Alox15b). Each simulation started from the energetically most favorable complex obtained in our docking studies. The evolution of the distances between the oxygen atom of the Fe(III)-OH^- cofactor (catalytically competent ALOX species) and the closest hydrogen atom attached to C7 (H7), C10 (H10) and C13 (H13) of AA along the MD simulations is pictured in Figure 7 and Figure S1 and the corresponding average distances are summarized in Table 3.

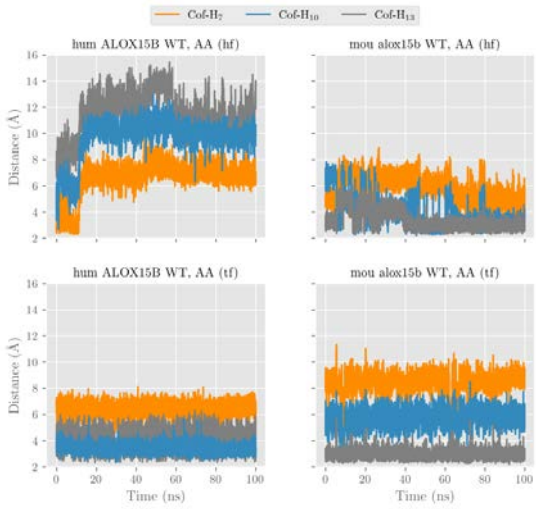

Figure 7. Distances from the oxygen atom in the Fe(III)-OH^- cofactor to the closest hydrogen atom attached to C7 (H7), C10 (H10), and C13 (H13) along the molecular dynamics simulations for AA (HF or TF) at the active site of wildtype human ALOX15B and wildtype mouse Alox15b.

Table 3. Average distances (Å) from the oxygen atom in the Fe(III)-OH^- cofactor to the closest hydrogen atom attached to C7 (H7), C10 (H10), and C13 (H13) along the molecular dynamics simulations for AA (HF or TF) at the active site of the different enzymes.

Substrate Orientation	Human						Mouse					
	WT			Mutant			WT			Mutant		
	H7	H10	H13	H7	H10	H13	H7	H10	H13	H7	H10	H13
AA (HF)	6.6	9.7	11.4	7.2	5.7	3.4	5.8	3.9	3.4	8.5	6.9	5.5
AA (TF)	6.4	3.4	4.2	6.5	4.6	4.8	8.4	5.8	3.0	7.4	4.8	3.2

In wildtype human ALOX15B the carboxylate group of AA in the HF alignment is destabilized by D602 and V603. A similar destabilizing effect was observed by D603 and V604 in the humanized Y603D+H604V double mutant of mouse Alox15b. Because of these

destabilizing effects, AA is unable to establish a strong non-covalent interaction with any residue in the depth of the enzyme cavity and it tends to move away towards the protein surface. The large average distances given in Table 3 confirm this trend.

Conversely, the strong interaction between the AA carboxylate and Arg428 stabilizes the position of TF AA alignment inside the substrate binding pocket. Thus, the tail-first orientation turns out to be the preferred way of substrate alignment and this data is consistent with the docking calculations and with the observed 15-HETE formation by wildtype human ALOX15B and the humanized mouse mutant. In our MD simulations many structures with H13 and/or H10 at distances suitable for hydrogen abstraction appear for both wildtype human ALOX15B, and the humanized Y603D+H604V double mutant of mouse Alox15b. Consequently, the average distances varying between 3.2 and 4.8 Å are rather small.

For those enzyme variants carrying a Tyr and a His in the core of the enzymes (wildtype mouse Alox15b and D602Y+V603H mutant of human ALOX15B) the AA carboxylate can form stabilizing hydrogen bonds independently of whether AA is aligned with HF or TF. In both cases, the enzyme-substrate complex remains stable, with H13 and H10 being located close to the oxygen of the cofactor (Figure 7 and Figure S1, Table 3).

In any alignment for any of the four studied enzymes H7 was always rather distant from Fe(III)-OH^- cofactor and thus hydrogen abstraction from this pro-chiral center is unlikely. However, our MD simulations cannot decide if the HF or the TF substrate alignment is more favorable, but our docking results already suggested that HF substrate orientation is the preferred choice for mouse Alox15b and the murinized human ALOX15B double mutant. The potential energy barriers for hydrogen abstractions from the pro-chiral bisallylic methylenes of AA (H7, H10, H13) tend to increase with the distance between the hydrogen to be abstracted and the oxygen atom of the Fe(III)-OH^- cofactor. However, there is no precise correlation between the energy barriers and the distances since many other factors are involved. AA 15-lipoxygenation by wildtype human ALOX15B and by the mouse Alox15b Tyr603Asp+His604Val double mutant involves hydrogen abstraction from C13 (H13). The nascent pentadienyl radical formed during hydrogen abstraction is close to planar (sp2 hybridization of the carbon atoms) and the π-electron density is completely delocalized over the entire pentadienoic system (C11 to C15). In contrast, AA 8-lipoxygenation by wildtype mouse Alox15b and by the human ALOX15B Asp602Tyr+Val603His double mutant involves hydrogen abstraction from C10 (H10). Here the π-electron density of the pentadienyl radical is delocalized over C8 to C12

We have previously suggested that the extent of conversion of the nonplanar structure of the fatty acid substrate to the planar structure of the evolving pentadienyl radical (geometric motion) severely impacts the energy barrier of the hydrogen abstraction. In fact, a high degree of geometric motion appears to increase the energy barrier [31]. The differential steric hindrance of this geometric motion by the C-terminal amino acids (Ile675 for human ALOX15B and Ile677 for mouse Alox15) as well as by Leu609 (for human ALOX15B) and Leu611 (for mouse Alox15b) appears to favor C13 hydrogen abstraction by human ALOX15B but C10 hydrogen abstraction by its mouse ortholog. For TF binding of AA in wildtype human ALOX15B (Figure 8) the dihedral angles C11-C12-C13-C14 and C12-C13-C14-C15 are closer to planarity (0° or 180°) than the dihedral angles C8-C9-C10-C11 and C9-C10-C11-C12. Thus, abstraction of H10 requires a high degree of geometric motion of AA in the region of the C8-C9 double bond but the side chains of Ile675 and Leu609 significantly hinder this motion. Thus, H13 abstraction and subsequent [+2] radical rearrangement is sterically preferred. For tail-first AA alignment at the active site of the Y603D+H604V double mutant of mouse Alox15b we observed a similar steric situation (Figure S2).

Int. J. Mol. Sci. **2023**, *24*, 10046

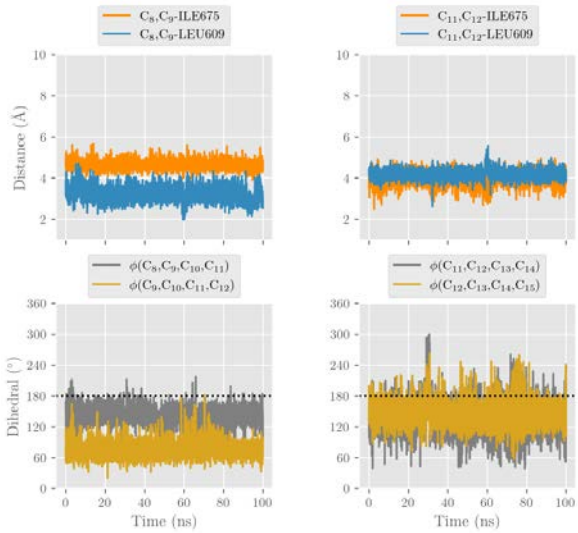

Figure 8. Shortest distances (Å) from the C8-C9 and C11-C12 double bonds to terminal Ile675 and Leu609, and dihedral angles C8-C9-C10-C11, C9-C10-C11-C12, C11-C12-C13-C14, and C12-C13-C14-C15 along the molecular dynamics simulation for AA (TF) at the active site of wildtype human ALOX15B.

On the other hand, the scenario is the opposite for head-first AA alignment. For wildtype mouse Alox15b (Figure S3) and for the D602Y+V603H double mutant of human ALOX15B (Figure S4) the steric effects of the above-mentioned amino acids favor the H10 abstraction and subsequent [−2] radical rearrangement.

2.7. D602Y+V603H Exchange in Human ALOX15B and Y603D+H604V Mutation in the Mouse Ortholog also Altered the Substrate Behavior of HETE Isomer

All canonic HETE-isomers involve bisallylic methylenes and thus they constitute suitable ALOX substrates. In theory, 15-HETE should be a good substrate for mouse Alox15b, and 8,15-diHETE is predicted as major reaction product. On the other hand, 8-HETE should not be accepted as substrate by wildtype mouse Alox15b. In contrast, human ALOX15B should well oxygenate 8-HETE and here again, 8,15-diHETE should be the major reaction product. However, 15-HETE should not be oxygenated by wildtype human ALOX15B. To test these hypotheses, in vitro activity assays were carried out with wildtype human and wildtype mouse ALOX15 orthologs and the reaction products were analyzed by RP-HPLC.

As indicated in Figure 9, wildtype human ALOX15B accepted 8-HETE but not 15-HETE as the substrate. As expected, mouse Alox15b exhibited an inverse substrate specificity. 15-HETE was a good substrate, but 8-HETE was not (Figure 9). D602Y+V603H exchange murinized the substrate specificity of the human ALOX15B since 15-HETE was a good substrate for this enzyme variant. In contrast, Y603D+H604V mutation in mouse Alox15b humanized the substrate specificity of mouse Alox15b since for this enzyme mutant 8-HETE was a good oxygenation substrate whereas 15-HETE was not oxygenated (Figure 9).

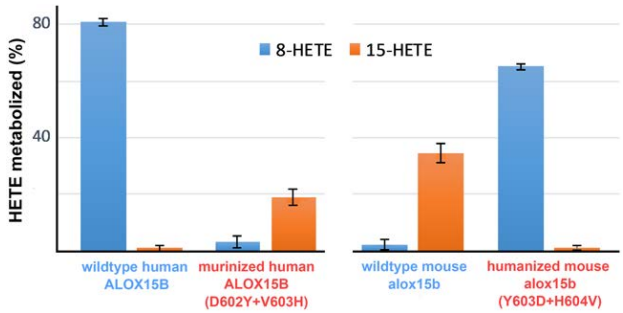

Figure 9. Substrate specificity of mouse and human wildtype ALOX15 orthologs and of their murinized (D602Y+V603H) and humanized (Y603D+H604V) double mutants using 15-HETE and 8-HETE as the substrate. The different ALOX15B variants were expressed as N-terminal his-tag fusion proteins in *E. coli* and aliquots of the bacterial lysis supernatants were used to perform in vitro activity assays using 15S-HETE and 8S-HETE (20 µM final concentration) as the substrate. The disappearance of the substrate during the incubation period was measured by RP-HPLC. Each activity assay was carried out in duplicate and each sample was analyzed twice by RP-HPLC.

2.8. Wildtype Mouse Alox15b Forms Significant Amounts of 8,15-diHETE from AA during Long Term Incubations

When we analyzed the mixture of oxygenation products formed from AA during short-term incubations by mouse Alox15b, we only detected the formation of 8-HETE and 15-HETE. However, after longer incubation periods we observed the additional formation of conjugated trienes that co-migrated with an authentic standard of 8S,15S-diHETE (Figure 10). This compound, which was absent in the product mixture of short-term incubations, involved the canonic conjugated triene chromophore (inset to Figure 10) and this data is consistent with its chemical structure.

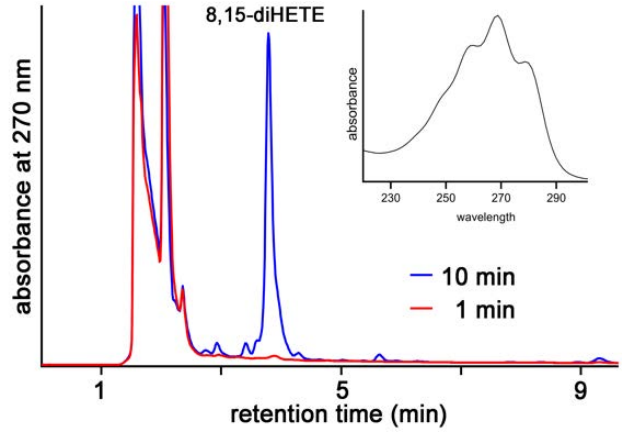

Figure 10. Formation of 8,15-diHETE during long-term incubations of AA with mouse Alox15b. Wildtype mouse Alox15b was expressed as N-terminal his-tag fusion protein in *E. coli* and aliquots of the bacterial lysis supernatant were used to perform in vitro AA oxygenation activity assays. The reaction was stopped after 1 (red) and 10 min (blue) by the addition of solid sodium borohydride and the reaction products were analyzed by RP-HPLC (legends to Figures 3 and 4) recording the absorbance at 270 nm. Inset: UV-spectrum of the peak eluting at about 4 min indicating the presence of the canonic conjugated triene chromophore.

Int. J. Mol. Sci. **2023**, *24*, 10046

In principle, there are two distinct biosynthetic pathways for 8,15-diHETE formation by mouse Alox15b. The first mechanism involves primary formation of 8-HETE, which can subsequently be used as substrate for secondary 15-lipoxygenation. The second pathway involves primary AA 15-lipoxygenation followed by 8-lipoxygenation.

2.9. The Product Pattern of AA Oxygenation by Mouse Alox15b Depends on the Duration of the In Vitro Incubation Period and on the Amounts of Enzyme Added

After a 3 min incubation period of mouse Alox15b with AA, a 93:7 mixture of 8-HETE and 15-HETE was analyzed (Figure 4A). Next, we explored whether the product pattern formed by mouse Alox15b depends on the enzyme concentration. For this purpose, we first incubated low amounts of enzymes for different time periods and analyzed the product pattern (Figure 11A). Here we found that at all time points 8-HETE was the dominant reaction product (black symbols) whereas 15-HETE as well as 8,15-diHETE were only formed in small amounts. However, at higher enzyme concentrations this product pattern was remarkably different (Figure 11B). When activity assays were carried out at a 10-fold higher enzyme concentration the relative share of 8-HETE formation was down, whereas 8,15-diHETE formation was augmented. In fact, at this enzyme concentrations 8,15-diHETE was the dominant AA oxygenation product (Figure 11B).

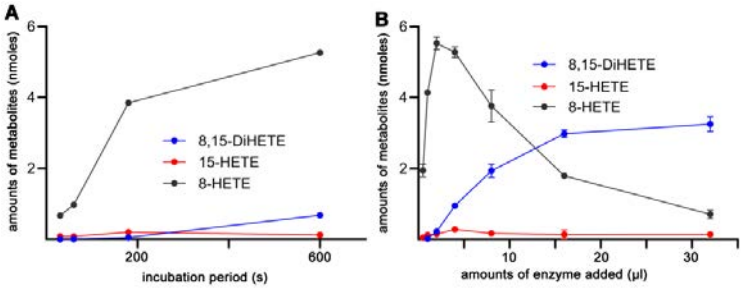

Figure 11. Formation of different oxygenation products by wildtype mouse Alox15b during the oxygenation of AA. Wildtype mouse Alox15b was expressed as N-terminal his-tag fusion protein in *E. coli* and aliquots of the bacterial lysis supernatant were used to perform in vitro AA oxygenation activity assays. The formation of 8-HETE, 15-HETE, and 8,15-diHETE (nmoles) was quantified. (**A**) Time dependence of product formation; single values are plotted. (**B**) Product formation at different enzyme concentrations. Each point represents the mean four different assays; means ± SD are given.

2.10. MD Simulations of 15-HETE and 8-HETE Binding

To explore the structural basis for differential oxygenation of 15- and 8-HETE by human and mouse ALOX15B orthologs, we ran four independent MD simulations (100 ns each). For wildtype human ALOX15B and for the humanized mouse Alox15b Y603D+H604V double mutant we analyzed TF alignment of 8-HETE. Since 15-HETE was not a good substrate for these two enzymes (Figure 9) we did not analyze the binding of this substrate. For wildtype mouse Alox15b and the murinized human ALOX15B D602Y+V603H double mutant, 15-HETE (HF) was the preferred substrate (Figure 9) and thus, we did not initially explore 8-HETE binding.

The evolution of the distances between the oxygen atom in the Fe(III)-OH^- cofactor to the closest hydrogen atom attached to C7 (H7), C10 (H10) or C13 (H13) along the MD simulations is pictured in Figure 12, and the average distances are summarized in Table 4. It can be seen that H13 in 8*S*-HETE (TF) is localized in close proximity to the Fe(III)-OH^- cofactor and thus, it is ready to be abstracted by the two enzymes. These steric configurations are consistent with the formation of 8S,15S-diHETE from the 8*S*-HETE substrate. On the other hand, H10 in 15*S*-HETE (TF) is also localized in close proximity to the Fe(III)-OH^- cofactor

and thus, it may also be ready to be abstracted by both wildtype mouse Alox15b and the murinized D602Y+V603H double mutant of human ALOX15B. These conformations of the enzyme-substrate complexes explain the formation of 8S,15S-diHETE from 15-HETE by these two enzymes, which was experimentally observed.

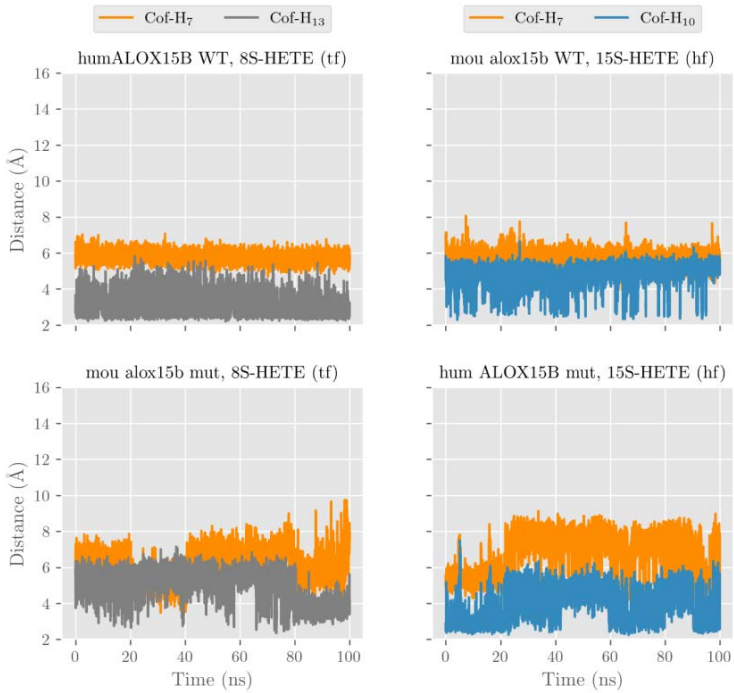

Figure 12. Distances from the oxygen atom in the Fe(III)-OH^- cofactor to the closest hydrogen atom attached to C7 (H7), C10 (H10), and C13 (H13) along the molecular dynamics simulations of tail-first 8*S*-HETE in wildtype human ALOX15B and Y603D+H604V mutant of mouse Alox15b, and head-first 15*S*-HETE in wildtype mouse Alox15b and D602Y+V603H mutant of human ALOX15B.

Table 4. Average distances (Å) between the oxygen atom in the Fe(III)-OH^- cofactor and the closest hydrogen atom attached to C7 (H7), C10 (H10), and C13 (H13) along the molecular dynamics simulations of TF 8*S*-HETE alignment in wildtype human ALOX15B, wildtype mouse Alox15b, and Y603D+H604V mutant of mouse Alox15b, and head-first 15*S*-HETE in wildtype mouse Alox15b and D602Y+V603H mutant of human ALOX15B. n.p., not possible since neither C13 nor C10 are bisallylic methylenes in the corresponding substrates, n.c., such MD simulations have not been performed.

Substrate and Orientation	Human						Mouse					
	WT			mut			WT			mut		
	H7	H10	H13	H7	H10	H13	H7	H10	H13	H7	H10	H13
15S-HETE (HF)	n.c.	n.c.	n.c.	6.7	4.0	n.p.	5.6	4.5	n.p.	n.c.	n.c.	n.c.
8S-HETE (TF)	5.8	n.p.	2.8	n.c.	n.c.	n.c.	6.9	n.p.	4.5	6.3	n.p.	5.2

Another aspect needs to be considered when the formation 8S,15S-diHETE from AA by wildtype mouse Alox15b is explored. We have shown that the primary formation of

Int. J. Mol. Sci. **2023**, *24*, 10046

8S-HETE is a favorable and fast process. In contrast, the formation of 8S,15S-diHETE from 8S-HETE is an unfavorable and slow process, but it is in fact possible. In effect, according to Table 2, the tail-first alignment of AA in wildtype mouse Alox15b is not the most favorable one, but it is possible. So, the tail-first alignment of 8S-HETE is also possible, and the corresponding MD simulation (Table 4 and Figure S5) shows that if this is the case, H13 is ready to be abstracted to yield the secondary 15-lipoxygenation. Moreover, Figure 9 shows that 8S-HETE is not a good substrate of wildtype mouse Alox15b, but it is somewhat metabolized. A second pathway would involve an initial slow 15-lipoxygenaton (it would imply an unfavorable tail-first orientation of AA), but a fast secondary 8-lipoxygenation of 15-HETE. Both pathways seem to be possible, as both are globally slow, because 15-lipoxygenation is always unfavorable.

2.11. Impact of Reaction Conditions on the Product Pattern of Mouse and Human ALOX15B

For the soybean LOX1 it has previously been reported [32] that the pattern of the reaction products formed from linoleic acid depends on the pH of the reaction mixture. On the other hand, the product patterns of a number of vertebrate ALOX isoforms [33] were remarkably stable when the pH of the reaction mixture was altered.

To explore the possible impact of the reaction conditions on the rate of EPA oxygenation, we incubated human and mouse ALOX15B orthologs with EPA at different pH (6.4, 7.4, and 8.4), different temperatures (15 °C, 25 °C, and 35 °C) and different substrate concentrations (50 μM, 100 μM, and 200 μM) for 5 min, quantified the reaction products formed during the incubation period and determined the chemical structure of the major EPA oxygenation products. As indicated in Table 5 (upper panel), human ALOX15B converted EPA most rapidly at pH 7.4. At pH 6.4 and 8.4 the oxygenation rates were gradually reduced but at all pH-values 15-HEPE was the exclusive oxygenation product. As expected, for mouse Alox15b 8-HEPE was the dominant EPA oxygenation product and 15-HEPE was only produced in small quantities. Interestingly, in contrast to human ALOX15B, which exhibited a higher EPA oxygenation rate at pH 7.4, mouse Alox15b was more active at pH 6.4. (Table 5, upper panel). When we explored the temperature dependence of EPA oxygenation (Table 5, middle panel) we found that both human and mouse ALOX15B oxygenated EPA with highest rates at 37 °C. At all temperatures 15-HEPE was the exclusive EPA oxygenation product of the human enzyme, whereas 8-HEPE was dominant for mouse Alox15b.

Finally, we also tested the impact of substrate concentrations (Table 5, lower panel). Human and mouse ALOX15B orthologs exhibited the highest EPA oxygenase activities at 200 μM substrate concentration. Here again, the exclusive EPA oxygenation product was identified as 15-HEPE for human ALOX15B at all substrate concentrations tested. For mouse Alox15b the situation was somewhat different. At low substrate concentrations (50 μM) a 1:2 mixture of 15- and 8-HEPE was analyzed but the relative share of 8-HEPE did increase with the increasing substrate concentrations. In fact, at 200 μM EPA 8-HEPE was rather dominant (Table 5, lower panel).

Table 5. Impact of reaction conditions on the rate of EPA oxygenation and the product pattern of human and mouse wildtype ALOX15B orthologs. Aliquots of bacterial lysis supernatants (5 µL) of recombinant ALOX15B preparations (wildtype human and mouse ALOX15B) were incubated for 5 min at different conditions (pH 6.4, 7.4, 8.4, 100 µM EPA, room temperature; temperatures 15 °C, 25 °C, 35 °C, 100 µM EPA, room temperature; EPA concentrations 50 µM, 100 µM, 200 µM, pH 7.4, room temperature). Sample workup and RP-HPLC analysis were carried out as described in the legend to Figure 4B. Three independent incubations were carried out under each condition (n = 3) and means ± SD are given.

pH Dependence			**Product Pattern**	
Enzyme	**pH**	**rel. Activity (%)**	**15-HEPE**	**8-HEPE**
Human ALOX15B	6.4	77.1 ± 3.6	100.0 ± 0.0	0.0 ± 0.0
	7.4	100.0 ± 6.3	100.0 ± 0.0	0.0 ± 0.0
	8.4	98.4 ± 6.6	100.0 ± 0.0	0.0 ± 0.0
Mouse Alox15b	6.4	100 ± 2.6	2.6 ± 0.5	97.4 ± 0.5
	7.4	62.1 ±1.0	1.5 ± 0.1	98.5 ± 0.1
	8.4	65.9 ± 10.4	3.8 ± 0.1	96.2 ± 0.1
Temperature Dependence			**Product Pattern**	
Enzyme	**Temperature (°C)**	**rel. Activity (%)**	**15-HEPE**	**8-HEPE**
Human ALOX15B	15	47.6 ±2.4	100.0 ± 0.0	0.0 ± 0.0
	25	73.7 ± 6.1	100.0 ± 0.0	0.0 ± 0.0
	35	100.0 ± 8.5	100.0 ± 0.0	0.0 ± 0.0
Mouse Alox15b	15	9.8 ± 0.9	5.8 ± 0.5	94.2 ± 0.5
	25	54.2 ± 7.0	6.7 ± 0.6	93.3 ± 0.6
	35	100.0 ±13.4	7.2 ± 1.3	92.8 ± 1.3
Substrate Concentration Dependence			**Product Pattern**	
Enzyme	**EPA Concentration (µM)**	**rel. Activity (%)**	**15-HEPE**	**8-HEPE**
Human ALOX15B	50	27.0 ± 3.6	100.0 ± 0.0	0.0 ± 0.0
	100	70.6 ± 0.8	100.0 ± 0.0	0.0 ± 0.0
	200	100.0 ± 10.9	100.0 ± 0.0	0.0 ± 0.0
Mouse Alox15b	50	11.6 ± 1.7	32.5 ± 1.3	67.5 ± 1.3
	100	88.7 ± 2.0	15.1 ± 1.2	84.9 ± 1.2
	200	100.0 ± 14.6	5.1 ± 0.5	94.9 ± 0.5

3. Discussion

3.1. Degree of Novelty, Advancement of Knowledge, and Limitations

The product pattern of wildtype mouse and human ALOX15B orthologs with AA as the substrate has previously been explored and product analysis indicated that human ALOX15B converts AA mainly to 15S-HETE [19,25] whereas 8S-HETE was the dominant AA oxygenation product of mouse Alox15b [25]. Y603D+H604V exchange in mouse Alox15b humanized the product pattern with AA as the substrate and the inverse mutagenesis strategy on the mouse enzyme partly humanized this enzyme property [25]. For wildtype human ALOX15B the product pattern with EPA and DHA has also been explored [34], but a number of important questions remained unanswered: (i) Which products are formed from other PUFAs by mouse Alox15b. (ii) Does D602Y+V603H exchange in human ALOX15B murinize the product pattern of this enzyme when EPA, DHA, and LA are used as the

Int. J. Mol. Sci. **2023**, *24*, 10046

substrate. (iii) Does Y603D+H604V exchange in mouse Alox15b humanize the product mixture of this enzyme when EPA, DHA, and LA are used as substrate. (iv) Do wildtype mouse and human ALOX15B orthologs and their humanized/murinized double mutants accept hydroxylated PUFAs (8-HETE and 15-HETE) as the substrate and what are the major products of these reactions. (v) Can the different reaction specificities of mouse and human ALOX15B orthologs and their humanized/murinized double mutants be explained by the different ways of substrate binding at the active site of the enzyme variants (docking studies and MD simulations).

To address these questions, we designed appropriate experiments and obtained the following results: (i) 8-HEPE and 10-HDHA were the dominant oxygenation products of mouse Alox15b with EPA and DHA, respectively (Figure 3). (ii) Mouse Alox15b (Figure 4) converted AA, EPA, and DHA to their n-12 oxygenation products (8-HETE, 8-HEPE, 10-HDHA) and the Y603D+H604V exchange humanized the product patterns with all three PUFAs. A similar humanization of the product mixture of mouse Alox15b was observed when linoleic acid was used as the substrate (Figure 5C,D). (iii) When an inverse mutagenesis strategy was employed for human ALOX15B, the D602Y+V603H exchange murinized the AA and EPA oxygenation products (Figure 4A,B). In contrast, when DHA was used as the substrate for the D602Y+V603H double mutant of human ALOX15B (Figure 4C) we did not see such murinization. Instead of 10-HDHA, which was expected to be formed by a murinized enzyme, we identified 7-HDHA as the major DHA oxygenation product. In other words, the D602Y+V603H double mutant of human ALOX15B converted DHA to the same reaction product that is formed from this substrate by ALOX5. This data suggests that the way of DHA binding at the active site of the D602Y+V603H double mutant of human ALOX15B should be similar in the way of substrate binding at ALOX5. When LA was used as the substrate, we neither observed murinization of the reaction products. In fact, the D602Y+V603H double mutant of human ALOX15B produced an unspecific product mixture of 13S-, 13R-, 9S-, and 9R-HODE and this data suggests that the oxygenation reaction with this fatty acid was not strictly controlled by the enzyme (Figure 5A,B). (iv) 15-HETE is a good substrate for wildtype mouse Alox15b and for the murinized human ALOX15B double mutant Y603D+H604V. In contrast, it is not well oxygenated by wildtype human ALOX15B and the humanized D602Y+V603H double mutant of mouse Alox15b. In contrast, 8-HETE is well oxygenated by wildtype human ALOX15B and the humanized mouse Alox15b double mutant Y603D+H604V. 8,15-diHETE was the major oxygenation product formed from both substrates. (v) Docking calculations indicate that the four polyenoic fatty acid substrates (AA, EPA, DHA, and LA) tested in this study preferentially tend to adopt a tail-first (TF) substrate alignment in wildtype human ALOX15B and in the humanized Y603D+H604V double mutant of mouse Alox15b. In contrast, a head-first (HF) substrate alignment was calculated for murinized D602Y+V603H mutant of human ALOX15B and wildtype mouse Alox15b. Molecular dynamics simulations using AA as the substrate revealed that binding of carboxylate group of the head-first oriented substrate in the substrate binding pocket would be destabilized by D602 and V603 in wildtype human ALOX15B, and by D603 and V604 in the humanized Y603D+H604V double mutant of mouse Alox15b. Thus, the substrate fatty acid is unable to establish a strong non-covalent interaction with any active site amino acid residue present at the bottom of the substrate binding pocket. Conversely, the strong interaction between the negatively charged carboxylic group of the substrate and the negatively charged side-chain of Arg428 stabilizes the TF substrate alignment. When Tyr and a His residues are present in the active site (wildtype mouse Alox15b and the murinized D602Y+V603H double mutant of human ALOX15B), the fatty acid carboxylate can form stabilizing hydrogen bonds with amino acid residues present either in the bottom region of the substrate binding cavity (HF substrate alignment) or with amino acids located close to the entrance of the substrate binding pocket (TF alignment). However, the docking results suggest that HF substrate orientation appears to be preferred. (vi) For each preferred substrate alignment both H13 (attached to C13) and H10 (attached to C10) of AA are located sufficiently close to the oxygen of the Fe(III)-OH^- cofactor for hydrogen abstraction, and steric hindrance by the N-terminal Ile675 and by the side-chain of Leu609 is

important. For TF, AA alignment at the active site of wildtype human ALOX15B and of the humanized Y603D+H604V double mutant of mouse Alox15b the H13 abstraction is preferred. In contrast, for HF, AA alignment at the active site of wild type mouse Alox15B and of the murinized D602Y+V603H double mutant of human ALOX15B H10 abstraction is preferred.

The most serious limitation of this study is that functional characterization of the four enzyme variants was carried out with crude enzyme preparations. Although we were able to purify wildtype human and mouse ALOX15B as well as theY603D+H604V double mutant of mouse Alox15b by affinity chromatography on Ni-agarose as catalytically active proteins, we experienced a >90% loss in catalytic of the D602Y+V603H double mutant of human ALOX15B during the purification procedure. The mechanistic basis for this loss in catalytic activity has not been clarified but to ensure strict comparability of the functional data we decided to use crude enzyme preparations (bacterial lysate supernatant) for functional characterization. For human and mouse wildtype ALOX15B orthologs we carried out similar experiments with the purified enzyme preparations and obtained similar data as for the bacterial lysates.

3.2. Complex Ester Lipids as Substrate for Mouse and Human ALOX15B

Despite the differential product patterns with free AA human and mouse ALOX15, orthologs convert AA-containing phospholipids incorporated in nanodiscs [35] mainly to the 15-HETE derivatives [11]. Thus, the product mixture of the two enzymes with this substrate appears to be similar. We carried out similar studies using AA containing phospholipid liposomes and mitochondrial membranes as substrates. These preliminary experiments indicated that 15S-HETE containing phospholipids were the major oxygenation products formed by mouse and human ALOX15B and this data is consistent with the results obtained in the nanodisc experiment [11]. However, when we employed mitochondrial membranes or liposomes involving linoleic acid as substrate for the two enzymes, we observed different product patterns. For human ALOX15B, esterified 15S-HETE and 13S-HODE were the major oxygenation products, and the corresponding R-enantiomers were only formed in small amounts. When incubations were carried out with mouse Alox15b, esterified AA oxygenation products were only detected in small amounts. As the dominant PUFA oxygenation product we identified 9S-HODE. Thus, when mitochondrial membranes and LA-containing liposomes were used as substrate the product specificities of human and mouse ALOX15B are different. Whether similar differences in the reaction specificities of the two enzymes can be observed when other lipid-protein such as plasma membranes of different cells or lipoproteins are used as substrate must be tested experimentally in the future.

3.3. Impact of Reaction Conditions on the Product Pattern of ALOX15B Variants

The composition of the reaction products of most ALOX-isoforms with a given substrate is well defined and alterations in the reaction conditions in the near physiological range do not dramatically alter this enzyme property. There may be minor modifications but in principle the reaction specificities of ALOX-isoforms are very robust. This conclusion is supported by the experimental date shown in Table 5. On the other hand, we found that the pattern of the arachidonic acid oxygenation products strongly depends on the amount of enzyme added to the incubation mixture (Figure 11B). However, these data do not indicate that the specificity of the enzyme has changed. In fact, the differences in the product pattern are the consequence of enzyme kinetics. At high enzyme concentrations the fatty acid substrate (AA) becomes rate limiting and the primary reaction product accumulates. Under these conditions the primary oxygenation product is used as the substrate for secondary oxygenation (formation of 8,15-diHETE). Thus, also at high enzyme concentration the specificity of the enzyme largely remains unchanged.

There are, however, rare exceptions from this rule. For instance, the specificity of soybean LOX1 is more variable since the pattern of linoleic acid oxygenation products formed by this enzyme is pH-sensitive [32]. This result might be related to the alkaline pH_{opt} of this ALOX isoform. On the other hand, the specificity of AA oxygenation by

most vertebrate ALOX-isoforms (human ALOX5, human ALOX12, human ALOX15, rabbit ALOX15, human ALOX15B, mouseAlox15, mouse Alox15b, zebrafishALOX12) was remarkable stable when the pH of the incubation mixture was varied in the near physiological range (pH 6.4–8.0) [33]. Here we observed (Table 5) that the product pattern of human ALOX15B was remarkably stable at different reaction conditions. At different pH-values (pH 6.4, 7.4, 8.4), at different temperatures (15 °C, 25 °C, 35°C), and at different substrate concentrations (50 μM, 100 μM, 200 μM) 15-HEPE was always identified as the exclusive EPA oxygenation product. In other words, in the near physiological range alterations in the reaction conditions did not impact the product pattern of human ALOX15B.

For mouse Alox15b the situation was somewhat different. For this enzyme we also observed that alterations in pH and temperature did hardly modify the product pattern of EPA oxygenation. Under all experimental conditions tested in our experiments (Table 5) 8-HEPE was identified as the dominant EPA oxygenation product (>90%) while 15-HEPE was only formed in smaller quantities (<10%). Interestingly, modification of the substrate concentration induced alterations in the reaction products of mouse Alox15b. At high substrate concentrations (200 μM) the relative share of the major EPA oxygenation product (8-HEPE) was about 95%. In contrast, at lower substrate concentrations we observed a gradual decline in the relative share of 8-HEPE formation. In fact, at 100 μM EPA 8-HEPE only contributed 85% to the product mixture and at 50 μM the 8-HEPE/15-HEPE ratio was only about 2:1. Thus, although at lower substrate concentrations 8-HEPE was still the major EPA oxygenation product, the relative share of 15-HEPE did significantly increase at lower substrate concentrations. The molecular basis for this observation was not explored but our findings need to be considered when the biosynthesis of oxygenated lipids in mouse cells, tissues, and body fluids (blood palsma, urine, liquor) are interpreted.

4. Materials and Methods

4.1. Chemicals

The chemicals used in this study were purchased from the following sources: Phosphate buffered saline without calcium and magnesium (PBS) from PAN Biotech (Aidenbach, Germany); nitrocellulose blotting membrane from Serva Electrophoresis GmbH (Heidelberg, Germany); EDTA (Merck KG, Darmstadt, Germany). Fatty acid substrates [5,8,11,14-eicosatetraenoic acid (AA), 5,8,11,14,17-eicosapentaenoic acid (EPA), 4,7,10,13,16,19-docosahexaenoic acid (DHA), 9,12-octadecadienoic acid (LA), 9,12,15-octadecatrienoic acid (ALA), 6,9,12-octadecatrienoic acid (GLA) 15S-HETE, 8S-HETE], and authentic HPLC standards of HETE-isomers used for HPLC analysis [15S-HETE, 15S/R-HETE, 12S/R-HETE, 12S-HETE, 8S/R-HETE, 5S-HETE, 8S,15S-diHETE] were obtained from Cayman Chem (distributed by Biomol GmbH, Hamburg, Germany). Acetic acid from Carl Roth GmbH (Karlsruhe, Germany); sodium borohydride from Life Technologies, Inc (Eggenstein, Germany); isopropyl-β-thiogalactopyranoside (IPTG) from Carl Roth GmbH (Karlsruhe, Germany); restriction enzymes from ThermoFisher (Schwerte, Germany); the E. coli strain Rosetta2 DE3 pLysS from Novagen (Merck-Millipore, Darmstadt, Germany). Oligonucleotide synthesis was performed at BioTez Berlin Buch GmbH (Berlin, Germany). Nucleic acid sequencing was carried out at Eurofins MWG Operon (Ebersberg, Germany). HPLC grade methanol, acetonitrile, n-hexane, 2-propanol, and water were from ThermoFisher (Schwerte, Germany).

4.2. Cloning and Expression of Mouse and Human ALOXB Orthologs

The cDNA sequences of mouse and human ALOX15B orthologs were extracted from the NCBI cDNA database and were chemically synthesized (BioCat GmbH, Heidelberg, Germany). For subcloning from the initial pUC57 synthesis vector into pET28b(+) (Novagen/Merck, Darmstadt, Germany) expression vector, a SalI restriction site was introduced immediately upstream of the start codon and a HindIII restriction site was generated immediately downstream of the stop codon. The sequences were optimized for bacterial expression by silent mutations.

The enzyme variants (wildtype and double mutants) were N-terminal hexa-his-tag fusion proteins, as described in Ref. [36]. Briefly, *E. coli* Rosetta2 (DE3)-pLysS cells were transformed with the recombinant plasmid pET28b and grown on an agar plate containing kanamycin and chloramphenicol. An isolated clone was selected and grown under shaking in a glucose free MSM with added trace elements and glucoamylase. Protein expression was induced by addition of IPTG. After 18 h, cells were harvested and homogenized by sonication, and the cell free supernatant was used as enzyme source.

4.3. Mutagenesis Studies

Site directed mutagenesis was performed as described in Ref. [36]. Plasmid DNA containing the coding sequence of the bony fish ALOX15 isoforms was incubated with specific primer pairs containing the required changes in their nucleotide sequence to achieve the intended amino acid exchanges and Pfu Ultra II Hot Start 2 × PCR Master Mix (Agilent Technologies, Waldbronn, Germany). After the PCR protocol (18 cycles), parent DNA was digested using *DpnI*. *E. coli* XL-1 Blue competent cells (Agilent Technologies Inc., Santa Clara, CA, USA) were transformed with the mutated plasmid and after replication the plasmid DNA of a selected bacterial colony was sequenced (Eurofins Genomics Germany GmbH, Ebersberg, Germany).

4.4. In Vitro Activity Assays and HPLC Analyses of the Reaction Products

Enzyme activity assays and analysis of the reaction products by HPLC were performed as described in Ref. [36]. Different amounts of the cell free supernatants were incubated with 100 μM substrate (AA, EPA, and DHA) and the reduced reaction products were analyzed by RP-HPLC on a Shimadzu instrument connected with a Hewlett Packard diode array detector 1040 A. Metabolites were separated on a Nucleodur C_{18} Gravity column (Macherey-Nagel, Düren, Germany; 250 × 4 mm, 5 μm particle size) coupled with a corresponding guard column (8 × 4 mm, 5 μm particle size). A solvent system consisting of acetonitrile:water:acetic acid (70:30:0.1, by volume for AA and DHA derivatives and 50:50:0.1, by volume for EPA derivatives) was used at a flow rate of 1 mL·min^{-1}. For more detailed analysis of the reaction products of linoleic acid oxygenation the conjugated dienes formed during the incubation period were prepared by RP-HPLC and further analyzed by normal-phase HPLC (NP-HPLC) and/or chiral-phase HPLC (CP-HPLC). Normal-phase HPLC was performed using the solvent system n-hexane/2-propanol/acetic acid (100/2/0.1, by volume) on a Nucleosil 100-5 column (250 × 4.6 mm, 5 μm particle size). 12-HETE enantiomers were resolved on a Chiralpak AD-H column (Daicel Corp., Osaka, Japan) with a solvent system consisting of n-hexane/methanol/ethanol/acetic acid (96:3:1:0.1, by vol; 1 mL/min).

4.5. Miscellaneous Methods including Statistics

For SDS/PAGE, approximately 100 μg denatured protein of the bacterial lysate supernatants were analyzed on a 7.5% polyacrylamide gel. The separated protein bands were then transferred onto a Protran BA 85 Membrane (Carl Roth GmbH, Karlsruhe, Germany) and the blots were probed with an anti-his-tag-HRP conjugated antibody (Miltenyi Biotec GmbH, Bergisch Gladbach, Germany). Immunoreactive bands were visualized using the SERVALight Polaris CL HRP WB Substrate Kit (Serva Electrophoresis GmbH, Heidelberg, Germany). Chemiluminescence was detected on a FUJIFILM Luminescent Image Analyzer LAS-1000plus & Intelligent Dark Box II. For testing the pH-dependence of the product mixture of wildtype human and mouse ALOX15B orthologs, a 1:1 mixtures of 0.05 M sodium phosphate buffer and 0.05 M sodium borate buffer were used and the different pH values were adjusted at room temperature by the addition of 5 M NaOH or HCl, respectively. The protein concentrations in the bacterial lysates were quantified using Bradford Reagent for quantitative protein determination (AppliChem, VWR International GmbH, Darmstadt, Germany) according to the instructions of the vendor. For statistical calculations and figure design we used the GraphPad prism program (version 8.00, GraphPad Software, La Jolla, CA, USA).

Int. J. Mol. Sci. **2023**, *24*, 10046

4.6. Structural Modeling

Four ALOX15B 3D models were built. Human ALOX15B coordinates were obtained from the X-ray structure with PDB ID 4NRE [37] and the mouse Alox15b model was obtained from AlphaFold DataBase (UniProt ID O35936) [38,39]. The double mutant versions of both human ALOX15B and mouse Alox15b were manually constructed using the Rotamers module by UCSF Chimera. Protonation was carried out at pH 7.4 using the ProteinPrepare tool by PlayMolecule.org [40].

4.7. Docking Calculations

The GOLD5.8 program [41] was used for the docking calculations. ChemScore [42] was employed for scoring purposes.

4.8. MD Simulations

The best-scored solutions for each substrate-enzyme complex (enzyme complexed with AA in head-first (HF) and in tail-first (TF) conformations, 15S-HETE in head-first conformation and 8S-HETE in tail-first conformation) from docking calculations were used as the initial structures for MD simulations. Ff19SB has been used as a force field for standard residues, while Fe and its coordinates have been parametrized following the Seminario Method from MCPB [43]. Force constants and RESP charges have been obtained using the Gaussian16 program at the B3LYP/6-31G(d) level of theory. As recommended in Ref. [44], OPC waters [45] were chosen as the water model. An orthorhombic solvation box of pre-equilibrated water molecules was built with a buffer of 10 Å around the molecule and Na^+ ions have been added for neutralization. The AMBER20's CUDA (GPU) pmemd package was used for running the simulations. The initial structure was minimized, heated at a rate of 50 K from 0 to 300 K, and the system was then equilibrated for 20 ps after each step. A total of 1 ns of NPT ensemble at 300 K and 1 atm was run for stabilization of the water box density. Prior to production, an equilibration of the system using the NVT ensemble at 300 K during 10 ns was performed. After equilibration, 100 ns of production was calculated using the same NVT ensemble.

5. Conclusions

Functional experiments with different polyenoic fatty acids, molecular docking studies and molecular dynamics simulations of substrate binding at the active site of human and mouse ALOX15B orthologs and their murinized/humanized double mutants suggest that AA 15-lipoxygenation by human ALOX15 involves tail-first (TF) substrate alignment. In contrast, for AA 8-lipoxygenation by mouse Alox15b head-first (HF) substrate orientation is preferred. The Asp602Tyr+Val603His exchange murinized the product mixture of human ALOX15B with arachidonic acid and eicosapentaenoic acid but not with docosahexaenoic acid. An inverse mutagenesis strategy on mouse Alox15b (Tyr603Asp+His604Val exchange) did humanize the product pattern of arachidonic acid, eicosapentaenoic acid, and docosahexaenoic acid oxygenation.

Supplementary Materials: The supporting information can be downloaded at: https://www.mdpi.com/article/10.3390/ijms241210046/s1.

Author Contributions: Conceptualization, H.K. and À.G.-L.; methodology, À.G.-L., K.R.K., H.K. and M.C.-N.; validation, H.K. and À.G.-L.; investigation, K.R.K., M.C.-N., X.C., J.M.L., À.G.-L. and H.K.; data curation, K.R.K., H.K., M.C.-N., J.M.L. and À.G.-L.; writing—original draft preparation, H.K. and À.G.-L.; writing—review and editing, all co-authors; visualization, K.R.K., H.K., M.C.-N., J.M.L. and À.G.-L.; supervision, H.K. and À.G.-L.; funding acquisition, À.G.-L. and J.M.L. All authors have read and agreed to the published version of the manuscript.

Funding: The experimental part of the study was supported by research grants of Deutsche Forschungsgemeinschaft to H.K. and D.H. (KU961/14-1, HE8295/1-1). The in silico part of this study was supported by a grant (PID2020-113764GB-I00) from the Spanish Ministerio de Ciencia e Innovación.

Institutional Review Board Statement: Not applicable.

Informed Consent Statement: Not applicable.

Data Availability Statement: All data generated or analyzed during this study are included in this published article. Original experimental raw data can be obtained upon request from K.R.K. (in vitro experiments) and A.G.L. (in silico experiments).

Acknowledgments: The authors acknowledge the methodological support of S. Stehling (Department of Biochemistry, Charité).

Conflicts of Interest: The authors declare that they do not have any conflict of interest with the content of this article.

Abbreviations

ALOX, arachidonic acid lipoxygenases; 5-HETE, 5S-hydroxy-6E,8Z,11Z,14Z-eicosatetraenoic acid; 8-HETE, 8-hydroxy-5Z,9E,11Z,14Z-eicosatetraenoic acid; 15-HETE, 15S-hydroxy-5Z,8Z,11Z, 13E-eicosatetraenoic acid; 12-HETE, 12-hydroxy-5Z,8Z,10E,14Z-eicosatetraenoic acid; AA, arachidonic acid; EPA, 5,8,11,14,17-eicosapentaenoic acid; DHA, 4,7,10,13,16,19-docosahexaenoic acid; LA, linoleic acid; 8-HEPE, 8-hydroxy-5Z,9E,11Z,14Z,17Z-eicosapentaenoic acid; 15-HEPE, 15S-hydroxy-5Z,8Z,11Z,13E,17Z-eicosapentaenoic acid; 5-HEPE, 5-hydroxy-6E,8Z,11Z,14Z,17Z-eicosapentaenoic acid; 17-HDHA, 17-hydroxy DHA, 17-hydroxy-4Z,7Z,10Z,13Z,15E,19Z-docosahexaenoic acid; 10-HDHA, 10-hydroxy-4Z,7Z,11E,13Z,16Z,19Z-docosahexaenoic acid; 7-HDHA, 7-hydroxy-4Z,8E,10Z,13Z,16Z,19Z-docosahexaenoic acid; 8,15-diHETE, 8S,15S-dihydroxy-5Z,9E,11Z,13E-eicosatetraenoic acid; TF, tail-first substrate alignment; HF, head-first substrate alignment.

References

1. Funk, C.D.; Chen, X.-S.; Johnson, E.N.; Zhao, L. Lipoxygenase genes and their targeted disruption. *Prostaglandins Other Lipid Mediat.* **2002**, *68–69*, 303–312. [CrossRef]
2. Kuhn, H.; Humeniuk, L.; Kozlov, N.; Roigas, S.; Adel, S.; Heydeck, D. The evolutionary hypothesis of reaction specificity of mammalian ALOX15 orthologs. *Prog. Lipid Res.* **2018**, *72*, 55–74. [CrossRef]
3. Funk, C.D.; Keeney, D.S.; Oliw, E.H.; Boeglin, W.E.; Brash, A.R. Functional expression and cellular localization of a mouse epidermal lipoxygenase. *J. Biol. Chem.* **1996**, *271*, 23338–23344. [CrossRef]
4. Haeggstrom, J.Z.; Funk, C.D. Lipoxygenase and leukotriene pathways: Biochemistry, biology, and roles in disease. *Chem. Rev.* **2011**, *111*, 5866–5898. [CrossRef] [PubMed]
5. Kuhn, H.; Banthiya, S.; van Leyen, K. Mammalian lipoxygenases and their biological relevance. *Biochim. Biophys. Acta* **2015**, *1851*, 308–330. [CrossRef]
6. Flohe, L.; Toppo, S.; Orian, L. The glutathione peroxidase family: Discoveries and mechanism. *Free Radic. Biol. Med.* **2022**, *187*, 113–122. [CrossRef] [PubMed]
7. Kanaoka, Y.; Austen, K.F. Roles of cysteinyl leukotrienes and their receptors in immune cell-related functions. *Adv. Immunol.* **2019**, *142*, 65–84. [CrossRef] [PubMed]
8. Jordan, P.M.; Werz, O. Specialized pro-resolving mediators: Biosynthesis and biological role in bacterial infections. *FEBS J.* **2022**, *289*, 4212–4227. [CrossRef] [PubMed]
9. Schebb, N.H.; Kuhn, H.; Kahnt, A.S.; Rund, K.M.; O'Donnell, V.B.; Flamand, N.; Peters-Golden, M.; Jakobsson, P.J.; Weylandt, K.H.; Rohwer, N.; et al. Formation, Signaling and Occurrence of Specialized Pro-Resolving Lipid Mediators-What is the Evidence so far? *Front. Pharmacol.* **2022**, *13*, 838782. [CrossRef]
10. Aloulou, A.; Rahier, R.; Arhab, Y.; Noiriel, A.; Abousalham, A. Phospholipases: An Overview. *Methods Mol. Biol.* **2018**, *1835*, 69–105. [CrossRef]
11. Bender, G.; Schexnaydre, E.E.; Murphy, R.C.; Uhlson, C.; Newcomer, M.E. Membrane-dependent Activities of Human 15-LOX-2 and Its Murine Counterpart: Implications for Murine Models of Atherosclerosis. *J. Biol. Chem.* **2016**, *291*, 19413–19424. [CrossRef] [PubMed]
12. Ulusan, S.; Sheraj, I.; Stehling, S.; Ivanov, I.; Das, A.; Kuehn, H.; Banerjee, S. Structural and functional evaluation mammalian and plant lipoxygenases upon association with nanodics as membrane mimetics. *Biophys. Chem.* **2022**, *288*, 106855. [CrossRef] [PubMed]
13. Schewe, T.; Halangk, W.; Hiebsch, C.; Rapoport, S.M. A lipoxygenase in rabbit reticulocytes which attacks phospholipids and intact mitochondria. *FEBS Lett.* **1975**, *60*, 149–152. [CrossRef] [PubMed]

14. Kuhn, H.; Belkner, J.; Wiesner, R.; Brash, A.R. Oxygenation of biological membranes by the pure reticulocyte lipoxygenase. *J. Biol. Chem.* **1990**, *265*, 18351–18361. [CrossRef]
15. Aldrovandi, M.; Banthiya, S.; Meckelmann, S.; Zhou, Y.; Heydeck, D.; O'Donnell, V.B.; Kuhn, H. Specific oxygenation of plasma membrane phospholipids by Pseudomonas aeruginosa lipoxygenase induces structural and functional alterations in mammalian cells. *Biochim. Biophys. Acta* **2017**, *1863*, 152–164. [CrossRef]
16. Belkner, J.; Wiesner, R.; Rathman, J.; Barnett, J.; Sigal, E.; Kuhn, H. Oxygenation of lipoproteins by mammalian lipoxygenases. *Eur. J. Biochem.* **1993**, *213*, 251–261. [CrossRef]
17. Pirillo, A.; Uboldi, P.; Kuhn, H.; Catapano, A.L. 15-Lipoxygenase-mediated modification of high-density lipoproteins impairs SR-BI- and ABCA1-dependent cholesterol efflux from macrophages. *Biochim. Biophys. Acta* **2006**, *1761*, 292–300. [CrossRef]
18. Kuhn, H.; Belkner, J.; Suzuki, H.; Yamamoto, S. Oxidative modification of human lipoproteins by lipoxygenases of different positional specificities. *J. Lipid Res.* **1994**, *35*, 1749–1759. [CrossRef]
19. Brash, A.R.; Boeglin, W.E.; Chang, M.S. Discovery of a second 15S-lipoxygenase in humans. *Proc. Natl. Acad. Sci. USA* **1997**, *94*, 6148–6152. [CrossRef]
20. Wuest, S.J.; Crucet, M.; Gemperle, C.; Loretz, C.; Hersberger, M. Expression and regulation of 12/15-lipoxygenases in human primary macrophages. *Atherosclerosis* **2012**, *225*, 121–127. [CrossRef]
21. Ebert, R.; Cumbana, R.; Lehmann, C.; Kutzner, L.; Toewe, A.; Ferreiros, N.; Parnham, M.J.; Schebb, N.H.; Steinhilber, D.; Kahnt, A.S. Long-term stimulation of toll-like receptor-2 and -4 upregulates 5-LO and 15-LO-2 expression thereby inducing a lipid mediator shift in human monocyte-derived macrophages. *Biochim. Biophys. Acta Mol. Cell Biol. Lipids* **2020**, *1865*, 158702. [CrossRef] [PubMed]
22. Benatzy, Y.; Palmer, M.A.; Brune, B. Arachidonate 15-lipoxygenase type B: Regulation, function, and its role in pathophysiology. *Front. Pharmacol.* **2022**, *13*, 1042420. [CrossRef] [PubMed]
23. Furstenberger, G.; Hagedorn, H.; Jacobi, T.; Besemfelder, E.; Stephan, M.; Lehmann, W.D.; Marks, F. Characterization of an 8-lipoxygenase activity induced by the phorbol ester tumor promoter 12-O-tetradecanoylphorbol-13-acetate in mouse skin in vivo. *J. Biol. Chem.* **1991**, *266*, 15738–15745. [CrossRef] [PubMed]
24. Jisaka, M.; Kim, R.B.; Boeglin, W.E.; Nanney, L.B.; Brash, A.R. Molecular cloning and functional expression of a phorbol ester-inducible 8S-lipoxygenase from mouse skin. *J. Biol. Chem.* **1997**, *272*, 24410–24416. [CrossRef]
25. Jisaka, M.; Kim, R.B.; Boeglin, W.E.; Brash, A.R. Identification of amino acid determinants of the positional specificity of mouse 8S-lipoxygenase and human 15S-lipoxygenase-2. *J. Biol. Chem.* **2000**, *275*, 1287–1293. [CrossRef]
26. Schafer, M.; Kakularam, K.R.; Reisch, F.; Rothe, M.; Stehling, S.; Heydeck, D.; Puschel, G.P.; Kuhn, H. Male Knock-in Mice Expressing an Arachidonic Acid Lipoxygenase 15B (Alox15B) with Humanized Reaction Specificity Are Prematurely Growth Arrested When Aging. *Biomedicines* **2022**, *10*, 1379. [CrossRef]
27. Goloshchapova, K.; Stehling, S.; Heydeck, D.; Blum, M.; Kuhn, H. Functional characterization of a novel arachidonic acid 12S-lipoxygenase in the halotolerant bacterium Myxococcus fulvus exhibiting complex social living patterns. *Microbiologyopen* **2019**, *8*, e00775. [CrossRef]
28. Wecksler, A.T.; Kenyon, V.; Deschamps, J.D.; Holman, T.R. Substrate specificity changes for human reticulocyte and epithelial 15-lipoxygenases reveal allosteric product regulation. *Biochemistry* **2008**, *47*, 7364–7375. [CrossRef]
29. Wecksler, A.T.; Kenyon, V.; Garcia, N.K.; Deschamps, J.D.; van der Donk, W.A.; Holman, T.R. Kinetic and structural investigations of the allosteric site in human epithelial 15-lipoxygenase-2. *Biochemistry* **2009**, *48*, 8721–8730. [CrossRef]
30. Suardiaz, R.; Jambrina, P.G.; Masgrau, L.; Gonzalez-Lafont, A.; Rosta, E.; Lluch, J.M. Understanding the Mechanism of the Hydrogen Abstraction from Arachidonic Acid Catalyzed by the Human Enzyme 15-Lipoxygenase-2. A Quantum Mechanics/Molecular Mechanics Free Energy Simulation. *J. Chem. Theory Comput.* **2016**, *12*, 2079–2090. [CrossRef]
31. Saura, P.; Suardíaz, R.; Masgrau, L.; Lluch, J.M.; González-Lafont, À. Unraveling How Enzymes Can Use Bulky Residues To Drive Site-Selective C–H Activation: The Case of Mammalian Lipoxygenases Catalyzing Arachidonic Acid Oxidation. *ACS Catal.* **2014**, *4*, 4351–4363. [CrossRef]
32. Gardner, H.W. Soybean lipoxygenase-1 enzymically forms both (9S)- and (13S)-hydroperoxides from linoleic acid by a pH-dependent mechanism. *Biochim. Biophys. Acta* **1989**, *1001*, 274–281. [CrossRef] [PubMed]
33. Walther, M.; Roffeis, J.; Jansen, C.; Anton, M.; Ivanov, I.; Kuhn, H. Structural basis for pH-dependent alterations of reaction specificity of vertebrate lipoxygenase isoforms. *Biochim. Biophys. Acta* **2009**, *1791*, 827–835. [CrossRef]
34. Kutzner, L.; Goloshchapova, K.; Heydeck, D.; Stehling, S.; Kuhn, H.; Schebb, N.H. Mammalian ALOX15 orthologs exhibit pronounced dual positional specificity with docosahexaenoic acid. *Biochim. Biophys. Acta* **2017**, *1862*, 666–675. [CrossRef] [PubMed]
35. Ravula, T.; Hardin, N.Z.; Ramamoorthy, A. Polymer nanodiscs: Advantages and limitations. *Chem. Phys. Lipids* **2019**, *219*, 45–49. [CrossRef]
36. Reisch, F.; Kakularam, K.R.; Stehling, S.; Heydeck, D.; Kuhn, H. Eicosanoid biosynthesis in marine mammals. *FEBS J.* **2021**, *288*, 1387–1406. [CrossRef]
37. Kobe, M.J.; Neau, D.B.; Mitchell, C.E.; Bartlett, S.G.; Newcomer, M.E. The structure of human 15-lipoxygenase-2 with a substrate mimic. *J. Biol. Chem.* **2014**, *289*, 8562–8569. [CrossRef]
38. Jumper, J.; Evans, R.; Pritzel, A.; Green, T.; Figurnov, M.; Ronneberger, O.; Tunyasuvunakool, K.; Bates, R.; Zidek, A.; Potapenko, A.; et al. Highly accurate protein structure prediction with AlphaFold. *Nature* **2021**, *596*, 583–589. [CrossRef]

39. Varadi, M.; Anyango, S.; Deshpande, M.; Nair, S.; Natassia, C.; Yordanova, G.; Yuan, D.; Stroe, O.; Wood, G.; Laydon, A.; et al. AlphaFold Protein Structure Database: Massively expanding the structural coverage of protein-sequence space with high-accuracy models. *Nucleic Acids Res.* **2022**, *50*, D439–D444. [CrossRef]
40. Martinez-Rosell, G.; Giorgino, T.; De Fabritiis, G. PlayMolecule ProteinPrepare: A Web Application for Protein Preparation for Molecular Dynamics Simulations. *J. Chem. Inf. Model.* **2017**, *57*, 1511–1516. [CrossRef]
41. Jones, G.; Willett, P.; Glen, R.C.; Leach, A.R.; Taylor, R. Development and validation of a genetic algorithm for flexible docking. *J. Mol. Biol.* **1997**, *267*, 727–748. [CrossRef] [PubMed]
42. Verdonk, M.L.; Cole, J.C.; Hartshorn, M.J.; Murray, C.W.; Taylor, R.D. Improved protein-ligand docking using GOLD. *Proteins* **2003**, *52*, 609–623. [CrossRef] [PubMed]
43. Li, P.F.; Merz, K.M. MCPB.py: A Python Based Metal Center Parameter Builder. *J. Chem. Inf. Model.* **2016**, *56*, 599–604. [CrossRef] [PubMed]
44. Tian, C.; Kasavajhala, K.; Belfon, K.A.A.; Raguette, L.; Huang, H.; Migues, A.N.; Bickel, J.; Wang, Y.Z.; Pincay, J.; Wu, Q.; et al. ff19SB: Amino-Acid-Specific Protein Backbone Parameters Trained against Quantum Mechanics Energy Surfaces in Solution. *J. Chem. Theory Comput.* **2020**, *16*, 528–552. [CrossRef]
45. Izadi, S.; Anandakrishnan, R.; Onufriev, A.V. Building Water Models: A Different Approach. *J. Phys. Chem. Lett.* **2014**, *5*, 3863–3871. [CrossRef]

SI6.2 Supporting information

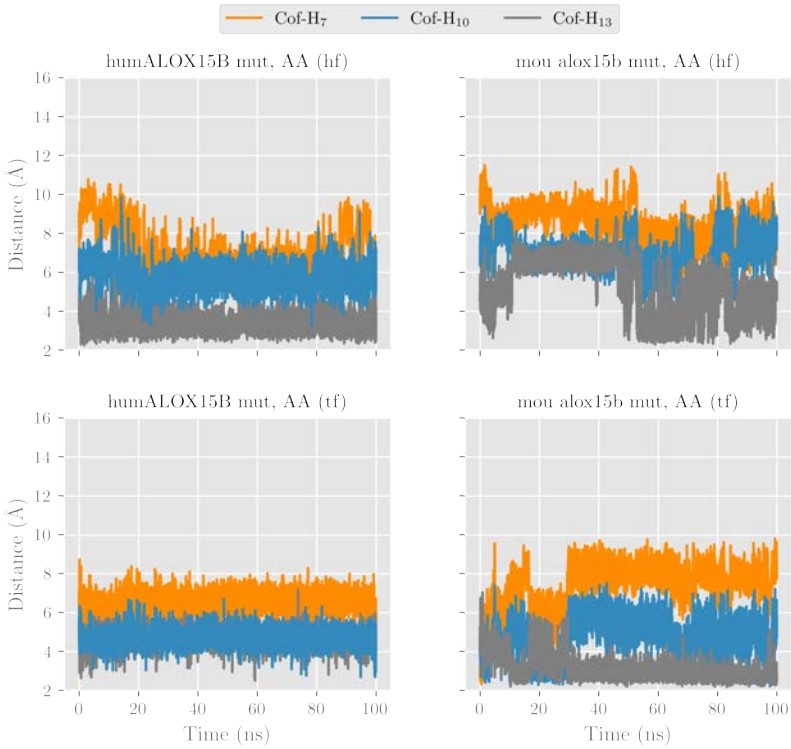

Figure SI6.1: Distances from H_7, H_{10}, and H_{13} to OH^- group along the MD simulations for AA and Asp602Tyr, Val603His humALOX15B's mutant and Tyr603Asp, His604Val mouAlox15b's mutant.

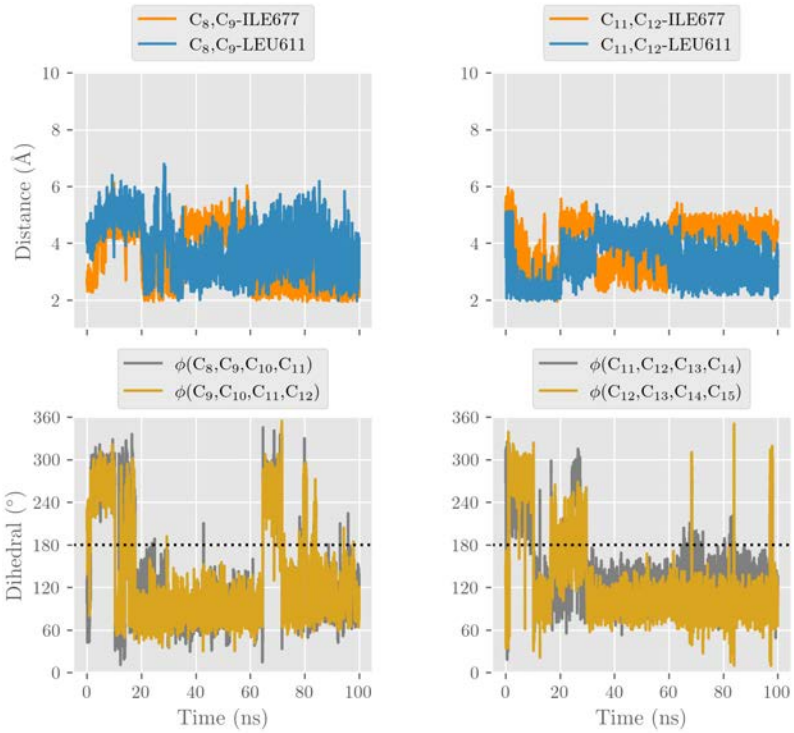

Figure SI6.2: Minimum distances from C_8C_9 and $C_{11}C_{12}$ to Leu611 and Ile 677, and dihedral angles around C_{10} and C_{15} along the MD simulation of the tail-first oriented AA complexed in Tyr603Asp, His604Val mouALOX15B's mutant.

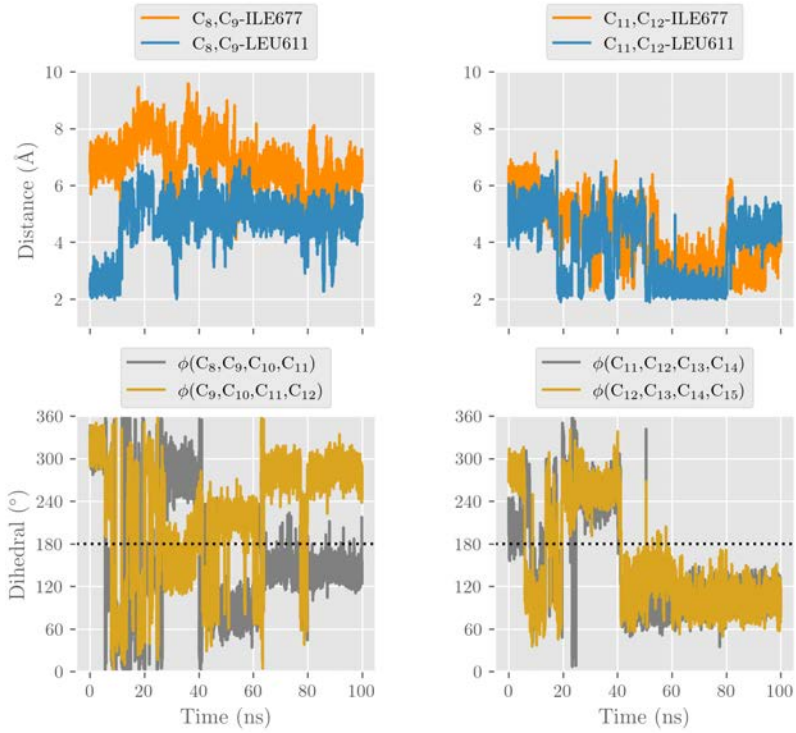

Figure SI6.3: Minimum distances from C_8C_9 and $C_{11}C_{12}$ to Leu611 and Ile 677, and dihedral angles around C_{10} and C_{15} along the MD simulation of the head-first oriented AA complexed in WT mouALOX15B.

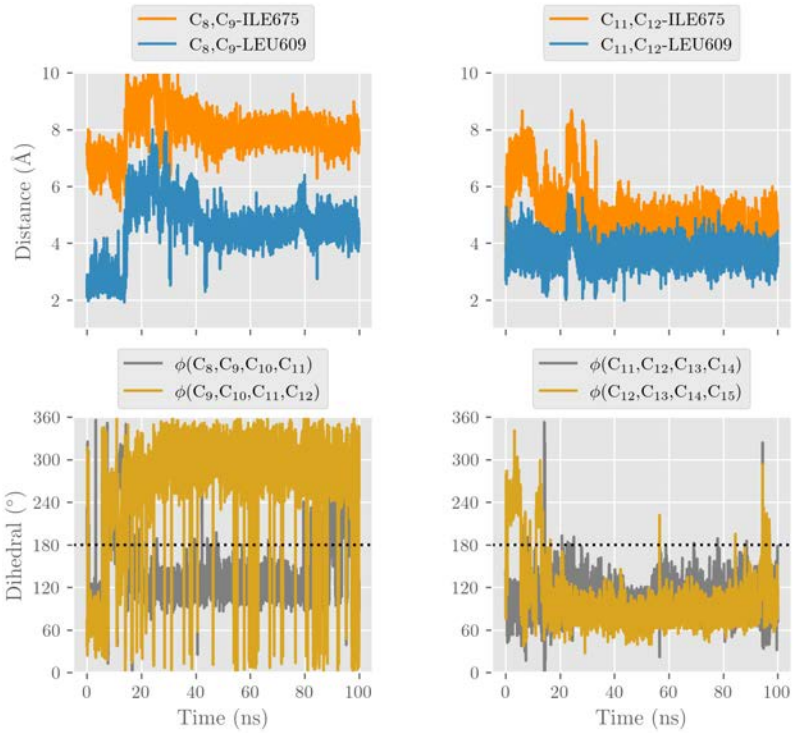

Figure SI6.4: Minimum distances from C_8C_9 and $C_{11}C_{12}$ to Leu609 and Ile 675, and dihedral angles around C_{10} and C_{15} along the MD simulation of the head-first oriented AA complexed in Asp602Tyr, Val603His humALOX15B's mutant.

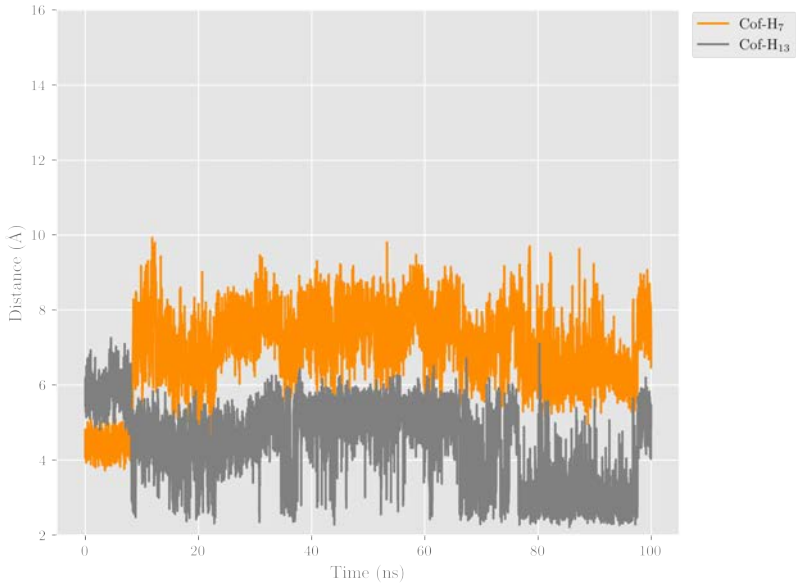

Figure SI6.5: Closest H_7 and H_{13} distances to OH^- cofactor along the MD simulation of the tail-first oriented 8S-HETE:WT mouAlox15b complex.

Chapter SI7

Exchanging ALOX5 regioselectivity to emulate ALOX15

SI7.1 Publication

ACS chemical biology

Articles

Cite This: ACS Chem. Biol. 2019, 14, 2768−2782

pubs.acs.org/acschemicalbiology

Mutations of Triad Determinants Changes the Substrate Alignment at the Catalytic Center of Human ALOX5

Igor Ivanov,*[,†] Alexey B. Golovanov,[†] Cristián Ferretti,[‡] Miquel Canyelles-Niño,[‡] Dagmar Heydeck,[§] Sabine Stehling,[§] José M. Lluch,[‡,∥] Àngels González-Lafont,[‡,∥] and Hartmut Kühn[§]

[†]Lomonosov Institute of Fine Chemical Technologies, MIREA - Russian Technological University, Vernadskogo pr. 86, 119571 Moscow, Russia

[‡]Departament de Química and [∥]Institut de Biotecnologia i de Biomedicina (IBB), Universitat Autònoma de Barcelona, 08193 Bellaterra, Barcelona, Spain

[§]Institute of Biochemistry, Charite - University Medicine Berlin, Corporate member of Free University Berlin, Humboldt University Berlin, and Berlin Institute of Health, Charitéplatz 1, D-10117 Berlin, Germany

Supporting Information

ABSTRACT: For the specificity of ALOX15 orthologs of different mammals, the geometry of the amino acids Phe353, Ile418, Met419, and Ile593 ("triad determinants") is important, and mutagenesis of these residues altered the reaction specificity of these enzymes. Here we expressed wild-type human ALOX5 and its F359W/A424I/N425M/A603I mutant in Sf9 insect cells and characterized the catalytic differences of the two enzyme variants. We found that wild-type ALOX5 converted arachidonic acid mainly to 5(*S*)-hydroperoxyeicosatetraenoic acid (HpETE). In contrast, 15(*S*)- and 8(*S*)-H(p)ETE were formed by the mutant enzyme. In addition to arachidonic acid, wild-type ALOX5 accepted eicosapentaenoic acid (EPA) as substrate, but C18 fatty acids were not oxygenated. The quadruple mutant also accepted linoleic acid and α- and γ-linolenic acid as substrate. Structural analysis of the oxygenation products and kinetic studies with stereospecifically labeled 11(*S*)- and 11(*R*)-deutero-linoleic acid suggested alternative ways of substrate orientation at the active site. *In silico* docking studies, molecular dynamics simulations, and quantum mechanics/molecular mechanics (QM/MM) calculations confirmed this hypothesis. These data indicate that "triad determinant" mutagenesis alters the catalytic properties of ALOX5 abolishing its leukotriene synthase activity but improving its biosynthetic capacity for pro-resolving lipoxins.

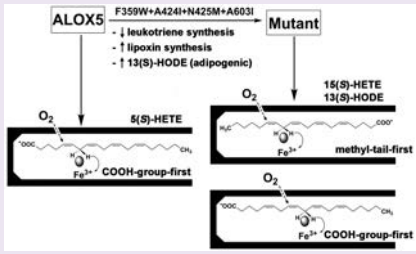

Lipoxygenases (ALOX isoforms) form a family of lipid dioxygenases that catalyze the oxygenation of free and esterified polyenoic fatty acids to hydroperoxy derivatives.[1,2] The catalytic cycle of the LOX reaction consists of four consecutive elementary reactions (stereoselective hydrogen abstraction, radical rearrangement, stereospecific oxygen insertion, radical reduction), and the rate-limiting step is the stereospecific abstraction of a hydrogen atom from a prochiral bisallylic methylene of the substrate fatty acid.[3,4] Although the molecular basis for the defined stereochemistry of the oxygenation reaction is not completely understood, the alignment of the fatty acid substrate at the active site of the enzyme plays a major role.[5,6] The human genome involves six functional *ALOX* genes,[7] which encode for six different ALOX isoforms (ALOX15, ALOX15B, ALOX12, ALOX12B, ALOX5, ALOXE3). The mouse genome involves an ortholog for each of the human *ALOX* genes but in addition the *Aloxe12* gene encodes for a seventh ALOX isoform.[7] Among the different human ALOX isoforms, ALOX5 is of particular biological relevance since it constitutes the key enzyme in the biosynthesis of leukotrienes.[8,9] These lipid mediators exhibit pro-inflammatory activities and play a major role in the pathogenesis of anaphylactic reactions.[10,11] In fact, leukotriene synthesis inhibitors[12] and a leukotriene receptor antagonist[13,14] are currently available for prescription as antiasthmatic drugs.

Human ALOX5 is a 75 kDa protein. It consists of a single polypeptide chain, which folds into a two-domain structure. The crystal structure of a mutant version of human ALOX5 has been solved,[15] and the X-ray data indicate that the small N-terminal domain, which involves specific binding sites for calcium and ATP, is composed of parallel and antiparallel β-sheets. This structural subunit has been implicated in membrane binding but might also exhibit regulatory activities.[9] The C-terminal domain involves the catalytic non-heme iron and consists of several α-helices, which form the substrate-binding pocket. This cavity is lined by hydrophobic amino acids, but there is no immediate connection to the protein

Received: August 20, 2019
Accepted: October 25, 2019
Published: October 30, 2019

DOI: 10.1021/acschembio.9b00674
ACS Chem. Biol. 2019, 14, 2768−2782

surface. The entrance into the substrate binding pocket is blocked by bulky amino acid side chains, and thus, substantial structural rearrangement is needed to allow substrate binding.[15] Although no direct X-ray data are currently available for ALOX5−substrate complexes, it has been suggested that during 5-lipoxygenation arachidonic acid (AA) slides into the substrate binding pocket with its carboxylate-end first and is aligned at the active site in such a way that the pro-*S*-hydrogen at C_7 is located close to the catalytic iron.[16]

Human ALOX5 oxygenates AA almost exclusively to 5(*S*)-HpETE, but previous mutagenesis studies have indicated that a phosphorylation mimicking mutant (Ser663Asn) of the stable ALOX5 induces a complete switch in the reaction specificity from arachidonic acid 5-lipoxygenation toward 15-lipoxygenation.[17] This change in reaction specificity would be of major biological interest since protein phosphorylation would convert the 5-lipoxygenating pro-inflammatory ALOX5 to a 15-lipoxygenating anti-inflammatory enzyme.[17] Unfortunately, this switch in reaction specificity, which has been related to an inverse substrate alignment at the active site of the enzyme,[17] could not be reproduced for human and other vertebrate ALOX5 orthologs in a follow up study.[18]

There is, however, an additional strategy to modify the reaction specificity of human ALOX5. Consecutive mutagenesis studies of the "triad determinants" transformed the 5-lipoxygenating enzyme stepwise to a 15-lipoxygenating enzyme species.[19] In fact, the F359W/A424I/N425M/A603I quadruple mutant of human ALOX5 exhibited a major 15*S*-lipoxygenase activity with 8-HETE being a minor side product.[19] These alterations were later on confirmed when similar mutagenesis strategies were applied for mouse[20] and zebrafish[18] ALOX5 orthologs. We recently performed corresponding *in vivo* mutagenesis on mouse alox5, and the resulting knock-in mice accumulated significantly more body weight when aging (unpublished data).

Compared with wild-type animals, the adipose tissue of the kinock-in mice contained elevated 13-HODE levels. 13-HODE has previously been identified as activating PPARγ ligand, which stimulates adipocyte differentiation and development.[21] Thus, the weight-gaining phenotype of our knock-in mice can be explained by the elevated 13-HODE concentrations in adipose tissue.

In the light of these new *in vivo* findings, the question of the molecular basis for the mutagenesis dependent specificity alterations of ALOX5 became of biological relevance. Previous studies[19] have indicated that the quadruple mutant of human ALOX5 (F359W/A424I/N425M/A603I) produces 15*S*-HETE as the major arachidonic acid oxygenation product. Alternative ways of substrate alignments at the active site have been suggested as mechanistic bases for the observed functional alterations, but this hypothesis has not been tested experimentally. To explore whether this hypothesis is correct, we expressed wild-type and mutant human ALOX5 in the baculovirus−insect cell system and characterized the enzymatic properties of the two enzyme variants. Structural analysis of the oxygenation products of different fatty acids by wild-type and mutant ALOX5, as well as kinetic studies with 11(*S*)- and 11(*R*)-deutero-linoleic acid suggested an inverse orientation of the substrate for arachidonic acid 5(*S*)- and 15(*S*)-lipoxygenation.

RESULTS

Expression of Wild-type and Mutant humALOX5 Variants. When we analyzed the lysis supernatants of Sf9 cells infected with the recombinant wild-type humALOX5 baculovirus by immunoblotting using an anti-His-tag antibody, we observed a band migrating with an apparent molecular weight of 75 kDa, and these data suggested that wild-type humALOX5 is expressed under our experimental conditions (Figure 1A). Similar amounts of immunoreactive protein were observed in the lysis pellet. This observation led to the conclusion that either cell lysis was incomplete or a major share of the recombinant protein was deposited as denatured

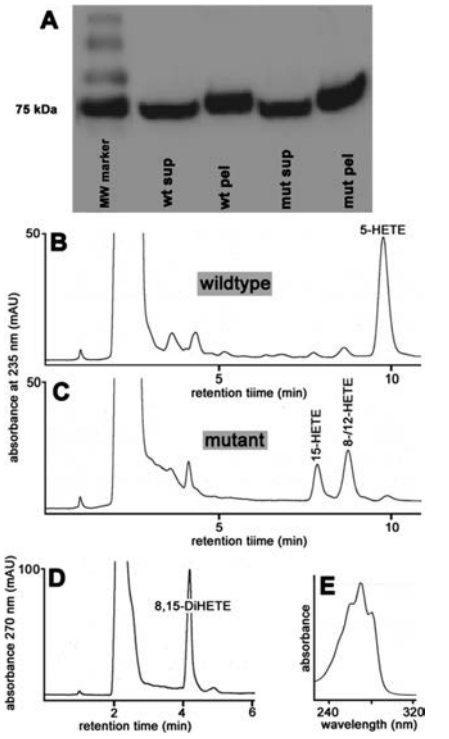

Figure 1. Expression of humALOX15 variants. Wild-type human ALOX5 and its F359W/A424I/N425M/A603I mutant were expressed in the baculovirus−insect cell system as described in the Methods. (A) Cell lysis supernatant (3 μL) and 3 μL of the reconstituted lysis pellet were applied to SDS-PAGE, and the blot was processed with an anti-His-tag antibody. (B, C) Activity assays were carried out with 20 μL of the lysis supernatant, and the reaction products were analyzed by RP-HPLC (see Methods). Retention times of authentic standards are given above the traces. (D) Following the chromatogram of the reaction products formed by the mutant enzyme at 270 nm, we observed a major conjugated triene that comigrated with an authentic standard of 8(*S*),15(*S*)-DiHETE. (E) The UV-spectrum of the reaction product exactly matched the spectrum of the standard. Activity assays were carried out in triplicate and representative RP-HPLC chromatograms are shown.

DOI: 10.1021/acschembio.9b00674
ACS Chem. Biol. 2019, 14, 2768−2782

protein in intracellular inclusion bodies. The quadruple mutant (F359/WA424I/N425M/A603I) of the human ALOX15 (humALOX15) was expressed at similar levels, and here again we detected large amounts of recombinant protein in the lysis pellet. When we calibrated the electrophoretic scale (data not shown) applying known amounts of pure His-tag fusion *M. fulvus* ALOX,[22] we estimated an expression level of 12.6 mg of recombinant wild-type humALOX5 per liter of Sf9 liquid culture (2×10^9 cells). Thus, our expression level was somewhat higher than that reported for the same enzyme (1−2 mg of human ALOX5 per $l \times 10^9$ cells) in a previous study.[23] It should be stressed at this point that we did not quantify the iron content of the recombinant enzymes preparations, and thus, it might well be that the different specific activities of the enzyme preparations might be related to a different iron load.

Conversion of Arachidonic Acid by Wild-type humALOX5 and Its F359WA424I/N425M/A603I Mutant. To test the catalytic activity of the recombinant humALOX5 variants, comparative activity assays were carried out. For this purpose, we incubated aliquots of the Sf9 cell lysis supernatant with arachidonic acid, and the amounts of conjugated dienes formed as major oxygenation products were quantified. As expected, large amounts of 5-HETE were formed by wild-type humALOX5 (Figure 1B). When the humALOX5 quadruple mutant was employed as catalyst (Figure 1C), 5-HETE formation was abolished. In contrast, large amounts of conjugated dienes comigrating with 15-HETE and 8-/12-HETE were detected (Figure 1C). To resolve 8- and 12-HETE, the 8/12-HETE peak was prepared by RP-HPLC and further analyzed by NP-HPLC.

With this combined RP/NP-HPLC strategy, the following product composition was quantified for the mutant enzyme expressed in Sf9 cells: 46.9 ± 3.5% 8-HETE, 44.9 ± 4.3% 15-HETE, and 8.9 ± 0.1% 12-HETE. In our previous study,[19] we obtained the following shares for the mutant enzyme expressed in *E. coli*: 20% 8-HETE, 71% 15-HETE, and 9% 12-HETE. Although the relative share of 15-HETE formation is somewhat higher for the mutant ALOX5 expressed in *E. coli*, 5-HETE formation is completely abolished for both mutant enzyme species.

When we recorded the chromatogram at 270 nm, we observed the formation of a conjugated triene, which comigrated with an authentic standard of 8(*S*),15(*S*)-diHETE (Figure 1D). Comparison of the UV-spectra of the reaction product (Figure 1E) with that of the authentic standard suggested chemical identity, and the mass spectra were virtually indistinguishable. It is of major biological relevance that the mutagenesis induced alterations in the reaction specificity and abolished the LTA_4-synthase activity of wild-type humALOX5 (Supplementary Figure S1), and these data indicate a strong reduction of the pro-inflammatory character of the enzyme. To identify the product enantiomer composition, we reanalyzed the major reaction products by combined NP/CP-HPLC (Figure 2). As expected, we found that the major product of the wild-type humALOX5 was 5(*S*)-HETE (Figure 2A). The two major oxygenation products formed by the mutant enzyme (Figure 2B) were also chiral [15(*S*)-HETE, 8(*S*)-HETE], whereas the minor oxygenation product (12-HETE) was a racemic mixture (data not shown). These data demonstrate that the stereochemistry of 15- and 8-HETE formation by the mutant enzyme was tightly enzyme controlled.

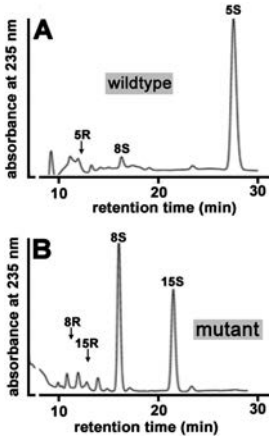

Figure 2. Combined NP/CP-HPLC analysis of the reaction products formed by wild-type human ALOX5 and its F359W/A424I/N425M/A603I mutant. The conjugated dienes formed during the activity assays (see Figure 1) were prepared by RP-HPLC (n = 3), pooled, and further analyzed by combined NP/CP-HPLC (see Methods). For each enzyme preparation, two separate analytical runs were carried out, and representative chromatograms are shown. (A) Wild-type human ALOX5, (B) F359W/A424I/N425M/A603I mutant. Retention times of authentic standards are given above the chromatographic traces. The combined triplicate samples presented in Figure 1 were analyzed.

Linoleic Acid Oxygenation by humALOX5 and Its F359W/A424I/N425M/A603I Mutant. The mutagenesis induced changes in the reaction specificity of humALOX5 with AA suggested that the quadruple mutant of humALOX5 might exhibit an altered substrate specificity. To characterize these alterations in more detail, we first incubated the two enzyme variants with linoleic acid. Recombinant wild-type humALOX5 did not accept linoleic acid as substrate (Figure 3A). These results are in agreement with the data obtained for native guinea pig ALOX5,[24] which shares a 91% amino acid sequence identity with human ALOX5. In contrast, the F359W/A424I/N425M/A603I mutant formed large amounts of conjugated dienes comigrating with 13- and 9-HODE (Figure 3B). Unfortunately, these two metabolites were not resolved in RP-HPLC, and thus, consecutive NP-HPLC and CP-HPLC were carried out. Here we found (Figure 3C) that 13-HODE was the major LA oxygenation product, and CP-HPLC revealed dominant formation of 13(*S*)-isomer (Figure 3C, left inset). 9-HODE (Figure 3C) was only produced in lower quantities (13-HODE/9-HODE ratio of 4:1). Surprisingly, this product was also chiral with strong preponderance of the *S*-enantiomer (Figure 3C, right inset).

The antarafacial character of the LOX reaction predicts that formation of 13(*S*)-HODE involves the abstraction of the pro-*S*-H atom from C_{11} of LA. To test whether the quadruple ALOX15 mutant also follows this mechanistic concept, we incubated the enzyme separately with 11(*S*)- and 11(*R*)-deutero-linoleic acid and found (Figure 4A) that 11(*S*)-deutero-linoleic acid was only oxygenated at a low rate. In contrast, 11(*R*)-deuterated substrate was effectively oxygenated (Figure 4B), and we calculated a primary isotopic effect of >30.

DOI: 10.1021/acschembio.9b00674
ACS Chem. Biol. 2019, 14, 2768−2782

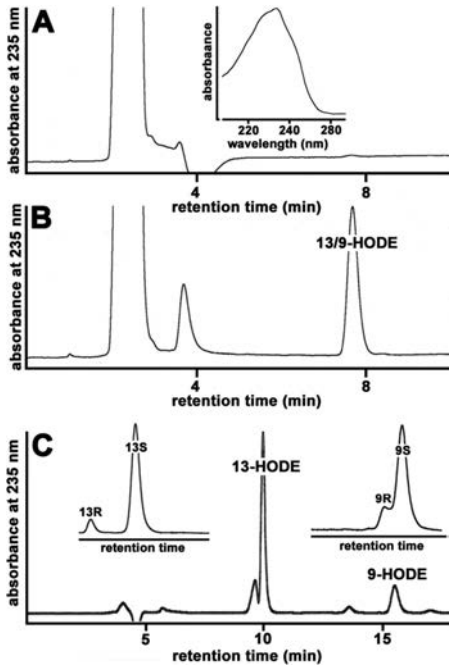

Figure 3. Analysis of the reaction products formed by human ALOX5 variants from linoleic acid. For linoleic acid (80 μM) oxygenase activity assays, the cell lysis supernatant was applied. Conjugated dienes formed during the incubation period were analyzed by RP-HPLC. (A) Wild-type human ALOX5. (B) Mutant human ALOX5. The UV-spectrum of the conjugated dienes formed by mutant human ALOX5 is shown by the inset in panel A. (C) Since 13-HODE and 9-HODE are not well resolved by RP-HPLC, the conjugated dienes were prepared by RP-HPLC and further analyzed NP-HPLC (Methods). 13- and 9-HODE were prepared by NP-HPLC, and their enantiomer compositions were analyzed by chiral phase HPLC (left inset, 13-HODE; right inset, 9-HODE). Three independent activity assays were carried out, and representative chromatograms are shown. NP- and CP-HPLC were performed with the pooled conjugated dienes prepared from the three independent activity assays.

These data indicated that the formation of 13(*S*)-HODE by the human ALOX5 quadruple mutant follows an antarafacial mechanism. When we analyzed the oxygenation products formed from 11(*S*)- and 11(*R*)-deutero-linoleic acid by both RP-HPLC and NP-HPLC, we found (Figure 4C, lower trace) that 13-HODE was the major product formed from 11(*R*)-deutero-linoleic acid and that 9-HODE only contributed about 20% to the product mixture (80.1 ± 0.6% 13-HODE vs 19.9 ± 0.6% 9-HODE). From this data, one can conclude that the formation of 13(*S*)-HODE from linoleic acid (Figure 3) is strongly inhibited when the deuterium isotope is localized at the 11(*S*)-position of the substrate. Finally, we analyzed the oxygenation products synthesized from 11(*S*)-deutero linoleic acid (Figure 4C, lower trace). Since the oxygenation rate of this substrate by the mutant enzyme was rather low (compare Figure 4A,B), we used a 10-fold higher enzyme concentration to prepare sufficient amounts of oxygenation products. In this case, 9-HODE appeared to be the major product (20.9 ± 2.5% 13-HODE vs 79.1 ± 2.5% 9-HODE). The most plausible explanation for the different product compositions is that the substrate fatty acid is inversely aligned [methyl-tail-first for 13(*S*)-HODE formation vs COOH-group-first for 9(*S*)-HODE formation] in the active site of the enzyme for the formation of the two linoleic acid oxygenation products (Figure 4D). It should be stressed at this point that the distance between C_{11} (only site of hydrogen abstraction in linoleic acid) and the methyl terminus of the fatty acid is much shorter than the corresponding distance to the carboxylic group, and this distance difference may contribute to the difference of 13-HODE and 9-HODE formation. However, recent MD simulations have indicated that the distance-based dip-stick model (Figure 4D) does not adequately mirror all aspects of substrate binding in the active site of ALOX isoforms.[25,26] In fact, our MD simulations of LA binding in the active site of the human ALOX5 quadruple mutant revealed (see below and Supplementary Figures S3 and S4) that C11 can even be located at a similar distance from the iron-bound hydroxyl in both orientations. According to our MD simulations, LA exhibits a higher degree of conformational flexibility when aligned at the active site allowing a large number of potential enzyme−substrate complexes. Which of these complexes are catalytically productive depends not only on the geometry (distances) but also on the energetic properties of these complexes.

Oxygenation of Other Fatty Acids by humALOX5 and Its F359W/A424I/N425M/A603I Mutant. Next, we analyzed the reaction specificity of the two enzyme variants with other naturally occurring polyenoic fatty acids. α-Linolenic acid (ALA) is not a good substrate for wild-type humALOX5 (Figure 5A). In contrast, the mutant enzyme formed large amounts of conjugated dienes (Figure 5B) that comigrated in RP-HPLC with an authentic standard of 13-HOTrE(n-3) and GC/MS analysis confirmed the chemical structure of this product (Table 1). γ-Linolenic acid (GLA) involves an additional double bond close to the carboxylate of the fatty acid substrate, and thus, this substrate is structurally more closely related to arachidonic acid. Nevertheless, this fatty acid was not well oxygenated by wild-type recombinant ALOX5 (Figure 5C). In contrast, the mutant enzyme oxygenated GLA to a mixture of 13-HOTrE(n-6) (early eluting diene) and 10-HOTrE(n-6) (late eluting diene) as indicated by GC/MS (Table 1).

Finally, we tested the reactivity of the two enzyme variants with EPA and DHA (Supplementary Figure S2). Wild-type human ALOX5 converted EPA with a 3-fold higher rate than arachidonic acid (Table 1), and as major oxygenation product 5-HEPA was identified (Table 1 and Supplementary Figure S2A). The quadruple mutant was catalytically much less effective on this substrate (Table 1), and here 12- and 15-HEPA were identified as major oxygenation products (Table 1 and Supplementary Figure S2B). Wild-type humALOX5 converted DHA with a 35% lower rate than arachidonic acid (Table 1), and as major oxygenation product 7-HDHA was identified (Table 1 and Supplementary Figure S2C). These results were consistent with previously obtained data for human ALOX5.[27] We also detected smaller amounts of 14- and 17-HDHA, but these compounds were already present as auto-oxidation products in the substrate solution. The ALOX5 quadruple mutant was catalytically similarly effective on this

DOI: 10.1021/acschembio.9b00674
ACS Chem. Biol. 2019, 14, 2768−2782

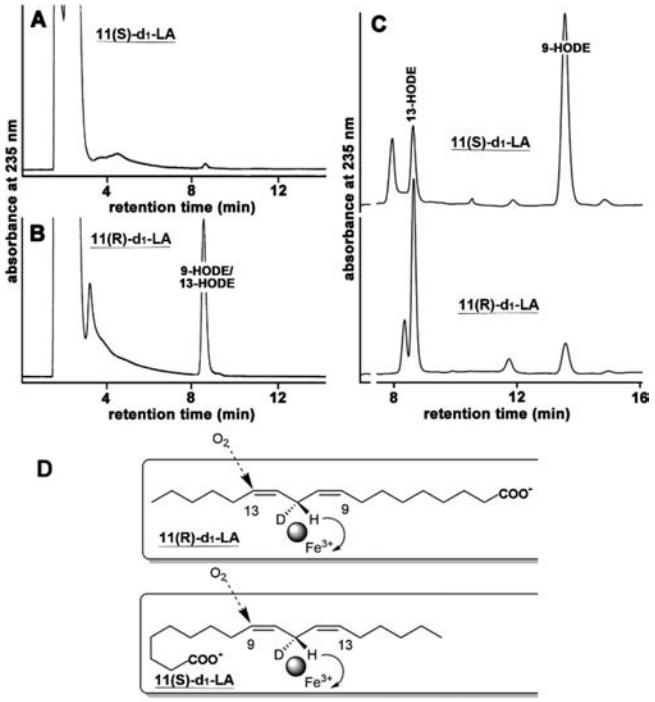

Figure 4. Analysis of the reaction products formed by human ALOX5 mutant (F359W/A424I/N425M/A603I) from 11(*S*)- and 11(*R*)-deuterolinoleic acid. Mutant human ALOX5 was expressed in the baculovirus−insect cell system (see Methods), and 50 μL of the cell lysis supernatant was used to quantify the oxygenation of stereospecifically deuterated linoleic acid (80 μM 11(*S*)- or 11(*R*)-d_1-linoleic acid). Conjugated dienes formed during the incubation period were analyzed by RP-HPLC. (A) 11(*S*)-d_1-Linoleic acid as substrate; (B) 11(*R*)-d_1-linoleic acid as substrate. The pronounced differences in product profile indicate a primary isotopic effect of >30. (C) The products formed from 11(*S*)- (upper trace) and 11(*R*)-d_1-linoleic acid (lower trace) were prepared by RP-HPLC and analyzed by NP-HPLC. Experiments were carried out in duplicate, and representative chromatograms are shown. (D) Mechanistic scenario explaining the stereochemistry of the hydrogen abstraction catalyzed by the ALOX5 quadruple mutant using 11-d_1-linoleic acid enantiomers as substrate.

substrate (Table 1), but here the major oxygenation products were 10- and 17-HDHA (Table 1 and Supplementary Figure S2D). There has been a long lasting discussion among ALOX5 experts about whether this enzyme forms significant amounts of 4-HDHA when acting on DHA. Although we cannot completely rule out this possibility, our data indicate that 4-HDHA is not among the major DHA oxygenation products of our recombinant enzyme preparation.

Lipoxin Synthase Activity. Lipoxins are specialized resolution mediators, formed from arachidonic acid by different ALOX isoforms.[28] In principle, there are two alternative mechanistic routes for lipoxin biosynthesis. (i) The epoxide pathway: Here polyenoic fatty acids are first oxygenated to mono- or dihydroperoxides. These peroxides may further be converted to epoxy derivatives, and this reaction may also be catalyzed by ALOX isoforms via their leukotriene A4 synthase activities.[29−31] These epoxides may then be hydrolyzed forming positional and optical diol isomers. (ii) The multiple oxygenation pathway: Lipoxins contain 3-hydroxy groups, and it might be possible that each of these functional groups is introduced by a separate ALOX-catalyzed oxygenation reaction. For instance, ALOX15 oxygenates arachidonic acid to 15-H(p)ETE (first oxygenation step). Next 15-H(p)ETE is oxygenated by the same enzyme or by ALOX5 to 5,15-DiH(p)ETE. This product still involves a bisallylic methylene (C_{10}), and thus, it constitutes a substrate for arachidonic acid 12- and 15-lipoxygenating ALOX isoforms (ALOX15, ALOX12, aspirin-treated COX2). When these enzymes oxygenate 5,15-DiH(p)ETE, either 5,6,15-tri-H(p)-ETE (hydroperoxy lipoxin A isomers) or 5,14,15-tri-H(p)ETE (hydroperoxy lipoxin B_4 isomers) are formed. In fact, 15-HETE or its methyl ester are oxygenated to LxB_4 (5,14,15-Tri-HETE), and the two oxygen atoms introduced at C_5 and C_{14} clearly originated from the atmosphere.[32,33] In other words, ALOX isoforms exhibit lipoxin synthase activities.[33−36] The extent of this catalytic activity is variable and depends on the enzyme characteristics but also on the availability of the substrate. To compare the lipoxin synthase activities of wild-type ALOX5 and its F359W/A424I/N425M/A603I mutant, we incubated the two enzyme variants with 5(*S*)-HETE, 15(*S*)-HETE, and 5(*S*),15(*S*)-DiHETE for 5 min and quantified by RP-HPLC the conjugated tetraenes formed.

DOI: 10.1021/acschembio.9b00674
ACS Chem. Biol. 2019, 14, 2768−2782

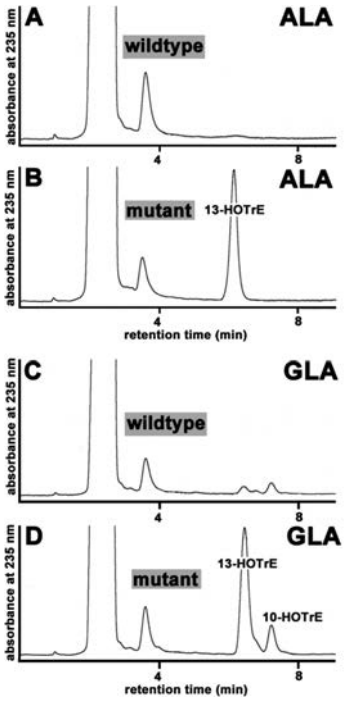

Figure 5. Analysis of the reaction products formed by human ALOX5 variants from α-linolenic acid (ALA) and γ-linolenic acid (GLA). Wild-type and mutant human ALOX5 were expressed in the baculovirus−insect cell system (see Methods), and 40 μL of the cell lysis supernatants was used for LA, ALA, and GLA (80 μM) oxygenase activity assays. Conjugated dienes formed during the incubation period were analyzed by RP-HPLC (see Methods). (A) Wild-type human ALOX5 with ALA as substrate. (B) Mutant human ALOX5 with ALA as substrate. (C). Wild-type human ALOX5 with GLA as substrate. (D) Mutant human ALOX5 with GLA as substrate. Three independent activity assays were carried out with each enzyme variant and each fatty acid, and representative chromatograms are shown. The conjugated dienes formed were prepared by RP-HPLC and pooled, and their chemical structures were identified by GC/MS (Table 1).

Wild-type human ALOX5 did not convert 5(*S*)-HETE to lipoxins (Table 2). In contrast, the mutant enzyme produced large amounts of conjugated tetraenes and LxA_4 isomers. When 15(*S*)-HETE was used as substrate (Table 2), the wild-type enzyme was the more efficient catalyst (596.3 ± 4.9 ng of lipoxin isomers per sample vs 108.0 ± 2.1 ng of lipoxin isomers per sample for the mutant enzyme). 5(*S*),15(*S*)-DiHETE was more effectively oxygenated to lipoxin isomers by the mutant enzyme (230.8 ng of lipoxin isomers per sample vs 29.1 ± 2.4 ng of lipoxin isomers per sample for the wild-type enzyme). These data show that wild-type human ALOX5 exhibits a higher lipoxin synthase activity than the mutant variant when 15(*S*)-HETE was used as substrate. In contrast, the F359W/A424I/N425M/A603I mutant exhibits a more pronounced lipoxin synthase activity when 5(*S*)- and 5(*S*),15(*S*)-DiHETE were used as substrate. When we employed arachidonic acid as substrate, no quantifiable amounts of lipoxin isomers could be detected in our *in vitro* assay system. It should be stressed at this point that we did not explore in this study whether the lipoxin isomers formed by the two enzyme variants were biosynthesized via the epoxide pathway or the multiple oxygenation route.

Membrane Oxygenase Activity. Mammalian ALOX5 orthologs do not accept esterified PUFAs as substrate and, thus, do not exhibit membrane oxygenase activity. In contrast, ALOX15 orthologs are capable of oxygenating membrane lipids.[37−39] Here we explored whether the quadruple mutant of human ALOX5 may also exhibit a membrane oxygenase activity. For this purpose, we incubated wild-type human ALOX5 and its quadruple mutant for 15 min *in vitro* with mitochondrial membranes and quantified the hydroxy-PUFA/PUFA ratio. As positive control, we employed recombinant rabbit ALOX15. We found only small amounts of hydroxy-PUFAs (0.07 ± 0.03%) in the membrane lipids when the membranes were incubated in the absence of any ALOX isoform (Table 3). In contrast, after incubation with the rabbit ALOX15 large amounts of conjugated dienes were observed in RP-HPLC, and almost 6% of the major PUFAs were present as oxygenated derivatives. As expected for wild-type ALOX5 (Table 3), no membrane oxygenase activity was detected (hydroxy-PUFA/PUFA ratio of 0.06 ± 0.03%). For the quadruple mutant, we obtained a hydroxy-PUFA/PUFA ratio of 0.25 ± 0.02%, and this data suggests only a minor membrane oxygenase activity. Compared with the rabbit enzyme this activity was rather low. These data indicate that recombinant wild-type human ALOX5 and its F359W/A424I/N425M/A603I mutant do not exhibit major membrane oxygenase activities.

Molecular Docking Studies and MD Simulations. To explore the molecular basis for the alterations in the reaction specificity of the F359W/A424I/N425M/A603I mutant of human ALOX5, we used the crystal structure of a mutant version of humALOX5 (pdb code 3O8Y).[15] Although the wild-type enzyme was heavily mutated to improve its crystallization behavior, the enzyme variant exhibits the same reaction specificity as the wild-type enzyme, and thus, the X-ray coordinates are suitable to perform substrate docking studies and MD simulations. First, we generated an *in silico* model for the F359W/A424I/N425M/A603I mutant and carried out a number of docking calculations of the enzyme−substrate complex using arachidonic acid (AA) as substrate. A plausible structure with high docking score for the COOH-group-first substrate alignment (COOH-group is buried deeply inside the substrate-binding pocket) was selected, and with this structure, MD simulations were carried out. During the first 100 ns of the simulation period, the bisallylic methylene C_{13} was localized close to the iron bound hydroxyl, but we also found structures in which C_{10} hydrogen atoms were close to the iron bound hydroxyl (Figure 6).

These structures might explain the formation of 15-HETE, which involves hydrogen abstraction from C_{13} but also of 8-HETE and 12-HETE, which involve hydrogen abstraction from C_{10}. At later time points of the simulation period (>100 ns) we observed reorientation of the substrate bringing the C_{10} hydrogens even closer to the iron-bound hydroxyl. During the entire simulation period, the bisallylic methylene C_7 remains far distant from the iron-bound hydroxyl (Figure 6A), and these data are in accordance with our experimental observation

DOI: 10.1021/acschembio.9b00674
ACS Chem. Biol. 2019, 14, 2768−2782

Table 1. GC/MS Analysis of the Major Oxygenation Products Formed from Different Polyenoic Fatty Acids[a]

enzyme	substrate	rel. catalytic activity (%)	major products	key ions (m/z) in MS; (rel. abundance, %)
wild-type human ALOX5	C_{18}:Δ9,12	<5	*b*	not performed
	C_{18}:Δ6,9,12	<5	*b*	not performed
	C_{18}:Δ9,12,15	<5	*b*	not performed
	C_{20}:Δ5,8,11,14,17	294	5-OH	**171** (37.4); **261** (46.6); 303 (1.1); 447 (1.8); 462(0.2)
	C_{22}:Δ4,7,10,13,16,19	65	7-OH	**287**(25.8); 473 (3.2)
mutant human ALOX5	C_{18}:Δ9,12	121	13-OH (85%)	73(100); 129 (11.2); **173** (8.5); **369** (14.6); 425 (1.9); 438(7.6)
			9-OH (15%)	73(100); 129 (10.5); **225** (12.5); 317 (0.8); 423 (1.0); 438(2.5)
	C_{18}:Δ6,9,12	106	13-OH (82%)	**225** (78.4); 315 (1.6), 423 (0.3); 438(0.2)
			10-OH (18%)	213 (0.5); **327** (6.4); 423 (0.3); 438(0.2)
	C_{18}:Δ9,12,15	45	13-OH	171(5.4); **369** (44.6); 423 (1.1); 438(0.3)
	C_{20}:Δ5,8,11,14,17	105	8-OH (56%)	**211** (7.5); 263 (2.3); **301** (44.6); 447 (2.3); 462(0.5)
			15-OH (44%)	**171** (9.8); 447 (2.3); 462(0.5)
	C_{22}:Δ4,7,10,13,16,19	86	10-OH (42%)	**237** (2.9); 327 (5.9); 473 (2.3); 488 (1.5)
			17-OH (58%)	**171** (24.9); 488 (2.8)

[a]Activity assays were carried out (see Methods). The major conjugated dienes were analyzed as bis-TMS derivatives. [b]Not applicable.

Table 2. Lipoxin Synthase Activity of Wild-type Human ALOX5 and Its F359W/A424I/N425M/A603I Mutant with Different Substrates[a]

substrate	wild-type enzyme (ng/sample)	mutant enzyme (ng/sample)	ratio (wild-type vs mutant)
5(*S*)-HETE	<1	491.9 ± 17.0	<0.002
15(*S*)-HETE	596.3 ± 4.9	108.0 ± 2.1	5.53
5(*S*),15(*S*)-DiHETE	29.1 ± 2.4	230.8 ± 19.5	0.13

[a]The ALOX protein content in the two recombinant enzyme variants was estimated by immunoblotting, and the aliquots with normalized protein content were incubated for 5 min in 0.5 mL of PBS containing 30 μM of different substrates in the presence of 1 μM linoleic acid acting as enzyme activator. After the incubation period, the reaction was terminated by the addition of solid sodium borohydride, which reduces the hydroperoxy products to the corresponding alcohols. The samples were acidified by the addition of 50 μL of acetic acid, proteins were precipitated with 1 mL of acetonitrile, and precipitate was spun down. Aliquots of the clear supernatant were injected for RP-HPLC quantification of the generated lipoxin isomers (see Methods). Experiments were carried out in duplicate and means ± standard errors are given.

Table 3. Membrane Oxygenase Activity of Wild-type Human ALOX5 and Its F359W/A424I/N425M/A603I Mutant[a]

enzyme	OH-PUFA/PUFA ratio (%)
no enzyme control	0.07 ± 0.03
rabbit ALOX15	5.82 ± 0.54
wild-type human ALOX5	0.06 ± 0.03
mutant human ALOX5	0.25 ± 0.02

[a]The membrane oxygenase activity assays were carried out as described in the Methods (membrane protein concentration in the assay sample 350 mg/mL) and the OH-PUFA/PUFA ratio was calculated as a suitable measure for the degree of oxygenation of the membrane phospholipids.[38] Experiments were carried out in duplicate and means ± standard errors are given. The amounts of the recombinant proteins were normalized with respect to a similar arachidonic acid oxygenase activity.

that in contrast to the wild-type enzyme no 5-HETE is formed by the F359W/A424I/N425M/A603I mutant. In Table 4, the average distances of the three bisallylic methylenes from the iron-bound hydroxyl calculated over the entire simulation

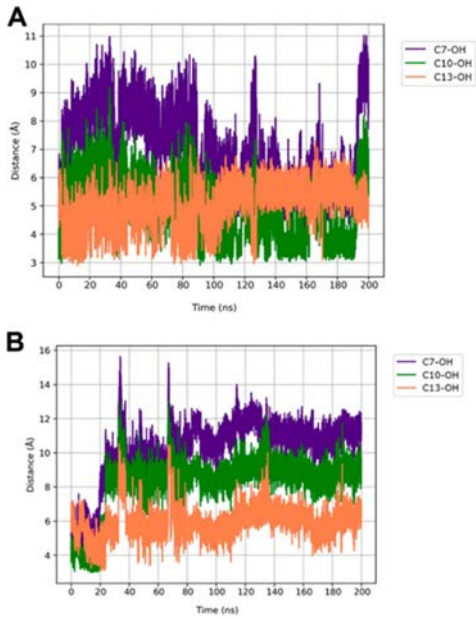

Figure 6. Evolution of the C−OH distances for C7, C10, and C13 of arachidonic acid vs time during 200 ns of molecular dynamics simulation: (A) COOH-group-first orientation; (B) methyl-tail-first orientation.

period are summarized. For the COOH-group-first substrate orientation, C_{10} and C_{13} are located on average at a similar distance from the iron-bound hydroxyl (4.95 Å for C_{10} and 5.00 Å for C_{13}), although, as mentioned, C_{10} gets closer than C_{13} during the second part of the trajectory. In contrast, C_7 is significantly displaced (7.02 Å) explaining the lack of 5-HETE formation. Next, we carried out similar MD simulations for the methyl-tail-first substrate alignment (Figure 6B). Here the average distances of the bisallylic methylenes from the iron-

DOI: 10.1021/acschembio.9b00674
ACS Chem. Biol. 2019, 14, 2768−2782

Table 4. Distances of the Bisallylic Methylenes of Arachidonic Acid from the Iron-Bound Hydroxyl Calculated from Our MD Simulations[a]

orientation		distances (Å)		
		C_7–OH	C_{10}–OH	C_{13}–OH
COOH-group-first	**average**	**7.02**	**4.95**	**5.00**
	minimum	3.99	2.91	2.90
	maximum	11.02	9.18	7.30
	max−min	7.03	6.27	4.40
methyl-tail-first	**average**	**10.23**	**8.29**	**5.94**
	minimum	4.05	2.99	3.07
	maximum	15.63	13.01	10.54
	max−min	11.58	10.02	7.46

[a]The MD simulations of the F359W/A424I/N425M/A603I mutant of humALOX5 were carried out as described in the Methods. The average distances of the AA bisallylic methylenes with respect to the oxygen atom of the iron-bound hydroxyl (C_7–OH, C_{10}–OH, and C_{13}–OH) for COOH-group-first and methyl-tail-first substrate alignments are given in Å.

bound hydroxyl were somewhat increased, and the order of C_{10} (8.29 Å) and C_{13} (5.94 Å) was inverted. As for the COOH-group-first alignment, the bisallylic C_7 was clearly displaced from the iron-bound hydroxyl in this methyl-tail-first substrate alignment. These data indicate that for the COOH-group-first substrate orientation hydrogen abstraction from C_{13} and C_{10} might be possible, even though the AA binding mode at the end of the MD trajectory suggests that H_{10} abstraction could be more favorable in the mutant enzyme.

For the methyl-tail-first substrate alignment, hydrogen is mainly abstracted from C_{13}, which is consistent with the formation of 15(*S*)-HETE (C13 hydrogen abstraction and [+2] radical rearrangement). Most importantly, in both substrate alignments hydrogen can hardly be abstracted from C_7, and this data is consistent with the lack of the 5-lipoxygenating activity of the humALOX15 quadruple mutant.

Similar docking studies and MD simulations were carried out with linoleic acid in the active site of the F359W/A424I/N425M/A603I mutant for the COOH-group-first and the methyl-tail-first substrate orientations. During both trajectories, the bisallylic methylene C_{11} is located in close proximity to the iron-bound hydroxyl (Supplementary Figures S3 and S4). The average C_{11}–OH distances are 4.48 and 5.17 Å for the COOH-group-first and the methyl-tail-first substrate orientation, respectively. These data suggest that hydrogen abstraction from C_{11} should be possible for both LA alignments. Snapshots of the MD simulations of the enzyme–arachidonic acid and the enzyme–linoleic acid complexes in the two orientations are given in Figure 7. It can be seen that C_{13} of arachidonic acid is located in the same region as the C_{11} of linoleic acid.

QM/MM Calculations. Only those enzyme–substrate complexes that have a methylene hydrogen of AA or LA close enough to the acceptor oxygen atom of the iron-bound hydroxyl might correspond to precatalytic structures of thermally feasible hydrogen transfer reactions. However, it is the calculation of the corresponding energy barriers that really establishes the viability of these H-abstraction reactions. To estimate the potential energy barriers for hydrogen abstraction in the different structures of the enzyme–substrate complexes for the COOH-group-first orientation, we selected three snapshots of the enzyme–arachidonic acid complex, in which the distance from one of the hydrogens attached to C_{13} to the

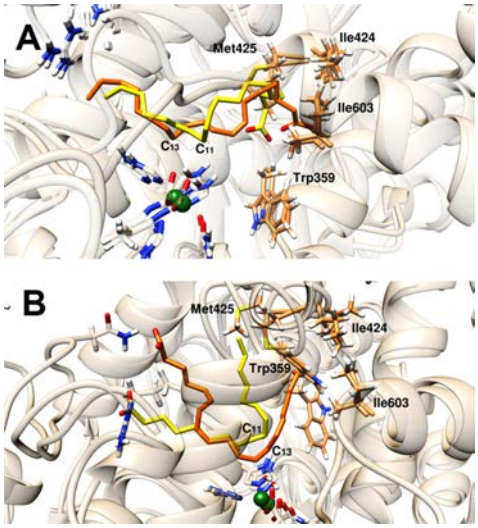

Figure 7. Comparison of AA and LA binding modes. (A) Overlay of COOH-group-first orientation of arachidonic acid (orange) and COOH-group-first orientation of linoleic acid (yellow) at the active site of the F359W/A424I/N425M/A603I mutant of humALOX5 at two snapshots of the corresponding MD simulations. (B) Overlay of arachidonic acid and linoleic acid methyl-tail-first orientations at two snapshots of the corresponding MD simulations.

iron bound hydroxyl was lower than 3 Å. In addition, we selected three snapshots, in which the distance from one of the two hydrogens attached to C_{10} to the iron bound hydroxyl was lower than 3 Å. The aim of our initial calculations was to explore which hydrogen abstraction process is energetically favored for COOH-group-first substrate binding as the distance values obtained in the MD simulations were not conclusive. From the values in Table 5, it can be seen that the potential energy barriers for H_{13} and H_{10} abstraction range from 19.7 to 22.6 kcal/mol and from 19.3 to 21.5 kcal/mol, respectively, confirming that both H-abstraction processes are possible. However, according to our theoretical calculations alone neither of these H-abstractions is favored over the other. In conjunction with experiments though, the formation as a major product of 8(*S*)-HETE can only be explained by H_{10}-abstraction followed by the [−2] radical rearrangement involved in COOH-group-first AA binding. For the methyl-tail-first substrate alignment, the distance calculations from the MD simulation clearly indicated that only H_{13} abstraction is feasible as mentioned above.

For the enzyme–linoleic acid complex, we selected some snapshots in which the distance of H_{11} from the iron bound hydroxyl was <3 Å. This selection procedure was carried out for COOH-group-first and methyl-tail-first substrate alignments to verify if H_{11} abstraction is possible for both substrate orientations. From Table 5, it can be seen that in average the potential energy barriers for hydrogen abstraction did not profoundly differ between the different enzyme–substrate complexes. Thus, according to our calculations neither of these alignments is catalytically more productive than the other.

DOI: 10.1021/acschembio.9b00674
ACS Chem. Biol. 2019, 14, 2768–2782

Table 5. H-Abstraction Potential Energy Barriers (in kcal/mol) for AA and LA Catalyzed by the F359W/A424I/N425M/A603I Mutant of humALOX5[a]

substrate	abstraction	orientation	$\Delta V^{\ddagger}$
AA	H_{10}	COOH-group-first	19.7
			22.6
			20.9
	H_{13}		21.0
			19.3
			21.5
LA	H_{11}	COOH-group-first	23.2
			14.2
			21.7
		methyl-tail-first	19.3

[a]The QM/MM H_{10} and H_{13} abstraction energy profiles from AA bound in a COOH-group-first orientation were calculated from three precatalytic snapshots of the MD simulation. The corresponding potential energy barriers are given in the last column. The same results are given for the H_{11}-abstraction reactions of LA from precatalytic snapshots of the MDs of the substrate COOH-group-first and methyl-tail-first orientations.

DISCUSSION

Mutation of the "Triad Determinants" Alters the Reaction Specificity of Recombinant humALOX5. Mammalian ALOX15 orthologs are either arachidonic acid 12- or arachidonic acid 15-lipoxygenating enzymes, and their reaction specificity depends on the geometry of critical amino acids.[4,40] These residues are localized in three distinct regions of the primary structure, and thus, this hypothesis has been referred to as the Triad Concept of ALOX15 specificity (Figure 8).[4,41] The substrate-binding pocket of mammalian ALOX15 orthologs is a U-shaped cavity the bottom of which is formed by three critical amino acids (triad positions Phe353, Ile418 /Met419, and Ile593). The side chain geometry of these residues determines the depth of the substrate binding pocket. When bulky amino acids are present at these positions, the bisallylic methylene C13 of AA is located in close proximity to the non-heme iron (Figure 8A). If less space-filling side chains are located at the triad positions, the bisallylic methylene C_{10} of the substrate is localized close to the catalytic iron. This substrate binding forces arachidonic acid 12-lipoxygenation (Figure 8B). Applying this concept to mammalian ALOX5 orthologs, one may conclude that AA penetrates into the substrate-binding pocket with its COOH-group ahead so that the bisallylic methylene C_7 is localized close to the catalytic iron (Figure 8C). This structure of the enzyme−substrate complex is consistent with the product pattern (5-lipoxygenation) formed by the wild-type enzyme. When more space-filling side chains are located at the "triad positions", the substrate can penetrate into the cavity in two different ways, with either its methyl-tail or its COOH-group ahead (Figure 8D). For methyl-first orientation, C_{13} of AA is located close the iron, which is required for 15(*S*)-lipoxygenation. In turn, for COOH-group first orientation, C_{10} appears to be closer to the non-heme iron, and such substrate alignment is required for (*S*)-lipoxygenation.

ALOX15 orthologs of highly developed primates carry bulky residues at the triad positions, and thus, they catalyze arachidonic acid 15-lipoxygenation. In contrast, those of lower primates and most other mammals involve less space filling amino acids at these positions, and thus, they function as arachidonic acid 12-lipoxygenating enzymes.[42,43] Previous mutagenesis studies on recombinant ALOX5 orthologs expressed in *E. coli* suggested that mutation of the "triad determinants" in human[19] and mouse[20] ALOX5 also altered the reaction specificity. Multiple mutations of the "triad determinants" gradually altered the reaction specificity from

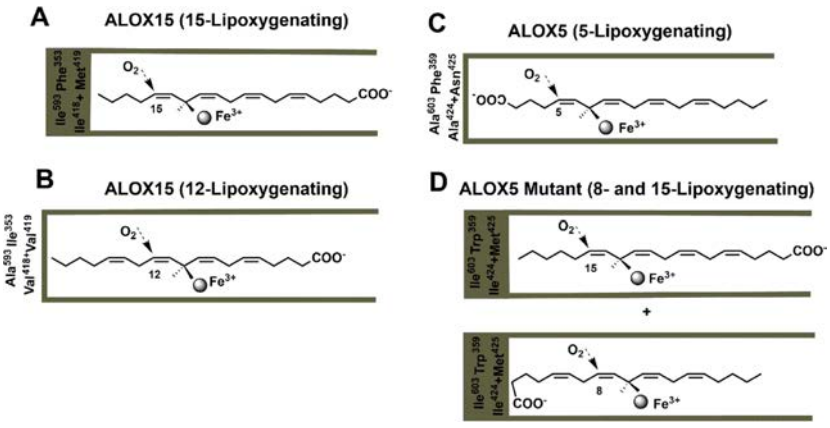

Figure 8. Triad concept of ALOX specificity. (A) Model of the substrate-binding pocket of rabbit ALOX15. AA is located at the substrate-binding pocket with its methyl-tail ahead. The depth of AA penetration is limited by the "triad determinants" (Phe353, Ile418 + Met419, and Ile593). (B) Less space-filling side chains at the triad positions allow the substrate to penetrate deeper into the cavity so that the bisallylic methylene C_{10} is localized close to the iron. (C) The substrate-binding pocket of human ALOX5. AA slides into the substrate-binding pocket with its COOH-group ahead so that the bisallylic methylene C_7 is localized close to the iron. (D) More space-filling side chains are located at the "triad positions". The substrate can penetrate into the cavity in two different ways either with its methyl-tail or COOH-group ahead so that the bisallylic methylenes at C_{13} (methyl-tail-first orientation) or C_{10} (COOH-group-first orientation) are localized close to catalytic iron.

DOI: 10.1021/acschembio.9b00674
ACS Chem. Biol. 2019, 14, 2768−2782

almost exclusively arachidonic 5-lipoxygenation to the formation of a mixture of 15(*S*)-HETE and 8(*S*)-HETE.[19,20] In fact, the F359W/A424I/N425M/A603I mutant of human ALOX5 produced 15(*S*)-HETE as the major oxygenation product.[19] Since human ALOX5 variants are expressed only at a low level in *E. coli*, we employed the baculovirus−insect cell system to express wild-type humALOX5[23,44] and its F359W/A424I/N425M/A603I mutant and characterized the two enzyme variants with respect to their reaction specificity using the most abundantly occurring mammalian polyenoic fatty acids as substrate. Wild-type humALOX5 is well expressed (12.6 mg/L culture fluid) in the baculovirus−insect cell system, and arachidonic acid is oxygenated by the wild-type human ALOX5 almost exclusively to 5(*S*)-H(p)ETE. The F359W/A424I/N425M/A603I mutant is expressed at similar levels (15.8 mg/L culture fluid) and converts this substrate to a mixture of 15(*S*)- and 8(*S*)-H(p)ETE and 12(*S*/*R*)-HETE. The 15(*S*)-HETE/8(*S*)-H(p)ETE ratios are somewhat different when the *E. coli* enzyme[19] is compared with the baculovirus−insect cell enzyme, but in principle, the two expression strategies yielded functionally similar enzymes.

Reaction Specificity with Linoleic Acid As Substrate. Wild-type human ALOX5 does not react with linoleic acid (Figure 3) since this fatty acid lacks a C_7 bisallylic methylene. However, since this substrate carries an *n*-8th bisallylic methylene (C_{11}), the F359W/A424I/N425M/A603I mutant should be able to oxygenate this fatty acid. In fact, we found that the mutant enzyme converted linoleic acid to a 4:1 mixture of 13(*S*)-HODE and 9(*S*)-HODE (Figure 3). In light of the product pattern formed from arachidonic acid [8(*S*)- and 15(*S*)-HETE], the simultaneous formation of 13(*S*)- and 9(*S*)-HODE is plausible. 13(*S*)-HODE is the major linoleic acid oxygenation product formed by the arachidonic acid 15-lipoxygenating activity of the mutant enzyme. Both reactions involve *n*-8 hydrogen abstraction and [+2] radical rearrangement. In contrast, 9(*S*)-HODE is likely to originate from the arachidonic acid 8-lipoxygenating activity. Although hydrogen is abstracted from different carbon atoms (C_{10} in case of arachidonic acid vs C_{11} of linoleic acid) both reactions involve [−2] radical rearrangement. For linoleic acid 13(*S*)-oxygenation, the substrate fatty acid is most probably methyl-tail-first aligned at the active site of the enzyme. In contrast, for linoleic acid 9(*S*)-lipoxygenation an inverse COOH-group-first alignment is likely. These data are consistent with the results we obtained using stereospecifically deuterated linoleic acid isomers (Figure 4).

Reaction Specificity with Other Polyenoic Fatty Acids. The two C18 polyenoic fatty acids ALA and GLA are hardly oxygenated by wild-type human ALOX5 (Table 1, Figure 5A). This observation is plausible for ALA since this substrate does not carry a bisallylic methylene in proximity to the carboxylic group. Interestingly, we also found that wild-type human ALOX5 does not effectively oxygenate GLA (Table 1, Figure 5C). With these fatty acids, activity assays suggested the presence of small amounts of conjugated dienes (Figure 5C), but these compounds were also present in nonenzyme control incubations. Thus, they are not of enzymatic origin. This result is somewhat surprising since GLA carries a bisallylic methylene at C_8, which is a potential target for hydrogen abstraction for the wild-type enzyme. The F359W/A424I/N425M/A603I mutant oxygenated the two linolenic acid isomers, and the 13-hydroxy derivatives were identified as major oxygenation products. With GLA, smaller amounts of 10-HOTrE were also formed, and this dual positional specificity suggests the ability of the enzyme to catalyze simultaneous hydrogen abstraction from C_{11} (13-HOTrE formation) and C_8 (10-HOTrE).

The formation of these products involves a [+2] radical rearrangement, and thus, one can conclude that the substrates may slide into the binding cavity with their methyl tail ahead. In contrast to the C18 polyenoic fatty acids, EPA and DHA are oxygenated by wild-type ALOX5. In fact, EPA was converted by the wild-type enzyme with a 3-fold higher rate than AA (Table 1), and the major oxygenation product was identified as 5-HEPA (Supplementary Figure S2A). The mutant enzyme converted this substrate to 8- (56%) and 15-HEPA (44%), and this product pattern was expected considering the arachidonic acid oxygenation products. With DHA, a more complex pattern of oxygenation products was observed. Here 7-HDHA was identified as major product of the wild-type enzyme, but in addition, we detected smaller amounts of 17-HDHA and 14-HDHA (Supplementary Figure S2C). The formation of 7-HDHA involves hydrogen abstraction from C9 and [−2] radical rearrangement, and thus, the fatty acid substrate may slide into the binding cavity with its carboxylic group ahead. In contrast, formation of 14-HDHA and 17-HDHA involves hydrogen abstraction from C12 and C15, respectively, and [+2] radical rearrangement. These data suggest a methyl-first alignment of the substrate at the active site. Thus, this polyenoic fatty acid can be bound at the substrate-binding pocket of wild-type human ALOX5 in either COOH-group-first or methyl-group-first orientation with COOH-group-first orientation being dominant. For the F359W/A424I/N425M/A603I quadruple mutant, 17-HDHA is the major oxygenation product (58%, Table 1). Formation of this product involves hydrogen abstraction from C15 and [+2] radical rearrangement, and these data suggest a methyl-group-first substrate orientation. However, we also detected significant amounts of 10-HDHA (42%, Table 1), and biosynthesis of this product involves C12 hydrogen abstraction and [−2] radical rearrangement. Thus, for 10-HDHA formation, the substrate might be bound at the enzyme in a COOH-group-first way. Taken together, the product patterns formed from DHA by wild-type and mutant human ALOX5 suggest that this fatty acid may be bound at the substrate-binding pocket in either orientation (methyl-group-first and carboxylic-group-first). For the wild-type enzyme, the carboxylic-group-first orientation is dominant, whereas for the mutant, the methyl-group-first orientation appears to prevail.

Molecular Docking Studies, MD Simulations, and QM/MM Calculations. Our docking studies and MD simulations revealed that arachidonic acid can present stable COOH-group-first and methyl-tail-first binding modes at the active site of the quadruple mutant of humALOX5. The structures generated from the MD trajectories and the calculated QM/MM barriers for H_{13} and H_{10} abstractions indicate that both H-abstractions may be possible for AA COOH-group first alignment. However, as the experimental results correlate COOH-group first orientation with a [−2] radical rearrangement, we conclude that in this orientation H_{10} abstraction takes place and this binding mode might explain the formation of 8(*S*)-HETE. For the AA methyl-tail-first orientation, docking and MD simulations show that only H_{13} abstraction is feasible. From the experiments, it is concluded that in a methyl-tail-first orientation there is a [+2] radical rearrangement and H_{13} abstraction explains the formation of

DOI: 10.1021/acschembio.9b00674
ACS Chem. Biol. 2019, 14, 2768−2782

15(*S*)-HETE. For LA, the *in silico* calculations show that H_{11} abstraction is possible for COOH-group-first as well as for methyl-tail-first orientations. The H_{11} abstraction for the COOH-group-first linoleic acid alignment explains the formation of 9(*S*)-HODE, and 13(*S*)-HODE originates from H_{11} abstraction from methyl-tail-first LA orientation. Finally, it is relevant to highlight again that the theoretical calculations confirm the switch of reaction specificity in the F359W/A424I/N425M/A603I mutant of humALOX5 at molecular level showing why the proS-hydrogen at C_7 is not abstracted.

Conclusions. The Triad Concept has been developed to explain the variable reaction specificities of mammalian ALOX15 orthologs. When this concept is applied for mammalian ALOX5 orthologs the reaction specificity of these enzymes is also altered and the 5S-lipoxygenating wild-type enzymes are gradually converted to 8*S*- and 15*S*-lipoxygenating mutants. This change in reaction specificity impacts the biological function of the enzymes since the biosynthetic capacity for pro-inflammatory leukotrienes is completely abolished. Analysis of the reaction products, kinetic studies with stereospecifically deuterated linoleic acid, molecular docking studies, MD simulations, and QM/MM calculations suggest alternative ways of substrate binding at the active site of the humALOX5 quadruple mutant.

METHODS

Chemicals. The chemicals used were obtained from the following sources: polyenoic fatty acid substrates and HPLC standards of 15(*S*)-HETE, 12(*S*)-HETE, and 5(*S*)-HETE, 5(*S*),6(*R*)-DiHETE, 5(*S*),6(*S*)-DiHETE, lipoxin A_4, and lipoxin B_4 from Cayman Chem (distributed by Biomol, Hamburg, Germany); HPLC grade methanol and acetic acid from Fisher Scientific (Nidderau, Germany); BSTFA used for hydroxy fatty acid derivatization from Sigma-Aldrich (Taufkirchen, Germany). The stereospecifically deuterated linoleic acid isomers were a kind gift of Dr. M. Hamberg from the Karolinska Institute in Stockholm. The degree of deuteration was different for the two isomers: 11(*R*)-deutero-linoleic acid, deuterium content 24%; 11(*S*)-deutero-linoleic acid, deuterium content 98%.

Cloning and Expression of Wild-type humALOX5 in the Baculovirus−Insect Cell System. Total RNA was extracted from a preparation of human mononuclear cells, and the humALOX5 cDNA was amplified using specific amplification primers involving a *Nco*I (upstream primer) and a *Hin*dIII (downstream primer) restriction site. The PCR product was first ligated into the TOPO TA cloning vector 2.1 (Invitrogen, Carlsbad, USA), and the recombinant plasmid was amplified. Next, the *Nco*I/*Hin*dIII restriction fragment was first subcloned in the pkk 233-2 (Pharmacia, Uppsala, Sweden) and further into the pRSET-A bacterial expression plasmid using *Xho*I/*Hin*dIII restriction sites. For this purpose an internal *Xho*I restriction site was deleted and an additional *Xho*I site was introduced in the pkk plasmid immediately upstream of the starting ATG. The recombinant enzyme was expressed in *E. coli*. Unfortunately, we noticed that the enzyme was expressed only at a low level in bacteria, and thus, we decided to employ a more efficient eukaryotic overexpression system. For this purpose, we excised the coding region of the His-tag fusion humALOX5 from the bacterial expression plasmid (*Bam*HI and *Hin*dIII digestion) after deletion of the internal *Bam*HI restriction site as described below, purified the restriction fragment after agarose gel electrophoresis, and subcloned it into the pFastBac HT-B shuttle vector (ThermoFisher Scientific, Schwerte, Germany). Preparation of the corresponding bacmid and the recombinant baculovirus was performed according to the instructions of the "Bac-to-Bac Baculovirus Expression System" (Invitrogen Life technologies/ThermoFisher, Schwerte, Germany). ALOX5 and the mutant were expressed in Sf9 cells (ATCC CRL-1711), cultured in Insect XPRESS Medium (Biozym, Hessisch Oldendorf, Germany) in the presence of 4 mM glutamine and 0.5% FCS. Insect cell culture (150 mL of 2 × 10^6 cells/mL) was infected with recombinant baculovirus (20 mL, second amplification, MOI of 1) and incubated in Erlenmeyer flasks at 27 °C for 72 h. After cells were harvested by centrifugation (4000*g*, 10 min, 4 °C), the cell pellet was resuspended in 6 mL of PBS and sonicated. The cell debris was spun down at (12000*g*, 10 min, 4 °C). The lysate supernatant (10−40 μL) was used as enzyme source for activity assays and further characterization. In additional experiments, we attempted to purify the recombinant enzyme by affinity chromatography. With this method, we could enrich the enzyme preparation but experienced severe loss in catalytic activity. Thus, we decided to carry out the experiments with crude enzyme preparations.

Site-Directed Mutagenesis and Expression of humALOX5 F359W/A424I/N425M/A603I Mutant. To obtain the humALOX5 quadruple mutant, three consecutive steps of mutagenesis were carried out with the bacterial expression plasmid. During the first step Phe359 was replaced with a more bulky Trp. During the second mutagenesis step, Ala424 and Asn425 were mutated to Ile and Met, respectively. Finally, Ala603 was mutated to a more bulky Ile. For each mutant, up to 5 clones were screened for the presence of the LOX-insert (digestion with *Xho*I and *Hin*dIII), and one clone was sequenced to confirm successful mutagenesis. Finally, we excised the 4-fold mutated coding region from the bacterial expression plasmid using *Bam*HI and *Hin*dIII after deletion of the internal *Bam*HI restriction site and subcloned the mutated restriction fragment into the pFastBac HT-B shuttle vector. Expression of the humALOX5 F359W/A424I/N425M/A603I mutant was carried out as described above for the wild-type enzyme.

Fatty Acid Oxygenase Activity. Each activity assay mixture was composed of aliquots of the Sf9 cell lysate supernatants (10−40 μL) in 500 μL of PBS containing 0.4 mM $CaCl_2$, 0.1 mM EDTA, 40 μg/mL dipalmitoylphosphatidyl-choline, and 0.1 mM ATP. The ALOX reaction was started by the addition of enzyme after a substrate fatty acid concentration of 40−100 μM (final concentration) had been adjusted. The mixture was incubated for 5 min at RT, the reaction was stopped by the addition of solid $NaBH_4$, the mixture was acidified to pH 3, and 0.5 mL of ice-cold acetonitrile was added. After 15 min of incubation on ice, the protein precipitate was spun down, the precipitate was removed, and aliquots of the protein-free supernatant were injected to HPLC for quantification of the conjugated dienes. Control incubations were run in the absence of enzyme (10 μL of PBS were used as enzyme equivalent), and these samples were taken through the same experimental protocol. The amounts of conjugated dienes present in the nonenzyme controls were subtracted from the diene content quantified for the enzyme incubations. Control and enzyme incubations were run side-by-side.

HPLC Analysis of Hydroxy Fatty Acids and Lipoxin Isomers. LOX products were analyzed on a HPLC Shimadzu instrument equipped with a Hewlett-Packard diode array detector 1040 A. The absorbance of the column effluent at 235 nm was used for detection of the conjugated dienes formed by the human ALOX5 variants. For RP-HPLC, a Nucleodur C18 column (Marcherey-Nagel, Düren, Germany; 250 mm × 4 mm, 5 μm particle size) coupled with a guard column (30 mm × 4 mm, 5 μm particle size) and a solvent system of acetonitrile/water/acetic acid (70/30/0.1, by vol) were used at a flow rate of 1 mL/min. Positional isomers of linoleic acid oxygenation (13-HODE vs 9-HODE), which were not well separated by RP-HPLC, were analyzed by NP-HPLC on a Nucleosil column (Marcherey-Nagel, Düren, Germany; 250 mm × 4 mm, 5 μm particle size) using a solvent system consisting of *n*-hexane/isopropanol/acetic acid (100/2/0.1, by vol) at a flow rate of 1 mL/min. Product enantiomers were separated by a mixed normal phase, chiral phase HPLC method. For this purpose, a small (30 mm × 4.6 mm) normal phase HPLC column (Marcherey-Nagel, Düren, Germany) was placed in front of a Chiralpak AD-H column (Daicel Corp, Osaka, Japan; 250 mm × 4.6 mm, 10 μm particle size) and an isocratic solvent system (*n*-hexane/methanol/ethanol/acetic acid, 96/3/1/0.1, by vol) was used at a flow rate of 1 mL/min. The absorbance of the column effluent at 235 nm was recorded.

Lipoxin isomers were quantified by RP-HPLC using a Nucleodur C18 column (Marcherey-Nagel, Düren, Germany; 250 mm × 4 mm,

DOI: 10.1021/acschembio.9b00674
ACS Chem. Biol. 2019, 14, 2768−2782

5 μm particle size) coupled with a guard column (30 mm × 4 mm, 5 μm particle size). The chromatogram was developed by isocratic elution with a solvent that consisted of acetonitrile/water/acetic acid (45/55/0.1, by vol) at a flow rate of 1 mL/min. The absorbance at 300 nm was recorded, and authentic standards of lipoxin A and lipoxin B were employed to calibrate the chromatographic system.

Membrane Oxygenase Activity. The membrane oxygenase activity of the two human ALOX5 variants and rabbit ALOX15 was quantified by incubation with sub-mitochondrial membranes (700 μg/mL membrane protein) in PBS for 15 min serving as model substrate for ALOX15 orthologs.[38] The amounts of the recombinant proteins applied were normalized with respect to their activity with AA. After the incubation period, the membrane lipids were extracted[45] and hydrolyzed under alkaline conditions. The resulting free fatty acid derivatives were analyzed by RP-HPLC on a Nucleodur C18 column (Marcherey-Nagel, Düren, Germany; 250 mm × 4 mm, 5 μm particle size) coupled with a guard column (30 mm × 4 mm, 5 μm particle size). A solvent system of acetonitrile/water/acetic acid (70/30/0.1, by vol) was used at a flow rate of 1 mL/min. Recording the chromatograms at 235 and 210 nm, we quantified both the conjugated dienes formed during the reaction (hydroxy-PUFAs) and the nonoxygenated polyenoic fatty acids (PUFAs). From these experimental raw data, we calculated the hydroxy-PUFA/PUFA ratio, which is a suitable measure for the degree of oxygenation of the membrane phospholipids. Calibration curves (6 point measurements) for 13-HODE (conjugated dienes), linoleic acid, and arachidonic acid were established.

GC/MS Analysis of the Reaction Products. The chemical structure of the major oxygenation products obtained from different substrates were analyzed by GC/MS on an Agilent 6897 gas chromatograph coupled with an Agilent 5973 N mass selective detector. For this purpose, the dominant conjugated dienes were prepared by RP-HPLC and silylated using BSTFA. The separation column (HP-5 ms, 25 m × 0.25 mm, coating thickness 0.25 μm) was coupled with a deactivated fused silica guard column (5 m × 0.32 mm). Helium was used as carrier gas at a total flow rate of 1.1 mL/min. The source temperature was set at 230 °C. To avoid sample degradation in the injector, the derivatized oxygenation products (1 μL) were injected using a cool on-column inlet. The analytes were eluted using the standard temperature program as described previously.[46]

Molecular Docking Simulations. GOLD5.2[47] was used to perform docking simulations of AA and LA binding modes inside the active site of F359W/A424I/N425M/A603I mutant of humALOX5. The crystallographic coordinates of subunit A of the apo enzyme (PDB ID 3O8Y)[15] were used. The quadruple mutant was created *in silico* by replacing the four residues in the WT enzyme with the UCSF CHIMERA code.[48] Prior to docking, crystallization agents were eliminated, and hydrogen atoms were included into the model by taking into account the protonation states of ionizable residues established by PROPKA 3.0 at pH = 7.0.[49] The docking protocol used in this study is the same as that employed in our previous work.[50] In all the docking runs, the protein coordinates have been kept fixed, whereas the maximum flexibility option has been adopted for the ligand. The substrate−metal ion interaction was described according to the algorithm included in GOLD for organic ligands in metalloenzymes, imposing in all the models hexacoordinated geometries for the iron metal. The genetic algorithm was applied by activating the most efficient protocol so that the ligand conformational search became as extensive as possible. The binding site cavity of the receptor was defined as a sphere centered at the iron atom with a radius of 19 Å. Binding affinities for the different docking solutions were evaluated with the ChemScore fitness function.[47]

MD Simulations. First, the ALOX5/AA and ALOX5/LA complexes were added to an orthorhombic box of pre-equilibrated TIP3P[51] water molecules. The water box dimensions were defined in such a way that a minimum distance of 10 Å exists between whatever atom of the protein and the edge of the unit cell. The overall charge of the different complexes was neutralized by including 20 Na^+ ions. The final biomolecular models contain around 75 500 atoms, protein atoms being about 11 000 of them. Molecular dynamics (MD) simulations were performed with the AMBER 16 GPU (CUDA) version of the PMEMD package.[52,53] The ff14SB force field[54] was used for protein atoms. The MM parameters for AA were taken from the literature,[55] whereas the ones for LA were obtained in this work using the standard protocol in AMBER[56] with Antechamber and Parmchk2 modules and GAFF as the source library.[57] The atomic MM charges for LA were calculated with the Restrained Electrostatic Potential (RESP) approach[58] at the HF/6-31G(d) level and on the LA optimized geometry at the same level. As for the Fe coordination sphere MM parameters specifically derived in this study were extracted from the MCPBY.py procedure[59] within the bonded model and using the Seminario method for the force constants calculation.[60]

The MD protocol used in this study is also quite similar to that employed in our previous work.[50] Initially, the systems were minimized with the steepest descent algorithm following a two-step MM minimization protocol. In the first step, 6000 energy minimization cycles were calculated to avoid bad contacts applying harmonic restraints (with a force constant of 5.0 kcal mol^{-1} $Å^{-2}$) to the protein and substrates atoms so that only solvent molecules and ions were allowed to move. In the following 16 000 minimization cycles, the overall systems were kept free of restraints. Next, MD simulations using periodic boundary conditions were performed. The systems were gradually heated from 0 to 300 K, with an increment of 30 K, during 10 steps of 20 ps each using a weak-coupling scheme (Berendsen temperature-bath).[61] Next, a 1 ns MD run at constant temperature (300 K) and pressure (1 bar) has been calculated to adjust the volume of the central box and to achieve an adequate density (around 1 g cm^{-3}). A weak-coupling algorithm was used for temperature and pressure (with isotropic position scaling and the Berendsen barostat)[61] and a weak restraint on backbone heavy atoms was applied. Finally, an equilibration stage of 10 ns followed by a production stage of 200 ns have been calculated at 300 K under the NVT ensemble without any restraints and with the temperature controlled by Langevin dynamics.[62] Along the whole MD trajectory, a time step of 2 fs was used. The SHAKE algorithm[63] was used to constrain all bonds with hydrogen atoms, and long-range electrostatic interactions were calculated with the Particle Mesh Ewald method.[64,65] A cutoff of 10 Å was defined to reduce the computational cost of including nonbonding interactions during the equilibration and production MD periods. The calculation of different magnitudes for the analysis of MD trajectories was carried out by a homemade python program and with the VMD[66] and Chimera visualizers.[48]

QM/MM Calculations. The QM/MM protocol used in this study follows the same general procedure employed in our previous work.[50] QM/MM calculations have been carried out with the ChemShell[67,68] package employing TURBOMOLE[69] for the QM calculations at the DFT level, and DL_POLY[70] for the MM energy computations with the AMBER force field. The electronic embedding scheme was used to account for the interactions between the QM and the MM regions. The link atom method, corrected using the charge-shift model,[71,72] has been employed to describe the QM/MM frontier. Nonbonding MM and QM/MM interactions were calculated without cutoffs. QM/MM optimized structures were obtained employing the Limited-memory Broyden−Fletcher−Goldfard−Shanno (L-BFGS) algorithm[73] using the microiterative method of the HDLCopt (Hybrid Delocalized Internal Coordinate Scheme)[74] module of ChemShell. All solvent molecules and ions outside a volume around AA or LA, with a radius of 17 Å, have been trimmed. In the active region (around 2000 atoms), the coordinates of all residues and water molecules in a sphere (with a radius of 15 Å and centered at C_{11} of AA or LA) along with the two complete substrates were optimized keeping frozen the rest of atoms. The overall number of atoms in those QM/MM calculations was around 12000.

The QM region has been described at the B3LYP/6-31G(d)[75,76] level for C, H, O, and N atoms and using the LANL2DZ basis set[77] for Fe. The QM region in the calculations for the AA complexes has 73 atoms (link atoms not included) being 24 atoms of the substrate, 3

DOI: 10.1021/acschembio.9b00674
ACS Chem. Biol. 2019, 14, 2768−2782

atoms of the Fe(III)—OH^- cofactor, and the following number of atoms for the residues coordinated to iron: 11 atoms of each of the three His residues (His367, His372, and His550), 8 atoms of Asn554, and 5 atoms of the Ile673 terminal residue. Eight link atoms were used: four along the bonds Cα−QM atom of the three histidines and the Asn554 residue, two between bonds Cα(QM)−C_β and Cα-(QM)−N of Ile673, and two more included in the aliphatic carbon chain of the lipid substrate (placed between C_6−C_7 and C_{16}−C_{17}). For the calculations for LA, the QM region has 66 atoms with 17 of them belonging to the substrate (with two link atoms between C_7−C_8 and C_{14}−C_{15}). The rest of QM atoms are the same as for the model with AA.

■ ASSOCIATED CONTENT

Supporting Information

The Supporting Information is available free of charge on the ACS Publications website at DOI: 10.1021/acschembio.9b00674.

List of nonstandard abbreviations, leukotriene A_4-synthase activity of ALOX5, analysis of the reaction products formed by human ALOX5 variants from EPA and DHA, and evolution of the C−OH distances for C_{11} of linoleic acid in MD simulations for both orientations (PDF)

■ AUTHOR INFORMATION

Corresponding Author

*I.I. E-mail: igor_ivanov@gmx.de.

ORCID

Igor Ivanov: 0000-0003-0543-2067

José M. Lluch: 0000-0002-7536-1869

Angels González-Lafont: 0000-0003-0729-2483

Author Contributions

I.I., H.K., A.G.L., and J.M.L. designed the study. I.I., H.K., S.S., and D.H. carried out expression of the recombinant enzymes and characterized the reaction specificity of the enzyme variants with different polyenoic fatty acids. A.B.G. and I.I. carried out GC/MS analysis of the reaction products. C.F. carried out the *in silico* docking and MD simulations. C.F. and M.C. performed the QM/MM calculations. H.K., D.H., I.I., and A.G.L. drafted the manuscript, and all authors contributed to prepare its final version.

Notes

The authors declare no competing financial interest.

■ ACKNOWLEDGMENTS

Deutsche Forschungsgemeinschaft (KU 961/14-1) and the Russian Foundation for Basic Research (19-54-12002) supported the experimental part of this work. We thank the Spanish "Ministerio de Ciencia, Innovación y Universidades" (Grants CTQ2017-83745-P). We also acknowledge CSUC for computational facilities and M. Hamberg from the Karolinska Institute in Stockholm for providing stereospecifically deuterated linoleic acid isomers.

■ REFERENCES

(1) Kuhn, H., Banthiya, S., and van Leyen, K. (2015) Mammalian lipoxygenases and their biological relevance. *Biochim. Biophys. Acta, Mol. Cell Biol. Lipids 1851*, 308−330.

(2) Haeggstrom, J. Z., and Funk, C. D. (2011) Lipoxygenase and leukotriene pathways: biochemistry, biology, and roles in disease. *Chem. Rev. 111*, 5866−5898.

(3) Brash, A. R. (1999) Lipoxygenases: occurrence, functions, catalysis, and acquisition of substrate. *J. Biol. Chem. 274*, 23679−23682.

(4) Ivanov, I., Kuhn, H., and Heydeck, D. (2015) Structural and functional biology of arachidonic acid 15-lipoxygenase-1 (ALOX15). *Gene 573*, 1−32.

(5) Schneider, C., Pratt, D. A., Porter, N. A., and Brash, A. R. (2007) Control of oxygenation in lipoxygenase and cyclooxygenase catalysis. *Chem. Biol. 14*, 473−488.

(6) Kuhn, H., Schewe, T., and Rapoport, S. M. (2006) The stereochemistry of the reactions of lipoxygenases and their metabolites. Proposed nomenclature of lipoxygenases and related enzymes. *Adv. Enzymol. Relat. Areas Mol. Biol. 58*, 273−311.

(7) Funk, C. D., Chen, X. S., Johnson, E. N., and Zhao, L. (2002) Lipoxygenase genes and their targeted disruption. *Prostaglandins Other Lipid Mediators 68−69*, 303−312.

(8) Radmark, O., Werz, O., Steinhilber, D., and Samuelsson, B. (2007) 5-Lipoxygenase: regulation of expression and enzyme activity. *Trends Biochem. Sci. 32*, 332−341.

(9) Radmark, O., Werz, O., Steinhilber, D., and Samuelsson, B. (2015) 5-Lipoxygenase, a key enzyme for leukotriene biosynthesis in health and disease. *Biochim. Biophys. Acta, Mol. Cell Biol. Lipids 1851*, 331−339.

(10) Liu, M., and Yokomizo, T. (2015) The role of leukotrienes in allergic diseases. *Allergol. Int. 64*, 17−26.

(11) Samuelsson, B., Dahlen, S. E., Lindgren, J. A., Rouzer, C. A., and Serhan, C. N. (1987) Leukotrienes and lipoxins: structures, biosynthesis, and biological effects. *Science 237*, 1171−1176.

(12) Berger, W., De Chandt, M. T., and Cairns, C. B. (2007) Zileuton: clinical implications of 5-Lipoxygenase inhibition in severe airway disease. *Int. J. Clin. Pract. 61*, 663−676.

(13) Matsuse, H., and Kohno, S. (2014) Leukotriene receptor antagonists pranlukast and montelukast for treating asthma. *Expert Opin. Pharmacother. 15*, 353−363.

(14) Singh, R. K., Tandon, R., Dastidar, S. G., and Ray, A. (2013) A review on leukotrienes and their receptors with reference to asthma. *J. Asthma 50*, 922−931.

(15) Gilbert, N. C., Bartlett, S. G., Waight, M. T., Neau, D. B., Boeglin, W. E., Brash, A. R., and Newcomer, M. E. (2011) The structure of human 5-lipoxygenase. *Science 331*, 217−219.

(16) Newcomer, M. E., and Brash, A. R. (2015) The structural basis for specificity in lipoxygenase catalysis. *Protein Sci. 24*, 298−309.

(17) Gilbert, N. C., Rui, Z., Neau, D. B., Waight, M. T., Bartlett, S. G., Boeglin, W. E., Brash, A. R., and Newcomer, M. E. (2012) Conversion of human 5-lipoxygenase to a 15-lipoxygenase by a point mutation to mimic phosphorylation at Serine-663. *FASEB J. 26*, 3222−3229.

(18) Adel, S., Hofheinz, K., Heydeck, D., Kuhn, H., and Häfner, A. K. (2014) Phosphorylation mimicking mutations of ALOX5 orthologs of different vertebrates do not alter reaction specificities of the enzymes. *Biochim. Biophys. Acta, Mol. Cell Biol. Lipids 1841*, 1460−1466.

(19) Schwarz, K., Walther, M., Anton, M., Gerth, C., Feussner, I., and Kuhn, H. (2001) Structural basis for lipoxygenase specificity. Conversion of the human leukocyte 5-lipoxygenase to a 15-lipoxygenating enzyme species by site-directed mutagenesis. *J. Biol. Chem. 276*, 773−779.

(20) Hofheinz, K., Kakularam, K. R., Adel, S., Anton, M., Polymarasetty, A., Reddanna, P., Kuhn, H., and Horn, T. (2013) Conversion of pro-inflammatory murine Alox5 into an anti-inflammatory 15S-lipoxygenating enzyme by multiple mutations of sequence determinants. *Arch. Biochem. Biophys. 530*, 40−47.

(21) Lefterova, M. I., Haakonsson, A. K., Lazar, M. A., and Mandrup, S. (2014) PPARgamma and the global map of adipogenesis and beyond. *Trends Endocrinol. Metab. 25*, 293−302.

(22) Goloshchapova, K., Stehling, S., Heydeck, D., Blum, M., and Kuhn, H. (2019) Functional characterization of a novel arachidonic acid 12S-lipoxygenase in the halotolerant bacterium Myxococcus

DOI: 10.1021/acschembio.9b00674
ACS Chem. Biol. 2019, 14, 2768−2782

fulvus exhibiting complex social living patterns. *MicrobiologyOpen 8*, No. e775.
(23) Funk, C. D., Gunne, H., Steiner, H., Izumi, T., and Samuelsson, B. (1989) Native and mutant 5-lipoxygenase expression in a baculovirus/insect cell system. *Proc. Natl. Acad. Sci. U. S. A. 86*, 2592−2596.
(24) Ochi, K., Yoshimoto, T., Yamamoto, S., Taniguchi, K., and Miyamoto, T. (1983) Arachidonate 5-lipoxygenase of guinea pig peritoneal polymorphonuclear leukocytes. Activation by adenosine 5′-triphosphate. *J. Biol. Chem. 258*, 5754−5758.
(25) Saura, P., Suardíaz, R., Masgrau, L., Lluch, J. M., and González-Lafont, À. (2014) Unraveling How Enzymes Can Use Bulky Residues To Drive Site-Selective C−H Activation: The case of mammalian lipoxygenases catalyzing arachidonic acid oxidation. *ACS Catal. 4*, 4351−4363.
(26) Suardíaz, R., Masgrau, L., Lluch, J. M., and González-Lafont, À. (2014) Introducing mutations to modify the C13/C9 ratio in linoleic acid oxygenations catalyzed by rabbit 15-lipoxygenase: a QM/MM and MD study. *ChemPhysChem 15*, 4049−4054.
(27) Cipollina, C., Salvatore, S. R., Muldoon, M. F., Freeman, B. A., and Schopfer, F. J. (2014) Generation and dietary modulation of anti-inflammatory electrophilic omega-3 fatty acid derivatives. *PLoS One 9*, No. e94836.
(28) Ryan, A., and Godson, C. (2010) Lipoxins: regulators of resolution. *Curr. Opin. Pharmacol. 10*, 166−172.
(29) Bryant, R. W., Schewe, T., Rapoport, S. M., and Bailey, J. M. (1985) Leukotriene formation by a purified reticulocyte lipoxygenase enzyme. Conversion of arachidonic acid and 15-hydroperoxyeicosatetraenoic acid to 14, 15-leukotriene A_4. *J. Biol. Chem. 260*, 3548−3555.
(30) Yamamoto, S., Ueda, N., Yokoyama, C., Kaneko, S., Shinjo, F., Yoshimoto, T., Oates, J. A., Brash, A. R., Fitzsimmons, B. J., and Rokach, J. (1987) Dioxygenase and leukotriene A synthase activities of arachidonate 5- and 12-lipoxygenases purified from porcine leukocytes. *Adv. Prostaglandin Thromboxane Leukot. Res. 17A*, 55−59.
(31) Rouzer, C. A., Matsumoto, T., and Samuelsson, B. (1986) Single protein from human leukocytes possesses 5-lipoxygenase and leukotriene A4 synthase activities. *Proc. Natl. Acad. Sci. U. S. A. 83*, 857−861.
(32) Kuhn, H., Wiesner, R., Alder, L., Schewe, T., and Stender, H. (1986) Formation of lipoxin B by the pure reticulocyte lipoxygenase. *FEBS Lett. 208*, 248−252.
(33) Kuhn, H., Wiesner, R., Alder, L., Fitzsimmons, B. J., Rokach, J., and Brash, A. R. (1987) Formation of lipoxin B by the pure reticulocyte lipoxygenase via sequential oxygenation of the substrate. *Eur. J. Biochem. 169*, 593−601.
(34) Banthiya, S., Kalms, J., Galemou Yoga, E., Ivanov, I., Carpena, X., Hamberg, M., Kuhn, H., and Scheerer, P. (2016) Structural and functional basis of phospholipid oxygenase activity of bacterial lipoxygenase from Pseudomonas aeruginosa. *Biochim. Biophys. Acta, Mol. Cell Biol. Lipids 1861*, 1681−1692.
(35) Ueda, N., Yamamoto, S., Fitzsimmons, B. J., and Rokach, J. (1987) Lipoxin synthesis by arachidonate 5-lipoxygenase purified from porcine leukocytes. *Biochem. Biophys. Res. Commun. 144*, 996−1002.
(36) Yamamoto, S., Ueda, N., Yokoyama, C., Fitzsimmons, B. J., Rokach, J., Oates, J. A., and Brash, A. R. (1988) Lipoxin syntheses by arachidonate 12- and 5-lipoxygenases purified from porcine leukocytes. *Adv. Exp. Med. Biol. 229*, 15−26.
(37) Schewe, T., Halangk, W., Hiebsch, C., and Rapoport, S. M. (1975) A lipoxygenase in rabbit reticulocytes which attacks phospholipids and intact mitochondria. *FEBS Lett. 60*, 149−152.
(38) Kuhn, H., Belkner, J., Wiesner, R., and Brash, A. R. (1990) Oxygenation of biological membranes by the pure reticulocyte lipoxygenase. *J. Biol. Chem. 265*, 18351−18361.
(39) Takahashi, Y., Glasgow, W. C., Suzuki, H., Taketani, Y., Yamamoto, S., Anton, M., Kuhn, H., and Brash, A. R. (1993) Investigation of the oxygenation of phospholipids by the porcine leukocyte and human platelet arachidonate 12-lipoxygenases. *Eur. J. Biochem. 218*, 165−171.
(40) Kuhn, H., Saam, J., Eibach, S., Holzhutter, H. G., Ivanov, I., and Walther, M. (2005) Structural biology of mammalian lipoxygenases: enzymatic consequences of targeted alterations of the protein structure. *Biochem. Biophys. Res. Commun. 338*, 93−101.
(41) Borngraber, S., Browner, M., Gillmor, S., Gerth, C., Anton, M., Fletterick, R., and Kuhn, H. (1999) Shape and specificity in mammalian 15-lipoxygenase active site. The functional interplay of sequence determinants for the reaction specificity. *J. Biol. Chem. 274*, 37345−37350.
(42) Adel, S., Karst, F., González-Lafont, À., Pekarova, M., Saura, P., Masgrau, L., Lluch, J. M., Stehling, S., Horn, T., Kuhn, H., and Heydeck, D. (2016) Evolutionary alteration of ALOX15 specificity optimizes the biosynthesis of antiinflammatory and proresolving lipoxins. *Proc. Natl. Acad. Sci. U. S. A. 113*, E4266−4275.
(43) Kuhn, H., Humeniuk, L., Kozlov, N., Roigas, S., Adel, S., and Heydeck, D. (2018) The evolutionary hypothesis of reaction specificity of mammalian ALOX15 orthologs. *Prog. Lipid Res. 72*, 55−74.
(44) Mancini, J. A., and Evans, J. F. (1993) Coupling of recombinant 5-lipoxygenase and leukotriene A4 hydrolase activities and trans-cellular metabolism of leukotriene A4 in Sf9 insect cells. *Eur. J. Biochem. 218*, 477−484.
(45) Bligh, E. G., and Dyer, W. J. (1959) A rapid method of total lipid extraction and purification. *Can. J. Biochem. Physiol. 37*, 911−917.
(46) Kozlov, N., Humeniuk, L., Ufer, C., Ivanov, I., Golovanov, A., Stehling, S., Heydeck, D., and Kuhn, H. (2019) Functional characterization of novel ALOX15 orthologs representing key steps in mammalian evolution supports the Evolutionary Hypothesis of reaction specificity. *Biochim. Biophys. Acta, Mol. Cell Biol. Lipids 1864*, 372−385.
(47) Verdonk, M. L., Cole, J. C., Hartshorn, M. J., Murray, C. W., and Taylor, R. D. (2003) Improved protein-ligand docking using GOLD. *Proteins: Struct., Funct., Genet. 52*, 609−623.
(48) Pettersen, E. F., Goddard, T. D., Huang, C. C., Couch, G. S., Greenblatt, D. M., Meng, E. C., and Ferrin, T. E. (2004) UCSF Chimera - A visualization system for exploratory research and analysis. *J. Comput. Chem. 25*, 1605−1612.
(49) Li, H., Robertson, A. D., and Jensen, J. H. (2005) Very fast empirical prediction and rationalization of protein pK(a) values. *Proteins: Struct., Funct., Genet. 61*, 704−721.
(50) Saura, P., Kaganer, I., Heydeck, D., Lluch, J. M., Kuhn, H., and González-Lafont, A. (2018) Mutagenesis of Sequence Determinants of Truncated Porcine ALOX15 Induces Changes in the Reaction Specificity by Altering the Catalytic Mechanism of Initial Hydrogen Abstraction. *Chem. - Eur. J. 24*, 962−973.
(51) Jorgensen, W. L., Chandrasekhar, J., Madura, J. D., Impey, R. W., and Klein, M. L. (1983) Comparison of Simple Potential Functions for Simulating Liquid Water. *J. Chem. Phys. 79*, 926−935.
(52) Le Grand, S., Gotz, A. W., and Walker, R. C. (2013) SPFP: Speed without compromise-A mixed precision model for GPU accelerated molecular dynamics simulations. *Comput. Phys. Commun. 184*, 374−380.
(53) Salomon-Ferrer, R., Gotz, A. W., Poole, D., Le Grand, S., and Walker, R. C. (2013) Routine Microsecond Molecular Dynamics Simulations with AMBER on GPUs. 2. Explicit Solvent Particle Mesh Ewald. *J. Chem. Theory Comput. 9*, 3878−3888.
(54) Maier, J. A., Martinez, C., Kasavajhala, K., Wickstrom, L., Hauser, K. E., and Simmerling, C. (2015) ff14SB: Improving the Accuracy of Protein Side Chain and Backbone Parameters from ff99SB. *J. Chem. Theory Comput. 11*, 3696−3713.
(55) Tosco, P. (2013) A mechanistic hypothesis for the aspirin-induced switch in lipid mediator production by cyclooxygenase-2. *J. Am. Chem. Soc. 135*, 10404−10410.
(56) Case, D. A., Betz, R. M., Cerutti, D. S., Cheatham, T. E. I., Darden, T. A., Duke, R. E., Giese, T. J., Gohlke, H., Goetz, A. W., Homeyer, N., Izadi, S., Janowski, P., Kaus, J., Kovalenko, A., Lee, T. S., S, L., Li, P., Lin, C., Luchko, T., Luo, R., Madej, B., Mermelstein, P. A., Merz, K. M., Monard, G., Nguyen, H., Nguyen, H. T., Omelyan, I.,

DOI: 10.1021/acschembio.9b00674
ACS Chem. Biol. 2019, 14, 2768−2782

Onufriev, A., Roe, D. R., Roitberg, A., Sagui, C., Simmerling, B.C. L., Botello-Smith, W. M., Swails, J., Walker, R. C., Wang, J., Wolf, R. M., Wu, X., Xiao, L., and Kollman, P. A. (2016) *Amber 2016*, University of California, San Francisco.
(57) Wang, J., Wolf, R. M., Caldwell, J. W., Kollman, P. A., and Case, D. A. (2004) Development and testing of a general amber force field. *J. Comput. Chem. 25*, 1157−1174.
(58) Bayly, C. I., Cieplak, P., Cornell, W. D., and Kollman, P. A. (1993) A Well-behaved electrostatic potential based method using charge restraints for deriving atomic charges - the resp model. *J. Phys. Chem. 97*, 10269−10280.
(59) Li, P. F., and Merz, K. M. (2016) MCPB.py: A python based metal center parameter builder. *J. Chem. Inf. Model. 56*, 599−604.
(60) Seminario, J. M. (1996) Calculation of intramolecular force fields from second-derivative tensors. *Int. J. Quantum Chem. 60*, 1271−1277.
(61) Berendsen, H. J. C., Postma, J. P. M., Vangunsteren, W. F., Dinola, A., and Haak, J. R. (1984) Molecular-Dynamics with Coupling to an External Bath. *J. Chem. Phys. 81*, 3684−3690.
(62) Leach, A. R. (1996) *Molecular Modeling: Principles and Applications*; Eddison Wesley Longman Limited, Essex, England.
(63) Ryckaert, J. P., Ciccotti, G., and Berendsen, H. J. C. (1977) Numerical-Integration of Cartesian Equations of Motion of a System with Constraints - Molecular-Dynamics of N-Alkanes. *J. Comput. Phys. 23*, 327−341.
(64) Darden, T., York, D., and Pedersen, L. (1993) Particle Mesh Ewald - an N.Log(N) Method for Ewald Sums in Large Systems. *J. Chem. Phys. 98*, 10089−10092.
(65) Essmann, U., Perera, L., Berkowitz, M. L., Darden, T., Lee, H., and Pedersen, L. G. (1995) A Smooth Particle Mesh Ewald Method. *J. Chem. Phys. 103*, 8577−8593.
(66) Humphrey, W., Dalke, A., and Schulten, K. (1996) VMD: visual molecular dynamics. *J. Mol. Graphics 14*, 27−38.
(67) Metz, S., Kastner, J., Sokol, A. A., Keal, T. W., and Sherwood, P. (2014) ChemShell-a modular software package for QM/MM simulations. *Wiley Interdiscip. Rev.: Comput. Mol. Sci. 4*, 101−110.
(68) Sherwood, P., de Vries, A. H., Guest, M. F., Schreckenbach, G., Catlow, C. R. A., French, S. A., Sokol, A. A., Bromley, S. T., Thiel, W., Turner, A. J., Billeter, S., Terstegen, F., Thiel, S., Kendrick, J., Rogers, S. C., Casci, J., Watson, M., King, F., Karlsen, E., Sjovoll, M., Fahmi, A., Schafer, A., and Lennartz, C. (2003) QUASI: A general purpose implementation of the QM/MM approach and its application to problems in catalysis. *J. Mol. Struct.: THEOCHEM 632*, 1−28.
(69) *TURBOMOLE*, http://www.turbomole.com (accessed March 15, 2018), Turbomole V7.0 2015, a development of University of Karlsruhe and Forschungszentrum Karlsruhe GmbH, 1989−2007, TURBOMOLE GmbH, since 2007.
(70) Smith, W., and Forester, T. (1996) DL_POLY_2.0: A general-purpose parallel molecular dynamics simulation package. *J. Mol. Graphics 14*, 136−141.
(71) Bakowies, D., and Thiel, W. (1996) Hybrid models for combined quantum mechanical and molecular mechanical approaches. *J. Phys. Chem. 100*, 10580−10594.
(72) Senn, H. M., and Thiel, W. (2009) QM/MM Methods for Biomolecular Systems. *Angew. Chem., Int. Ed. 48*, 1198−1229.
(73) Liu, D. C., and Nocedal, J. (1989) On the Limited Memory BFGS Method for Large Scale Optimization. *Math. Program. 45*, 503−528.
(74) Billeter, S., Turner, A., and Thiel, W. (2000) Linear scaling geometry optimization and transition state search in hybrid delocalised internal coordinates. *Phys. Chem. Chem. Phys. 2*, 2177−2186.
(75) Stephens, P. J., Devlin, F. J., Chabalowski, C. F., and Frisch, M. J. (1994) *Ab Initio* calculation of vibrational absorption and circular dichroism spectra using density functional force fields. *J. Phys. Chem. 98*, 11623−11627.
(76) Hariharan, P., and Pople, J. (1973) Influence of polarization functions on molecular-orbital hydrogenation energies. *Theor. Chim. Acta 28*, 213−222.
(77) Hay, P., and Wadt, W. (1985) Abinitio effective core potentials for molecular calculations - potentials for the transition-metal atoms Sc to Hg. *J. Chem. Phys. 82*, 270−283.

DOI: 10.1021/acschembio.9b00674
ACS Chem. Biol. 2019, 14, 2768−2782

SI7.2 Supporting information

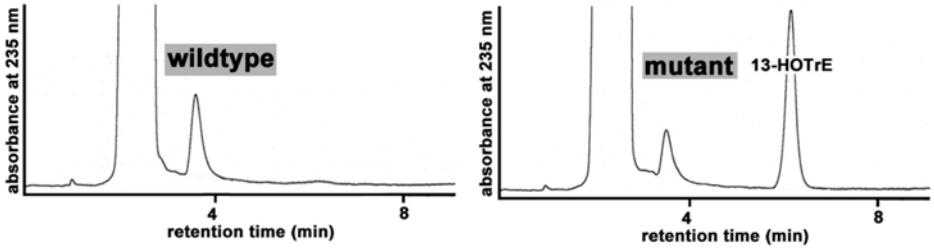

(a) Wild-type humALOX5 *(b) humALOX5 mutant*

Figure SI7.1: RP-HPLC chromatograms of α-LA incubations with WT humALOX5 and its quadruple mutant

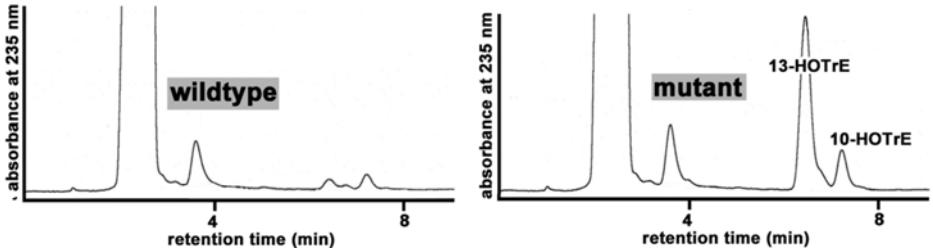

(a) Wild-type humALOX5 *(b) humALOX5 quadruple mutant*

Figure SI7.2: RP-HPLC chromatograms of γ-LA incubations with WT humALOX5 and its quadruple mutant

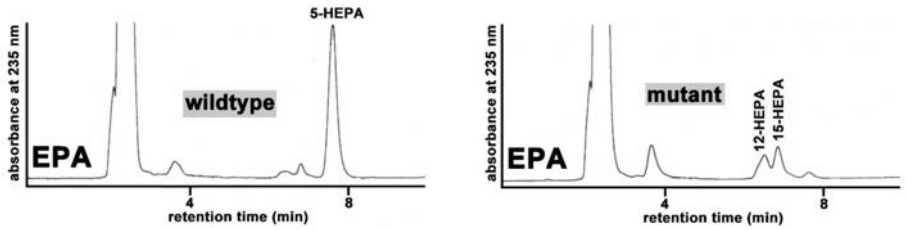

(a) Wild-type humALOX5 *(b) humALOX5's quadruple mutant*

Figure SI7.3: RP-HPLC chromatograms of EPA incubations with WT humALOX5 and its quadruple mutant

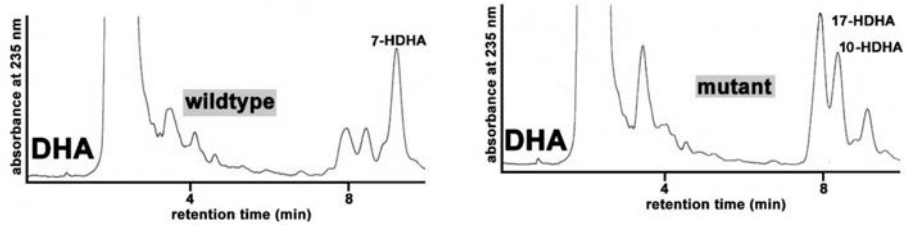

(a) Wild-type humALOX5 *(b) humALOX5 quadruple mutant*

Figure SI7.4: RP-HPLC chromatograms of DHA incubations with WT humALOX5 and its quadruple mutant

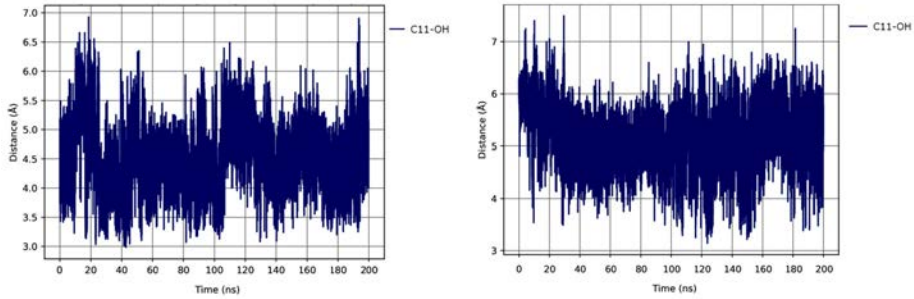

(a) Head-first orientation *(b) Tail-first orientation*

Figure SI7.5: C_{11}-OH^- distances for head- and tail-first binding modes of the LA:humALOX5's quadruple mutant complex during 200 ns ***of MD simulation***

Chapter SI8

Exploring FLAP in an AA-containing membrane

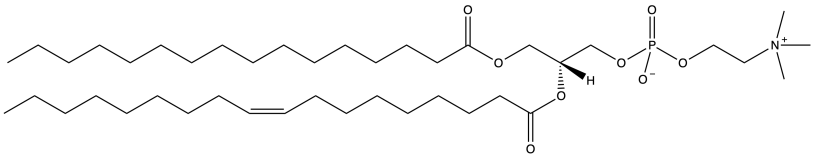

(a) POPC

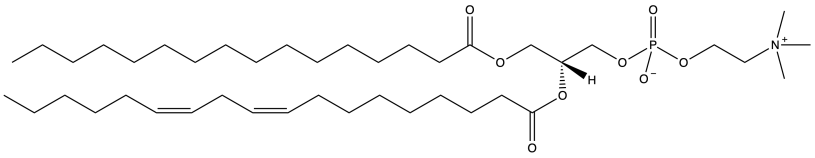

(b) PLPC

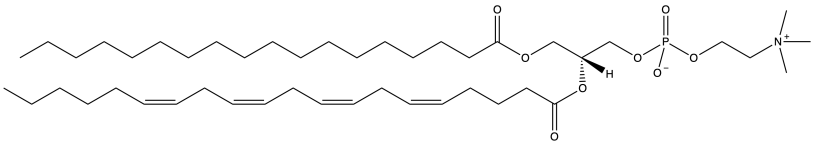

(c) SPC

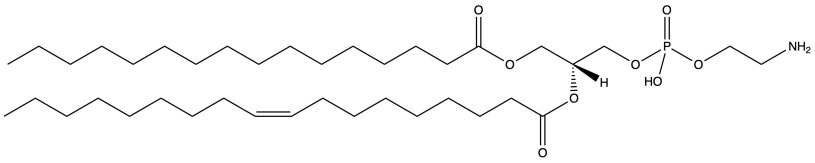

(d) POPE

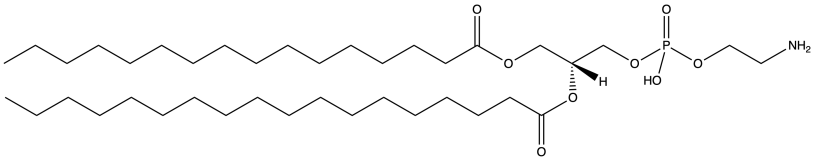

(e) PSPE

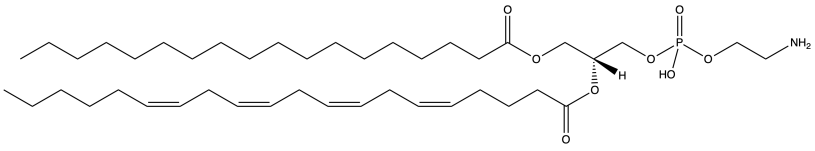

(f) SAPE

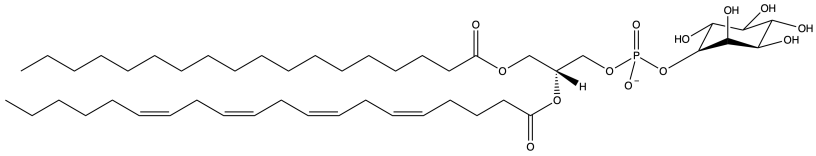

(g) SAPI

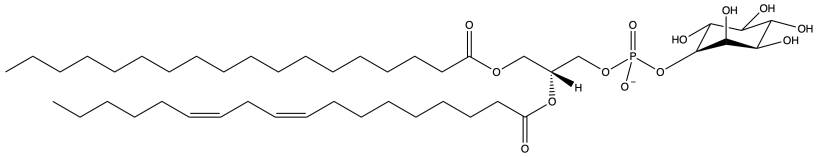

(h) SLPI

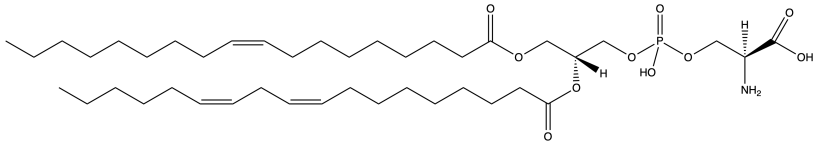

(i) OLPS

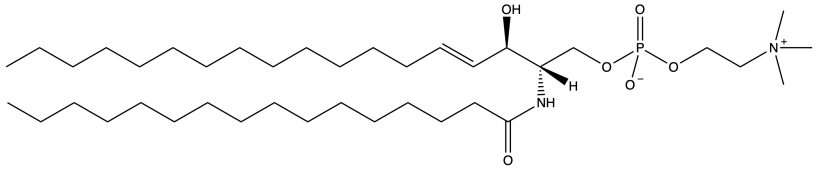

(j) PSM

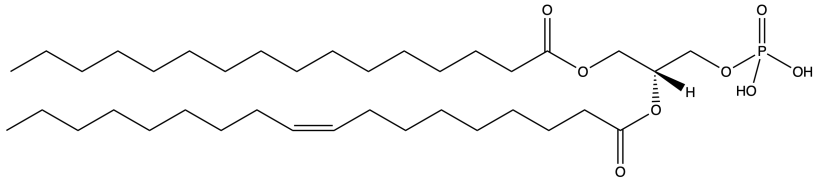

(k) POPA

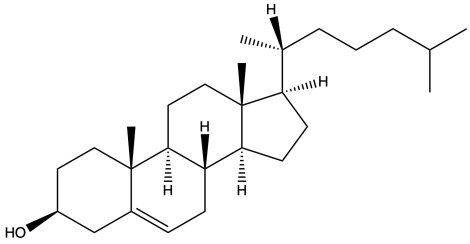

(l) Cholesterol

Figure SI8.1: Endoplasmic reticulum membrane components

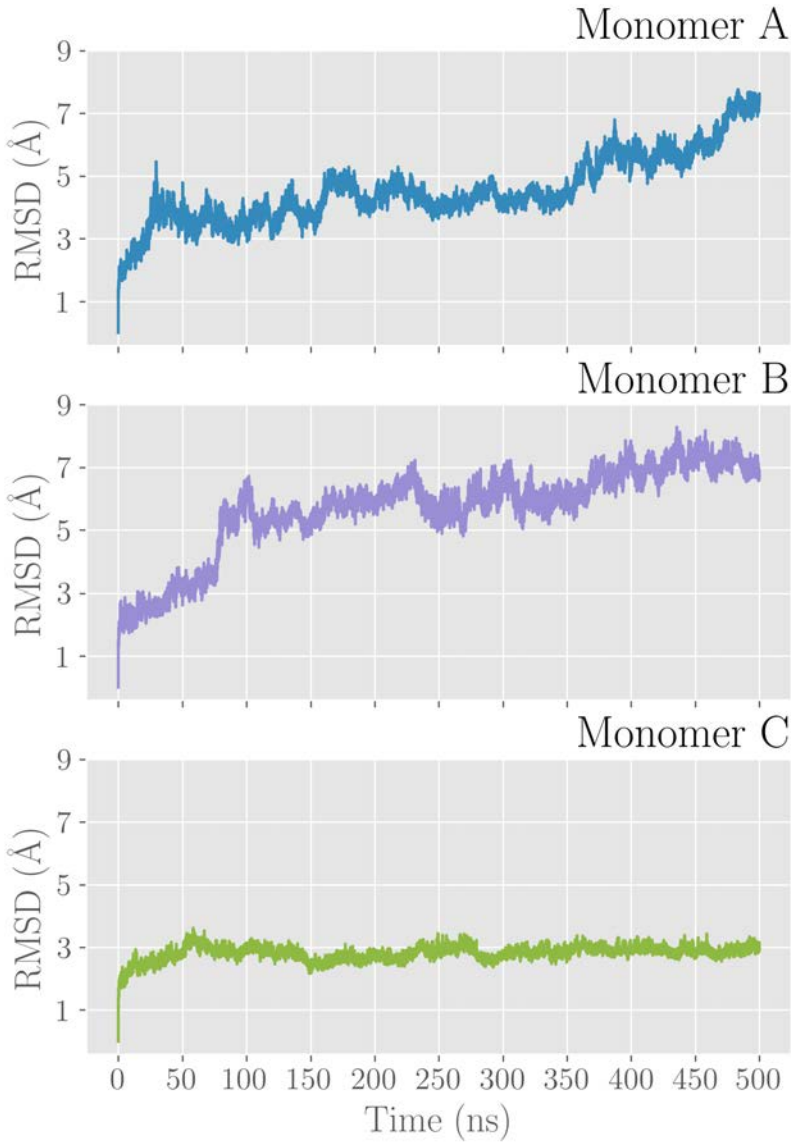

Figure SI8.2: All-atom RMSD of FLAP's monomers A, B and C

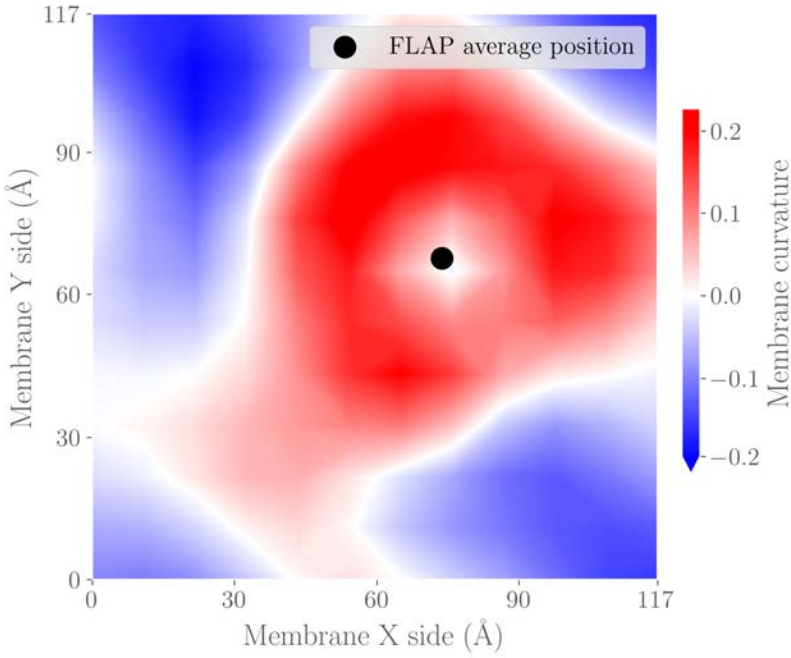

(a) Upper leaflet

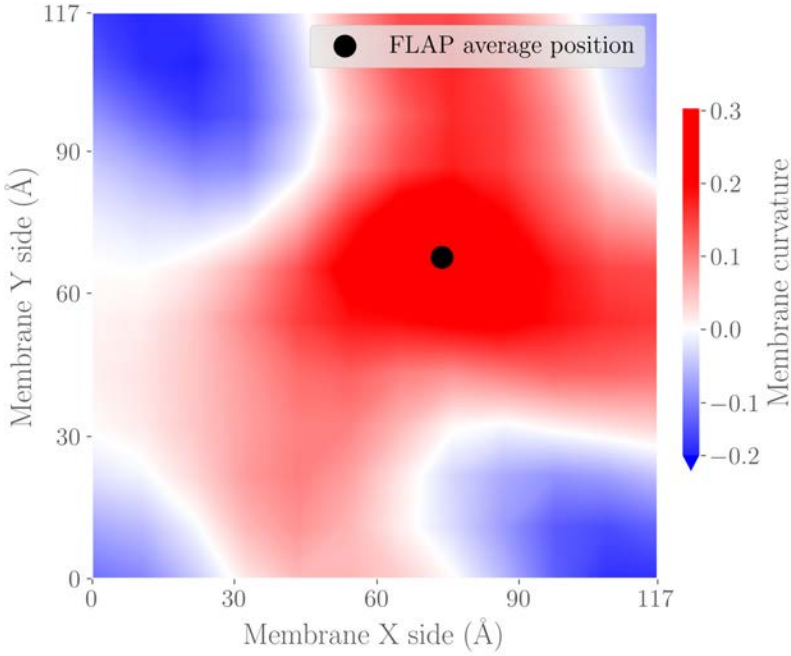

(b) Lower leaflet

Figure SI8.3: Upper and lower leaflets' curvature. *Blue indicates a convex curvature, while red indicates a concave curvature. The mean position of the FLAP is indicated as a black dot.*

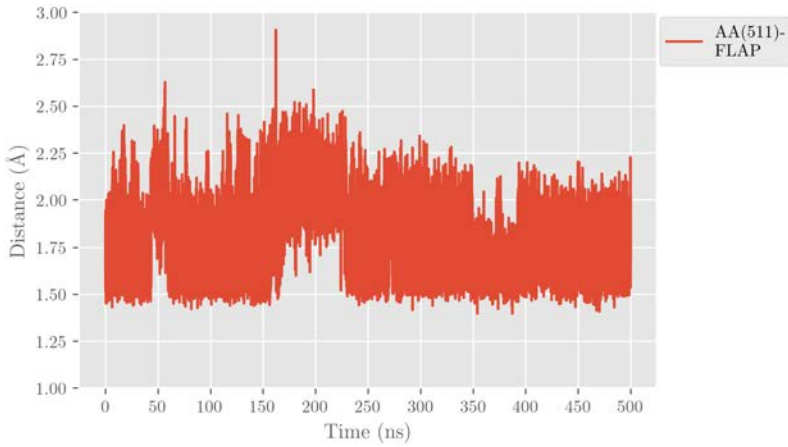

Figure SI8.4: Minimum distance from FLAP to AA511 along the trajectory

Chapter SI9

Computational study on the conversion from LTA_4 to LTB_4 driven by LTA_4H

SI9.1 Publication

International Journal of
Molecular Sciences

MDPI

Article

Theoretical Characterization of the Step-by-Step Mechanism of Conversion of Leukotriene A_4 to Leukotriene B_4 Catalysed by the Enzyme Leukotriene A_4 Hydrolase

Miquel Canyelles-Niño [1,2], Àngels González-Lafont [1,3] and José M. Lluch [1,3,*]

[1] Departament de Química, Universitat Autònoma de Barcelona, 08193 Bellaterra, Barcelona, Spain; miquel.canyelles@uab.cat (M.C.-N.); angels.gonzalez@uab.cat (À.G.-L.)
[2] Biochemize SL, Carrer de Zamora, 45, 08005 Barcelona, Barcelona, Spain
[3] Institut de Biotecnologia i de Biomedicina (IBB), Universitat Autònoma de Barcelona, 08193 Bellaterra, Barcelona, Spain
* Correspondence: josemaria.lluch@uab.cat

Abstract: LTA_4H is a bifunctional zinc metalloenzyme that converts leukotriene A_4 (LTA_4) into leukotriene B_4 (LTB_4), one of the most potent chemotactic agents involved in acute and chronic inflammatory diseases. In this reaction, LTA_4H acts as an epoxide hydrolase with a unique and fascinating mechanism, which includes the stereoselective attachment of one water molecule to the carbon backbone of LTA_4 several methylene units away from the epoxide moiety. By combining Molecular Dynamics simulations and Quantum Mechanics/Molecular Mechanics calculations, we obtained a very detailed molecular picture of the different consecutive steps of that mechanism. By means of a rather unusual 1,7-nucleophilic substitution through a clear S_N1 mechanism, the epoxide opens and the triene moiety of the substrate twists in such a way that the bond C_6-C_7 adopts its *cis* (*Z*) configuration, thus exposing the *R* face of C_{12} to the addition of a water molecule hydrogen-bonded to ASP375. Thus, the two stereochemical features that are required for the bioactivity of LTB_4 appear to be closely related. The noncovalent π-π stacking interactions between the triene moiety and two tyrosines (TYR267 and, especially, TYR378) that wrap the triene system along the whole reaction explain the preference for the *cis* configuration inside LTA_4H.

Keywords: leukotriens; leukotriene A_4 hydrolase; enzyme catalysis; QM/MM calculations; molecular dynamics simulations; proinflammatory lipid mediators

Citation: Canyelles-Niño, M.; González-Lafont, À.; Lluch, J.M. Theoretical Characterization of the Step-by-Step Mechanism of Conversion of Leukotriene A_4 to Leukotriene B_4 Catalysed by the Enzyme Leukotriene A_4 Hydrolase. *Int. J. Mol. Sci.* **2022**, *23*, 3140. https://doi.org/10.3390/ijms23063140

Academic Editor: Francesco Mallamace

Received: 17 February 2022
Accepted: 11 March 2022
Published: 15 March 2022

1. Introduction

Nowadays, it is recognised that inflammatory-based human diseases represent the leading causes of present-day morbidity and mortality worldwide [1]. Infection of the host, tissue injury or surgical trauma trigger the release of proinflammatory lipid and protein mediators by cells in the site of challenge. These chemical mediators act as chemoattractants to recruit neutrophiles. This initial inflammatory response occurs to protect the host and produces the very well know signs of acute inflammation (redness, heat, swelling and pain) [2]. After this onset phase, the inflammatory reaction must be resolved to prevent the inflammation from spreading. The resolution phase is regulated by a number of specialised proresolving lipid mediators (produced by human cells called macrophages). If resolution does not work well, the acute inflammation evolves to chronic inflammation [3–7]. Chronic inflammatory diseases are the most significant cause of death in the world today [1].

The lipid mediator Leukotriene B_4 (LTB_4, 5*S*,12*R*-dihydroxy-6*Z*,8*E*,10*E*,14*Z*-eicosatetraenoic acid) (Figure 1a) exerts one of the most potent chemotactic effects on polymorphonuclear leukocytes in the onset phase. In addition, excessive formation of LTB_4 can be related to the maintenance of chronic inflammatory diseases [8]. The biosynthesis of LTB_4 from arachidonic acid (AA) is the result of the action of several proteins. To start,

Int. J. Mol. Sci. **2022**, *23*, 3140

the 5-lipoxygenase-activating protein (FLAP), an integral membrane protein, facilitates the transfer of the substrate AA to the enzyme 5-lipoxygenase (5-LOX) [9–11]. 5-LOX produces 5*S*-hydroperoxy-6*E*,8*Z*,11*Z*,14*Z*-eicosatetraenoic acid (5-HpETE) as a result of the hydroperoxidation of C5 of AA. Then, 5-LOX catalyses the formation of the highly labile epoxide intermediate Leukotriene A_4 (LTA_4, 5*S*,6*S*-epoxy-7*E*,9*E*,11*Z*,14*Z*-eicosate-traenoic acid) (Figure 1b) by dehydration of 5-HpETE. FLAP regulates the 5-LOX activity, increasing the efficiency of the formation of LTA_4 from 5-HpETE [8,12–14]. Finally, after having been released from 5-LOX, LTA_4 is hydrolased into LTB_4 by the enzyme leukotriene A_4 hydrolase (LTA_4H) (EC 3.3.2.6) [8].

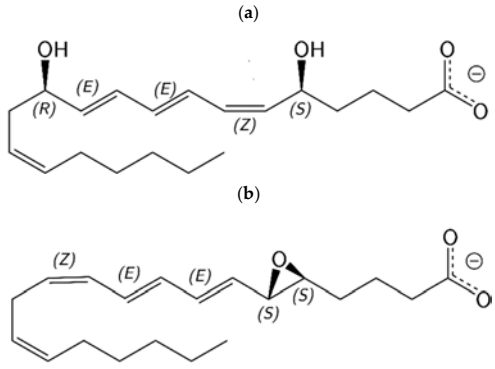

Figure 1. Structures corresponding to LTB_4 (**a**) and LTA_4 (**b**).

LTA_4H is a monomeric bifunctional zinc metalloenzyme. It is detected in almost all mammalian cells, and it has both aminopeptidase activity and epoxide hydrolase activity. In this paper, we will focus on the second one. This epoxide hydrolase reaction is interesting because involves the stereoselective introduction of one water molecule to the carbon backbone (C_{12}) of LTA_4 in a position several methylene units away from the epoxy moiety (carbons C_5 to C_6) [15].

A high-resolution crystal structure of human LTA_4H in the complex with the competitive inhibitor bestatin revealed that the protein includes three domains, an N-terminal domain, a Zn-containing catalytic domain and an α-helical C-terminal domain. The active site is placed in a deep cleft in between the domains, where the Zn^{2+} is coordinated to HIS295, HIS299 and one carboxylic oxygen of GLU318 [16,17]. Because of the LTA_4 instability (half-life of about 10 s at neutral pH) high-resolution crystal structures of LTA_4H complexed to LTA_4 were not determined until recently by Haeggström and coworkers [18]. They described six different structures of human LTA_4H from five distinct crystal forms, finding two conformational states of the enzyme and several conformations of the substrate LTA_4, and showing that LTA_4H undergoes domain movements. From this structural information and previous site-directed mutagenesis experiments [15,19,20], Haeggström and coworkers [18] propose a mechanism for the epoxide hydrolase reaction. In short, the C_1 carboxylate group of LTA_4 anchors to ARG563, while Zn^{2+} and TYR383 are coordinated to the epoxide oxygen. A catalytic water molecule (WAT1), polarised by Zn^{2+} and GLU271, transfers a proton to produce an S_N1 acid-induced opening of the epoxide ring. The positive charge of the resulting carbonium ion is delocalised over the triene system, with the C_6-C_7 bond in a pro-*cis* configuration stabilised by the L-shape of the tight pocket. Finally, a second water molecule, activated by ASP375, adds to C_{12} to generate an *R*-hydroxyl group. It has to be underlined that the 12*R*-hydroxyl group and the 6*Z*,8*E*,10*E* configuration of the conjugated triene system are required for the bioactivity of LTB_4 [15]. It seems that ASP375 is needed for the generation of the former [15], whereas TYR378 could be involved in the formation of the right configuration of the triene moiety [21,22].

To our knowledge, only a theoretical study of the epoxide hydrolase reaction exists so far [23]. However, this work was just restricted to the step corresponding to the epoxy ring opening, using the self-consistent-charge density-functional tight-binding (SCC-DFTB) theory [24–26] for the Quantum Mechanics calculations and the CHARMM force field for the molecular mechanics part [27]. Thus, considering only the first reaction step and using a low level of calculation, it provided a rather incomplete view of the whole reaction mechanism to obtain LTB_4.

In this paper, we combine Molecular Dynamics (MD) simulations and Quantum Mechanics/Molecular Mechanics (QM/MM) calculations, using the B3LYP hybrid functional to describe the QM part, to disclose the molecular details of the complete step-by-step mechanism of conversion of leukotriene A_4 to leukotriene B_4 catalysed by the enzyme leukotriene A_4 hydrolase. In particular, we analyse the key factors that drive the 12*R* and the 6*Z*,8*E*,10*E* stereochemistries of the hydroxyl group and the triene moiety, respectively, that are essential for the bioactivity of LTB_4.

2. Results and Discussion

2.1. QM/MM Structural Analysis

According to the crystallographic structures [18], the catalytic water molecule WAT1 is hydrogen-bonded to two Glutamate residues, GLU271 and GLU296. However, the positions of the corresponding hydrogen atoms are not a priori clear. That is, which of these Glutamate residues, GLU271 or GLU296, is the protonated one is not known. Thus, as explained below, two versions of the protonation state of the LTA_4:LTA_4H Michaelis complex have been prepared starting from (GLU271, protonated GLU296) or (protonated GLU271, GLU296), leaving all the other protonation states untouched. These two initial structures have been QM/MM-optimised, and the same minimum energy structure was obtained in both cases, showing that the protonated residue is GLU296, as pictured in Figure 2, where the QM/MM partition used is also shown. Thus, WAT1 coordinates to GLU271 through a donor water hydrogen bond, while it connects to GLU296 through an acceptor hydrogen bond. The remaining water hydrogen atom is the one interacting with the oxygen atom of the epoxide. A complete view of this QM/MM-optimised LTA_4:LTA_4H Michaelis complex is pictured in Figure 3. A scheme of the main noncovalent interactions between the substrate LTA_4 and the enzyme LTA_4H in this optimised Michaelis complex is shown in Figure 4.

LTA_4 fits into the L-shaped hydrophobic cavity of the LTA_4H. The substrate docks to the protein through the interaction between the polar head of the LTA_4 and ARG563 and LYS565 from the protein, which are located in the depth of the cavity. Thus, the substrate is placed in a head-first conformation. Moreover, this fitting conformation lets the epoxide oxygen move near the Zn environment, while it places C_{12} near ASP375 (with WAT3 between them). The epoxide is not only stabilised by being in the second coordination sphere of the Zn atom, but also thanks to two hydrogen bonds from TYR383 and WAT1, the catalytic water which is also coordinated to Zn. With this conformation, TYR267 and TYR378 are the two residues closest to the triene moiety of the substrate. The main interactions between the substrate LTA_4 and the enzyme LTA_4H in this optimised Michaelis complex are schematised in Figure 4. The role of all these residues is to limit the available space and give a shape to the cavity. TYR267 and TYR378 are key residues of the selectivity of the reaction too (see below).

The Zn ion is the central atom of the catalytic domain of the protein. In good agreement with the crystallographic structures [18], in the optimised structure it is pentacoordinated to two HISs (HIS295, HIS299), GLU318, WAT1 and WAT2 with an octahedral geometry (distance RMSD compared to the ideal octahedron: 0.490 Å) [28], so a vacancy for the coordination is available (Figure 5). The free O from GLU318 is linked to WAT2 through a hydrogen bond. Moreover, there is a second coordination sphere, which initially contains the epoxide of LTA_4, GLU271 (hydrogen-bonded to WAT1 and WAT2) and GLU296 (linked to WAT1 through a hydrogen bond).

Int. J. Mol. Sci. **2022**, *23*, 3140

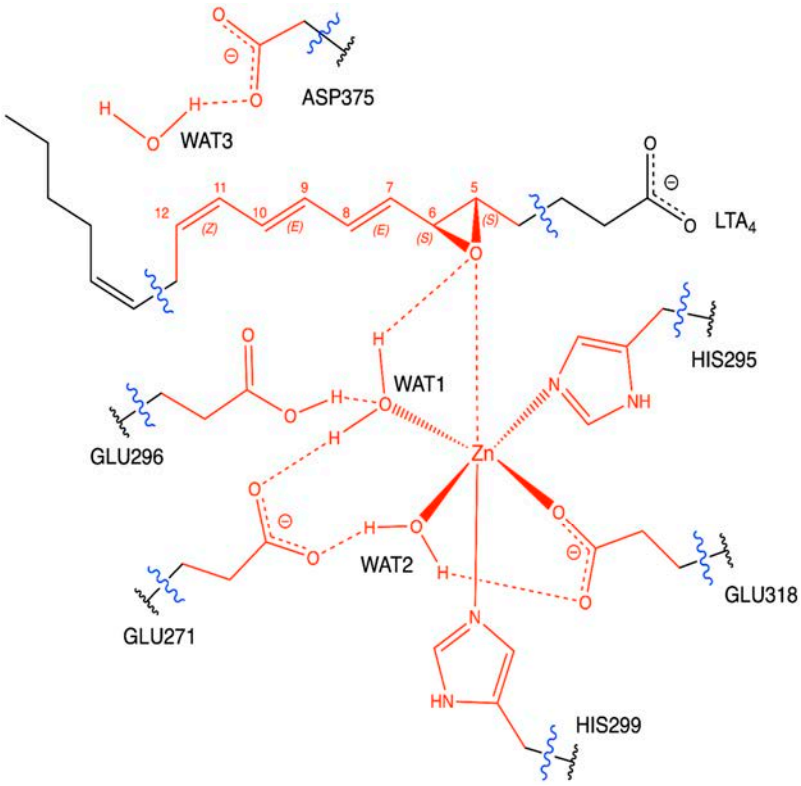

Figure 2. QM/MM partition. QM atoms are depicted in red. The boundary between the QM and MM regions is indicated by blue wavy lines.

2.2. Molecular Dynamics Simulation

In the above section we have analysed the structure of the optimised LTA_4:LTA_4H Michaelis complex and we have identified some key points for the reaction mechanism. However, we might wonder if these features correspond just to this particular minimum energy structure, or if they hold throughout the dynamic fluctuations of the enzyme system. To unravel this point, we analysed 100 ns extracted from a Molecular Dynamics simulation of that Michaelis complex carried out following the protocol explained below. The QM/MM-optimised structure described in Section 2.1. was taken as starting point for the MD simulation.

Firstly, we selected the snapshots along the Molecular Dynamics simulation where there is a water molecule with a distance ASP375-WAT up to 3 Å and a distance C_{12}-WAT smaller than 5 Å at once. In Figure 6, we illustrate where the water molecule appears in those selected snapshots as a function of the distances ASP375-WAT and C_{12}-WAT. This water molecule is the one that appears between ASP375 and C_{12}. Along the simulation there is exchange between the water molecules, in such a way that the water molecule that is represented in this figure is not always the same. In the optimised QM/MM structure, this is WAT3. Almost all the snapshots (96% of the generated snapshots) include a bridging water molecule closer than 3 Å and 5 Å to ASP375 and $C_{12,}$ respectively. Even as many as 58% of the generated snapshots involve a bridging water molecule closer than 3 Å and 4.5 Å

to ASP375 and $C_{12,}$ respectively. It is clear that in most configurations a water molecule, activated by ASP375, appears to be ready to attack C_{12}, thus forming a hydroxyl group.

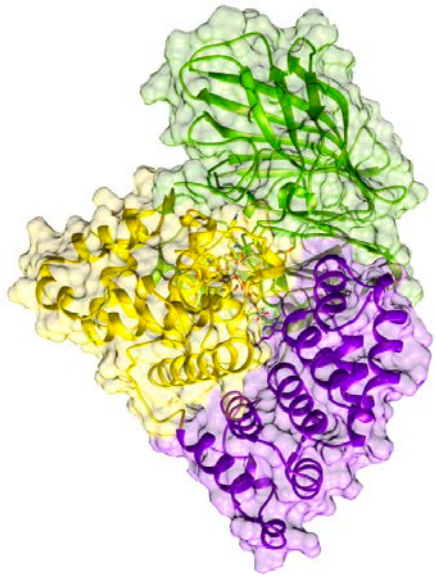

Figure 3. Complete view of the QM/MM-optimised LTA_4:LTA_4H Michaelis complex (the solvation waters are not shown for the sake of clarity). LTA_4H has three domains that are pictured here in different colours: The N-terminal domain (in green), the catalytic domain (in yellow) and the C-terminal domain (in violet). The substrate LTA_4 is represented using a stick model.

On the other hand, the evolution of distances shown in Figure 7 confirms that the epoxide of LTA_4 maintains two hydrogen bonds with TYR383 and WAT1, and that it remains in the second coordination sphere of Zn ion along the Molecular Dynamics simulation.

Finally, we can see in Figure 8 that the C_6-C_7 bond of LTA_4 (the single bond next to the epoxide) keeps a rather pro-*cis* configuration along the Molecular Dynamics simulation. A total of 91% of the snapshots correspond to a pro-*cis* configuration $|dihedral\ angle\ H6-C6-C7-H7| \leq 90°$, whereas only 9% are associated with a pro-*trans* configuration $|dihedral\ angle\ H6-C6-C7-H7| \geq 90°$. The evolution of this dihedral angle along the complete enzyme reaction is a key point for the formation of LTB_4, as will be explained below.

2.3. QM/MM Reaction Mechanism Calculations

The conversion of LTA_4 to LTB_4 is unique because the water molecule is proposed [15,17] to be introduced stereoespecifically at a site (C_{12}) six methylene units away from the epoxide moiety (C_5 to C_6), in what would be a 1,7-nucleophilic substitution. Although it is believed [17] to proceed by means of an S_N1 mechanism, an S_N2 mechanism should also be considered as possible. To unravel this point, a two-dimensional potential energy surface was built (see Figure 9) using a reaction coordinate r_c^1 for the epoxide ring opening ($r_c^1 = d(C_6(LTA_4) - O_{epox}(LTA_4))$, that is, the epoxide breaking bond length, and a reaction coordinate r_c^2 for the water addition to C_{12} ($r_c^2 = (d(O(WAT3) - H(WAT3)) - d(O(WAT3) - C_{12}(LTA_4))$), that is, the difference between the water breaking bond length and the forming O–C bond length. The rest of the geometrical parameters in the active region have been fully optimised. R stands for the optimised structure (Figures 3–5). Using the Dijsktra algorithm [29] we have also defined in Figure 6 the minimum energy reaction path (white points) on that surface and the minimum (R, INT1 and INT2) and maximum energy points along it (TS1 and TS2).

Int. J. Mol. Sci. **2022**, *23*, 3140

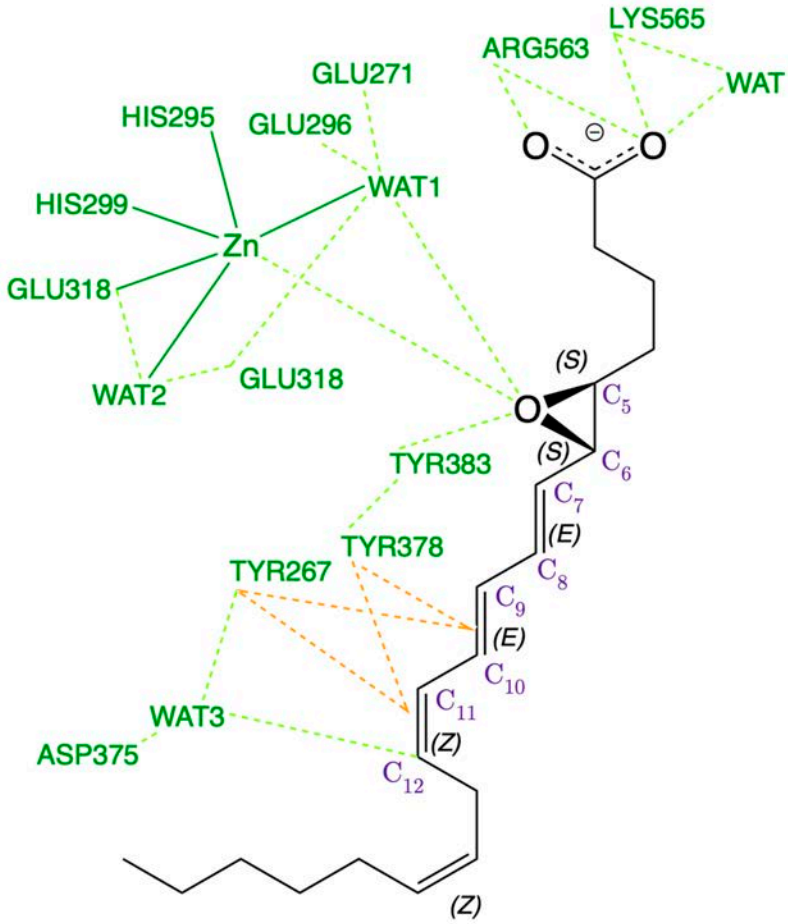

Figure 4. Scheme of the main noncovalent interactions (in dashed lines) between the substrate LTA_4 (in black) and the enzyme LTA_4H (in green) in the optimised Michaelis complex and the Zn environment. The dashed orange lines indicate π-π stacking interactions.

As shown in Figure 9, the reaction takes place in two well-separated steps. Firstly, the $C_6 - O_{epox}$ bond progressively breaks, thus opening the epoxide ring. In the intermediate INT1, the epoxide is already open (the distance $C_6 - O$epox is 2.3 Å), but the value of the reaction coordinate r_c^2 has not significantly changed yet. From here on, in the second step the distance C6 − Oepox remains quite invariant, while a clear evolution of the reaction coordinate r_c^2 occurs, indicating the water (WAT3) addition to C_{12} and the breakage of an O-H bond in this water molecule and finally reaching the intermediate INT2. Thus, the 1,7-nucleophilic substitution clearly takes place through an S_N1 mechanism. As a matter of fact, it is an extreme case of S_N1 reaction, because the minimum energy reaction paths corresponding to each step appear to be roughly orthogonal (each one parallel to one coordinate axis) in the two-dimensional potential energy surface shown in Figure 9. Any deviation of the mechanism towards the region near the diagonal of that energy surface (that is, any approach to the S_N2 mechanism) implies the penetration in high-energy

regions, which turns out to be forbidden. An NBO charge analysis in INT1 gives a charge of +0.71 a.u. delocalised over the triene system (from C_6 to C_{12}) of the substrate, which confirms the existence of the carbocation required in the intermediate of an S_N1 mechanism.

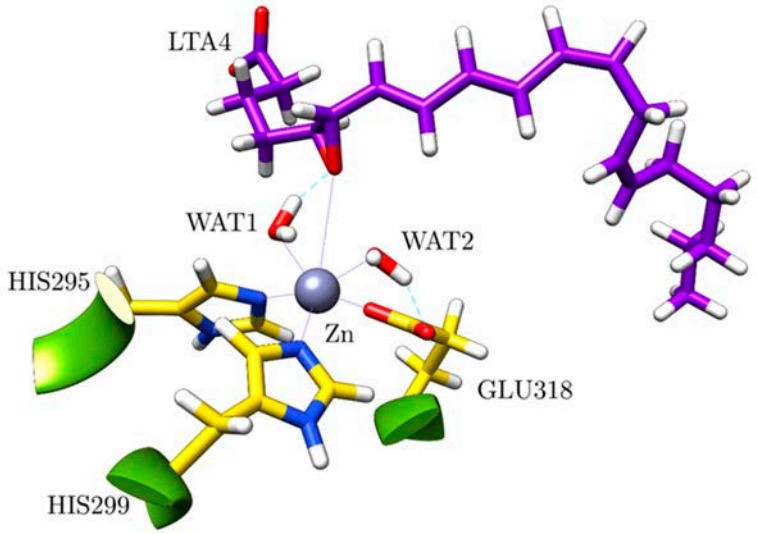

Figure 5. Zn environment in the optimised structure.

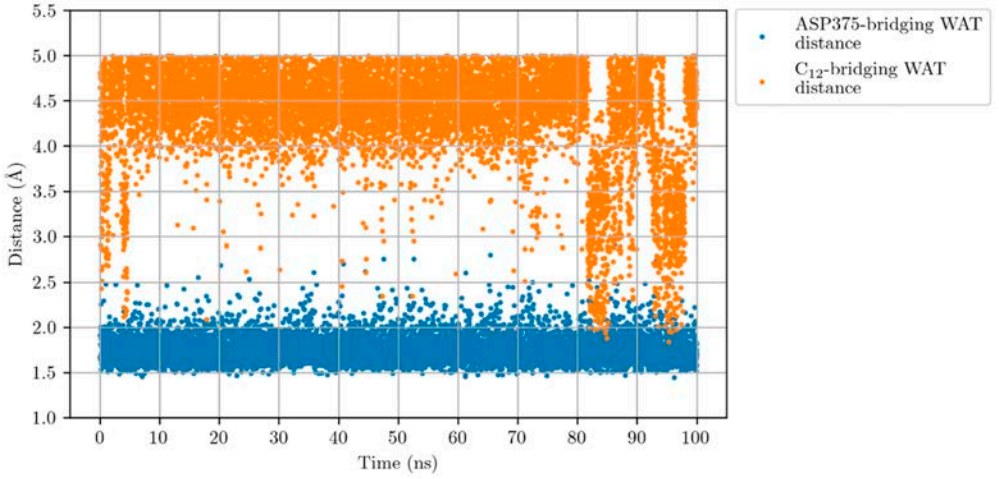

Figure 6. Distances ASP375-WAT (blue points) and C_{12}-WAT (orange points) along the Molecular Dynamics simulation for the LTA_4:LTA_4H Michaelis complex. WAT stands for a water molecule placed between ASP375 and C_{12}.

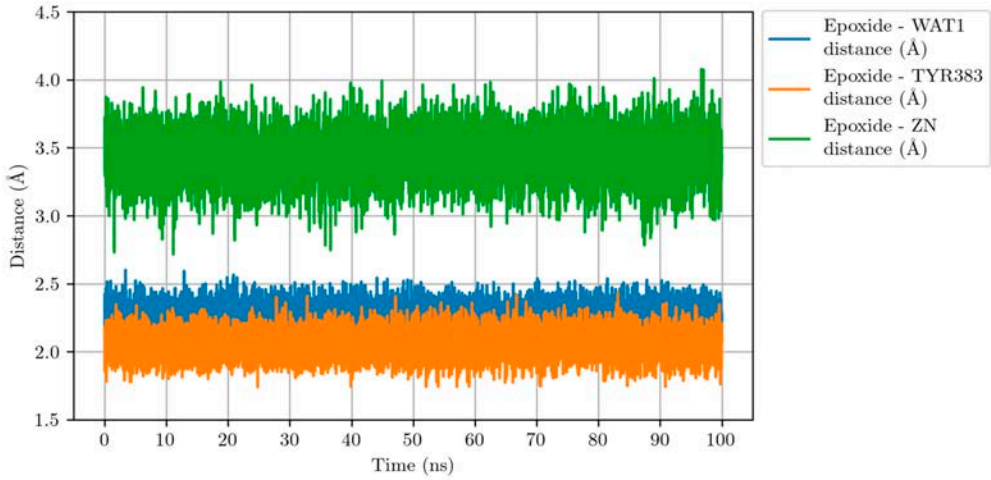

Figure 7. Distances epoxide-WAT1 (blue line), epoxide-TYR383 (orange line) and epoxide-Zn (green line) along the Molecular Dynamics simulation for the LTA_4:LTA_4H Michaelis complex.

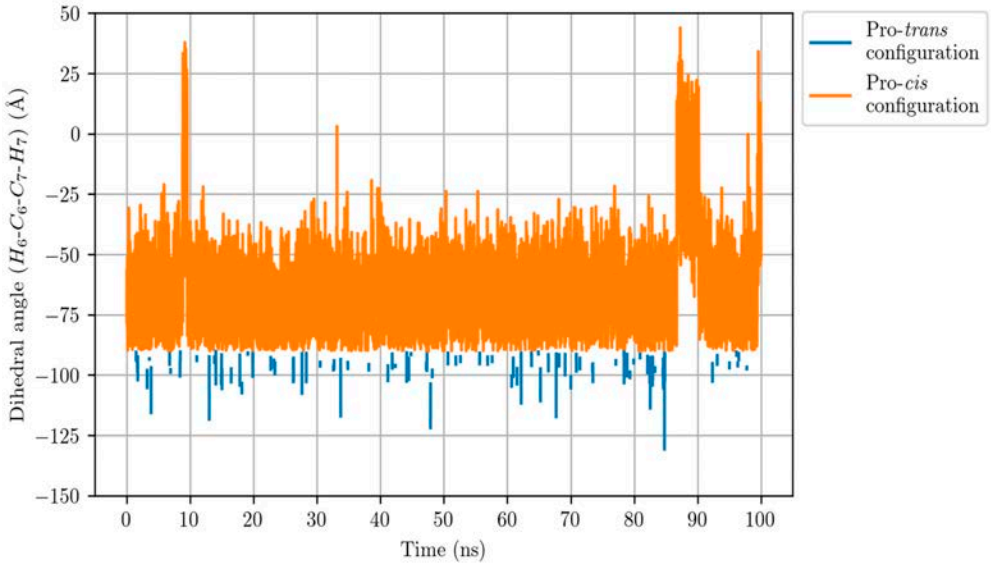

Figure 8. Dihedral angle H_6-C_6-C_7-H_7 along the Molecular Dynamics simulation for the LTA_4:LTA_4H Michaelis complex. The pro-*cis* configuration (orange line) corresponds to $|dihedral\ angle| \leq 90°$, whereas $|dihedral\ angle| \geq 90°$ indicates a pro-*trans* configuration (blue line).

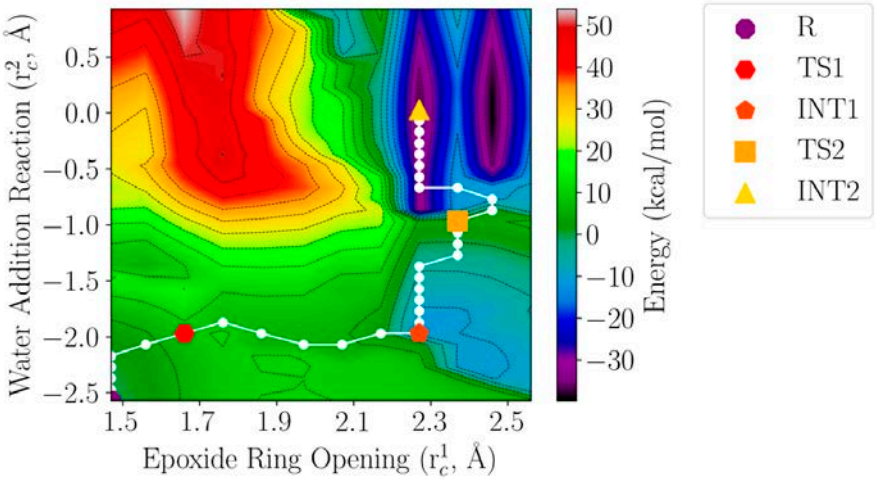

Figure 9. Two-dimensional potential energy surface as a function of the epoxide ring opening and water addition reaction coordinates defined in the text. Isoenergetic lines correspond to intervals of 5 kcal/mol.

To our surprise, a structural analysis of the intermediate INT2 shows that the conjugated triene moiety has a 6*E*,8*E*,10*E* configuration that would not lead to LTB_4 but to its stereoisomer 12*S*-6-*trans*-LTB_4 (5*S*,12*S*-dihydroxy-6*E*,8*E*,10*E*,14*Z*-eicosatetraenoic acid). Following the evolution of the structures along the S_N1 mechanism shown in Figure 9, we found that an unexpected rotation of the C_6-C_7 bond from the initial rather pro-*cis* configuration in LTA_4 to a pro-*trans* configuration in INT1 occurs, which leads to the 6*E* inadequate configuration of C_6-C_7 in INT2. To analyse this fact, we built a two-dimensional potential energy surface (see Figure 10) as a function of the rotation of the C_6-C_7 bond (r_c^3 = dihedral angle H_6-C_6-C_7-H_7) and the epoxide ring opening (r_c^1 = d(C_6(LTA_4) − O_{epox}(LTA_4)). Starting from the reactant R, the Dijsktra algorithm [29] localises two minimum energy reaction paths (grey and white points) on the surface shown in Figure 10, and the minimum (R, INT1trans and INT1cis) and maximum (TS1trans and TS1cis) energy points along them. One path involves the pro-*trans* (grey points) configuration (as a matter of fact, it corresponds to the first step of the S_N1 mechanism shown in Figure 9). The other one maintains a pro-*cis* configuration (white points) to reach an intermediate INT1cis with the adequate pro-*cis* structure. The two paths are competitive, with the pro-*trans* being the one that implies the lowest potential energy barrier. This explains why only the *trans* configuration was obtained in the two-dimensional potential energy surface shown in Figure 9, where the rotation of the C_6-C_7 bond was not included to define the reaction coordinate. This result also agrees with our B3LYP/6-31G(d) calculation that shows that in the gas phase, 12*S*-6-*trans*-LTB_4 is 0.3 kcal/mol more stable than LTB_4 in terms of potential energy. However, the experimental result is that LTA_4H converts LTA_4 into LTB_4, that is, with a 6*Z*,8*E*,10*E* configuration for the conjugated triene moiety.

An especially interesting point is that the configuration of the C_6-C_7 bond in INT1 determines the stereochemistry of the ingoing water into C_{12}. In Figure 11, we have displayed the position of WAT3 with respect to the plane generated by the triene moiety (from C_6 to C_{12}) in the reactant LTA_4 (pro-*cis*, yellow disk) in INT1trans (pro-*trans*, brown disk) and in INT1cis (pro-*cis*, violet disk). It can be clearly seen that the face of attack of WAT3 in the pro-*trans* configuration is just the opposite than in the case of the pro-*cis* configuration in INT1, leading to the 12*S*-hydroxyl or the 12*R*-hydroxyl configurations,

Int. J. Mol. Sci. **2022**, *23*, 3140

respectively. Thus, the two main stereochemical features that are required for the bioactivity of LTB_4 appear to be closely linked.

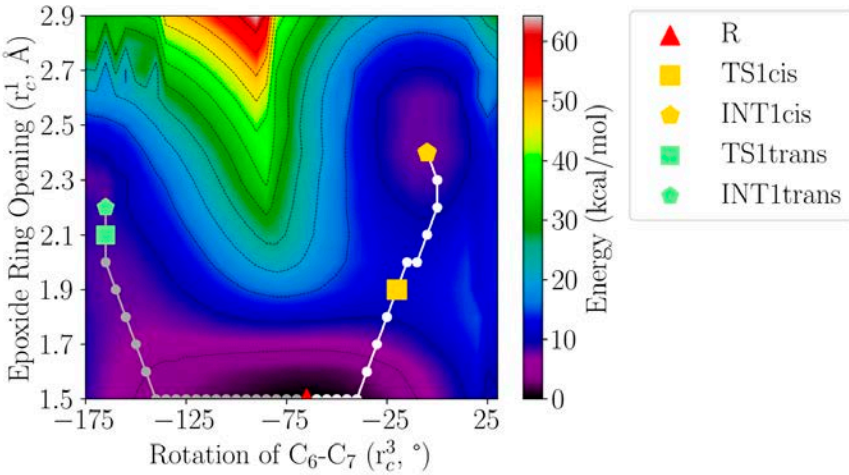

Figure 10. Two-dimensional potential energy surface as a function of the rotation of the C_6-C_7 bond and the epoxide ring-opening reaction coordinates defined in the text. Isoenergetic lines correspond to intervals of 5 kcal/mol.

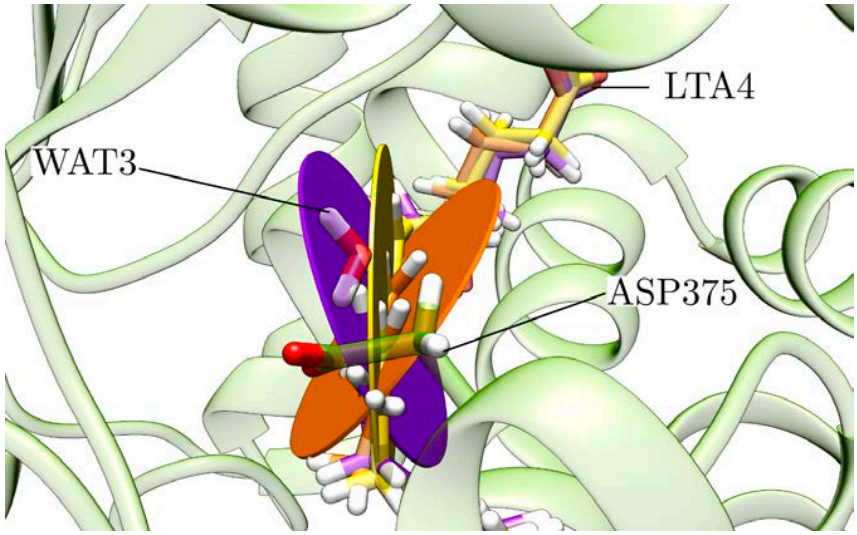

Figure 11. Position of WAT3 with respect to the plane generated by the triene moiety in the reactant LTA_4 (pro-*cis*, yellow disk), in INT1trans (pro-*trans*, brown disk) and in INT1cis (pro-*cis*, violet disk).

At this point, it is clear that a complete and comparative study of the pro-*cis* and the pro-*trans* reaction paths is needed to understand the mechanism of this enzyme reaction. To this aim, firstly we fully optimised the structures INT1cis, INT1trans, TS1cis and TS1trans, which appear in Figure 10, in order to locate the corresponding stationary

structures (minima and transition-state structures) in the complete potential hypersurface of the reaction. Then, for each reaction path, we followed the reaction coordinates d(O(WAT3)-H(WAT3))-d(O(WAT3)-C_{12}(LTA_4)) and d(O(WAT1)-H(WAT1))-d(H(WAT1)-O_{epox}) to describe, respectively, the water addition (WAT3) to C_{12} and the final protonation of the oxygen atom bonded to C_6 (the former oxygen atom of the epoxide) by WAT1 and to locate the corresponding stationary structures. The relative potential energies for all the stationary points we localised are shown in Figure 12.

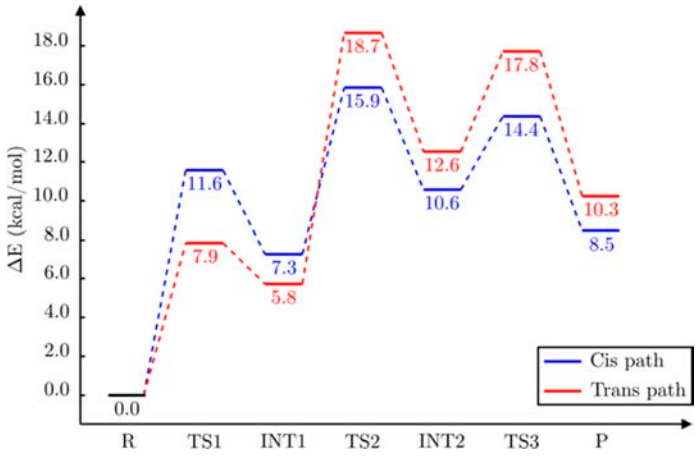

Figure 12. Diagram of potential energies of the stationary structures of the complete mechanism of conversion of LTA_4 to LTB_4 (pro-*cis* reaction path, in blue) catalysed by LTA_4H and of the competitive pro-*trans* reaction path (in red).

We focused firstly on the pro-*cis* reaction path. In Figure 13 we show a succession of pictures of the stationary structures along this path, intending to capture LTA_4H in action. For the sake of clarity, in Figures S1–S3 we display representations of those stationary structures focused on the region where the corresponding step occurs in each case.

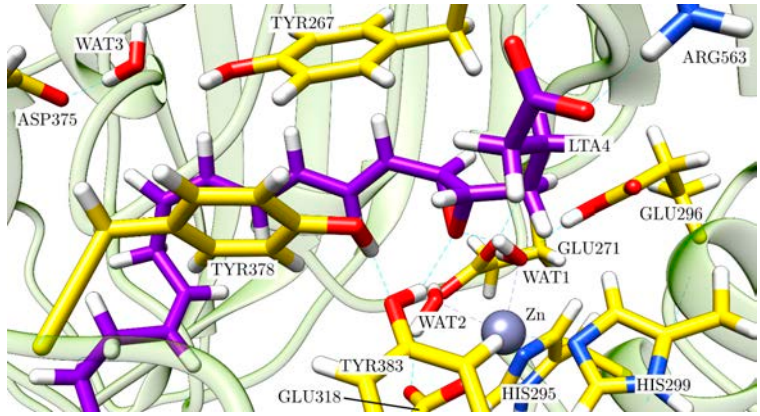

R

Figure 13. *Cont.*

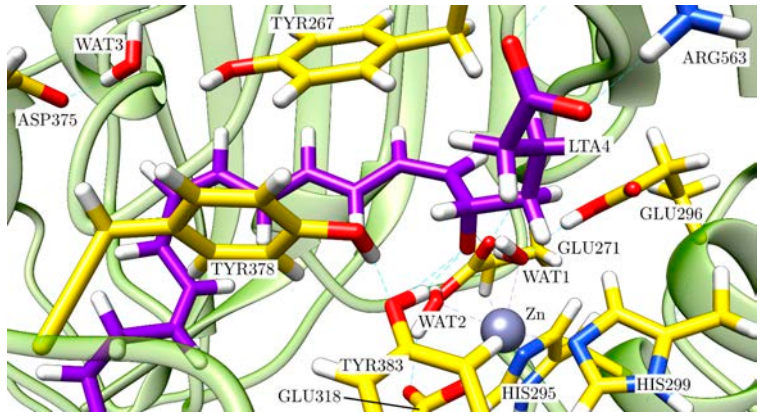

TS1cis

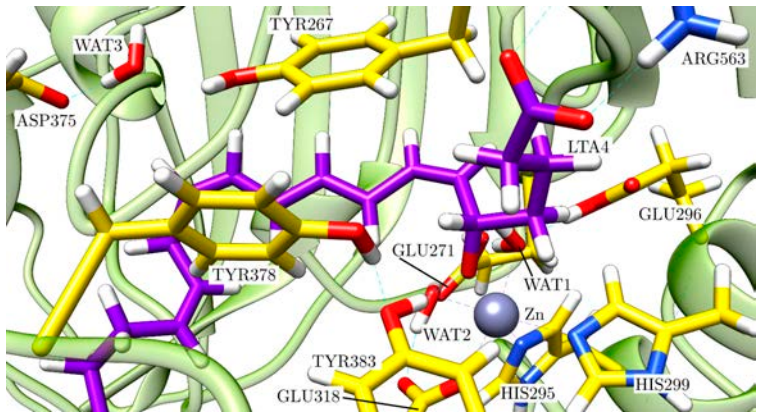

INT1cis

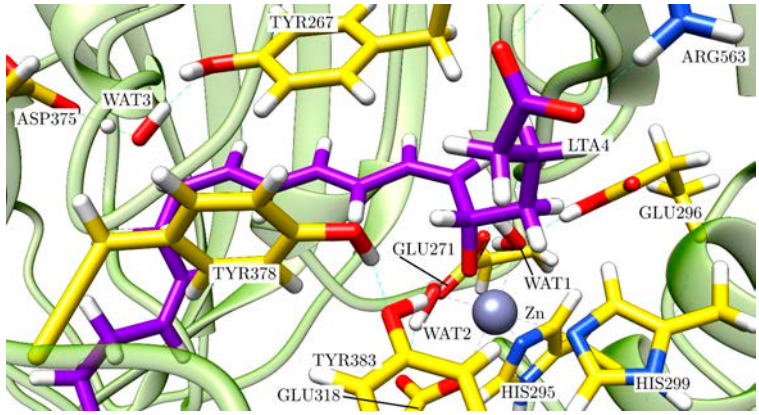

TS2cis

Figure 13. *Cont.*

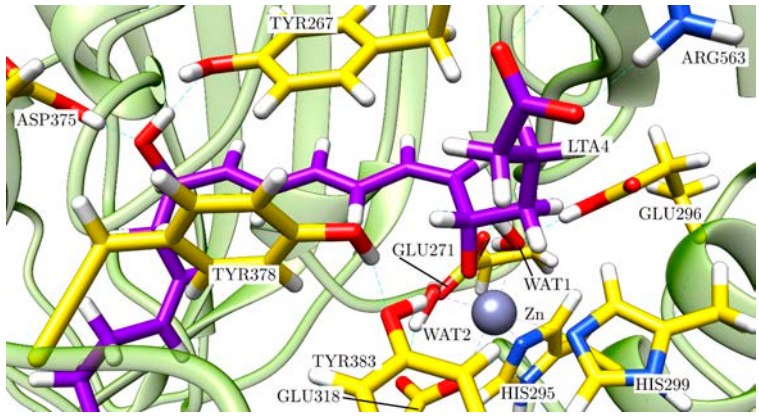

INT2cis

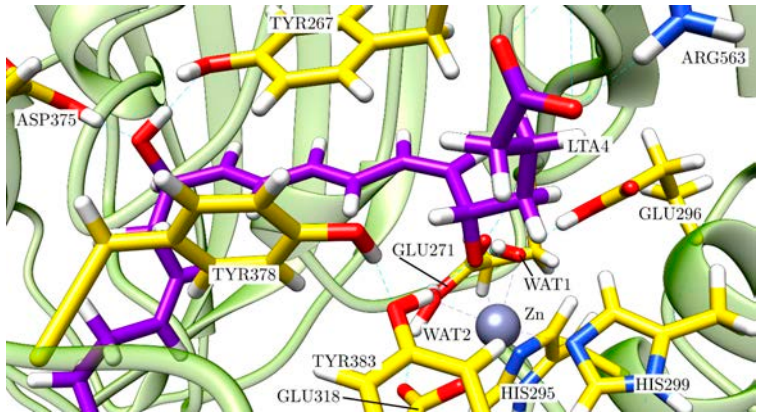

TS3cis

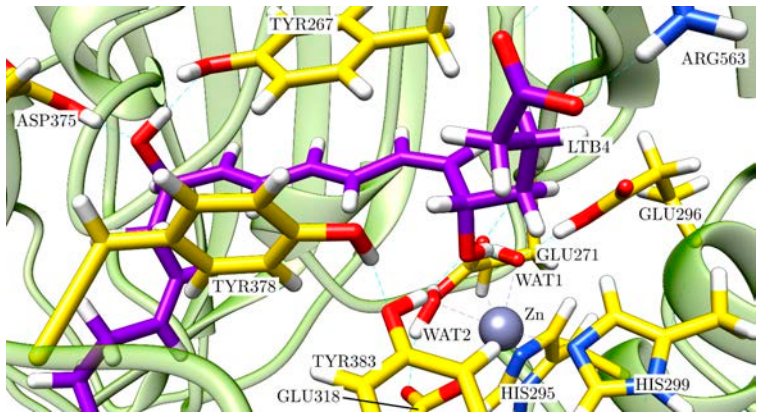

Pcis

Figure 13. Stationary structures of the complete mechanism of conversion of LTA_4 to LTB_4 (pro-*cis* reaction path) catalysed by LTA_4H: R, TS1cis, INT1cis, TS2cis, INT2cis, TS3cis and Pcis.

Int. J. Mol. Sci. **2022**, *23*, 3140

The evolution of the main geometrical parameters along the pro-*cis* reaction path leading to LTB_4 is indicated in Table 1. As indicated above, the first step consists of the epoxide opening. The formation of a nascent negative charge in the oxygen of the epoxide is stabilised by the interaction of this oxygen with the Zn atom, the hydroxyl group of TYR383 and the hydrogen bond interaction with WAT2 and WAT1, although WAT1 moves away from INT1cis. Conversely, the Zn-O_{epox} bond is significantly shortened from 3.39 Å in R to 1.99 Å at INT1cis, in such a way that epoxide completes the coordination sphere of Zn by occupying its free vacancy (see Figure 5). The epoxide is fully opened at INT1cis, while O_{epox}-C_5 is stronger at INT1cis than in R. This step implies a potential energy barrier of 11.6 kcal/mol. As explained above, at INT1cis no significant changes have occurred with respect to WAT3 and ASP375 yet, thus indicating an S_N1 mechanism. Very interestingly, the dihedral angle H_6-C_6-C_7-H_7 goes from −65.6° in R (a value close to an intermediate situation of the bond C_6-C_7 between pro-*cis* and pro-*trans*) to −15.9° at TS1cis and −7.1° at INT1cis, a clearly *cis* stereochemistry. As a result of the twist that the triene moiety must perform to adopt this *cis* stereochemistry, WAT3 becomes ready to attack the *R* face of C_{12} (by the side opposite to the Zn atom, see Figure S2) at INT1cis. Then, WAT3 adds to C_{12} (the distance O(WAT3)-C_{12} evolves from 3.69 Å at INT1cis to 1.53 Å at INT2cis), while one of its hydrogen atoms is fully transferred to ASP375 through the corresponding hydrogen bond. This second step involves a potential energy barrier of 15.9 kcal/mol. Finally, in the third step, the final transfer of a proton from WAT1 to the oxygen atom bonded to C_6 (the former oxygen atom of the epoxide, O_{epox}) takes place, while the distance Zn-O_{epox} clearly increases through a potential energy barrier of 14.4 kcal/mol, thus forming LTB_4. Note that Haeggström and coworkers [18] have proposed that the catalytic water WAT1 transfers a proton to promote an S_N1 acid-induced opening of the epoxide ring. However, we have found here that this proton donation is not the first step of the reaction, but the last one. That is, when the epoxide ring opens, the nascent negative charge in its oxygen atom is quite stabilised through the interaction with atoms surrounding it, in such a way that a previous proton transfer from WAT1 is not needed.

Table 1. Most relevant distances (in Å) and dihedral angle (in degrees) defining the *E*/*Z* character of the C_6-C_7 bond for the stationary structures of the complete mechanism of conversion of LTA_4 to LTB_4 (pro-*cis* reaction path) catalysed by LTA_4H.

Pro-*cis* Reaction Path	**R**	**TS1**	**INT1**	**TS2**	**INT2**	**TS3**	**P**
Zn-O_{epox}	3.39	2.94	1.99	1.97	1.95	2.45	2.96
O_{epox}-C_5	1.45	1.41	1.39	1.39	1.39	1.41	1.43
O_{epox}-C_6	1.47	1.92	2.40	2.41	2.42	2.37	2.39
H(WAT1)-O_{epox}	1.75	1.65	2.42	2.46	2.49	1.39	1.02
O(WAT1)-H(WAT1)	0.99	1.00	0.97	0.97	0.98	1.09	1.59
O(WAT3)-C_{12}	3.84	3.69	3.69	1.82	1.53	1.53	1.53
H(WAT3)-O(ASP375)	1.71	1.69	1.67	1.36	1.03	1.03	1.03
O(WAT3)-H(WAT3)	0.99	0.99	0.99	1.11	1.53	1.53	1.53
H_6-C_6-C_7-H_7	−65.6	−15.9	−7.1	1.5	1.5	−0.5	−0.7

Let us describe the pro-*trans* reaction path now. In Figure 14, we show a succession of pictures of the stationary structures along this path. For the sake of clarity, in Figures S4–S6, we display representations of those stationary structures focused on the region where the corresponding step occurs in each case.

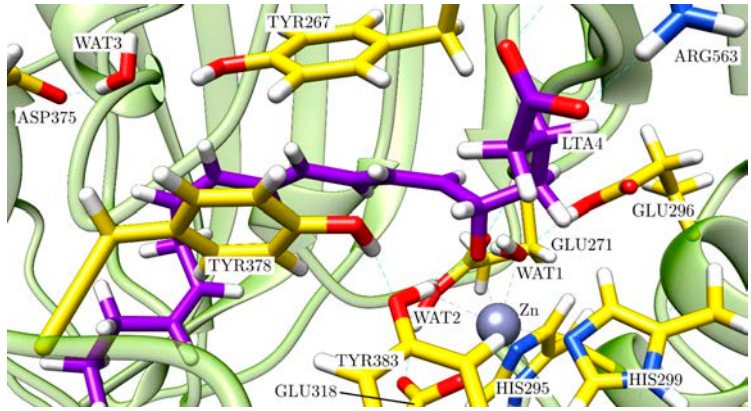

TS1trans

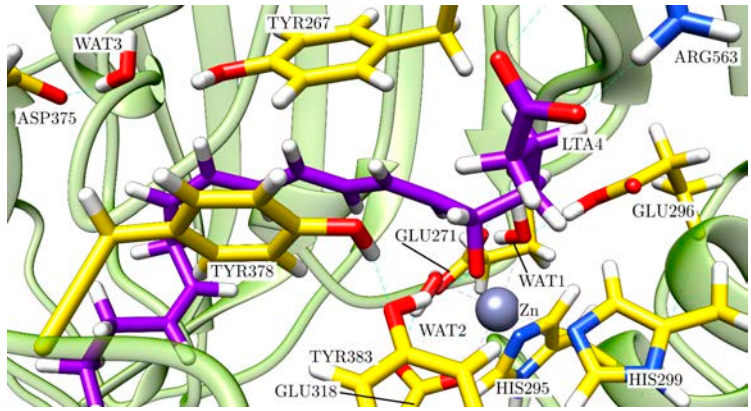

INT1trans

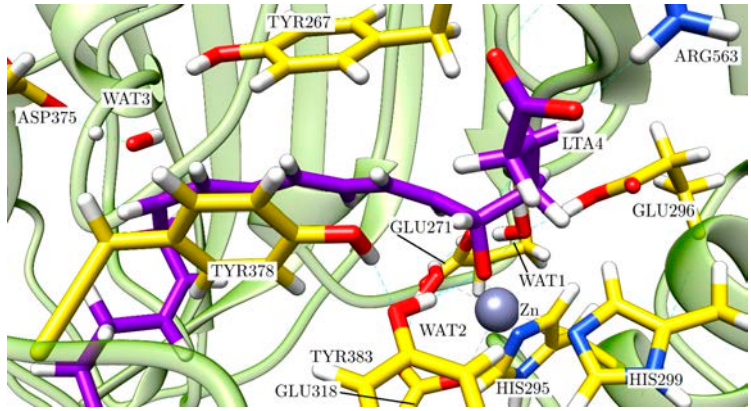

TS2trans

Figure 14. *Cont.*

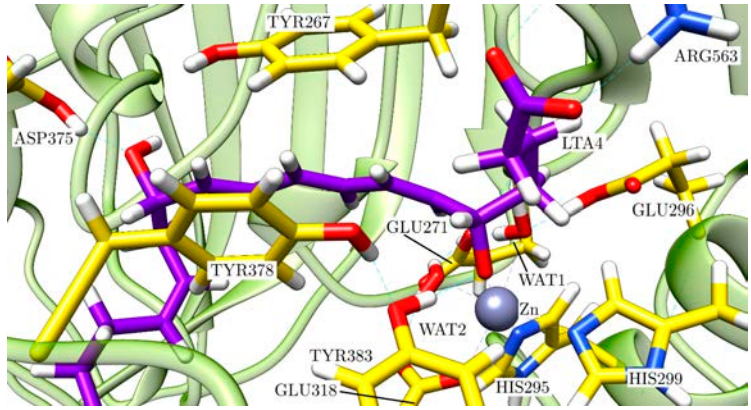

INT2trans

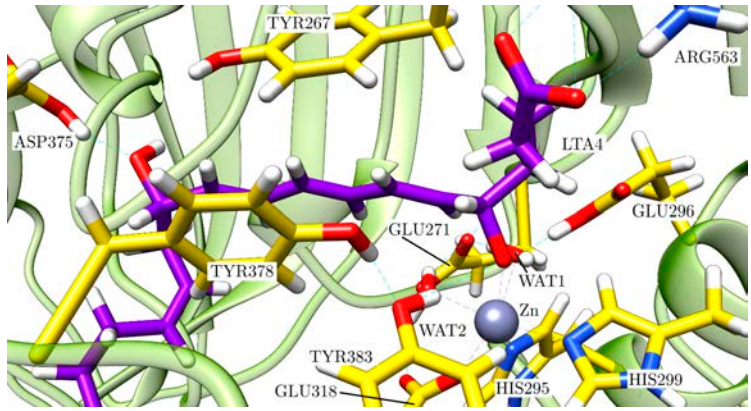

TS3trans

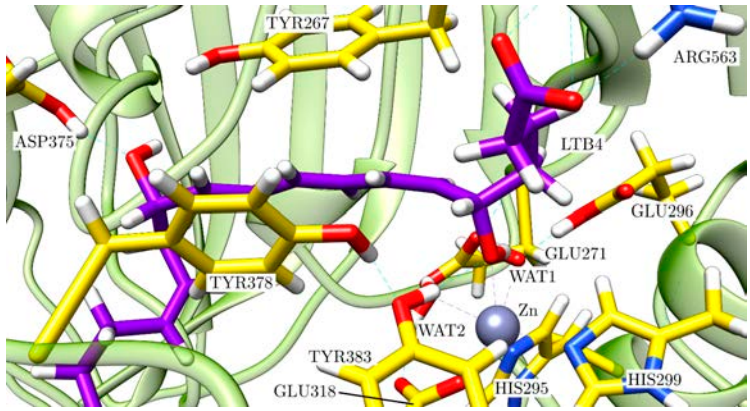

Ptrans

Figure 14. Stationary structures of the complete mechanism of the pro-*trans* reaction path catalysed by LTA_4H: TS1trans, INT1trans, TS2trans, INT2trans, TS3trans and Ptrans.

The evolution of the main geometrical parameters along the pro-*trans* reaction path is indicated in Table 2. Analogously to the case of the pro-*cis* reaction path, in the first step of the pro-*trans* reaction path, the oxygen of the epoxide is stabilised by the interaction with the Zn atom, the hydroxyl group of TYR383 and the hydrogen bond interaction with WAT2 and WAT1, although WAT1 also moves away at INT1trans. Conversely, the Zn-O_{epox} bond is significantly shortened from 3.39 Å in R to 1.98 Å at INT1trans. The epoxide is fully opened at INT1trans of this S_N1 mechanism. This step implies a potential energy barrier of only 7.9 kcal/mol. The key stereochemical features of the complete reaction are determined in this first step, where the fate of the process is decided. Thus, the dihedral angle H_6-C_6-C_7-H_7 is 196.9° at TS1trans and 183.7° at INT1trans, a clearly *trans* stereochemistry. This twist of the triene moiety takes place in the opposite direction to the twist that happens in the pro-*cis* reaction path. This way, WAT3 now becomes ready to attack the *S* face of C_{12} (by the same side as the Zn atom, see Figure S5) at INT1trans. Then, WAT3 adds to C_{12} (the distance O(WAT3)-C_{12} evolves from 3.66 Å at INT1trans to 1.51 Å at INT2trans), while one of its hydrogen atoms is fully transferred to ASP375 through the corresponding hydrogen bond. This second step involves a potential energy barrier of 18.7 kcal/mol. Finally, in the third step, the final transfer of a proton from WAT1 to the oxygen atom bonded to C_6 takes place, while the distance Zn-O_{epox} clearly increases through a potential energy barrier of 17.8 kcal/mol, thus forming 12*S*-6-*trans*-LTB_4, the stereoisomer of LTB_4.

Table 2. Most relevant distances (in Å) and dihedral angle (in degrees) defining the *E*/*Z* character of the C_6-C_7 bond for the stationary structures of the pro-*trans* reaction path catalysed by LTA_4H.

Pro-*trans* Reaction Path	**R**	**TS1**	**INT1**	**TS2**	**INT2**	**TS3**	**P**
Zn-O_{epox}	3.39	2.64	1.98	1.93	1.92	3.26	2.96
O_{epox}-C_5	1.45	1.40	1.39	1.39	1.39	1.44	1.43
O_{epox}-C_6	1.47	2.04	2.20	2.30	2.32	2.39	2.34
H(WAT1)-O_{epox}	1.75	1.66	3.00	3.12	3.12	0.97	1.02
O(WAT1)-H(WAT1)	0.99	1.00	0.98	0.98	0.98	2.39	1.59
O(WAT3)-C_{12}	3.84	3.68	3.66	1.79	1.51	1.50	1.50
H(WAT3)-O(ASP375)	1.71	1.66	1.66	1.32	1.01	1.01	1.01
O(WAT3)-H(WAT3)	0.99	1.00	1.00	1.12	1.60	1.64	1.62
H_6-C_6-C_7-H_7	294.4	196.9	183.7	178.1	177.5	180.7	181.5

A final point to discuss is why LTA_4H converts LTA_4 into LTB_4 instead of the stereoisomer 12*S*-6-*trans*-LTB_4, which is more stable in the gas phase. In other words, why the pro-*cis* reaction path is the dominant one instead of the pro-*trans* reaction path. As seen in Figure 12, as for the epoxide opening the *trans* path is more favourable than the *cis* path. However, from here on, the *cis* energy profile appears clearly below the *trans* energy profile. In particular, taking into account the complete mechanism, the higher energy transition state structure of the *trans* path (18.7 kcal/mol) and the *trans* final product (10.3 kcal/mol) are significantly above the corresponding values of the *cis* path (15.9 kcal/mol and 8.5 kcal/mol, respectively), what means that the inside of the LTA_4H formation of LTB_4 is more favourable than the formation of 12*S*-6-*trans*-LTB_4 both kinetically and thermodynamically. This energy crossing can be explained by observing some of the most important noncovalent interactions that take place between the substrate and the enzyme. TYR267 and TYR378 are the two residues closest to the triene system, which is practically wrapped by these two tyrosines along the reaction paths (see the sequence of structures shown in Figures 13 and 14). The key point here is that these two tyrosines and the triene moiety can interact among them through noncovalent π-π stacking interactions that are different depending on the reaction path (see Figure 15 for the angles between the respective planes). The angle of the π-π interaction between TYR267 and TYR378 is kept quite invariant (between 50° and 60°)

Int. J. Mol. Sci. **2022**, *23*, 3140

throughout the complete reaction for both reaction paths, and it has not been depicted. It has to be recalled here that the closer the planes to the face-to-face orientation, the more stabilising the interaction. Thus, TYR267 slightly favours the pro-*trans* reaction path up to INT1 (the first step), but the pro-*cis* reaction path in the second and third steps. Much more relevant is the role of TY378. As explained above, during the epoxide opening the triene moiety twists in two opposite directions depending on which reaction path it takes, pro-*cis* or pro-*trans*. As a result of this twist, the π-π stacking interaction with TY378 becomes clearly face-to-face (pro-*trans*) or clearly edge-to-face (pro-*cis*). At INT1trans (see Figure 11) the planes of the triene moiety and TY378 are roughly parallel. This way, TYR378 favours the formation of a broken epoxide with a *trans* C_6-C_7 bond. However, along the second and third steps, edge-to-face interaction is kept for the pro-*cis* reaction path, while the face-to-face interaction for the pro-*trans* reaction path becomes significantly broken, thus destabilising the formation of 12*S*-6-*trans*-LTB_4 and leading to LTB_4 as a product of the reaction catalysed by LTA_4H. Indeed, those two tyrosines do not exist in the gas phase, where the 12*S*-6-*trans*-LTB_4 is more stable than LTB_4. Our theoretical result agrees with experimental data [21,22] showing that mutations of TY378 lead not only to LTB_4 but also to products with a *trans* stereochemistry in the C_6-C_7 bond.

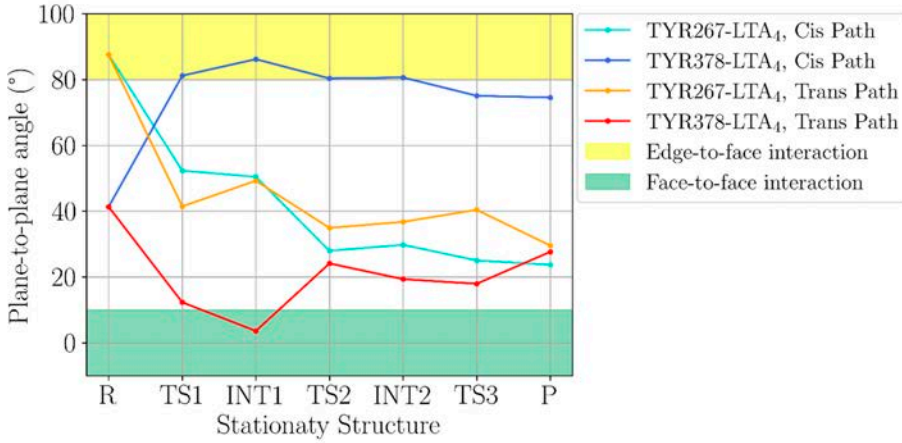

Figure 15. Angles between the plane of the triene moiety of the substrate and the planes of the aromatic rings of TYR267 and TYR378 for the different stationary structures located along the pro-*cis* and the pro-*trans* reaction paths. The closest plane to the whole number of C and H atoms of the triene system was taken as the plane of this triene moiety.

3. Materials and Methods

3.1. Protein Setup

Numerous crystallographic structures [18] have been reported for human LTA_4H, some of them complexing a wide variety of inhibitors and a few of them containing the LTA_4 substrate but including one or more mutations. Here, a single-mutated version of human LTA_4H (ASP375ASN) complexed with LTA_4 was used (PDB code: 5NI6) [18]. The mutation was reverted to the WT enzyme. The protein was protonated at pH 7.0 using PropKa3.0 [30] through a web interface (www.playmolecule.org, accessed on 1 July 2019). Two versions of the protonation state were prepared: (GLU271, protonated GLU296) and (protonated GLU271, GLU296), leaving all the other protonation states untouched. A box of TIP3P [31] water molecules was built around the protein for solvation. The box was built up considering 10 Å from the outermost protein's atom in each direction of the space.

3.2. QM/MM Calculations

The solvation model was cropped, so only the water molecules inside a 17 Å radius sphere around whatever atom of the substrate were kept for the QM/MM calculations. The modular software package ChemShell [32,33] was used as the interface between the QM and the MM calculations. TURBOMOLE [34] was used for the density functional theory (DFT) calculations, while AMBER [35] force fields were employed for the MM calculations using the DL_POLY [36] module in ChemShell. AMBER's ff14SB [37] force field was used for generating the protein MM parameters. GAFF2 [38] force field was used for parameterising the substrate (LTA_4), whose RESP charges [39] were calculated using Gaussian09 [40]. An electrostatic embedding scheme [41] was employed in order to treat the QM mm interactions. Additionally, a link atom scheme was used to treat the QM/MM boundary by using the charge shift model [42]. No cut-offs were introduced for the nonbonding QM/MM and MM interactions [43].

The active region of the system was built by selecting all atoms within a radius of 15 Å around the oxygen atom of the epoxide group of the substrate. These atoms were allowed to move freely (almost 3000 atoms), while the nonactive ones were frozen (almost 8000 atoms). For the QM part of the system (see Figure 2), 86 atoms were selected involving the Zn and its immediate environment (HIS295, HIS299, GLU318, WAT1, WAT2), GLU271 and GLU296, from C_4 to C_{13} of the substrate (thus including the epoxide and the triene group and ASP375 and its nearest water molecule (WAT3). From this selection, eight link atoms were added: six between the corresponding bonds C(MM)-C(QM) atoms of the six residues and two bonded to the aliphatic carbon atoms of the lipid substrate (placed between C_3-C_4 and C_{13}-C_{14}). Moreover, a microiterative scheme [44] was applied for the energy optimisation to minima. All residues containing at least one atom in the QM region were added to the 'micro' region of the microiterative scheme, while all other atoms were kept in the 'macro' region.

The QM/MM energy optimisations to minima and scan calculations were performed using the HDLCopt (hybrid delocalised internal coordinate) coordinates scheme [45] and the limited-memory Broyden–Fletcher–Goldfard–Shanno (L-BFGS) algorithm [46,47]. For optimisations to minima, tolerance was set to 0.0045 Bohr, while for potential energy surface (PES) calculations it was set to 0.01 Bohr. PES calculations have at least one angle, bond or bond distance differences fixed in order to carry out the exploration. The transition-state searches were carried out employing the HDLC coordinates scheme and the partitioned rational function optimiser (P-RFO) [48,49] combined with the L-BFGS algorithm. P-RFO and the L-BFGS algorithm were used as implemented in the HDLCopt module and the DL_FIND geometry optimisation library [50] of ChemShell, respectively. A set of core atoms including only the 6 atoms directly implicated in the reaction was defined in order to ease the calculation of the Hessian along the optimisation. Frequencies of the optimised structures were calculated using the force module from ChemShell for the whole QM region. The nature of the stationary structures was confirmed by means of the analysis of the number of imaginary frequencies.

We used the Dijsktra algorithm [29] to obtain the minimum energy reaction path on the two-dimensional potential energy surfaces.

The QM region was described by the B3LYP hybrid functional [51]. The 6-31G(d) Pople basis set [52] was employed for the C, H, O and N atoms, while the Stuttgart RLC ECP basis set [53] was used for the Zn atom.

3.3. Molecular Dynamics Simulation

The crystallographic structure optimised at the QM/MM level and with the proper protonation (deprotonated GLU271, protonated GLU296) was chosen as the initial structure for the MD simulation. Protein parameters and charges were obtained from the ff14SB [37] force field from AMBER [35]. The substrate was parametrised using the parmchk2 module from AmberTools [54]. It was optimised at the B3LYP/6-31G(d) level, and then Merz–Kollman RESP charges [39] were calculated. Zn parameters were obtained following the

Int. J. Mol. Sci. **2022**, *23*, 3140

Seminario Method [55] and the bonded model from AMBER using MCPB.py [56]. All residues within 3 Å around Zn were included in the model (HIS295, HIS299, GLU318, WAT1, WAT2). The model has not been optimised since the global structure corresponds to a QM/MM minimum, but frequencies were calculated as well as Merz–Kollman RESP charges [39] at the B3LYP/6-31G(d) level. MM parameters were derived from the frequencies' calculation.

AMBER's tLEAP module was used to generate an orthorhombic box of pre-equilibrated TIP3P [31] water molecules, including 9 Na^+ ions, to neutralise the protein's charge. Thus, a resulting box of 78.7 × 116.5 × 94.7 $Å^3$ containing almost 72,000 atoms, around 9700 of them coming from the protein, was obtained. Bonds between substrate's epoxide and WAT1′s H and substrate's epoxide and H of TYR383 were manually added by adding bond force constants of 25 kcal/mol·$Å^2$ in order to describe the detected H-bonds between these atoms.

MD calculations were performed in GPUs using the PMEMD module [57,58] in its CUDA version from the AMBER18 package.

Three initial MM minimisations were performed, combining the steepest descent method and the conjugate gradient method for 5000 steps each. In the first one, the protein, cofactors and substrate were kept frozen by applying a restraint of 150.0 kcal/mol·$Å^2$. In the second one, only the backbone was restrained, while in the third minimisation, all the system was set free to move. A cut-off of 9 Å was applied in the three minimisations. Then, the system was heated from 0 to 300 K in steps of 30 K for 200 ps. SHAKE algorithm [59] was deactivated for the H of WAT and of TYR383, which are bonded to the epoxide. A restraint of 5 kcal/mol·$Å^2$ was applied to the backbone, and a cut-off of 9 Å was used.

Once heated, an NPT step of 5 ns was performed at 1 bar and at 300 K with a restraint of 5 kcal/mol·$Å^2$ applied to the backbone, a cut-off of 9 Å and with the SHAKE algorithm deactivated for the hydrogens bonded to the substrate's epoxide. A density of 1.0025 g/mL was achieved, and so the system was equilibrated. The temperature was controlled by Langevin dynamics [60] while the pressure was adjusted by the Berendsen barostat [61].

Finally, an NVT equilibration step was performed before the NVT production step. Both share the same configuration: 300 K, no restraints and no SHAKE algorithm for hydrogens bonded to substrate's epoxide. A total of 10 ns of equilibration were calculated followed by 150 ns of production, from which the last 100 ns have been selected for further analysis.

4. Conclusions

LTB_4 is a very potent lipid inflammatory mediator involved in acute and chronic inflammatory diseases. The chirality of the 12*R*-hydroxyl group and the 6*Z*,8*E*,10*E* configuration of the conjugated triene moiety are key features for its bioactivity. LTB_4 is obtained when LTA_4 is hydrolysed by the enzyme LTA_4H. In this paper, our Molecular Dynamics simulations and Quantum Mechanics/Molecular Mechanics calculations allowed us to theoretically capture LTA_4H in action, revealing the molecular details of the complete step-by-step mechanism of that enzyme reaction, in good agreement with the available experimental results.

The first step of the reaction consists of the opening of the epoxide of LTA_4. In a second, well-separated step, a water molecule is added to C_{12} of LTA_4, while one of its hydrogen atoms is fully transferred to ASP375. The set of these two orthogonal steps constitutes a rather unusual 1,7-nucleophilic substitution through a clear S_N1 mechanism.

In LTA_4, the bond C_6-C_7 has a configuration rather similar to pro-*cis*, although intermediate between the pro-*cis* and the pro-*trans* ones. As a result of the epoxide opening, the bond C_6-C_7 evolves either to a *cis* (*Z*) or to a *trans* (*E*) configuration. The triene moiety must twist to allow the bond C_6-C_7 to adopt its *cis* (*Z*) or *trans* (*E*) configuration, in such a way that it exposes the *R* face of C_{12} (by the side opposite to the Zn atom) or the *S* face of C_{12} (by the same side as the Zn atom), respectively, to the water addition. Only the *cis* (*Z*) configuration will lead to LTB_4 (5*S*,12*R*-dihydroxy-6*Z*,8*E*,10*E*,14*Z*-eicosatetraenoic acid),

whereas the *trans* (*E*) configuration would eventually form its stereoisomer 12*S*-6-*trans*-LTB_4 (5*S*,12*S*-dihydroxy-6*E*,8*E*,10*E*,14*Z*-eicosatetraenoic acid). Thus, the two main stereochemical features that are required for the bioactivity of LTB_4 appear to be closely linked.

In the gas phase, 12*S*-6-*trans*-LTB_4 is more stable than LTB_4. Inside LTA_4H, the epoxide opening (first step) to give the *trans* (*E*) configuration of the bond C_6-C_7 turns out to be more favourable than the opening to the *cis* (*Z*) configuration, both kinetically and thermodynamically. However, from here on, the *cis* energy profile becomes clearly below the *trans* energy profile. This can be explained through noncovalent π-π stacking interactions between the triene moiety and TYR267 and, especially, between the triene moiety and TYR378. Both tyrosines wrap the triene system along the whole reaction.

Finally, in the third step, the final transfer of a proton from a water molecule to the oxygen atom bonded to C_6 (the former oxygen atom of the epoxide) takes place, thus forming LTB_4. This proton transfer does not occur in the first step of the reaction to trigger an S_N1 acid-induced opening of the epoxide ring

This is an excellent example of how the role of an enzyme is not only to accelerate the reaction rate, but to govern the stereochemistry of the product, making it possible for the bioactive product (LTB_4 in this case) to be formed.

Supplementary Materials: The following supporting information can be downloaded at: https://www.mdpi.com/article/10.3390/ijms23063140/s1.

Author Contributions: Conceptualization, À.G.-L. and J.M.L.; investigation, M.C.-N.; writing—original draft preparation, M.C.-N., À.G.-L. and J.M.L.; writing—review and editing, À.G.-L. and J.M.L.; funding acquisition, À.G.-L. and J.M.L. All authors have read and agreed to the published version of the manuscript.

Funding: This study was supported by a grant (PID2020-113764GB-I00) from the Spanish "Ministerio de Ciencia e Innovación". We also acknowledge CSUC for computational facilities.

Data Availability Statement: The data presented in this study are contained within the article.

Conflicts of Interest: The authors declare no conflict of interest.

References

1. Furman, D.; Campisi, J.; Verdin, E.; Carrera-Bastos, P.; Targ, S.; Franceschi, C.; Ferrucci, L.; Gilroy, D.W.; Fasano, A.; Miller, G.W.; et al. Chronic Inflammation in the Etiology of Disease across the Life Span. *Nat. Med.* **2019**, *25*, 1822–1832. [CrossRef] [PubMed]
2. Serhan, C.N.; Chiang, N.; van Dyke, T.E. Resolving Inflammation: Dual Anti-Inflammatory and pro-Resolution Lipid Mediators. *Nat. Rev. Immunol.* **2008**, *8*, 349–361. [CrossRef] [PubMed]
3. Ayoub, S.S. *Fundamentals of Inflammation*; Serhan, C.N., Ward, P.A., Gilroy, D.W., Eds.; Cambridge University Press: Cambridge, UK, 2010; ISBN 9781139195737.
4. Buckley, C.D.; Gilroy, D.W.; Serhan, C.N. Proresolving Lipid Mediators and Mechanisms in the Resolution of Acute Inflammation. *Immunity* **2014**, *40*, 315–327. [CrossRef]
5. Serhan, C.N. Discovery of Specialized Pro-Resolving Mediators Marks the Dawn of Resolution Physiology and Pharmacology. *Mol. Asp. Med.* **2017**, *58*, 1–11. [CrossRef] [PubMed]
6. Dalli, J. Does Promoting Resolution Instead of Inhibiting Inflammation Represent the New Paradigm in Treating Infections? *Mol. Asp. Med.* **2017**, *58*, 12–20. [CrossRef]
7. Serhan, C.N. Treating Inflammation and Infection in the 21st Century: New Hints from Decoding Resolution Mediators and Mechanisms. *FASEB J.* **2017**, *31*, 1273–1288. [CrossRef] [PubMed]
8. Wan, M.; Tang, X.; Stsiapanava, A.; Haeggström, J.Z. Biosynthesis of Leukotriene B4. *Semin. Immunol.* **2017**, *33*, 3–15. [CrossRef] [PubMed]
9. Mancini, J.A.; Abramovitz, M.; Cox, M.E.; Wong, E.; Charleson, S.; Perrier, H.; Wang, Z.; Prasit, P.; Vickers, P.J. 5-Lipoxygenase-Activating Protein Is an Arachidonate Binding Protein. *FEBS Lett.* **1993**, *318*, 277–281. [CrossRef]
10. Peters-Golden, M.; Brock, T.G. 5-Lipoxygenase and FLAP. *Prostaglandins Leukot. Essent. Fat. Acids* **2003**, *69*, 99–109. [CrossRef]
11. Evans, J.F.; Ferguson, A.D.; Mosley, R.T.; Hutchinson, J.H. What's All the FLAP about?: 5-Lipoxygenase-Activating Protein Inhibitors for Inflammatory Diseases. *Trends Pharmacol. Sci.* **2008**, *29*, 72–78. [CrossRef]
12. Gerstmeier, J.; Weinigel, C.; Rummler, S.; Rådmark, O.; Werz, O.; Garscha, U. Time-resolved in Situ Assembly of the Leukotriene-synthetic 5-lipoxygenase/5-lipoxygenase-activating Protein Complex in Blood Leukocytes. *FASEB J.* **2016**, *30*, 276–285. [CrossRef]
13. Abramovitz, M.; Wong, E.; Cox, M.E.; Richardson, C.D.; Li, C.; Vickers, P.J. 5-Lipoxygenase-Activating Protein Stimulates the Utilization of Arachidonic Acid by 5-Lipoxygenase. *Eur. J. Biochem.* **1993**, *215*, 105–111. [CrossRef]

14. Basavarajappa, D.; Wan, M.; Lukic, A.; Steinhilber, D.; Samuelsson, B.; Radmark, O. Roles of Coactosin-like Protein (CLP) and 5-Lipoxygenase-Activating Protein (FLAP) in Cellular Leukotriene Biosynthesis. *Proc. Natl. Acad. Sci. USA* **2014**, *111*, 11371–11376. [CrossRef]
15. Rudberg, P.C.; Tholander, F.; Thunnissen, M.M.G.M.; Samuelsson, B.; Haeggstrom, J.Z. Leukotriene A4 Hydrolase: Selective Abrogation of Leukotriene B4 Formation by Mutation of Aspartic Acid 375. *Proc. Natl. Acad. Sci. USA* **2002**, *99*, 4215–4220. [CrossRef]
16. Thunnissen, M.M.G.M.; Nordlund, P.; Haeggström, J.Z. Crystal Structure of Human Leukotriene A4 Hydrolase, a Bifunctional Enzyme in Inflammation. *Nat. Struct. Biol.* **2001**, *8*, 131–135. [CrossRef]
17. Rinaldo-Matthis, A.; Haeggström, J.Z. Leukotriene A4 Hydrolase and Leukotriene C4 Synthase. In *Lipoxygenases in Inflammation*; Springer: Frankfurt, Germany, 2016; pp. 31–46. [CrossRef]
18. Stsiapanava, A.; Samuelsson, B.; Haeggström, J.Z. Capturing LTA4 Hydrolase in Action: Insights to the Chemistry and Dynamics of Chemotactic LTB4 Synthesis. *Proc. Natl. Acad. Sci. USA* **2017**, *114*, 9689–9694. [CrossRef]
19. Rudberg, P.C.; Tholander, F.; Thunnissen, M.M.G.M.; Haeggström, J.Z. Leukotriene A4 Hydrolase/Aminopeptidase: Glutamate 271 is a catalytic residue with specific roles in two distinct enzyme mechanisms. *J. Biol. Chem.* **2002**, *277*, 1398–1404. [CrossRef]
20. Rudberg, P.C.; Tholander, F.; Andberg, M.; Thunnissen, M.M.G.M.; Haeggström, J.Z. Leukotriene A4 Hydrolase: Identification of a common carboxylate recognition site for the epoxide hydrolase and aminopeptidase substrates. *J. Biol. Chem.* **2004**, *279*, 27376–27382. [CrossRef]
21. Mueller, M.J.; Blomster, M.; Oppermann, U.C.; Jornvall, H.; Samuelsson, B.; Haeggstrom, J.Z. Leukotriene A4 Hydrolase: Protection from Mechanism-Based Inactivation by Mutation of Tyrosine-378. *Proc. Natl. Acad. Sci. USA* **1996**, *93*, 5931–5935. [CrossRef]
22. Mueller, M.J.; Blomster Andberg, M.; Samuelsson, B.; Haeggstrom, J.Z. Leukotriene A4 Hydrolase Mutation of Tyrosine 378 Allows Conversion of Leukotriene A4 into an Isomer of Leukotriene B4. *J. Biol. Chem.* **1996**, *271*, 24345–24348. [CrossRef]
23. Mu, X.; Xu, D. QM/MM Molecular Dynamics Investigations of the Substrate Binding of Leucotriene A4 Hydrolase: Implication for the Catalytic Mechanism. *J. Phys. Chem. B* **2018**, *122*, 7253–7263. [CrossRef]
24. Elstner, M.; Porezag, D.; Jungnickel, G.; Elsner, J.; Haugk, M.; Frauenheim, T.; Suhai, S.; Seifert, G. Self-Consistent-Charge Density-Functional Tight-Binding Method for Simulations of Complex Materials Properties. *Phys. Rev. B* **1998**, *58*, 7260–7268. [CrossRef]
25. Elstner, M.; Frauenheim, T.; Kaxiras, E.; Seifert, G.; Suhai, S. A Self-Consistent Charge Density-Functional Based Tight-Binding Scheme for Large Biomolecules. *Phys. Status Solidi* **2000**, *217*, 357–376. [CrossRef]
26. Elstner, M. The SCC-DFTB Method and Its Application to Biological Systems. *Theor. Chim. Acta* **2006**, *116*, 316–325. [CrossRef]
27. Cui, Q.; Elstner, M.; Kaxiras, E.; Frauenheim, T.; Karplus, M. A QM/MM Implementation of the Self-Consistent Charge Density Functional Tight Binding (SCC-DFTB) Method. *J. Phys. Chem. B* **2001**, *105*, 569–585. [CrossRef]
28. Pettersen, E.F.; Goddard, T.D.; Huang, C.C.; Couch, G.S.; Greenblatt, D.M.; Meng, E.C.; Ferrin, T.E. UCSF Chimera? A Visualization System for Exploratory Research and Analysis. *J. Comput. Chem.* **2004**, *25*, 1605–1612. [CrossRef] [PubMed]
29. Dijkstra, E.W. Invariance and Non-Determinacy. *Numer. Math.* **1959**, *1*, 269–271. [CrossRef]
30. Olsson, M.H.M.; Søndergaard, C.R.; Rostkowski, M.; Jensen, J.H. PROPKA3: Consistent Treatment of Internal and Surface Residues in Empirical pK_a Predictions. *J. Chem. Theory Comput.* **2011**, *7*, 525–537. [CrossRef]
31. Jorgensen, W.L.; Chandrasekhar, J.; Madura, J.D.; Impey, R.W.; Klein, M.L. Comparison of Simple Potential Functions for Simulating Liquid Water. *J. Chem. Phys.* **1983**, *79*, 926–935. [CrossRef]
32. Sherwood, P.; de Vries, A.H.; Guest, M.F.; Schreckenbach, G.; Catlow, C.R.A.; French, S.A.; Sokol, A.A.; Bromley, S.T.; Thiel, W.; Turner, A.J.; et al. QUASI: A General Purpose Implementation of the QM/MM Approach and Its Application to Problems in Catalysis. *J. Mol. Struct. THEOCHEM* **2003**, *632*, 1–28. [CrossRef]
33. Metz, S.; Kästner, J.; Sokol, A.A.; Keal, T.W.; Sherwood, P. ChemShell—A Modular Software Package for QM/MM Simulations. *WIREs Comput. Mol. Sci.* **2014**, *4*, 101–110. [CrossRef]
34. Ahlrichs, R.; Bär, M.; Häser, M.; Horn, H.; Kölmel, C. Electronic Structure Calculations on Workstation Computers: The Program System Turbomole. *Chem. Phys. Lett.* **1989**, *162*, 165–169. [CrossRef]
35. Case, D.A.; Ben-Shalom, I.Y.; Brozell, S.R.; Cerutti, D.S.; Cheatham, T.E., III; Cruzeiro, V.W.D.; Darden, T.A.; Duke, R.E.; Ghoreishi, D.; Gilson, M.K.; et al. *Amber 18*; University of California: San Francisco, CA, USA, 2018.
36. Smith, W.; Forester, T.R. DL_POLY_2.0: A General-Purpose Parallel Molecular Dynamics Simulation Package. *J. Mol. Graph.* **1996**, *14*, 136–141. [CrossRef]
37. Maier, J.A.; Martinez, C.; Kasavajhala, K.; Wickstrom, L.; Hauser, K.E.; Simmerling, C. Ff14SB: Improving the Accuracy of Protein Side Chain and Backbone Parameters from Ff99SB. *J. Chem. Theory Comput.* **2015**, *11*, 3696–3713. [CrossRef]
38. Wang, J.; Wolf, R.M.; Caldwell, J.W.; Kollman, P.A.; Case, D.A. Development and Testing of a General Amber Force Field. *J. Comput. Chem.* **2004**, *25*, 1157–1174. [CrossRef]
39. Bayly, C.I.; Cieplak, P.; Cornell, W.D.; Kollman, P.A. A Well-Behaved Electrostatic Potential Based Method Using Charge Restraints for Deriving Atomic Charges: The RESP Model. *J. Phys. Chem.* **1993**, *97*, 10269–10280. [CrossRef]
40. Frisch, M.J.; Trucks, G.W.; Schlegel, H.B.; Scuseria, G.E.; Robb, M.A.; Cheeseman, J.R.; Scalmani, G.; Barone, V.; Petersson, G.A.; Nakatsuji, H.; et al. *Gaussian09*; Gaussian, Inc.: Wallingford, CT, USA, 2009.

41. Bakowies, D.; Thiel, W. Hybrid Models for Combined Quantum Mechanical and Molecular Mechanical Approaches. *J. Phys. Chem.* **1996**, *100*, 10580–10594. [CrossRef]
42. Senn, H.M.; Thiel, W. QM/MM Methods for Biomolecular Systems. *Angew. Chem. Int. Ed.* **2009**, *48*, 1198–1229. [CrossRef]
43. De Vries, A.H.; Sherwood, P.; Collins, S.J.; Rigby, A.M.; Rigutto, M.; Kramer, G.J. Zeolite Structure and Reactivity by Combined Quantum-Chemical−Classical Calculations. *J. Phys. Chem. B* **1999**, *103*, 6133–6141. [CrossRef]
44. Kästner, J.; Thiel, S.; Senn, H.M.; Sherwood, P.; Thiel, W. Exploiting QM/MM Capabilities in Geometry Optimization: A Microiterative Approach Using Electrostatic Embedding. *J. Chem. Theory Comput.* **2007**, *3*, 1064–1072. [CrossRef]
45. Billeter, S.R.; Turner, A.J.; Thiel, W. Linear Scaling Geometry Optimisation and Transition State Search in Hybrid Delocalised Internal Coordinates. *Phys. Chem. Chem. Phys.* **2000**, *2*, 2177–2186. [CrossRef]
46. Liu, D.C.; Nocedal, J. On the Limited Memory BFGS Method for Large Scale Optimization. *Math. Program.* **1989**, *45*, 503–528. [CrossRef]
47. Nocedal, J. Updating Quasi-Newton Matrices with Limited Storage. *Math. Comput.* **1980**, *35*, 773–782. [CrossRef]
48. Baker, J. An Algorithm for the Location of Transition States. *J. Comput. Chem.* **1986**, *7*, 385–395. [CrossRef]
49. Banerjee, A.; Adams, N.; Simons, J.; Shepard, R. Search for Stationary Points on Surfaces. *J. Phys. Chem.* **1985**, *89*, 52–57. [CrossRef]
50. Kästner, J.; Carr, J.M.; Keal, T.W.; Thiel, W.; Wander, A.; Sherwood, P. DL-FIND: An Open-Source Geometry Optimizer for Atomistic Simulations. *J. Phys. Chem. A* **2009**, *113*, 11856–11865. [CrossRef] [PubMed]
51. Becke, A.D. Density-functional Thermochemistry. III. The Role of Exact Exchange. *J. Chem. Phys.* **1993**, *98*, 5648–5652. [CrossRef]
52. Hariharan, P.C.; Pople, J.A. The Influence of Polarization Functions on Molecular Orbital Hydrogenation Energies. *Theor. Chim. Acta* **1973**, *28*, 213–222. [CrossRef]
53. Schautz, F.; Flad, H.-J.; Dolg, M. Quantum Monte Carlo Study of Be 2 and Group 12 Dimers M 2 (M = Zn, Cd, Hg). *Theor. Chim. Acta* **1998**, *99*, 231–240. [CrossRef]
54. Case, D.A.; Ben-Shalom, I.Y.; Brozell, S.R.; Cerutti, D.S.; Cheatham, T.E., III; Cruzeiro, V.W.D.; Darden, T.A.; Duke, R.E.; Ghoreishi, D.; Giambasu, G.; et al. *Amber19*; University of California: San Francisco, CA, USA, 2019.
55. Seminario, J.M. Calculation of Intramolecular Force Fields from Second-Derivative Tensors. *Int. J. Quantum Chem.* **1996**, *60*, 1271–1277. [CrossRef]
56. Li, P.; Merz, K.M. MCPB.Py: A Python Based Metal Center Parameter Builder. *J. Chem. Inf. Model.* **2016**, *56*, 599–604. [CrossRef] [PubMed]
57. Le Grand, S.; Götz, A.W.; Walker, R.C. SPFP: Speed without Compromise—A Mixed Precision Model for GPU Accelerated Molecular Dynamics Simulations. *Comput. Phys. Commun.* **2013**, *184*, 374–380. [CrossRef]
58. Götz, A.W.; Williamson, M.J.; Xu, D.; Poole, D.; le Grand, S.; Walker, R.C. Routine Microsecond Molecular Dynamics Simulations with AMBER on GPUs. 1. Generalized Born. *J. Chem. Theory Comput.* **2012**, *8*, 1542–1555. [CrossRef] [PubMed]
59. Ryckaert, J.P.; Ciccotti, G.; Berendsen, H.J.C. Numerical Integration of the Cartesian Equations of Motion of a System with Constraints: Molecular Dynamics of n-Alkanes. *J. Comput. Phys.* **1977**, *23*, 327–341. [CrossRef]
60. Leach, A.R. *Molecular Modelling: Principles and Applications*; Pearson Education: London, UK, 2001.
61. Berendsen, H.J.C.; Postma, J.P.M.; van Gunsteren, W.F.; Dinola, A.; Haak, J.R. Molecular Dynamics with Coupling to an External Bath. *J. Chem. Phys.* **1984**, *81*, 3684–3690. [CrossRef]

SI9.2 Supporting information

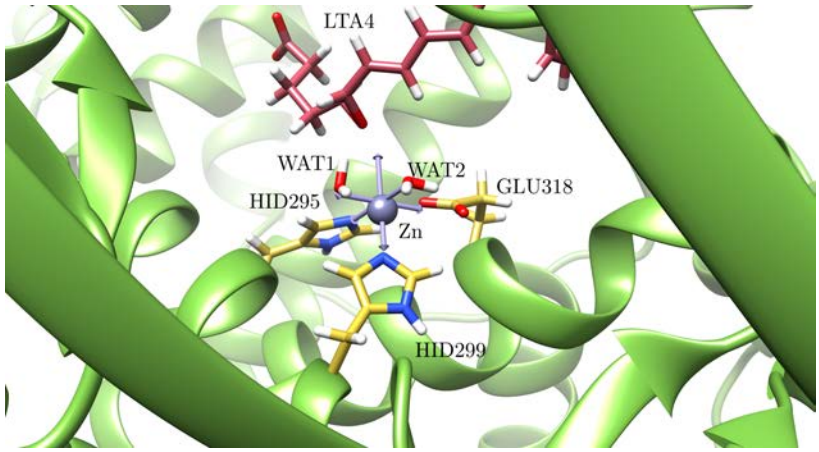

Figure SI9.1: Zn environment with drawing of the ideal octahedral coordination geometry

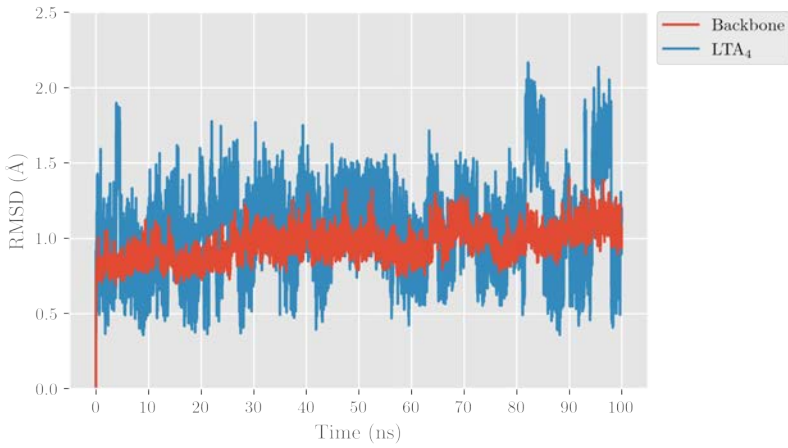

Figure SI9.2: RMSD of backbone and LTA_4 along the MD simulation

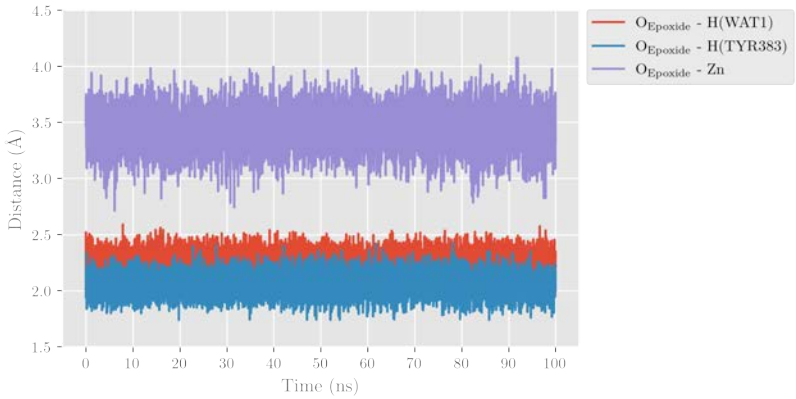

Figure SI9.3: Evolution of distances from LTA_4's epoxide to Zn, Tyr383 and Wat1

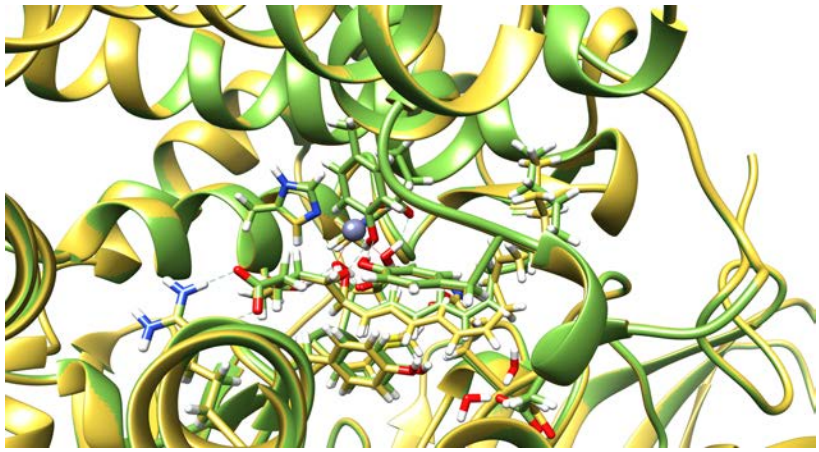

Figure SI9.4: Structural comparison of the crystallographic structure and the reactant structure obtained from INT2

(a) *R*

(b) *TS1*-E

(c) *INT1*-E

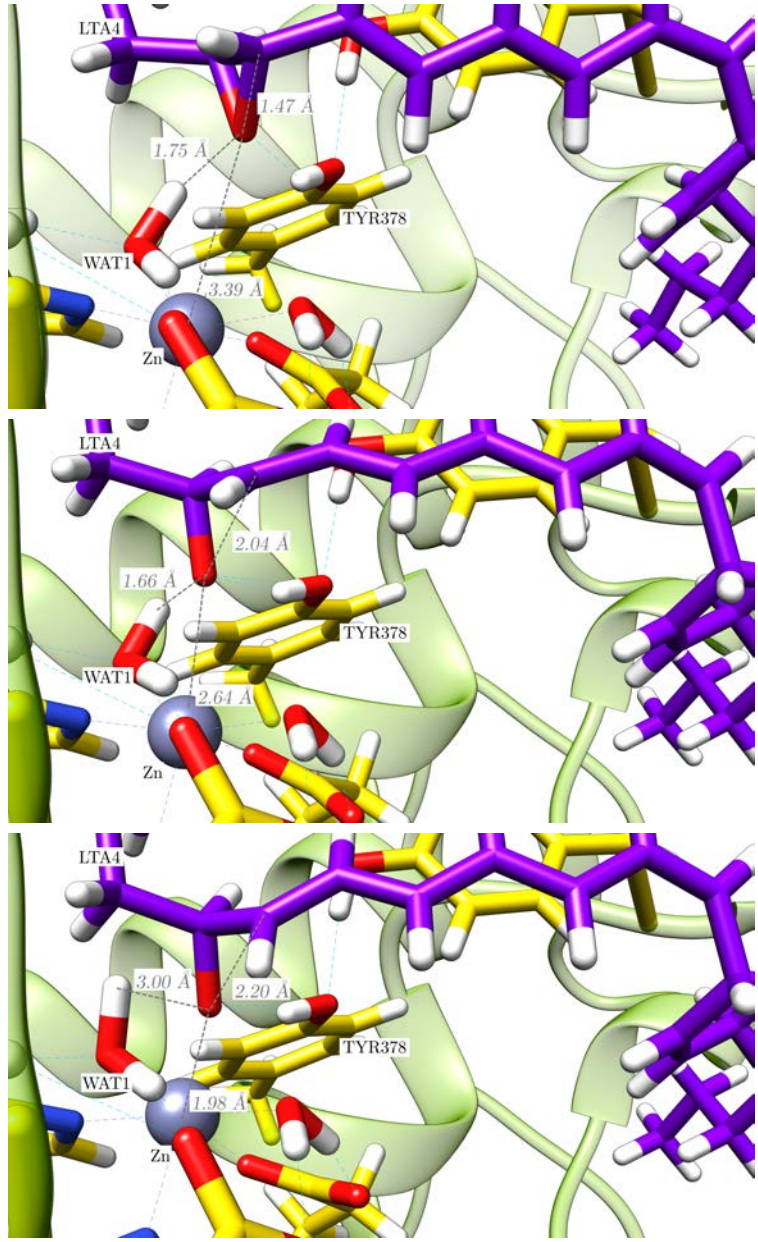

Figure SI9.5: Closer view of stationary structures along Epoxide Ring Opening reaction for* E *path. *Most relevant distances are labelled in grey.*

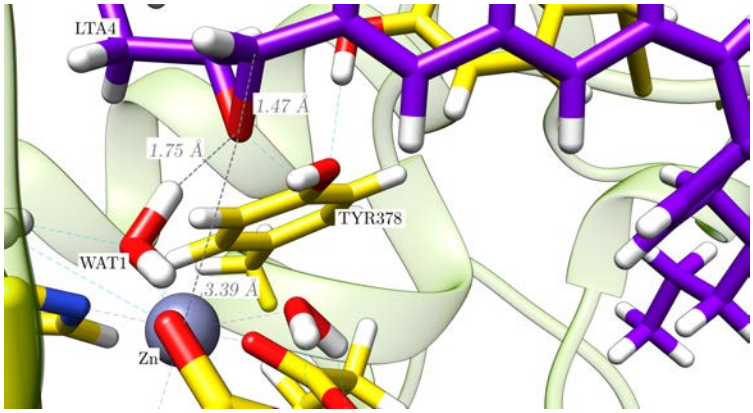

(a) R

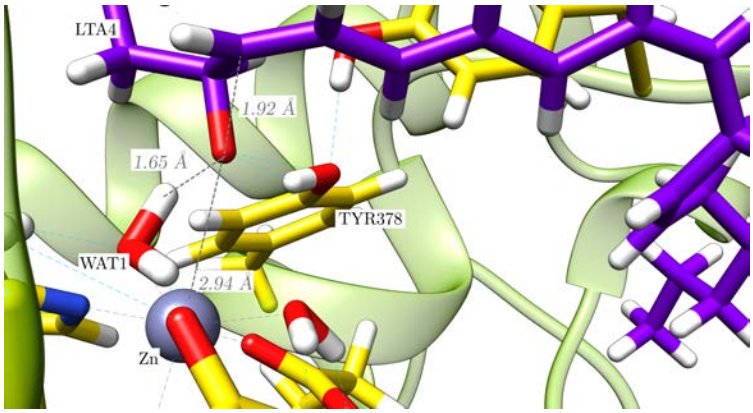

(b) TS1-Z

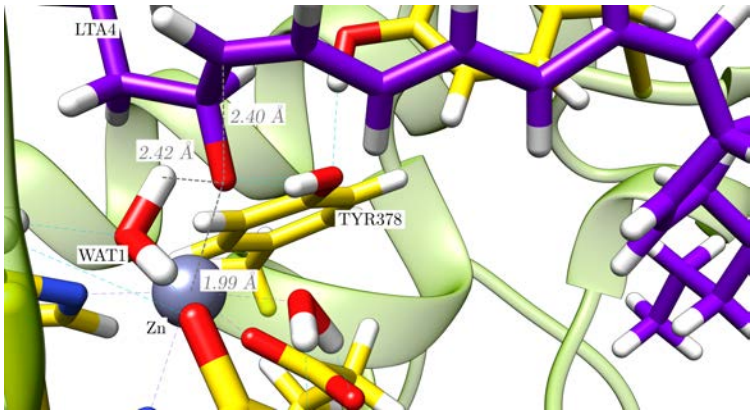

(c) INT1-Z

Figure SI9.6: Closer view of stationary structures along Epoxide Ring Opening reaction for Z path. *Most relevant distances are labelled in grey.*

(a) *INT1*-E

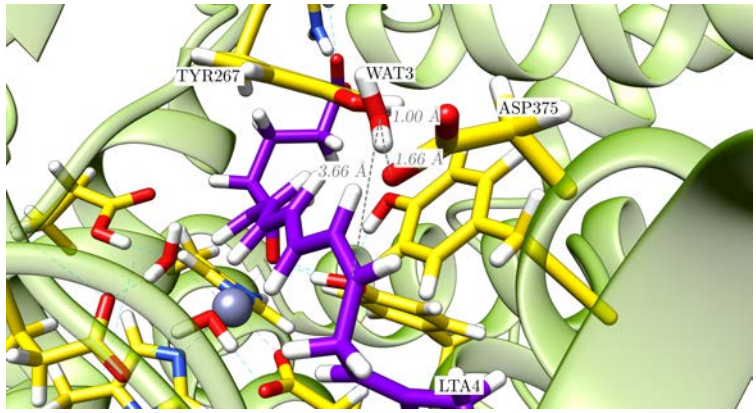

(b) *TS2*-E

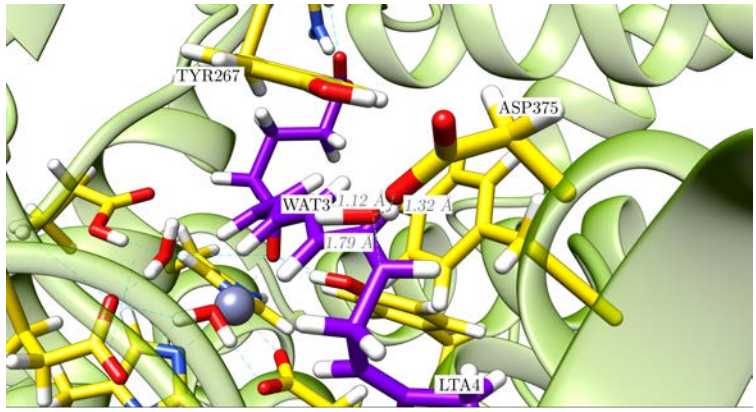

(c) *INT2*-E

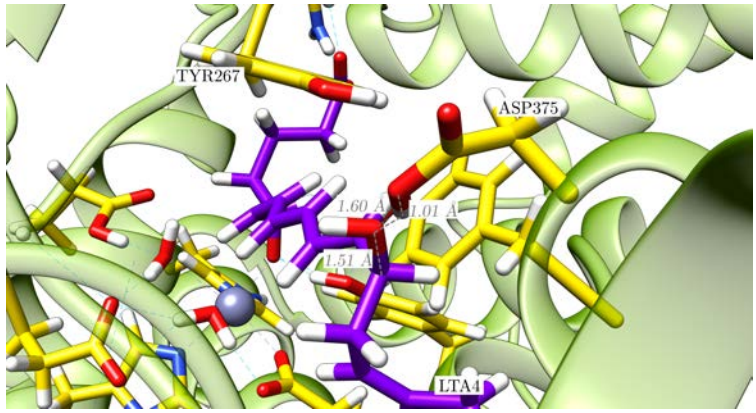

Figure SI9.7: Closer view of stationary structures along Water Addition reaction for* E *path. *Most relevant distances are labelled in grey.*

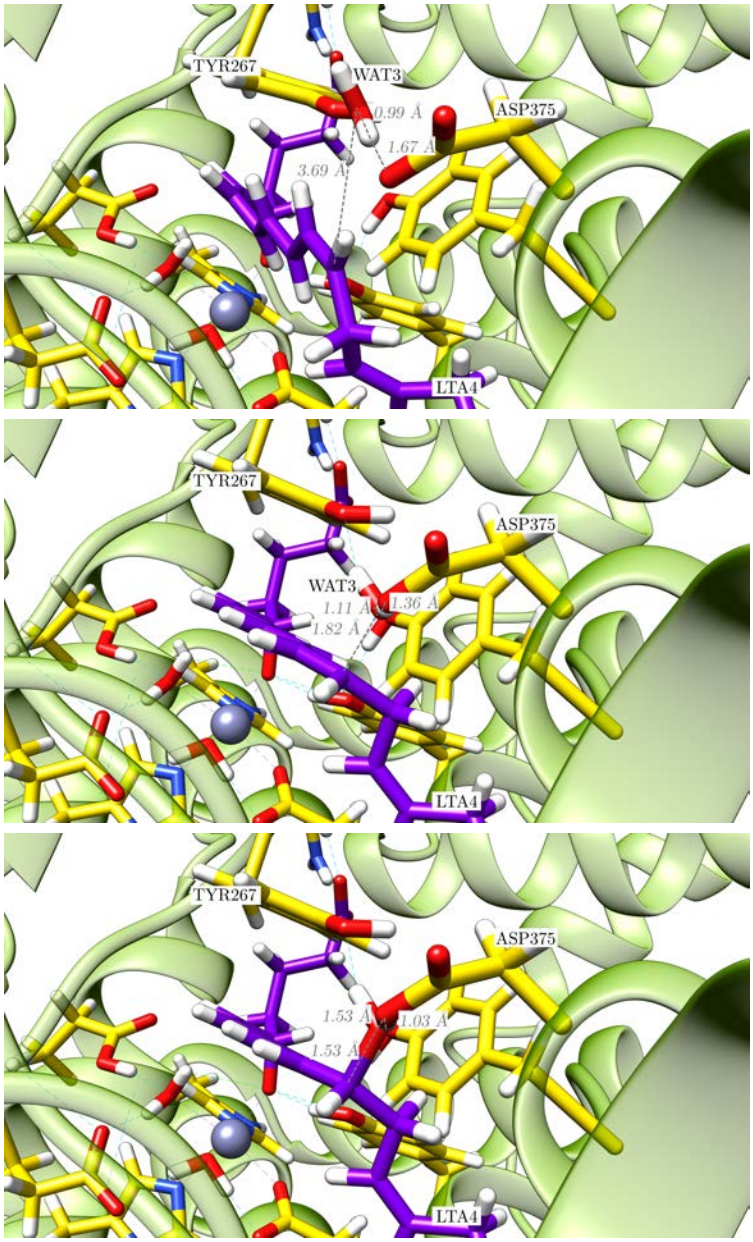

(a) INT1-Z

(b) TS2-Z

(c) INT2-Z

Figure SI9.8: Closer view of stationary structures along Water Addition reaction for Z path. *Most relevant distances are labelled in grey.*

(a) *INT2*-E

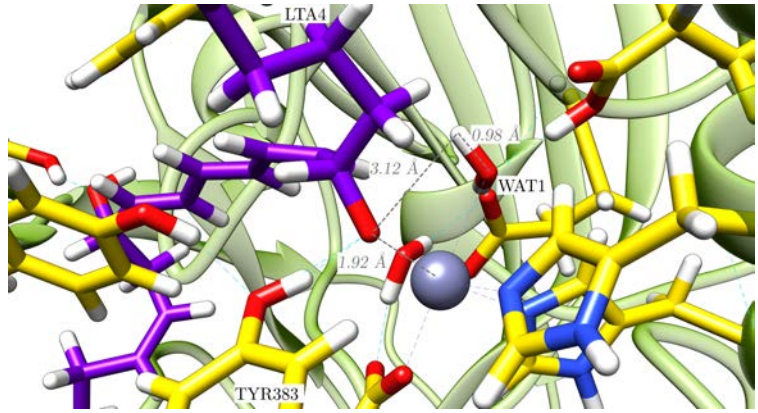

(b) *TS3*-E

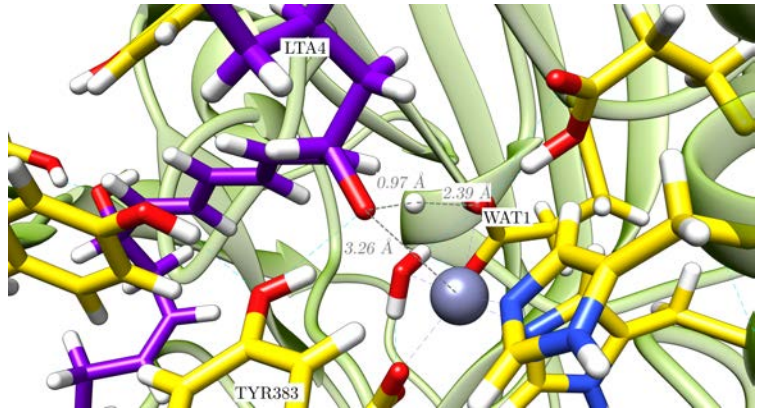

(c) *P*-E

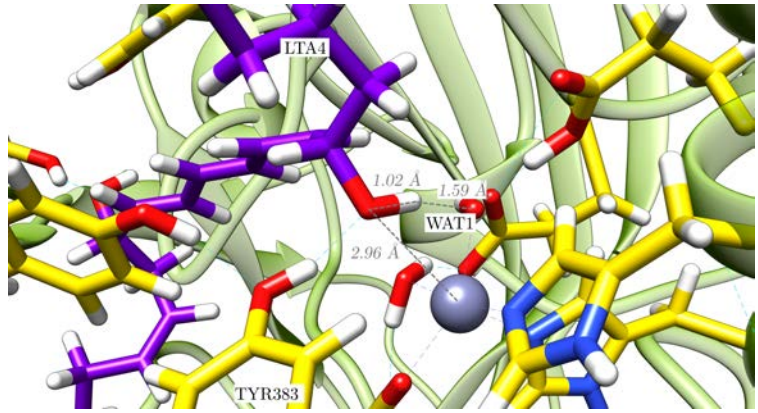

Figure SI9.9: Closer view of stationary structures along Protonation reaction for* E *path. *Most relevant distances are labelled in grey.*

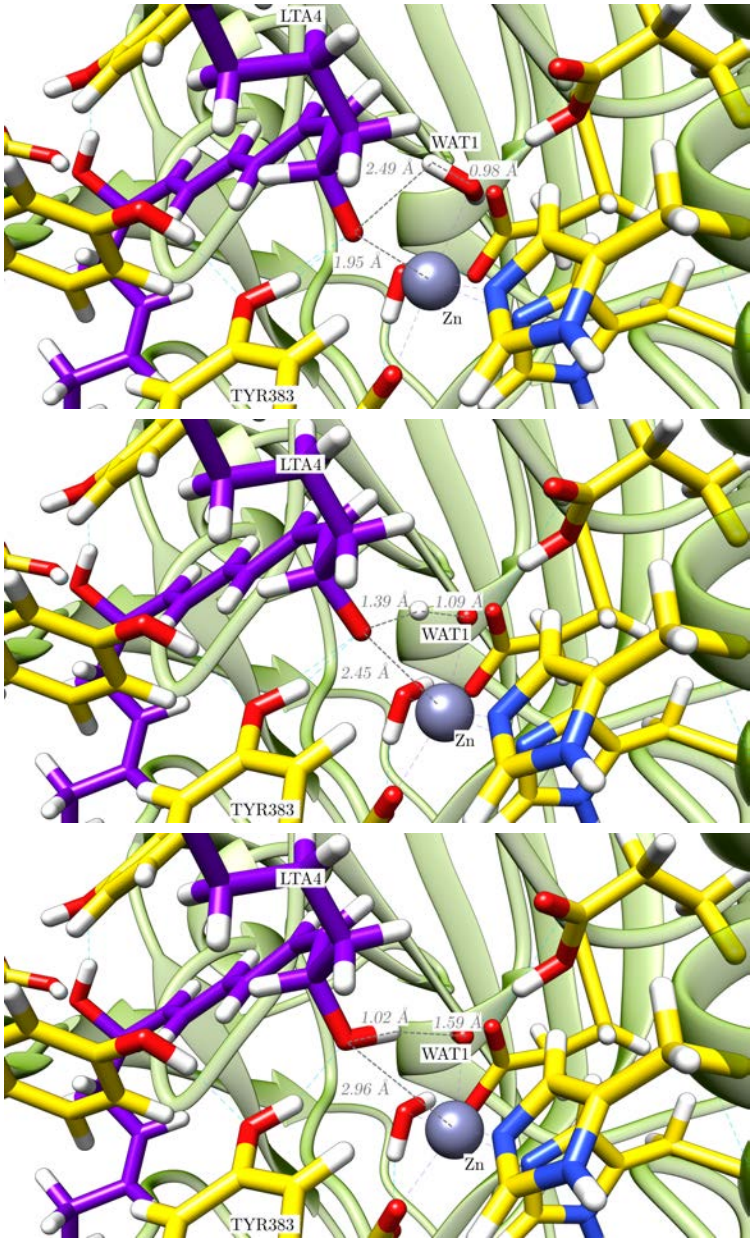

(a) INT2-Z

(b) TS3-Z

(c) P-Z

Figure SI9.10: Closer view of stationary structures along Protonation reaction for Z path. *Most relevant distances are labelled in grey.*

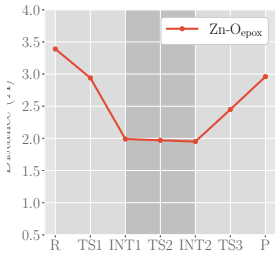

(a) Zn–O

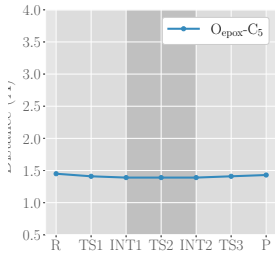

(b) $O_{epoxide}$–C_5

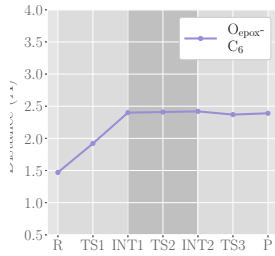

(c) $O_{epoxide}$–C_6

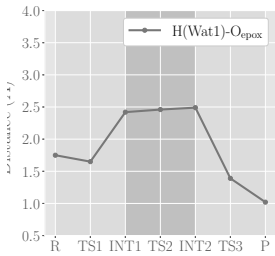

(d) H(Wat1)–$O_{epoxide}$

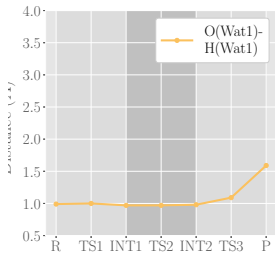

(e) O(Wat1)–H(Wat1)

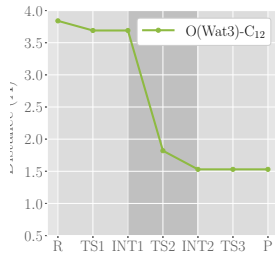

(f) O(Wat3)–C_{12}

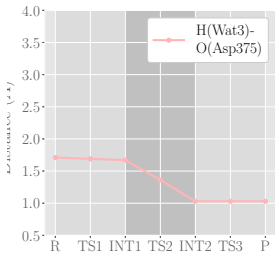

(g) H(Wat3)–O(Asp375)

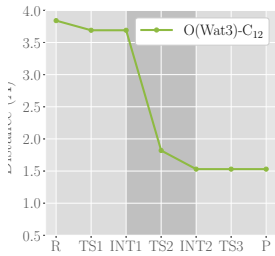

(h) O(Wat3)–H(Wat3)

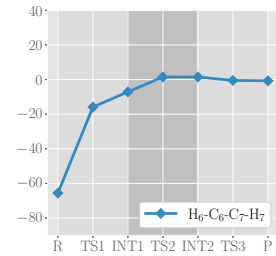

(i) H_6–C_6-C_7-H_7

Figure SI9.11: Evolution of most relevant distances along Z path from LTA_4 to LTB_4. *Different grey areas indicate different steps along the mechanism.*

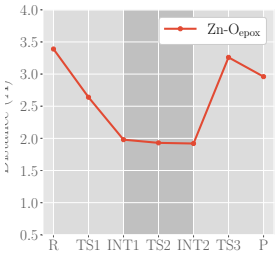

(a) Zn–O

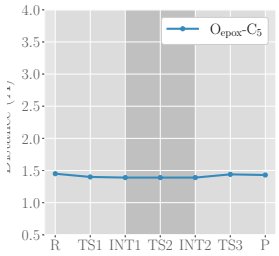

(b) $O_{epoxide}$–C_5

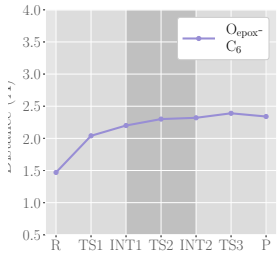

(c) $O_{epoxide}$–C_6

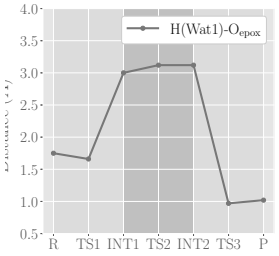

(d) H(Wat1)–$O_{epoxide}$

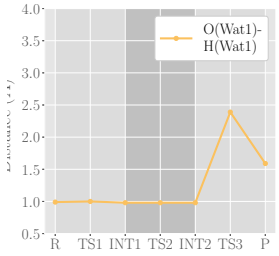

(e) O(Wat1)–H(Wat1)

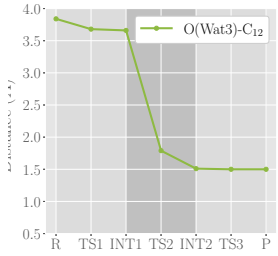

(f) O(Wat3)–C_{12}

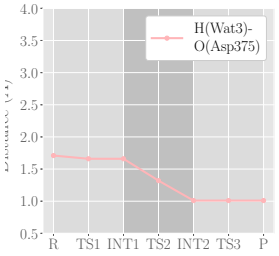

(g) H(Wat3)–O(Asp375)

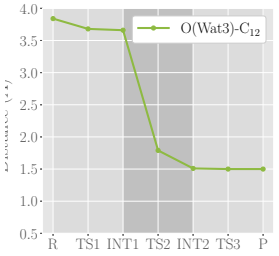

(h) O(Wat3)–H(Wat3)

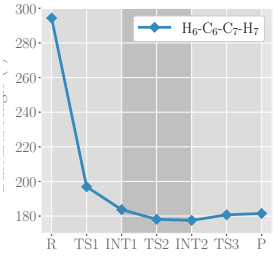

(i) H_6–C_6-C_7-H_7

Figure SI9.12: Evolution of most relevant distances along* E *path from LTA_4 to LTB_4. *Different grey areas indicate different steps along the mechanism.*

Chapter SI11

Conversion of Docosahexaenoic Acid by pig ALOX15/*pig*12LOX

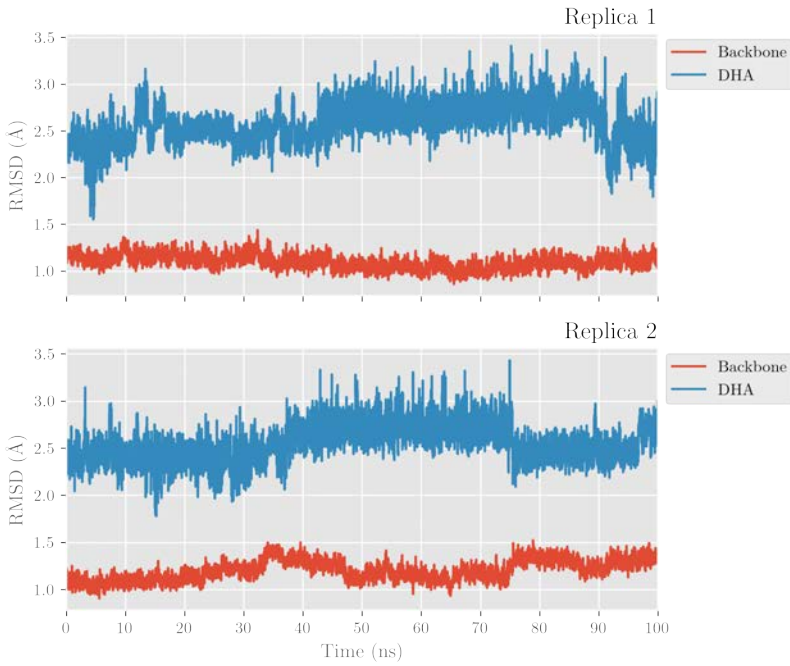

Figure SI11.1: RMSD of backbone and DHA along replicas 1 and 2 of MD simulation

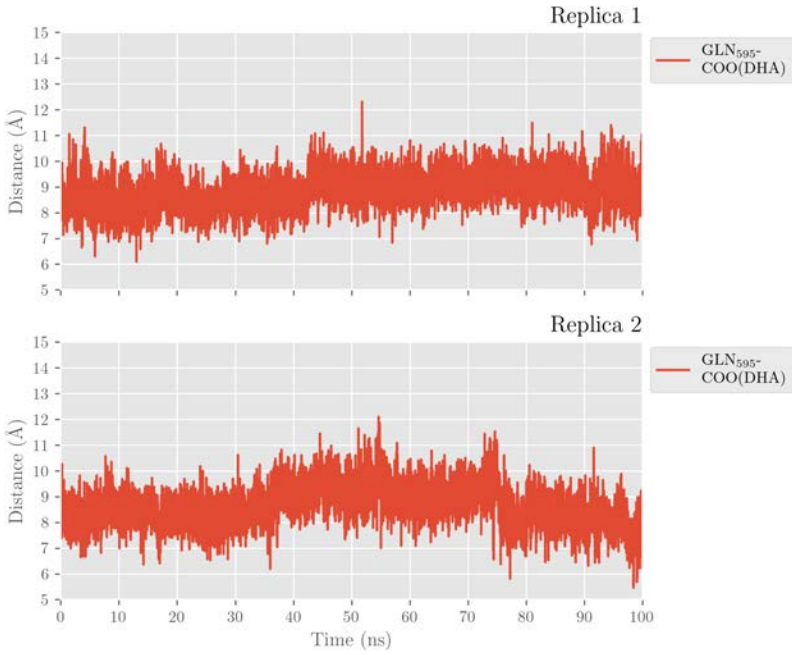

Figure SI11.2: GLN595-COO(DHA) distance along replicas 1 and 2 of MD simulation

Chapter SI12

Peroxidation: Formation of 14*S*-hydroperoxy-DHA from Docosahexaenoic Acid by human ALOX12

SI12.1 Publication

International Journal of
Molecular Sciences

MDPI

Article

Hydroperoxidation of Docosahexaenoic Acid by Human ALOX12 and pigALOX15-mini-LOX

Miquel Canyelles-Niño [1,2], Àngels González-Lafont [1,3,*] and José M. Lluch [1,3]

[1] Departament de Química, Universitat Autònoma de Barcelona, Bellaterra, 08193 Barcelona, Spain
[2] Arquebio SL, Carrer de Álava 51, 08005 Barcelona, Spain
[3] Institut de Biotecnologia i Biomedicina (IBB), Universitat Autònoma de Barcelona, Bellaterra, 08193 Barcelona, Spain
* Correspondence: angels.gonzalez@uab.cat

Abstract: *Human* lipoxygenase 12 (hALOX12) catalyzes the conversion of docosahexaenoic acid (DHA) into mainly 14S-hydroperoxy-4Z,7Z,10Z,12E,16Z,19Z-docosahexaenoic acid (14S-H(p)DHA). This hydroperoxidation reaction is followed by an epoxidation and hydrolysis process that finally leads to maresin 1 (MaR1), a potent bioactive specialized pro-resolving mediator (SPM) in chronic inflammation resolution. By combining docking, molecular dynamics simulations, and quantum mechanics/molecular mechanics calculations, we have computed the potential energy profile of DHA hydroperoxidation in the active site of hALOX12. Our results describe the structural evolution of the molecular system at each step of this catalytic reaction pathway. Noteworthy, the required stereospecificity of the reaction leading to MaR1 is explained by the configurations adopted by DHA bound to hALOX12, along with the stereochemistry of the pentadienyl radical formed after the first step of the mechanism. In *pig* lipoxygenase 15 (pigALOX15-mini-LOX), our calculations suggest that 14S-H(p)DHA can be formed, but with a stereochemistry that is inadequate for MaR1 biosynthesis.

Keywords: hydroperoxidation mechanism; human platelet ALOX12; enzyme catalysis; molecular dynamics simulations; QM/MM calculations

check for updates

Citation: Canyelles-Niño, M.; González-Lafont, À.; Lluch, J.M. Hydroperoxidation of Docosahexaenoic Acid by Human ALOX12 and pigALOX15-mini-LOX. *Int. J. Mol. Sci.* **2023**, *24*, 6064. https://doi.org/10.3390/ijms24076064

Academic Editor: Jan Korabecny

Received: 13 February 2023
Revised: 15 March 2023
Accepted: 17 March 2023
Published: 23 March 2023

1. Introduction

Mammalian lipoxygenases (LOXs) form a heterogeneous family of non-heme iron-containing enzymes that catalyze the dioxygenation of polyunsaturated fatty acids (PUFAs) with cis-methylene-interrupted double bonds. The peroxidation process is highly regio- and stereospecific, leading to the corresponding conjugated hydroperoxides [1]. Then, along the biological pathway, those hydroperoxy fatty acids formed by the different LOXs isoforms generate a wide variety of bioactive lipid mediators that are involved in a plethora of pro- and anti-inflammatory processes [1–3].

The first lipoxygenase discovered in animal tissues by Nobel Laureate Samuelsson and his colleague Hamberg was the *human* 12-lipoxygenase of blood platelets [4]. This enzyme was named 12S-LOX because it oxidizes arachidonic acid (AA) to generate almost exclusively one regio- and stereospecific isomer, the 12S-hydro(per)oxyeicosa-5,8,10,14-tetraenoic acid (12S-H(p)ETE) [5]. However, this nomenclature was confusing because the regio- and stereospecificity of LOX isoforms depend on the substrate and are species-specific [6,7]. Moreover, this nomenclature is not related to the biological function of LOX isoforms. For this reason, terminology based on the gene encoding each LOX isoform is more recommended. In humans, the platelet-type 12-LOX (12S-LOX) is encoded by the *ALOX12* gene and is named *human* ALOX12 (hALOX12) [7]. The hALOX12 peroxidation reaction is initiated by H-abstraction of the H_{10} atom of AA by the Fe(III)-OH^- cofactor. Next, an oxygen molecule inserts on C_{12} following an antarafacial approach and gives a hydroperoxide with S stereochemistry. Finally, the reduced product, 12S-HETE, is obtained by the action of glutathione peroxidase.

Human ALOX12 is the unique LOX isoform expressed in *human* platelets [4]. Nowadays this LOX has been found in platelets of several other mammals such as *bovine*, *mouse*, *rat*, *rabbit*, *sheep*, and *dog* [8–11] but is not expressed in *porcine* platelets [12]. Through hALOX12 oxidized metabolites, this enzyme regulates platelet activity in hemostasis and thrombosis, and controls platelet role in inflammatory processes. According to several studies with *human* patients, hALOX12 and its derived oxylipin 12S-HETE seem to present prothrombotic effects [13]. However, the prothrombotic role of 12S-HETE in vivo is not fully understood yet. There are contradictory experimental results with animal models in which 12S-HETE could either promote or inhibit or even not participate in platelet aggregation [14,15]. In this respect, the first selective hALOX12 inhibitor, ML355, has been shown to impair thrombus formation and vessel occlusion in vivo with minimal effects on hemostasis [16,17]. It has also been recognized that platelets are involved in the pathogenesis of several diseases, such as asthma, cancer, neurodegenerative disorders, gastrointestinal and hepatic inflammation, insulin resistance, and atherosclerosis, in which chronic inflammation plays an underlying role [7,18]. So, 12-HETE has been described as a pro-inflammatory molecule. However, it is not always clear whether the 12-HETE present in the inflamed tissue originated from platelets or from other cells because hALOX12 is also expressed in leucocytes, *human* islets, and epidermal keratinocytes [19]. On the other hand, hALOX12, in conjunction with other LOX isoforms, is involved in the transcellular biosynthesis of AA-derived anti-inflammatory agents such as lipoxins [20].

Human ALOX12 also catalyzes the oxygenation of the ω-3 fatty acid 4,7,10,13,16,19-docosahexaenoic acid (DHA). DHA can be converted by hALOX12 into two different products, depending on the experimental conditions. In this respect, there are different results in the literature concerning the regioselectivity of the DHA oxygenation reaction with hALOX12. According to Kühn and co-workers [21], the ω-9 hydroperoxide product 14-hydroperoxydocosahexaenoic acid (14-H(p)DHA) is dominant over DHA. Those experimental results did not show significant amounts of any other product with this enzyme. Thus, hALOX12 catalysis with DHA was classified as singular ω-9 oxygenase activity. Two years later, Holman and co-workers [22] published new kinetic results that confirmed 14-H(p)DHA as the main product of DHA peroxidation by hALOX12. However, the obtained percentage of 11-HDHA:14-HDHA (29:71) products (the reduced forms of 11-hydroperoxydocosahexaenoic acid (11-H(p)DHA) and 14-H(p)DHA, respectively) was higher than previously reported. According to the authors, those differences appear because they expressed hALOX12 in *insect* cells, whereas Kühn and co-workers used E. coli as the expression system [21]. In a following paper, Holman and co-workers report a smaller in vitro proportion of 11S-HDHA (19%) to 14S-HDHA (81%), and an even smaller ex vivo percentage (6:94) [23]. The DHA peroxidation mechanism is proposed to initiate with an H-abstraction reaction (described as a proton-coupled electron transfer, PCET [24,25]) of H_{12} or $H_{9,}$ in this case, by the Fe(III)-OH^- cofactor. Next, an oxygen molecule inserts on C_{14} or C_{11} of DHA, following an antarafacial approach, and gives the corresponding hydroperoxides with S stereochemistry, which are immediately reduced to 14-HDHA and 11-HDHA, respectively. Moreover, steady-state kinetic measurements of this catalytic mechanism of hALOX12 have demonstrated that the rates of substrate capture and product release are similar between DHA and AA [23,26].

The biological relevance of DHA-derived oxylipins, 11-HDHA and 14-HDHA, is currently a focus of interest. The cardiovascular benefits of a diet rich in ω-3 fatty acids such as DHA have been known for decades, but the mechanisms involved in their anti-aggregatory effects on platelets are still under study. Recent in vitro and ex vivo experiments [27] with *mice* and *human*-washed platelets have confirmed that DHA, as well as 11-HDHA and 14-HDHA, inhibit collagen-induced platelet aggregation. Interestingly, the in vivo thrombosis data in *mice* showed that only acute concentrations of 11-HDHA or 14-HDHA attenuated overall thrombus formation. This fact suggests that under physiological conditions (at similar basal ALOX12-derived oxylipin levels than those used in the assays mentioned), 11-HDHA and 14-HDHA may play a central role in the regulation of throm-

bus formation by activating Protein Kinase A (PKA). Nevertheless, the authors of the experimental study do not discard additional complex mechanisms driven by specialized pro-resolving mediators (SPMs), also derived from DHA, that could contribute to antithrombotic effects. Maresin 1 (7R,14S-dihydroxy-4Z,8E,10E,12Z,16Z,19Z- docosahexaenoic acid, MaR1) is an SPM derived from 14S-H(p)DHA that is subsequently converted to 13S,14S-epoxy-4Z,7Z,9E,11E,16Z,19Z-docosahexaenoic acid through an epoxidation mechanism. Then, this epoxide intermediate is proposed to be enzymatically hydrolyzed to form the stereochemistry of bioactive MaR1 [23,28]. MaR1 is a potent SPM that actively participates in the inflammation-resolution phase of many different diseases, and it has also been described as a novel antiplatelet agent crucial in the resolution of inflammation in cardiovascular injuries [29,30].

At the molecular level, the structural basis of hALOX12's product selectivity has been much less studied than in the case of *rabbit* and *human* ALOX15. Remarkably, some mutagenesis experiments back in 2010 already showed that the triad concept (which established that the three residues, Phe353, Ile418, and Phe593, at the bottom of *rabbit* ALOX15's cavity were critical for AA positioning) only partially applies to hALOX12 [31,32]. Instead, this hypothesis has been supported several times for ALOX15 orthologs. By mutagenesis of the residues of the triad, an AA 15-lipoxigenating ALOX15 ortholog has been converted into an AA 12-lipoxygenating enzyme or vice versa. However, a U-shaped binding pocket [33–35] was introduced to complete the description of the substrate binding cavity of LOX isoforms versus the triad concept [6]. Moreover, the regioselectivity of LOX isoforms has also been shown to depend on the orientation of the substrate bound to the enzyme. That is, which end of the substrate (carboxylate-head or hydrophobic-tail) is innermost in the cavity [6,35]. Recently, Holman and co-workers [22] have thoroughly studied, by site-directed mutagenesis and, using docking calculations, the main interactions of AA with hALOX12 active-site residues, establishing the main differences between hALOX12 and hALOX15 regioselectivities. In that work, the double mutant A417I/V418M of hALOX12 increased 15-HpETE production by only 24 $\pm$ 2%, whereas the single mutation of hALOX15 (I418A) augmented the yield of 12-HETE to 94% [31]. Also, the docking simulations by Holman and co-workers supported the U-shaped binding mode [35] for AA in hALOX12 with a tail-first orientation [22]. However, the calculations in that paper were performed using a model of the catalytic domain of hALOX12 built from the crystallographic coordinates of an N-terminal truncation variant of pigALOX15 [36], so-called pigALOX15-mini-LOX. As the same authors explain, the X-ray structure for hALOX12's catalytic domain, available at the Protein Data Bank (PDB code 3D3L), is not adequate for modeling the AA/hALOX12 complex.

The *porcine* LOX isoform is encoded by the *ALOX15* gene, and for that reason, it is called pigALOX15. It presents a high degree (86%) of sequence conservation with rabALOX15, but much less similarity with hALOX12 (66%). This *porcine* LOX was purified from the cytosolic fraction of leukocytes [37], and it was later also mainly found in the anterior pituitary gland of *pigs* [38]. As with the other ALOX15 orthologs, pigALOX15 presents dual specificity when reacting with AA. The main pigALOX15 peroxidation products are 12S- and 15S-HpETE in a ratio of about 10:1 [39,40]. However, as mentioned above, this regioselectivity has been inverted by site-directed mutagenesis based on the triad concept. In a study by some of the authors [41], the complete wild-type pigALOX15 and its pigALOX15-mini-LOX variant were expressed, and both showed the same regiospecificity, mainly producing 12-H(p)ETE. However, catalytic activity was strongly reduced for the isolated catalytic domain. The specificity switch of pigALOX15-mini-LOX induced by experimental mutagenesis of Val418 and Val419 sequence determinants was demonstrated. Moreover, docking, MD simulations, and quantum mechanics/molecular mechanics calculations using a solvated model of wild-type and the Val418Ile + Val419Met double mutant of pigALOX15-mini-LOX were performed. In agreement with experiments, the lower energy barriers in the wild-type LOX were found for the H_{10}-abstraction process leading to 12-lipoxygenation whereas the double mutant was dominantly 15-lipoxygenating with lower barriers for the H_{13}-abstraction.

Int. J. Mol. Sci. 2023, 24, 6064

In this study, we have built for the first time an in silico model of the DHA/hALOX12 complex using the AlphaFold [42,43] server to retrieve the initial coordinates of the *human* LOX protein. Docking and MD simulations have been performed to simulate the binding mode of DHA at the active site of hALOX12. Next, we have calculated within a QM/MM scheme the potential energy profile of the hydroperoxidation mechanistic steps that convert DHA to the fully characterized 14S-hydroperoxy-4Z,7Z,10Z,12E,16Z,19Z-docosahexaenoic acid (14S-H(p)DHA). Special attention has been devoted to the stereochemistry of the reaction because the biosynthesis of maresin 1, which is the potent bioactive SPM derived from 14S-H(p)DHA, is highly stereospecific. For the sake of comparison, the viability of DHA peroxidation by pigALOX15 has also been analyzed using the crystallographic coordinates of an N-terminal truncation variant of pigALOX15 (pigALOX15-mini-LOX) that has been previously used as a model of the hALOX12 structure.

2. Results and Discussion

Docking calculations were carried out for the DHA/hALOX12 and DHA/pigALOX15-mini-LOX complexes. The binding mode of the substrate with the best score in the active site of each LOX was selected to initiate the corresponding MD simulations.

2.1. MD Simulations of the DHA/hALOX12 Complex

In this section, the achieved outcomes from the two MD trajectories of the solvated DHA/hALOX12 complex are presented. In Figure 1, we have plotted the protein backbone RMSDs versus time. The protein RMSD along the first replica remains quite stable during 170 ns. Then, a conformational change occurs that increases the RMSD. This conformational change corresponds to an opening of the PLAT (Polycystin-1,Lipoxygenase, Alpha-Toxin) domain (N-terminal domain from residues 1–110) away from the catalytic domain (C-terminal domain) (Figure 2). The average distance between the geometrical centers of the two domains changes from 42.3 Å to 47.2 Å when the domains separate (see Figure S1). The angle between the longest axes of the two ellipsoids that enclose the PLAT and the catalytic domain, respectively, is 38.2° in the closed conformation and 58.8° in the open structure. Experimentally, the flexibility of the PLAT domain of hALOX12, described as a pendulum-like movement, was proposed for fitting SAXS measurements [44,45]. The C-skeleton of DHA also experiences a sudden conformational change just before the N-terminal displacement (see Figure 1, replica 1). In the second MD replica, the PLAT domain remains more tightly bound to the catalytic domain in a close conformation (see Figure 1, replica 2). Moreover, in this second MD replica, the DHA substrate shows the same binding mode all along the trajectory.

In the hALOX12 active site, DHA adopts a U-shaped binding mode [35], like that described for AA by Holman and co-workers using docking calculations [22], while the two-domain LOX remains closed. There is a modification of the DHA pose bound to hALOX12 when the PLAT domain separates. An overlay of both DHA binding modes is depicted in Figure 3.

In Figure 4, the interatomic distances of the main interactions between the carboxylate head of DHA and hALOX12 residues have been plotted along the two MD trajectories. As DHA has two more carbons than AA, its carboxylate group is hydrogen-bonded to Arg402 instead of being bound to His596 like AA (see Figure 3). Arg402 is a more solvent-exposed residue than His596 that can only be reached by DHA being a longer substrate. The average hydrogen-bond distance between Arg402 and the carboxylate of DHA (2.41 Å and 2.12 Å in replicas 1 and 2, respectively) is similar in both MD replicas, but in replica 2, the interaction remains more stable all along the trajectory.

The carboxylate group of DHA also interacts with Gln406, but this interaction is less favorable and more fluctuating than with Arg402. In turn, Arg402 and Gln406 interact by hydrogen bonds along the MD trajectory, as can be seen in Figure 5 for replica 1. However, Gln406 flips repeatedly away from the cavity, losing contact with DHA's carboxylate and Arg402. In contrast, Arg402 remains more fixed along the trajectory due to its electro-

static interactions with Glu175 of the α2-helix. Several water molecules also contribute to stabilizing the substrate's carboxylate head.

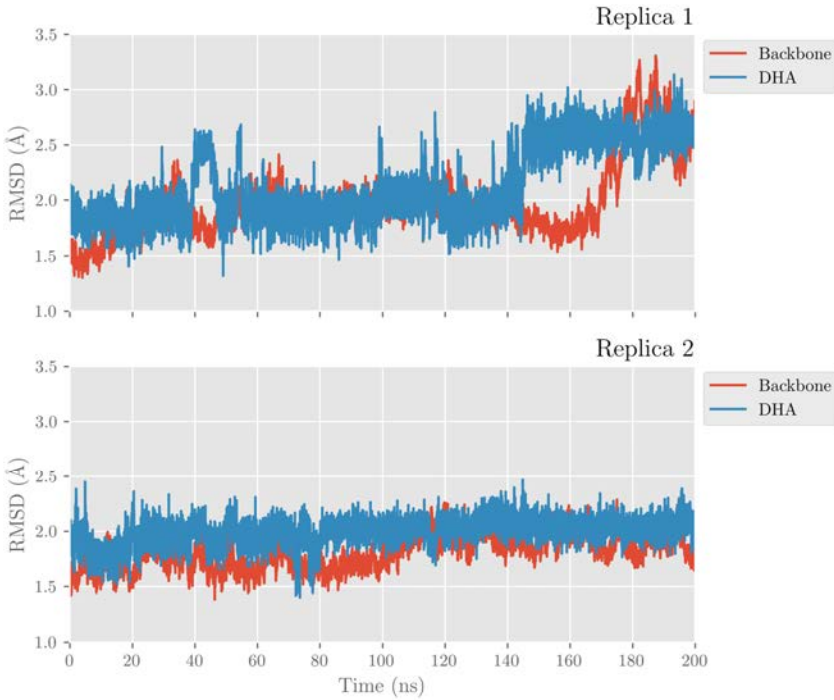

Figure 1. Protein and substrate backbone RMSDs versus time for the MD replica 1 and replica 2 in hALOX12.

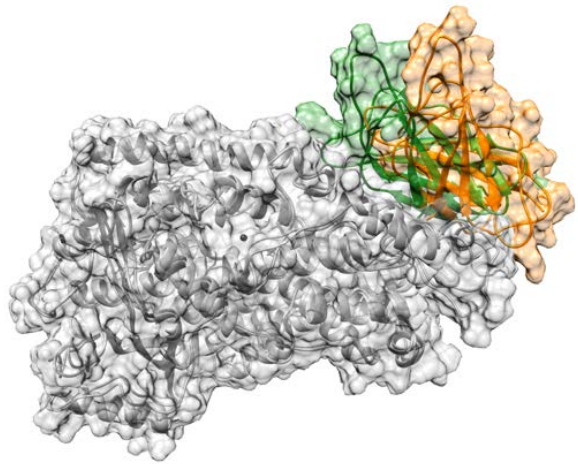

Figure 2. PLAT domain of hALOX12 in the closed (in green) and in the open (in orange) conformation. The C-terminal domain is shown in grey.

Int. J. Mol. Sci. 2023, 24, 6064

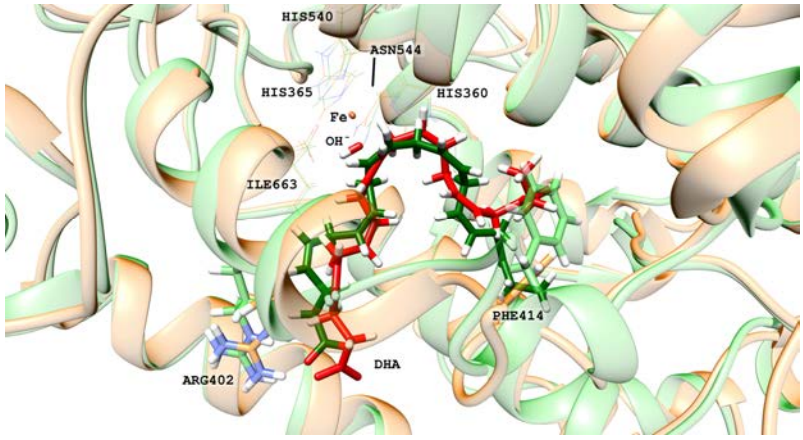

Figure 3. DHA binding mode in the closed (in green) and the open (in red) conformations of hALOX12. The interaction between Arg402 and the carboxylate group of DHA is shown as well as the rotation of Phe414.

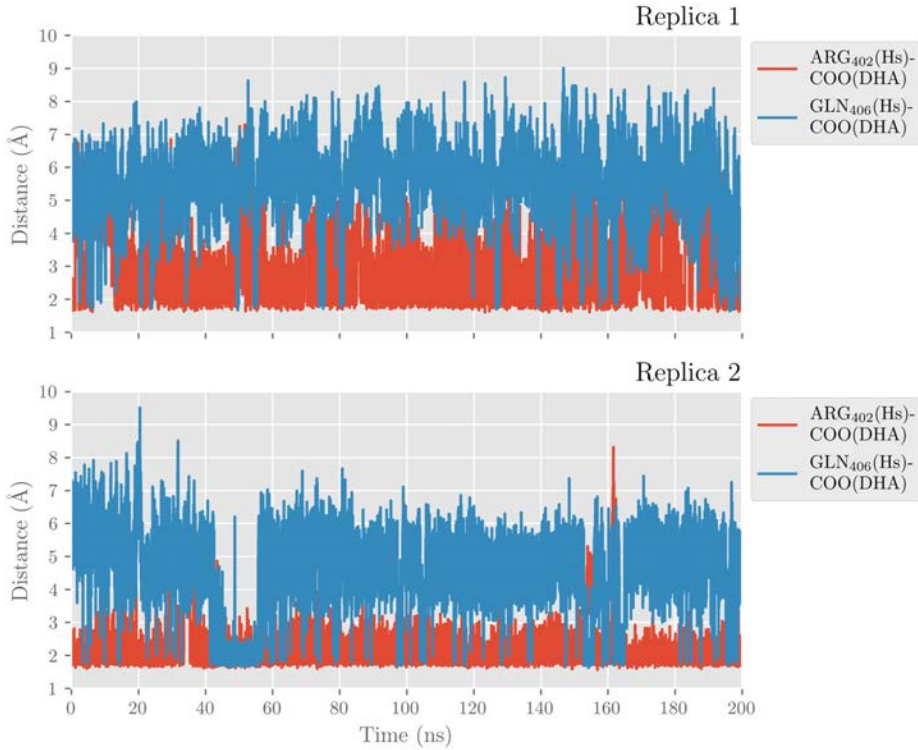

Figure 4. Distances of a carboxylate's oxygen atom of DHA to the closest hydrogen atom in Arg402 and Gln406 versus time for the MD replica 1 and replica 2 in hALOX12.

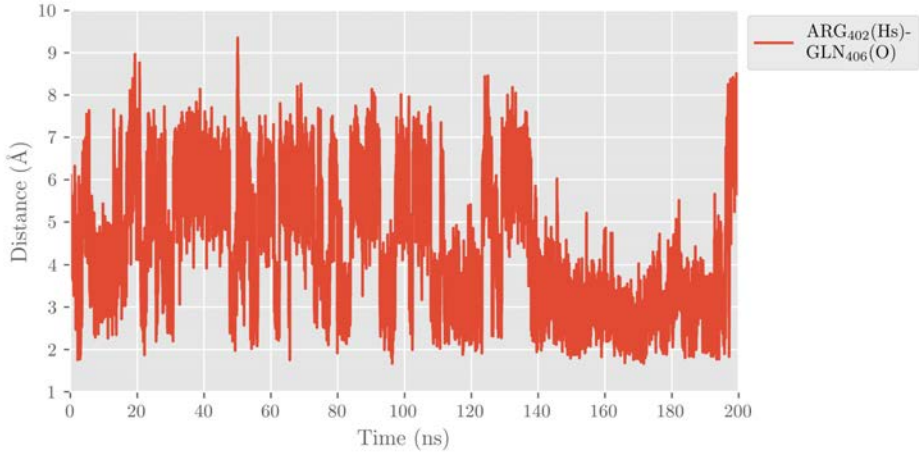

Figure 5. Distance between the oxygen atom in Gln406 and the closest hydrogen atom in Arg402 versus time for the MD replica 1 in hALOX12.

Holman and co-workers mutated the Arg402 residue by a hydrophobic Leu and did not observe any significant change in the reactivity of hALOX12 with DHA [22]. However, this result does not necessarily mean that Arg402 does not interact with the carboxylate group of DHA in WT hALOX12, as was suggested by the authors of the mutagenesis experiment. In the Arg402Leu mutant, the DHA carboxylate group might reinforce its interaction with Gln406 and the closer water molecules. Thus, the change of hydrogen-bonded partner (mainly Arg402 in WT hALOX12 by Gln406 in the Arg402Leu mutant) would not imply any relocation of DHA.

DHA also establishes π–π interactions between its six double bonds and aromatic residues of the hALOX12 active site that stabilize the substrate binding mode. In Figure 6, we plotted the distances between Phe174 and the closer carbon atom of Δ^4 and Δ^7 double bonds along the MD trajectory of replica 1. This π–π stacking stabilizes the Δ^4 double bond during the first 150 ns of the trajectory until the DHA substrate moves to the cavity entrance. Then, Phe174 switches its stacking interactions from the Δ^4 to the Δ^7 double bond. In Figure S2, the rest of the stacking interactions between the substrate and the enzyme residues are plotted. As can be observed, there are also π–π interactions between Phe352 and the Δ^{19} double bond and His365 and the Δ^{10} double bond. The stacking interaction of DHA with Phe414, which has been described for AA, is established with two double bonds (Δ^{13} and Δ^{16}). In the MD replica 1, all those interactions weaken when the PLAT domain separates from the catalytic domain. The principal hALOX12 residues interacting with DHA's double bonds by stacking interactions are plotted in Figure 7 for the two binding modes observed along the MD replica 1. In replica 2, the stacking interactions with Phe174 remain stable after 80 ns (Figure 6). In Figure S2, it can be observed that the interactions with Phe352 and Phe414 remain very stable all along the trajectory. In contrast, the π–π stacking with His365 is not present in this MD replica.

The PLAT movement also correlates with structural changes in some α-helices of the catalytic domain. In this respect, it is noteworthy that there is a loss of the secondary structure of the α-helix from residue 408 to residue 418, which flips the sidechain of Phe414. With the displacement of the PLAT domain, Phe414 rotates, blocking the U-shaped cavity bottom and opening a new cavity to accommodate the DHA tail. This rotation of the Phe414 sidechain is depicted in Figures 3, 7 and S3. Then, Ile408 approaches the DHA tail that simultaneously rotates around the C_{17}–C_{18} single bond, losing the U-shaped binding mode.

Int. J. Mol. Sci. 2023, 24, 6064

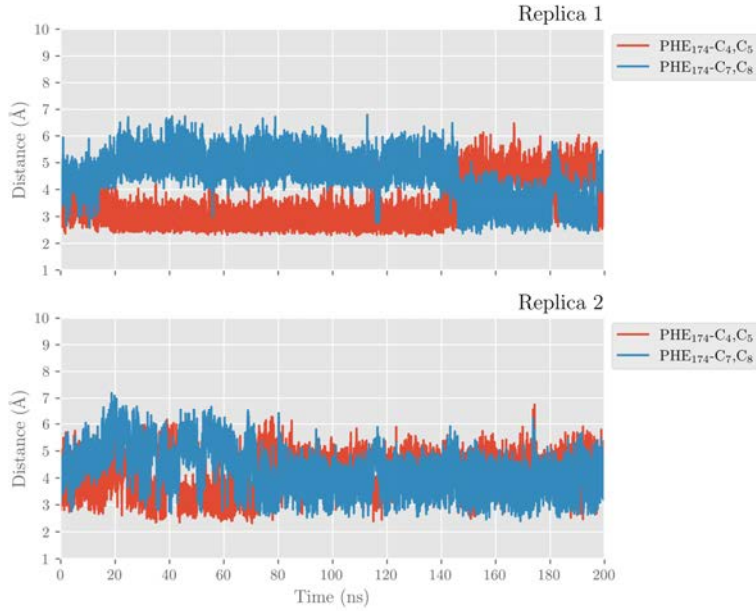

Figure 6. Distances between Phe174 side chain and the closest atom of the Δ^4 and Δ^7 double bonds versus time for the MD replica 1 and replica 2 in hALOX12.

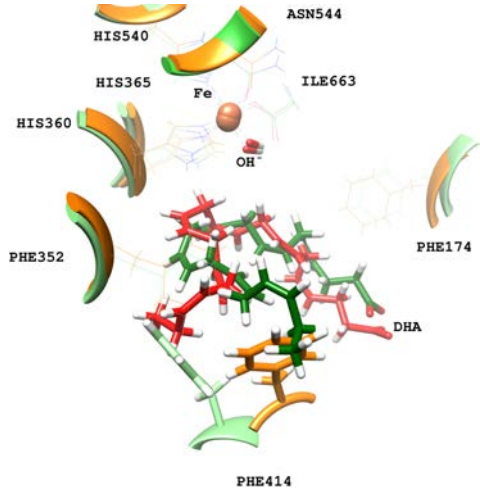

Figure 7. Main stacking interactions between hALOX12 residues and DHA. The protein residues and DHA are shown in green for the closed conformation, and in orange and red, respectively, for the open conformation of the MD replica 1.

For the U-shaped DHA binding mode, the residues at the cavity bottom that mainly interact with the substrate are Phe352, Ala417, Cys559, and Gln590. For the more twisted DHA orientation in replica 1, the bottom cavity is formed by the sidechains of Ile357, His425, and Ile408. Those residues at the cavity bottom are shown in Figure 8. The changes

in the interactions between the substrate's tail and the protein residues at the cavity bottom could explain why hALOX12 might only partially follow the triad hypothesis. However, kinetic experiments with A417I and V418M mutants would be necessary to confirm this prediction that has already been shown for AA. Finally, it is worth mentioning that Leu407 is also a critical residue defining the U-shaped binding mode of DHA in hALOX12, as has been described for AA [22].

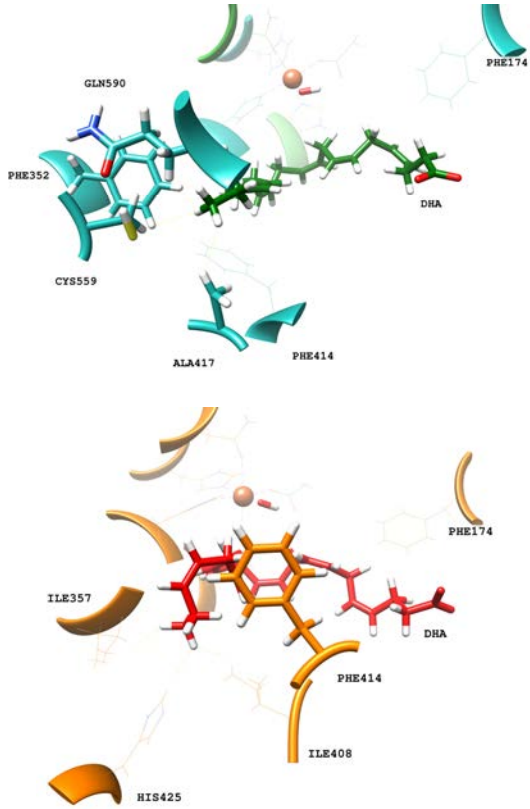

Figure 8. Main interactions between the terminal methyl of DHA and residues of the bottom of hALOX12′s cavity for the close (upper, blue) and open (lower, orange) conformations.

Here, we also analyzed the evolution of the hydrogen atoms H_9, H_{12}, and H_{15}, which are candidates to be abstracted in the first step of the catalytic mechanism. That is, we recorded the distances from the oxygen atom in the Fe(III)-OH^- cofactor to the closest H_9, H_{12}, and H_{15} atoms (attached to C_9, C_{12}, and C_{15}, respectively) along the MD trajectory (see Figure 9). During the MD replica 1, hydrogen H_{12} remains at precatalytic distances (that is, smaller than 4 Å), although with some structural fluctuations. H_9 also remains quite stable at precatalytic distances from the cofactor but moves farther away when the PLAT domain separates. The average H_{12}-OH^- and H_9-OH^- distances before the PLAT movement are 3.60 Å and 3.16 Å, respectively. The smaller average H_9-OH^- distance compared to the H_{12}-OH^- one does not agree with the regioselectivity of hALOX12, which gives 14-H(p)DHA as the main product. However, we have shown in previous mechanistic studies on the reactivity of other ALOXs that interatomic distances alone cannot explain

the molecular origin of enzyme regiospecificity. As can be observed in Figure 9, H_{15} is more distant from the cofactor than H_{12} and H_9 when the two-domain protein is closed but approaches when the two domains open. The evolution of those three distances indicates that the opening of the two-domain protein is correlated with a movement of DHA to the entrance of the cavity, as mentioned above. Along the MD replica 2, the three distances maintain more stable values in accordance with the stability of the DHA binding mode in this trajectory. In this case, the average H_{12}-OH^- distance is the smallest (2.99 Å) followed by the average H_9-OH^- distance (3.44 Å), and the H_{15}-OH^- one (4.49 Å), in agreement with the regiospecificity observed for hALOX12.

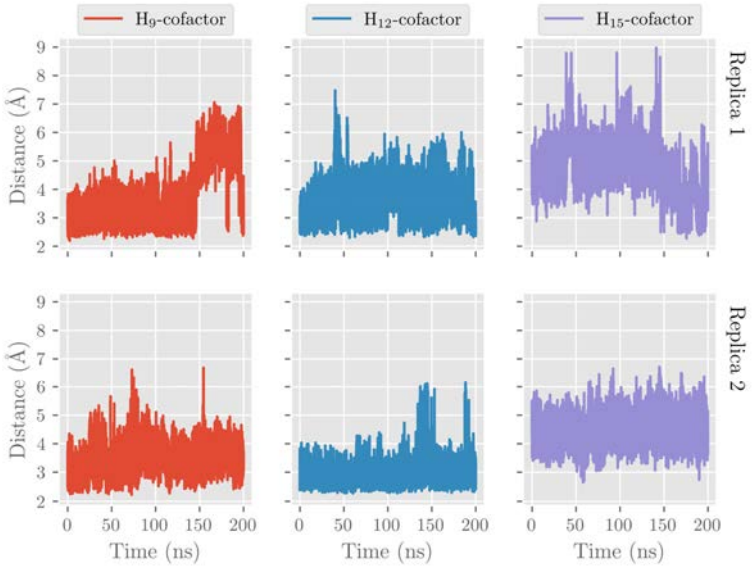

Figure 9. Evolution with time of the H_{12}-OH^-, H_9-OH^-, and H_{15}-OH^- distances along the MD replica 1 and replica 2 in hALOX12.

As mentioned above, ALOXs are also enzymes that are highly stereospecific. ALOX12 catalyzes the formation of 14S-hydroperoxy-4Z,7Z,10Z,12E,16Z,19Z-docosahexaenoic acid (14S-H(p)DHA), which is the intermediate that forms 13S,14S-epoxy-4Z,7Z,9E,11E,16Z,19Z-docosahexaenoic acid (13S,14S-epoxy-DHA). This epoxide is then enzymatically hydrolyzed to form the final maresin product (MaR1, 7R,14S-dihydroxy-4Z,8E, 10E,12Z,16Z,19Z-docosahexaenoic acid). The stereochemistry of the bonds around C_{12} in 14S-H(p)DHA is critical for the formation of MaR1. We analyzed the MD trajectories of the DHA/hALOX12 complex and concluded that configurations of DHA with the angle between planes $\Pi(C_{10}C_{11}C_{12})$ and $\Pi(C_{12}C_{13}C_{14})$ smaller than 90° are prompted to give the E stereochemistry of the Δ^{12} bond in 14S-H(p)DHA. Most of the configurations of the MD replica 1 before the PLAT movement accomplish that structural condition, and there is also a fraction of those configurations when the two domains are separated (see Figure 10). In contrast, many DHA configurations present angles between the $\Pi(C_7C_8C_9)$ and $\Pi(C_9C_{10}C_{11})$ planes with values above 90°. These configurations would lead to a Z stereochemistry of the Δ^9 bond in 11S-H(p)DHA.

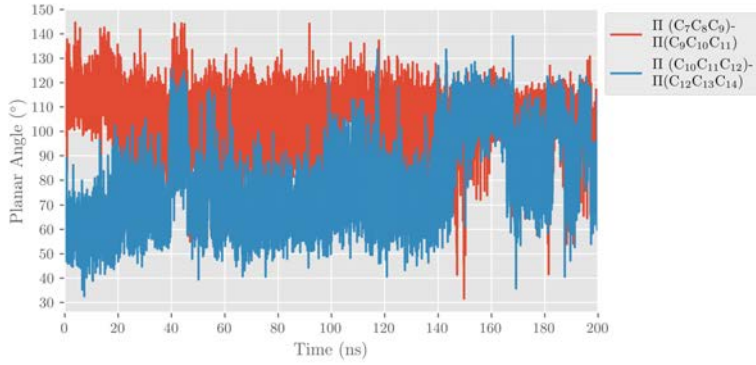

Figure 10. Evolution with time of the angle between planes formed by $C_7C_8C_9$ and $C_9C_{10}C_{11}$ (in red) and by $C_{10}C_{11}C_{12}$ and $C_{12}C_{13}C_{14}$ (in blue) along the MD replica 1 in hALOX12.

2.2. QM/MM Calculations of DHA Hydroperoxidation Catalyzed by hALOX12

2.2.1. Hydrogen Abstraction Reactions Catalyzed by hALOX12

In Table 1 and Table S1, the QM/MM results corresponding to the first step of the catalytic mechanism are given (see Figure 11). We have calculated the potential energy profiles for the H_{12}, H_9, and H_{15} abstraction reactions using as initial structures several selected snapshots of the MD trajectory for replica 1. Those initial or precatalytic structures were filtered according to the following criteria. We searched precatalytic snapshots in which the initial distance between the three hydrogen atoms, H_{12}, H_9, and H_{15}, and the oxygen atom of the hydrogen acceptor, that is, the oxygen of the Fe(III)-OH^- cofactor, was smaller than 4.0 Å.

Table 1. Number of the MD frame used as initial coordinates for the QM/MM optimization in hALOX12, optimized H_{12proS}-OH^- and H_{9proR}-OH^- distances (in Å) at reactants, potential energy barriers, and reaction energies (in kcal/mol) for the H_{12proS} and H_{9proR} abstraction processes. The stereochemistry of the pentadienyl radicals centered at C_{12} and C_9 is also given. Exponential average (in kcal/mol) energy barriers [46] for the two H-abstractions are included in the last row.

	H_{12proS}				H_{9proR}			
Frame	$d^{react}_{H-OH^-}$ [a]	$\Delta E^{\ddagger}$	ΔE	**Pentadienyl Stereochemistry**	$d^{react}_{H-OH^-}$ [b]	$\Delta E^{\ddagger}$	ΔE	**Pentadienyl Stereochemistry**
322	3.5	15.9	−18.3	ZE	3.5	36.4	−13.9	ZZ
2253	5.4	20.5	−19.0	ZE	3.5	23.4	−19.1	ZZ
4986	5.4	19.3	−17.0	ZE	5.0	35.0	−14.1	ZZ
6993	3.9	18.0	−18.5	ZE	3.1	29.7	−14.5	ZZ
8721	5.0	21.9	−17.3	ZE	3.3	22.7	−13.6	ZZ
10,106	5.5	24.3	−16.8	ZE	3.4	25.6	−17.4	ZZ
12,860	5.2	22.9	−18.5	ZE	3.9	29.2	−15.3	ZZ
14,423	4.1	21.8	−19.1	ZE	3.4	27.5	−13.6	ZZ
18,168	3.7	17.1	−17.0	ZE	3.3	31.8	−13.8	ZZ
19,729	3.4	17.1	−17.0	ZE	3.9	43.7	−18.4	ZZ
$\Delta E^{\ddagger}_{AV}$		17.1				23.9		

[a] H stands for H_{12proS}; [b] H stands for H_{9proR}.

Int. J. Mol. Sci. **2023**, *24*, 6064

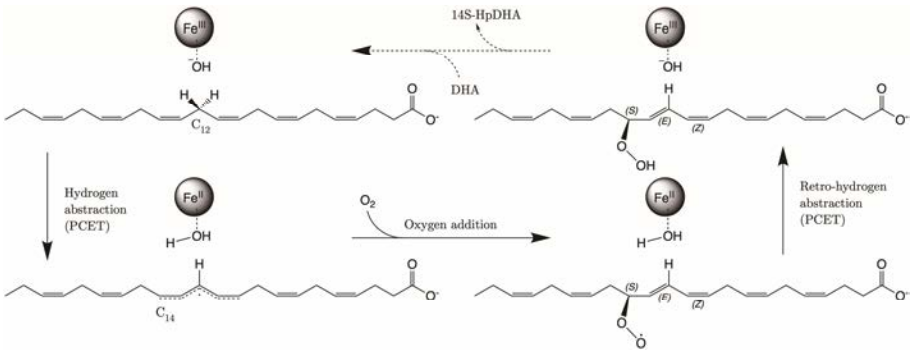

Figure 11. Scheme of the DHA hydroperoxidation mechanism. PCET stands for proton coupled electron transfer.

Then, several of those precatalytic snapshots were optimized according to the QM/MM model described in the methodology section, and the corresponding minima were located. From those minima, the potential energy profile for the H-abstraction was calculated using the difference between the C_X-H_X distances and the corresponding H_X-OH^- ones as the reaction coordinate. In Table 1, the results for the most favorable abstraction reactions, the H_{12proS} and H_{9proR} abstractions, are collected. In Table S1, we have included the results for the rest of the H-abstraction energy profiles. The values of the H_{proX}-OH^- distances in Table 1 are given for the optimized reactants of the H_{12} and H_9 abstraction processes. As can be observed, the QM/MM optimized distances are longer than the initial distances of the precatalytic structures. As for the potential energy barriers, there is no correlation between their values and those of the optimized H_{12proS}-OH^- or H_{9proR}-OH^- distances. Thus, the H_{9proR}-OH^- distances are shorter in almost all the optimized reactants, but the individual barriers are higher for the H_9-abstraction than for the H_{12}-abstraction. At the optimized radical products of both H-abstractions, the corresponding pentadienyl group is planar, and the electronic density is delocalized over five carbon atoms. In DHA, the set of carbon atoms around C_{12} that will form the pentadienyl radical after H_{12}-abstraction is closer to planarity than the set of carbon atoms around C_9, which will form the pentadienyl radical after H_9-abstraction. The larger the geometrical change from an initially nonplanar structure to a planar pentadienyl and, especially, the greater steric hindrance to that motion, the higher the contribution to the potential energy barrier [24]. Both abstraction processes are exoergic, as has already been obtained in other ALOXs with AA. All in all, the exponential average energy barrier is 6.8 kcal/mol lower for H_{12}-abstraction than for H_9-abstraction. This result agrees with the regioselectivity of hALOX12, which favors the abstraction of H_{12}, leading to the formation of 14S-H(p)DHA after the addition of O_2 at C_{14} (see next section). In Table 1, the pentadienyl stereochemistry is given at both product radicals. It is remarkable that the stereochemistry of all the pentadienyl radicals from C_{10} to C_{14} (ZE) is the one needed for leading to the fully characterized 14S-hydroperoxo-4Z,7Z,10Z,12E,16Z,19Z-docosahexaenoic acid (see next section). (ZE) stands for the stereochemistry in the pentadienyl radical that will become 10Z, and 12E in 14S-H(p)DHA. Hence, the geometry of the QM/MM optimized products ratifies the analysis made of the most stable configurations of DHA along the MD trajectory (See Figure 10). In contrast, the stereochemistry of the pentadienyl radical centered at C_9 is (ZZ). In this case, the stereochemistry of 11-H(p)DHA, being the minor product, has not been reported. In Figure 12, the structures of the optimized reactant, transition state structure, and product of the H_{12proS}-abstraction initiated from snapshot 8721 are depicted.

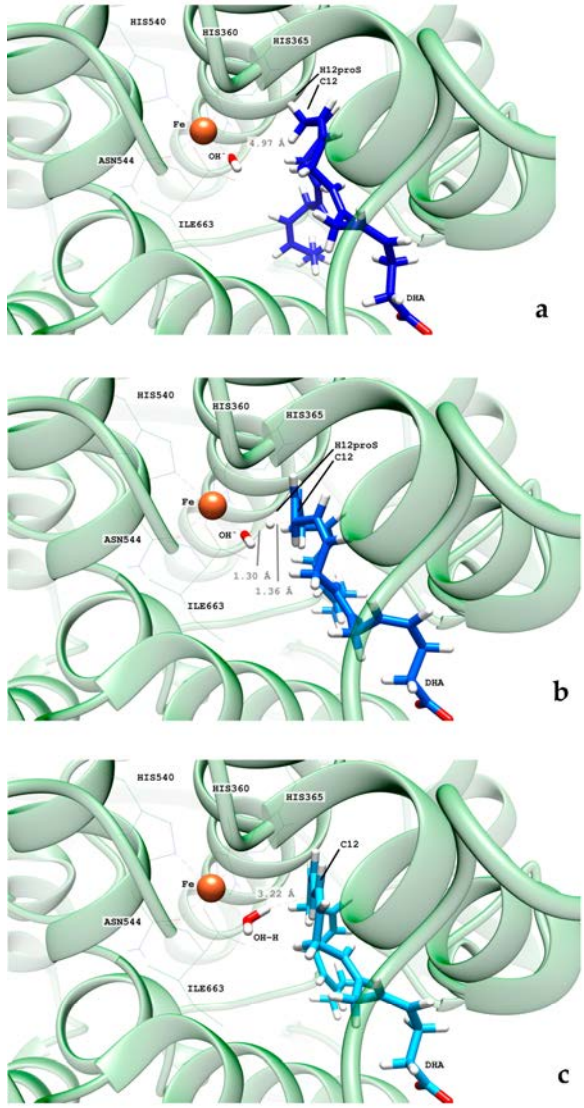

Figure 12. Images of the optimized reactant (**a**), transition state structure (**b**), and product (**c**) of the H_{12proS} abstraction initiated from snapshot 8721 in hALOX12. The distance between H_{12proS} and the oxygen atom in OH^- is shown for the optimized reactant (**a**). At the transition state structure, the distances between the shifting hydrogen with respect to C_{12} (donor atom) and the oxygen atom in OH^- (acceptor atom) are depicted (**b**). The distance between the H atom in the nascent water molecule and C_{12} is plotted at the optimized product (**c**).

On the other hand, the H_{15}-abstraction (Table S1) has a low probability of occurring since the percentage of precatalytic structures (10%, see Figure 9) is quite lower than for the H_{12} (74%) and H_9 (73%) abstractions.

Int. J. Mol. Sci. 2023, 24, 6064

2.2.2. O_2 Addition and Retro-Hydrogen Abstraction Reactions Catalyzed by hALOX12

The second step of the overall DHA hydroperoxidation process that leads to the final products consists of adding an oxygen molecule to the C_{10}–C_{14} or C_7–C_{11} DHA pentadienyl radicals, formed once H_{12} or H_9 has been abstracted, respectively. Here, we only calculated the reaction pathway for O_2 addition to the delocalized C_{10}–C_{14} radical that gives the main hydroperoxide product, 14S-H(p)DHA.

We have explored different initial locations for the O_2 molecule around C_{14} at the conformation of the DHA pentadienyl radical obtained from the different MD snapshots. The O_2 molecules around C_{14}, taken as the origin of coordinates, have been initially placed at 3.0 Å along the x, y, and z Cartesian axes and along the bisector axes contained in the xy, xz, and yz planes. The structures selected were chosen by a visual analysis. This means that all the O_2 molecules with close contacts or clashes with other residues were discarded. Then, QM/MM single-point energy calculations were carried out for the selected positions, and the higher energy structures were discarded. The most stable structures were optimized and then taken as starting points to build the reaction path for the oxygen addition to C_{14}. The addition pathway was calculated in the forward and backward directions using the distance from the attacking oxygen of the O_2 molecule to C_{14} as the reaction coordinate. From the last structure of the backward path, the addition reactant structure was optimized. The O-C_{14} distance values for the converged QM/MM minimum energy geometries are presented in Table 2. All the oxygen addition reaction pathways present low potential energy barriers. The chirality of the oxygenated product and the geometry of the addition pathway are also included in Table 2. We have obtained three converged addition pathways corresponding to antarafacial additions leading to peroxyl radicals with S stereochemistry at C_{14}, in agreement with the experimental stereochemistry assigned to the final hydroperoxide product, 14S-H(p)DHA. In Figure 13, the reactant, transition state structure, and the product of the addition process to C_{14}, initiated from frame 8721, are depicted.

The final step of the overall hydroperoxidation mechanism consists of a retro-hydrogen abstraction from the Fe(II)-H_2O cofactor to the peroxyl DHA radical. This reaction leads to the final 14S-H(p)DHA product, and hALOX12 recovers the initial Fe(III)-OH^- cofactor's state. However, as the oxygen molecule has been added following an antarafacial approach with respect to the cofactor, the carbon chain of the peroxyl radical needs to rotate before the proper retro-hydrogen transfer can take place. We calculated the potential energy profiles for this carbon chain rotation using the $C_{13}C_{14}C_{15}C_{16}$ dihedral as the reaction coordinate for the three pathways initiated at snapshots 8721, 10,106, and 18,168. The potential energy barriers measured from the corresponding previous minima (that is, the addition products) on the QM/MM potential energy surface for the three rotations range from 5.8 to 6.6 kcal/mol. In Figure 14, the reactant, transition state structure, and the product of the rotation process, initiated from frame 8721, are presented. Note that the reactant minimum in Figure 14a has the same structure as the addition product minimum in Figure 13c but is plotted from a different perspective to better follow the carbon chain rotation.

Table 2. Number of the MD frame used as initial coordinates for the QM/MM optimization in hALOX12; optimized O-C_{14} distances (in Å) at the reactants and potential energy barriers for the addition reaction as well as the chirality of the peroxyl product and the geometry of the addition approach; potential energy barriers for the rotation of the peroxyl radical's carbon chain and for the retro-hydrogen abstraction (reorganization of the peroxyl radical and retro-hydrogen abstraction itself). All energies are in kcal/mol.

Frame	$d^{react}_{O-C_{14}}$	$\Delta E^{\ddagger}_{O_2 add}$	Chirality of Product	Geometry of Addition	$\Delta E^{\ddagger}_{Crot}$	$\Delta E^{\ddagger}_{reorg}$	$\Delta E^{\ddagger}_{retro-Habs}$
8721	3.2	3.0	S	Antarafacial	6.6	10.2	33.3
10,106	3.2	4.3	S	Antarafacial	5.8	-	-
18,168	3.1	3.1	S	Antarafacial	5.9	13.1	20.6

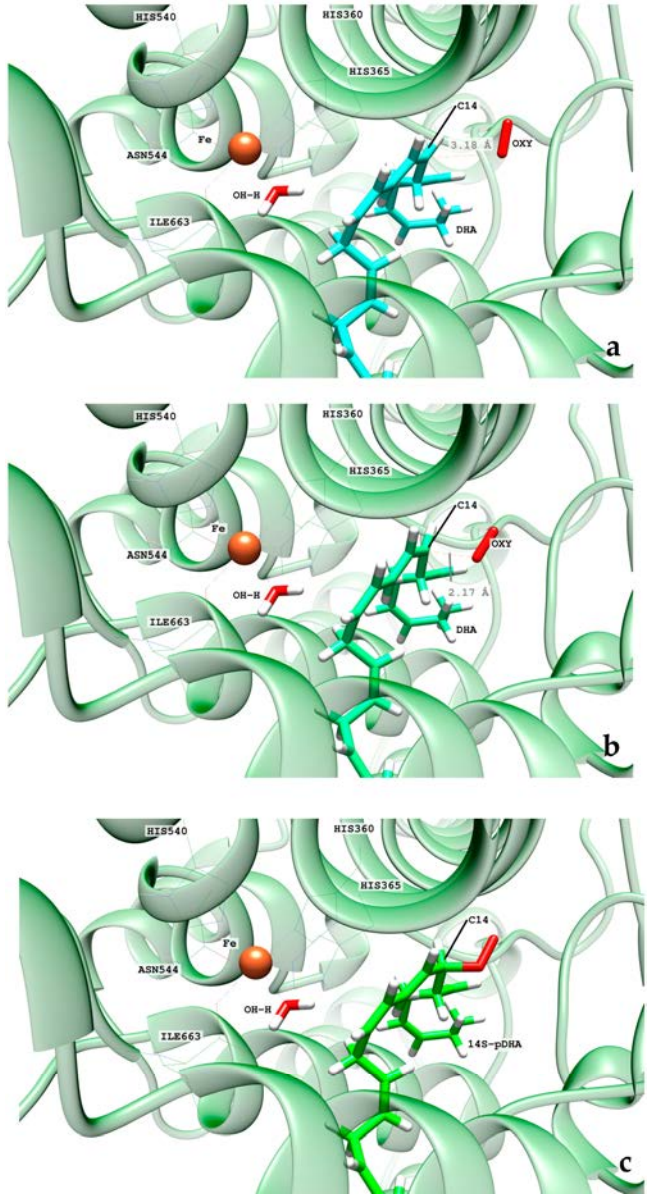

Figure 13. Images of the optimized reactant (**a**), transition state structure (**b**), and product (**c**) of the O_2 addition at C_{14} (frame 8721) in hALOX12. The distances between C_{14} and the attacking oxygen atom are given for the reactant and transition state structures.

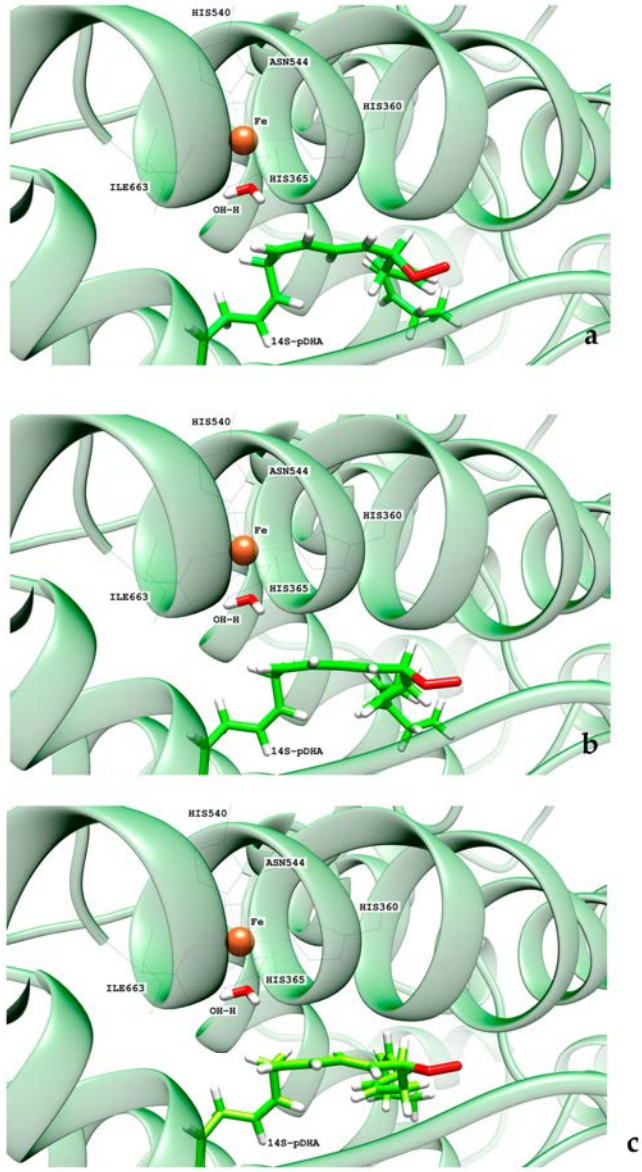

Figure 14. Images of the optimized reactant (**a**), transition state structure (**b**), and product (**c**) of the carbon chain rotation of the peroxyl radical (frame 8721) in hALOX12.

From the rotated peroxyl radical the retro-hydrogen abstraction from the Fe(II)-H_2O cofactor to the peroxyl DHA radical can be initiated. We calculated the corresponding QM/MM potential energy profile versus a reaction coordinate defined as the difference between the breaking H-OH (water ligand) bond distance and the forming H-OOC_{14} one. This abstraction process involves two different structural steps. First, there is a reorgani-

zation of the peroxyl radical that correlates with the rotation of the peroxo group at C_{14} from the antarafacial to the suprafacial side. The potential energy barriers given in Table 2 for this structural reorganization (10.2 and 13.1 kcal/mol for the pathways initiated from snapshots 8721 and 18,168, respectively) are calculated from the corresponding reactant minima, which are the products obtained from the rotation pathway. The reorganization corresponding to snapshot 10,106 did not converge. The transition state structure (TS1) and the product geometry or intermediate (INT1) of this reorganization process are depicted in Figure 15 for the reaction initiated from snapshot 8721. The final step of the mechanism corresponds to the movement of the shifting hydrogen. The abstraction potential energy barriers calculated from the optimized intermediate are 33.3 and 20.6 kcal/mol for the pathways initiated from frames 8721 and 18,168, respectively. In Figure 15, the plots of the stationary-point structures (transition state (TS2) and product) of this final step are also depicted for the pathway of snapshot 8721.

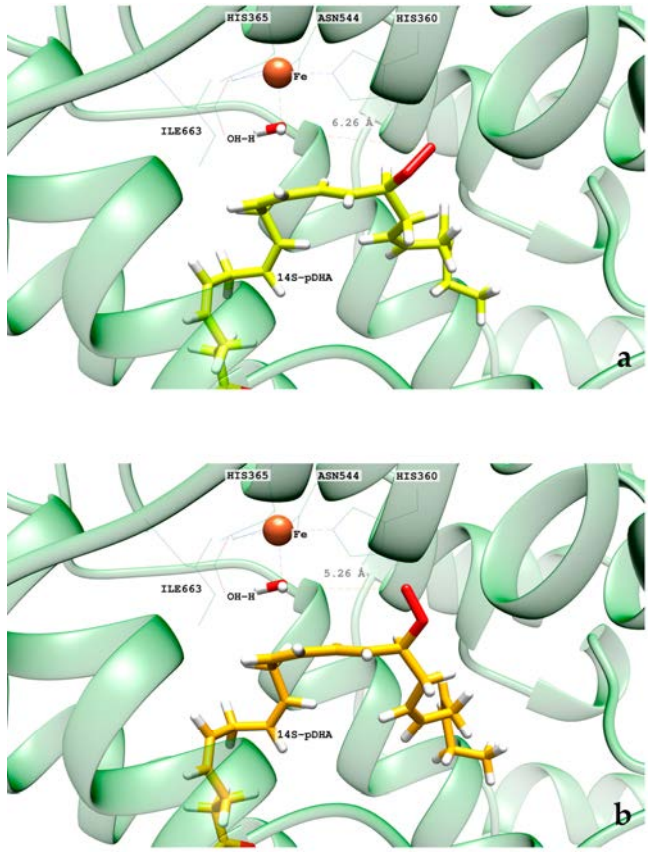

Figure 15. *Cont.*

Int. J. Mol. Sci. **2023**, *24*, 6064

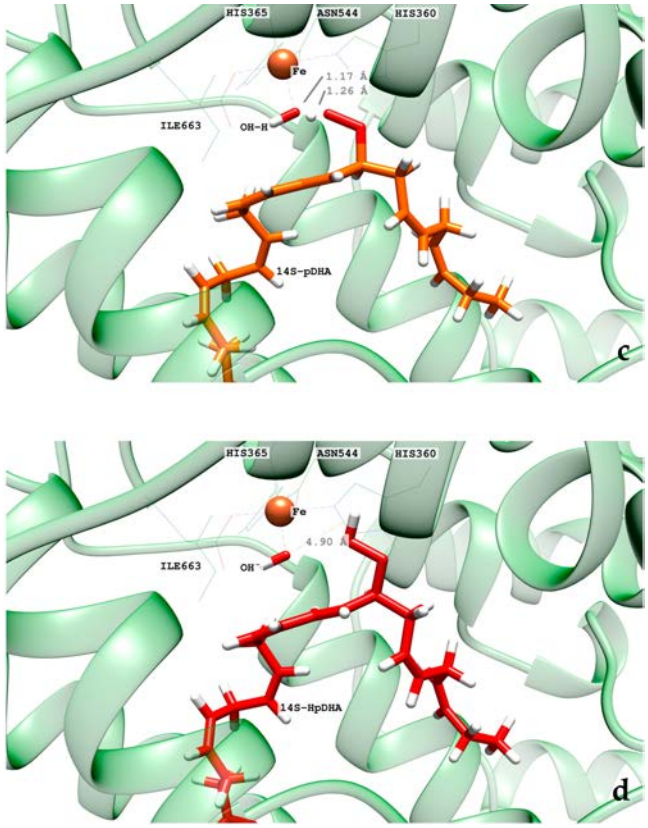

Figure 15. Images of the transition state structure (TS1) (**a**), intermediate (INT1) (**b**), transition state structure (TS2) (**c**), and the final 14S-H(p)DHA product (**d**) (frame 8721) in hALOX12. The distances between the outer oxygen of the peroxo group and the water hydrogen atom are given for TS1 and INT1. The distances corresponding to the shifting hydrogen atom are indicated for TS2 and the final 14S-H(p)DHA product.

In Figure 16, we have depicted an overall energy scheme of the mechanistic steps initiated from the reactant of the H_{12proS}-abstraction reaction (frame 8721) bound to the solvated enzyme plus an oxygen molecule within the water box at the entrance of the enzyme cavity. The position of the oxygen molecule has been optimized at 12.1 Å from the C_{14} atom of the substrate. This structure has been taken as the zero of energy of the overall energy scheme. The approach of the oxygen molecule to 3.1 Å from C_{14} at the addition reactant structure represents a falloff in energy of 53.3 kcal/mol with respect to the H_{12proS}-abstraction product. Consequently, the barriers for the O_2 addition, carbon chain rotation, and retro-hydrogen abstraction are very far below the reference structure. Therefore, none of those processes can be the rate-determining step of the hydroperoxidation reaction. In contrast, the H_{12proS}-abstraction transition state structure is 17.3 kcal/mol above the reference structure (see Table 1 and Figure 16), so it is the rate-determining step. Here, we are assuming that the oxygen molecule approaches the enzyme once the H-abstraction process has taken place.

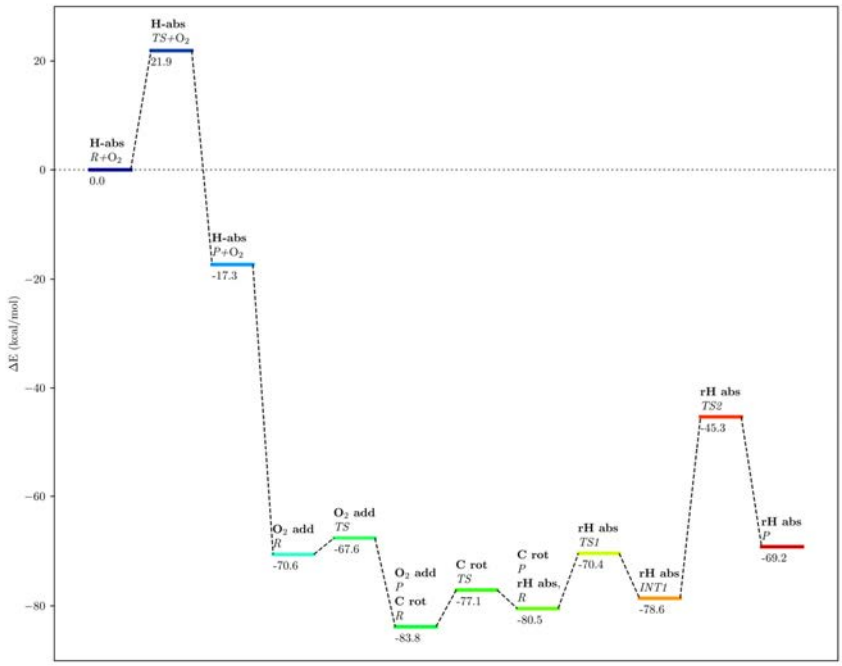

Figure 16. Overall energy scheme of the H_{12proS}-abstraction, oxygen addition, carbon chain rotation, and retro-hydrogen abstraction steps of the DHA hydroperoxidation mechanism in hALOX12. All energies are in kcal/mol. The zero of energies corresponds to the reactant of the H_{12proS} abstraction step bound to the solvated enzyme plus an oxygen molecule within the water box whose position has been optimized at 12.1 Å from the substrate's C_{14}.

2.3. MD Simulations of the DHA/pigALOX15-mini-LOX Complex

In this section, the results corresponding to the two MD trajectories of the solvated DHA/pigALOX15-mini-LOX complex are presented for the sake of comparison with DHA/hALOX12 behavior. In Figure S4, we have plotted the protein backbone RMSD versus time for the two MD replicas. The results show a stable conformation of the C-terminal domain of pigALOX15-mini-LOX, even though the N-terminal domain is not present. The carbon-chain RMSD of DHA also indicates a rather steady binding mode along the two trajectories.

In the pigALOX15-mini-LOX active site, DHA also adopts a U-shaped binding mode like that described in hALOX12. However, the carboxylate head of DHA does not interact with Arg403 (Arg402 in hALOX12), as can be observed in Figure 17 along the two MD trajectories.

This interaction is lost because a displacement of the α2-helix in pigALOX15-mini-LOX moves away from the Glu176 … Arg403 pair (Glu175 … Arg402 in hALOX12) from the cavity entrance. Moreover, pigALOX15-mini-LOX has a Gly in position 407 instead of the Gln406 of hALOX12, which does not interact with Arg403 and cannot maintain this arginine close to the DHA carboxylate. Therefore, in its location in pigALOX15-mini-LOX, the carboxylate head of DHA only interacts with some water molecules. In addition, DHA also establishes π–π interactions between its double bonds and aromatic residues of the active site that stabilize the substrate binding mode. The stacking interactions between Phe175 and Δ^4 and Δ^7 are plotted in Figure 18. Along the MD replicas, Phe175 exchanges its interaction between those two double bonds, except during the first 30 ns of replica 2

when the stacking is present with both double bonds at the same time. The rest of the π–π interactions presented in Figure S5 are weaker in pigALOX15-mini-LOX than in hALOX12.

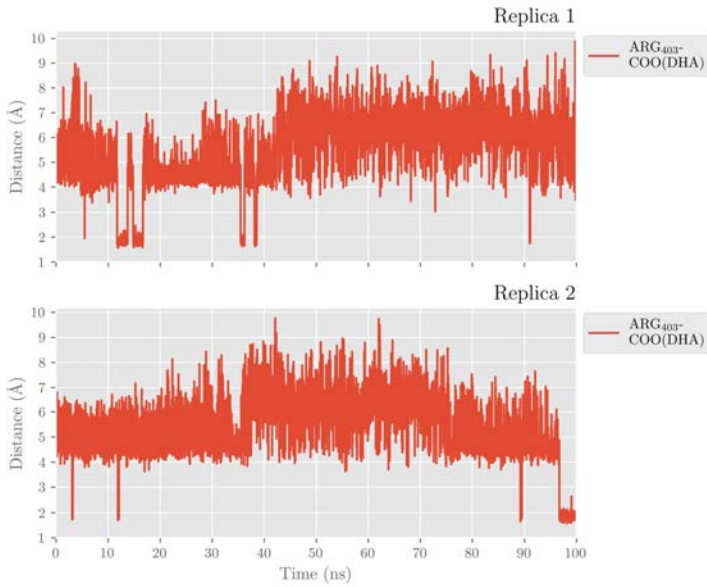

Figure 17. Distances of a carboxylate's oxygen atom of DHA to the closest hydrogen atom in Arg403 versus time for the MD replica 1 and replica 2 in pigALOX15-mini-LOX.

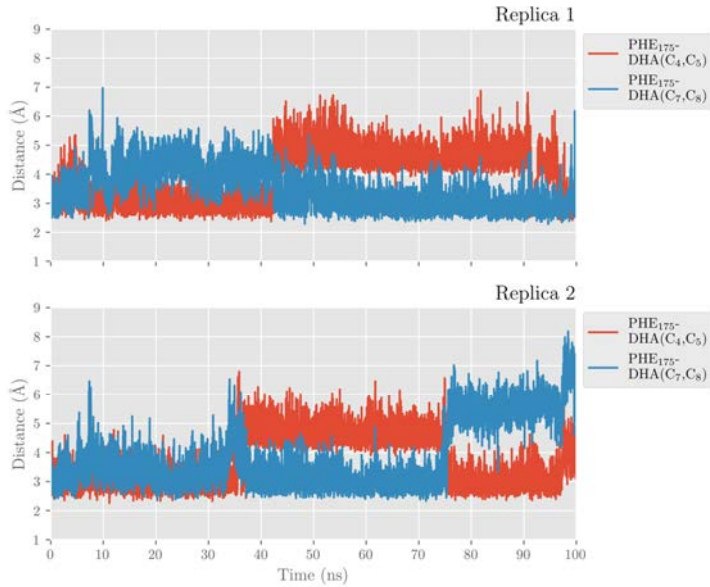

Figure 18. Distances between Phe175 sidechain and the closest atom of the Δ^4 and Δ^7 double bonds versus time for the MD replica 1 and for replica 2 in pigALOX15-mini-LOX.

As for H_{12}-OH^-, H_9-OH^-, and H_{15}-OH^- distances along the MD replica 1 and replica 2, we have plotted them in Figure 19. H_{12} remains the closest to the OH- group of the cofactor the main part of the trajectory. H_9 and H_{15} present a similar number of precatalytic structures when considering both MD replicas. However, when H_9 is closer, H_{15} is farther away, and vice versa. Our MD simulation indicates that the DHA binding mode in pigALOX15-mini-LOX could lead to 14-H(p)DHA as a major product but also, with less probability, to 11-H(p)DHA and 17-H(p)DHA as minor products. Experimentally, Kühn and coworkers obtained a relative share of 76.4% for 14-H(p)DHA and 23.6% for 17-H(p)DHA for the specificity of pigALOX15 [21].

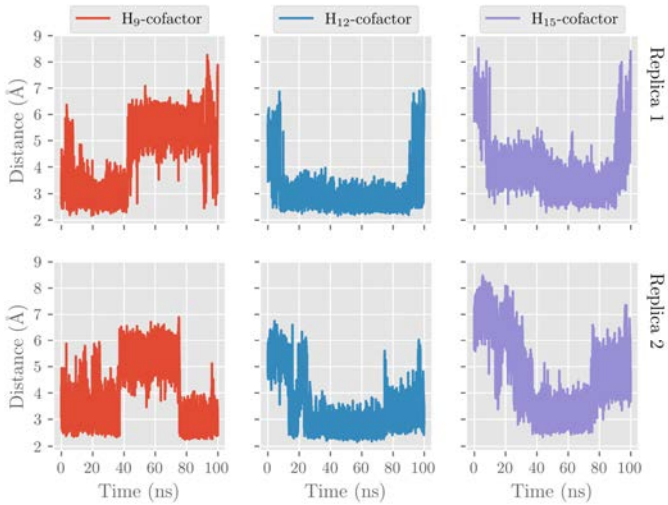

Figure 19. Evolution with time of the H_{12}-OH^-, H_9-OH^-, and H_{15}-OH^- distances along the MD replica 1 and replica 2 in pigALOX15-mini-LOX.

When we calculated the angle between planes $\Pi(C_{10}C_{11}C_{12})$ and $\Pi(C_{12}C_{13}C_{14})$ of DHA, the values obtained are above 90° most of the time (see Figure 20). As indicated before, this result means that the configurations of DHA would give a Z stereochemistry of the Δ^{12} bond in 14S-H(p)DHA. The angle between planes $\Pi(C_7C_8C_9)$ and $\Pi(C_9C_{10}C_{11})$ of DHA behaves similarly all along the trajectory.

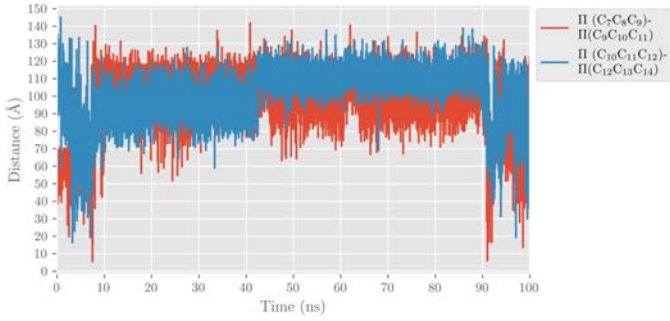

Figure 20. Evolution with time of the angle between planes formed by $C_7C_8C_9$ and $C_9C_{10}C_{11}$ (in red) and by $C_{10}C_{11}C_{12}$ and $C_{12}C_{13}C_{14}$ (in blue) along the MD replica 1 in pigALOX15-mini-LOX.

2.4. QM/MM Calculations of H_{12}-Abstraction from DHA Catalyzed by pigALOX15-mini-LOX

In this section, we present the results of the QM/MM calculations corresponding to the H_{12}-abstraction. We have calculated the potential energy profiles for the H_{12} transfer using as initial structures several selected snapshots of the MD trajectory for replica 1. Following the methodology explained in the corresponding section, we calculated the potential energy profile of this catalytic step using, as a reaction coordinate, the difference between the C_{12}-H_{12} and the H_{12}-OH^- distances. In Table 3, the potential energy barriers are given along with their exponential average. The obtained value of 17.6 kcal/mol is nearly the same as for the H_{12proS}-abstraction in hALOX12. This theoretical result verifies, in agreement with experiments, that pigALOX15-mini-LOX is active and can catalyze the conversion of DHA to 14-H(p)DHA beginning with the abstraction of H_{12proS} [21]. In Table 3 the stereochemistry of the pentadienyl radical centered at C_{12} is given. All the radical products present a (ZZ) stereochemistry, as the configurations of the MD trajectory had predicted. This is not such a stable stereochemistry for those pentadienyl radicals in the enzyme's binding pocket as the (ZE) configuration obtained in hALOX12. Hence, the corresponding reaction energies are not as negative as in hALOX12 (Table 1). Moreover, as commented above, the (ZZ) stereochemistry is not the adequate configuration for the formation of 13S,14S-epoxy-4Z,7Z,9E,11E,16Z,19Z-docosahexaenoic acid and for finally leading to 7R,14S-dihydroxy-4Z,8E, 10E,12Z,16Z,19Z-docosahexaenoic acid (MaR1). For this reason, our hypothesis here is that pigALOX15-mini-LOX forms 14S-hydroperoxo-4Z,7Z,10Z,12Z,16Z,19Z-docosahexaenoic acid, but this hydroperoxide would not give the bioactive SPM MaR1 that it is synthesized by hALOX12.

Table 3. Optimized H_{12proS}-OH^- distances (in Å) at reactants, potential energy barriers, and reaction energies (in kcal/mol) for the H_{12proS} abstraction process. The stereochemistry of the pentadienyl group around C_{12} at the product radical is also given. The exponential average potential energy barrier [46] (in kcal/mol) for the H_{12proS}-abstraction is included in the last row.

	H_{12proS}			
Frame	$d^{react}_{H-OH^-}$ [a]	$\Delta E^{\ddagger}$	ΔE	**Pentadienyl Stereochemistry**
940	3.2	20.9	−12.5	ZZ
1548	3.0	19.8	−11.8	ZZ
1709	2.9	24.5	−12.4	ZZ
2132	2.8	22.1	−9.7	ZZ
2515	3.2	27.2	−8.9	ZZ
3020	2.8	19.8	−10.8	ZZ
3556	3.2	24.5	−9.9	ZZ
4502	2.7	15.9	−16.1	ZZ
5758	2.6	20.4	−12.1	ZZ
9207	2.6	22.6	−13.1	ZZ
$\Delta E^{\ddagger}_{AV}$		17.6		

[a] H stands for H_{12proS}.

3. Materials and Methods

3.1. Protein Setup

The model structure of *human* ALOX12 was taken from the AlphaFold Data Base (UniprotID P18054) [42]. For pigALOX15-mini-LOX, we used the x-ray structure launched at the Protein Data Bank with PDB code 3RDE [36], removing the ligand bound to the protein. The two structures were protonated through a web interface (www.playmolecule.org) (accessed

on 19 January 2021) [47]. A pH = 7.0 was employed for the titratable residues. The protonation state for the iron coordination sphere was corrected by hand to ensure a correct description.

3.2. Molecular Docking Simulations

Docking calculations were performed with GOLD5.8 [48] to obtain stable binding modes of DHA in the active site of hALOX12 and pigALOX15-mini-LOX. For the conformational search of the ligand, the torsion angle distribution of the Cambridge Database was used. In contrast, some protein side chains were treated as flexible. The GOLD's option to consider the interactions of organic ligands with metal ions in metalloenzymes was activated, but it restricted the docking exploration to hexacoordinated geometries of iron. The binding side was defined as a sphere of 20 Å around the iron atom. This conformational space was explored using the Lamarckian algorithm included in GOLD. One hundred DHA-binding poses were generated and grouped into clusters. We used the ChemScore fitness function to rank the docking poses and estimate their binding free energies.

3.3. Molecular Dynamics Simulations

The best-ranked docking poses of DHA bound to hALOX12 and pigALOX15-mini-LOX were selected to initiate the MD simulations. For the solvated DHA/hALOX12 complex, we used the ff19SB force field [49] to calculate the potential energy of the protein and the OPC force field [50] to describe the water molecules, as recommended [49]. For the solvated DHA/pigALOX15-mini-LOX complex, we used the ff14SB force field [51] for the protein and the TIP3P force field to describe the water molecules as recommended [51]. We developed specific parameters for DHA using the AMBER standard protocol with Antechamber and Parmchk2 modules. The GAFF2 library [52] was used as the source for these parameters. The substrate structure was optimized employing the B3LYP/6-31G(d) level of theory. The atomic charges were set to fit the electrostatic potential generated at the B3LYP/6-31G(d) level of theory by the restrained electrostatic potential (RESP) model. The atomic charges were calculated according to the Merz–Kollman scheme [53] using Gaussian16 [54]. An unprotonated state was established for the DHA substrate in the two complexes, considering the physiological conditions. We also developed specific MM parameters for the iron atom and its first coordination sphere using the MCPB.py procedure [55] within the bonded model and the Seminario method for the force constant calculations [56]. For hALOX12, the iron ligands are His360, His365, His540, Asn544, Ile663, and the OH^- group. For pigALOX15-mini-LOX, the iron ligands are His250, His255, His430, His434, Ile552, and the OH^- group.

The protocol recommended by the AMBER package using the tLeap module was used to assemble the DHA/hALOX12 and DHA/pigALOX15-mini-LOX systems, solvate those complexes with an orthorhombic box of pre-equilibrated water molecules with a buffer of 10 Å and neutralize the total charge by adding sodium cations. The resulting systems contain around 80,000 atoms, of which about 10,600 belong to the protein, for the DHA/hALOX12 system, and 64,000 atoms, of which about 8800 belong to the protein, for the DHA/pigALOX15-mini-LOX. The rest of the atoms correspond to water molecules and salt ions.

The molecular dynamics (MD) simulations were run using either the AMBER20 (hALOX12) [57] or AMBER16 (pigALOX15-mini-LOX) [58] GPU (CUDA) version of the PMEMD package [59,60]. Initially, the systems were submitted to 110,000 energy minimization steps combining the steepest decent and conjugate gradient methods to remove close contacts. In the first 5000 steps, harmonic restraints were applied to the protein and substrate atoms with a force constant of 5.0 kcal mol^{-1} $Å^{-2}$ so that only the solvent and ions were relaxed. In the following 5000 steps, harmonic restraints were applied to the protein backbone with the same force constant as before. Finally, the whole system was kept free during the last 100,000 steps. Then, MD simulations using periodic boundary conditions and the particle-mesh Ewald approach to introduce long-range electrostatic effects were performed. The DHA/hALOX12 system was gently heated using six 20 ps steps, incrementing the temperature by 50 K each step (0–300 K) under constant volume.

For the DHA/pigALOX15-mini-LOX system, the temperature was increased by 10 steps of 30 K (0–300 K) during 20 ps each step. After heating, we calculated an MD trajectory of 1 ns within the NPT ensemble (300 K, 1 atm) to adjust the volume of the orthorhombic box and relax the density to a value of around 1 g cm^{-3}. During the heating and the compressing, harmonic restraints were applied to the protein backbone with a force constant of 5.0 kcal mol^{-1} $Å^{-2}$, whereas the rest of the system was kept free. The Langevin equilibration scheme [61] was used to control and equalize the temperature, while the pressure was adjusted by the Berendsen barostat [62]. Next, an equilibration stage of 10 ns at constant volume and temperature (300 K) was performed. Finally, we ran production MD trajectories of 250 ns and 100 ns for hALOX12 and pigALOX15-mini-LOX, respectively, within the same NVT ensemble. For each system, two MD replicas were calculated. A time step of 1 fs was used along the whole MD trajectories. Bonds involving hydrogen were constrained with the SHAKE algorithm [63]. The non-bonding interactions have been calculated with a cutoff of 9 Å.

The analysis of the MD trajectories was carried out with a Python package and RCBS.py [64]. Matplotlib was used for plotting [65].

3.4. QM/MM Calculations

The modular program package ChemShell 3.7 [66,67] was employed to carry out the QM/MM computations. TURBOMOLE 7.0 [68] was used for the DFT calculations and the DL_POLY 5.0 [69] module in ChemShell for the MM part.

The QM region was described by the B3LYP hybrid function [70]. The 6–31G(d) Pople basis set [71] was employed for the C, H, O, and N atoms, while the LANL2DZ basis set [72] was used for the Fe atom. The QM/MM partition is depicted in Figure 21. As for the hydrogen abstractions, the QM region was defined by all the atoms of the DHA substrate, which are found between C_6 and C_{17}; 11 atoms for each His residue of the iron coordination sphere (His360, His365, and His540 in hALOX12 and His250, His255 His430, and His434 in pigALOX15-mini-LOX); 8 atoms of the iron ligand Asn554 in hALOX12; and 3 atoms of the iron ligand Ile residue (Ile 663 in hALOX12 and Ile552 in pigALOX15-mini-LOX) and the Fe^{III}-OH^- cofactor. For oxygenations, the DHA carbon chain rotation, and the hydrogen retrodonation, this region was enlarged by an oxygen molecule. Seven link atoms were included to define the QM/MM boundary: five between the bonds Cα-QM atoms of the five residues in the iron coordination sphere and two bonded to the aliphatic carbon atoms of the lipid substrate (placed between C_5-C_6 and C_{17}-C_{18}). An electronic embedding scheme was employed to treat the interaction between the QM and MM subsystems. We also used the charge shift algorithm to minimize overpolarization effects. Cutoffs were not introduced to treat the nonbonding MM and QM/MM interactions [73].

The QM/MM optimizations have been carried out by employing the limited-memory Broyden–Fletcher–Goldfarb–Shanno (L-BFGS) algorithm [74] for energy minimizations and scans of reaction pathways. For these optimizations to minima, a microiterative scheme [75] was considered using hybrid delocalized coordinates (HDLC) [76]. As for the transition-state searches, the dimer method was used [77]. These algorithms are implemented in the DL_FIND geometry optimization library [78] of ChemShell.

For these QM/MM models, all water molecules outside a 17 Å radius volume centered on the ligand molecule were removed. The active region was defined by all residues and water molecules inside a 15 Å radius sphere centered on C_{12} of the ligand molecule. This region was allowed to move freely (≈2200 atoms), while the atoms left out were kept frozen during the optimization. Roughly 12,000 atoms were considered in the QM/MM calculations.

The images of structures were plotted with UCSF CHIMERA [79].

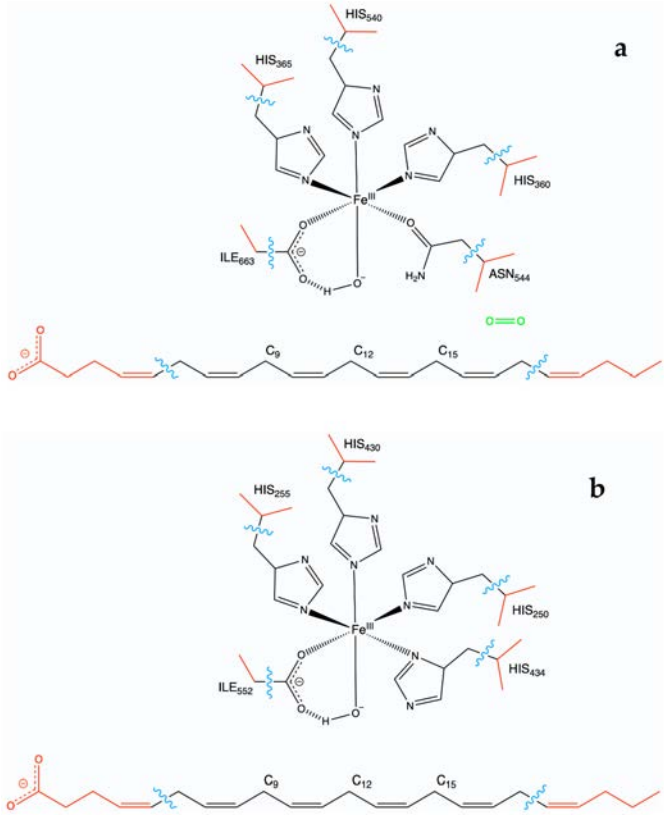

Figure 21. QM/MM partition in the DHA/hALOX12 (**a**) and DHA/pigALOX15-mini-LOX systems (**b**).

4. Conclusions

Human ALOX12 is a lipoxygenase that catalyzes the oxidation of the ω-3 fatty acid 4,7,10,13,16,19-docosahexaenoic acid (DHA), forming the hydroperoxides, 14S-H(p)DHA and 11S-H(p)DHA, as major and minor products, respectively. The biological relevance of the corresponding reduced oxylipins, 14S-hydroxydocosahexaenoic acid (14S-HDHA) and 11S-hydroxydocosahexaenoic acid (11S-HDHA), has been associated with the regulation of thrombus formation in vivo. PigALOX15 also catalyzes the conversion of DHA to 14S-H(p)DHA, but the minor product detected is 17S-H(p)DHA.

In this paper, we have carried out docking and molecular dynamics simulations, plus QM/MM calculations, to analyze the molecular details of the complete DHA hydroperoxidation mechanism in hALOX12. For the first time, the protein setup of hALOX12 has been modeled using the structure provided by the AlphaFold server. For pigALOX15, the same methodology has been used to calculate the energy barrier of the first step of the catalytic mechanism using the X-ray structure of an N-terminal truncation variant of pigALOX15.

The DHA peroxidation reaction is initiated by the H-abstraction of H_{12}, H_9, or H_{15} of DHA by the Fe (III)-OH^- cofactor. Next, an oxygen molecule inserts on C_{14}, C_{11}, or C_{17} following an antarafacial approach. Finally, there is a retro-hydrogen donation from the Fe (II)-H_2O cofactor to the peroxyl radical, leading to the corresponding hydroperoxides with S stereochemistry. The calculated QM/MM energy barriers for each mechanistic step confirm that the reaction process is viable in the hALOX12 active site. Interestingly, the stereochem-

istry (ZE) of the pentadienyl radicals from C_{10} to C_{14}, formed after H_{12pros} abstraction, is the one needed for leading to the fully characterized 14S-hydroperoxy-4Z,7Z,10Z,12E,16Z,19Z-docosahexaenoic acid because (ZE) in the pentadienyl radical becomes 10Z and 12E in 14S-H(p)DHA. Only with this stereochemistry can 14S-H(p)DHA be converted by ALOX12 to 7R,14S-dihydroxy-4Z,8E,10E,12Z,16Z,19Z-docosahexaenoic acid (MaR1). This fact is relevant because MaR1 is a potent SPM that actively participates in the inflammation-resolution phase of many diseases and has also been described as a novel antiplatelet agent.

In pigALOX15-mini-LOX, our calculations support that 14S-H(p)DHA can be formed, but the stereochemistry (ZZ) of the pentadienyl radicals from C_{10} to C_{14}, obtained after H_{12pros} abstraction, is not adequate for MaR1 formation.

This is an excellent example of how an enzyme governs the stereochemistry of the catalytic mechanism that leads to a given bioactive product (MaR1 in this case) and how this stereochemistry control might be species specific.

Supplementary Materials: The supporting information can be downloaded at: https://www.mdpi.com/article/10.3390/ijms24076064/s1.

Author Contributions: Conceptualization, À.G.-L. and J.M.L.; investigation, M.C.-N.; writing—original draft preparation, M.C.-N., À.G.-L. and J.M.L.; writing—review and editing, À.G.-L. and J.M.L.; funding acquisition, À.G.-L. and J.M.L. All authors have read and agreed to the published version of the manuscript.

Funding: This study was supported by a grant (PID2020-113764GB-I00) from the Spanish "Ministerio de Ciencia e Innovación". We also acknowledge CSUC for computational facilities.

Institutional Review Board Statement: Not applicable.

Informed Consent Statement: Not applicable.

Data Availability Statement: The data presented in this study are contained within the article.

Conflicts of Interest: The authors declare no conflict of interest.

References

1. Steinhilber, D. Lipoxygenases: An Introduction. In *Lipoxygenases in Inflammation*; Steinhilber, D., Ed.; Springer: Cham, Switzerland, 2016; pp. 1–6; ISBN 978-3-319-27764-6.
2. Serhan, C.N.; Chiang, N.; Van Dyke, T.E. Resolving Inflammation: Dual Anti-Inflammatory and pro-Resolution Lipid Mediators. *Nat. Rev. Immunol.* **2008**, *8*, 349–361. [CrossRef]
3. Serhan, C.N. Treating Inflammation and Infection in the 21st Century: New Hints from Decoding Resolution Mediators and Mechanisms. *FASEB J.* **2017**, *31*, 1273–1288. [CrossRef]
4. Hamberg, M.; Samuelsson, B. Prostaglandin Endoperoxides. Novel Transformations of Arachidonic Acid in Human Platelets. *Proc. Natl. Acad. Sci. USA* **1974**, *71*, 3400–3404. [CrossRef] [PubMed]
5. Ikei, K.N.; Yeung, J.; Apopa, P.L.; Ceja, J.; Vesci, J.; Holman, T.R.; Holinstat, M. Investigations of Human Platelet-Type 12-Lipoxygenase: Role of Lipoxygenase Products in Platelet Activation. *J. Lipid Res.* **2012**, *53*, 2546–2559. [CrossRef] [PubMed]
6. Ivanov, I.; Heydeck, D.; Hofheinz, K.; Roffeis, J.; O'Donnell, V.B.; Kuhn, H.; Walther, M. Molecular Enzymology of Lipoxygenases. *Arch. Biochem. Biophys.* **2010**, *503*, 161–174. [CrossRef] [PubMed]
7. Kulkarni, A.; Nadler, J.L.; Mirmira, R.G.; Casimiro, I. Regulation of Tissue Inflammation by 12-Lipoxygenases. *Biomolecules* **2021**, *11*, 717. [CrossRef]
8. Nugteren, D.H. Arachidonate Lipoxygenase in Blood Platelets. *Biochim. Biophys. Acta (BBA)/Lipids Lipid Metab.* **1975**, *380*, 299–307. [CrossRef]
9. Bürger, F.; Krieg, P.; Marks, F.; Fürstenberger, G. Positional- and Stereo-Selectivity of Fatty Acid Oxygenation Catalysed by Mouse (12S)-Lipoxygenase Isoenzymes. *Biochem. J.* **2000**, *348*, 329–335. [CrossRef]
10. Yu, J.Y.; Lee, J.J.; Jung, J.K.; Min, Y.K.; Ma, J.Y.; Kim, T.J.; Lee, M.Y.; Yun, Y.P. Anti-Platelet Activity of Diacetylated Obovatol through Regulating Cyclooxygenase and Lipoxygenase Activities. *Arch. Pharm. Res.* **2012**, *35*, 2191–2198. [CrossRef]
11. Katoh, A.; Ikeda, H.; Murohara, T.; Haramaki, N.; Ito, H.; Imaizumi, T. Platelet-Derived 12-Hydroxyeicosatetraenoic Acid Plays an Important Role in Mediating Canine Coronary Thrombosis by Regulating Platelet Glycoprotein IIb/IIIa Activation. *Circulation* **1998**, *98*, 2891–2898. [CrossRef]
12. Yoshimoto, T.; Takahashi, Y. Arachidonate 12-Lipoxygenases. *Prostaglandins Other Lipid Mediat.* **2002**, *68–69*, 245–262. [CrossRef]
13. Matsuda, S.; Murakami, J.; Yamamoto, Y.; Konishi, Y.; Yokoyama, C.; Yoshimoto, T.; Yamamoto, S.; Mimura, Y.; Okuma, M. Decreased Messenger RNA of Arachidonate 12-Lipoxygenase in Platelets of Patients with Myeloproliferative Disorders. *BBA-Mol. Basis Dis.* **1993**, *1180*, 243–249. [CrossRef] [PubMed]

14. Sekiya, F.; Takagi, J.; Sasaki, K.; Kawajiri, K.; Kobayashi, Y.; Sato, F.; Saito, Y. Feedback Regulation of Platelet Function by 12 S-Hydroxyeicosatetraenoic Acid: Inhibition of Arachidonic Acid Liberation from Phospholipids. *Biochim. Biophys. Acta (BBA)/Lipids Lipid Metab.* **1990**, *1044*, 165–168. [CrossRef]
15. Holm, A.C.B.S.; Grenegård, M.; Öllinger, K.; Lindström, E.G. Inhibition of 12-Lipoxygenase Reduces Platelet Activation and Prevents Their Mitogenic Function. *Platelets* **2014**, *25*, 111–117. [CrossRef]
16. Adili, R.; Tourdot, B.E.; Mast, K.; Yeung, J.; Freedman, J.C.; Green, A.; Luci, D.K.; Jadhav, A.; Simeonov, A.; Maloney, D.J.; et al. First Selective 12-LOX Inhibitor, ML355, Impairs Thrombus Formation and Vessel Occlusion in Vivo with Minimal Effects on Hemostasis. *Arterioscler. Thromb. Vasc. Biol.* **2017**, *37*, 1828–1839. [CrossRef] [PubMed]
17. Tsai, W.C.; Aleem, A.M.; Tena, J.; Rivera-Velazquez, M.; Brah, H.S.; Tripathi, S.; D'silva, M.; Nadler, J.L.; Kalyanaraman, C.; Jacobson, M.P.; et al. Docking and Mutagenesis Studies Lead to Improved Inhibitor Development of ML355 for Human Platelet 12-Lipoxygenase. *Bioorganic Med. Chem.* **2021**, *46*, 116347. [CrossRef]
18. Contursi, A.; Tacconelli, S.; Hofling, U.; Bruno, A.; Dovizio, M.; Ballerini, P.; Patrignani, P. Biology and Pharmacology of Platelet-Type 12-Lipoxygenase in Platelets, Cancer Cells, and Their Crosstalk. *Biochem. Pharmacol.* **2022**, *205*, 115252. [CrossRef]
19. Dobrian, A.D.; Lieb, D.C.; Cole, B.K.; Taylor-Fishwick, D.A.; Chakrabarti, S.K.; Nadler, J.L. Functional and Pathological Roles of the 12- and 15-Lipoxygenases. *Prog. Lipid Res.* **2011**, *50*, 115–131. [CrossRef]
20. Serhan, C.N.; Romano, M. Lipoxin Biosynthesis and Actions: Role of the Human Platelet LX-Synthase. *J. Lipid Mediat. Cell Signal.* **1995**, *12*, 293–306. [CrossRef]
21. Kutzner, L.; Goloshchapova, K.; Heydeck, D.; Stehling, S.; Kuhn, H.; Schebb, N.H. Mammalian ALOX15 Orthologs Exhibit Pronounced Dual Positional Specificity with Docosahexaenoic Acid. *Biochim. Biophys. Acta—Mol. Cell Biol. Lipids* **2017**, *1862*, 666–675. [CrossRef]
22. Aleem, A.M.; Tsai, W.C.; Tena, J.; Alvarez, G.; Deschamps, J.; Kalyanaraman, C.; Jacobson, M.P.; Holman, T. Probing the Electrostatic and Steric Requirements for Substrate Binding in Human Platelet-Type 12-Lipoxygenase. *Biochemistry* **2019**, *58*, 848–857. [CrossRef]
23. Freedman, C.; Tran, A.; Tourdot, B.E.; Kalyanaraman, C.; Perry, S.; Holinstat, M.; Jacobson, M.P.; Holman, T.R. Biosynthesis of the Maresin Intermediate, 13S,14S-Epoxy-DHA, by Human 15-Lipoxygenase and 12-Lipoxygenase and Its Regulation through Negative Allosteric Modulators. *Biochemistry* **2020**, *59*, 1832–1844. [CrossRef]
24. Saura, P.; Suardíaz, R.; Masgrau, L.; Lluch, J.M.; González-Lafont, À. Unraveling How Enzymes Can Use Bulky Residues to Drive Site-Selective c-h Activation: The Case of Mammalian Lipoxygenases Catalyzing Arachidonic Acid Oxidation. *ACS Catal.* **2014**, *4*, 4351–4363. [CrossRef]
25. Weinberg, D.R.; Gagliardi, C.J.; Hull, J.F.; Murphy, C.F.; Kent, C.A.; Westlake, B.C.; Paul, A.; Ess, D.H.; McCafferty, D.G.; Meyer, T.J. Proton-Coupled Electron Transfer. *Chem. Rev.* **2012**, *112*, 4016–4093. [CrossRef] [PubMed]
26. Perry, S.C.; Kalyanaraman, C.; Tourdot, B.E.; Conrad, W.S.; Akinkugbe, O.; Freedman, J.C.; Holinstat, M.; Jacobson, M.P.; Holman, T.R. 15-Lipoxygenase-1 Biosynthesis of 7S,14S-DiHDHA Implicates 15-Lipoxygenase-2 in Biosynthesis of Resolvin D5. *J. Lipid Res.* **2020**, *61*, 1087–1103. [CrossRef] [PubMed]
27. Yamaguchi, A.; Stanger, L.; Freedman, C.J.; Standley, M.; Hoang, T.; Adili, R.; Tsai, W.C.; van Hoorebeke, C.; Holman, T.R.; Holinstat, M. DHA 12-LOX-Derived Oxylipins Regulate Platelet Activation and Thrombus Formation through a PKA-Dependent Signaling Pathway. *J. Thromb. Haemost.* **2021**, *19*, 839–851. [CrossRef]
28. Dalli, J.; Zhu, M.; Vlasenko, N.A.; Deng, B.; Haeggström, J.Z.; Petasis, N.A.; Serhan, C.N. The Novel 13S,14S-Epoxy-Maresinis Converted by Human Macrophages to Maresin 1 (MaR1), Inhibits Leukotriene A4 Hydrolase (LTA4H), and Shifts Macrophage Phenotype. *FASEB J.* **2013**, *27*, 2573–2583. [CrossRef]
29. Tang, S.; Wan, M.; Huang, W.; Stanton, R.C.; Xu, Y. Maresins: Specialized Proresolving Lipid Mediators and Their Potential Role in Inflammatory-Related Diseases. *Mediat. Inflamm.* **2018**, *2018*, 2380319. [CrossRef]
30. Serhan, C.N.; Dalli, J.; Karamnov, S.; Choi, A.; Park, C.-K.; Xu, Z.-Z.; Ji, R.-R.; Zhu, M.; Petasis, N.A. Macrophage Proresolving Mediator Maresin 1 Stimulates Tissue Regeneration and Controls Pain. *FASEB J.* **2012**, *26*, 1755–1765. [CrossRef]
31. Vogel, R.; Jansen, C.; Roffeis, J.; Reddanna, P.; Forsell, P.; Claesson, H.E.; Kuhn, H.; Walther, M. Applicability of the Triad Concept for the Positional Specificity of Mammalian Lipoxygenases. *J. Biol. Chem.* **2010**, *285*, 5369–5376. [CrossRef]
32. Chen, X.-S.; Funk, C.D. Structure-function Properties of Human Platelet 12-lipoxygenase: Chimeric Enzyme and in Vitro Mutagenesis Studies. *FASEB J.* **1993**, *7*, 694–701. [CrossRef] [PubMed]
33. Neau, D.B.; Gilbert, N.C.; Bartlett, S.G.; Boeglin, W.; Brash, A.R.; Newcomer, M.E. The 1.85 Å Structure of an 8R-Lipoxygenase Suggests a General Model for Lipoxygenase Product Specificity. *Biochemistry* **2009**, *48*, 7906–7915. [CrossRef]
34. Neau, D.B.; Bender, G.; Boeglin, W.E.; Bartlett, S.G.; Brash, A.R.; Newcomer, M.E. Crystal Structure of a Lipoxygenase in Complex with Substrate: The Arachidonic Acid-Binding Site of 8R-Lipoxygenase. *J. Biol. Chem.* **2014**, *289*, 31905–31913. [CrossRef] [PubMed]
35. Newcomer, M.E.; Brash, A.R. The Structural Basis for Specificity in Lipoxygenase Catalysis. *Protein Sci.* **2015**, *24*, 298–309. [CrossRef] [PubMed]
36. Xu, S.; Mueser, T.C.; Marnett, L.J.; Funk, M.O. Crystal Structure of 12-Lipoxygenase Catalytic-Domain-Inhibitor Complex Identifies a Substrate-Binding Channel for Catalysis. *Structure* **2012**, *20*, 1490–1497. [CrossRef] [PubMed]
37. Yokoyama, C.; Shinjo, F.; Yoshimoto, T.; Yamamoto, S.; Oates, J.A.; Brash, A.R. Arachidonate 12-Lipoxygenase Purified from Porcine Leukocytes by Immunoaffinity Chromatography and Its Reactivity with Hydroperoxyeicosatetraenoic Acids. *J. Biol. Chem.* **1986**, *261*, 16714–16721. [CrossRef] [PubMed]

38. Ueda, N.; Hiroshima, A.; Natsui, K.; Shinjo, F.; Yoshimoto, T.; Yamamoto, S.; Ii, K.; Gerozissis, K.; Dray, F. Localization of Arachidonate 12-Lipoxygenase in Parenchymal Cells of Porcine Anterior Pituitary. *J. Biol. Chem.* **1990**, *265*, 2311–2316. [CrossRef]
39. Reddy, R.G.; Yoshimoto, T.; Yamamoto, S.; Marnett, L.J. Expression, Purification, and Characterization of Porcine Leukocyte 12-Lipoxygenase Produced in the Methylotrophic Yeast, Pichia Pastoris. *Biochem. Biophys. Res. Commun.* **1994**, *205*, 381–388. [CrossRef]
40. Suzuki, H.; Kishimoto, K.; Yoshimoto, T.; Yamamoto, S.; Kanai, F.; Ebina, Y.; Miyatake, A.; Tanabe, T. Site-Directed Mutagenesis Studies on the Iron-Binding Domain and the Determinant for the Substrate Oxygenation Site of Porcine Leukocyte Arachidonate 12-Lipoxygenase. *Biochim. Biophys. Acta (BBA)/Lipids Lipid Metab.* **1994**, *1210*, 308–316. [CrossRef]
41. Saura, P.; Kaganer, I.; Heydeck, D.; Lluch, J.M.; Kühn, H.; González-Lafont, À. Mutagenesis of Sequence Determinants of Truncated Porcine ALOX15 Induces Changes in the Reaction Specificity by Altering the Catalytic Mechanism of Initial Hydrogen Abstraction. *Chem.—Eur. J.* **2018**, *24*, 962–973. [CrossRef]
42. Jumper, J.; Evans, R.; Pritzel, A.; Green, T.; Figurnov, M.; Ronneberger, O.; Tunyasuvunakool, K.; Bates, R.; Žídek, A.; Potapenko, A.; et al. Highly Accurate Protein Structure Prediction with AlphaFold. *Nature* **2021**, *596*, 583–589. [CrossRef] [PubMed]
43. Varadi, M.; Anyango, S.; Deshpande, M.; Nair, S.; Natassia, C.; Yordanova, G.; Yuan, D.; Stroe, O.; Wood, G.; Laydon, A.; et al. AlphaFold Protein Structure Database: Massively Expanding the Structural Coverage of Protein-Sequence Space with High-Accuracy Models. *Nucleic Acids Res.* **2022**, *50*, D439–D444. [CrossRef]
44. Aleem, A.M.; Jankun, J.; Dignam, J.D.; Walther, M.; Kühn, H.; Svergun, D.I.; Skrzypczak-Jankun, E. Human Platelet 12-Lipoxygenase, New Findings about Its Activity, Membrane Binding and Low-Resolution Structure. *J. Mol. Biol.* **2008**, *376*, 193–209. [CrossRef] [PubMed]
45. Shang, W.; Ivanov, I.; Svergun, D.I.; Borbulevych, O.Y.; Aleem, A.M.; Stehling, S.; Jankun, J.; Kühn, H.; Skrzypczak-Jankun, E. Probing Dimerization and Structural Flexibility of Mammalian Lipoxygenases by Small-Angle X-Ray Scattering. *J. Mol. Biol.* **2011**, *409*, 654–668. [CrossRef] [PubMed]
46. Romero-Téllez, S.; Cruz, A.; Masgrau, L.; González-Lafont, À.; Lluch, J.M. Accounting for the Instantaneous Disorder in the Enzyme-Substrate Michaelis Complex to Calculate the Gibbs Free Energy Barrier of an Enzyme Reaction. *Phys. Chem. Chem. Phys.* **2021**, *23*, 13042–13054. [CrossRef]
47. Martínez-Rosell, G.; Giorgino, T.; De Fabritiis, G. PlayMolecule ProteinPrepare: A Web Application for Protein Preparation for Molecular Dynamics Simulations. *J. Chem. Inf. Model.* **2017**, *57*, 1511–1516. [CrossRef]
48. Jones, G.; Willett, P.; Glen, R.C.; Leach, A.R.; Taylor, R. Development and Validation of a Genetic Algorithm for Flexible Docking. *J. Mol. Biol.* **1997**, *267*, 727–748. [CrossRef]
49. Tian, C.; Kasavajhala, K.; Belfon, K.A.A.; Raguette, L.; Huang, H.; Migues, A.N.; Bickel, J.; Wang, Y.; Pincay, J.; Wu, Q.; et al. Ff19SB: Amino-Acid-Specific Protein Backbone Parameters Trained against Quantum Mechanics Energy Surfaces in Solution. *J. Chem. Theory Comput.* **2020**, *16*, 528–552. [CrossRef]
50. Izadi, S.; Anandakrishnan, R.; Onufriev, A.V. Building Water Models: A Different Approach. *J. Phys. Chem. Lett.* **2014**, *5*, 3863–3871. [CrossRef]
51. Maier, J.A.; Martinez, C.; Kasavajhala, K.; Wickstrom, L.; Hauser, K.E.; Simmerling, C. Ff14SB: Improving the Accuracy of Protein Side Chain and Backbone Parameters from Ff99SB. *J. Chem. Theory Comput.* **2015**, *11*, 3696–3713. [CrossRef]
52. Wang, J.; Wolf, R.M.; Caldwell, J.W.; Kollman, P.A.; Case, D.A. Development and Testing of a General Amber Force Field. *J. Comput. Chem.* **2004**, *25*, 1157–1174. [CrossRef]
53. Bayly, C.I.; Cieplak, P.; Cornell, W.D.; Kollman, P.A. A Well-Behaved Electrostatic Potential Based Method Using Charge Restraints for Deriving Atomic Charges: The RESP Model. *J. Phys. Chem.* **1993**, *97*, 10269–10280. [CrossRef]
54. Frisch, M.J.; Trucks, G.W.; Schlegel, H.B.; Scuseria, G.E.; Robb, M.A.; Cheeseman, J.R.; Scalmani, G.; Barone, V.; Petersson, G.A.; Nakatsuji, H.; et al. *Gaussian 16*; Gaussian, Inc.: Wallingford, CT, USA, 2016.
55. Li, P.; Merz, K.M. MCPB.Py: A Python Based Metal Center Parameter Builder. *J. Chem. Inf. Model.* **2016**, *56*, 599–604. [CrossRef]
56. Seminario, J.M. Calculation of Intramolecular Force Fields from Second-Derivative Tensors. *Int. J. Quantum Chem.* **1996**, *60*, 1271–1277. [CrossRef]
57. Case, D.A.; Ben-Shalom, I.Y.; Brozell, S.R.; Cerutti, D.S.; Cheatham, T.E., III; Cruzeiro, V.W.D.; Darden, T.A.; Duke, R.E.; Ghoreishi, D.; Gilson, M.K.; et al. *Amber 20*; University of California: San Francisco, CA, USA, 2020.
58. Case, D.A.; Betz, R.M.; Cerutti, D.S.; Cheatham III, T.E.; Darden, T.A.; Duke, R.E.; Giese, T.J.; Gohlke, H.; Goetz, A.W.; Homeyer, N.; et al. *Amber 16*; University of California: San Francisco, CA, USA, 2016.
59. Le Grand, S.; Götz, A.W.; Walker, R.C. SPFP: Speed without Compromise—A Mixed Precision Model for GPU Accelerated Molecular Dynamics Simulations. *Comput. Phys. Commun.* **2013**, *184*, 374–380. [CrossRef]
60. Salomon-Ferrer, R.; Götz, A.W.; Poole, D.; Le Grand, S.; Walker, R.C. Routine Microsecond Molecular Dynamics Simulations with AMBER on GPUs. 2. Explicit Solvent Particle Mesh Ewald. *J. Chem. Theory Comput.* **2013**, *9*, 3878–3888. [CrossRef] [PubMed]
61. Leach, A.R. *Molecular Modelling. Principles and Applications*, 2nd ed.; Pearson Education: London, UK, 2001; ISBN 978-0-582-38210-7.
62. Berendsen, H.J.C.; Postma, J.P.M.; Van Gunsteren, W.F.; Dinola, A.; Haak, J.R. Molecular Dynamics with Coupling to an External Bath. *J. Chem. Phys.* **1984**, *81*, 3684–3690. [CrossRef]
63. Ryckaert, J.P.; Ciccotti, G.; Berendsen, H.J.C. Numerical Integration of the Cartesian Equations of Motion of a System with Constraints: Molecular Dynamics of n-Alkanes. *J. Comput. Phys.* **1977**, *23*, 327–341. [CrossRef]

64. Canyelles-Niño, M. MolBioMedUAB/RCBS.Py: 0.2.0bis. GitHub: San Franciso, CA, USA, 2023. [CrossRef]
65. Hunter, J.D. Matplotlib: A 2D Graphics Environment. *Comput. Sci. Eng.* **2007**, *9*, 90–95. [CrossRef]
66. Sherwood, P.; De Vries, A.H.; Guest, M.F.; Schreckenbach, G.; Catlow, C.R.A.; French, S.A.; Sokol, A.A.; Bromley, S.T.; Thiel, W.; Turner, A.J.; et al. QUASI: A General Purpose Implementation of the QM/MM Approach and Its Application to Problems in Catalysis. *J. Mol. Struct. THEOCHEM* **2003**, *632*, 1–28. [CrossRef]
67. Metz, S.; Kästner, J.; Sokol, A.A.; Keal, T.W.; Sherwood, P. ChemShell-a Modular Software Package for QM/MM Simulations. *Wiley Interdiscip. Rev. Comput. Mol. Sci.* **2014**, *4*, 101–110. [CrossRef]
68. Ahlrichs, R.; Bär, M.; Häser, M.; Horn, H.; Kölmel, C. Electronic Structure Calculations on Workstation Computers: The Program System Turbomole. *Chem. Phys. Lett.* **1989**, *162*, 165–169. [CrossRef]
69. Smith, W.; Forester, T.R. DL_POLY_2.0: A General-Purpose Parallel Molecular Dynamics Simulation Package. *J. Mol. Graph.* **1996**, *14*, 136–141. [CrossRef]
70. Becke, A.D. Density-Functional Thermochemistry. III. The Role of Exact Exchange. *J. Chem. Phys.* **1993**, *98*, 5648–5652. [CrossRef]
71. Hariharan, P.C.; Pople, J.A. The Influence of Polarization Functions on Molecular Orbital Hydrogenation Energies. *Theor. Chim. Acta* **1973**, *28*, 213–222. [CrossRef]
72. Hay, P.J.; Wadt, W.R. Ab Initio Effective Core Potentials for Molecular Calculations. Potentials for the Transition Metal Atoms Sc to Hg. *J. Chem. Phys.* **1985**, *82*, 270–283. [CrossRef]
73. De Vries, A.H.; Sherwood, P.; Collins, S.J.; Rigby, A.M.; Rigutto, M.; Kramer, G.J. Zeolite Structure and Reactivity by Combined Quantum-Chemical-Classical Calculations. *J. Phys. Chem. B* **1999**, *103*, 6133–6141. [CrossRef]
74. Liu, D.C.; Nocedal, J. On the Limited Memory BFGS Method for Large Scale Optimization. *Math. Program.* **1989**, *45*, 503–528. [CrossRef]
75. Kästner, J.; Thiel, S.; Senn, H.M.; Sherwood, P.; Thiel, W. Exploiting QM/MM Capabilities in Geometry Optimization: A Microiterative Approach Using Electrostatic Embedding. *J. Chem. Theory Comput.* **2007**, *3*, 1064–1072. [CrossRef]
76. Billeter, S.R.; Turner, A.J.; Thiel, W. Linear Scaling Geometry Optimisation and Transition State Search in Hybrid Delocalised Internal Coordinates. *Phys. Chem. Chem. Phys.* **2000**, *2*, 2177–2186. [CrossRef]
77. Heyden, A.; Bell, A.T.; Keil, F.J. Efficient Methods for Finding Transition States in Chemical Reactions: Comparison of Improved Dimer Method and Partitioned Rational Function Optimization Method. *J. Chem. Phys.* **2005**, *123*, 224101. [CrossRef] [PubMed]
78. Kästner, J.; Carr, J.M.; Keal, T.W.; Thiel, W.; Wander, A.; Sherwood, P. DL-FIND: An Open-Source Geometry Optimizer for Atomistic Simulations. *J. Phys. Chem. A* **2009**, *113*, 11856–11865. [CrossRef] [PubMed]
79. Pettersen, E.F.; Goddard, T.D.; Huang, C.C.; Couch, G.S.; Greenblatt, D.M.; Meng, E.C.; Ferrin, T.E. UCSF Chimera—A Visualization System for Exploratory Research and Analysis. *J. Comput. Chem.* **2004**, *25*, 1605–1612. [CrossRef] [PubMed]

SI12.2 Supporting information

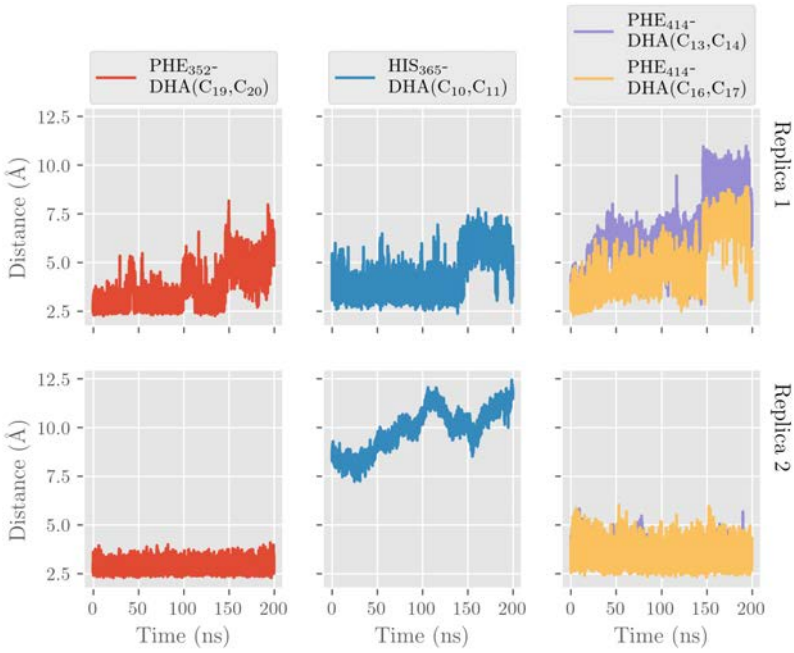

Figure SI12.1: Shortest distances between Δ^{10}, Δ^{13}, Δ^{16} and Δ^{19}, and close aromatic residue for each double bond versus time for replica 1 and 2.

Table SI12.1: Initial H-OH$^-$ distance of the QM/MM-optimised structure, potential energy barrier, and stereochemistry of the pentadienyl for the abstraction of hydrogens 12, 9 and 15 for the ten selected frames. *Distances are in* Å *and energies are in* kcal/mol. *Exponential average energy barriers [–ref 46 paper–] are included in the last row.*

	H_{12proS}			H_{12proR}			H_{9proS}			H_{9proR}			H_{15proS}			H_{15proR}		
Frame	d^r_H	$\Delta E^\ddagger$	**P.S.**	d^r_H	$\Delta E^\ddagger$	**P.S.**	d^r_H	$\Delta E^\ddagger$	**P.S.**	d^r_H	$\Delta E^\ddagger$	**P.S.**	d^r_H	$\Delta E^\ddagger$	**P.S.**	d^r_H	$\Delta E^\ddagger$	**P.S.**
322	3.5	15.9	ZE	3.5	27.3	ZZ	4.7	41.1	ZE	3.5	36.4	ZZ	6.0	34.9	ZZ	4.8	31.2	ZE
2253	5.4	20.5	ZE	4.4	29.7	ZZ	3.6	29.4	ZE	3.5	23.4	ZZ	7.5	34.4	ZE	5.8	42.8	ZZ
4986	5.4	19.3	ZE	4.9	34.6	ZZ	4.5	53.5	ZE	5.0	35.0	ZZ	7.9	31.7	ZE	6.1	43.1	ZE
6993	3.9	18.0	ZE	3.5	29.3	ZZ	4.1	39.1	ZE	3.1	29.7	ZZ	6.0	32.5	ZZ	4.7	43.4	ZZ
8721	5.0	21.9	ZE	4.3	28.8	ZZ	3.4	34.6	ZE	3.3	22.7	ZZ	7.4	39.6	ZE	5.6	51.4	ZZ
10106	5.5	24.3	ZE	4.3	28.5	ZZ	3.7	37.9	ZE	3.4	25.6	ZZ	6.9	36.6	ZE	5.3	43.2	ZE
12860	5.2	22.9	ZE	4.5	37.3	ZZ	4.1	40.3	ZE	3.9	29.2	ZZ	7.3	43.2	ZE	5.7	54.7	ZE
14423	4.1	21.8	ZE	3.7	29.4	ZZ	3.9	36.3	ZE	3.4	27.5	ZZ	6.3	51.2	ZZ	5.1	44.3	ZZ
18168	3.7	17.1	ZE	3.2	23.7	ZZ	4.5	38.5	ZE	3.3	31.8	ZZ	6.0	25.3	ZZ	4.9	31.8	ZE
19729	3.4	17.1	ZE	3.0	24.8	ZZ	5.3	46.7	ZE	3.9	43.7	ZZ	4.6	35.1	ZZ	5.4	21.9	ZZ
$\Delta E^\ddagger_{AV}$		17.1			25.0			30.7			23.9			26.7			23.2	

d^r_H stands for $d^{react}_{H-OH^-}$ –the initial distance between the H to be abstracted and the O of the cofactor–,
and P.S. stands for Pentadienyl Stereochemistry

Chapter SI14

Design of LTA_4H mutants for hydrolysis of eMaR1

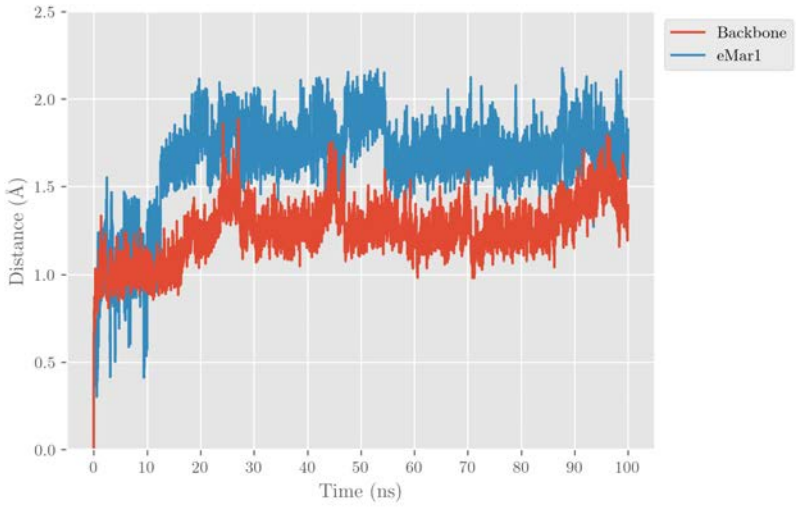

Figure SI14.1: RMSD of backbone and 13S,14S-eMaR1 along the MD trajectory for mutant 0 of LTA_4H

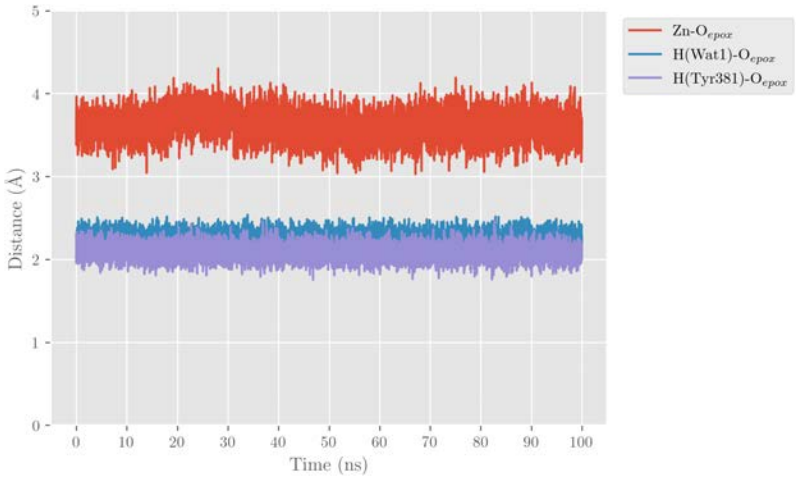

Figure SI14.2: Evolution of distances from eMaR1's epoxide to Zn, Tyr383 and Wat1 along the MD trajectory for mutant 0 of LTA_4H

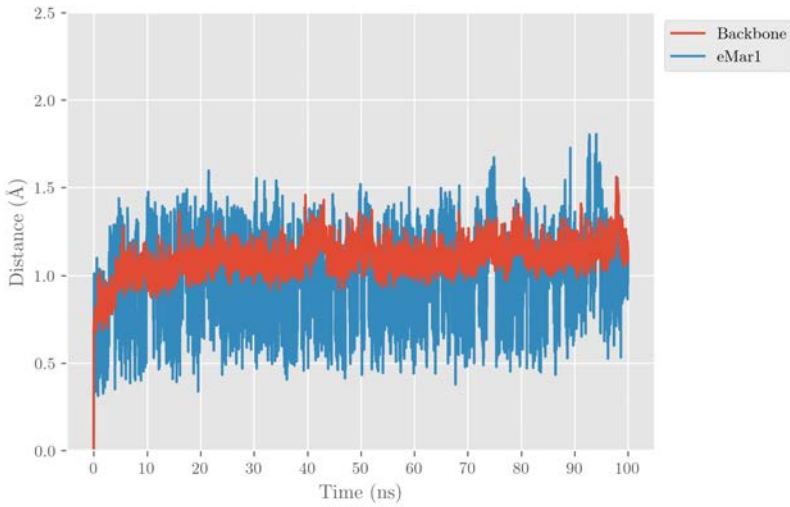

Figure SI14.3: RMSD of backbone and 13S,14S-eMaR1 along the MD trajectory for mutant 0 with set B of mutations of LTA_4H at the depth of the cavity

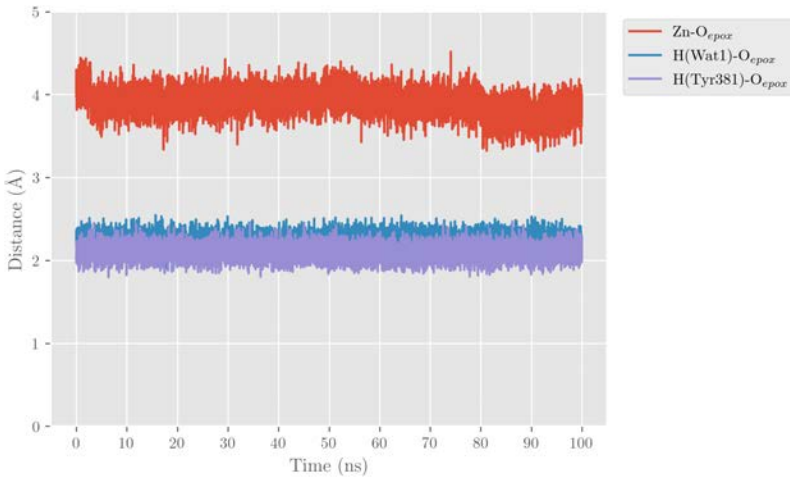

Figure SI14.4: Evolution of distances from eMaR1's epoxide to Zn, Tyr383 and Wat1 along the MD trajectory for 0 with set B of mutations of LTA_4H at the depth of the cavity

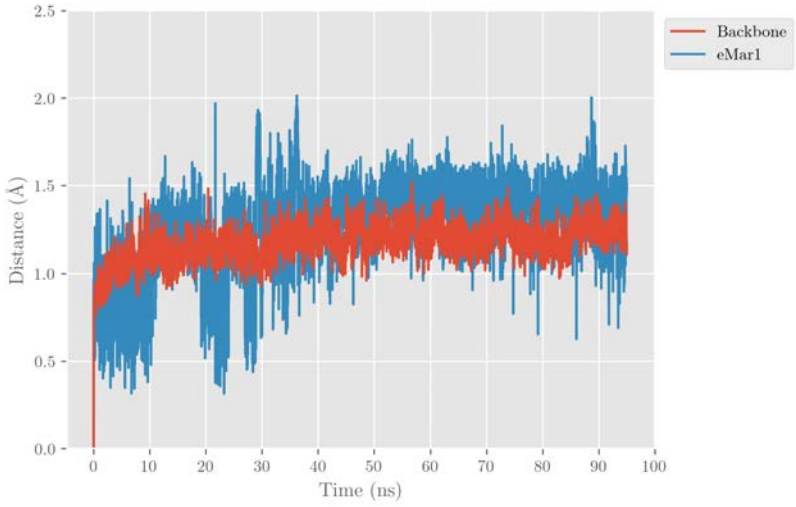

Figure SI14.5: RMSD of backbone and 13S,14S-eMaR1 along the MD trajectory for mutant 1 (or mutant 0 with set A of mutations) of LTA_4H

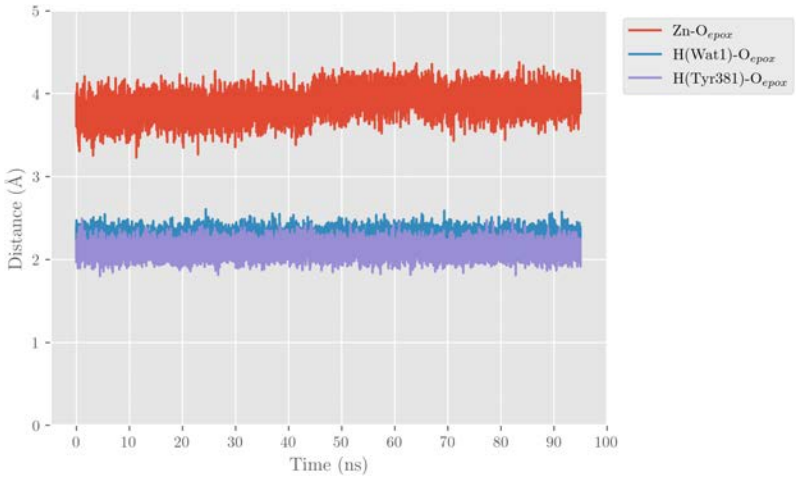

Figure SI14.6: Evolution of distances from eMaR1's epoxide to Zn, Tyr383 and Wat1 along the MD trajectory for mutant 1 (or mutant 0 with set A of mutations) of LTA_4H

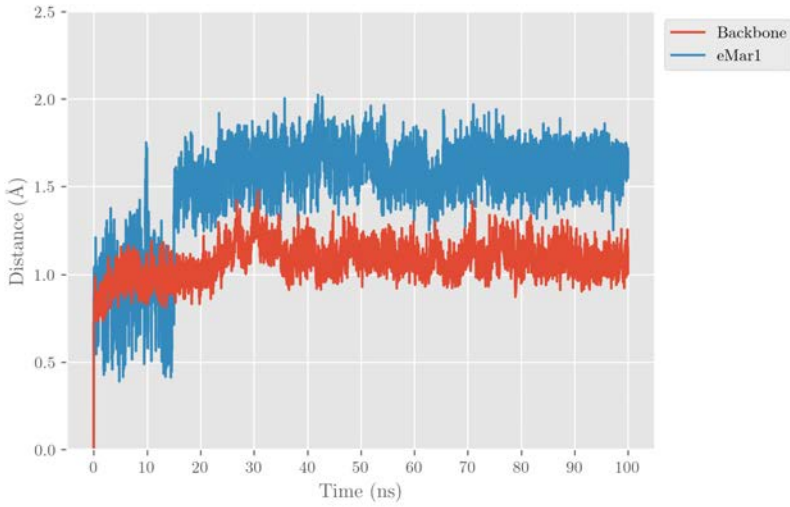

Figure SI14.7: RMSD of backbone and 13S,14S-eMaR1 along the MD trajectory for the mutant 2 of LTA_4H

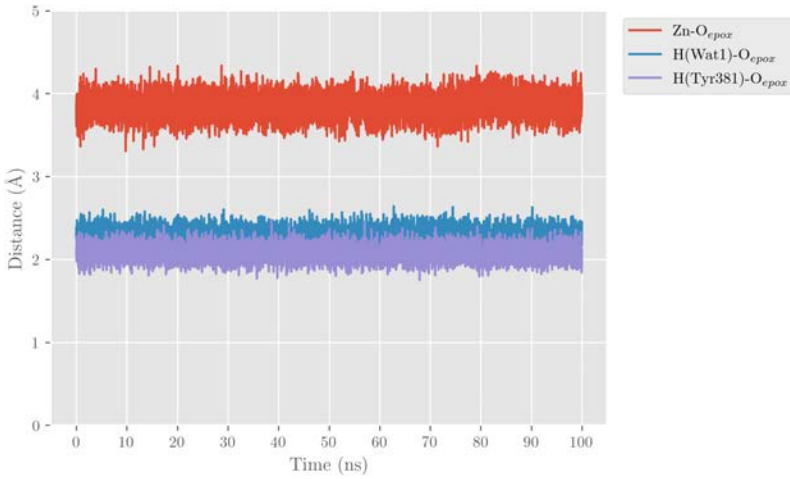

Figure SI14.8: Evolution of distances from eMaR1's epoxide to Zn, Tyr383 and Wat1 along the MD trajectory for the mutant 2 of LTA_4H

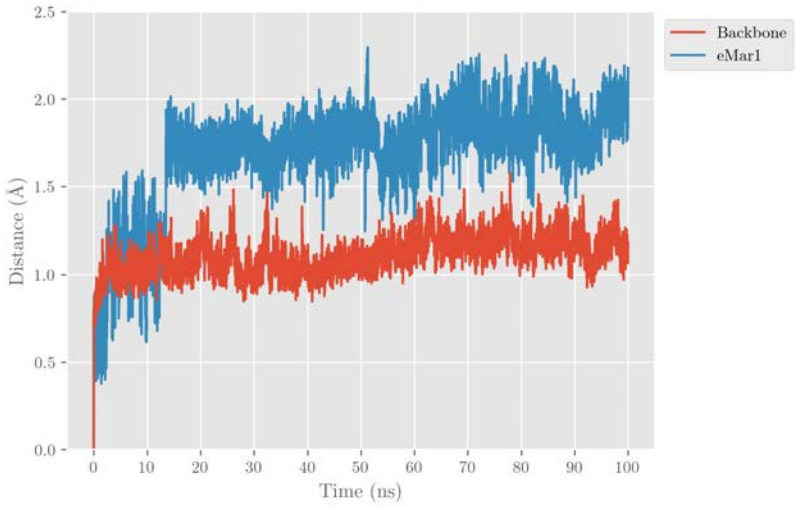

Figure SI14.9: RMSD of backbone and 13S,14S-eMaR1 along the MD trajectory for the mutant 3 of LTA_4H

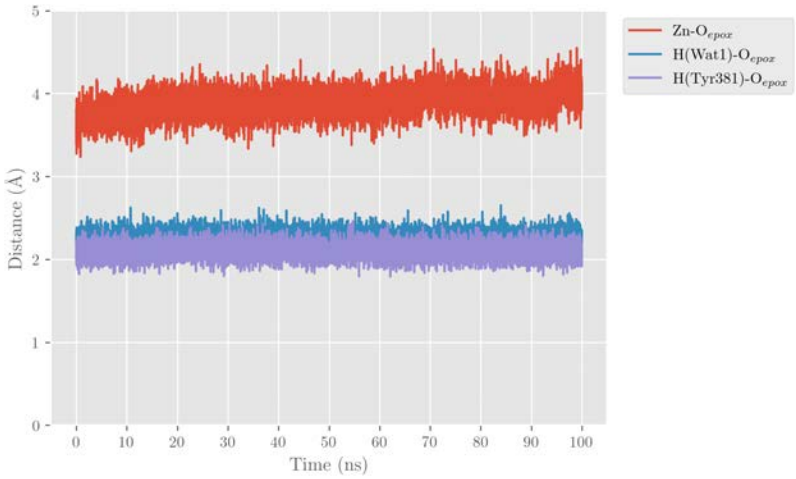

Figure SI14.10: Evolution of distances from eMaR1's epoxide to Zn, Tyr383 and Wat1 along the MD trajectory for the mutant 3 of LTA_4H

Chapter SI15

Experimental synthesis of MaR1 from DHA

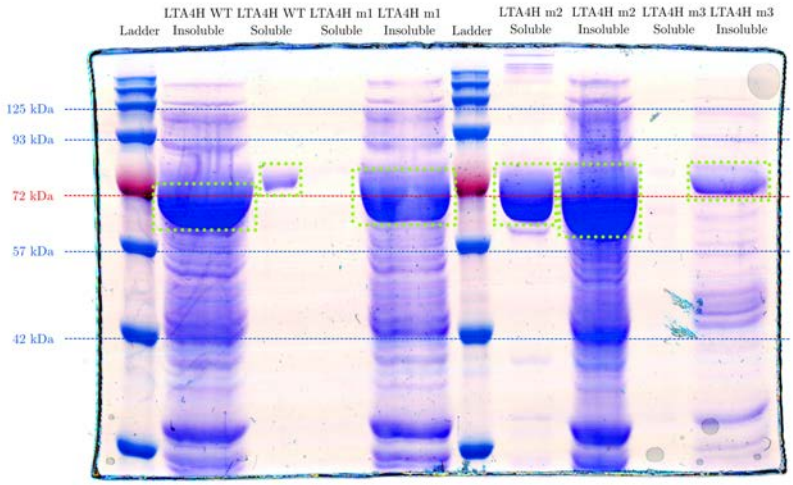

Figure SI15.1: Comassie-stained SDS-PAGE gel of expression of WT, mutant 1, 2 and 3 of LTA_4H in low IPTG concentration conditions. 24 h *of incubation time,* 0.25 mM *of IPTG,* 20 °C. 72 kDa *and* 57 kDa *weight marks are indicated with red and blue dashed lines, respectively. Bands corresponding to LTA_4H's are indicated with a purple square.*

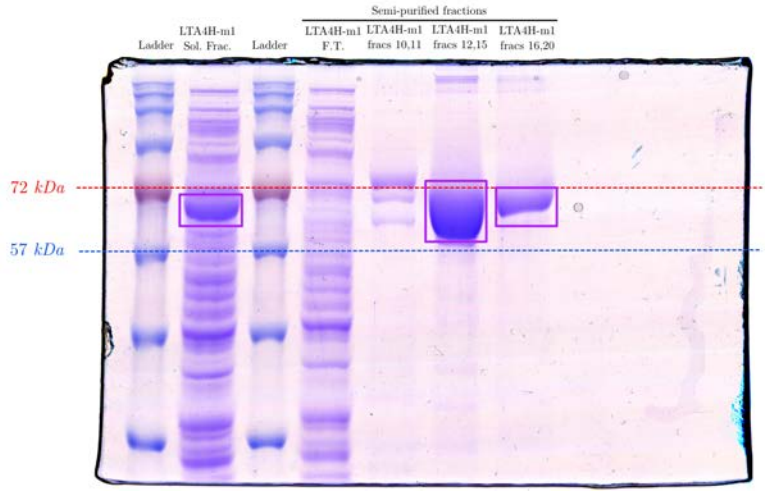

(a) Comassie stained SDS-PAGE

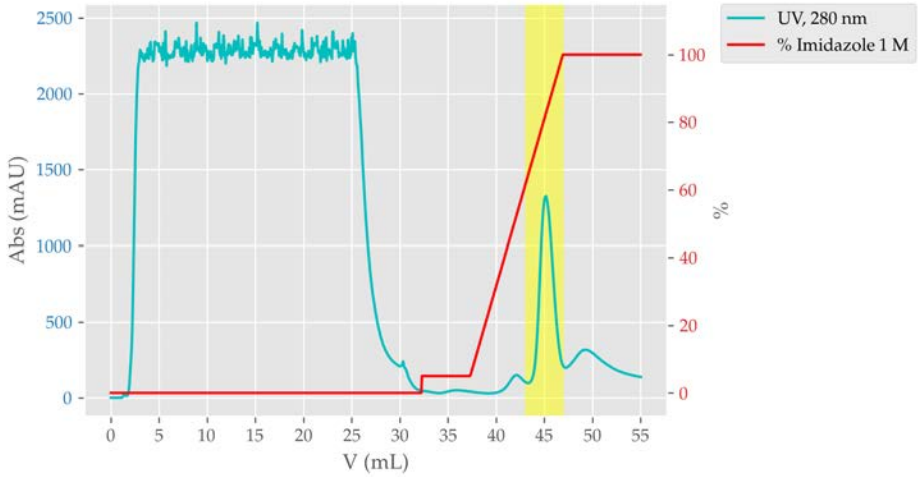

(b) UV measure and imidazole concentration along the FPLC purification

Figure SI15.2: FPLC purification of mutant 1 of LTA$_4$H. *FPLC purification of WT LTA$_4$H. For (a), 72 kDa and 57 kDa weight marks are indicated with red and blue dashed lines, respectively. Bands corresponding to LTA$_4$H's are indicated with a purple square. For (b), yellow region indicates the elution volume where the purified protein is detected.*

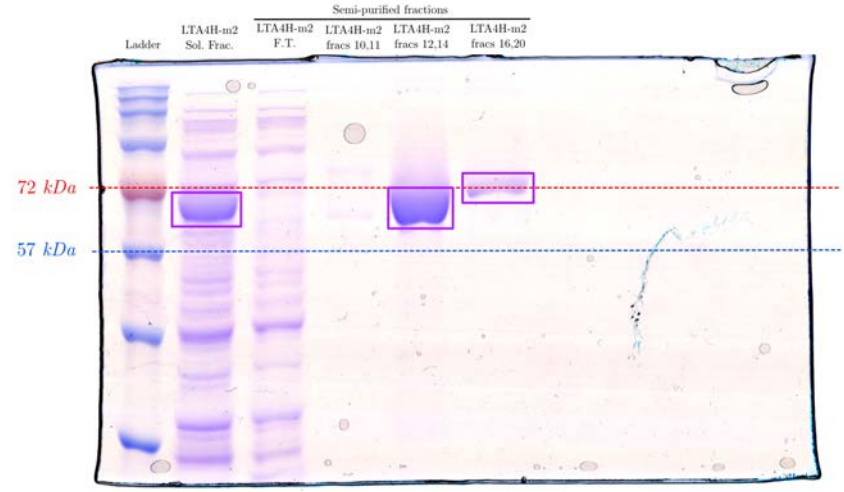

(a) Comassie stained SDS-PAGE

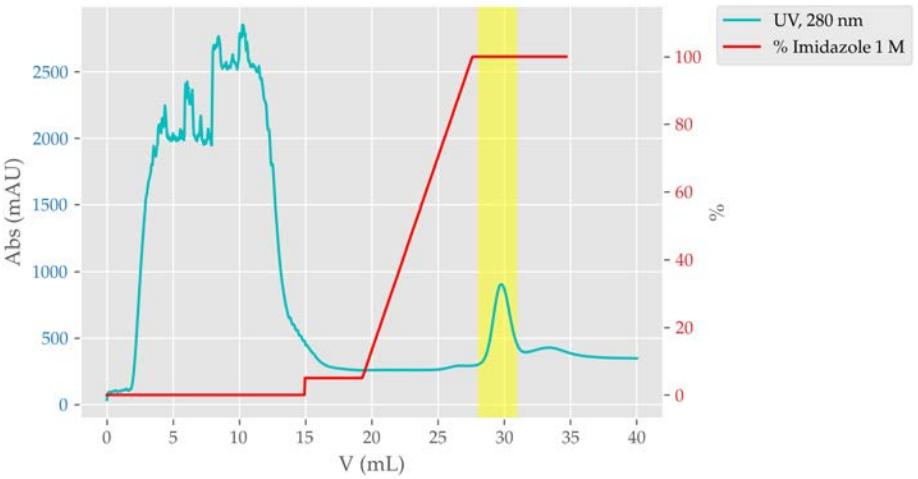

(b) UV measure and imidazole concentration along the FPLC purification

Figure SI15.3: FPLC purification of mutant 2 of LTA$_4$H. *FPLC purification of WT LTA$_4$H. For (a), 72 kDa and 57 kDa weight marks are indicated with red and blue dashed lines, respectively. Bands corresponding to LTA$_4$H's are indicated with a purple square. For (b), yellow region indicates the elution volume where the purified protein is detected.*

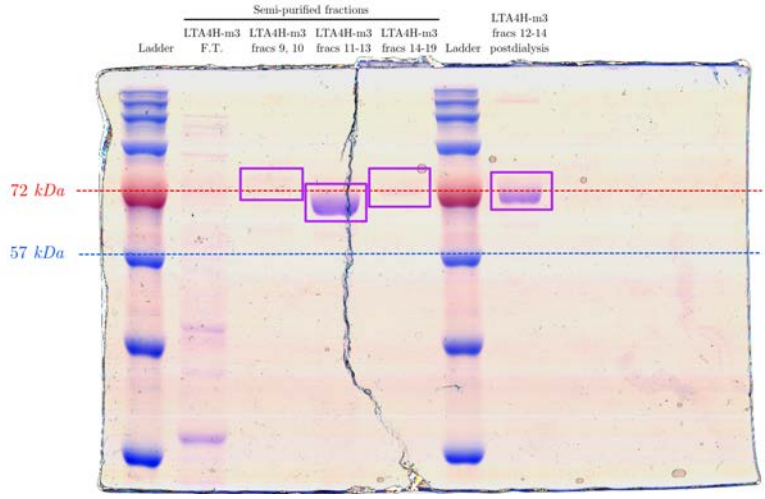

(a) Comassie stained SDS-PAGE

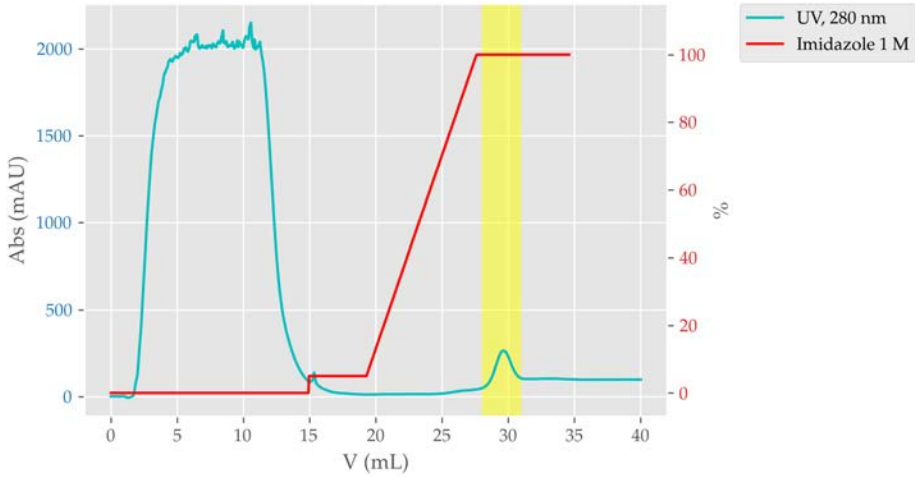

(b) UV measure and imidazole concentration along the FPLC purification

Figure SI15.4: FPLC purification of mutant 3 of LTA$_4$H. *FPLC purification of WT LTA$_4$H. For (a), 72 kDa and 57 kDa weight marks are indicated with red and blue dashed lines, respectively. Bands corresponding to LTA$_4$H's are indicated with a purple square. For (b), yellow region indicates the elution volume where the purified protein is detected.*

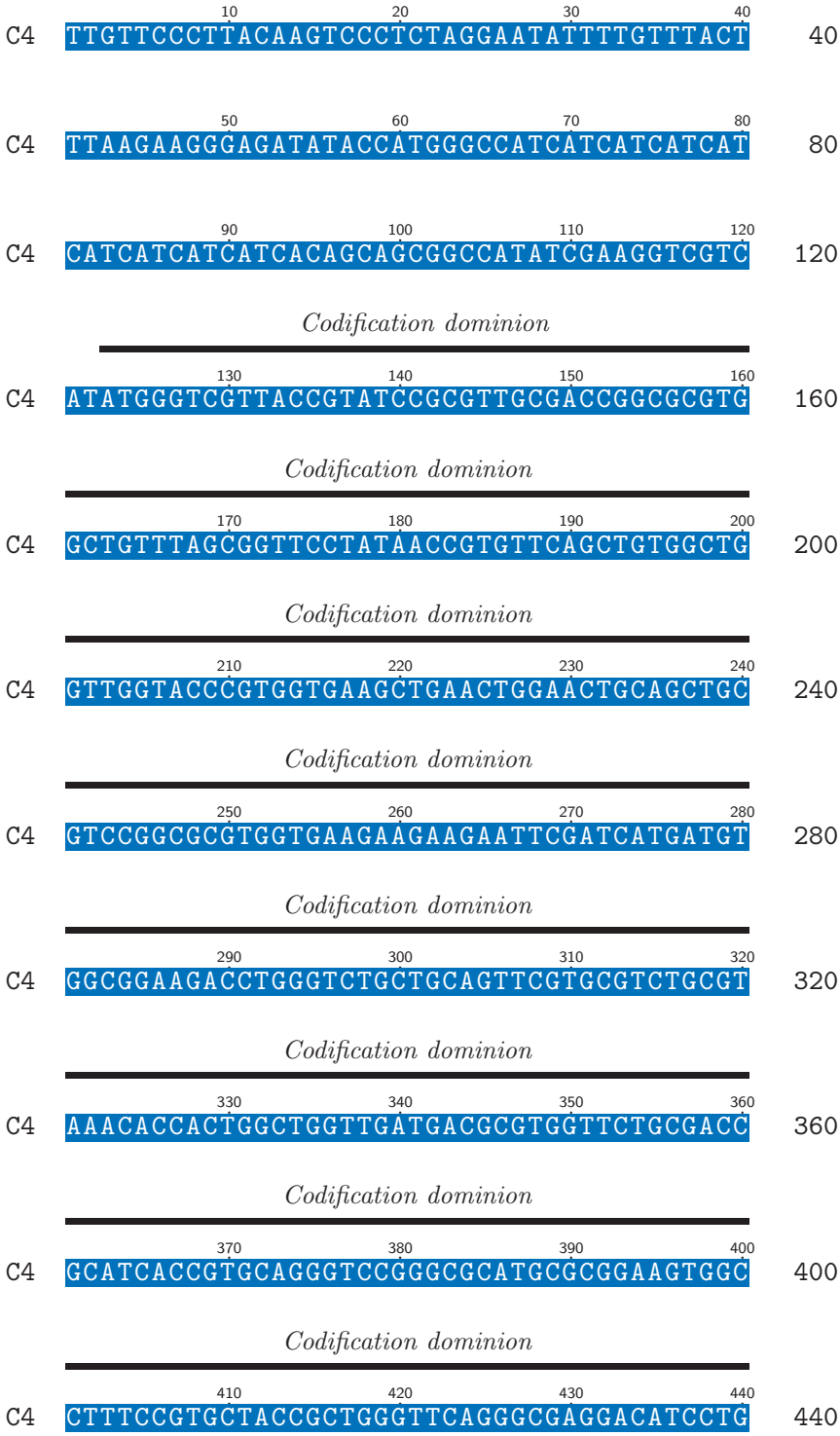
10 20 30 40
C4 TTGTTCCCTTACAAGTCCCTCTAGGAATATTTTGTTTACT 40
50 60 70 80
C4 TTAAGAAGGGAGATATACCATGGGCCATCATCATCATCAT 80
90 100 110 120
C4 CATCATCATCATCACAGCAGCGGCCATATCGAAGGTCGTC 120
Codification dominion
130 140 150 160
C4 ATATGGGTCGTTACCGTATCCGCGTTGCGACCGGCGCGTG 160
Codification dominion
170 180 190 200
C4 GCTGTTTAGCGGTTCCTATAACCGTGTTCAGCTGTGGCTG 200
Codification dominion
210 220 230 240
C4 GTTGGTACCCGTGGTGAAGCTGAACTGGAACTGCAGCTGC 240
Codification dominion
250 260 270 280
C4 GTCCGGCGCGTGGTGAAGAAGAAGAATTCGATCATGATGT 280
Codification dominion
290 300 310 320
C4 GGCGGAAGACCTGGGTCTGCTGCAGTTCGTGCGTCTGCGT 320
Codification dominion
330 340 350 360
C4 AAACACCACTGGCTGGTTGATGACGCGTGGTTCTGCGACC 360
Codification dominion
370 380 390 400
C4 GCATCACCGTGCAGGGTCCGGGCGCATGCGCGGAAGTGGC 400
Codification dominion
410 420 430 440
C4 CTTTCCGTGCTACCGCTGGGTTCAGGGCGAGGACATCCTG 440

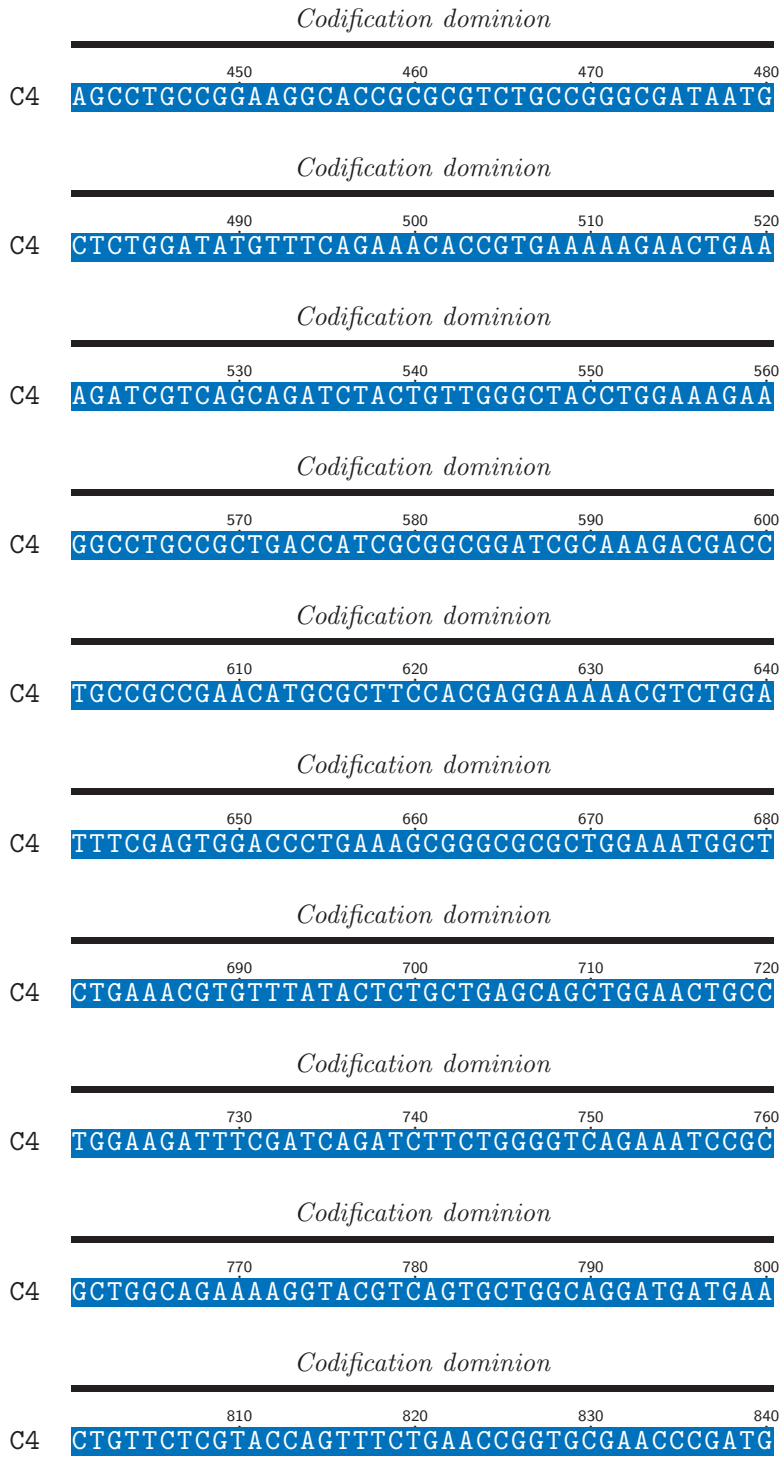
Codification dominion
450 460 470 480
C4 AGCCTGCCGGAAGGCACCGCGCGTCTGCCGGGCGATAATG 480
Codification dominion
490 500 510 520
C4 CTCTGGATATGTTTCAGAAACACCGTGAAAAAGAACTGAA 520
Codification dominion
530 540 550 560
C4 AGATCGTCAGCAGATCTACTGTTGGGCTACCTGGAAAGAA 560
Codification dominion
570 580 590 600
C4 GGCCTGCCGCTGACCATCGCGGCGGATCGCAAAGACGACC 600
Codification dominion
610 620 630 640
C4 TGCCGCCGAACATGCGCTTCCACGAGGAAAAACGTCTGGA 640
Codification dominion
650 660 670 680
C4 TTTCGAGTGGACCCTGAAAGCGGGCGCGCTGGAAATGGCT 680
Codification dominion
690 700 710 720
C4 CTGAAACGTGTTTATACTCTGCTGAGCAGCTGGAACTGCC 720
Codification dominion
730 740 750 760
C4 TGGAAGATTTCGATCAGATCTTCTGGGGTCAGAAATCCGC 760
Codification dominion
770 780 790 800
C4 GCTGGCAGAAAAGGTACGTCAGTGCTGGCAGGATGATGAA 800
Codification dominion
810 820 830 840
C4 CTGTTCTCGTACCAGTTTCTGAACCGGTGCGAACCCGATG 840

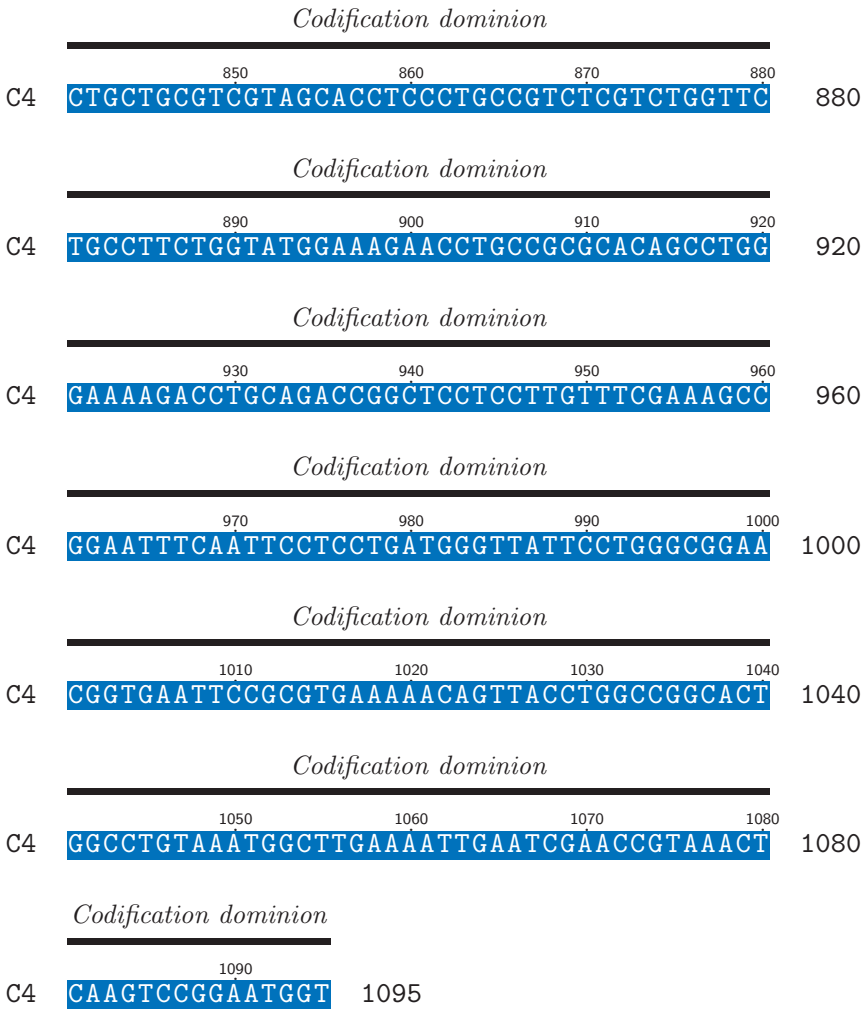

Figure SI15.4: Sequence from DNA sequencing of colony 4 of hum-ALOX12* E. coli *transformant cells

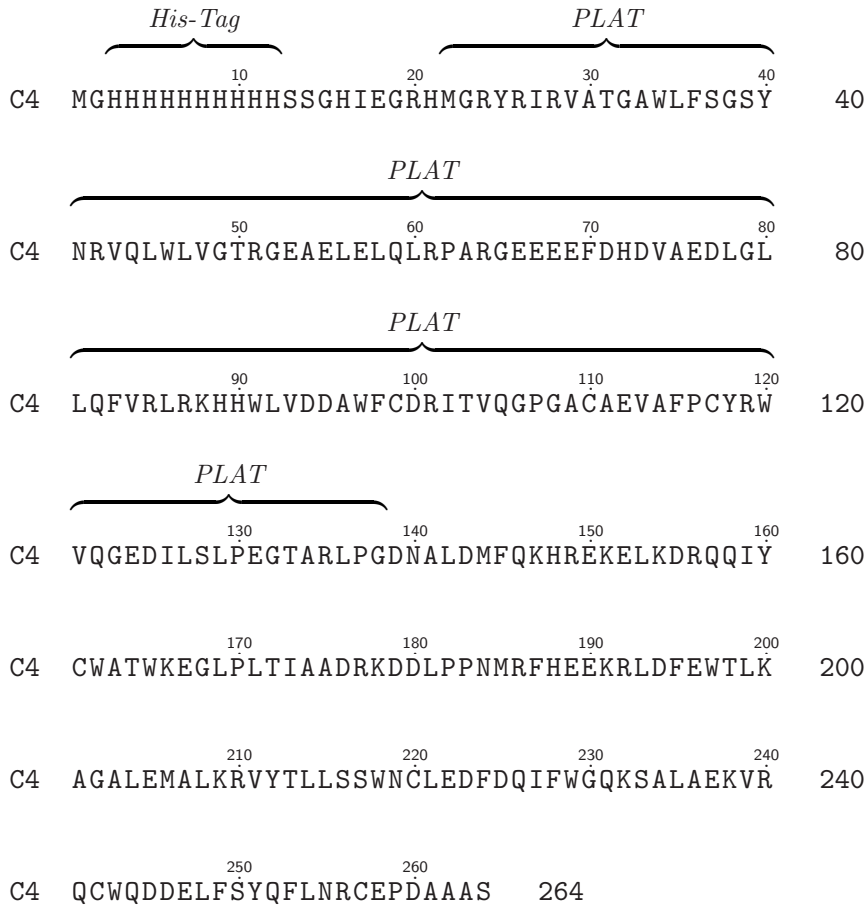

Figure SI15.5: Amino acidic sequence from DNA sequencing of colony 4 of humALOX12* E. coli *transformant cells

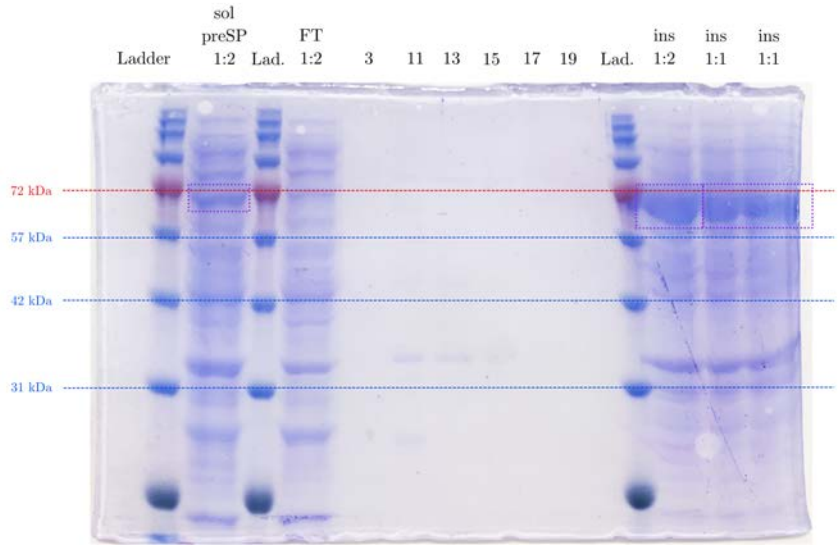

Figure SI15.6: Comassie-stained SDS-PAGE gel of humALOX12 from "BCZ" transformant's FPLC purification. *Red and blue, dashed lines indicate molecular weight marks. "sol" stands for soluble sample, "preSP" stands for pre-purification sample, "ins" stands for insoluble sample, and numbers corresponds to the fraction number of elution.*